DCT 262

Analysis of the Field Behavior of a Geosynthetic Reinforced Soil Integrated Bridge System During Construction and Operation

By

Christopher Meehan
Majid Talebi
Tyler Poggiogalle

December, 2016

Delaware Center for Transportation
University of Delaware
355 DuPont Hall
Newark, Delaware 19716
(302) 831-1446

The Delaware Center for Transportation is a university-wide multi-disciplinary research unit reporting to the Chair of the Department of Civil and Environmental Engineering, and is co-sponsored by the University of Delaware and the Delaware Department of Transportation.

DCT Staff

Christopher Meehan
Director

Jerome Lewis
Associate Director

Ellen Pletz
Business Administrator I

Earl "Rusty" Lee
T^2 Program Coordinator

Matheu Carter
T^2 Engineer

Sandra Wolfe
Event Coordinator

The research reported in this document was prepared through participation in an Agreement sponsored by the State of Delaware's Department of Transportation and the Federal Highway Administration. The views and conclusions contained in this document are those of the author(s) and should not be interpreted as presenting the official policies or position, either expressed or implied, of the State of Delaware's Department of Transportation or the U.S. Federal Government unless so designated by other authorized documents.

Delaware Center for Transportation
University of Delaware
Newark, DE 19716
(302) 831-1446

ACKNOWLEDGEMENTS

The findings presented in this report are based upon work supported by the Delaware Department of Transportation (DelDOT). The authors would like to acknowledge the suggestions and assistance of Mike Adams, Jennifer Nicks, Tom Stabile, and other members of the Federal Highway Administration's Turner-Fairbank Highway Research Center for their continued support throughout this research. The authors would also like to acknowledge student colleagues who have provided support for this project in various ways: Daniel Cacciola, Matthew Becker, Will Baker, Truxton Boyce, Marc Toussant, and Scott Forsythe.

TABLE OF CONTENTS

APPENDIX

LIST OF TABLES

LIST OF FIGURES

ABSTRACT

The Geosynthetic Reinforced Soil Integrated Bridge System (GRS-IBS) is a composite bridge structure built using GRS abutments and prefabricated bridge superstructure elements. This accelerated bridge construction technology has been developed and promoted by researchers and engineers from the United States of America's Federal Highway Administration (FHWA). GRS-IBS technology has proven itself useful for rapid, cost-effective bridge construction in other regions of the United States. Consequently, the Delaware Department of Transportation (DelDOT) constructed the first GRS-IBS in the state of Delaware (Br. 1-366) in 2013 to explore the effectiveness of this technology for use within their own bridge inventory.

This report provides an overview of the design, construction, and monitoring process that was utilized to deploy the first constructed GRS-IBS in Delaware. Recorded performance data for the structure from the time of construction, live load testing, and over three years of in-service operation were collected using different types of instruments and analyzed.

Details regarding GRS-IBS technology, Br. 1-366 project requirements, the design and construction procedure, and the instrumentation system that was utilized for monitoring the health of the structure have been presented in Chapters 1 through 3.

The collected engineering data from different phases of the project are presented in Chapter 4, including construction, live load testing, and over three years of in-service operation.

Since the amount of collected data was quite large, some techniques were utilized to manage and filter the recorded data, as described in Chapter 5. A technique for statistical correlation analysis is also presented in this chapter, which was found to be very useful for

developing an understanding of interrelationships between various sensor measured values. The correlation between different types of readings are investigated using this technique, and the corresponding findings from this analysis are presented in this chapter.

A strong effect of temperature on the measured strain readings was observed, as discussed in Chapter 5. Chapter 6 presents a correction procedure to account for the effects of temperature on the measured strain values. The use of this correction technique allows for significant refinement of the measured strain values within the GRS abutment.

The details and findings from a robust live load testing program are presented in Chapter 7. More specifically, the effect of the live load on the strain in the abutments and the pressure within and beneath the abutments have been investigated in this chapter. It is shown that the structure was quite stable during each of the live load test events, with the induced pressure and deformation by the live loads being quite low, and with little corresponding strain being measured within the GRS abutments.

The applied pressure distribution beneath the west GRS abutment foundation was investigated during construction and live load testing, as described in Chapter 8. It is shown that the pressure distribution is not uniform and the maximum pressure is measured beneath the facing wall. An approach is suggested in this chapter to predict the applied pressure induced by the abutment and the surcharge loads.

The long term performance of the structure is analyzed in Chapter 9 using the data collected by different sensors over three years of in-service operation. The data analysis shows the effect of the precipitation amount and type (rain and snow) on the abutment water content. The abutment performance that occurs as a result of changes in water content appears satisfactory. Creep deformation did occur in the abutment, but its overall magnitude was quite small over the

monitoring period, with the maximum strain being less than 0.5%. The lateral deflection and settlement of the facing walls was small, less than 12 mm. The concrete bridge deformation was also small, with the measured results being affected by the air temperature change. The abutment temperature distribution was different in hot and cold weather. The clay foundation beneath the abutment experienced some minor creep deformation. The results also indicated the effect of temperature on the measured foundation and abutment pressure.

Finally, the overall conclusions of this report are presented in Chapter 10 and some recommendations are made for future research.

Chapter 1

INTRODUCTION

According to Federal Highway Administration (FHWA) reports, there are approximately 600,000 bridges in the United States, and many of them have functional or structural deficiencies (e.g., FHWA 2011c). In most regions in the U.S., insufficient financial resources are available to allow for complete repair or replacement of these bridges (e.g., FHWA 2011a). Therefore, the use of more economical means of bridge construction has been of interest over the last few decades (e.g., Wu 1994). In the retaining wall community, development of Mechanically Stabilized Earth (MSE) and Geosynthetic Reinforced Soil (GRS) structures has allowed for significant cost savings, and concepts from these technologies can also be applied to bridge construction, to save costs and reduce construction time.

Although reinforced earth structures have been constructed for thousands of years using straw, tree branches, and plant material, MSE walls in their modern form first appeared in the 1960s, when the use of embedded steel reinforcing strips affixed to rigid facing elements was used for soil reinforcement (Berg et al. 2009). Later, in the 1980s, geosynthetic reinforcement was introduced into the reinforced soil industry, solving some of the problems that are present with corrosion of steel reinforcement strips in MSE structures (Berg et al. 2009). Later developments in reinforced earth

technology, particularly GRS construction techniques, would prove instrumental for some of FHWA's more recent advances in bridge construction.

Generally, the term GRS has been used in the literature to describe reinforced soil systems with geosynthetic reinforcement at any spacing, though varying definitions exist. According to the Federal Highway Administration (FHWA), however, GRS is a type of reinforced earth that is characterized by very close reinforcement spacing (i.e., about 0.2 m), much closer spacing than what is typically employed in traditional MSE structures (Adams et al. 2011). In GRS systems, the reinforcement does not just serve as a tensile inclusion to resist tensile forces (as it does with MSE systems that utilize larger spaced reinforcement); it also provides increased confinement, restrains dilation, and reduces lateral deformation (e.g., Adams et al. 2011). Over the last 30 years, more than 100,000 square facing feet of GRS retaining walls have been constructed in the U.S. (FHWA 2011a).

The Geosynthetic Reinforced Soil Integrated Bridge System (GRS-IBS) is a composite bridge structure built using GRS abutments and prefabricated bridge superstructure elements. GRS-IBS technology has been developed through on-going research at the FHWA (Adams et al. 2011). GRS-IBS structures have shown significant savings in both construction time and cost over conventional bridge structures (FHWA 2011a). They also typically exhibit fewer construction difficulties and easier maintenance over the life cycle of the structure than conventional bridges, and can be constructed in variable weather conditions. GRS-IBS technology has historically performed well under a variety of static and dynamic loading conditions if designed and

constructed properly (e.g., Helwany et al. 2007, 2012; Adams et al. 2011; Tatsuoka et al. 2013). By the end of 2012, more than 100 GRS-IBS structures had been designed or constructed in the U.S. in more than 20 states (FHWA 2011b). This number had increased significantly to 150 GRS-IBS structures in more than 35 states by mid 2014 (Talebi et al. 2014), which shows the increasing popularity of this new technology, and which is also a product of its promotion through FHWA's "Every Day Counts" initiative.

Figure 1.1 shows a schematic of the critical elements of a GRS-IBS (Adams et al. 2011).

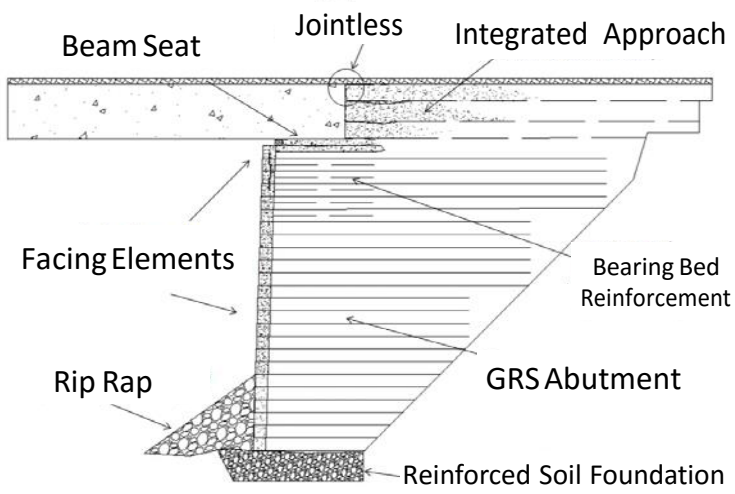

Figure 1.1 Typical cross-section for a GRS-IBS structure (modified after Adams et al. 2011)

The particularly innovative component of this integrated system is the GRS abutment, which is constructed by compacting soil and geosynthetic reinforcement in a

series of thin alternating layers. Facing elements at the front of the GRS abutment are frictionally connected to the geosynthetic (i.e., no pins or other connection elements are used for the geosynthetic, as is common in MSE structures). A variety of facing element types can be used; to date, concrete masonry unit (CMU) blocks have been the most common for GRS-IBS deployments (Adams et al. 2011). Due to the close spacing of the reinforcement, the facing elements are not required to hold back as much soil as typical MSE facing elements, and stress arching between soil reinforcement layers can play a more significant role. Consequently, pinned connections are not necessary for the facing blocks, in contrast with most typical MSE structures. For good to intermediate foundation conditions, the base of the reinforced soil zone is typically supported using a reinforced soil foundation (RSF), which is created by encapsulating a series of compacted soil layers with geosynthetic.

If the GRS-IBS passes over a waterway, rip rap scour protection is placed in front of the wall facing blocks at the base of the abutment, to prevent soil erosion and undermining of the GRS-IBS.

The resulting composite soil/geosynthetic mass has significant compressive and tensile strength, and is strong enough to directly support the dead loads and live loads that are applied by the bridge superstructure. A variety of steel, concrete, or composite superstructures can be used for the bridge span itself; for shorter span bridges like the one that is described in this report, a concrete box beam superstructure has proven to be fairly popular, for both cost and ease of construction reasons (e.g., Russell 2011). If a concrete box beam configuration is used, it is common practice to support

the bridge beams on a beam seat that is built directly into the GRS abutment. Beneath the beam seat area, additional bearing bed reinforcement is used to help with load shedding from the bridge loads, by helping to serve as an embedded footing in the reinforced soil mass (Adams et al. 2011). The bearing bed reinforcement spacing directly underneath the beam seat should be, at a minimum, half the primary spacing (Adams et al. 2011). In this configuration, an integrated approach reinforced backfill zone is used on either end of the bridge beams, in conjunction with a jointless continuous pavement interface.

Since GRS-IBS technology has proven useful for rapid, cost-effective bridge construction in other regions of the United States, the Delaware Department of Transportation (DelDOT) decided to explore the effectiveness of this technology for use within their own bridge inventory. As a first step in this process, DelDOT constructed a new GRS-IBS (Br. 1-366) in 2013 in New Castle County, on Chesapeake City Road over Guthrie Run (Figure 1.2) to replace a bridge that had reached the end of its usable service life. This construction project represents the first use of GRS-IBS technology in the state of Delaware.

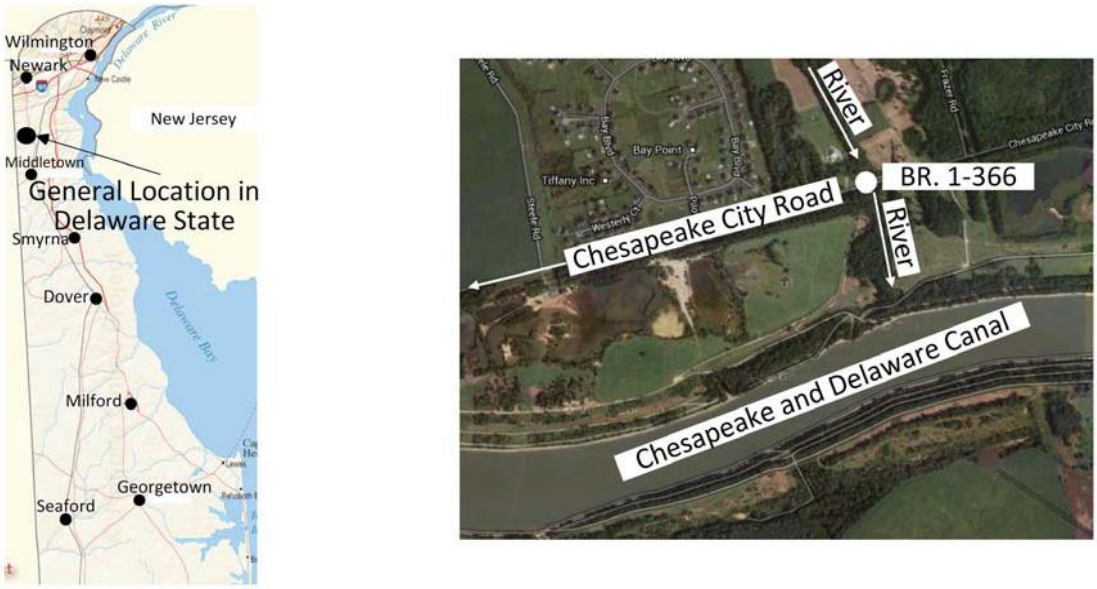

Figure 1.2 GRS-IBS project location in Delaware

As the project owner, DelDOT managed the associated design and construction processes for this GRS-IBS project. The University of Delaware (UD) and the authors of this report worked closely with DelDOT during this process to provide technical guidance through design assistance and construction inspection. UD personnel also designed an innovative system of sensors that was used to monitor the performance of the structure over an extended period.

This report provides an overview of the design, construction, and monitoring process that was performed for this GRS-IBS project. Short-term data recorded during the construction process and from a load test immediately following construction are presented. Long-term monitoring data was collected over the course of three years to assess the performance of the structure over an extended period of time beyond project completion, i.e. under "in service" load

conditions, is also presented. The overall objective of this research is to evaluate the performance of the designed GRS-IBS structure during construction and operation. Particular focus is given to field observations and other findings that can be used to improve existing GRS-IBS design, construction, and/or monitoring processes. In particular, there were six main objectives:

- Design and construction of the abutments of the first GRS-IBS structure in Delaware.
- Evaluation of the performance of the structure during construction and load testing.
- Examination of relationships between various sensor-measured values over time for the constructed GRS-IBS.
- Assessment of the effect of temperature on the data collected by the sensors, specifically the effect on strain gauges and pressure cells.
- Evaluation of the applied pressure distribution beneath the foundation during construction and after surcharge application.
- Investigation of the performance of the structure over three years of operation post-construction.

REFERENCES

Adams, M., Nicks, J., Stabile, T., Wu, J., Schelatter, W. and Hartmann, J., (2011). "Geosynthetic Reinforced Soil Integrated Bridge System Interim Implementation Guide", Publication No. FHWA-HRT-11-026, Federal Highway Administration, Washington, DC.

Berg, R. Christopher, B. and Samtani, N. (2009). "Design and Construction of Mechanically Stabilized Earth Walls and Reinforced Soil Slopes", Publication No. FHWA-NHI-10-024, Federal Highway Administration, Washington, DC

FHWA, (2011a). "Geosynthetic Reinforced Soil Integrated Bridge System (GRSIBS)". EDC1 Regional Summits, www.fhwa.dot.gov/everydaycounts/pdfs/summits/GRSIBS_full_presentation.pdf

FHWA, (2011b). "Semi-Annual Project Delivery Report". www.fhwa.dot.gov/wadiv/preports/semiannual_ix.pdf

FHWA (2011c). "Bridge guide", Publication No. FHWA-HIF-11-042, Federal Highway Administration, Washington, DC.

Helwany, S., Wu, J. and Kitsabunnarat, A. (2007), "Simulating the Behavior of GRS Bridge Abutments." Journal of Geotechnical and Geoenvironmental Engineering, 133 (10): 1229-1240.

Russell, H., (2011). "Adjacent Precast Concrete Box-Beam Bridges: State of the Practice." Precast/Prestressed Concrete Institute Journal, 56 (1): 75-91.

Tatsuoka, F., Tateyama, M., Koda, M. and Koseki, J. (2013). "Seismic Design, Construction and Performance of Geosynthetic-Reinforced Soil Retaining Walls and Bridge Abutments for Railways in Japan." Proceeding of the 2013 Geo-Congress, San Diego, CA, 1143-1157.

Talebi, M., Meehan, C., Cacciola, D. and Becker, M. (2014). "Rapid Replacement." Journal of Civil Engineering, ASCE, April 2014, 64-69 and 81.

Wu, J. (1994). "Design and construction of low cost retaining walls: The next generation in technology." CTI-UCD-1-94, Colorado Transportation Institute, Denver

Chapter 2

LITERATURE REVIEW

The objective of this chapter is to summarize and synthesize the observations, ideas, and viewpoints that have been presented by previous researchers on the behavior of GRS structures and their performance.

In order to improve the performance and stability of compacted fills, the application of Geosynthetic-Reinforced Soil (GRS) has seen increasing usage over the last few decades, in the construction of many types of earth structures, including retaining walls, bridge abutments, embankments, slopes, and shallow foundations. Historically, the first GRS wall was built in 1970, near Poitiers, France (Allen et al. 2002). Geosynthetic-reinforced walls have been in use in the United States since 1974 (Allen et al. 2002). Allen and Holtz (1991) and Berg et al. (1998) described the history of geosynthetic wall design in North America.

GRS walls typically exhibit some differences in behavior relative to other reinforced earth technologies, such as Mechanically Stabilized Earth (MSE) walls. In particular, GRS walls and bridge abutments are often more ductile and consequently more tolerant to differential settlement, they can be more adaptable to low quality backfill materials, for some projects can be easier to construct, and for some applications

can be more economical (e.g., Wu 1994; Bathurst et al. 1997, Abu-Hejleh et al. 2002; Adams et al. 2011; Nicks et al. 2013).

The behavior of GRS structures has been examined by a number of researchers through the use of case history assessment, scale model testing, and numerical simulation. Ten laboratory tests were conducted by Tatsuoka et al. (1989) on small scale GRS retaining walls using five different types of facing having varying rigidities. Tatsuoka (1993) also evaluated the effect of facing rigidity on the performance of GRS retaining walls using lab and field tests. Test results clearly showed the effect of facing rigidity on GRS behavior, for both deformation (i.e., service limit state) and stability (i.e., ultimate limit state) conditions. For GRS structures with higher facing rigidity, it was determined that higher earth pressure is applied to the facing wall, which results in an increase in confinement and stability of the wall. Wu (1994) summarized the various types of facing elements used for GRS and other reinforced walls ranging from rigid to flexible facing elements. Helwany et al. (1996) investigated the effects of facing rigidity and reinforcement length on the performance of GRS walls using numerical analysis, full scale tests, and four real cases. From this study, it was shown that numerical modeling can accurately predict the behavior of GRS walls under service load conditions. In addition, Helwany et al. (1996) observed that continuous facing panels generally exhibited more favorable performance than discreet facing panels, as the required length of reinforcement can be shorter and the associated displacement can be smaller for GRS walls with continuous facing. Allen et al. (2002) discussed a summary of 20 GRS wall case histories which covered a wide variety of

wall heights, surcharge conditions, foundation conditions, facing types and batter, reinforcement types and stiffness, and reinforcement spacing. Based on their studies, Allen et al. (2002) stated that the current design criteria at the time (AASHTO 2002) was very conservative and suggested that the approach used to design geosynthetic walls against internal reinforcement rupture be reevaluated. Lee and Wu (2004) synthesized the measured behavior and experiences gained from 10 case histories of flexible facing GRS bridge-supporting structures from around the world (including four in-service GRS bridge abutments and six full-scale field experiments). Their study illustrated the effects of facing wall rigidity, reinforcement spacing, backfill strength, fill placement density, and reinforcement length and type on the short- and long-term performance of GRS structures. Generally, flexible facing was shown to exhibit satisfactory performance (Lee and Wu 2004). The overall quality of the granular backfill and the reinforcement spacing were shown to have a significant effect on the load carrying capacity of the GRS abutment, on the maximum settlement beneath the bridge, the lateral displacement of the GRS abutment, and on the associated creep behavior of the system (Lee and Wu 2004).

Benjamin et al. (2007) studied the performance of eight prototype GRS structures. Different types of field instruments were utilized for this purpose, including surveying to evaluate face displacements, magnetic extensometers to evaluate vertical settlements, and tell-tales to monitor horizontal displacements within the reinforcements as well as on the wall facing. For the structures that were examined, the horizontal extensometers generally showed that the lateral displacement of the wall face had its

maximum value at the mid-height of the wall. In addition, there was generally an increase in lateral displacement with time for the GRS walls, which was attributed to precipitation events that had occurred during the summer season in Brazil. Larger displacements were measured by surveying points installed on the walls, as compared to those measured by the extensometers; this difference was attributed to soil particle rearrangement at the flexible facing. The largest horizontal strain observed for the walls was less than 1 percent during construction, which increased to 1.3 percent over time after construction had been completed. The location of largest strain was consistent with the development of a potential failure surface. There was generally good agreement between the maximum reinforcement tension that was predicted using the *K*-stiffness method (Bathurst et al. 2005) and what was measured in the field (Benjamin et al. 2007).

Hatami and Bathurst (2005, 2006) used the results from four full load tests on GRS walls to verify predicted behavior using numerical modeling. Results for two GRS walls with stiff modular block facing and with a very flexible wrapped-face were reported by Bathurst et al. (2006, 2007). The flexible-face wall had higher deformations and reinforcement load levels, which indicated that the facing wall played a structural role in carrying the applied earth loads. Wu (2007) evaluated the behavior of a couple of field cases to investigate the lateral earth pressure acting on the facing wall. It was concluded that the lateral earth pressure on the facing of a segmental GRS wall does not follow either the Rankine or Coulomb earth pressure theories. In reality, the magnitude of earth pressure is much smaller than what is calculated by these methods, and its value depends on the reinforcement spacing. For uniform reinforcement spacing, the

magnitude of applied horizontal earth pressure was generally observed to be constant. Miyata and Bathurst (2007) used a database of 9 new vertical face geosynthetic reinforced soil walls to investigate the effect of non-cohesive and cohesive backfill strength on the response of the structure. They concluded that the peak internal strain in the case of cohesive backfill is generally higher. In addition, the AASHTO simplified design method (AASHTO 2002) was determined to excessively overestimate measured reinforcement loads for both cohesive and non-cohesive backfill soils.

A series of FEM analyses were conducted by Wu et al. (2006) to examine the effect of sill type, sill width, soil stiffness/strength, reinforcement spacing, and foundation stiffness on the load-carrying capacity of GRS abutment sills. Two performance criteria were considered to determine the allowable bearing pressure of a given GRS abutment: a limiting displacement criterion and a limiting shear strain criterion. Data from five well-instrumented full-scale experiments were used to evaluate the FEM program. From the results, Wu et al. (2006) recommended a design procedure for determining the allowable bearing pressure.

Wu et al. (2008) conducted two full-scale load tests on GRS abutment walls to examine the behavior of segmental facing GRS abutment walls under increasing vertical loads on the associated bridge sill. Maximum sill settlement, maximum angular distortion, maximum lateral wall movement, the safety factor and the failure loads were investigated in this research. It was concluded that the real factor of safety inferred by the measurement was much higher than the one calculated by the design method; the design method is consequently deemed to be very conservative. Bathurst et al. (2009)

utilized the results from four full-load tests to investigate the influence of reinforcement stiffness and compaction effort on deformations. The influence of compaction effort on the wall deformation during construction and after surcharge application was investigated in this research. Significant downdrag forces were observed behind the facing wall and were consequently reported.

Ehlrich et al. (2012) investigated the effect of compaction on the behavior of two GRS walls using two walls constructed in the lab. Two different compaction techniques were utilized for this purpose. For Wall 1, a vibrating plate and vibratory tamper were used for soil compaction (heavy compaction), while only the vibrating plate was used for Wall 2 (light compaction). According to the results, the maximum tension in the reinforcement layers at the end of construction for Wall 1 was much higher. However, the difference in reinforcement tension was observed to decrease as a result of surcharge application. In addition, the maximum reinforcement tension was nearer to the wall face for Wall 1.

The long-term performance of GRS structures has been examined by a few researchers (e.g., Fannin 2001; Koerner and Soong 2001; Allen and Bathurst 2002; Farrag et al. 2004; Benjamim et al. 2007; Won and Kim 2007). The most important overall finding from these projects was that the creep deformation of GRS walls is more significant if marginal backfill is used instead of a high-quality granular backfill. In addition, as creep occurs in the backfill, the load in the reinforcement can be increased. Liu et al (2009) investigated the effect of implementing marginal backfill instead of clean granular backfill on the long-term response of a GRS structure using the FE

analysis method in conjunction with load test results. An elastoplastic viscoplastic model having a Drucker-Prager yield criterion and a Singh-Mitchell creep component with nonlinear elastic properties was utilized in this study to describe the nonlinearity, creep, and stress relaxation of the cohesive soil. Liu et al. (2009) showed that an increase in the backfill creep not only increases the wall deformation, it could also increase reinforcement load. Furthermore, the reinforcement creep also increases the deformation in the reinforced zone, as the stress transfers from the reinforcement to the soil which mobilizes a higher level of stress in the backfill. An increase in reinforcement stiffness and a decrease in reinforcement spacing were both observed to have a restrictive effect on long-term soil deformation in this research. The results also showed that the relative creep rate of reinforcement and backfill soil needs to be considered in the design process, especially for backfill with a significant cohesive fines content. Liu (2011) investigated the lateral facing displacements of segmental GRS walls at the end of construction and after 10 years of creep using Finite Element analyses. It was shown that the deformation of the reinforced soil zone was only slightly affected by the reinforcement length, but was much more significantly affected by the reinforcement spacing and reinforcement stiffness. In addition, the soil stiffness was observed to play an important role in the lateral deformation for cases where the soil strength was not significantly mobilized because of large reinforcement stiffness and/or small reinforcement spacing.

A few investigations have shown the satisfactory performance of constructed GRS structures on low- to intermediate-quality foundation soils (e.g.,

Adams 2000; Abu-Hejleh et al. 2002; Helwany et al. 2003). Rowe and Skinner (2001) simulated the behavior of an eight meter high GRS wall constructed on a layered soil foundation using the finite element method. The effect of the soft soil foundation drained and undrained strength, stiffness and its thickness on the wall performance were investigated in this research. The results from this study indicated generally better performance for a GRS wall than a MSE wall of similar height on the soft foundation. Skinner and Rowe (2005) investigated the behavior of a GRS abutment on a 10m thick yielding clayey soil deposit. They showed that a geosynthetic reinforced soil wall can resist against the excessive deformations caused by unexpected significant yielding of the foundation soil and even reduce the differential settlement and potential bridge bump effect at the top of the wall.

Wu and Pham (2013) presented an analytical model for predicting the ultimate load-carrying capacity and required reinforcement strength of a GRS mass based on a semi empirical equation which was verified by measured data from available field-scale experiments. Iwamato et al. (2014) used the results of some load tests performed on GRS walls to estimate the capacity of footings on geosynthetic reinforced soils. The results were compared with those predicted using the Wu and Pham (2013) equation employing using both the peak and fully softened soil shear strength parameters. The results from fully softened shear strength parameters agreed better with the measured capacities. This behavior was attributed to development of relatively large strains at failure because of the high strength of the reinforced soil. For large strain levels, the soil behavior is generally better simulated using fully softened strength parameters.

Generally, the term GRS has been used in the literature to describe reinforced soil systems with geosynthetic reinforcement at any spacing. However, the Federal Highway Administration (FHWA) (Adams et al. 2011) defines GRS as a reinforced soil mass having reinforcement spacing that is less than 0.3 m (and usually less than 0.2 m). The decrease in reinforcement spacing relative to other reinforced earth technologies is believed to increase the confinement and integrity of the system, as the reinforcement does not just serve as a tensile inclusion to resist tensile forces; it also restrains dilation, and reduces lateral deformation (Wu et al. 2014). The benefits of closely spaced reinforcement have been demonstrated through many field-scale experiments (e.g., Adams et al. 2002; Wu et al. 2011).

A particular GRS system of interest that has been introduced by the FHWA is the Geosynthetic Reinforced Soil Integrated Bridge System (GRS-IBS). The GRS-IBS is a composite bridge structure built using GRS abutments and prefabricated bridge superstructure elements. In this system, the approach roadway is also reinforced by layers of geosynthetic. Therefore, this system has all of the benefits of GRS structures and it also does not have the "bump at the end-of-the-bridge" problem, which is commonly caused by differential settlement between the bridge abutment and the approach roadway for conventional bridges.

Current GRS-IBS design guidelines (Adams et al. 2011) suggest the use of concrete masonry unit (CMU) blocks as facing elements for GRS-IBS structures. For GRS-IBS reinforcement elements, Adams et al. (2011) noted that biaxial, woven polypropylene (PP) geotextile is commonly used since it is inexpensive, easily placed

and compatible with the friction connection that is used between CMU block facing elements and the GRS mass. The suggested ultimate strength for the geotextile is 70 kN/m.

The next chapter presents details regarding the design, construction and instrumentation of a specific GRS-IBS structure, the first of its kind in Delaware.

REFERENCES

AASHTO (2002), "Standard Specifications for Highway Bridges", American Association of State Highway and Transportation Officials, Seventeenth Edition.

Abu-Hejleh, N., Zornberg, J., Wang, T. and Watcharamonthein, J. (2002). "Monitored displacements of unique geosynthetic-reinforced soil bridge abutments." Geosynthetics International, 9 (1), 71–95.

Adams, M. (2000). "Reinforced soil technology at FHWA, making old technology new." Geotechnical Fabrics Report, August, 34–37.

Adams, M., Lillis, C., Wu, J. and Ketchart, K. (2002). "Vegas mini pier experiment and postulate of zero volume change." In Proceedings, Seventh International Conference on Geosynthetics, 389-394.

Adams, M., Nicks, J., Stabile, T., Wu, J., Schelatter, W. and Hartmann, J. (2011). "Geosynthetic Reinforced Soil Integrated Bridge System Interim Implementation Guide", Publication No. FHWA-HRT-11-026, Federal Highway Administration, Washington, DC.

Allen, T., and Holtz, R. (1991). "Design of retaining walls reinforced with geosynthetics." In Geotechnical Engineering Congress, 970-987.

Allen T, Bathurst R and Berg R. (2002). "Global level of safety and performance of geosynthetic walls: an historical perspective." Geosynthetics International, 9(5–6), 395-450

Allen, T. and Bathurst, R. (2002). "Observed long-term performance of geosynthetic walls, and implications for design." Geosynthetics International, 9 (5–6), 567–606.

Bathurst, R., Cai, Z., Alfaro, M. and Pelletier, M. (1997). "Seismic design issues for geosynthetic reinforced segmental retaining walls." Mechanically stabilized backfill, Balkema, Rotterdam, Netherlands, 79–97.

Bathurst, R., Allen, T. and Walters, D. (2005). "Reinforcement loads in geosynthetic walls and the case for a new working stress design method." Geotextiles and Geomembranes, 23, No. 4, 287–322

Bathurst, R., Vlachopoulos, N., Walters, D., Burgess, P. and Allen, T. (2006). “The influence of facing rigidity on the performance of two geosynthetic reinforced soil retaining walls.” Canadian Geotechnical Journal, 43 (12), 1225–1237.

Bathurst, R., Vlachopoulos, N., Walters, D., Burgess, P. and Allen, T. (2007). Reply to the discussions on ‘The influence of facing rigidity on the performance of two geosynthetic reinforced soil retaining walls’. Canadian Geotechnical Journal, 44 (12), 1484– 1490.

Bathurst, R., Nernheim, A., Walters, D., Allen, T., Burgess, P. and Saunders, D. (2009). “Influence of Reinforcement Stiffness and Compaction on the Performance of Four Geosynthetic Reinforced Soil Walls.” Geosynthetics International, 16(1), 43-59.

Benjamim, C., Bueno, B. and Zornberg, J. (2007). “Field monitoring evaluation of geotextile-reinforced soil-retaining walls.” Geosynthetics International, 14 (2), 100–118

Berg, R., Allen, T. and Bell, J. (1998). “Design Procedures for Reinforced Soil Walls - A Historical Perspective”, Proceedings of the Sixth International Conference on Geosynthetics, IFAI, Vol. 2, Atlanta, Georgia, USA, 491-496.

Ehrlich, M., Mirmoradi, S. and Saramago, R. (2012). “Evaluation of the effect of compaction on the behavior of geosynthetic-reinforced soil walls.” Geotextiles and Geomembranes, 34, 108-115.

Fannin, R. (2001). “Long-term variations of force and strain in a steep geogridreinforced soil slope.” Geosynthetics International, 8 (1), 81–96.

Farrag, K., Abu-Farsakh, M., Morvant, M. (2004). “Stress and strain monitoring of reinforced soil test wall.” Transportation Research Record 1868, 89–99.

Hatami, K. and Bathurst, R. (2005). “Development and verification of a numerical model for the analysis of geosynthetic reinforced soil segmental walls under working stress conditions.” Canadian Geotechnical Journal, 42 (4), 1066–1085.

Hatami, K. and Bathurst, R. (2006). “A numerical model for reinforced soil segmental walls under surcharge loading.” Journal of Geotechnical and Geoenvironmental Engineering, 132 (6), 673– 684.

Helwany, S., Tatsuoka, F., Tateyama, M. and Kojima, K. (1996). "The Effects of Facing Rigidity on the Performance of GRS Structures." Soils and Foundations, Japanese Geotechnical Society, 36(1), 27-38.

Helwany, S., Wu, J. and Froessl, B. (2003). “GRS bridge abutments—an effective means to alleviate bridge approach settlement.” Geotextiles and Geomembranes, 21, 177–196.

Iwamoto, M, Ooi, P., Nicks, J., Adams, M.and Manoa, U. (2013). “Use of fully softened versus peak strength to predict the capacity of footings on geosynthetic reinforced soil.” In Third International Conference on Geotechnique, Construction Materials and Environment, Nagoya, Japan, 252-257.

Koerner, R., Soong, T. (2001). “Geosynthetic reinforced segmental retaining walls.” Geotextiles and Geomembranes, 19, 359–386.

Lee, K. and Wu, J. (2004). “A Synthesis of Case Histories on GRS Bridge-Supporting Structures with Flexible Facing.” Geotextiles and Geomembranes, Journal of the International Geosynthetics Society, Vol. 22, pp. 181-204.

Liu, H., Wang, X. and Song, E. (2009). “Long-term behavior of GRS retaining walls with marginal backfill soils.” Geotextiles and Geomembranes, 27(4), 295-307

Liu, H. (2011). “Long-term lateral displacement of geosynthetic-reinforced soil segmental retaining walls.” Geotextiles and Geomembranes, 32, 18-27.

Miyata, Y. and Bathurst, R. (2007). “Development of K-stiffness method for geosynthetic reinforced soil walls constructed with c-ϕ soils.” Canadian Geotechnical Journal, 44(12), 1391-1416.

Nicks, J., Adams, M., Ooi, P. and Stabile, T. (2013). “Geosynthetic reinforced soil performance testing—Axial load deformation relationships.” Publication No. HRT-13-066, Federal Highway Administration (FHWA), Washington, DC.

Rowe, R. and Skinner, G. (2001). “Numerical analysis of geosynthetic reinforced retaining wall constructed on a layered soil foundation.” Geotextiles and Geomembranes, 19, 387–412.

Skinner, G. and Rowe, R. (2005). “Design and behaviour of a geosynthetic reinforced retaining wall and bridge abutment on a yielding foundation.” Geotextiles and Geomembranes, 23(3), 234-260.

Tatsuoka, F., Tateyama, M. and Murata, O. (1989). “Earth retaining wall with a short geotextile and a rigid facing.” In Proceedings, 12th ICSMFE, 1311-1314.

Tatsuoka F. (1993). “Roles of facing rigidity in soil reinforcing.” Keynote Lecture, Proceedings International Symposium on Earth Reinforcement Practice, IS Kyushu 92, Balkema, 2, 831-870.

Won, M., Kim, Y. (2007). “Internal deformation behavior of geosynthetic-reinforced soil walls.” Geotextiles and Geomembranes, 25 (1), 10–12.

Wu, J. (1994). “Design and construction of low cost retaining walls: The next generation in technology.” CTI-UCD-1-94, Colorado Transportation Institute, Denver.

Wu, J., Lee, K. and Pham, T. (2006). “Allowable bearing pressures of bridge sills on GRS abutments with flexible facing.” Journal of Geotechnical and Geoenvironmental Engineering, 132(7), 830-841.

Wu, J. (2007). “Lateral earth pressure against the facing of segmental GRS walls.” Proceedings of Geo-Denver.

Wu, J., Ketchart, K. and Adams, M. (2008). “Two full-scale loading experiments of geosynthetic-reinforced soil (GRS) abutment wall.” International Journal of Geotechnical Engineering, 2(4), 305-317.

Wu, J., Ma, C., Pham, T. and Adams, M. (2011). “Required minimum reinforcement stiffness and strength in geosyntheticreinforced soil (GRS) walls and abutments.” International Journal of Geotechnical Engineering, 5(4), 395–404

Wu, J. and Pham, T. (2013). “Load-carrying capacity and required reinforcement strength of closely spaced soil-geosynthetic composites.” Journal of Geotechnical and Geoenvironmental Engineering, 139(9), 1468-1476.

Wu, J., Yang, K., Mohamed, S., Pham, T. and Chen, R. (2014). “Suppression of Soil Dilation—A Reinforcing Mechanism of Soil-Geosynthetic Composites.” Transportation Infrastructure Geotechnology, 1(1), 68-82.

Chapter 3

DESIGN, CONSTRUCTION, AND INSTRUMENTATION OF A GRS-IBS STRUCTURE IN DELAWARE

3.1 Introduction

In this chapter, the details regarding the design, construction, and instrumentation of a GRS-IBS structure, the first of its kind in Delaware, are presented. As noted in Chapter 1, this GRS-IBS structure is located in New Castle County, on Chesapeake City Road over Guthrie Run (Figure 1.2). This structure, Br. 1-366, was constructed in 2013 as a replacement for an existing bridge that had had reached the end of its usable service life. The design for this structure was conducted following current FHWA interim implementation guidelines for GRS-IBS structures (Adams et al. 2011). Following this guidance document, the GRS-IBS should be designed to be internally and externally stable. The corresponding design criteria presented in this guidance document were considered in the design process to achieve these goals.

3.2 Project specifications

3.2.1 Geometrical specifications

Preliminary geometrical details for this project were provided by engineers from the Delaware Department of Transportation (DelDOT). From the geometrical

requirements, it was determined that the maximum height from the road elevation to bottom of the foundation needed to be about 6.1 m (Figure 3.1), which was less than the allowable height (about 9 m) that is specified for GRS-IBS structures (Adams et al. 2011.) The width of the bridge including two lanes and two shoulders was 12.2 m and the span length was determined to be 8.7 m (Figure 3.2). As shown in Figure 3.1, 1.3 m of the bridge was placed on each abutment, yielding a total bridge length of 11.3 m. The width and the length of each abutment were determined to be 9.8 m and 14.6 m, respectively (Figure 3.2).

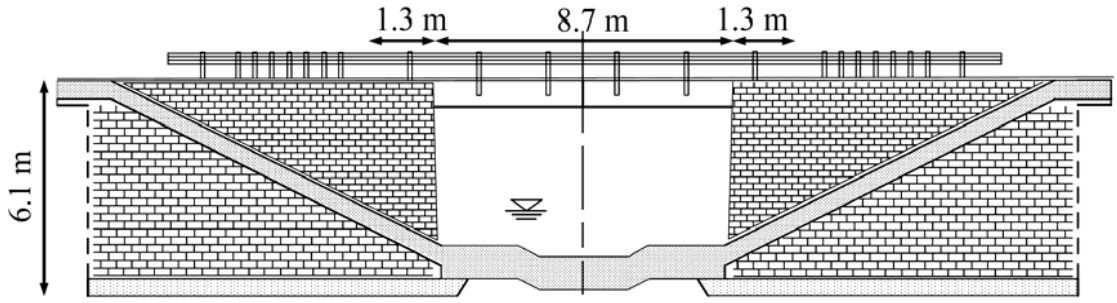

Figure 3.1 General cross-section view of the GRS-IBS structure, along the road centerline

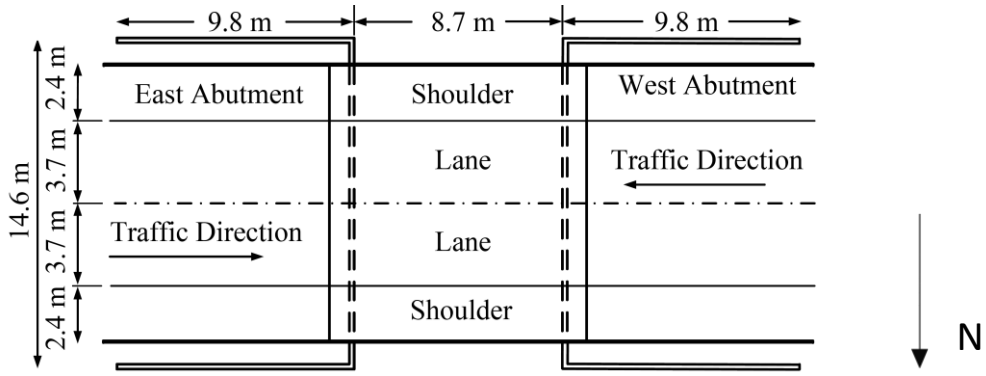

Figure 3.2 Plan view of the GRS-IBS structure

3.2.2 Geotechnical specifications

As part of the geotechnical exploration process, two boreholes were drilled at the site, one in each abutment. The respective depth of these boreholes, which was determined beased on the height of the wall and the applied loads, is presented in Table 3.1. The resulting borehole data sheets are provided in Appendix A. In addition, a variety of geotechnical laboratory tests were performed on soils obtained from these borings, including 41 soil classification tests, six consolidation tests, two unconfined compression tests, four UU triaxial shear tests, and 11 organic content tests. The corresponding test results have been provided in Appendices B through F.

Table 3.1 Overview of borehole exploration program

Borehole No.	Borehole Depth (m)	Observed Depth to Groundwater (m)	Observed Depth to Bedrock (m)
CC-1	18.3	3.3	Not Encountered
CC-2	18.3	3.5	Not Encountered

Using the results from these laboratory tests, published correlations, and engineering judgment, a simplified soil layer geometry, associated soil unit weights, and necessary strength parameters for design of the GRS-IBS were determined; this information is provided in Figure 3.3 (note that some conservatism was used in the determination of some of the estimated parameters).

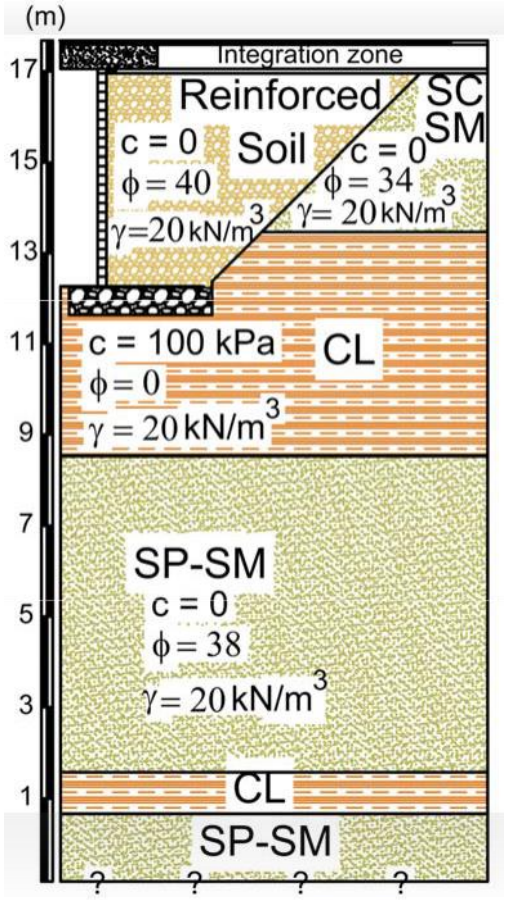

Figure 3.3 Soil layering and engineering properties used for the design of the GRS-IBS

As shown in Figure 3.3, the soil encountered during the site exploration consisted of both granular and fine materials, ranging in USCS classification from SM-SC to CL. The uppermost soil layer, ranging from approximately 0 to 4.0 m or so in thickness, was generally a fine sandy material with silt and clay. According to the standard penetration test results, this material was generally at a "medium dense" state. Beneath this sandy layer, a fairly thin stiff orange sandy clay layer was observed, which transitioned rather

quickly to a grayish-brown silty fine sandy clay layer. This layer continued to an approximate depth of 9.0 m. This layer is medium stiff to stiff and in some depths includes organic material. Generally, it appears as if this layer became siltier with depth. After this clay layer, a fine sand layer with some silt was observed again. This fine sand layer was classified as dense to very dense and was shown to extend to the end of the borehole exploration (with only a minor occurrence of a thin clay layer at the very end).

3.2.3 Reinforced fill material

Following the interim implementation guidelines for GRS-IBS structures (Adams et al. 2011), the following requirements should be considered for the reinforced fill material:

- The abutment backfill materials should consist of crushed, hard, durable particles or fragments of stone or gravel.
- These materials should be free from organic matter or deleterious material such as shale or other soft particles that have poor durability.
- The backfill should follow the size and quality requirements for crushed aggregate material normally used locally in the construction and maintenance of highways by Federal or State agencies.
- Abutment backfill typically consists of either well-graded or open-graded aggregates.
- Lower quality granular or natural fill materials can be used if the amount of fines is limited to less than 12 percent for drainage.

Based on these requirements, No. 8 stone was utilized for the backfill material in the reinforced soil zone. This crushed stone is a coarse material with a relatively uniform gradation, as shown in Figure 3.4. This material has DelDOT approval for use in construction and generally conforms to the associated material specifications (Adams et al. 2011) for GRS-IBS backfill material.

Figure 3.4 No. 8 stone material utilized in the project

Figure 3.5 shows the maximum and minimum allowable range for No. 8 stone which is specified in the standard provided by DelDOT (2001). To assure that the borrow materials used were in agreement with the DelDOT standard, seven gradation tests were conducted at University of Delaware lab. The results are shown in Figure 3.5. As shown in this figure, all gradation curves fit the allowable range.

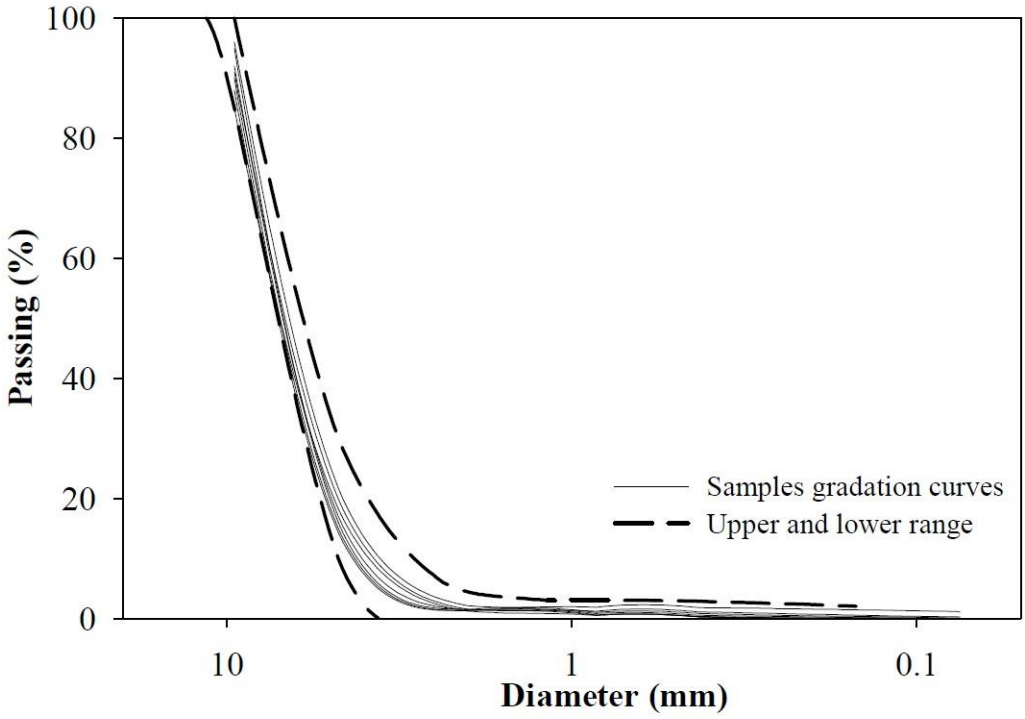

Figure 3.5 No. 8 stone gradation ranges and the samples gradation test results

For this specified material, the engineering properties shown in Table 3.2 were utilized for the design of the GRS-IBS structure; these values are also shown accordingly in Figure 3.3.

Table 3.2 Reinforced fill properties

Property	Notation	Unit	Estimated parameters
Reinforced fill unit weight	γ_r	kN/m^3	20
Maximum diameter of reinforced fill	d_{max}	m	0.013
Reinforced fill cohesion	c_r	kPa	0
Reinforced fill friction angle	ϕ_r	deg	40

3.2.4. Reinforced soil foundation (RSF)

In accordance with FHWA recommendations (Adams et al. 2011), the backfill material that was used to construct the RSF was the same as that used for abutment construction (No. 8 stone).

3.2.5 Road base material

The road base is a granular fill material that is placed and compacted as part of the roadway approach to the bridge. For this project, the estimated properties of the road base are presented in Table 3.3. As this material had not been specified at the time of design, it should be noted that these properties are only estimates, which were determined based on values presented in Adams et al. (2011).

Table 3.3 Road base soil properties

Property	Notation	Unit	Estimated parameters
Road base unit weight	γ_{rb}	kN/m^3	22
Road base cohesion	c_{rb}	kPa	0
Road base friction angle	ϕ_{rb}	deg	40

3.2.6 Concrete Masonry Unit (CMU) blocks

The most commonly used facing element for GRS walls and abutments is the split-face concrete masonry unit (CMU) with nominal dimensions of 0.2 m by 0.2 m by 0.4 m**.** CMU blocks are lightweight and easy to place. The soil is compacted every 8-inches (0.2 m), which is the thickness of the CMU block; this allows for easier monitoring of soil compaction in the field.

3.2.7 Geosynthetic

Adams et al. (2011) stated that the utilization of biaxial, woven polypropylene (PP) geotextile is very common for the reinforcement elements in GRS-IBS structures. Consequently, it was decided to use the same material for this project. An ultimate strength of 70 kN/m (Adams et al. 2011) was used for this material for GRS load-bearing applications.

The geotextile reinforcement (HPG-57) was provided by Hanes Geo Component and is a polypropylene woven fabric. According to the manufacturer's specifications, this geotextile is stabilized to resist degradation due to ultraviolet

exposure. It is resistant to commonly encountered soil chemicals, mildew and insects, and is non-biodegradable. Polypropylene is stable within a pH range of 2 to 13, making it one of the most stable polymers available for geotextiles today. The main properties of this material are presented in Table 3.4.

Table 3.4 Utilized geotextile properties

Property	**Test Method**	**Value**
Wide Width Tensile Strength (Maximum)	ASTM D4595	70 x 70 kN/m
Wide Width Tensile Strength (2% Strain)	ASTM D4595	14 x 19.3 kN/m
Wide Width Tensile Strength (5% Strain)	ASTM D4595	35 x 39.4 kN/m
Permittivity [1]	ASTM D4491	0.400 sec^{-1}
UV Resistance	ASTM D4355	80 % @ 500 hrs

3.3. Determination of design layout for the proposed GRS-IBS

The beam seat (b) and the setback (a_b) should be determined at the beginning of the design process, as shown in Figure 3.6. Adams et al. (2011) considered the following requirements for this purpose (Figure 3.6):

If $L_{span} > 7.6$ m then $b > 0.76$ m (3.1)

If $L_{span} < 7.6$ m then $b > 0.61$ m (3.2)

$a_b > 0.2$ m (3.3)

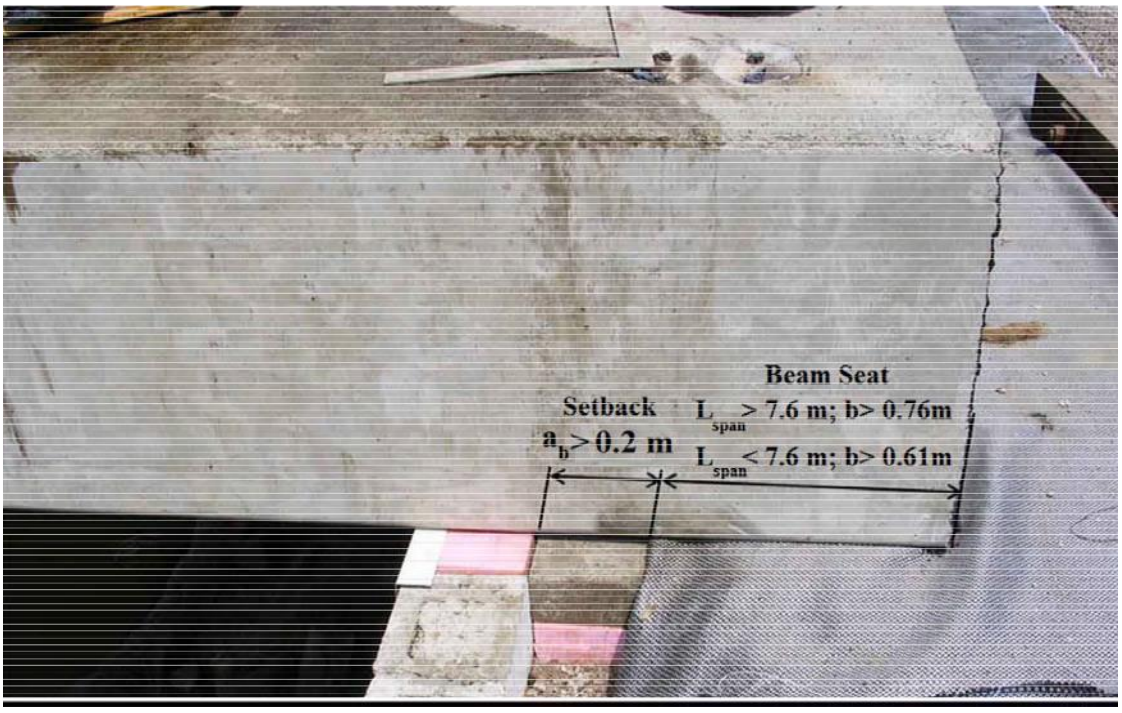

Figure 3.6 Bridge seat and setback distances (modified after Adams et al. 2011)

Based on the anticipated dead load (DL) and live load (LL) loading and the associated design calculations for this project (which are presented in the next section), a bearing width of 0.9 m was selected for design. The setback distance (a_b) between the back of the wall face and the front edge of the bridge beam seat should be the height of a standard CMU block, 0.2 m. The clear space between the top of the CMU block wall and the bottom of the bridge superstructure should be greater than 2 percent of the wall height. Consequently, for this project, a minimum clear space dimension of 0.1 m was required.

A foundation width of 2.5 m (B_{total}) was selected based on the sliding and bearing capacity requirements (presented in the next section). Additionally, the depth of the excavation for the RSF (D_{RSF}) should equal one-quarter the total width of the base of the GRS abutment (Figure 3.7); for this project, this yielded a D_{RSF} of 0.63 m. The foundation should be extended forward a distance of 0.25 B_{total} (x_{RSF} = 0.63 m), as shown in Figure 3.5. This results in a total length of the foundation (B_{RSF}) equal to 3.13 m. The reinforcement spacing is 0.2 m at the wall face, corresponding to the height of the CMU blocks. The reinforcement spacing within the bearing reinforcement bed is 0.1 m, half of the primary reinforcement spacing distance (Adams et al. 2011).

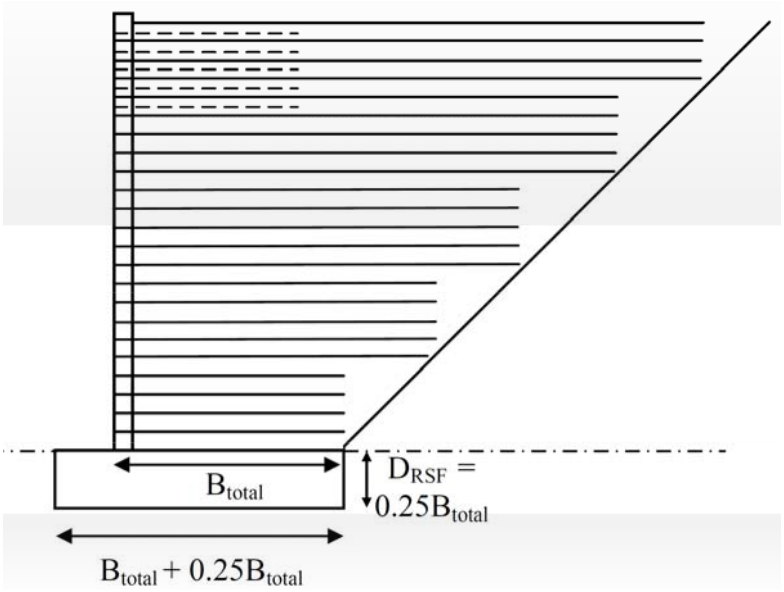

Figure 3.7 Reinforced soil foundation (RSF) dimensions

As part of the design process, the minimum reinforcement length at the base of the wall was found to be equal to 2.5 m and the reinforcement lengths moving upwards in the structure from this point were chosen based on the cut slope angle (which was 45°).

The primary reinforcement spacing is 0.2 m at the wall face. The reinforcement spacing within the bearing reinforcement bed is 0.1 m, half of the primary spacing. The required depth of the bearing reinforcement bed was determined later following the results from the internal stability analysis that was conducted. At a minimum, however, there would be five intermediate layers between the primary reinforcement layers (at 0.2 m spacing) in the bearing reinforcement zone.

3.4 Loading

The most common pressures on a typical GRS-IBS structure that may be resolved into forces for stability computations (after Adams et al. 2011) are depicted in Figure 3.8.

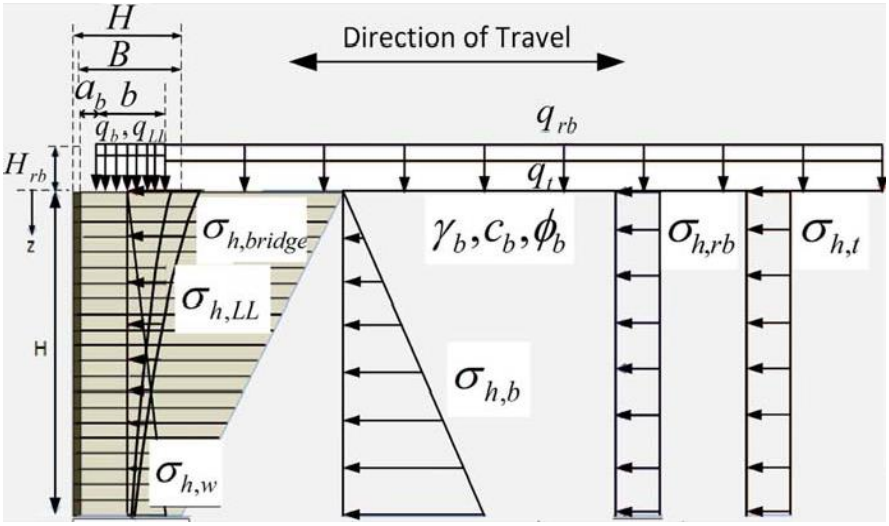

Figure 3.8 Vertical and lateral pressures on a GRS abutment (modified after Adams et al. 2011)

The applicable pressures on a GRS abutment after the Adams et al. (2011) design approach are as follows:

q_t = equivalent roadway LL surcharge

$\sigma_{h,t}$ = lateral stress distribution due to the equivalent roadway LL surcharge

q_{rb} = surcharge due to the structural backfill of the integrated approach (road base)

$\sigma_{h,rb}$ = lateral stress distribution due to the structural backfill of the integrated approach

q_b = equivalent superstructure DL pressure

$\sigma_{h,bridge}$ = lateral stress distribution due to the equivalent superstructure DL pressure

$\sigma_{h,b}$ = equivalent lateral stress distribution due to retained soil behind the GRS abutment

q_{LL} = equivalent superstructure LL pressure

$\sigma_{h,LL}$ = lateral stress distribution due to the equivalent superstructure LL pressure

$\sigma_{h,W}$ = lateral stress distribution due to the weight of the GRS fill

The lateral earth pressure is calculated according to classical soil mechanics theory for active earth pressure with no cohesion, utilizing Equation 3.4:

$$P_a = \frac{1}{2} K_a \gamma h^2 \tag{3.4}$$

In this equation, P_a is the lateral force applied by the retained soil, K_a is the active earth pressure coefficient, γ is the soil density and h is the height of the structure. For the vertical walls that were used in this study, with a horizontal backfill, we have:

$$K_a = tan^2(45 - \frac{\phi'}{2}) \tag{3.5}$$

where ϕ' is the effective stress soil friction angle.

The lateral pressure due to surcharge loading ($\sigma_{h,q}$) is calculated using the following equation:

$$a_{h,q} = \frac{q}{rr}[a + sin(a)\, cos(a + 2/f)]K_a \tag{3.6}$$

Where q is the surcharge pressure, K_a is the coefficient of active earth pressure (Equation 3.5), and α and β are the angles shown in Figure 3.9, found using Equation 3.7 and Equation 3.8, respectively.

$$a = tan^{-1}\left(\frac{x}{z}\right) - /f \quad (3.7)$$

$$/f \quad tan^{-1}\left(\frac{x-b_q}{z}\right) \quad (3.8)$$

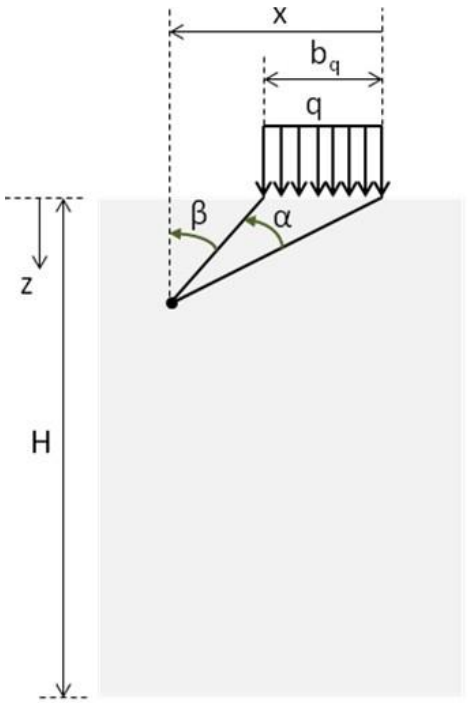

Figure 3.9 Geometry used to calculate Boussinesq elastic theory solution describing the horizontal pressure beneath an applied strip load as a function of depth (Adams et el. 2011)

The associated dead loads and live loads that were used for design of the GRS-IBS structures are summarized in Table 3.5. Other parameters defined in Table

3.5 are: h_{eq} = equivalent height of overburden for traffic surcharge, h_{rb} = height of road base, H = height of the GRS abutment, B_{RSF} and D_{RSF} = width and depth of the RSF, respectively, B = base length of reinforcement, γ_b = unit weight of retained backfill, γ_{rb} = unit weight of road base material, γ_r = unit weight of reinforced backfill, and K_{ab} = coefficient of active earth pressure (Adams et al. 2011).

To determine the bridge DL, the criteria to select the maximum weight is based on the AASHTO LRFD Design Load of HL93, which consists of the Design Truck of total weight of 72 kips and Lane Load of 0.64 kip/ft and the Design Tandem of total weight of 50 kips and Lane Load of 0.64 kip/ft. The number of trucks is dependent on the number of 12 ft design lanes. The bridge weight was considered to calculate the corresponding pressure per abutment.

Table 3.5 Loads and surcharges for 1-366 Bridge

Property	Notation	Measurement	Equation
Bridge DL	q_b	73.1 kPa	Calculated using the bridge weight
Bridge LL	q_{LL}	97.5 kPa	In accordance with AASHTO LRFD Bridge Design
Roadway LL	q_t	15 kPa	$q_t = (h_{eq})\ (y_b)$, h_{eq} = 0.76 m
Road base DL	q_{rb}	11.7 kPa	$q_{rb} = (h_{rb})(y_{rb})$, $h_{rb} = 1.75\ ft$
Weight of GRS abutment	W	200 kN/m	$W = BHy_r$
Weight of RSF	W_{RSF}	36.4 kN/m	$W_{RSF} = B_{RSF}D_{RSF}y_r$
Lateral load (retained backfill)	F_b	65.9 kN/m	$F_b = 0.5(y_b)(H^2)K_{ab}$
Lateral load (q_{rb} effect)	F_{rb}	16.1 kN/m	$F_{rb} = (q_{rb})(H)K_{ab}$
Lateral load (q_t effect)	F_t	20.6 kN/m	$F_t = (q_t)(H)K_{ab}$

3.5 External stability analysis

The external stability of the GRS-IBS was evaluated by looking at the following potential external failure mechanisms:

- Direct sliding
- Bearing capacity
- Global stability

3.5.1 Direct sliding

The GRS abutment must resist horizontal translation, which is also commonly described as a “direct sliding” mode of failure; this corresponds to an ultimate limit state failure mechanism in the horizontal direction. The factor of safety against direct sliding occurring is determined by examining the ratio between the sliding resisting forces (R_n) and the sliding driving forces (F_n).

The driving forces on the GRS abutment include the lateral forces due to the retained backfill (F_b), the road base (F_{rb}), and the traffic surcharge (F_t) (Table 3.5).

$$F_n = F_b + F_{rb} + F_t \tag{3.9}$$

$$F_b = \frac{1}{2} y_b K_{ab} H^2 \tag{3.10}$$

$$F_{rb} = q_{rb} K_{ab} H \tag{3.11}$$

$$F_t = q_t K_{ab} H \tag{3.12}$$

The resisting force (R_n) is calculated using the equation:

$$R_n = \mu X W_t \tag{3.13}$$

The total resisting weight (W_t) includes the weight of the GRS abutment plus the weight of the bridge beam plus the weight of the road base over the GRS abutment (Table 3.5, Equation 3.14). Since the live loads are not permanent, they cannot be counted in the determination of the resisting force.

$$W_t = W + q_b b + q_{rb} b_{rb} \tag{3.14}$$

The friction force (μ) is the friction factor between the wall base and the foundation; its value can be determined from tan (ϕ_{crit}), *where* ϕ_{crit} is the critical interface friction angle. It is generally best to determine the interface friction angle using an interface direct shear test for the particular combination of geosynthetic and reinforced fill material that will be used for construction (ASTM D5321). For the current project, this information was not accessible in a timely fashion during the design process; consequently, it was assumed that the friction factor would be equal to 2/3 times the tangent of the reinforced granular fill friction angle (Adams et al. 2011)*:*

$$\mu = \frac{2}{3} tan(\phi) \tag{3.15}$$

The calculated factor of safety against sliding determined following the above approach was equal to 1.57, which is greater than the minimum required value of 1.5 (Adams et al. 2011).

3.5.2 Bearing capacity

The GRS abutment must also be designed against bearing capacity failure, which corresponds to an ultimate limit state failure mechanism in the vertical direction. To prevent bearing capacity failure, the applied vertical pressure at the base of the RSF must not exceed the allowable bearing capacity of the underlying soil foundation. The applied vertical pressure is a result of the weight of the GRS abutment (W), the weight of the RSF (W_{RSF}), the bridge dead load (q_b), the LL on the superstructure (q_{LL}), and the LL on the approach pavement (q_t). The pressure at the base ($\sigma_{v,base,n}$) is calculated utilizing a Meyerhof-type distribution, as shown in Equation 3.16.

$$\sigma_{v,base,n} = \frac{\sum}{B_{RSF}-2e_{b,n}} \tag{3.16}$$

Before calculating the applied vertical bearing pressure, the eccentricity of the resulting force at the base of the wall must first be calculated using the following equation:

$$e_{b,n} = \frac{\sum M_D - \sum M_R}{\sum} \tag{3.17}$$

In the above equation, ΣM_D, ΣM_R, and ΣV are the total driving moment, the total resisting moment, and the total vertical load, respectively.

The moments are calculated around the center of the base of the RSF. The driving moments (calculated as a counterclockwise moment) include the lateral force due to the retained backfill, the road base DL, and the roadway LL.

$$\sum M_D = F_b\left(\frac{H}{3}\right) + F_{rb}\left(\frac{H}{2}\right) + F_t\left(\frac{H}{2}\right) \quad (3.18)$$

The resisting moments (calculated as a clockwise moment) include the vertical force due to the bridge and road base DLs and the bridge and roadway LLs. The weight of the GRS abutment is also included as a resisting moment.

$$\sum M_R = (q_b b + q_{LL} b)\left[\left(\frac{b}{2} + a_b\right) - \left(\frac{B_{RSF}}{2} - x_{RSF} - b_{block}\right)\right] + (q_t b_{rb,t} + q_{rb} b_{rb,t})\left(\frac{B_{RSF}}{2} - \frac{b_{rb,t}}{2}\right) + W\left(\frac{B_{RSF}}{2} - \frac{B_{total}}{2}\right) \quad (3.19)$$

The variables b, a_b, x_{RSF} and B_{total} are defined in Section 3.3. The variable b_{block} is the width of the CMU block, and $b_{rb,t}$ is the width over the GRS abutment where the road base DL acts.

The total vertical load is equal to the sum of the weight of the GRS abutment, the weight of the RSF, and the load due to the DLs (bridge and road base) and LLs (bridge and roadway):

$$\sum V = W + W_{RSF} + W_{face} + q_t b_{rb,t} + q_{rb} b_{rb,t} + q_b b + q_{LL} b \quad (3.20)$$

The variable W_{face} corresponds to the weight of the facing elements. The other parameters are as denoted previously.

For the designed GRS-IBS, substituting in for the appropriate variables results in $e_{b,n}$ and $\sigma_{v,base,n}$ values of 0.25 m and 163 kPa, respectively. Using these values, the ultimate bearing capacity can be calculated. The general formulation for the ultimate bearing capacity calculation is as follows (AASHTO, 2010):

$$q_n = c_f N_c + \frac{1}{2} B' \gamma_f N_\gamma + \gamma_f D_f N_q \quad (3.21)$$

where c_f is the cohesion of the foundation soil, N_c, N_γ, and N_q are dimensionless bearing capacity coefficients which depend on the RSF foundation friction angle (ϕ), γ_f is the unit weight of the foundation soil, B' is the effective foundation width (equal to B_{RSF}-$2e_{b,n}$), and D_f is the depth of embedment. The calculated q_n that results is 530 kPa.

From the calculated values of $\sigma_{v,base,n}$ and q_n, the factor of safety against bearing capacity failure is about 3.3; this is greater than the minimum required value of 3.0 (Adams et al. 2011), which indicates that the structure can be considered stable against bearing capacity failure.

3.5.3 Global stability

Global stability was also checked as an essential part of the external stability analysis using different failure mechanisms that were assessed using the Slope/W program (Geo-Slope Ltd 2010). Different situations for varying water level were assessed, using the appropriate undrained and drained shear parameters of the foundation clay layer determined by the field and laboratory test results. A variety of slip surface shapes were checked as part of this analysis, using different slope stability analysis methods. The overall results of these analysis indicated that the structure was stable against global stability failure with a calculated factor of safety value of 1.51 (Figure 3.10); this meets the required minimum factor of safety against failure criterion of 1.5 (Adams et al. 2011).

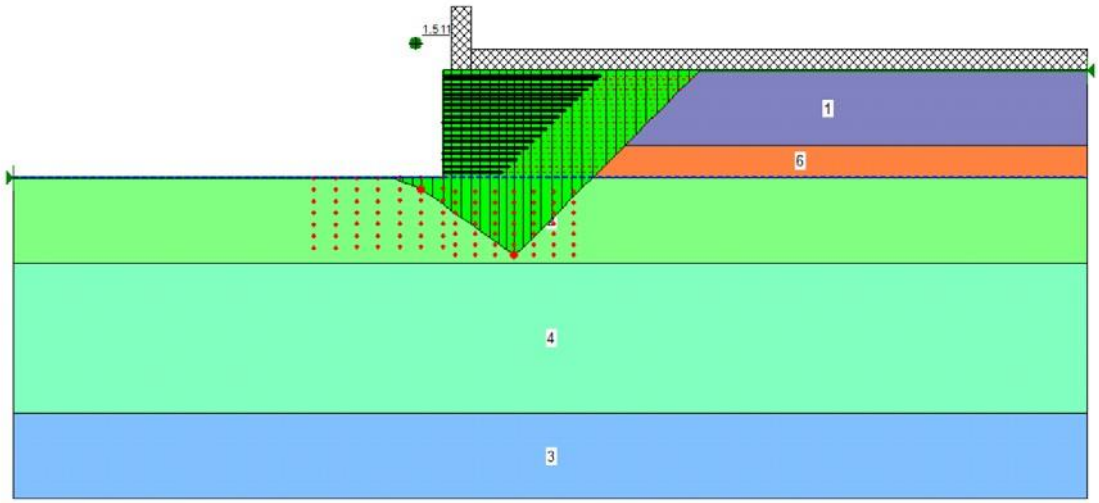

Figure 3.10 Results from the global stability analysis

3.6 Internal stability analysis

3.6.1 Ultimate capacity

The ultimate capacity of a GRS abutment corresponds to the ultimate load that can be applied by the superstructure before failure occurs; following current GRS-IBS design guidelines, its value should be determined using two different but complementary methods, one having an empirical basis and another having an analytical basis (Adams et al. 2011).

3.6.1.1 Empirical method

The empirical method uses the load test results of a performance test on a GRS composite material identical (or very similar) to that used in the field. The ultimate capacity (q_{ult}) is found empirically as the stress at 5 percent vertical strain from the stress-strain curve determined from the load test. For the current project, there was no performance test data available; consequently, the performance test results determined by Adams et al. (2011) were used (Figure 3.11).

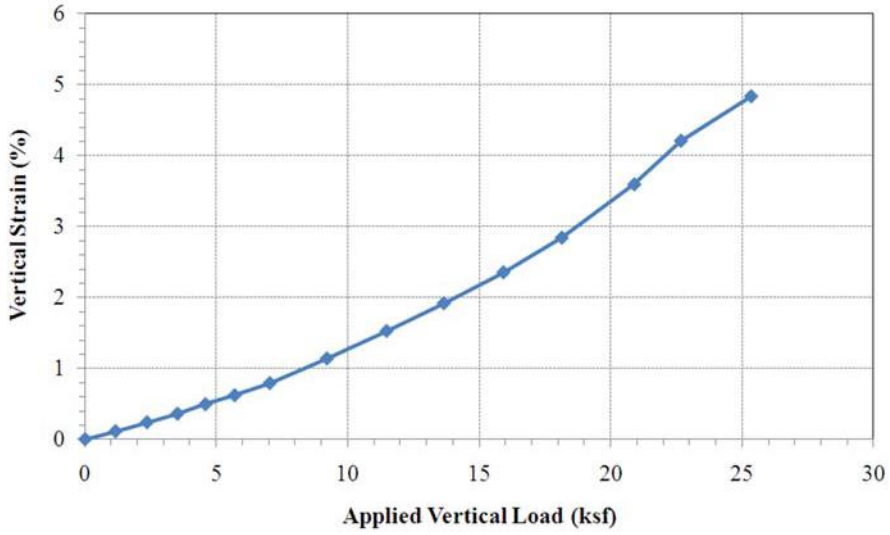

Figure 3.11 Assumed design envelope for vertical capacity and strain at 8-inch reinforcement spacing (Adams et al. 2011)

As shown in Figure 3.11, the ultimate capacity found empirically as the stress at 5 percent vertical strain is about 26 ksf (1245 kPa). The total allowable pressure on the GRS abutment ($V_{allow,emp}$) is therefore 355.7 kPa, which is the ultimate capacity (q_{ult}) divided by a factor of safety for capacity ($FS_{capacity}$) of 3.5 (Adams et al. 2011).

The applied vertical stress ($V_{applied}$), which is equal to the unfactored sum of the vertical pressures on the bridge bearing area, must be less than $V_{allow,emp}$. This includes the DL and LL from the bridge (q_b, q_{LL}):

$V_{applied} = q_b + q_{LL} = 170.5 \text{ kPa} < V_{allow,emp}$ (3.22)

Consequently, as $V_{allow,emp}$ = 355.7 kPa, the empirical design approach yields satisfactory results.

3.6.1.2 Analytical method

Alternatively, the ultimate capacity can be found analytically for a granular backfill using the following equation (Adams et al. 2011):

$$q_{ult} = [0.7^{(\frac{S_v}{6d_{max}})} \frac{T_f}{S_v} K_r \quad (3.23)$$

where S_v is the reinforcement spacing (equal to 0.2 m in this project), d_{max} is the maximum grain size of the reinforced backfill (equal to 0.0125 m in this project), T_f is the ultimate strength of the reinforcement (equal to 70 kN/m in this project), and K_{pr} is the coefficient of passive earth pressure for the reinforced fill:

$$K_r = tan^2(45 + \frac{\phi_r}{2}) \quad (3.24)$$

The variable ϕ_r is the friction angle of the reinforced backfill (equal to 40 degrees in this project, see Table 3.2). From the calculations that were conducted $q_{ult,an}$= 612 kPa and $V_{allow,an}$= 612/3.5=174.9> $V_{applied}$. Therefore, the structure is stable against ultimate internal capacity failure, by both the analytical and empirical design approaches.

3.6.2 Deformation

Both the vertical and horizontal deformation applied by the superstructure dead load (q_b) need to be checked, which correspond to service limit state assessments (Adams et al. 2011).

3.6.2.1 Vertical Deformation

The vertical strain should not exceed 0.5 percent according to the interim implementation guidelines (Adams et al. 2011). It is recommended that a performance test be conducted to determine the vertical deformation. For cases where no performance test has been conducted, but where the reinforced backfill materials used are similar to what is recommended in the interim implementation guide, then the curve shown in Figure 3.8 can be used (Adams et al. 2011). As shown in Figure 3.11, the vertical load at 0.5 percent is about 4.5 ksf (215 kPa). Dividing this by q_b results in a factor of safety about 2.9 against vertical deformation failure.

3.6.2.2 Horizontal Deformation

In response to a vertical load, the composite behavior of a properly constructed GRS mass is such that both the reinforcement and soil strain laterally together (Adams et al. 2011). This fact can be used to predict both the maximum lateral reinforcement strain and the maximum face deformation at a given load. The maximum lateral displacement and the maximum horizontal strain of the abutment face wall can be estimated using Equations 3.25 and 3.26 (Adams et al. 2011):

$$D_L = \frac{2b_{q,vol}D_v}{H} \quad (3.25)$$

$$E_L = \frac{D_L}{b_{q,vol}} \quad (3.26)$$

Where $b_{q,vol}$ is the width of the load along the top of the wall (including the setback), D_v is the vertical settlement in the GRS abutment, H is the wall height including the clear space distance, and ε_L is the lateral strain. Replacing the corresponding values results in D_L = 0.01m and $E_L = 0.9\%$.

According to the GRS-IBS interim implementation guide (Adams et al. 2011), the maximum lateral strain should be limited to 1 percent. It should be noted that Equations 3.25 and 3.26 come from the assumptions of a triangular lateral deformation and a uniform vertical deformation. This assumption is based on the observed deformation behavior of GRS structures. In addition, the location of the maximum lateral deformation depends on the loading and fill conditions, with the assumption that the volume gained equals the volume lost. The maximum deformation of a GRS abutment often occurs in the top third of the abutment/wall (Adams et al. 2011).

3.6.2.3 Required reinforcement strength

The strength of the reinforcement used at this project (T_{ult}) is 70 kN/m. Applying a factor of safety of 3.5 (Adams et al. 2011), the allowable reinforcement strength (T_{all}) is 23.3 kN/m. According to the interim implementation guide (Adams et

al. 2011), the geotextile strength at 2 percent strain ($T_{\varepsilon=2\%}$) should not be less than 23.3 kN/m.

The maximum required reinforcement strength (T_{req}) is found as a function of depth (Adams et al. 2011):

$$T_{req} = \frac{\sigma_h}{0.7\left(\frac{S_v}{6d_{max}}\right)} S_v \quad (3.27)$$

Where S_v is the reinforcement spacing, d_{max} is the maximum grain size of the backfill material, and σ_h is the total lateral stress within the GRS abutment at a given depth and location (Equation 3.28).

$$\sigma_h = \sigma_{h,W} + \sigma_{h,bridge,eq} + \sigma_{h,rb} + \sigma_{h,t} \quad (3.28)$$

As shown in Equation 3.28, the lateral stress (σ_h) is a combination of the lateral stresses due to the road base DL ($\sigma_{h,rb}$), the roadway LL ($\sigma_{h,t}$), the self-weight of the GRS reinforced soil mass ($\sigma_{h,W}$), and an equivalent bridge load ($\sigma_{h,bridge,eq}$).

The lateral stress due to the equivalent bridge load ($\sigma_{h,bridge,eq}$) is calculated using elastic earth pressure theory (using Boussinesq's assumptions). The location of interest to determine the maximum lateral pressure is directly underneath the centerline of the bridge bearing width (i.e., $= \frac{b}{2}$, as shown in Figure 3.9).

$$\sigma_{h,bridge,eq} = \frac{(q_b+q_{LL})-(q_{rb}+q_t)}{rr}[a + sin(a)\, cos(a + 2/f)]K_{ar} \quad (3.29)$$

Where α and β (shown in Figure 3.9) are determined following Equations 3.6 and 3.7.

Using this approach, the required reinforcement strength at different depths was calculated (Table 3.6). As shown in this table, the maximum calculated value of T_{req}, which occurs at the top of the GRS abutment, is less than 20 kN/m. This value is less than the allowable reinforcement strength (T_{all}) and therefore no bearing bed reinforcement is needed; however, the minimum requirement is that the bearing bed reinforcement should extend through five courses of blocks (Adams et al. 2011). Consequently, five courses of block was chosen to extend the bearing reinforcement bed in this case (to a depth of 1.0 m below the top of the wall).

Table 3.6 Depth of bearing bed reinforcement calculations

Layer	Dist. from top of wall	Total	Req. Strength	Ultimate Check	2% Check
	z (m)	$\sigma_{h,total}$ (kPa)	T_{req} (kN/m)	$T_{req} > T_{allow}$	$T_{req} > T@2\%$
1	0.20	37.0	19.5	NO	NO
2	0.41	34.2	18.0	NO	NO
3	0.61	30.8	16.2	NO	NO
4	0.81	28.0	14.7	NO	NO
5	1.01	26.0	13.7	NO	NO
6	1.22	24.7	13.0	NO	NO
7	1.42	23.9	12.6	NO	NO
8	1.62	23.4	12.3	NO	NO
9	1.83	23.2	12.2	NO	NO
10	2.03	23.2	12.2	NO	NO
11	2.23	23.3	12.2	NO	NO
12	2.44	23.5	12.4	NO	NO
13	2.64	23.8	12.5	NO	NO
14	2.84	24.2	12.7	NO	NO
15	3.05	24.7	13.0	NO	NO
16	3.25	25.2	13.3	NO	NO
17	3.45	25.8	13.6	NO	NO
18	3.66	26.3	13.9	NO	NO
19	3.86	27.0	14.2	NO	NO
20	4.06	27.6	14.5	NO	NO
21	4.27	28.2	14.9	NO	NO
22	4.47	28.9	15.2	NO	NO
23	4.67	29.6	15.6	NO	NO

3.7 Final typical geometrical section

From the calculations that are described in the previous sections, coupled with the overall project geometrical requirements, the final geometry of the first GRS-IBS to be constructed in Delaware was determined; the pertinent section can be observed in Figure 3.12.

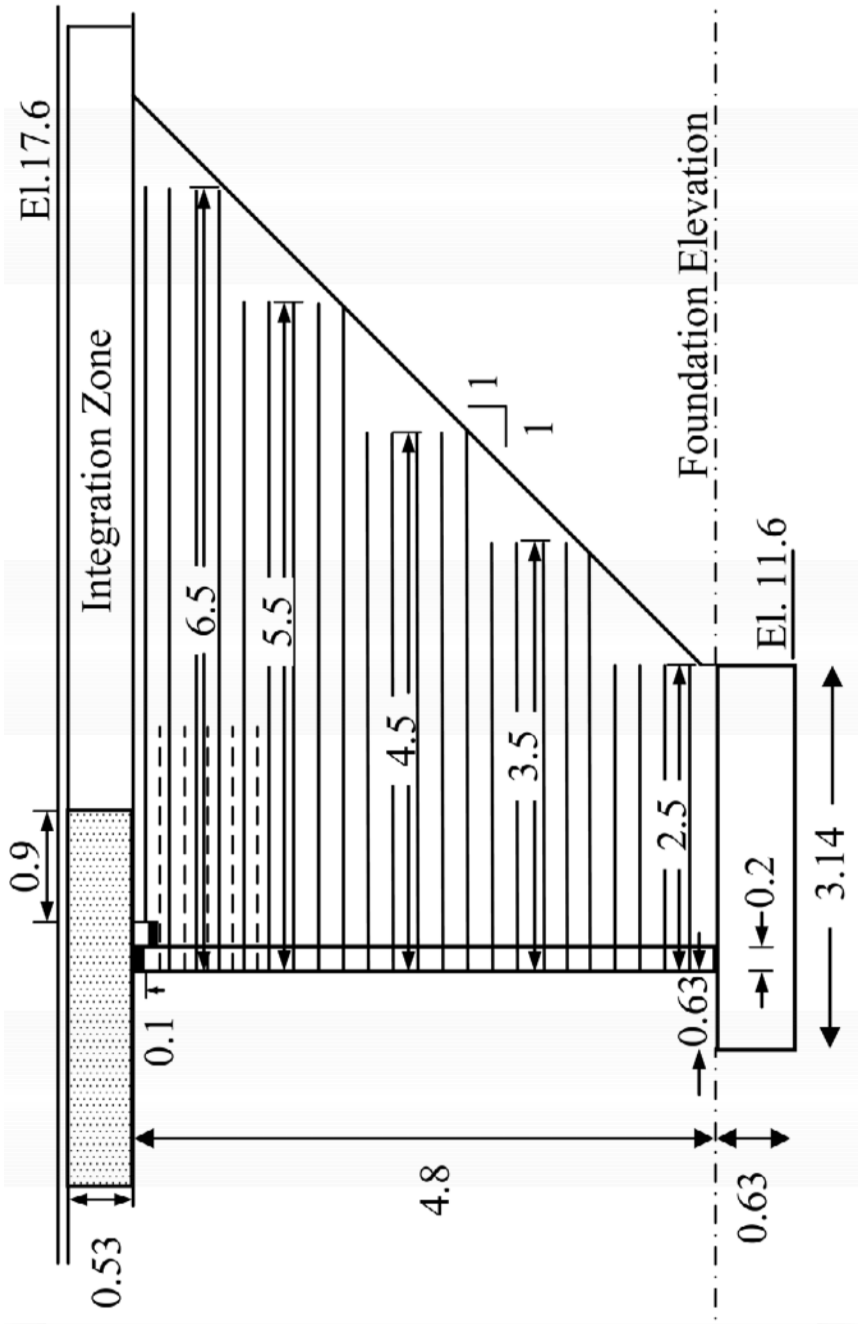

Figure 3.12 Typical section of GRS-IBS wall

3.8. Construction

Construction of Delaware's first GRS-IBS structure, in New Castle County on Chesapeake City Road over Guthrie Run, began in March 2013 via demolition of the existing bridge and abutments at this location. Figure 3.13 shows some photos related to the existing bridge, before and after its demolition. Excavation for the east abutment foundation began on March 22, 2013; construction of the new east abutment was completed on April 5, 2013. Figures 3.14 through 3.19 show photos of the east abutment construction process. Excavation for the west abutment foundation began on April 3, 2013; construction of the new west abutment was completed on April 23, 2013. Figures 3.20 through 3.24 show some photos of the west abutment construction process.

Figure 3.13 Existing bridge before and after demolition

Figure 3.13 (Continued)

Figure 3.14 East abutment excavation and construction (3-25-13)

Figure 3.15 East abutment excavation and construction (3-28-13)

Figure 3.16 East abutment excavation and construction (4-2-13)

Figure 3.17 East abutment excavation and construction (4-3-13)

Figure 3.18 East abutment excavation and construction (4-3-13)

Figure 3.19 East abutment excavation and construction (4-4-13)

Figure 3.20 West abutment excavation and construction (4-4-13)

Figure 3.21 West abutment excavation and construction (4-15-13)

Figure 3.22 West abutment excavation and construction (4-16-13)

Figure 3.23 West abutment excavation and construction (4-17-13)

Figure 3.24 West abutment excavation and construction (4-23-13)

After abutment completion, the bridge beams were placed using a crane on April 25, 2013, and the integrated zone was constructed over the following three weeks. Figure 3.25 and 3.26 show some photos of the bridge placement and integration zone construction process.

Figure 3.25 Bridge placement operation

Figure 3.26 Integration zone construction

After paving and guard rail installation, the GRS-IBS was completed; a picture showing the GRS-IBS in service months after its initial construction (during the first winter) is provided in Figure 3.27. Although this was the first GRS-IBS constructed

in Delaware, the speed of construction was fairly quick, as predicted. It is anticipated that future GRS-IBS projects can be built on an even faster time schedule, as local contractors become more familiar with the technology.

Figure 3.27 Completed bridge and abutments, eight months after construction

3.9 Instrumentation

As this was the first GRS-IBS that had been constructed in Delaware, an instrumentation system was designed to monitor the behavior of the structure over time after construction. Figure 3.28 shows the instrumented section. The instruments shown were located down the roadway centerline. Table 3.7 lists the various sensors that were used, including in-place inclinometers, piezometers, pressure cells, strain gauges, thermistors, volumetric water content sensors, and surveying points. The following sections provide additional details about the purpose of each sensor that was used in the instrumentation system.

Table 3.7 Instrument types, locations, and numbers

Instrument types	Location	No.
Inclinometer sensors	Foundation, West Abutment	4
Piezometers	Foundation, West Abutment	3
Pressure cells	Foundation, GRS Abutment, between Bridge and Integrated Zone, West Abutment	8
Strain gauges	West GRS Abutment, East GRS Abutment and beneath the Bridge	110
Thermistors	West GRS Abutment and East GRS Abutment	50
Volumetric water content sensors	West GRS Abutment	5
Surveying points	West and East Facing Walls	30

3.9.1 Inclinometer Sensors

Four In-Place Inclinometer (IPI) sensors were installed in the clay foundation layer (Figure 3.3) to monitor displacement of this layer during construction and subsequent bridge operations. There is a relatively stiff sandy layer beneath the clay layer; consequently, the inclinometer casing was advanced through the clay layer and was terminated in the sandy soil. Figure 3.29 shows the sensor and its installation at the site.

Given the site foundation conditions, drilling after removal of the existing bridge would have been time consuming and difficult. Consequently, the inclinometer (and piezometer) holes were drilled before deconstruction through the existing bridge abutments, the hole casing was left in place during excavation of the existing abutment,

and the sensors were installed once excavation had reached the base elevation from which new construction was to take place. The IPI sensors that were utilized in this project provide an in-place alternative to traditional traversing probe-type inclinometers, by employing a fixed chain of sensors affixed to a series of connected rods. Vertical biaxial IPIs were used, allowing for displacement measurements in both the N-S and E-W directions.

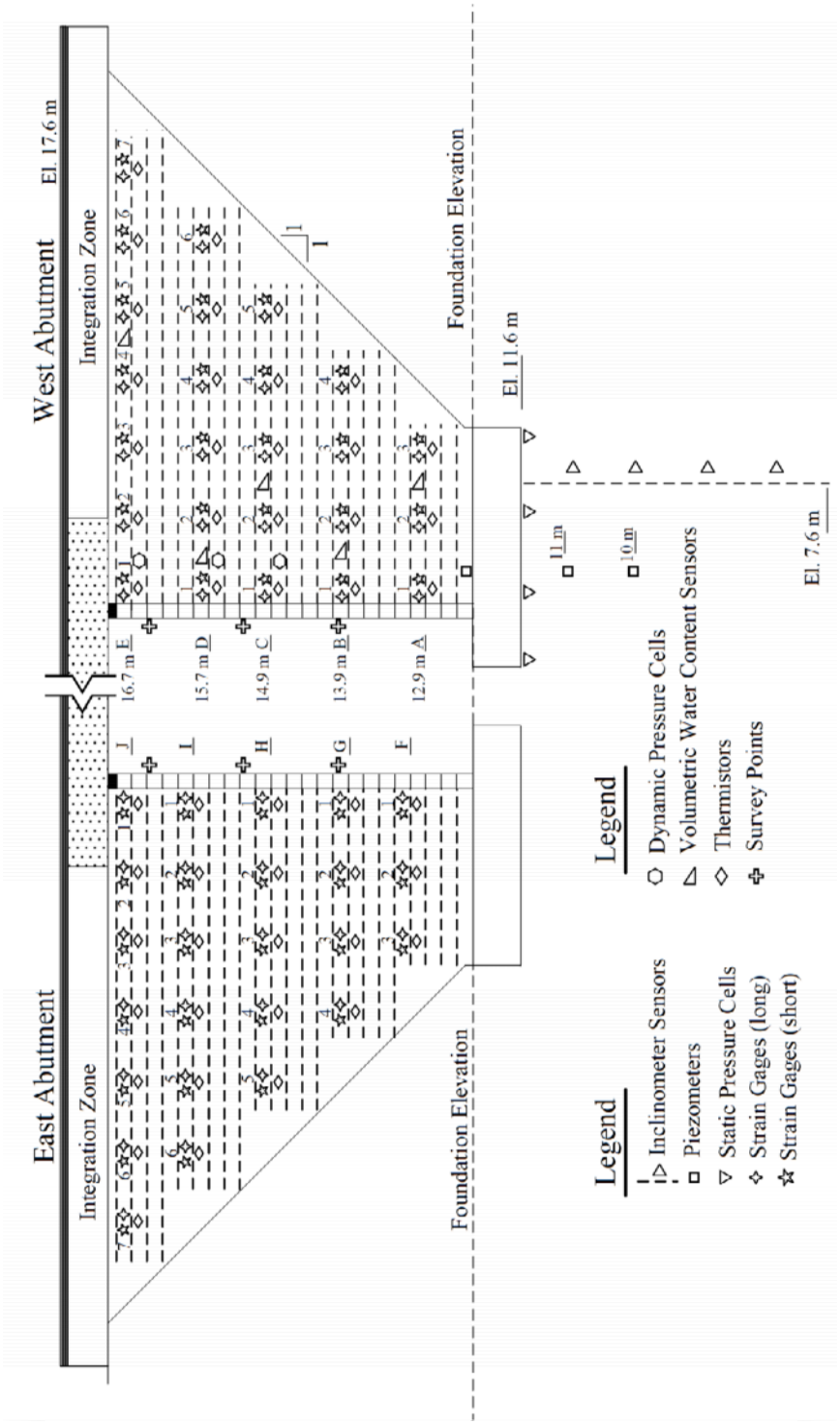

Figure 3.28 Instrumented Section

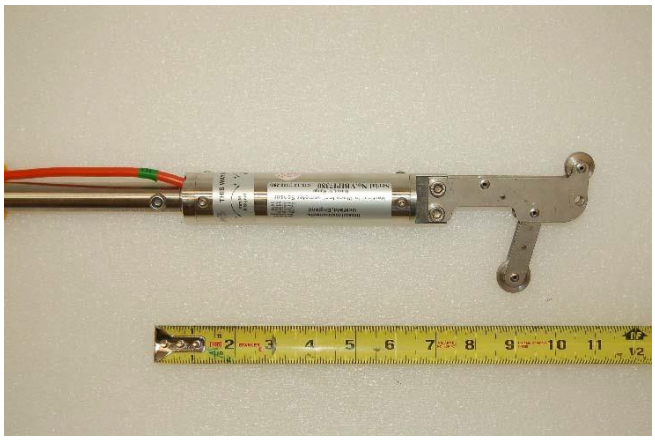

Figure 3.29 Inclinometer sensor and its installation

3.9.2 Piezometers

Three vibrating wire piezometers were installed to monitor pore water pressure in the clay foundation during construction and operation of the GRS-IBS. The pressure range for the installed piezometers was 0-300 kPa. As noted previously, the borehole for the piezometers was drilled before demolition, and the casing that was used to protect the cabling was cut during excavation down to the foundation elevation.

Figure 3.30 shows the piezometer sensor and its installation. The data from the upper piezometer can be used to determine the water elevation in the abutments.

Figure 3.30 Piezometer sensor and its installation

3.9.3 Pressure Cells

Eight vibrating wire pressure cells were installed for the GRS-IBS, including four beneath the foundation, three within the west abutment, and one between the end of the concrete bridge and the integration zone (Figure 3.28). The cells installed in the foundation measured the static pressure and its distribution in the foundation. Finally, the pressure cell between the concrete bridge and integration zone measured the horizontal stress induced by loads and temperature-induced changes in the bridge deck. The pressure cells installed within the abutment are capable of measurement of both static and instantaneous pressure produced by live load on the road provided a data logger with high frequency of data collection is utilized. As seen in Figure 3.31, sand bags were utilized at the top and the bottom of the cells to provide a flat surface around the cells, to hopefully prevent stress concentrations from forming at the location of the sensor. The pressure range for these cells is 0-300 kPa. Figure 3.31 shows a typical pressure cell and its installation process. The results measured using the foundation static pressure cells will be discussed in Chapters 4, 7, 8 and 9. The results measured using the abutment pressure cells will be discussed in Chapters 4, 7 and 9.

Figure 3.31 A total pressure cell and its installation

3.9.4 Strain gauges

Fifty (50) strain gauges (EA-06-20CBW-120 and EP-08-250BG-120 provided by Micro-Measurements) were installed in each abutment to monitor the strain in the geotextile (Figure 3.28). Two different types of strain gauges (long and short) and two different attachment techniques (Leshchinsky and Fowler 1990; Wu et al. 2013) were utilized to assess the effect of the strain gauge installation methodology on the resulting strain readings. Figure 3.32 shows the strain gauges being attached to the geotextile (Figure 3.32a and 3.32b) and their protection in the field (Figure 3.32c). The strain gauges were installed on the geotextiles, waterproofed and wired in the University of Delaware lab before construction (Figure 3.32d). As shown in Figure 3.32, the gauges were protected against the granular fill material by placing sand above and below each sensor area. All operational gauges survived the construction process intact using this installation approach. Ten (10) additional strain gauges were attached on the underside of the bridge beams to monitor the response of the concrete superstructure during GRS-IBS operation (Figure 3.28).

The details regarding the strain gauges preparation, attachment techniques and the corresponding results are presented in the following section.

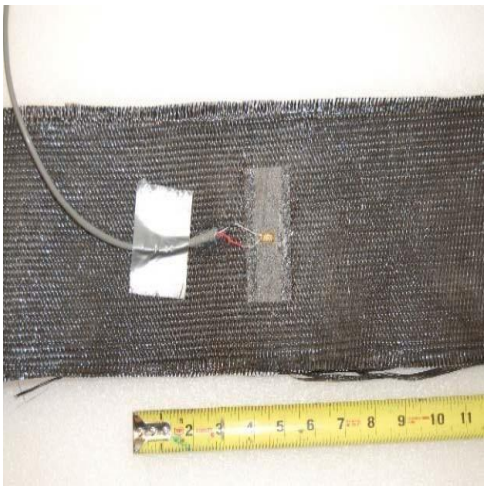

(a)

(b)

(c)

(d)

Figure 3.32 Strain gauges and their installation: (a) short gauge, (b) long gauge, (c) gauge wiring in the lab before their installation at the site, and (d) gauge protection at the site

3.9.4.1 Strain gauges attachment techniques

As noted earlier, two different attachment techniques were utilized to bond the long and short gauges to geotextile layers.

The following steps were followed to attach the long gauges (after Leshchinsky and Fowler, 1999):

1- The geotextile surface was cleaned off with hydrogen peroxide.

2- Dow Corning 3145 Silicone Adhesive (RTV) was applied to the geotextile surface, where the strain gauge is to be placed (Figure 3.33).

Figure 3.33 RTV application to the geotextile surface

3- The RTV was smeared out (with a popsicle stick) so that the underside of the strain gauge and tab were covered (Figure 3.34).

Figure 3.34 RTV smearing out on geotextile

4- Using tweezers, the strain gauge was removed from its packaging, and placed in the RTV that was spread in step 3 (Figure 3.35).

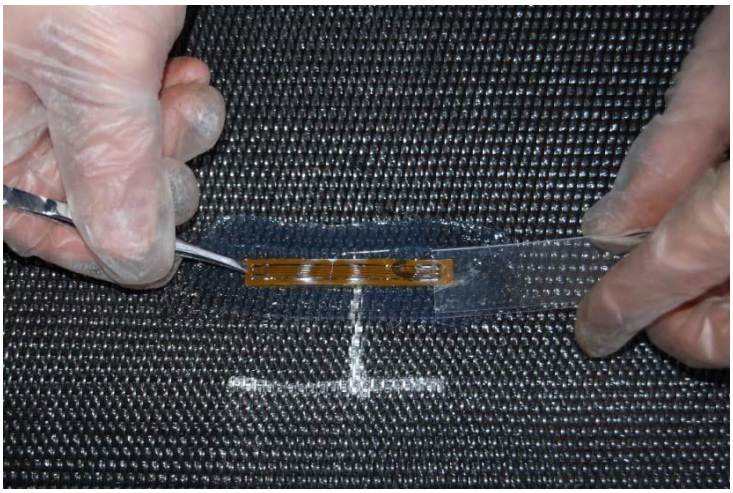

Figure 3.35 Placing strain gauge on the RTV

5- Again using tweezers, a soldering tab was placed about 0.5” (13mm) away from the lead end of the strain gauge.

6- The strain gauge and tab were covered with a piece of Teflon tape (Figure 3.36).

Figure 3.36 Covering the gauge using Teflon tape

7- After the Teflon tape placement, the tape was carefully pressed downward so the gauge and tab were moved into place, becoming embedded into the RTV.

8- A Teflon plate was then placed on top of the Teflon tape. A weight was also placed on top of Teflon plate (Figure 3.37).

Figure 3.37 Placing a Teflon plate and a weight on the gauge

9- The RTV was cured for approximately 24 hours. This time frame was varied using judgment for thicker RTV applications, as necessary.

10- After the time frame set in step 9, the weight and Teflon block were removed after assuring that the RTV was fully dried. The Teflon tape was also removed.

11- Wires were then soldered onto the gauge leads and tabs. (Figure 3.38)

12- To provide a water seal (and provide additional protection), a thick coat of RTV was spread over the top of the gauge, tab and surrounding wires for waterproofing purposes, so that the gauge was effectively sealed (Figure 3.39).

Figure 3.38 Wired long strain gauge

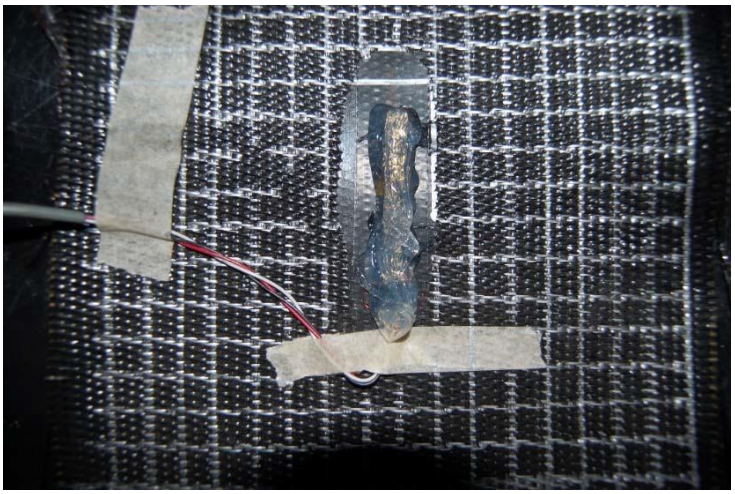

Figure 3.39 Spread RTV on top of the gauge

The following steps were followed in case of short gauges (Wu et al. 2013):

1- A small rectangle of a dummy fabric was cut and was cleaned off with hydrogen peroxide (Figure 3.40).

Figure 3.40 Cleaning off the dummy fabric with hydrogen peroxide

2- The geotextile surface was cleaned off with hydrogen peroxide.

3- Using a small piece of scotch tape, the top surface of the strain gauge was covered and the gauge was placed on the dummy fabric (Figure 3.41).

4- Mbond epoxy provided by VISHAY was mixed in this step and a few drops of epoxy were placed on one end of the underside of the strain gauge using the mixing rod (Figure 3.42).

5- Step 4 was repeated for the opposite end of the strain gauge.

Figure 3.41 Attaching the gauge to the dummy fabric using a piece of scotch tape

Figure 3.42 Adding epoxy to the ends of the gauge

6- Two rubber pads surrounded the tape, gauge and dummy fabric and this pad-dummy fabric-gauge-tape-pad system was compressed using a clamp for about 24 hours (Figure 3.43)

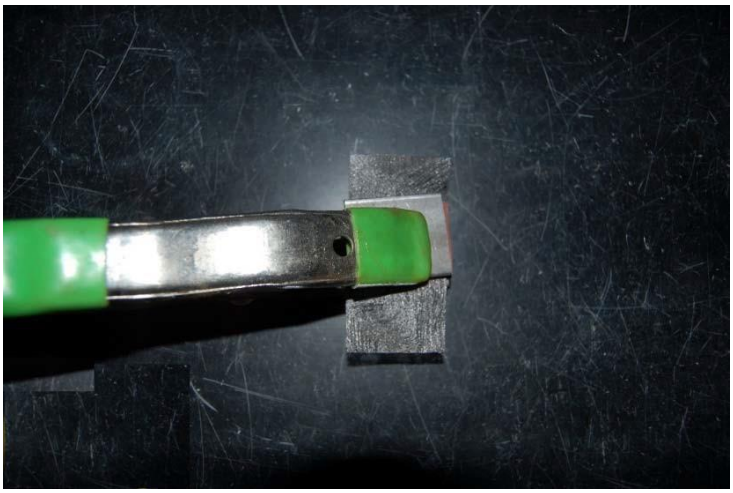

Figure 3.43 Surrounding the gauge using rubber pads and compressing it using a clamp

7- After drying process completed, the scotch tape was removed from the system (Figure 3.44).

8- The dummy fabric (with previously attached strain gauge), was laid down in the location of final attachment on geotextile.

   Epoxy was carefully spread only on each end of the dummy fabric. Then, the dummy fabric/system was flipped over and placed in the location and an additional layer of epoxy was applied to the top surface of the dummy fabric (Figure 3.45).

Figure 3.44 Removing the scotch tape from the system

Figure 3.45 Spreading epoxy only on each end of the dummy fabric

9- After epoxy dried, wires were soldered on the gauge leads and M coat B provided by micromeasurement was utilized to waterproof the strain gauges. Figure 3.46 displays an attached short strain gauge on the geotextile after wiring and waterproofing.

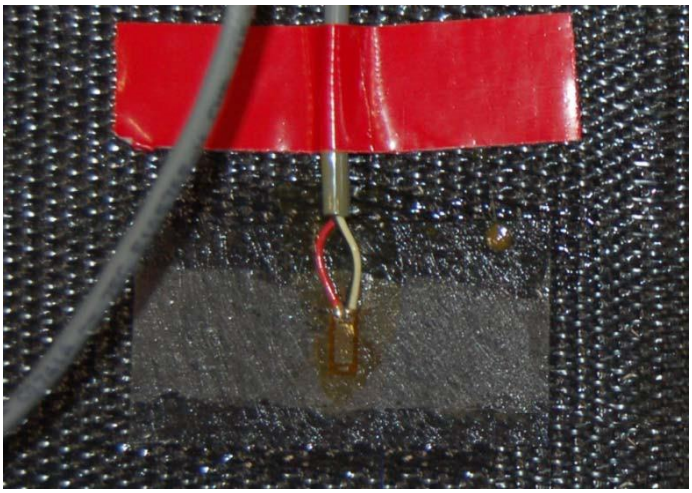

Figure 3.46 Wired short gauge

3.9.5 Thermistors

Twenty-five (25) thermistors (the YSI 55000 series, provided by Therm-x) were installed per abutment to monitor temperature and its effect on measured strains in the geotextile (Figure 3.28). The thermistors were waterproofed and wired in the University of Delaware lab before construction. One thermistor was placed at each installed strain-gauge location on the geotextile (between the two types of strain gauges that were installed), as shown in Figure 3.28. Figure 3.47 shows a typical thermistor and its installation. The goal of using thermistors was to investigate the effect of the temperature on the readings. The details about this effect will be discussed in more detail in Chapters 5 and 6.

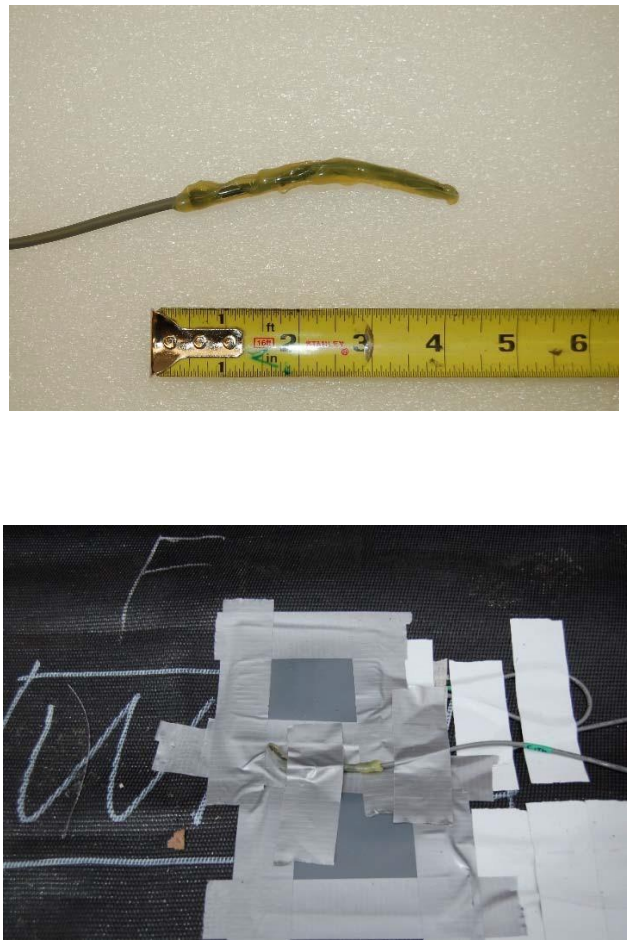

Figure 3.47 Thermistor and its installation

3.9.5.1 Thermistors waterproofing procedure

Before their installation, the thermistors were waterproofed for protection against existing water in the abutment. The waterproofing process that was utilized was as follows:

- 24 AWG 3 conductor wire provided by Carol was utilized in this project to connect the thermistors to the data acquisition system. In order to connect the wire to the thermistor, approximately 2 to 3 cm of one end of each wire was stripped and tinned.

- 3/32" (nominal) Polyolefin heat shrink tubing was first slid over the end of the wire.

- In the next step, poly tubing was utilized around the thermistor. First, one piece of Tygon Micro Bore PVC Tubing .020" ID x .060" OD was cut and slid over one of the thermistor leads. Then, one of the conductors was soldered to the lead.

- After that, the small diameter heat shrink tubing was slid onto the unsoldered lead of the extension wire. The purpose of this heat shrink tubing is to isolate the two leads, not to isolate the second lead from the environment. Then the other conductor was soldered to the unsoldered lead of the thermistor. Figure 3.48 displays the wire, soldered thermistor with the small heat shrink and PVC tubing on.

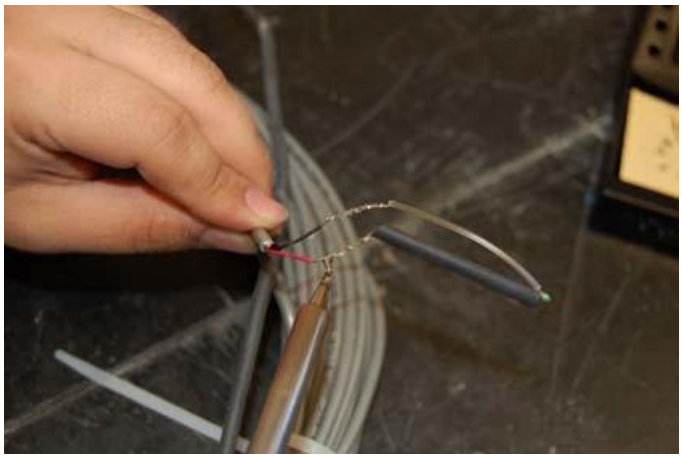

Figure 3.48 The soldered thermistor with the PVC and small diameter shrink tubing

- In this step, the small diameter heat shrink tubing was slid down to cover the second solder joint. Then the lighter was utilized to shrink the tubing, as shown in Figure 3.49.

Figure 3.49 Shrinking the heat shrink tubing around the thermistor

- The large diameter shrink tubing was then slid down to cover the two solder joints. This tubing was then shrunk using a heat gun. Figure 3.50 shows the large diameter shrink tubing covering the whole thermistor length.

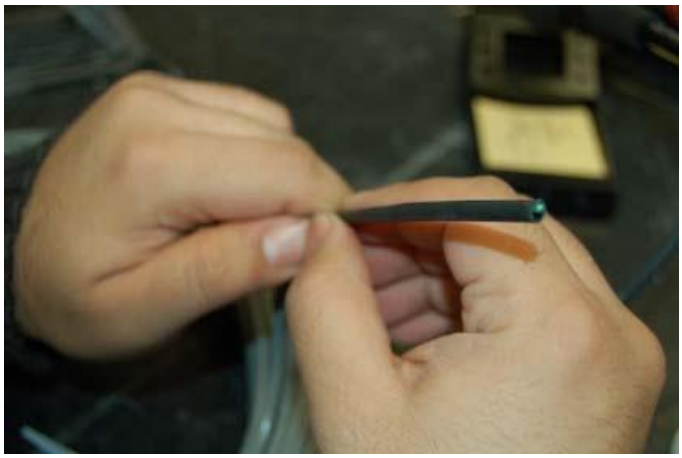

Figure 3.50 Sliding the large diameter heat shrink tubing to cover the thermistor leads

- Finally, to make the thermistor as waterproof as possible, it was completely covered by hot glue, as shown in Figure 3.51. As can be observed in this figure, the hot glue formed a thick layer over the thermistor probe.

Figure 3.51 Hot glue utilization to waterproof the thermistor

3.9.6 Volumetric moisture content sensors

Five volumetric moisture content sensors (MAS-1, provided by Decagon) were installed in the west abutment to monitor soil moisture content and its effect on strains in the geotextile (Figure 3.28). The effect of increase in water content because of precipitation or increase in river water level on the structure's response was investigated by these sensors. Figure 3.52 shows a typical MAS-1 sensor.

Figure 3.52 Volumetric moisture content sensor

3.9.7 Surveying targets

Fifteen surveying targets were installed in each abutment to monitor facing wall deflection during GRS-IBS operation. The targets were installed on both abutments at three elevations, and there are five targets at each elevation across the facing walls. The data were collected on a weekly basis for the first year of the project, a reading

frequency which was then changed to monthly after the first year, once no significant displacements had been observed. The finest graduation of surveying measurement was 0.02 ft (or 6 mm) in the surveying operation. Figure 3.53 and Figure 3.54 show the surveying points that were used on the west and the east abutment, respectively. The corresponding surveying results are presented and discussed in Chapters 4, 7 and 9.

Figure 3.53 Surveying points on the west abutment

Figure 3.54 Surveying points on the east abutment

3.10 Data collection process

For the west abutment, a data logger system provided by itmsoil USA was utilized for data collection. Logger 1 consists of the following components:

- One CR1000 data logging and control module
- One AVW200 vibrating wiring sensor interface
- One PS100 power supply
- Three BCM-1's bridge completion modules
- Six AM16/32 multiplexers
- Two 16" x 16" GRP enclosures

Based on the types of the readings taken, different multiplexer configurations were utilized and the sensors were connected to the corresponding multiplexer. The inclinometer sensors, piezometers, static pressure cells and strain gauge data were collected by this logger.

Logger 2 consists of the following components:

- One CR800 data logging and control module
- Three AM16/32 multiplexers
- One 16" x 16" GRP enclosures

All items above were installed in one enclosure. The thermistors, dynamic pressure cells and volumetric water content sensors data were collected by this logger.

The logger is programmed with CRBasic. The source code of the logger program named Logger1 CR1000.CR1 is supplied on the USB drive. It can be viewed with an ASCII editor such as Notepad. The logger program was already loaded into logger 1 by itmsoil USA before shipping. The PC200W program provided by itmsoil USA was used to send the program to the logger.

Figure 3.55 and Figure 3.56 illustrated the implemented loggers for this project.

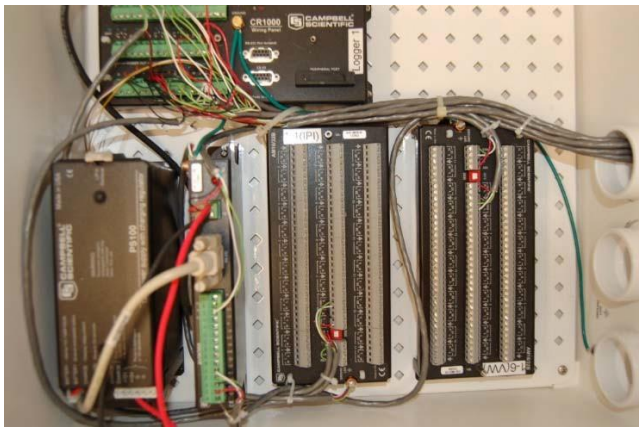

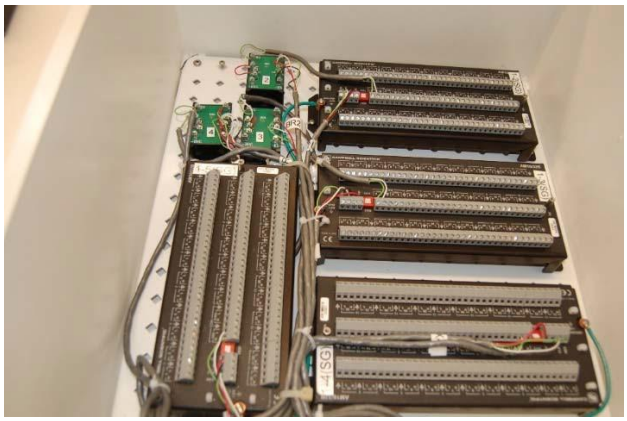

Figure 3.55 Logger CR1000 and its multiplexers

Figure 3.56 Logger CR800 and its multiplexers

For 75 sensors installed in the east abutment, two rotary data switches manufactured by Omega (OSWG5-40) were utilized to collect the data, as shown in Figure 3.57. In case of the east abutment, the raw data (in ohms) was taken manually approximately every week over the long term using the rotary switches. In the early stages of the project (i.e., immediately post-construction), the data was collected every day to monitor the stability of the abutment.

Figure 3.57 The rotary data switches, (a) front view, (b) back view

For the west abutment, simultaneous recordings of sensor data were collected every 10 minutes using the loggers provided by itmsoil USA. This short time interval data collection was selected to assure that high quality data were collected and the data for any incidence such as raining or increase in river water level were available. This implies that a large dataset was collected and the length of the dataset increased over time post-construction. However, collecting this large amount of data came with some cost. Managing and analyzing this large amount of data to investigate the change in trends of different responses is not an easy task and could not be done manually. It was decided to use a powerful program which could handle a large dataset and its related analysis requirements. As a result, the R programming language was selected for this purpose. The details pertaining to the R program and the data management procedure that was utilized are discussed in Chapter 5.

REFERENCES

Adams, M., Nicks, J., Stabile, T., Wu, J., Schelatter, W. and Hartmann, J. (2011). "Geosynthetic Reinforced Soil Integrated Bridge System Interim Implementation Guide", Federal Highway Administration, Publication No. FHWA-HRT-11-026, Washington, DC.

AASHTO (2010). LRFD Bridge Design Specifications, Fifth Edition, American Association of State Highway and Transportation Officials, Washington, DC.

Delaware department of transportation (2001), "Standard Specifications for Road and Bridge Construction Manual".

GEO-SLOPE Ltd., (2010). Stability modeling With SLOPE/W 2007 Version: An engineering methodology [Computer Program]. GEO-SLOPE International Ltd., Calgary, Alberta, Canada

Leshchinsky, D., and Fowler, J. (1990). "Laboratory measurement of load-elongation relationship of high-strength geotextiles" Geotextiles and Geomembranes, 9(2), 145-164.

Wu, J., Nicks, J., Pham, T.and Adams, M. (2013). "Composite Behavior of Geosynthetic Reinforced Soil Mass", Federal Highway Administration, Publication No. FHWA-HRT-10-077, Washington, DC.

Chapter 4

RECORDED SENSOR DATA DURING CONSTRUCTION, DURING LIVE LOAD TESTING, AND OVER THE LONG TERM

4.1 Introduction

As described in Chapter 3, different types of instruments including inclinometers, piezometers, total pressure cells, strain gauges, thermistors, water content sensors, and surveying targets were installed in both of the GRS-IBS abutments. These instruments were utilized to monitor the structure's responses during construction, during live load testing, and over the long term, during the first three years of the structure's operational life. The purpose of this chapter is to present the recorded sensor data during these three different time periods; this data will then be examined in closer detail in subsequent chapters of this report.

4.2 Volumetric water content sensors

As discussed in Chapter 3, five volumetric water content sensors were installed in the west abutment in order to measure the change in the moisture content of the abutment and its possible effects on the response of the structure. Figure 4.1 depicts the changes in the west abutment volumetric water content during live load testing, and over a three-year period post-construction. No data was recorded using these sensors during the construction process.

As shown in Figure 4.1, the volumetric water content is fairly constant for most of the period of observation, varying in the range of 20-25% for most of the sensors. Sensor t5, the lowermost sensor, stopped working after a few months. The reason for this sensor failure is not clear, but may have been due to waterproofing issues with the sensor, as this sensor is generally always submerged.

The later winter and spring months tended to exhibit a fairly significant increase in volumetric moisture content, which was observed across the three years of monitoring. This behavior is not surprising, given Delaware's generally wet spring weather, which can increase water infiltration into the abutment, and which can also cause the water level in the river channel to increase significantly. Interestingly, the peak moisture content values for the second year and the beginning of the third year were appreciably higher than the first year. The data from sensor t4 has fluctuated more than the other three working sensors. This is not surprising, as this sensor is generally located near the surface of the water level in the channel beneath the bridge; this water level tends to fluctuate with different weather events and the associated water runoff conditions that then feed water into the channel beneath the bridge.

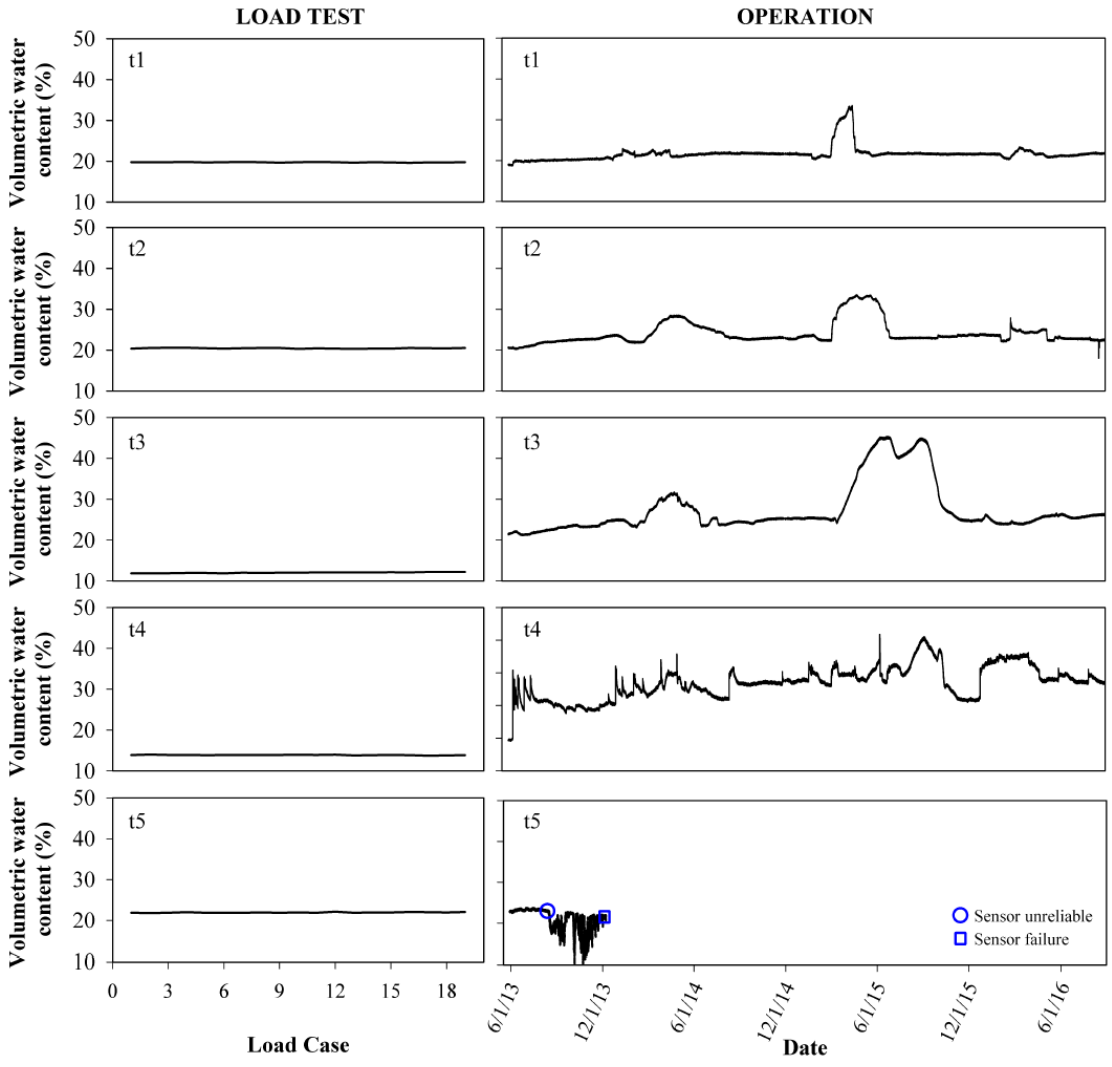

Figure 4.1 Change in the west abutment volumetric water content during load testing and over more than three years of operation

4.3 Thermistors

As discussed in Chapter 3, there are 50 thermistors installed in this project, 25 per abutment. The thermistors were installed at the same location as the strain gauges

to investigate the effect of temperature changes on the gauge readings. Figure 4.2 presents the changes in thermistor temperatures for all instrumented layers in the west abutment (A to E) during construction, load testing and for the first three years of operation.

The temperature data for the thermistors installed in the east abutment were collected manually using a rotary switch data logger. Figure 4.3 presents the corresponding results for the installed thermistors in the east abutment. Based on the collected data, the seasonal temperature changes in both abutments follow the same trend, which is rational. However, since the data for the east abutment were collected manually approximately every two to three weeks, the daily changes in temperature were not measured for the east abutment.

For comparison purposes, Figure 4.4 shows the ambient air temperature recorded at the datalogger location, over the same monitoring period as the abutments. As shown, changes in abutment temperature follow changes in ambient air temperature, in a logical fashion. The temperature recorded by the thermistors closest to the facing wall (i.e., A1-E1) generally experienced more fluctuation in response to daily, weekly, or monthly ambient temperature changes, while thermistors located further from the face of the abutment (i.e., A3-E7) generally responded more slowly, following seasonal fluctuations in ambient air temperature. In a similar fashion, the top layer of geosynthetic (Layer E) generally fluctuated more in temperature then deeper embedded layers (i.e., Layer A or B), with the general trend in behavior trending consistently with depth.

A few of the thermistors began exhibiting unusual measurements or stopped working outright during the long-term monitoring process, i.e. A1-th, A-2th, A3-th, C1-th, C4-th, D2-th, G1-th, H2-th, J6-th and J7-th, as shown in Figures. 4.2 and 4.3. The reason for sensor failure is not clear from the data that is presented; it is speculated that the presence of water or moisture is potentially to blame, as the lowest thermistors located in Layer A (beneath the general level of water in the channel) exhibited a higher failure rate than elsewhere in the abutment. Failure of other sensors may have been caused by eventual failure of the sensor waterproofing over time.

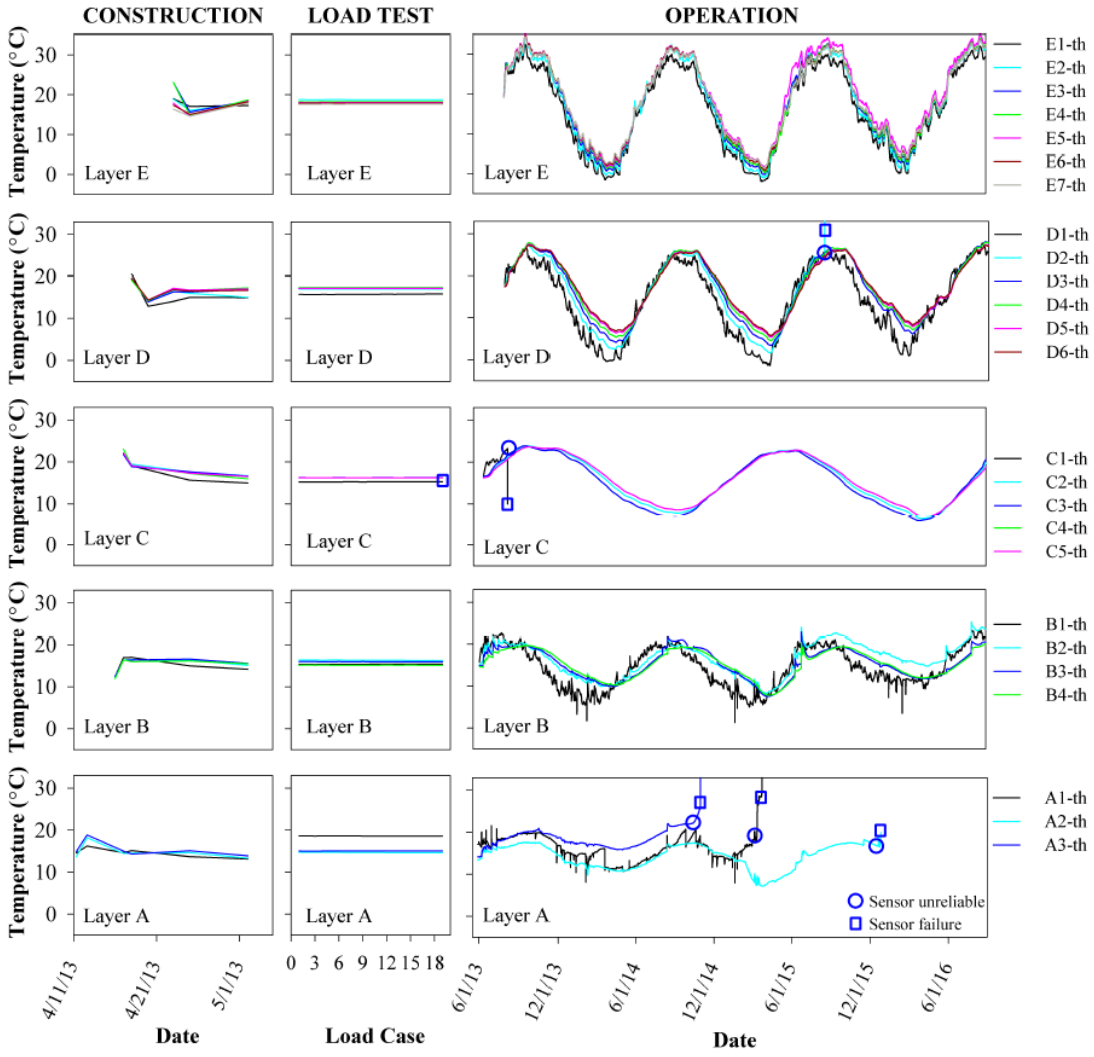

Figure 4.2 Temperature recorded by the thermistors in the west abutment during construction, load testing and for three years of operation

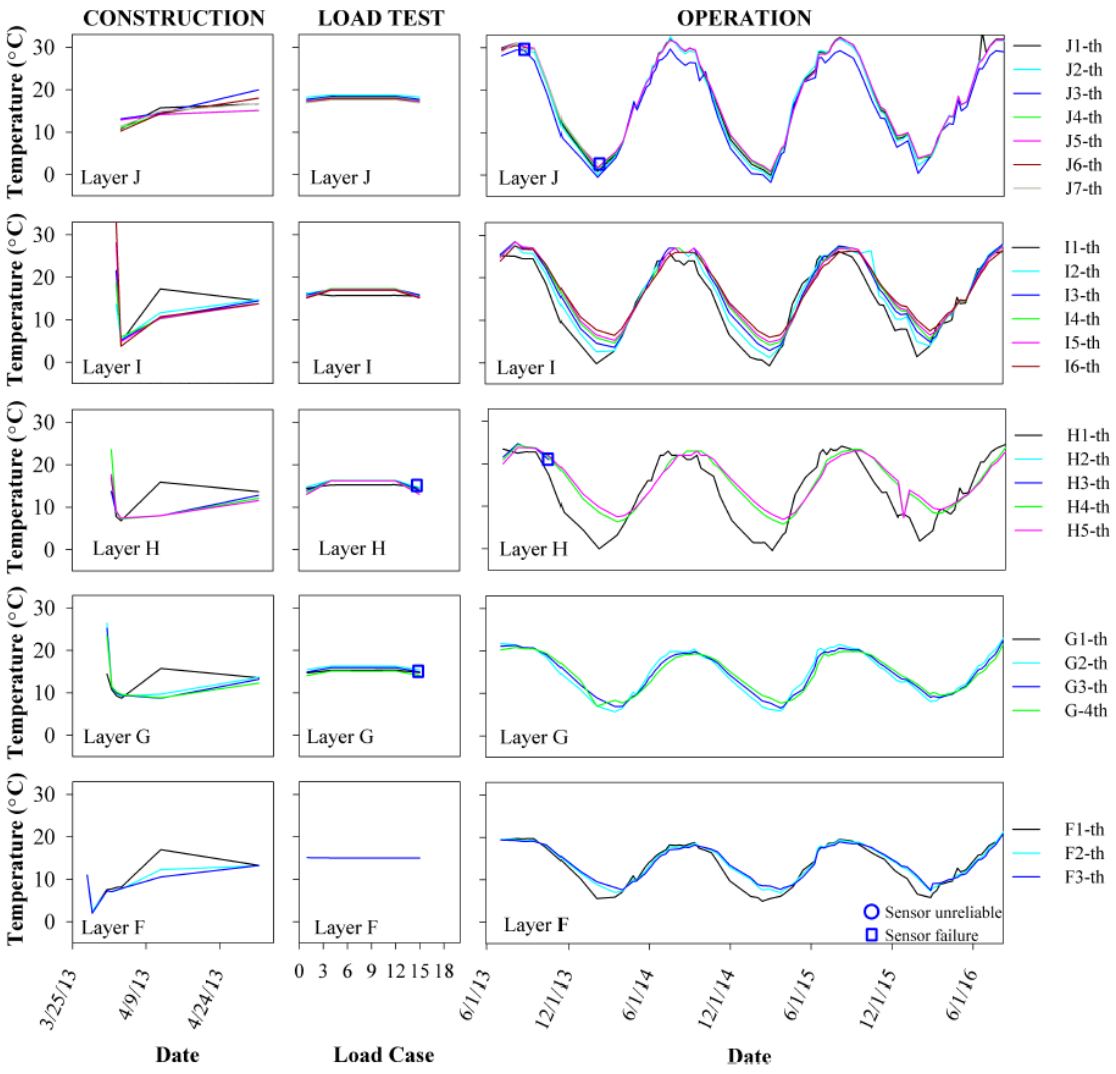

Figure 4.3 Temperature recorded by the thermistors in the east abutment during construction, load testing and for three years of operation

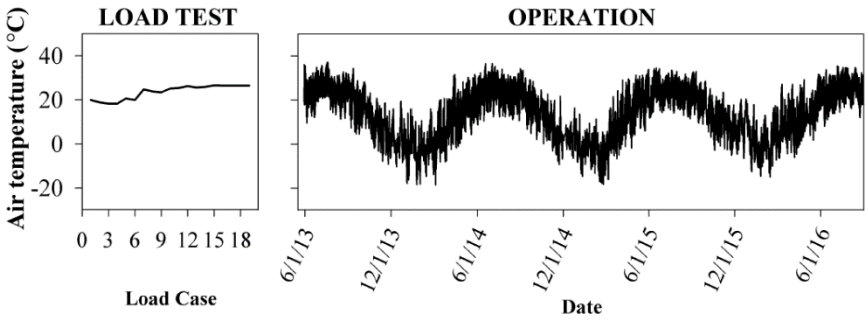

Figure 4.4 Air temperature recorded by the datalogger

4.4 Surveying targets

Surveying of mounted targets for this project was performed by DelDOT personal using a TOPCON Pulse Total Station, GPT-3000 series instrument, survey legs tripod legs, prisms and mini prisms. The measurement precision and resolution for the utilized system was 6 mm and 0.3 mm, respectively. The state plane coordinate system (SPCS) was implemented as the surveying grid in this project. As discussed previously in Chapter 3, there were 15 targets installed on each facing wall in three rows and five columns. Both lateral deflection and settlement were measured during the surveying process. Figure 4.5 shows the lateral (horizontal) deflection of the installed targets on the middle section of the east abutment right beneath the road centerline, while Figure 4.6 presents the same data for the middle section of the west abutment. In both of these figures, data are shown for the live load test and over three years of operation post-construction. Surveying data was not available during the construction phase for this project because the surveying targets were not installed until after the GRS abutments

had been completely constructed. Figure 4.7 shows the settlement of the installed targets on the middle section of the east abutment right beneath the road centerline. Figure 4.8 presents the same data for the middle section of the west abutment.

Also shown in Figures 4.5 through 4.8 is a grayscale error band that illustrates the general measurement uncertainty associated with the surveying technique that was utilized for the current study. The magnitude of this error band was determined based on the general precision of the surveying operation ($\pm$6 mm). As shown, measured deflection readings tended to not fluctuate significantly outside of the expected error band. Measured horizontal deflections were generally in the range of 2-10 mm over time, and measured settlements were generally in the range of 0-5 mm over time. The fluctuations in movement that were observed can reasonably be attributed to errors associated with the surveying process that was utilized. Overall, measured horizontal deflections did not exceed 10 mm, and measured settlements did not exceed 10 mm.

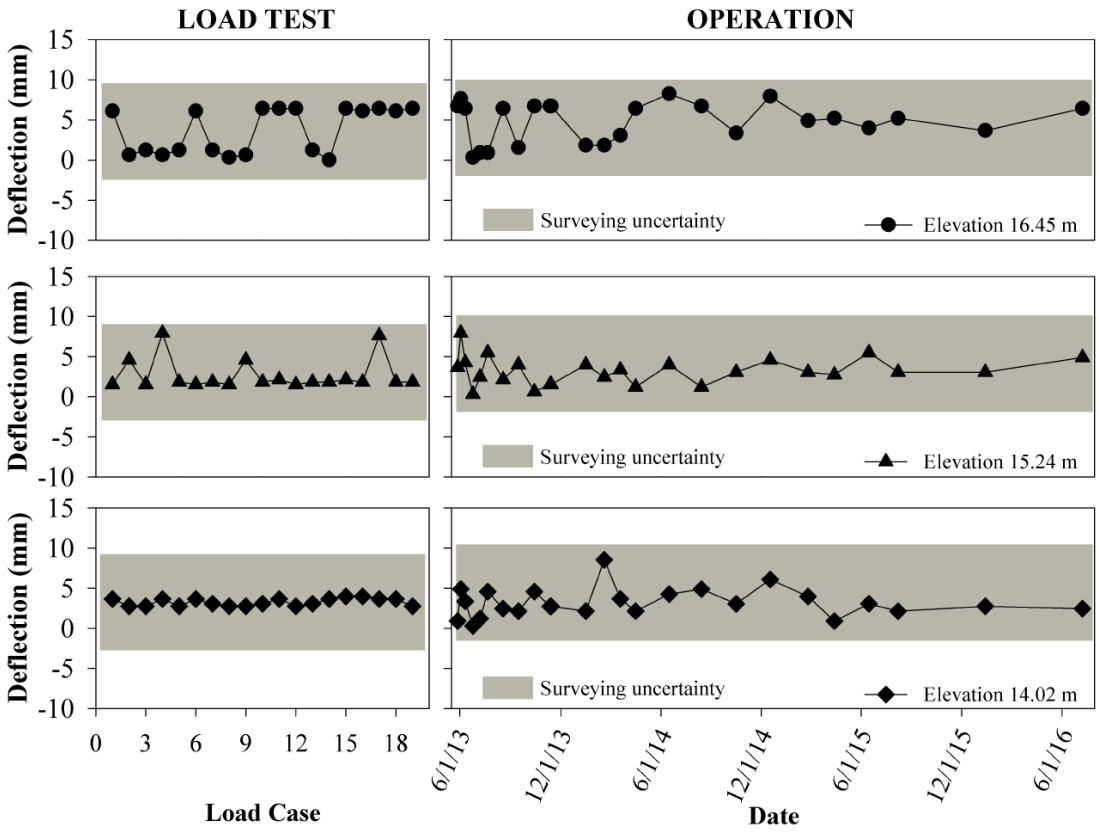

Figure 4.5 Lateral deflection of the east facing wall at the abutment centerline

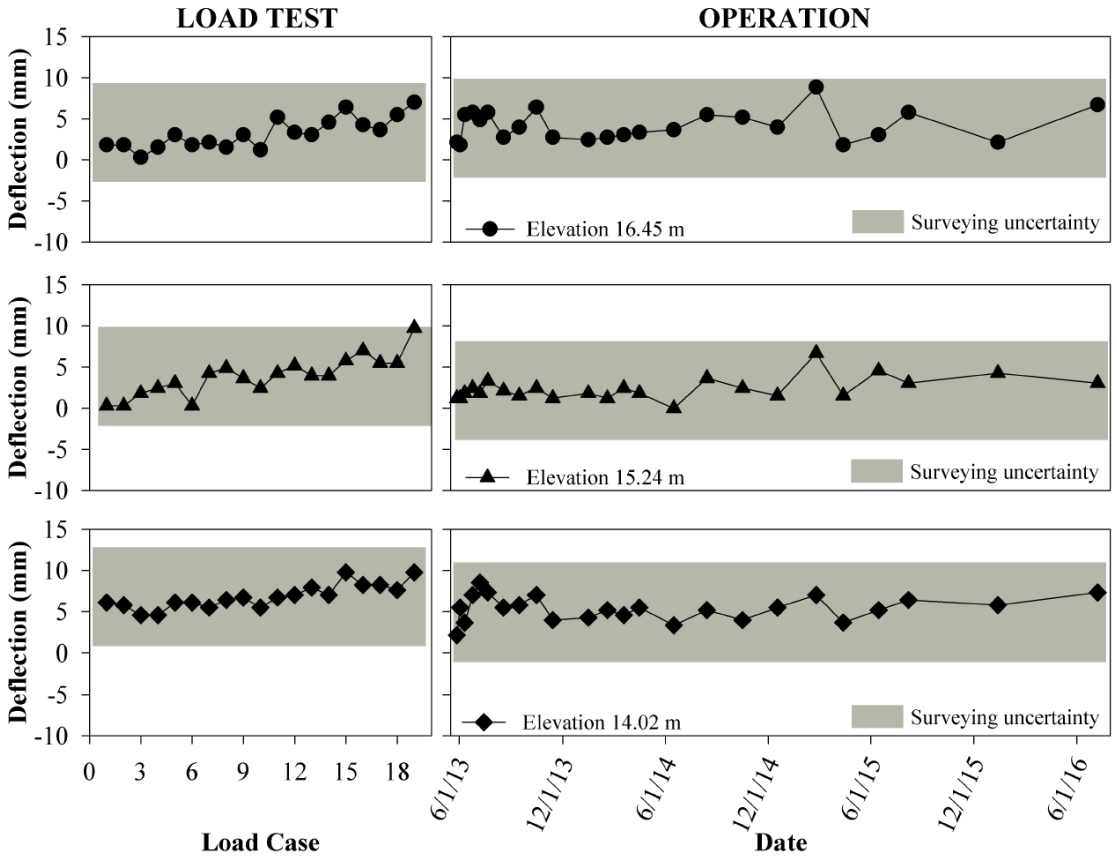

Figure 4.6 Lateral deflection of the west facing wall at the abutment centerline

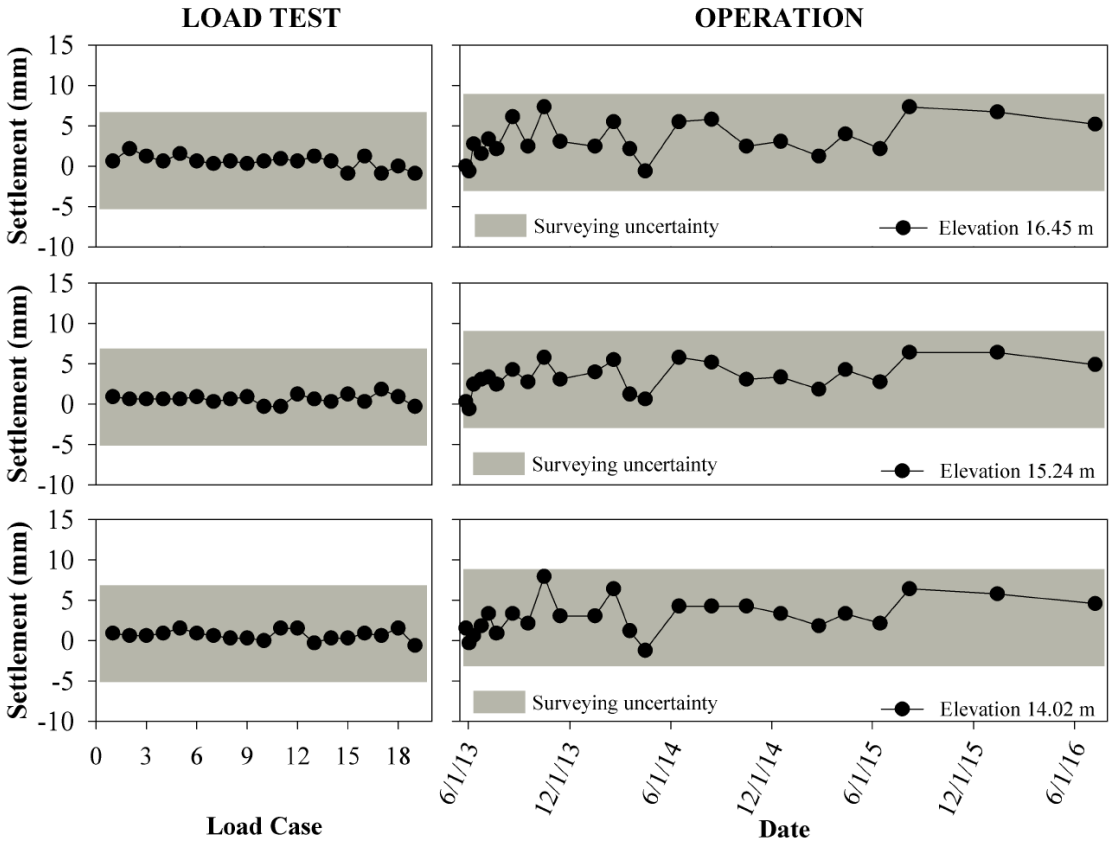

Figure 4.7 Settlement of the east facing wall at the abutment centerline

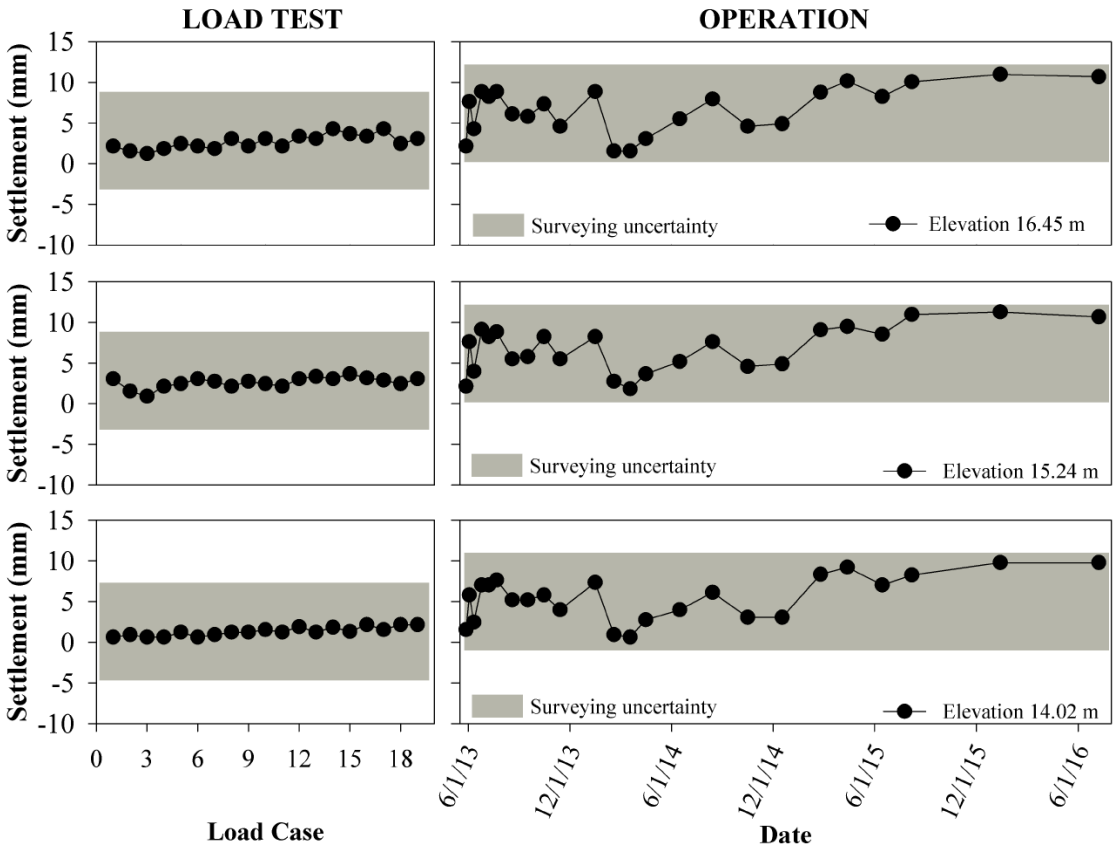

Figure 4.8 Settlement of the west facing wall at the abutment centerline

Figures 4.9 through 4.24 show the measured deflection and settlement for cross-sections through the west and east facing walls of the GRS-IBS that are offset from the abutment/bridge centerline. For comparison purpose, the corresponding data for the same elevation of the middle section are also presented in these figures. As shown, the measured values for these other targets are generally in the same range as the measured values for the targets on the centerline. This data demonstrates that overall the movement of the facing walls either horizontally or vertically was very low for both abutments, within the range of error for the surveying method that was utilized. This relatively small amount of movement should correspond to fairly low induced strains in

the geosynthetic reinforcement; this behavior will be examined in more detail later in this chapter and in subsequent chapters.

It can be noted that the error position (the mean position of the long-term recorded data) is sometimes offset slightly between the load test period and the long-term operation period. This offset can be observed in many of the figures that are shown in this section, with a shift that is typically on the order of a few millimeters; from this observation, it could possibly be inferred that the facing walls continued to deform slightly from the construction induced loads and load test loads into the long-term operational period.

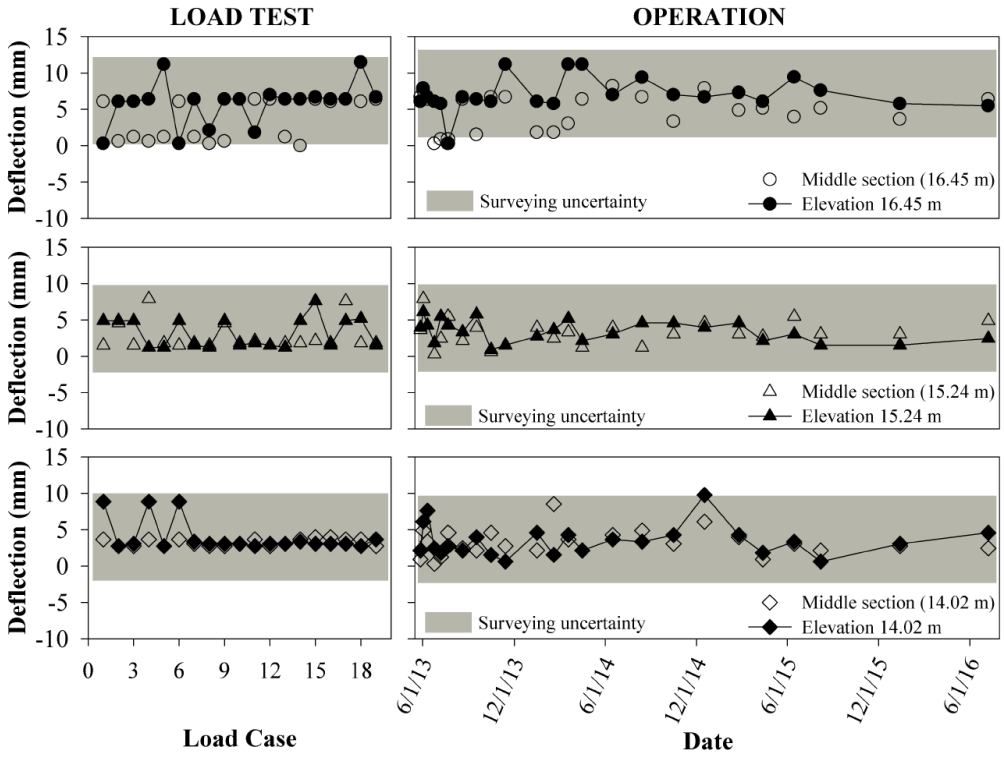

Figure 4.9 Lateral deflection of the east facing wall at 5.6 m offset from the abutment centerline, in the upstream direction

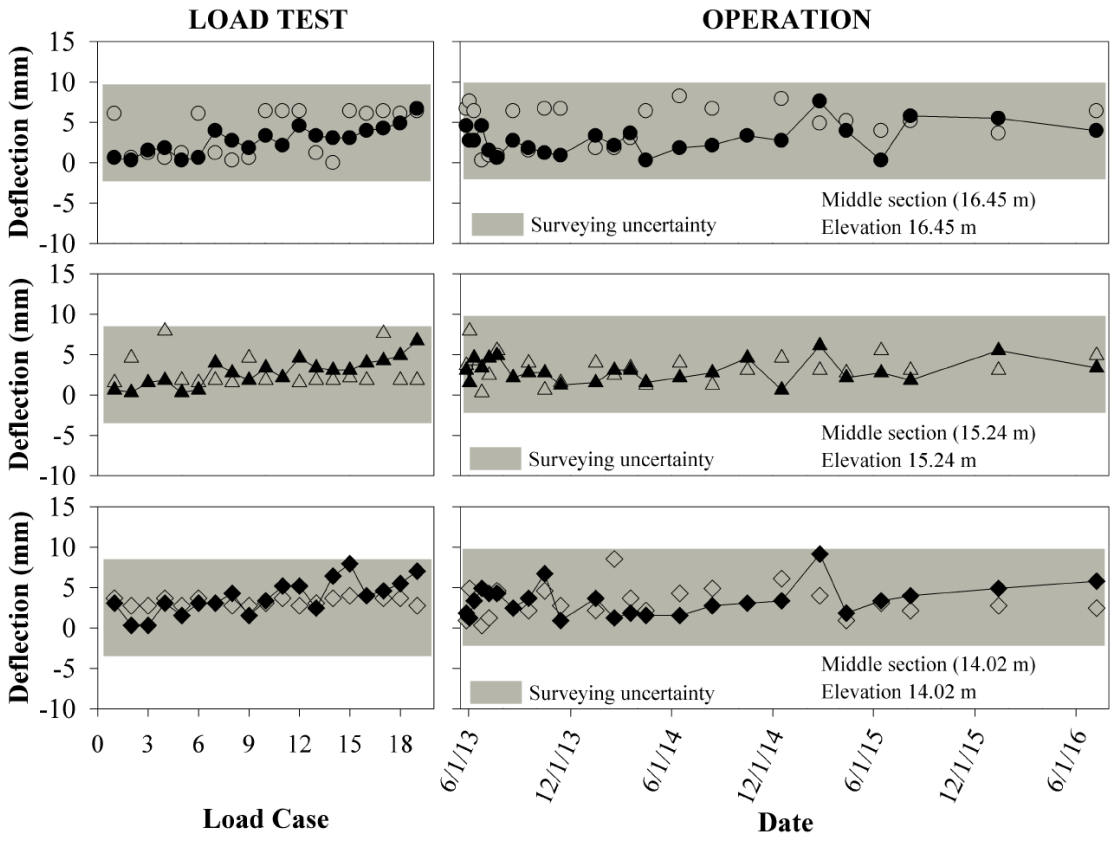

Figure 4.10 Lateral deflection of the west facing wall at 5.6 m offset from the abutment centerline, in the upstream direction

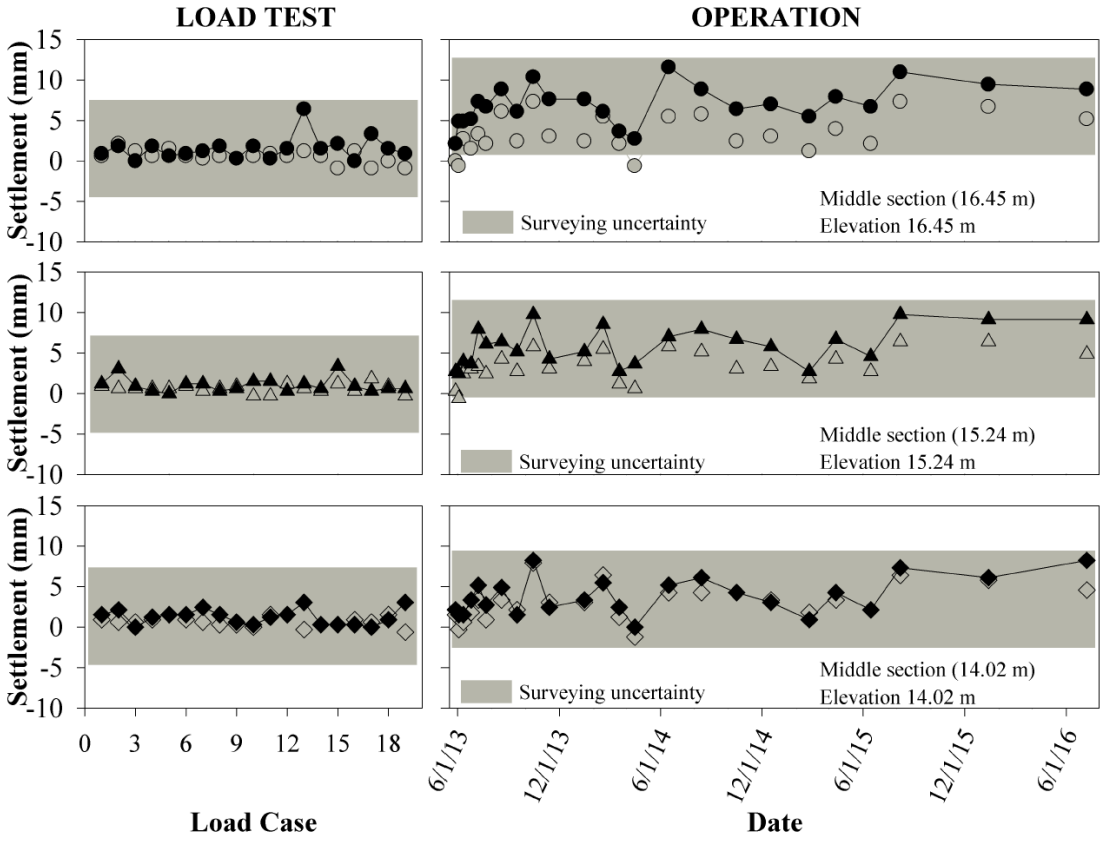

Figure 4.11 Settlement of the east facing wall at 5.6 m offset from the abutment centerline, in the upstream direction

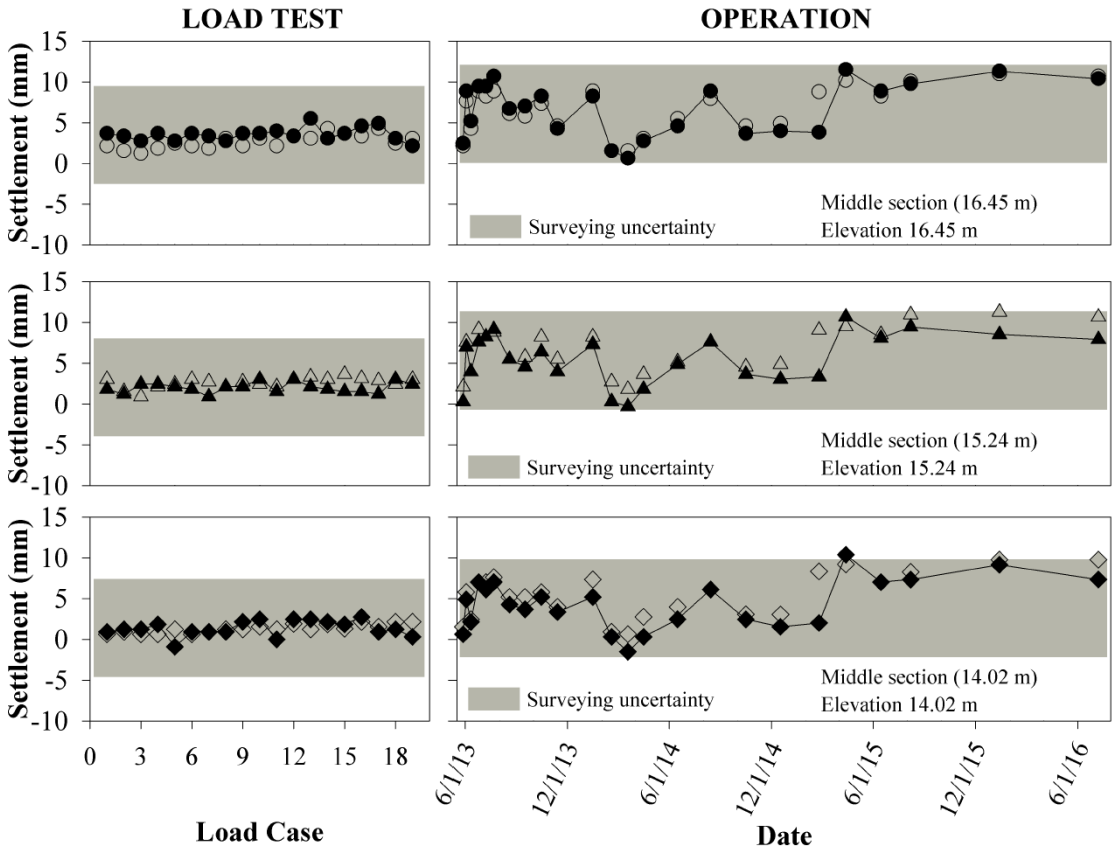

Figure 4.12 Settlement of the west facing wall at 5.6 m offset from the abutment centerline, in the upstream direction

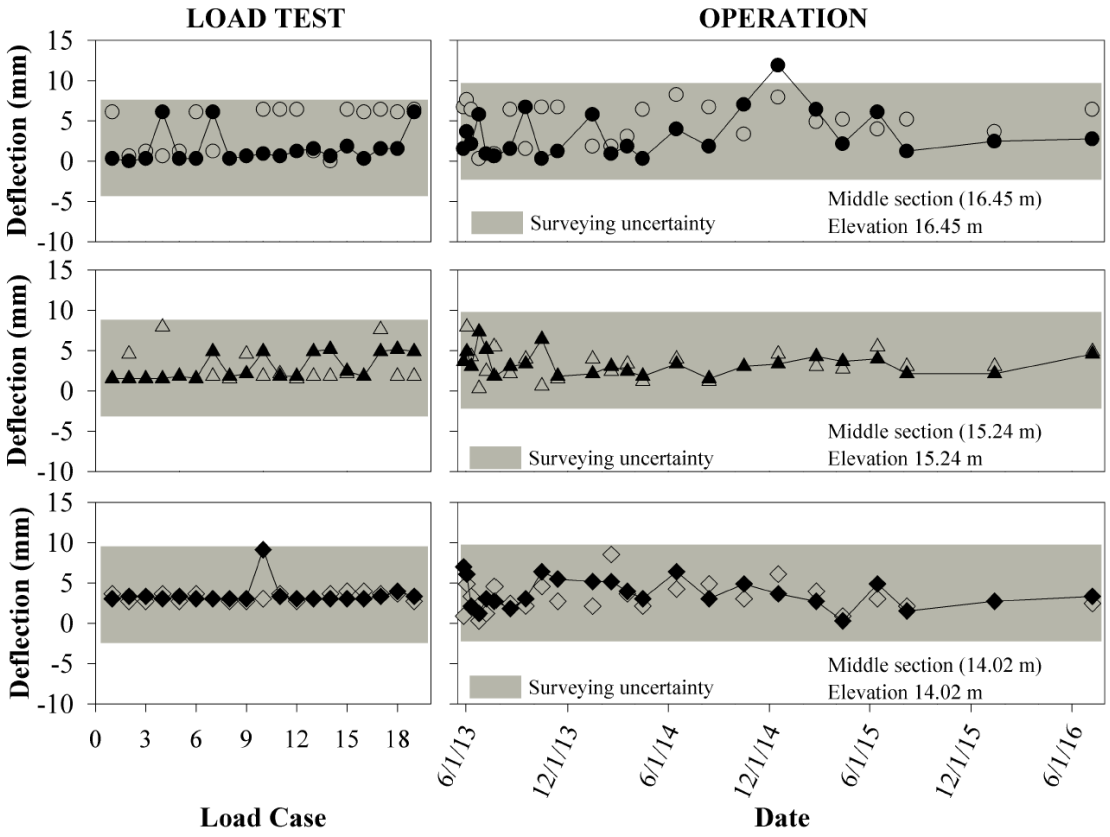

Figure 4.13 Lateral deflection of the east facing wall at 2.8 m offset from the abutment centerline, in the upstream direction

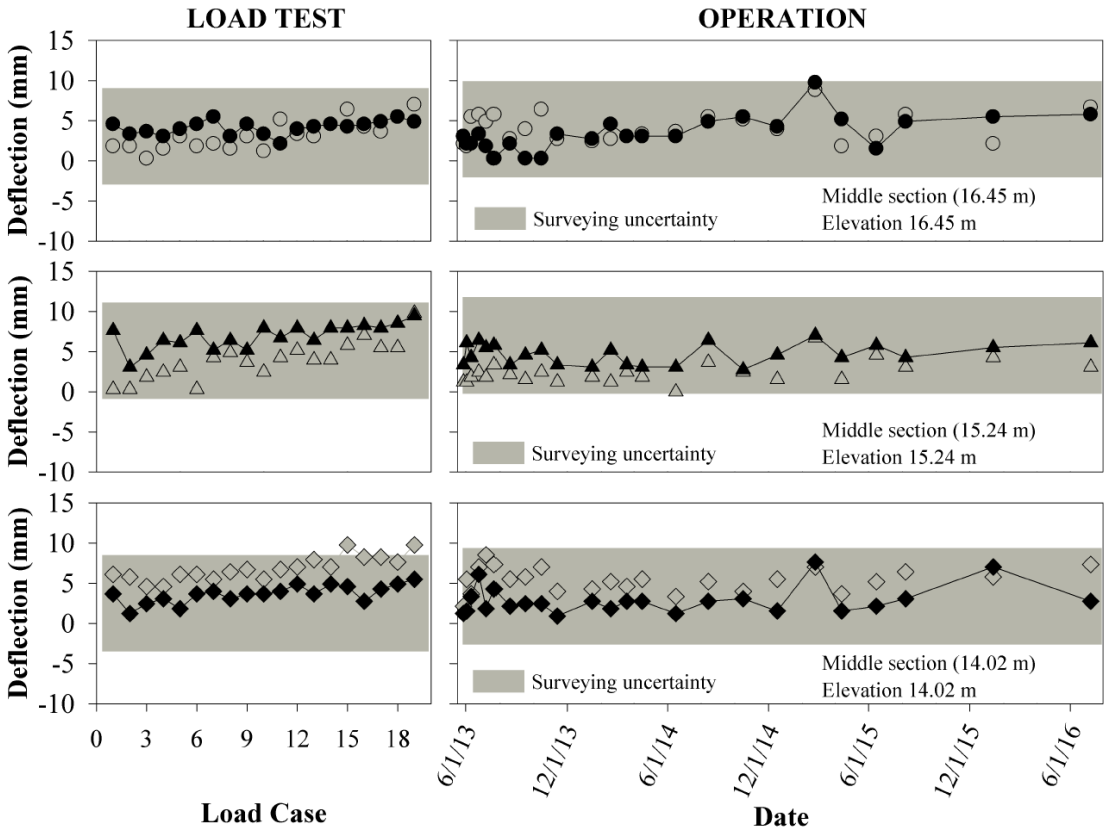

Figure 4.14 Lateral deflection of the west facing wall at 2.8 m offset from the abutment centerline, in the upstream direction

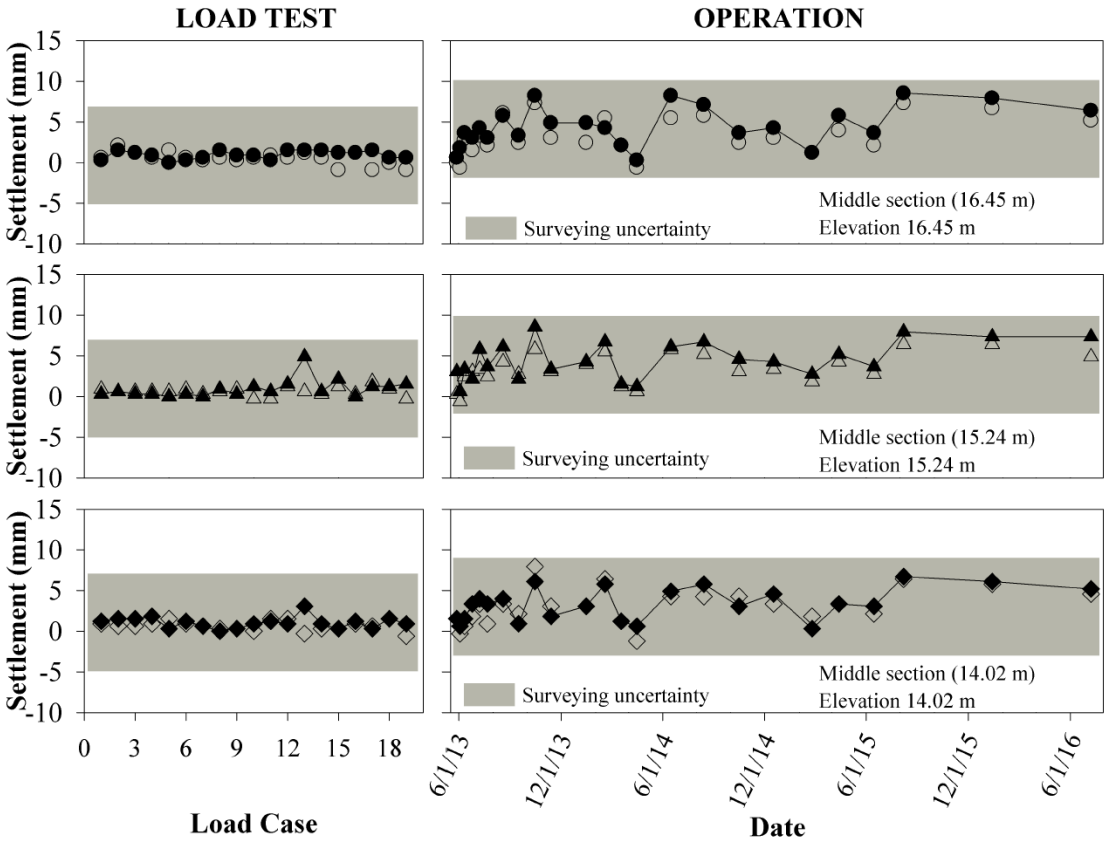

Figure 4.15 Settlement of the east facing wall at 2.8 m offset the from the abutment centerline, in the upstream direction

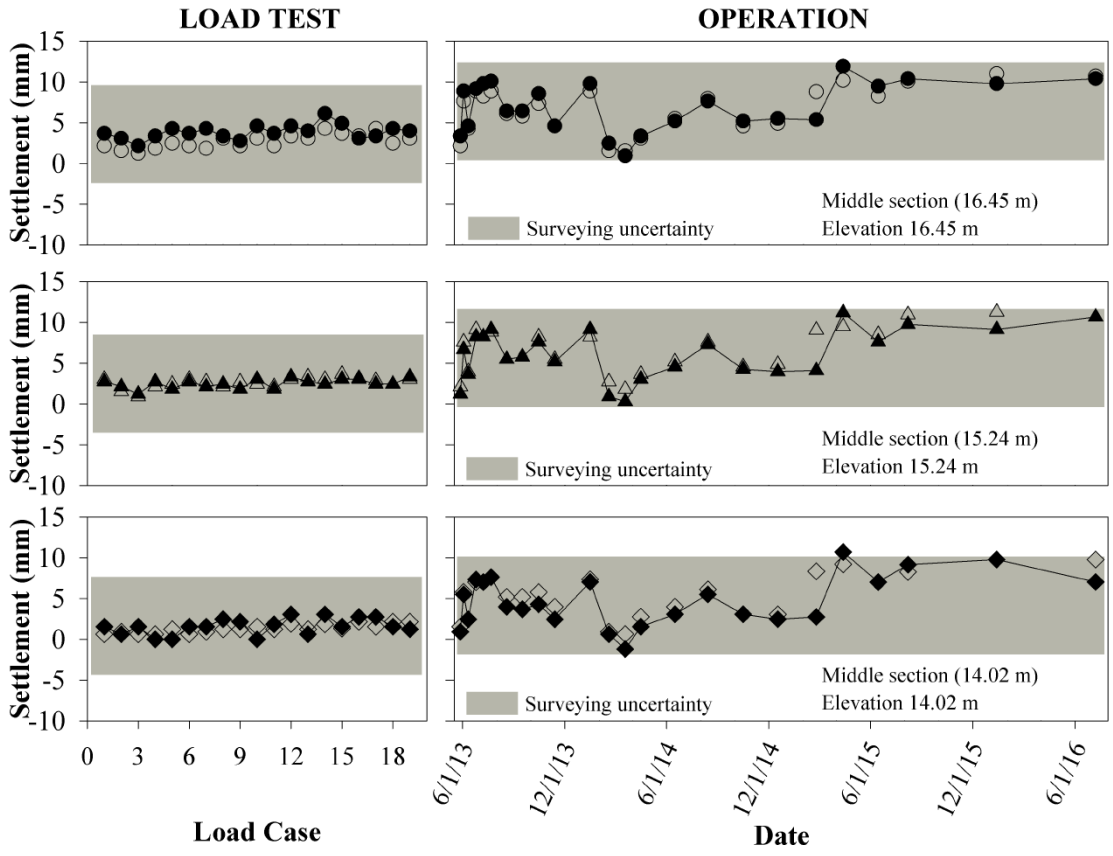

Figure 4.16 Settlement of the west facing wall at 2.8 m offset from the abutment centerline, in the upstream direction

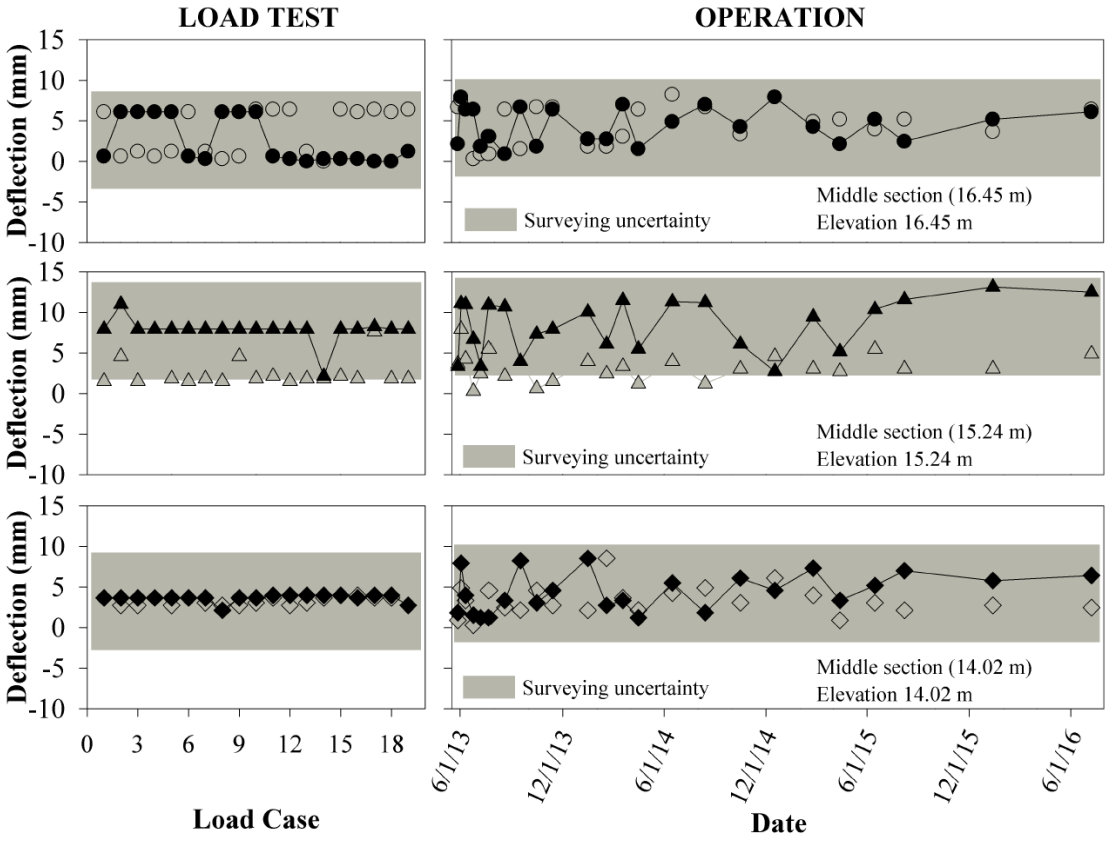

Figure 4.17 Lateral deflection of the east facing wall at 2.8 m offset from the abutment centerline, in the downstream direction

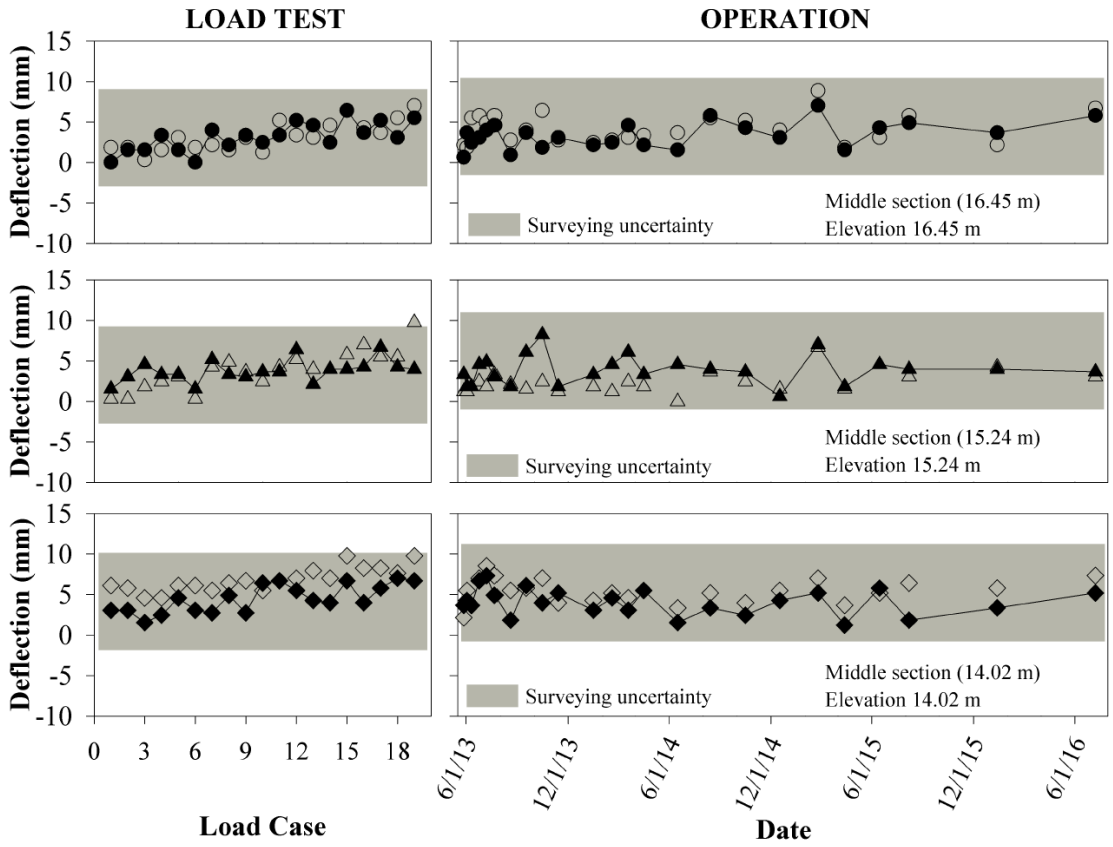

Figure 4.18 Lateral deflection of the west facing wall at 2.8 m offset from the abutment centerline, in the downstream direction

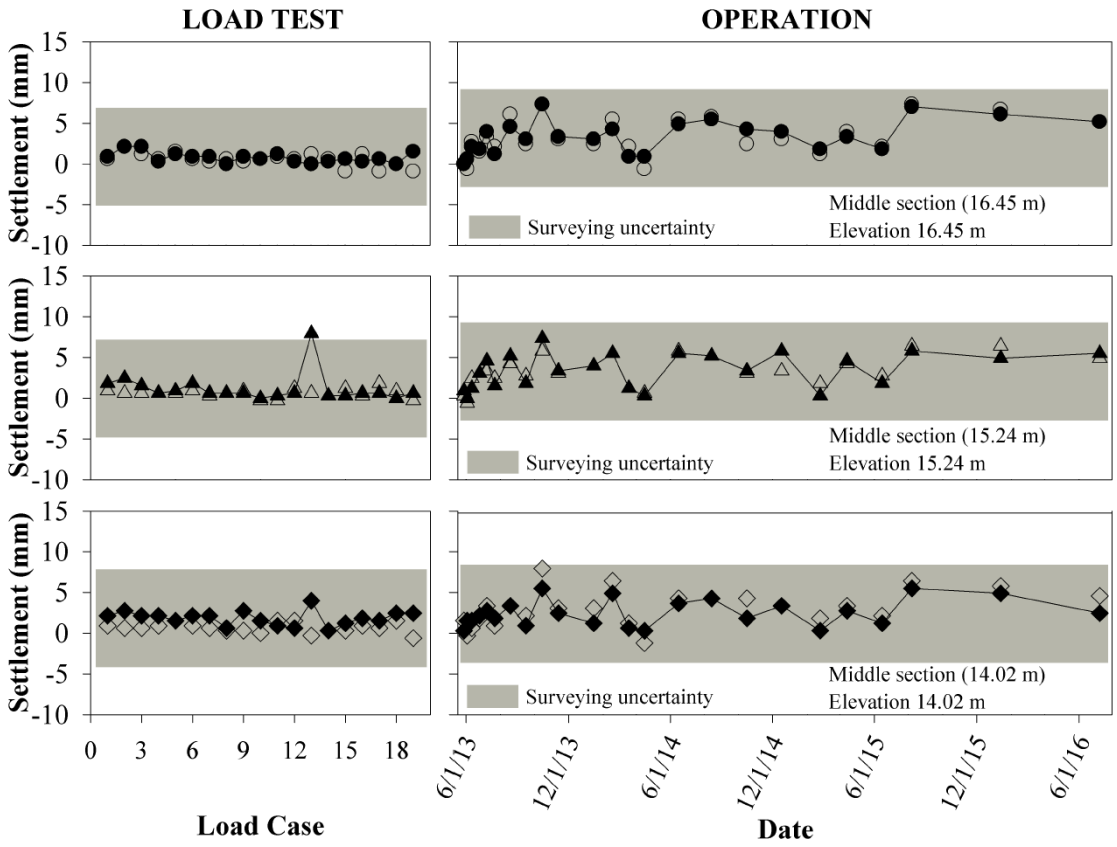

Figure 4.19 Settlement of the east facing wall at 2.8 m offset from the abutment centerline, in the downstream direction

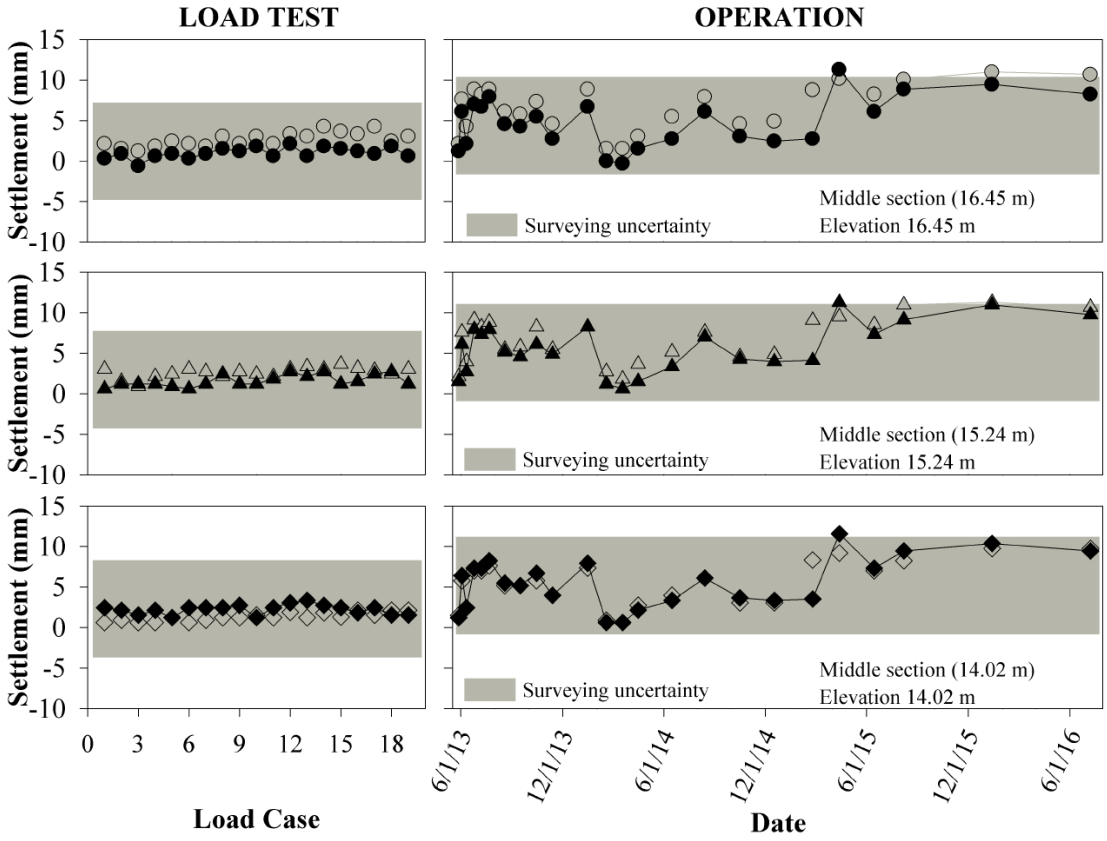

Figure 4.20 Settlement of the west facing wall at 2.8 m offset from the abutment centerline, in the downstream direction

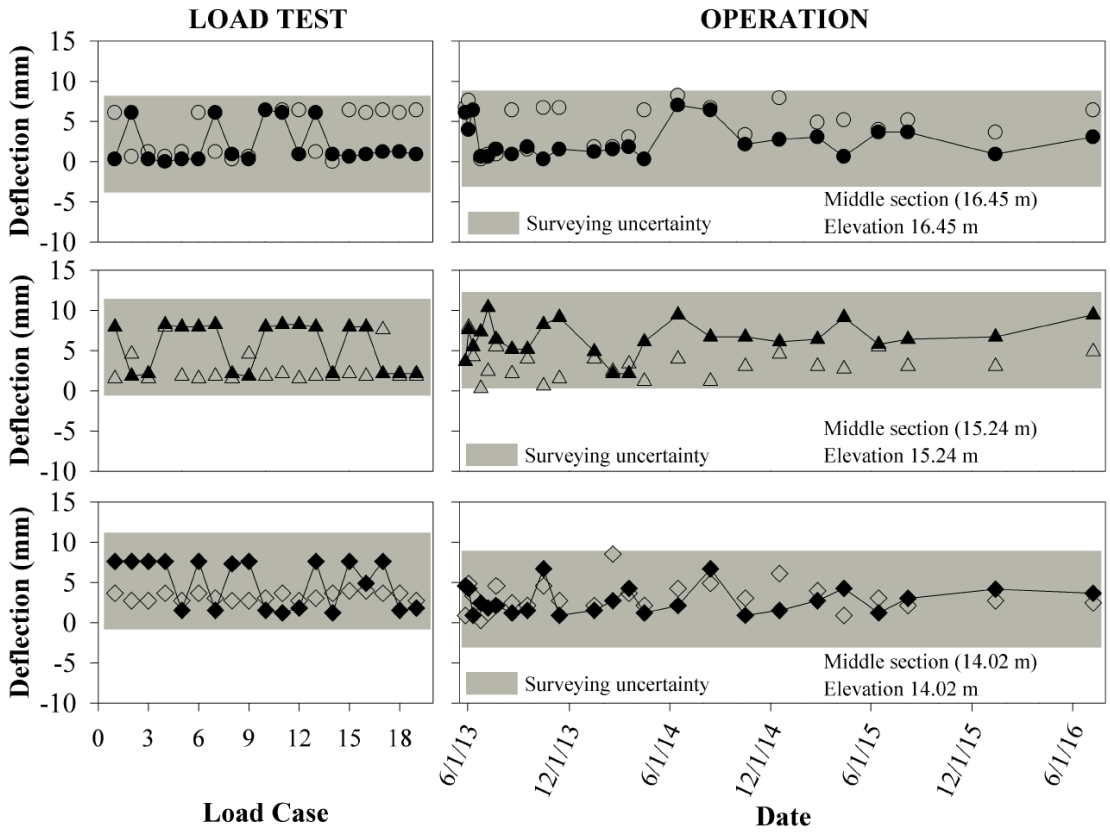

Figure 4.21 Lateral deflection of the east facing wall at 5.6 m offset from the abutment centerline, in the downstream direction

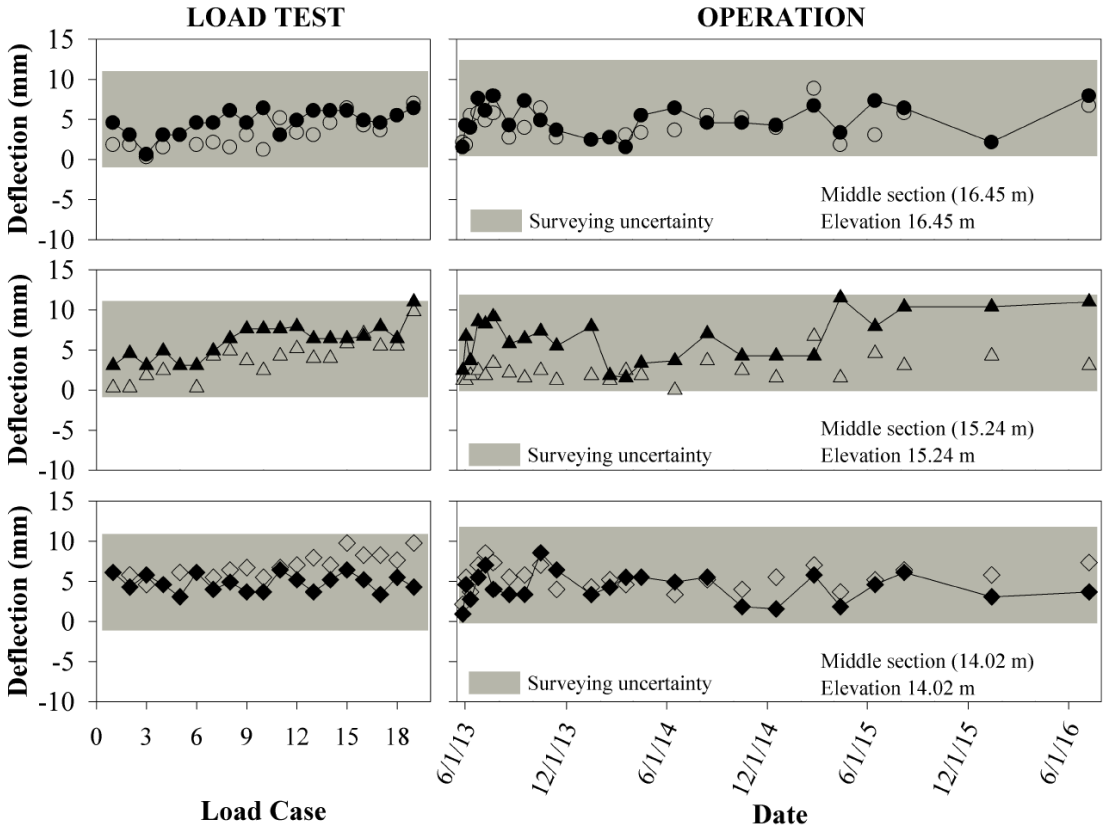

Figure 4.22 Lateral deflection of the west facing wall at 5.6 m offset from the abutment centerline, in the downstream direction

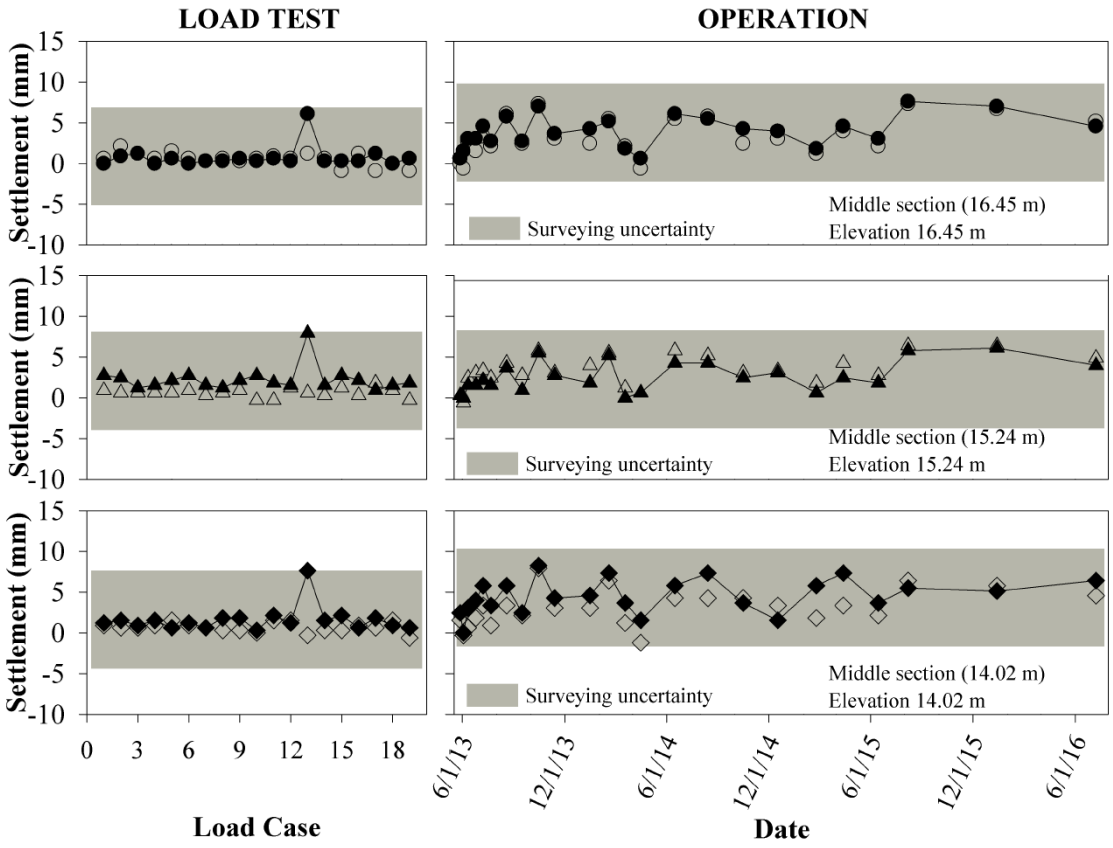

Figure 4.23 Settlement of the east facing wall at 5.6 m offset from the abutment centerline, in the downstream direction

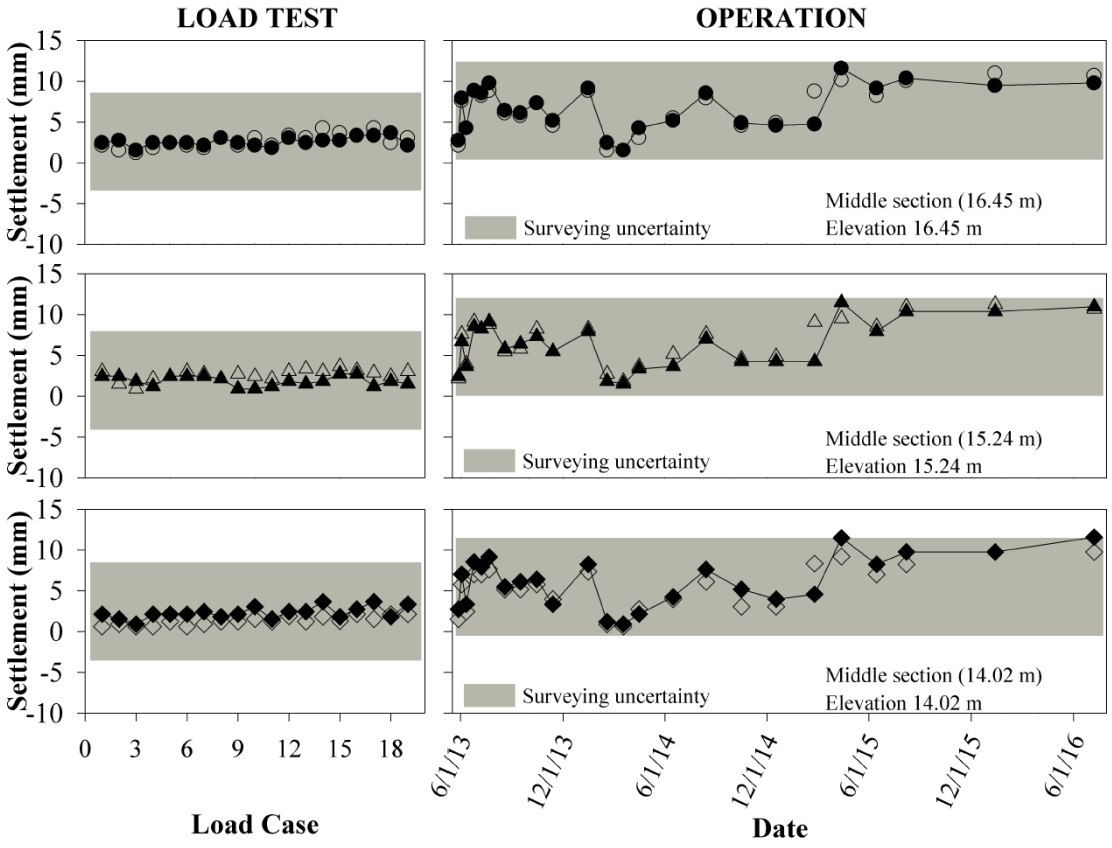

Figure 4.24 Settlement of the west facing wall at 5.6 m offset from the abutment centerline, in the downstream direction

4.5 Piezometers

Figure 4.25 presents measured pore pressures in the GRS-IBS foundation during construction, load testing and for three years of operation. Some load-induced changes in pore water pressure in the GRS-IBS foundation were observed in each of the piezometers during construction. No significant changes in pore water pressure were observed during the live load testing period. Given that this structure is a replacement

for an existing structure having generally similar dimensions, the overall change in load after unloading (existing structure deconstruction) and reloading (GRS-IBS construction) is not believed to be overly significant. It can consequently be inferred that no significant consolidation settlements should be expected post-construction. This observation is consistent with the long-term settlement data that was presented in the previous section. The jump in pore pressure between the end of construction and the beginning of the load test is attributed to the filling of the river channel beneath the bridge post-construction.

As can be observed, over the long-term monitoring period post-construction, all of the pore pressure transducers exhibit consistent spikes in pore pressure at the same point in time. As will be shown later in Chapter 8, these spikes are due to increases in pore pressure caused by storm events, which raise the water level in the river channel and consequently increase the pore pressure beneath the structure. Some disagreement in results began to occur in the Spring of 2015 for the lowest piezometer (P3) and it eventually reached full failure in January of 2016. Since the other two piezometers still show the same result, it appears that the lowest piezometer may not be properly functioning past this point in time. The data from the piezometers were utilized to calculate the effective pressure beneath the RSF, which is discussed in more detail in Chapters 6 and 8.

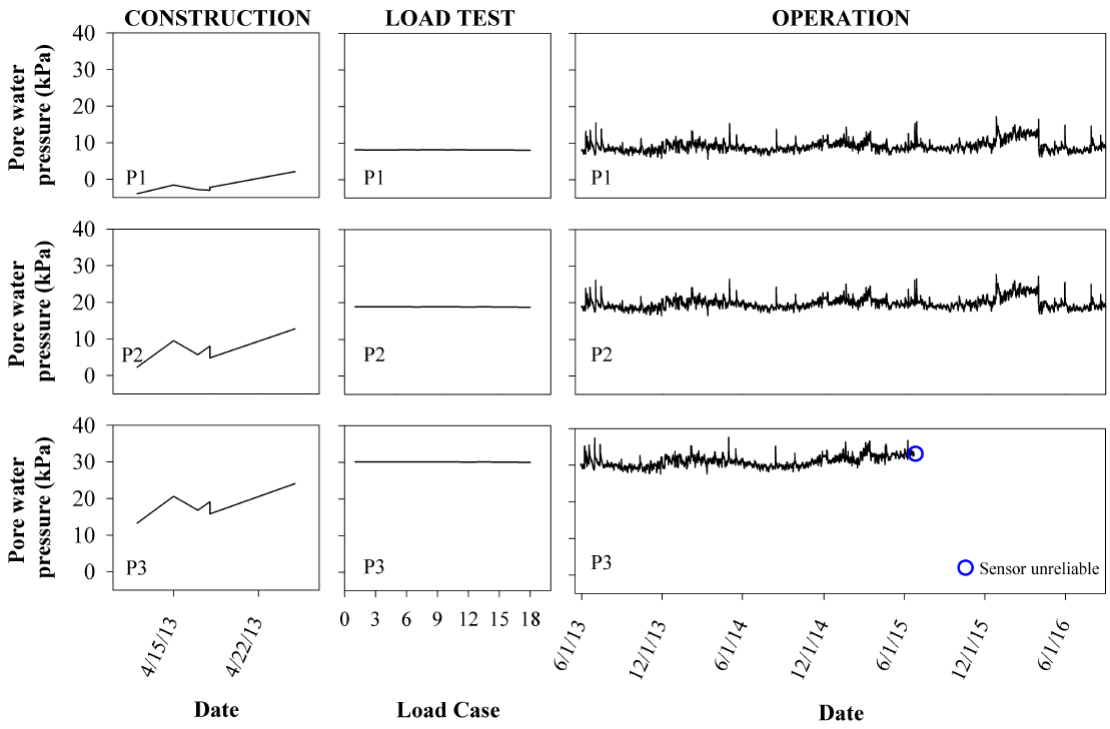

Figure 4.25 Measured pore water pressure by piezometers during construction, load testing and over three years of operation

4.6 Inclinometer sensors

Figures 4.26 and 4.27 show the recorded lateral deflection in the GRS-IBS foundation in the East-West and North-South directions respectively, during construction, live load testing, and over three years of operation post-construction. As shown, the deflection increases during construction and at the beginning of operation, and then tends to stabilize over time. Over the long-term some very small additional trends in movement are observed; these displacements are attributed to long-term creep behavior of the foundation soils. The maximum deflection in E-W and N-S directions

are 10 and 12 mm, respectively. The significantly noisier behavior was observed in the N-S direction relative to the E-W direction since in "biaxial" IPI, the A direction readings are always more stable than those in the B direction because the wheels are on the same plane as the A direction.

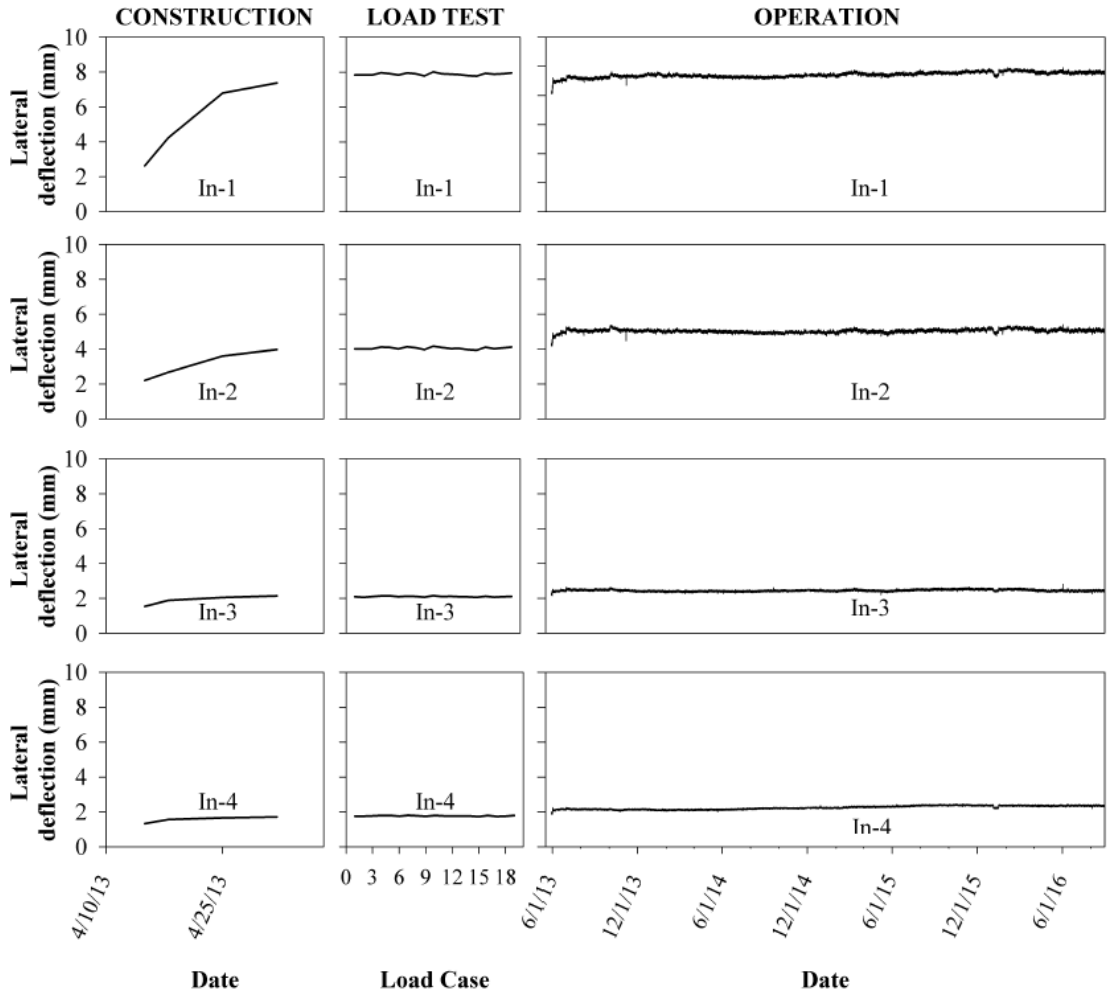

Figure 4.26 Lateral deflection in the E-W direction recorded by the inclinometer sensors during construction, live load testing and over three years of operation

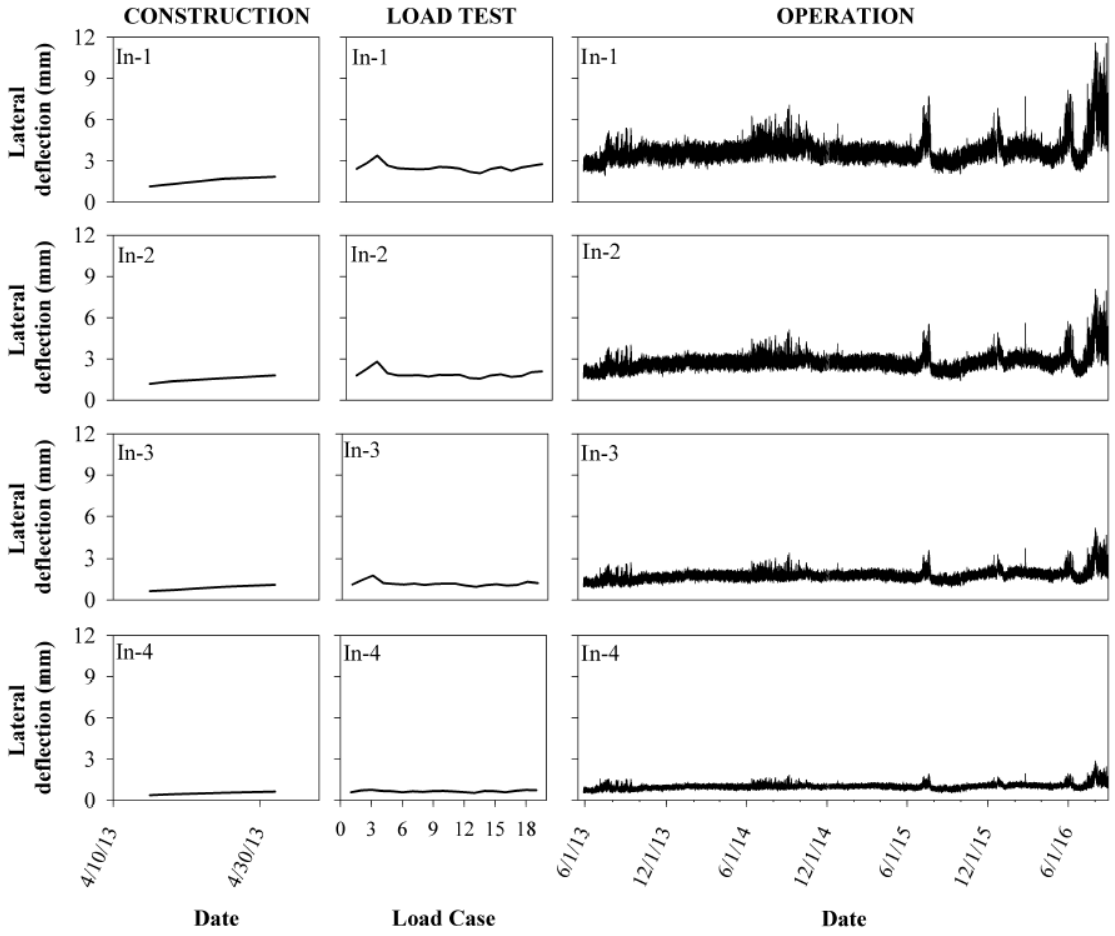

Figure 4.27 Lateral deflection in the N-S direction recorded by the inclinometer sensors during construction, live load testing and over three years of operation

Figure 4.28 displays the changes in lateral deflection of the foundation during construction and after bridge placement. As shown, the lateral deflection increases following a corresponding increase in the abutment loads. The maximum deflection, which occurred after the bridge placement in the E-W direction, was less than 8 mm.

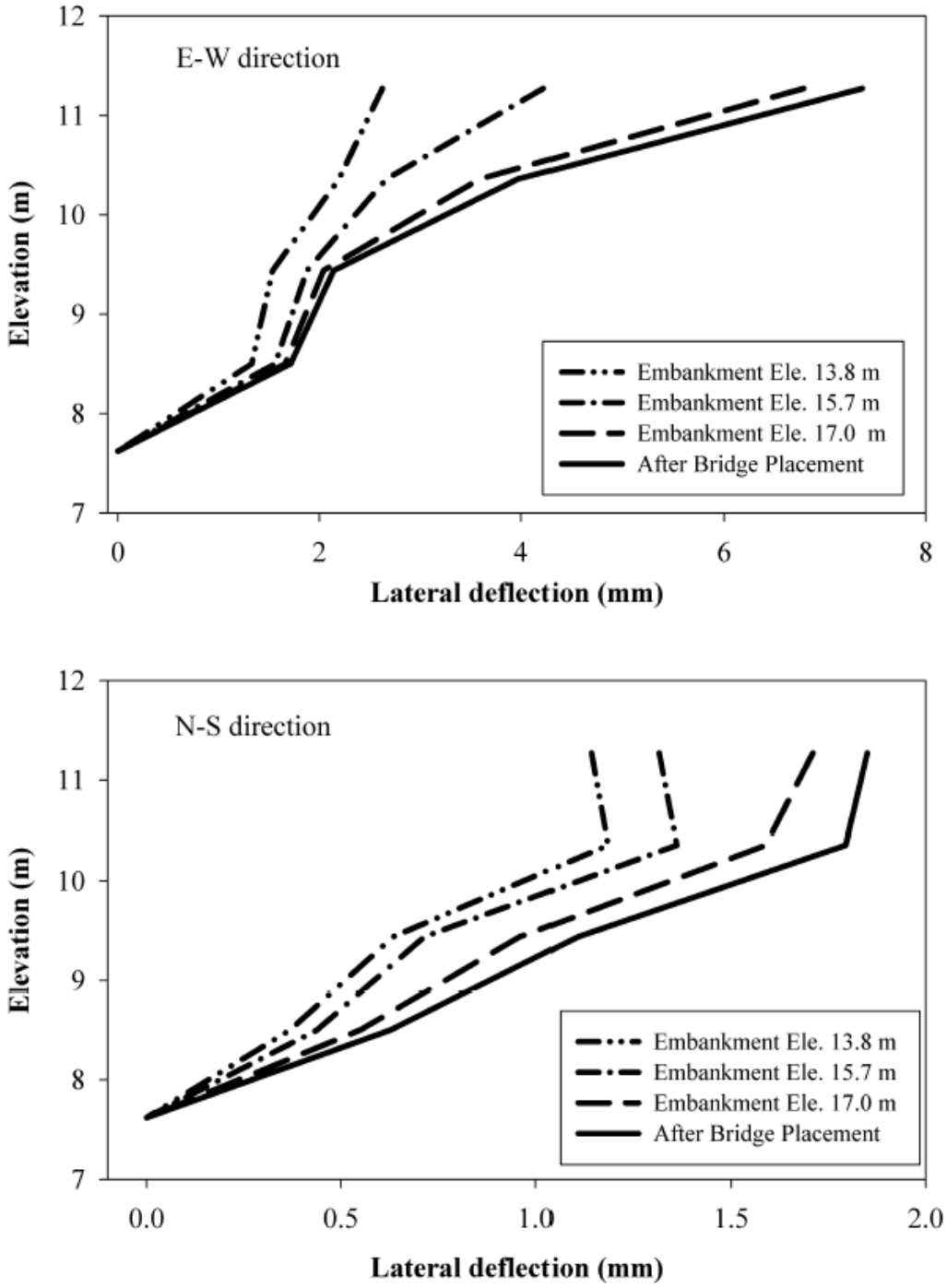

Figure 4.28 Foundation deflection during abutment construction and after the bridge placement in E-W and N-S directions

4.7 Foundation pressure cells

Total pressure values measured by the four pressure cells located beneath the RSF (S1 to S4) are presented in Figure 4.29 for GRS-IBS monitoring that was performed during construction, live load testing, and over three years of operation post-construction. In order to calculate the effective pressure, the measured pore pressure by the installed piezometers (P1 to P3) should be used; the calculated effective pressures for these sensors are presented later in Chapters 6 and 8. As shown, the total pressure varies beneath the foundation and is not constant from point to point beneath the foundation. The maximum pressure was measured beneath the facing wall and the minimum pressure was measured in front of the RSF. Over the long-term, some sensor noise is present for the measured values; this noise is attributed to the effect of temperature changes. These observations will be discussed in more detail in subsequent chapters of this report.

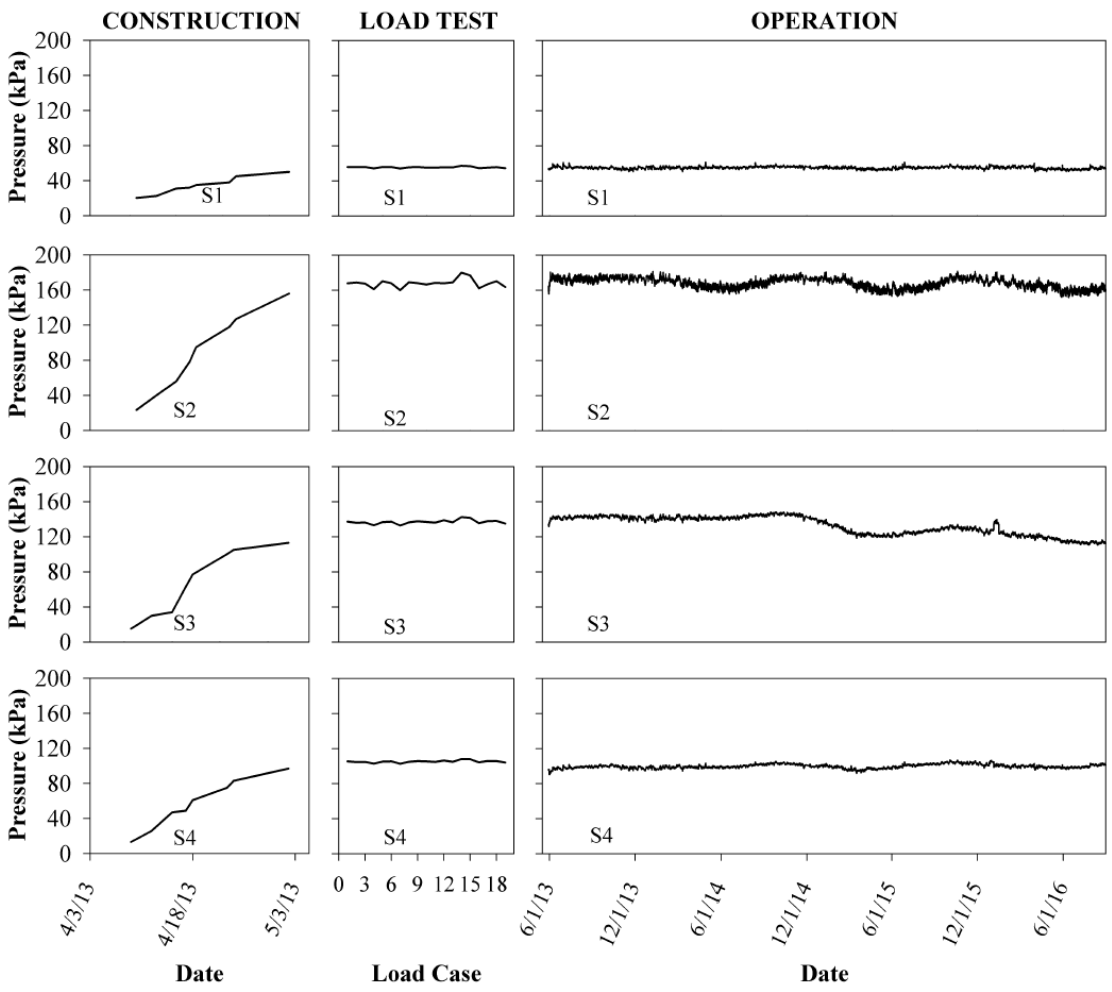

Figure 4.29 Total pressure values recorded by four pressure cells in the GRS-IBS foundation during construction, live load testing and over three years of operation

4.8 Abutment pressure cells

Figure 4.30 displays measured total pressure values during construction, live load testing and over three years of operation. As shown in this figure, the total

stress increases significantly during construction; the large increment of stress increase that is shown for all sensors corresponds to the placement of the bridge superstructure, which induced significant load directly into the total pressure cells. The total pressure response for these sensors was also generally responsive to different live load levels during the live load test. There is significant noise and fluctuation in the recorded data over the long term, which is not surprising since a foil based pressure transducer was used for these total pressure cells rather than a vibrating wire one. There is both an electrical and structural effect on the measured pressure values over time. These effects will be discussed in more detail in Chapter 8.

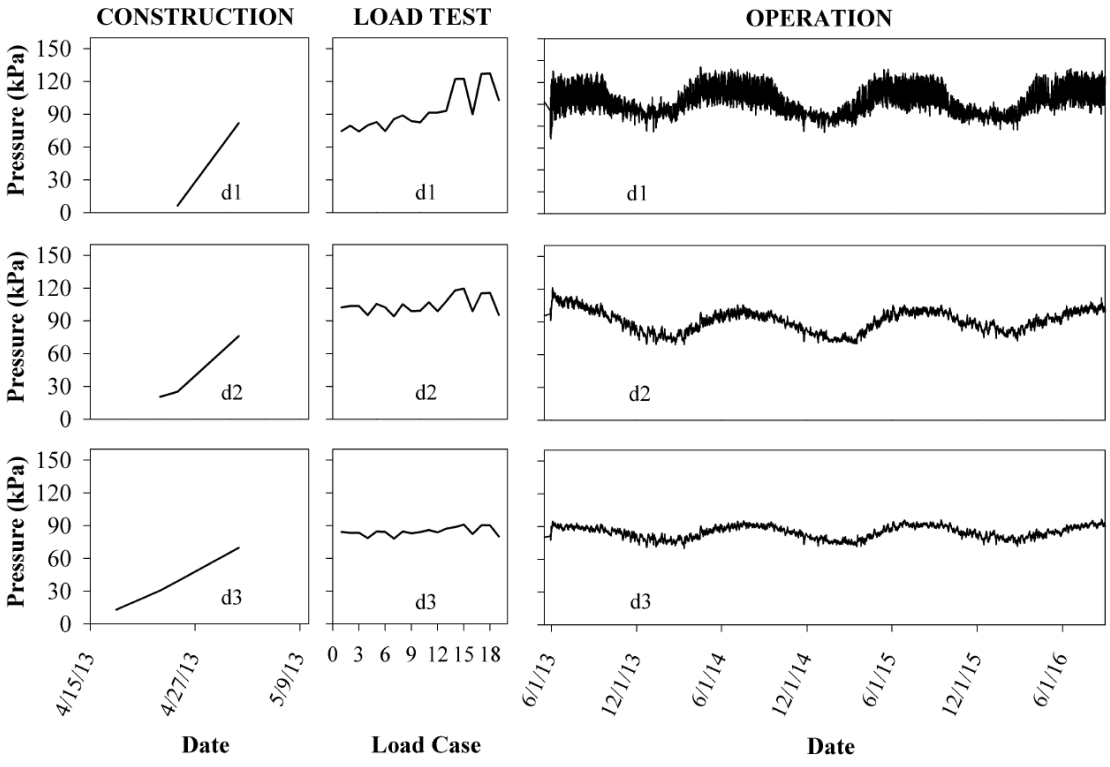

Figure 4.30 Abutment measured pressure recorded by three pressure cells during construction, live load testing and over three years of operation

Figure 4.31 displays the measured pressure at the end of the abutment construction and also after the bridge placement. As shown in this figure, the pressure is changing linearly before the bridge placement since the only applied pressure in this case is the weight of the soil on top of the cells. Therefore, the maximum pressure was measured at the location of the lowest cell (d3) and the minimum pressure was measured by the uppermost cell (d1). Right after the bridge placement, a significant increase occurred in the measured pressure, as shown in the figure. The increase in measured pressure by d1, d2 and d3 was 75.57, 51.01 and 38.49 kPa, respectively. In this case, the maximum pressure was recorded by d1, which is logical since this is the uppermost cell and the closest one to the point of load application by the bridge superstructure.

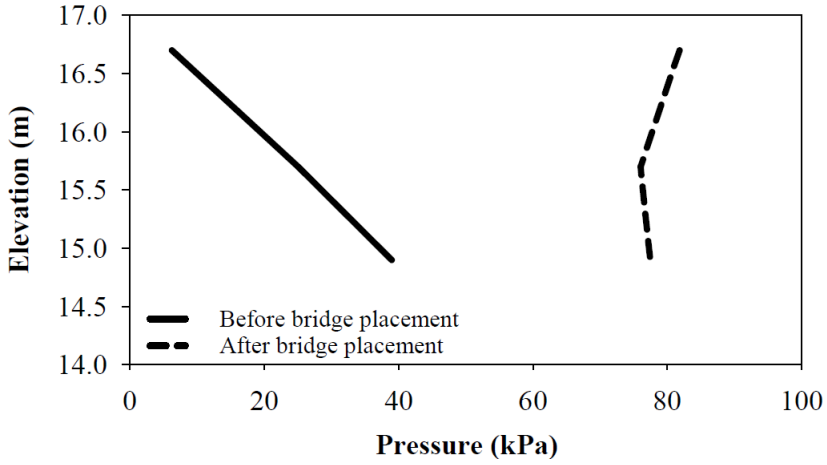

Figure 4.31 Abutment measured pressure before and after bridge placement

The increase in pressure can be calculated using theory of elasticity and the methods such as Boussinesq's or Westergard's formulations. Since Boussinesq's

method (Boussinesq 1885) was utilized in the GRS-IBS manual (Adams et al. 2011), this method was utilized here to calculate the pressure induced by the bridge. For comparison purposes, the 1H:2V method was also utilized to calculate the induced pressure by the bridge. Figure 4.32 illustrates the induced pressure by the bridge measured by the cells and also using Boussinesq's and the 1H:2V methods. As shown, the measured pressure by the cells are higher for all three cells and elevations. The calculated values by 1H:2V method are between the measured values and Boussinesq's method in the lower depth but they are lower than Boussinesq's method for the uppermost cell.

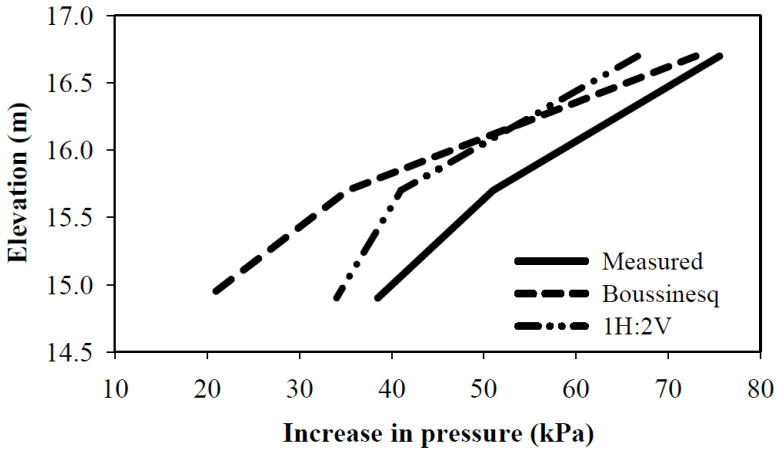

Figure 4.32 Increase in measured pressure by the bridge placement vs values calculated by Boussinesq's method and the 1H:2V "load spread" method

4.9 Strain gauges

As discussed in Chapter 3, two different types of strain gauges (EA-06-20CBW-120 and EP-08-250BG-120 provided by Micro-Measurements) were installed

in the abutments to monitor strain in the geotextile. These sensors were utilized to monitor the behavior of the structure during construction, load testing, and over three years of operation.

Figures 4.33 and 4.34 present the measured strain in the west abutment by the long and short gauges, respectively, while Figures 4.35 and 4.36 present the corresponding results for the east abutment. As noted in Chapter 3, the east abutment data were collected manually while the west abutment data were collected automatically using data loggers.

A few of the strain gauges began exhibiting unusual measurements or stopped working outright during the long-term monitoring process, including: A1-l, A1-s, A2-l, A2-s, A3-l, A3-s, B1-l, B2-s, B3-s, B4-l, C1-s, C2-l, C2-s, C3-l, C3-s, C4-l, C4-s, D1-s, D2-l, D2-s, D3-s, D5-l, D5-s, D6-l, D6-s, E4-l, E4-s, E6-s, E7-l, F1-s, F1-l, H3-s, H3-l and I4-s, as shown in Figures 4.33 through 4.36. The water level in the river channel impacted the long-term performance and survivability of most of the strain gauges in the A and F layers during operation, as these geosynthetic layers were generally continuously submerged once the river was allowed to resume its natural course in the channel post-construction.

Comparing these figures with Figures 4.2, 4.3 and 4.4, a clear effect of temperature on the measured strain can be observed. Details regarding the effect of temperature on the strain readings is presented in Chapter 7, and a new procedure is

provided for correcting measured strain data to account for temperature effects, using an observational approach.

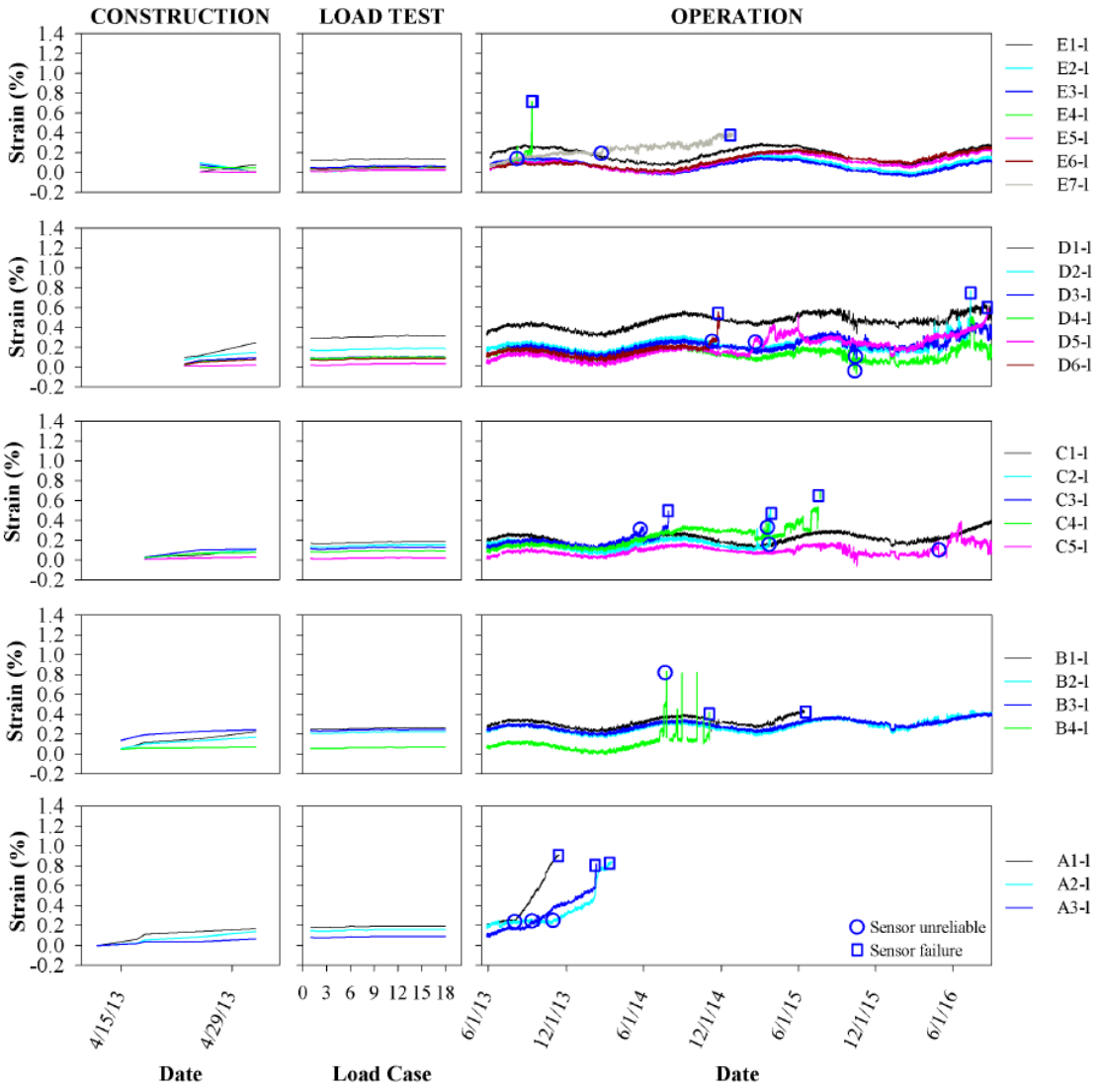

Figure 4.33 Strain measured by the "long" gauges in the west abutment during construction, live load testing and over three years of operation

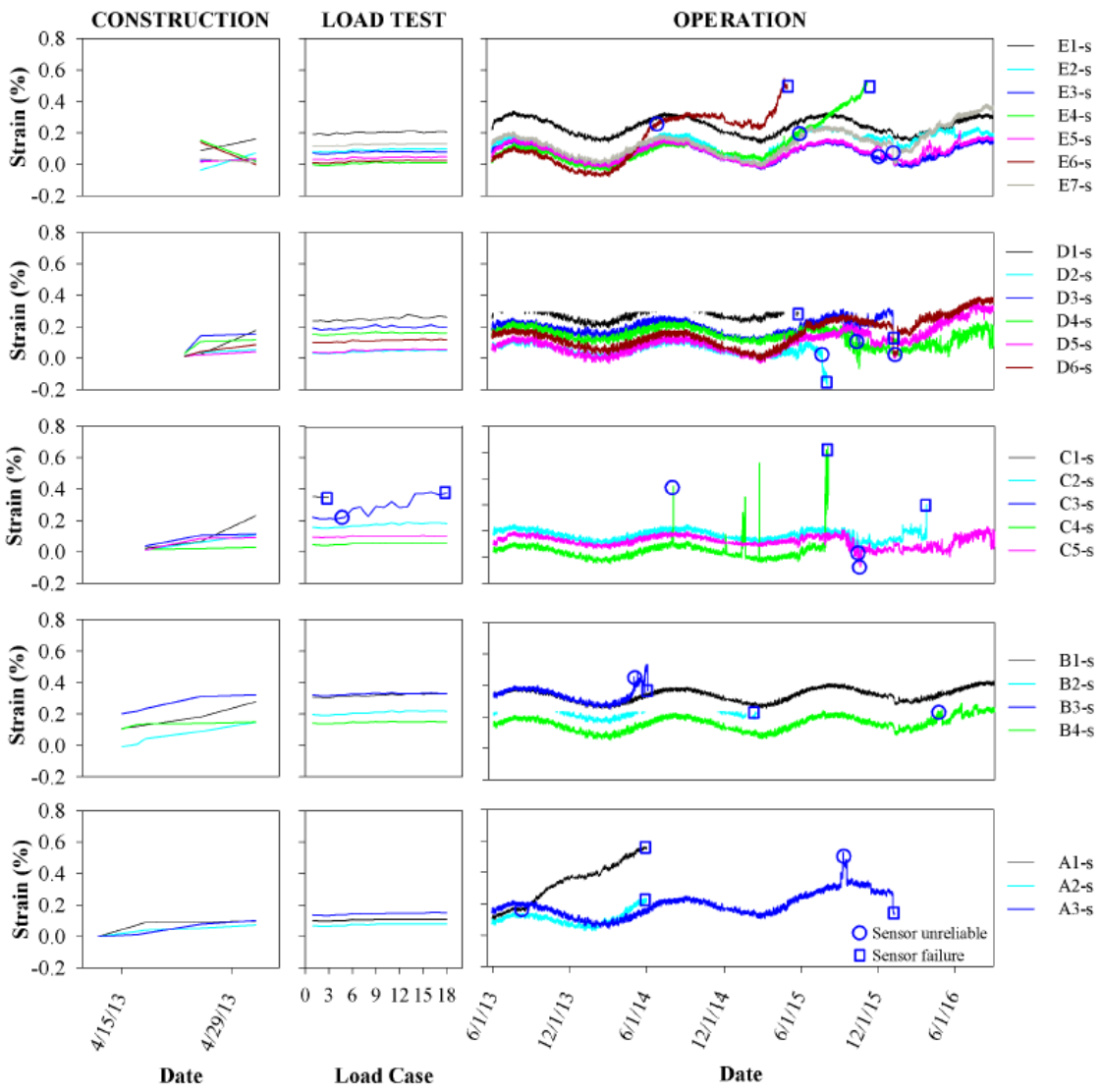

Figure 4.34 Strain measured by the "short" gauges in the west abutment during construction, live load testing and over three years of operation

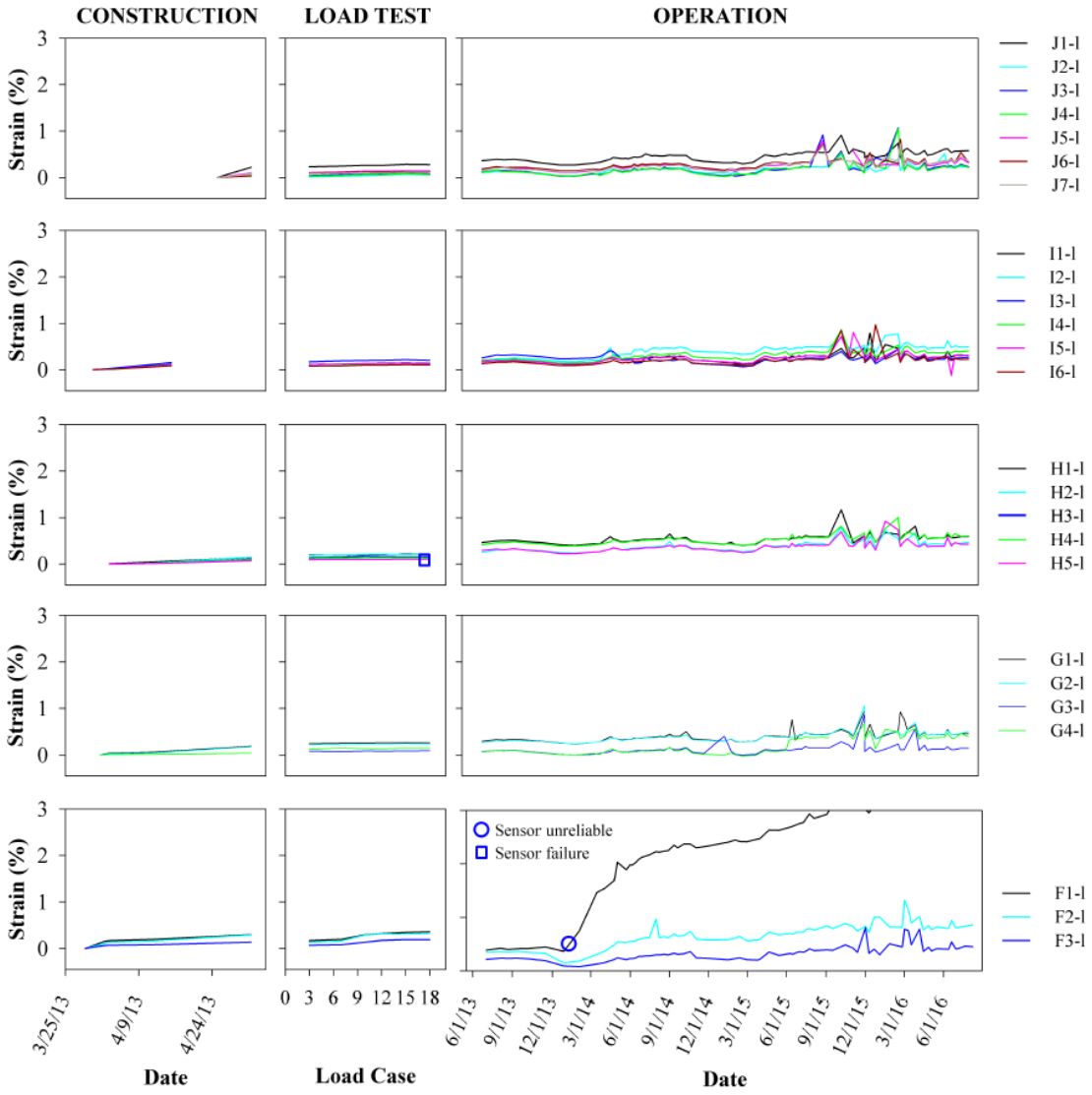

Figure 4.35 Strain measured by the "long" gauges in the east abutment during construction, live load testing and over three years of operation

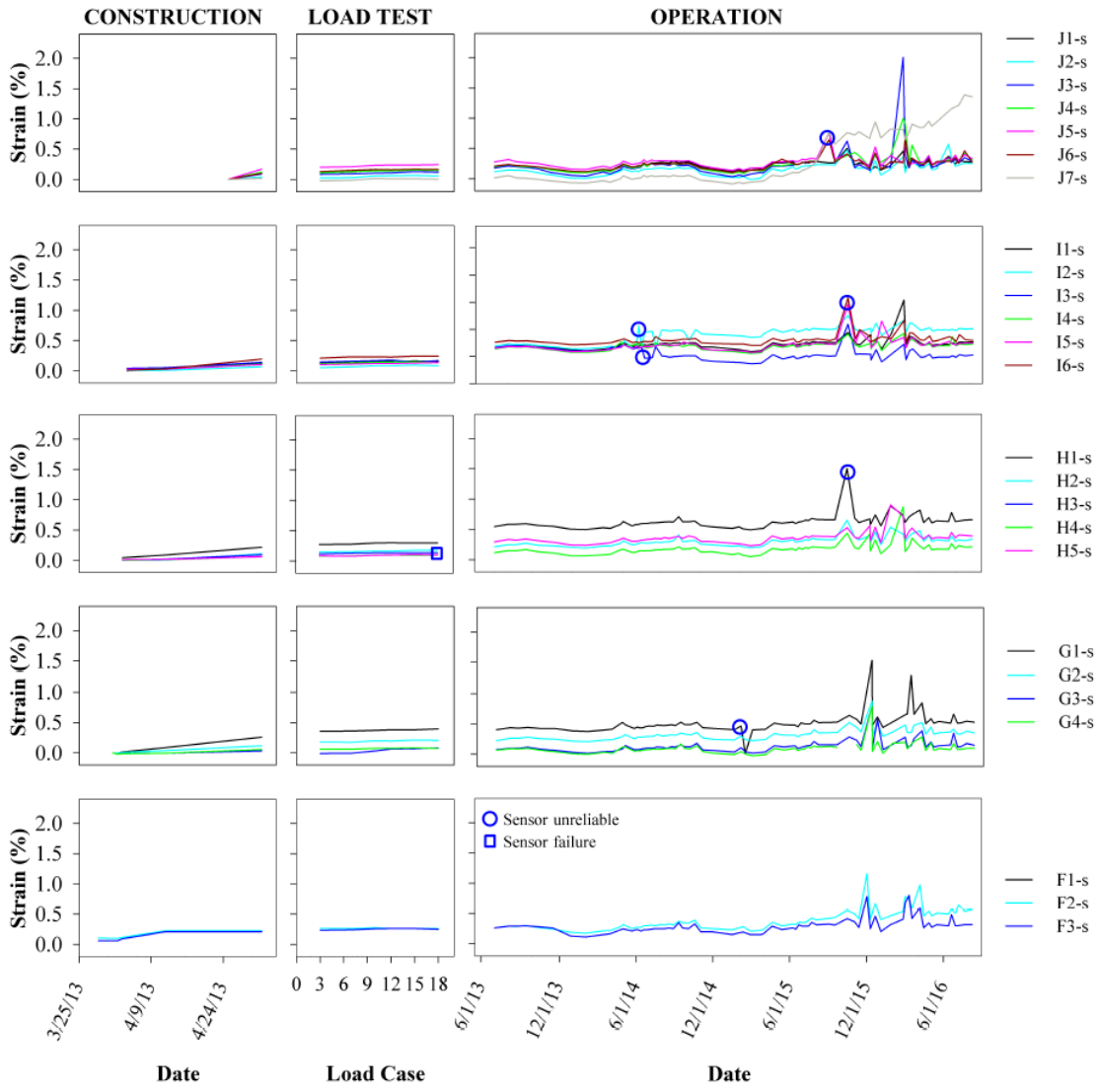

Figure 4.36 Strain measured by the "short" gauges in the east abutment during construction, live load testing and over three years of operation

4.9.1 Measured strain during construction and bridge superstructure placement

In order to examine the deformation behavior of the GRS abutments during construction and bridge superstructure placement, the data from the strain gauges were utilized. Figures 4.37 and 4.38 present the strain changes by long and short strain gauges for the instrumented layers in the west abutment during construction. As expected, the strain increased during construction because of the load applied by the self-weight of the abutment materials. As shown in these figures, the measured strain by both types of gauges is generally quite low, with a maximum value of less than 0.3% strain being observed, even after bridge placement. Overall, the maximum level of strain was observed for reinforcement layer B for both gauge types.

The measured strain results from the long and short gauges are often not very consistent. For example, for layer A, the minimum and maximum measured strain values for the long gauges after bridge placement are 0.07 and 0.16, respectively, while the corresponding values for the short gauges are 0.08 and 0.10, respectively. In addition, the strain distribution measured by the long and the short gauges are different. For example, for the B layer, the minimum and maximum measured strain by the long gauges are 0.07 and 0.25, respectively, while the corresponding strains measured using the short gauges are 0.15 and 0.33, respectively. The strain distribution measured by the long and the short gauges for Layer B was more similar than what was observed for Layer A. In layer C, the minimum and maximum measured strains by the long gauges are 0.03 and 0.12, respectively, while the corresponding numbers for the short gauges are 0.09 and 0.23. In layer D, the minimum and maximum measured strains by the long

gauges are 0.02 and 0.25, respectively, while the corresponding numbers for the short gauges are 0.04 and 0.18. In addition, the strain distribution measured by the long and the short gauges are different. For layer E, the minimum and maximum measured strains by the long gauges are 0.00 and 0.08, respectively, while the corresponding numbers for the short gauges are 0.00 and 0.16. For a number of the short and long strain gauges, the strain near the back end of the reinforced soil zone tended to increase after the bridge placement.

Generally, the strains measured by the short strain gauges were slightly higher than the values measured by the long strain gauges. At the end of abutment construction and before bridge placement, the average measured strains by the long and short gauges was 0.08% and 0.09%, respectively. The average measured strain by the short gauges was 0.1% after bridge placement while the corresponding value for the long gauges was 0.09%, which is very close to average measured by the short gauges. Except for layer A, the maximum values measured by the short gauges are generally higher than the values measured by the long gauges, for the other instrumented layers. In general, it can be observed that all of the measured strains tend to be very small. As noted, the maximum measured strain after bridge superstructure placement was about 0.3%.

In order to evaluate the effect of bridge placement on the strain values, Figure 4.39 shows the increase in measured strain by the long and short gauges. As shown, there is a very small increase in measured strain by both types of gauges. The increase in the strain behind the facing wall is more obvious than the strain in the back

of the abutment. The maximum increases in measured strain by the short gauges are 0.16%, 0.15%, 0.16%, 0.10% and 0.02% for layers E, D, C, B and A, respectively. The corresponding values for the long strain gauges are 0.08%, 0.13%, 0.06%, 0.07% and 0.05% for layers E, D, C, B and A, respectively. The measured values by the short gauges behind the facing wall were typically larger, except for layer A.

The strain gauge results for the east abutment during construction are shown in Figures 4.40 and 4.41 for long and short gauges, respectively. As shown in these figures, the maximum measured strain was about 0.3% which again occurred after bridge placement. There is not a good consistency between the long gauge and short gauge measured strains. Figure 4.42 indicates the increase in measured strain in the east abutment because of bridge placement. As shown, the maximum increase in strain recorded by both the long and the short gauges is about 0.2%. As shown in these figures, there is no measured data for the first short gauge in layer F since this gauge was not working from the beginning.

At the end of abutment construction and before bridge placement, the average measured strain by the long and short gauges in the east abutment was 0.02% and 0.03%, respectively, which was less than what was measured in the west abutment. The average measured strain by the short gauges was 0.11% after bridge placement while the corresponding value for the long gauges was 0.10%, which is very close to average measured by the short gauges. These measured values were generally similar to those that were measured in the west abutment after bridge placement.

From the data presented in this section it can be inferred that overall the value of the strain in the GRS-IBS structure was limited to less than 0.3% even after the placement of the bridge superstructure elements. This indirectly indicates that the abutment lateral deformations should be generally small and less than the allowable lateral deformation. These results are generally expected, since the abutment in this GRS-IBS structure was constructed using a very strong and high quality granular material and closely spaced high strength geotextile. These two factors considerably limit the maximum deformation that can occur in the abutments.

The long term performance of the strain gauges is discussed in more detail in Chapter 7 and the effect of the temperature changes on the strain readings is also investigated in that chapter.

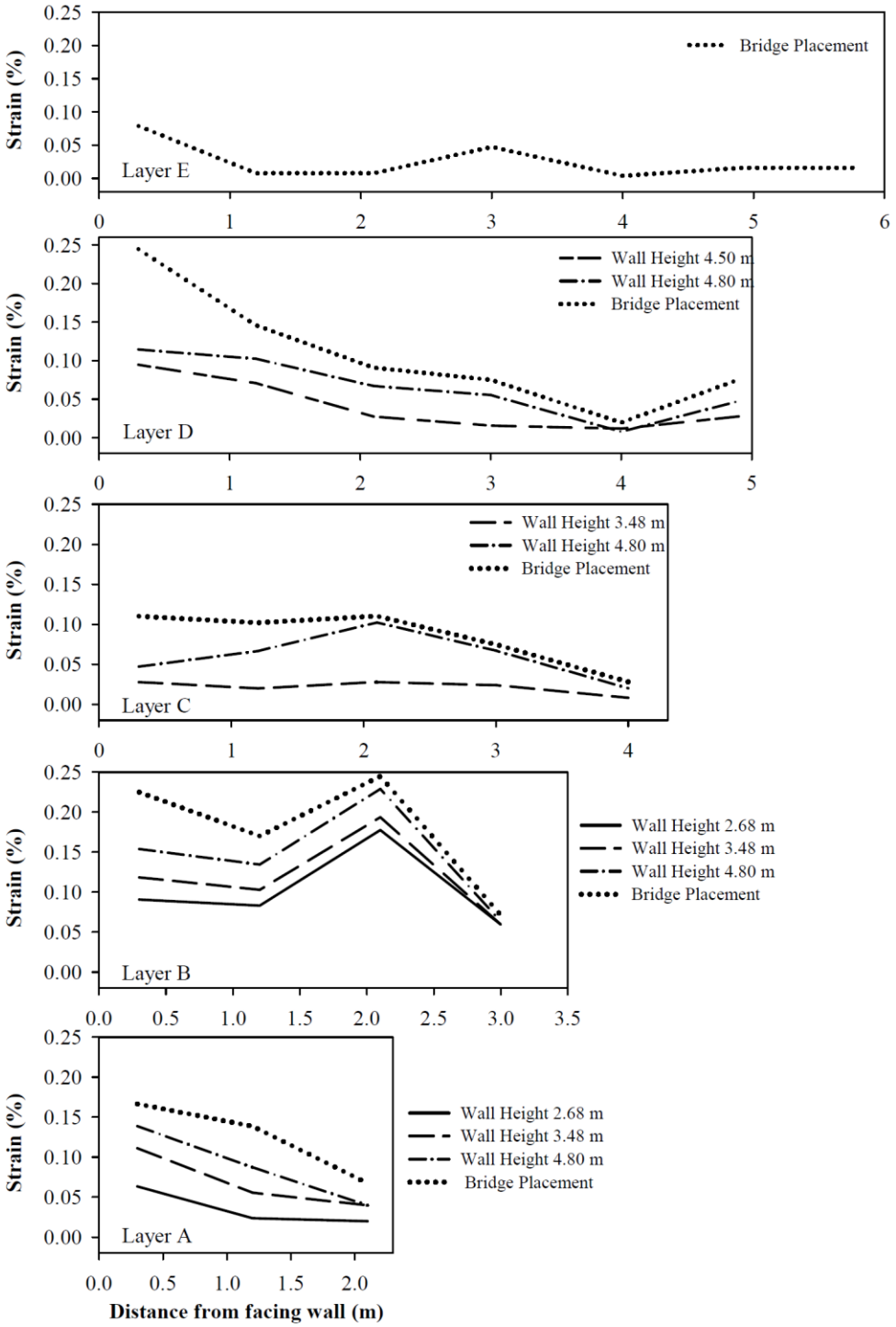

Figure 4.37 Measured strain by "long" gauges in the west abutment during construction and after bridge superstructure placement

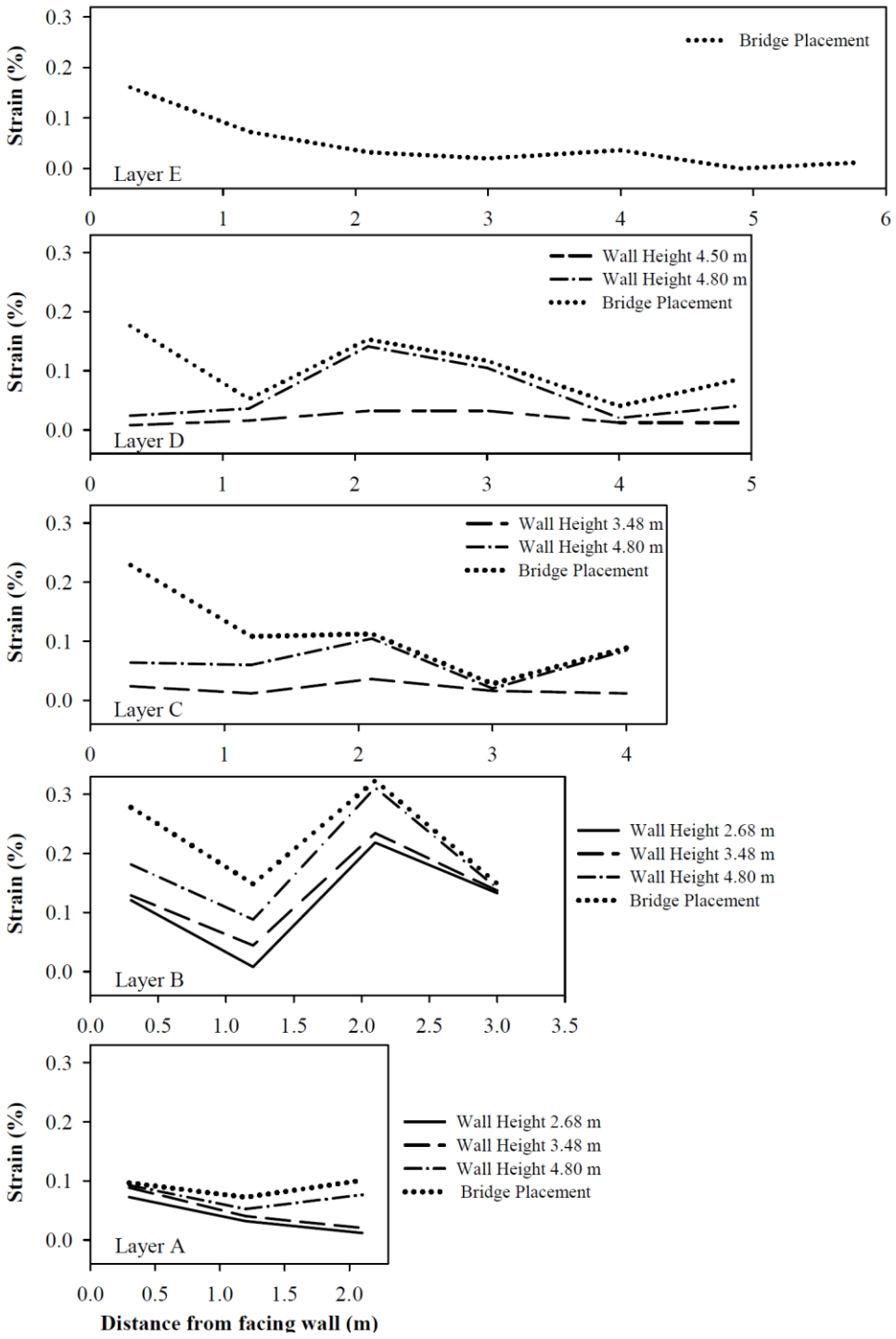

Figure 4.38 Measured strain by "short" gauges in the west abutment during construction and after bridge superstructure placement

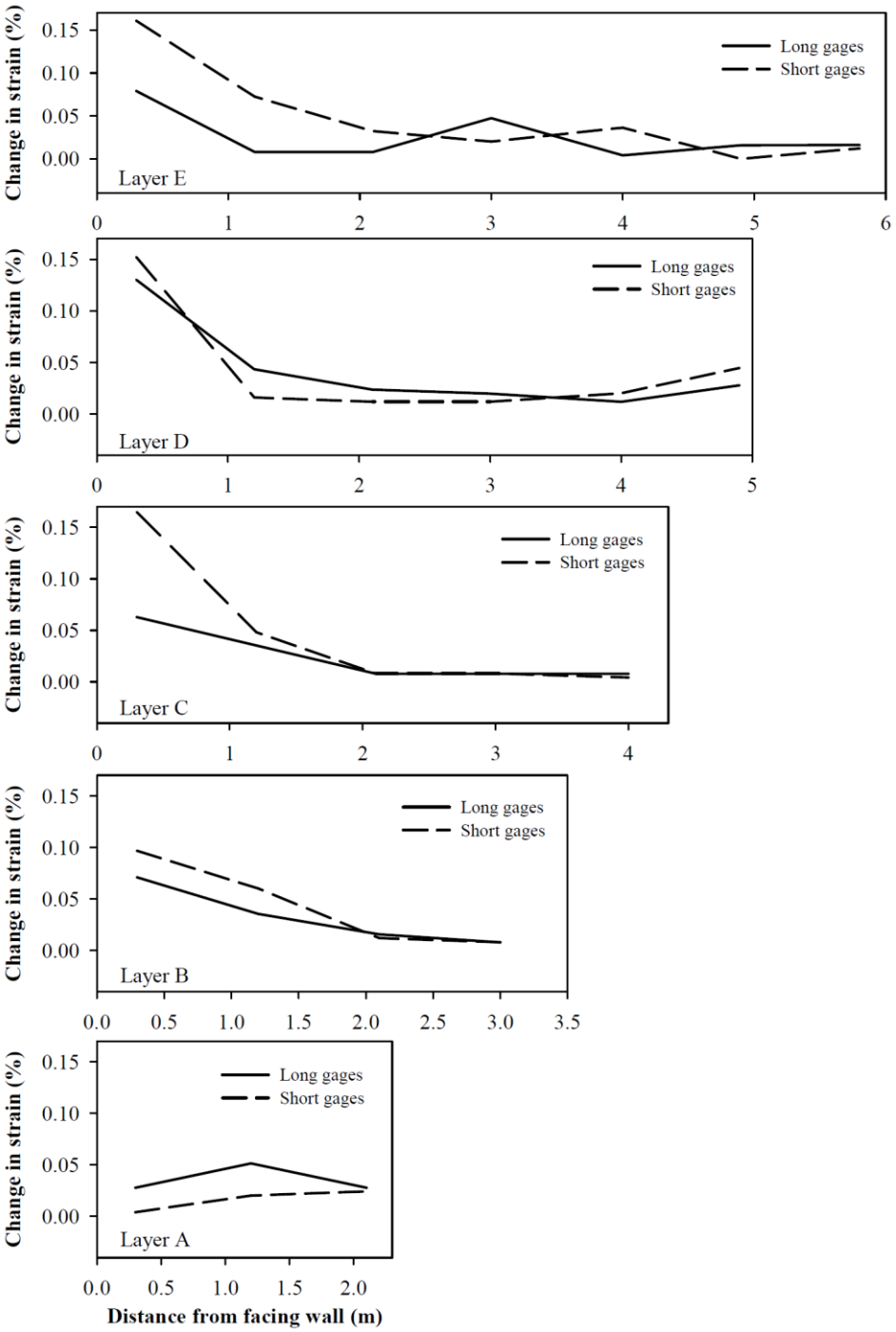

Figure 4.39 Increase in strain in the west abutment after bridge superstructure placement measured by the "long" and the "short" strain gauges

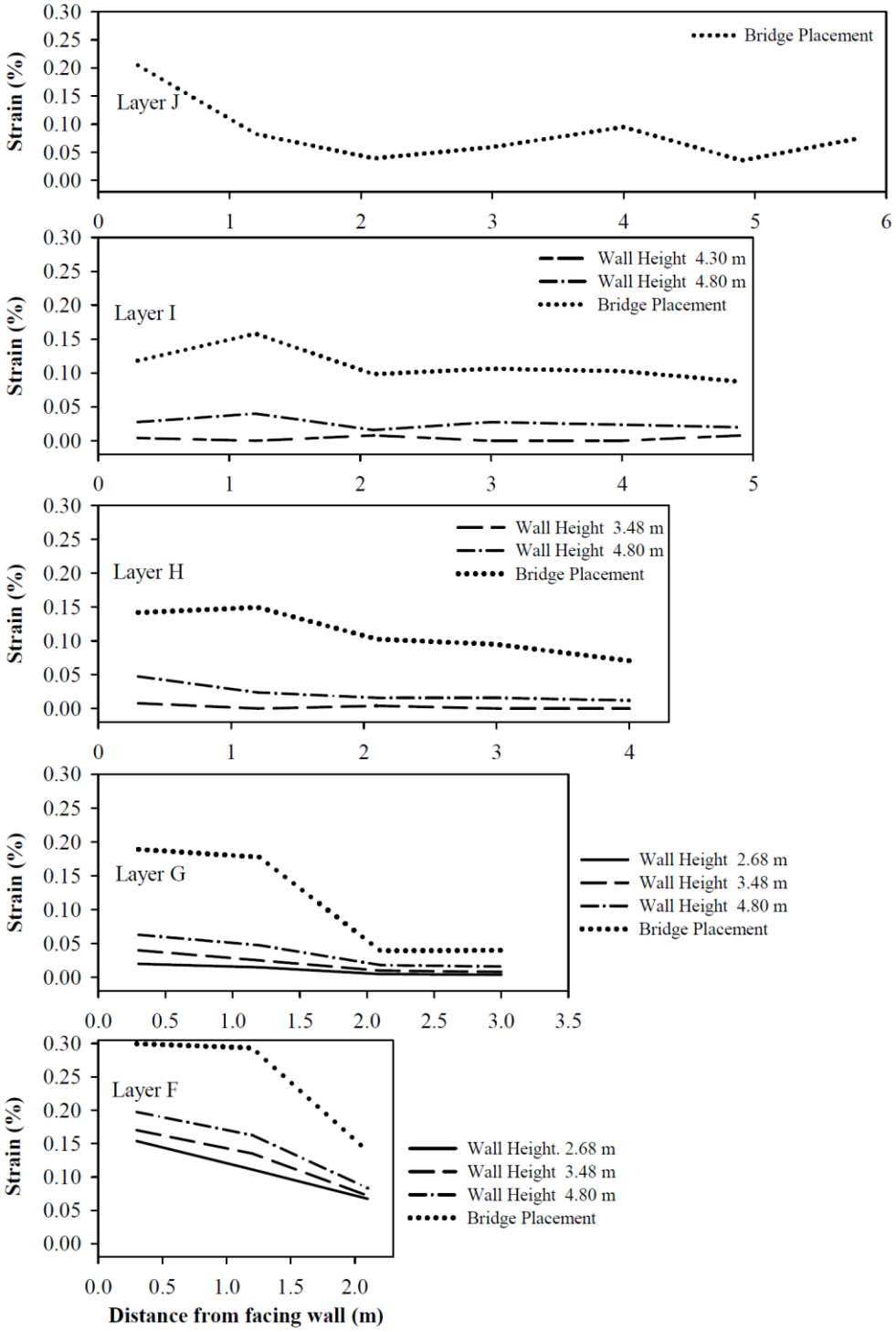

Figure 4.40 Measured strain by "long" gauges in the east abutment during construction and after bridge superstructure placement

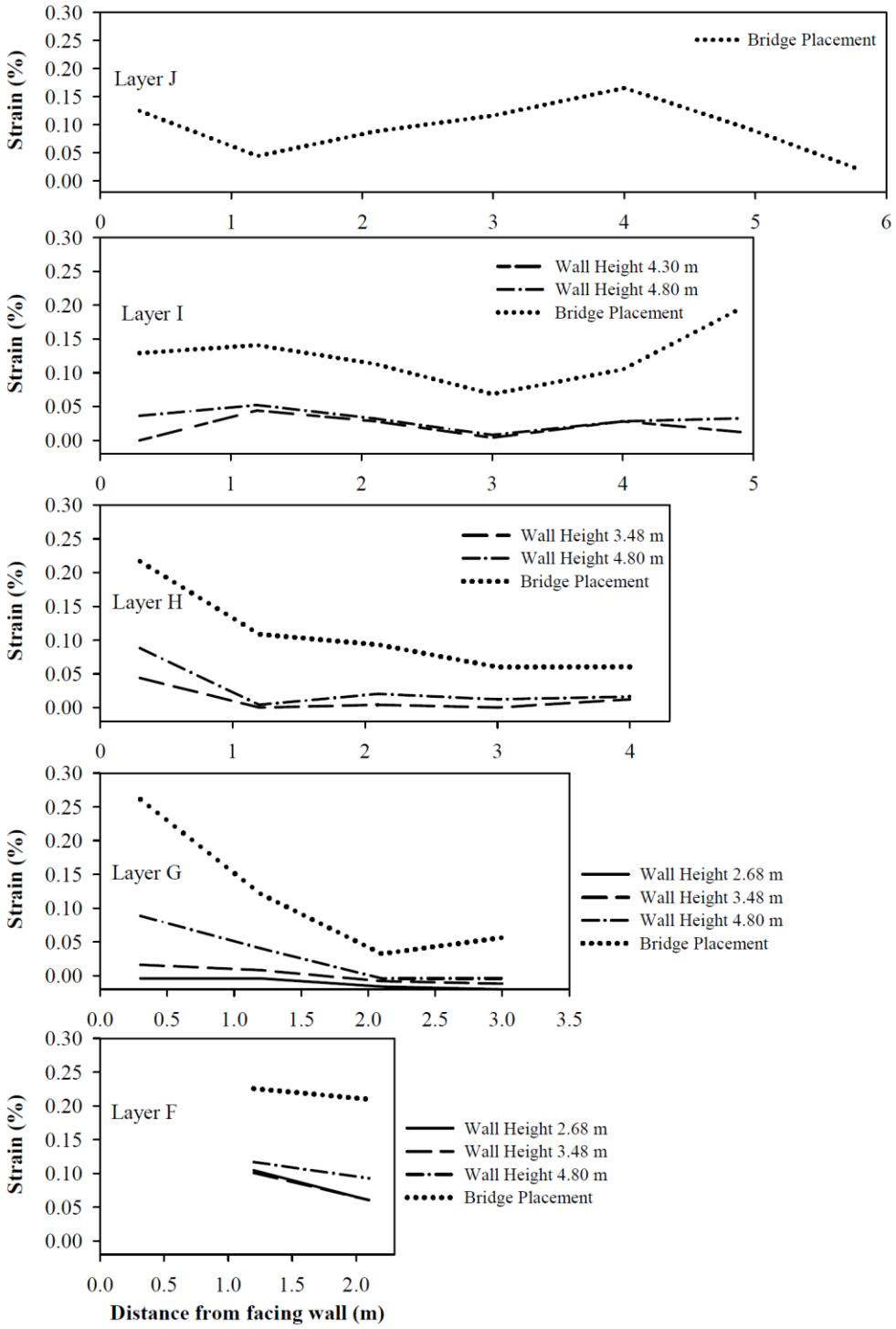

Figure 4.41 Measured strain by "short" gauges in the east abutment during construction and after bridge superstructure placement

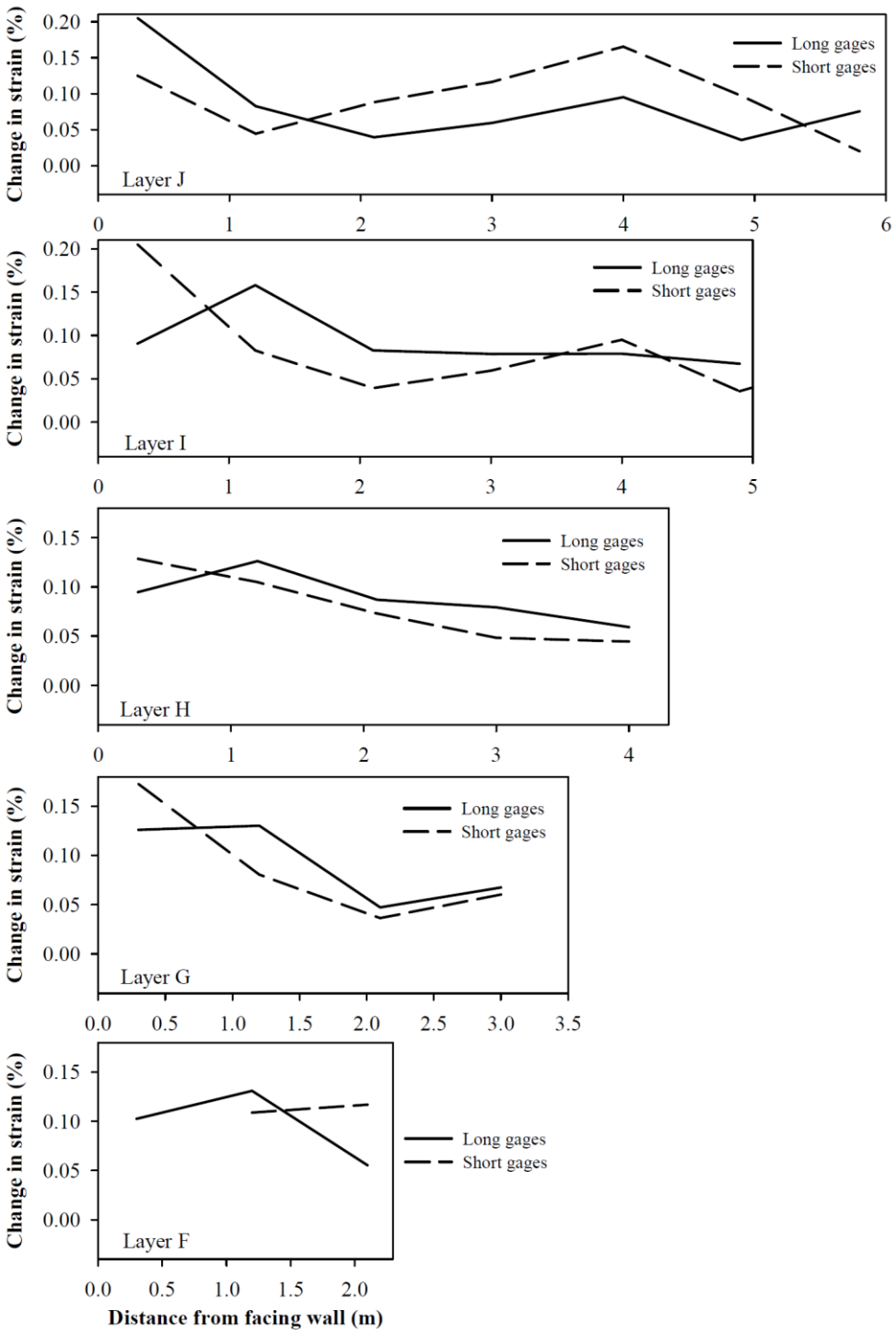

Figure 4.42 Increase in strain in the east abutment after bridge placement measured by the "long" and the "short" strain gauges

4.10 Bridge strain gauges

In order to monitor the deformations of the bridge, 10 Vishay strain gauges (EA-06-20CBW-120) were attached to the bottom of the bridge across its middle span (Figure 3.28) before its placement on the abutments and their data were collected after bridge placement had occurred. Five of the gauges stopped working at the very beginning of the data collection period. The results for the remaining working gauges are shown in Figure 4.43. Since the changes in the measured strain is mainly induced by the air temperature (as will be discussed in detail for the abutment strain gauges in Chapter 6) it can be generally observed that the bridge strain is low and no significant structural strain occurred within three years of operation to the bridge. The bridge strain and its relationship with the air temperature are discussed in more detail in Chapter 9.

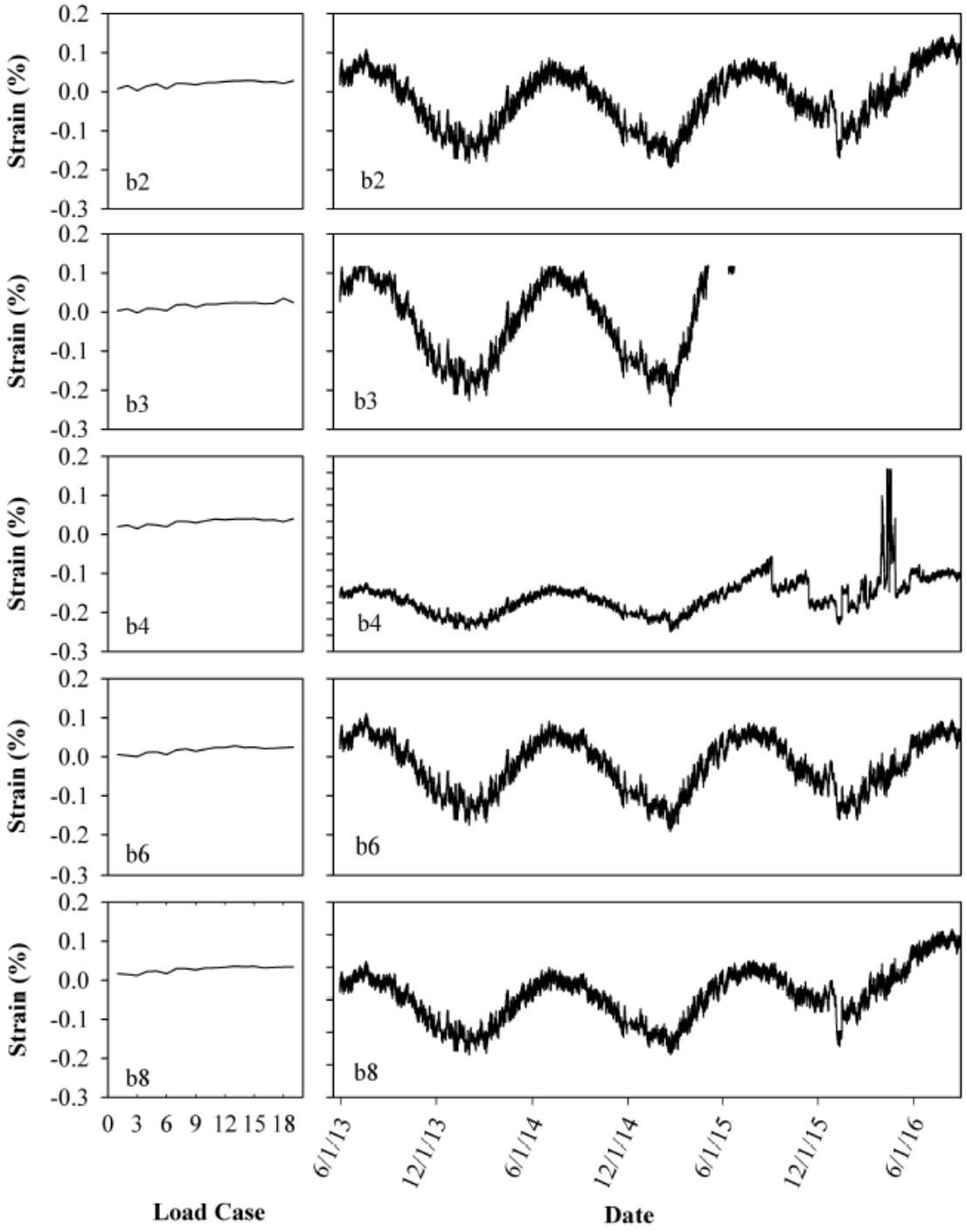

Figure 4.43 The strain beneath the bridge across its middle span measured by the bridge strain gauges during live load testing and over three years of operation

4.11 Conclusion

In this chapter, the data collected by different sensors were presented for the time of construction, live load testing, and over three years of operation. The results and major findings from this data are as follows:

1- The abutment's water content sensors were mostly changing between 20 to 30 percent. The peak values were observed in the winter and spring seasons. The highest values were observed at mid-height in the abutment.

2- The abutment's temperature was changing in accordance with the air temperature. The seasonal fluctuations were higher for the top elevation and parallel to the facing wall.

3- The foundation pore water pressure was changing in accordance with the water level in the river. No significant excess pore pressures were produced during construction.

4- The maximum lateral deflection and settlement of the facing walls was less than 15 mm over the three years of operation.

5- The maximum lateral deflection in the foundation was less than 10 mm.

6- The pressure in the foundation increased during construction and live load testing. The pressure distribution beneath the foundation for the time of construction and live load testing is discussed in more detail in Chapter 6. The temperature changes also affected the collected

measurements within three years of operation. A discussion of the effect of the temperature on the readings is presented in Chapter 8.

7- The abutment pressure changes were measured using three pressure cells in the upper elevations. The results showed that the pressure increased during construction and live load testing. The temperature also affected the measured pressure; the corresponding details are discussed in Chapter 8.

8- The strain in the abutments increased during construction and live load testing. The maximum measured strain was mostly less than 0.5 percent (for the sensors which were properly working). The effect of temperature on the strain measurements is discussed in more detail in the next chapter.

As presented in this chapter, significant amounts of data were collected over three years of operation. In Chapter 5, relationships between different sensor measured values are investigated using correlation analysis. It will be shown that correlation analysis is a powerful and useful tool for the evaluation of the interdependency of different types of sensor responses.

As a result of this analysis, the effect of temperature changes on measured strain is illustrated and a procedure is presented to correct the measured strain values in Chapter 6. In addition, the effect of temperature on the foundation and abutment pressure readings is also shown through the correlation analysis.

The load test was conducted after the bridge installation and before the pavement construction to monitor the behavior of the structure under the live loads. The results for the live load test will be presented in Chapter 7.

The pressure distribution beneath the foundation of reinforced structures is a challenging issue, which was investigated in depth in the current study, as discussed in Chapter 8, using the corresponding collected data for the time of construction and live load testing; a detailed discussion on this issue is presented in this chapter.

The long term performance of the structure is analyzed in Chapter 9 using the collected data by all installed sensors. Based on the results, it will be shown that the structure is internally and externally stable and all responses are in the allowable range.

REFERENCES

Adams, M., Nicks, J., Stabile, T., Wu, J., Schelatter, W. and Hartmann, J. (2011). "Geosynthetic reinforced soil integrated bridge system Interim Implementation Guide." Publication No. FHWA-HRT-11-026. Federal Highway Administration, Washington, DC.

Boussinesq, J. (1885). "Application des potentiels à l'étude de l'équilibre et du mouvement des solides élastiques: principalement au calcul des déformations et des pressions que produisent, dans ces solides." des efforts quelconques exercés sur une petite partie de leur surface ou de leur intérieur: mémoire suivi de notes étendues sur divers points de physique. mathematique et d'analyse, (Vol. 4). Gauthier-Villars. (In French).

Chapter 5

DATA MANAGEMENT AND CORRELATION ANALYSIS

5.1 Introduction

This chapter describes the techniques that were utilized to manage and filter the large amounts of data that were collected from the GRS-IBS instrumentation over the long-term monitoring period. A technique for statistical correlation analysis is presented that was found to be very useful for developing an understanding of interrelationships between various sensor measured values. From the correlation analysis that was performed, it can be observed that there is a strong correlation between the temperature changes and the strain measured by the strain gages.

5.2 R programming language

Supported by the R Foundation for Statistical Computing (2011), R is a programming language and software environment for statistical computing and graphics. This program has a command line interface with several available graphical front-ends, and it is widely utilized by statisticians and data analysts for performing statistical analyses.

A wide variety of statistical and graphical techniques are implemented with R and its libraries, including linear and nonlinear modeling, classical statistical tests,

time-series analysis, classification, clustering, and others. R is easily extensible through functions and extensions, and the R community is noted for its active contributions in terms of packages. Many of R's standard functions are written in R itself, which makes it easy for users to follow the algorithmic choices that are made. For computationally intensive tasks, C, C++, and FORTRAN code can be linked and called at run time. Another strength of R is its static graphics, which can produce publication-quality graphs, including mathematical symbols. Dynamic and interactive graphics are available through additional packages (R Development Core Team 2011).

Given its data analysis capabilities, the R program can easily handle fairly large data sets. Consequently, this program was selected for analysis of the data that was collected from the different sensors that were installed in the west GRS abutment. The process of collecting and analyzing the data was as follows:

- First, the raw data was transferred from the loggers to a laptop at the site. These raw data needed to be converted to engineering data using calibration relationships provided for each individual sensor. The data was saved in text files in different columns corresponding to readings that were taken over time by the different sensors.
- At the University of Delaware, a code was written in the R environment to read the text file and convert the raw data to engineering data in the desired units.
- Since a large volume of data was collected from the data logger, some memory issues occurred during the conversion process after a couple of

months of data collection, as the data set rapidly grew to be very large. Consequently, it was decided to round the data. The rounding operation was conducted very carefully for each type of sensor to make sure that the outcome was still precise and reliable. The degree of rounding for each sensor type was selected following the general accuracy and precision values reported by the manufacturer for each sensor.

- Another technique that was used to overcome the memory issue was filtering. Examination of recorded data indicated that filtering every other row of recorded data allowed for presentation of essentially the same results, with very little loss of shape or resolution in the recorded data sets; this filtering process reduced the recorded data from a time interval of every 10 minutes to a time interval of 20 minutes.
- The graph for the engineering data was plotted using R for all sensors and trends were evaluated to investigate any change in the abutment behavior.

This process was followed after every data collection event from the data loggers in the field, with the graphs being updated accordingly after each round of data collection. Data from the field were generally collected manually from the data logger every 2-3 weeks or so over the long-term monitoring period.

5.3 Correlation analysis using R

Different types of instruments followed different trends in behavior over the long-term monitoring period. In some cases, direct observation of recorded sensor values indicated a general behavioral trend that was similar between various sensors. For example, all strain gages tended to show somewhat similar trends in behavior, relative to each other. Additionally, the strain gauges seemed to have similar behavior as what was observed with the air temperature values, as recorded by the thermistor at the data logger location. From these initial observations, it was felt that utilizing a mathematical methodology to identify sensors that exhibited similar trends in behavior would be useful for assessing the overall response of the structure. In addition, some of the sensors' responses might be dependent on the change of measured values from different sensors (for example, changes in total pressure corresponding to a change in the river level, which might also change volumetric moisture contents, or changes in temperature causing thermal strains of the bridge superstructure or GRS abutments, etc). As a result, a correlation analysis approach was utilized to identify commonalities between data that was collected from different sensors.

This correlation analysis was conducted using R with data collected over the first year of in-service operation of the GRS-IBS. As observed weather patterns and temperature trends follow a generally annual cycle, similar behavioral trends were observed for future years of data collection. Using correlation analysis, the correlation coefficient between any two sets of recorded data can be calculated using the following approach (Johnson and Wichem 2002):

$$\rho_{X,Y} = \frac{cov(X,Y)}{\sigma_X \sigma_Y} \quad (5.1)$$

$$cov(X,Y) = E[(X - \mu_X)(Y - \mu_y)] \quad (5.2)$$

$$\mu_X = E[X] \quad (5.3)$$

$$\mu_Y = E[Y] \quad (5.4)$$

$$\sigma^2{}_X = E[X^2] - E[X]^2 \quad (5.5)$$

$$\sigma^2{}_{XY} = E[XY^2] - E[Y]^2 \quad (5.6)$$

$$E\big[(X - \mu_X)(Y - \mu_y)\big] = E[XY] - E[x]E[Y] \quad (5.7)$$

In Equations 5.1 through 5.7, *X* and *Y* are the data sets of interest (i.e, data from sensor 1 and sensor 2), $\rho_{X,Y}$ is Pearson's correlation coefficient (Pearson 1920), cov is the covariance, σ is the standard deviation of a data set, μ is the mean of a data set, and *E* is the expected value, which is calculated using Equation 5.8:

$$E[X] = x_1 p_1 + x_2 p_2 + \cdots + x_k p_k \quad (5.8)$$

Where the x_is are the variables and the p_ks are the corresponding probabilities.

The correlation coefficient ranges from −1 to 1. A value of 1 implies that a linear equation describes the relationship between *X* and *Y* perfectly, with all data points lying on a line for which *Y* increases as *X* increases. A value of −1 implies that all data

points lie on a line for which *Y* decreases as *X* increases. A value of 0 implies that there is no linear correlation between the variables (Johnson and Wichem 2002).

Correlation analysis was performed by breaking up the recorded data for each sensor into single-day increments. In this way, the effect of daily trends in behavior could be separated from longer-term (i.e., seasonal or annual) trends in behavior. In this analysis, the correlation was conducted between the data recorded by one sensor versus the data recorded by all other sensors, one-by-one. For example, one strain gage was selected and the correlation coefficient was calculated between its daily data and the other sensors' data. As a result, for each sensor, a large matrix of data was formed with 365 rows and 97 columns. The number of rows represents the number of days in one year for which comparisons are being made and the number of columns indicates the results for the sensors whose data the primary sensor is being compared against. There will be a total of 97 of these matrices that result from this analysis process.

To aggregate the daily correlation results, an average correlation coefficient can be determined by averaging the 365 rows of daily correlation data for each sensor. This allows a 97 x 97 matrix to be developed, which presents the average degree of daily correlation between the different sensor types in the current study, as shown in Figures 5.1 through 5.4. As shown in these figures, different colors are attributed to different ranges of average values, which vary between dark green (between 0.9 and 1 or -0.9 and -1) to dark red (between -0.1 and 0.1).

As shown in these figures, there is a very high correlation between the strain gages and air temperature data with ρ>0.99 for almost every sensor. The largest block of green shown is the correlation of different strain gauges relative to each other; this illustrates the significant behavioral similarities of data measured by the different strain gauges. It can also be observed in these figures that the correlation coefficients between air temperature (T_a) and temperatures measured by the thermistors closer to the facing wall are greater than the corresponding values for T_a and temperatures measured further away from the facing wall. This behavior is rational, as the closer thermistors are more exposed to the air and their temperature changes, which are driven by air temperature changes, should be more consistent. Thermistors further away from the wall show less correlation, because deeper soil temperatures are not as affected by daily swings in temperature, but rather move with seasonal changes in temperature.

Another finding from Figures 5.1 through 5.4 is the very strong correlation between the measured pore pressure by the three piezometers (P1 to P3), which is equal to 1. Piezometer P1 was placed in the lower part of the abutment while the other two were installed in the foundation. This indicates that the change in pore pressure in the abutment and the foundation has the same root cause, which was believed to be the change in water level in the river; more data and analysis in this regard will be presented in Chapter 9. Measured results also did not show any correlation between the changes in pore pressure and the strain changes in the abutment, since the corresponding correlation coefficients are low and less than 0.38 (with an average value of 0.35), as shown in Figures 5.1 through 5.4. The same conclusion can be made for the correlation

between the water content measured by the abutment water content sensors and the abutment deformation since the corresponding correlation coefficients are very close to 0 in Figure 5.1. It can consequently be inferred that changes in abutment water content did not induce any significant changes in abutment strain. Finally, the pore pressure and water content changes of the foundation and abutment did not correlate strongly with foundation deformation.

Figure 5.1 The average correlation coefficient between different sensors

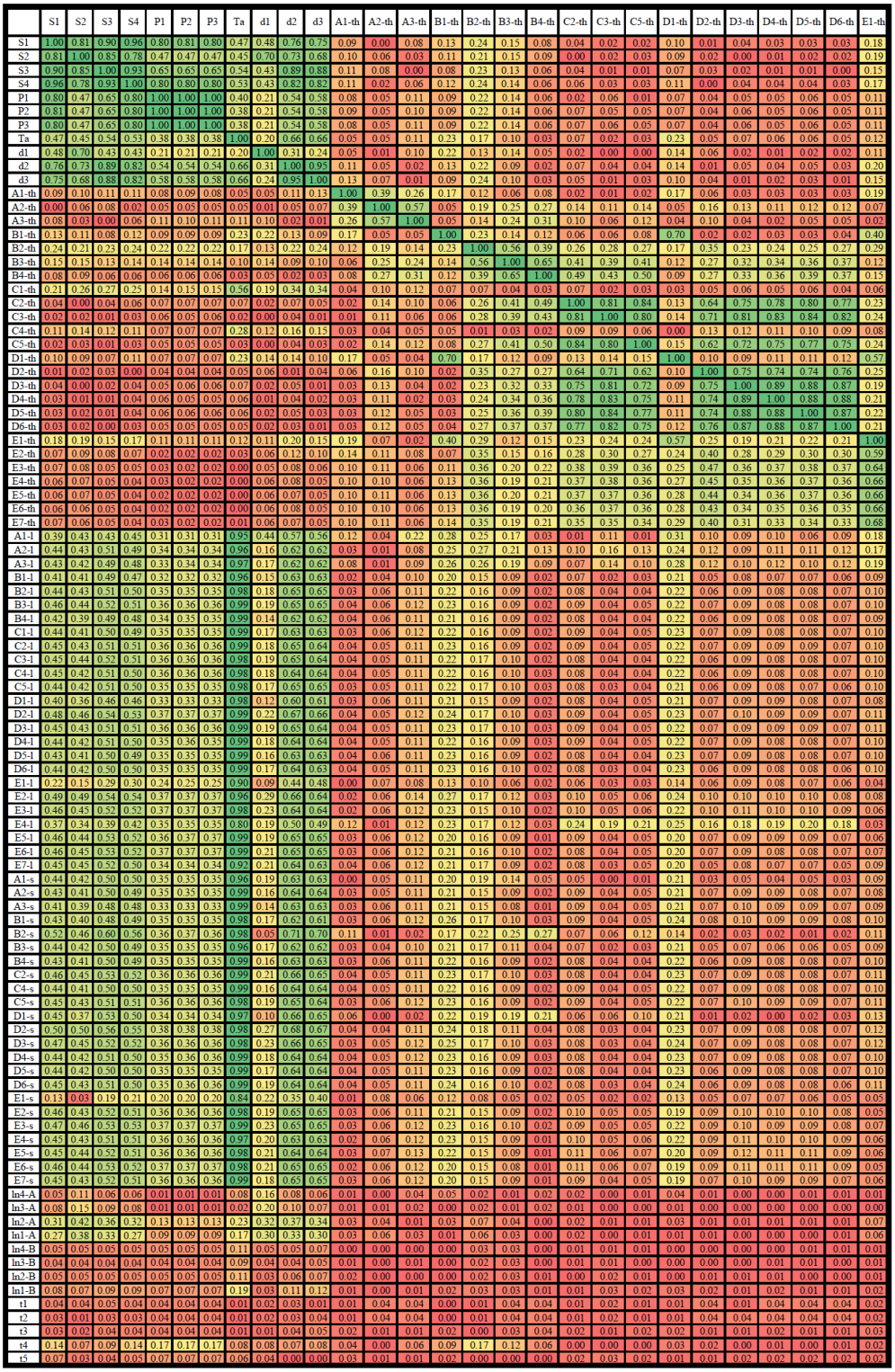

	S1	S2	S3	S4	P1	P2	P3	Ta	d1	d2	d3	A1-th	A2-th	A3-th	B1-th	B2-th	B3-th	B4-th	C2-th	C3-th	C5-th	D1-th	D2-th	D3-th	D4-th	D5-th	D6-th	E1-th
S1	1.00	0.81	0.90	0.96	0.80	0.81	0.80	0.47	0.48	0.76	0.75	0.09	0.00	0.08	0.13	0.24	0.15	0.08	0.04	0.02	0.02	0.10	0.01	0.04	0.03	0.03	0.03	0.18
S2	0.81	1.00	0.85	0.78	0.47	0.47	0.47	0.45	0.70	0.73	0.68	0.10	0.06	0.03	0.11	0.21	0.15	0.09	0.00	0.02	0.03	0.09	0.02	0.00	0.01	0.02	0.02	0.19
S3	0.90	0.85	1.00	0.93	0.65	0.65	0.65	0.54	0.43	0.89	0.88	0.11	0.08	0.00	0.08	0.23	0.13	0.06	0.04	0.01	0.01	0.07	0.03	0.02	0.01	0.01	0.00	0.15
S4	0.96	0.78	0.93	1.00	0.80	0.80	0.80	0.53	0.43	0.82	0.82	0.11	0.02	0.06	0.12	0.24	0.14	0.06	0.06	0.03	0.03	0.11	0.00	0.04	0.04	0.04	0.03	0.17
P1	0.80	0.47	0.65	0.80	1.00	1.00	1.00	0.40	0.21	0.54	0.58	0.08	0.05	0.11	0.09	0.22	0.14	0.06	0.02	0.06	0.01	0.07	0.04	0.05	0.05	0.06	0.05	0.11
P2	0.81	0.47	0.65	0.80	1.00	1.00	1.00	0.38	0.21	0.54	0.58	0.09	0.05	0.10	0.09	0.22	0.14	0.06	0.07	0.05	0.05	0.07	0.04	0.06	0.05	0.06	0.05	0.11
P3	0.80	0.47	0.65	0.80	1.00	1.00	1.00	0.38	0.21	0.54	0.58	0.08	0.05	0.11	0.09	0.22	0.14	0.06	0.07	0.06	0.05	0.07	0.04	0.06	0.05	0.06	0.05	0.11
Ta	0.47	0.45	0.54	0.53	0.38	0.38	0.38	1.00	0.20	0.66	0.66	0.05	0.05	0.11	0.23	0.17	0.10	0.03	0.07	0.02	0.03	0.23	0.05	0.07	0.06	0.06	0.05	0.12
d1	0.48	0.70	0.43	0.43	0.21	0.21	0.21	0.20	1.00	0.31	0.24	0.05	0.01	0.10	0.22	0.13	0.14	0.05	0.02	0.00	0.00	0.14	0.06	0.02	0.01	0.02	0.02	0.11
d2	0.76	0.73	0.89	0.82	0.54	0.54	0.54	0.66	0.31	1.00	0.95	0.11	0.05	0.02	0.13	0.22	0.09	0.02	0.07	0.04	0.04	0.14	0.01	0.05	0.04	0.05	0.03	0.20
d3	0.75	0.68	0.88	0.82	0.58	0.58	0.58	0.66	0.24	0.95	1.00	0.13	0.07	0.01	0.09	0.24	0.10	0.03	0.05	0.01	0.03	0.10	0.04	0.01	0.02	0.03	0.01	0.15
A1-th	0.09	0.10	0.11	0.11	0.08	0.09	0.08	0.05	0.05	0.11	0.13	1.00	0.39	0.26	0.17	0.12	0.06	0.08	0.02	0.01	0.02	0.17	0.06	0.03	0.03	0.03	0.03	0.19
A2-th	0.00	0.06	0.08	0.02	0.05	0.05	0.05	0.05	0.01	0.05	0.07	0.39	1.00	0.57	0.05	0.19	0.25	0.27	0.14	0.11	0.14	0.05	0.16	0.13	0.11	0.12	0.12	0.07
A3-th	0.08	0.03	0.00	0.06	0.11	0.10	0.11	0.11	0.10	0.02	0.01	0.26	0.57	1.00	0.05	0.14	0.24	0.31	0.10	0.06	0.12	0.04	0.10	0.04	0.02	0.05	0.05	0.02
B1-th	0.13	0.11	0.08	0.12	0.09	0.09	0.09	0.23	0.22	0.13	0.09	0.17	0.05	0.05	1.00	0.23	0.14	0.12	0.06	0.06	0.08	0.70	0.02	0.02	0.03	0.03	0.04	0.40
B2-th	0.24	0.21	0.23	0.24	0.22	0.22	0.22	0.17	0.13	0.22	0.24	0.12	0.19	0.14	0.23	1.00	0.56	0.39	0.26	0.28	0.27	0.17	0.35	0.23	0.24	0.25	0.27	0.29
B3-th	0.15	0.15	0.13	0.14	0.14	0.14	0.14	0.10	0.14	0.09	0.10	0.06	0.25	0.24	0.14	0.56	1.00	0.65	0.41	0.39	0.41	0.12	0.27	0.32	0.34	0.36	0.37	0.12
B4-th	0.08	0.09	0.06	0.06	0.06	0.06	0.06	0.03	0.05	0.02	0.03	0.08	0.27	0.31	0.12	0.39	0.65	1.00	0.49	0.43	0.50	0.09	0.27	0.33	0.36	0.39	0.37	0.15
C1-th	0.21	0.26	0.27	0.25	0.14	0.15	0.15	0.56	0.19	0.34	0.34	0.04	0.10	0.12	0.07	0.07	0.04	0.03	0.07	0.02	0.03	0.03	0.05	0.06	0.05	0.06	0.04	0.06
C2-th	0.04	0.00	0.04	0.06	0.07	0.07	0.07	0.07	0.02	0.07	0.05	0.02	0.14	0.10	0.06	0.26	0.41	0.49	1.00	0.81	0.84	0.13	0.64	0.75	0.78	0.80	0.77	0.23
C3-th	0.02	0.02	0.01	0.03	0.06	0.05	0.06	0.02	0.00	0.04	0.01	0.01	0.11	0.06	0.06	0.28	0.39	0.43	0.81	1.00	0.80	0.14	0.71	0.81	0.83	0.84	0.82	0.24
C4-th	0.11	0.14	0.12	0.11	0.07	0.07	0.07	0.28	0.12	0.16	0.15	0.03	0.04	0.05	0.05	0.01	0.03	0.02	0.09	0.09	0.06	0.00	0.13	0.12	0.11	0.10	0.09	0.08
C5-th	0.02	0.03	0.01	0.03	0.05	0.05	0.05	0.03	0.00	0.04	0.03	0.02	0.14	0.12	0.08	0.27	0.41	0.50	0.84	0.80	1.00	0.15	0.62	0.72	0.75	0.77	0.75	0.24
D1-th	0.10	0.09	0.07	0.11	0.07	0.07	0.07	0.23	0.14	0.14	0.10	0.17	0.05	0.04	0.70	0.17	0.12	0.09	0.13	0.14	0.15	1.00	0.10	0.09	0.11	0.11	0.12	0.57
D2-th	0.01	0.02	0.03	0.00	0.04	0.04	0.04	0.05	0.06	0.01	0.04	0.06	0.16	0.10	0.02	0.35	0.27	0.27	0.64	0.71	0.62	0.10	1.00	0.75	0.74	0.74	0.76	0.25
D3-th	0.04	0.00	0.02	0.04	0.05	0.06	0.06	0.07	0.02	0.05	0.01	0.03	0.13	0.04	0.02	0.23	0.32	0.33	0.75	0.81	0.72	0.09	0.75	1.00	0.89	0.88	0.87	0.19
D4-th	0.03	0.01	0.01	0.04	0.06	0.05	0.05	0.06	0.01	0.04	0.02	0.03	0.11	0.02	0.03	0.24	0.34	0.36	0.78	0.83	0.75	0.11	0.74	0.89	1.00	0.88	0.88	0.21
D5-th	0.03	0.02	0.01	0.04	0.06	0.06	0.06	0.06	0.02	0.05	0.03	0.03	0.12	0.05	0.03	0.25	0.36	0.39	0.80	0.84	0.77	0.11	0.74	0.88	0.88	1.00	0.87	0.22
D6-th	0.03	0.02	0.00	0.03	0.05	0.05	0.05	0.05	0.02	0.03	0.01	0.03	0.12	0.05	0.04	0.27	0.37	0.37	0.77	0.82	0.75	0.12	0.76	0.87	0.88	0.87	1.00	0.21
E1-th	0.18	0.19	0.15	0.17	0.11	0.11	0.11	0.12	0.11	0.20	0.15	0.19	0.07	0.02	0.40	0.29	0.12	0.15	0.23	0.24	0.24	0.57	0.25	0.19	0.21	0.22	0.21	1.00
E2-th	0.07	0.09	0.08	0.07	0.02	0.02	0.02	0.03	0.06	0.12	0.10	0.14	0.11	0.08	0.07	0.35	0.15	0.16	0.28	0.30	0.27	0.24	0.40	0.28	0.29	0.30	0.30	0.59
E3-th	0.07	0.08	0.05	0.05	0.03	0.02	0.02	0.00	0.05	0.08	0.06	0.10	0.11	0.06	0.11	0.36	0.20	0.22	0.38	0.39	0.36	0.25	0.47	0.36	0.37	0.38	0.37	0.64
E4-th	0.06	0.07	0.05	0.04	0.03	0.02	0.02	0.00	0.06	0.08	0.05	0.10	0.10	0.06	0.13	0.36	0.19	0.21	0.37	0.38	0.36	0.27	0.45	0.35	0.36	0.37	0.36	0.66
E5-th	0.06	0.07	0.05	0.04	0.02	0.02	0.02	0.00	0.06	0.07	0.05	0.10	0.11	0.06	0.13	0.36	0.20	0.21	0.37	0.37	0.36	0.28	0.44	0.34	0.36	0.37	0.36	0.66
E6-th	0.06	0.06	0.05	0.04	0.02	0.02	0.02	0.00	0.06	0.08	0.05	0.10	0.10	0.06	0.13	0.36	0.19	0.20	0.36	0.37	0.36	0.28	0.43	0.34	0.35	0.36	0.35	0.66
E7-th	0.07	0.06	0.05	0.04	0.03	0.02	0.02	0.01	0.06	0.07	0.05	0.10	0.11	0.06	0.14	0.35	0.19	0.21	0.35	0.35	0.34	0.29	0.40	0.31	0.33	0.34	0.33	0.68
A1-1	0.39	0.43	0.43	0.45	0.31	0.31	0.31	0.95	0.44	0.57	0.56	0.12	0.04	0.22	0.28	0.25	0.17	0.03	0.01	0.11	0.01	0.31	0.10	0.09	0.10	0.06	0.09	0.18
A2-1	0.44	0.43	0.51	0.49	0.34	0.34	0.34	0.96	0.16	0.62	0.62	0.03	0.01	0.08	0.25	0.27	0.21	0.13	0.10	0.16	0.13	0.24	0.12	0.09	0.11	0.11	0.12	0.17
A3-1	0.43	0.42	0.49	0.48	0.33	0.34	0.34	0.97	0.17	0.62	0.62	0.08	0.01	0.09	0.26	0.26	0.19	0.09	0.07	0.14	0.10	0.28	0.12	0.10	0.12	0.10	0.12	0.19
B1-1	0.41	0.41	0.49	0.47	0.32	0.32	0.32	0.96	0.15	0.63	0.63	0.02	0.04	0.10	0.20	0.15	0.09	0.02	0.07	0.02	0.03	0.21	0.05	0.08	0.07	0.07	0.06	0.09
B2-1	0.44	0.43	0.51	0.50	0.35	0.35	0.35	0.98	0.18	0.65	0.65	0.03	0.06	0.11	0.22	0.16	0.09	0.02	0.08	0.04	0.04	0.22	0.06	0.09	0.08	0.08	0.07	0.10
B3-1	0.46	0.44	0.52	0.51	0.36	0.36	0.36	0.99	0.19	0.65	0.65	0.04	0.06	0.12	0.23	0.16	0.09	0.02	0.09	0.04	0.05	0.22	0.07	0.09	0.08	0.08	0.07	0.10
B4-1	0.42	0.39	0.49	0.48	0.34	0.35	0.35	0.99	0.14	0.62	0.62	0.04	0.06	0.11	0.21	0.16	0.09	0.02	0.08	0.04	0.04	0.22	0.06	0.09	0.08	0.08	0.07	0.09
C1-1	0.44	0.41	0.50	0.49	0.35	0.35	0.35	0.99	0.17	0.63	0.63	0.03	0.06	0.12	0.22	0.16	0.09	0.02	0.09	0.04	0.05	0.23	0.07	0.09	0.08	0.08	0.07	0.10
C2-1	0.45	0.43	0.51	0.51	0.36	0.36	0.36	0.99	0.18	0.65	0.64	0.04	0.05	0.11	0.23	0.16	0.09	0.02	0.09	0.04	0.05	0.22	0.07	0.09	0.09	0.09	0.07	0.10
C3-1	0.45	0.44	0.52	0.51	0.36	0.36	0.36	0.98	0.19	0.65	0.64	0.04	0.05	0.11	0.22	0.17	0.10	0.02	0.08	0.04	0.04	0.22	0.06	0.09	0.08	0.08	0.07	0.10
C4-1	0.45	0.42	0.51	0.50	0.36	0.36	0.36	0.98	0.18	0.64	0.64	0.04	0.05	0.11	0.22	0.16	0.10	0.03	0.08	0.04	0.04	0.22	0.06	0.09	0.08	0.08	0.07	0.10
C5-1	0.44	0.42	0.51	0.50	0.35	0.35	0.35	0.98	0.17	0.65	0.65	0.03	0.05	0.11	0.22	0.17	0.10	0.03	0.08	0.03	0.04	0.21	0.06	0.09	0.08	0.07	0.06	0.10
D1-1	0.40	0.36	0.46	0.46	0.33	0.33	0.33	0.98	0.12	0.60	0.61	0.03	0.06	0.11	0.21	0.15	0.09	0.02	0.08	0.04	0.05	0.21	0.07	0.09	0.09	0.08	0.07	0.08
D2-1	0.48	0.46	0.54	0.53	0.37	0.37	0.37	0.99	0.22	0.67	0.66	0.04	0.05	0.12	0.24	0.17	0.10	0.03	0.09	0.04	0.05	0.23	0.07	0.10	0.09	0.09	0.07	0.11
D3-1	0.45	0.43	0.51	0.51	0.36	0.36	0.36	0.99	0.19	0.65	0.64	0.04	0.05	0.11	0.23	0.17	0.10	0.03	0.09	0.04	0.05	0.22	0.07	0.09	0.09	0.09	0.07	0.11
D4-1	0.44	0.42	0.51	0.50	0.35	0.36	0.35	0.99	0.18	0.64	0.64	0.04	0.05	0.11	0.22	0.16	0.09	0.03	0.09	0.04	0.05	0.22	0.07	0.09	0.08	0.08	0.07	0.10
D5-1	0.43	0.41	0.50	0.49	0.35	0.35	0.35	0.99	0.16	0.63	0.63	0.04	0.06	0.11	0.23	0.16	0.09	0.02	0.08	0.04	0.04	0.23	0.07	0.09	0.08	0.08	0.07	0.10
D6-1	0.44	0.42	0.50	0.50	0.35	0.35	0.35	0.99	0.17	0.64	0.63	0.04	0.05	0.11	0.23	0.16	0.10	0.02	0.08	0.03	0.04	0.23	0.06	0.09	0.08	0.08	0.06	0.10
E1-1	0.22	0.15	0.29	0.30	0.24	0.25	0.25	0.90	0.09	0.44	0.48	0.00	0.07	0.08	0.13	0.10	0.06	0.02	0.06	0.03	0.03	0.14	0.06	0.09	0.08	0.07	0.06	0.04
E2-1	0.49	0.49	0.54	0.54	0.37	0.37	0.37	0.96	0.29	0.66	0.64	0.02	0.06	0.14	0.27	0.17	0.12	0.03	0.10	0.05	0.06	0.24	0.10	0.10	0.10	0.10	0.08	0.08
E3-1	0.46	0.45	0.52	0.52	0.37	0.37	0.37	0.98	0.23	0.64	0.64	0.02	0.06	0.12	0.23	0.15	0.10	0.02	0.10	0.05	0.06	0.22	0.10	0.11	0.10	0.10	0.09	0.06
E4-1	0.37	0.34	0.39	0.42	0.35	0.35	0.35	0.80	0.19	0.50	0.49	0.12	0.01	0.12	0.23	0.17	0.12	0.03	0.24	0.19	0.21	0.25	0.16	0.18	0.19	0.20	0.18	0.03
E5-1	0.46	0.44	0.53	0.52	0.36	0.37	0.37	0.99	0.19	0.65	0.65	0.03	0.06	0.12	0.20	0.16	0.09	0.01	0.09	0.04	0.05	0.20	0.07	0.09	0.09	0.09	0.07	0.06
E6-1	0.46	0.45	0.53	0.52	0.37	0.37	0.37	0.99	0.21	0.65	0.65	0.03	0.06	0.12	0.21	0.16	0.10	0.02	0.08	0.04	0.05	0.20	0.07	0.09	0.08	0.08	0.07	0.07
E7-1	0.45	0.45	0.52	0.50	0.34	0.34	0.34	0.92	0.21	0.64	0.63	0.04	0.06	0.12	0.21	0.17	0.09	0.02	0.08	0.03	0.05	0.20	0.05	0.08	0.07	0.07	0.05	0.09
A1-s	0.44	0.42	0.50	0.50	0.35	0.35	0.35	0.96	0.19	0.63	0.63	0.00	0.05	0.11	0.20	0.19	0.14	0.05	0.05	0.00	0.01	0.21	0.03	0.05	0.04	0.05	0.03	0.09
A2-s	0.43	0.41	0.50	0.49	0.35	0.35	0.35	0.99	0.16	0.64	0.64	0.03	0.05	0.11	0.21	0.15	0.09	0.02	0.09	0.04	0.05	0.21	0.07	0.09	0.09	0.08	0.07	0.08
A3-s	0.41	0.39	0.48	0.48	0.33	0.33	0.33	0.99	0.14	0.63	0.63	0.03	0.06	0.11	0.21	0.15	0.08	0.01	0.09	0.04	0.05	0.21	0.07	0.10	0.09	0.09	0.07	0.09
B1-s	0.43	0.40	0.48	0.49	0.35	0.35	0.35	0.98	0.17	0.62	0.61	0.03	0.06	0.12	0.26	0.17	0.10	0.03	0.09	0.04	0.05	0.24	0.08	0.10	0.09	0.09	0.08	0.10
B2-s	0.52	0.46	0.60	0.56	0.36	0.37	0.36	0.98	0.05	0.71	0.70	0.11	0.01	0.02	0.17	0.22	0.25	0.27	0.07	0.06	0.12	0.14	0.02	0.03	0.02	0.01	0.02	0.11
B3-s	0.44	0.42	0.50	0.49	0.35	0.35	0.35	0.96	0.17	0.62	0.62	0.03	0.04	0.10	0.21	0.17	0.11	0.04	0.07	0.02	0.03	0.21	0.05	0.07	0.06	0.06	0.05	0.09
B4-s	0.43	0.41	0.50	0.49	0.35	0.35	0.35	0.99	0.16	0.63	0.63	0.03	0.06	0.11	0.22	0.16	0.09	0.02	0.08	0.04	0.04	0.22	0.06	0.09	0.08	0.08	0.07	0.10
C2-s	0.46	0.45	0.53	0.52	0.36	0.36	0.36	0.99	0.21	0.66	0.65	0.04	0.05	0.11	0.23	0.17	0.10	0.03	0.08	0.04	0.04	0.23	0.07	0.09	0.08	0.08	0.07	0.11
C4-s	0.44	0.41	0.50	0.50	0.35	0.35	0.35	0.99	0.16	0.64	0.64	0.04	0.05	0.11	0.22	0.16	0.09	0.02	0.09	0.04	0.05	0.22	0.07	0.09	0.08	0.08	0.07	0.10
C5-s	0.45	0.43	0.51	0.51	0.36	0.36	0.36	0.98	0.19	0.65	0.64	0.03	0.06	0.12	0.23	0.16	0.09	0.02	0.09	0.04	0.05	0.22	0.07	0.10	0.09	0.09	0.07	0.11
D1-s	0.45	0.37	0.53	0.50	0.34	0.34	0.34	0.97	0.10	0.66	0.65	0.06	0.00	0.02	0.22	0.19	0.19	0.21	0.06	0.06	0.10	0.21	0.01	0.02	0.00	0.02	0.03	0.13
D2-s	0.50	0.50	0.56	0.55	0.38	0.38	0.38	0.98	0.27	0.68	0.67	0.04	0.04	0.11	0.24	0.18	0.11	0.04	0.08	0.03	0.04	0.23	0.07	0.09	0.08	0.08	0.07	0.12
D3-s	0.47	0.45	0.52	0.52	0.36	0.36	0.36	0.98	0.23	0.66	0.65	0.03	0.05	0.12	0.25	0.17	0.10	0.03	0.08	0.03	0.04	0.24	0.07	0.09	0.08	0.08	0.07	0.12
D4-s	0.44	0.42	0.51	0.50	0.35	0.36	0.36	0.99	0.18	0.64	0.64	0.04	0.05	0.12	0.23	0.16	0.09	0.03	0.08	0.04	0.04	0.23	0.07	0.09	0.08	0.08	0.07	0.10
D5-s	0.44	0.42	0.50	0.50	0.35	0.35	0.35	0.99	0.17	0.64	0.64	0.04	0.05	0.11	0.23	0.16	0.09	0.02	0.08	0.04	0.04	0.23	0.06	0.09	0.08	0.08	0.07	0.10
D6-s	0.45	0.43	0.51	0.50	0.35	0.36	0.36	0.99	0.19	0.64	0.64	0.04	0.05	0.11	0.24	0.16	0.10	0.02	0.08	0.03	0.04	0.24	0.06	0.09	0.08	0.08	0.06	0.11
E1-s	0.13	0.03	0.19	0.21	0.20	0.20	0.20	0.84	0.22	0.35	0.40	0.01	0.08	0.06	0.12	0.08	0.05	0.02	0.05	0.02	0.02	0.13	0.05	0.07	0.07	0.06	0.05	0.05
E2-s	0.46	0.43	0.52	0.51	0.36	0.36	0.36	0.98	0.19	0.65	0.65	0.03	0.06	0.11	0.21	0.15	0.09	0.02	0.10	0.05	0.05	0.19	0.09	0.10	0.10	0.10	0.08	0.05
E3-s	0.47	0.46	0.53	0.53	0.37	0.37	0.37	0.99	0.23	0.65	0.65	0.03	0.06	0.12	0.23	0.16	0.10	0.02	0.09	0.05	0.05	0.22	0.09	0.10	0.09	0.09	0.08	0.07
E4-s	0.45	0.43	0.51	0.51	0.36	0.36	0.36	0.97	0.20	0.63	0.63	0.02	0.06	0.12	0.23	0.15	0.09	0.01	0.10	0.05	0.06	0.22	0.09	0.11	0.10	0.10	0.09	0.06
E5-s	0.45	0.44	0.52	0.51	0.36	0.36	0.36	0.98	0.21	0.64	0.64	0.03	0.07	0.13	0.22	0.15	0.09	0.01	0.11	0.06	0.07	0.20	0.09	0.12	0.11	0.11	0.09	0.06
E6-s	0.46	0.44	0.53	0.52	0.37	0.37	0.37	0.98	0.21	0.65	0.65	0.02	0.06	0.12	0.20	0.15	0.08	0.01	0.11	0.06	0.07	0.19	0.09	0.11	0.11	0.11	0.09	0.05
E7-s	0.45	0.43	0.52	0.51	0.36	0.36	0.36	0.99	0.18	0.65	0.65	0.03	0.06	0.12	0.20	0.15	0.09	0.01	0.09	0.04	0.05	0.19	0.07	0.10	0.09	0.09	0.07	0.06
ln4-A	0.05	0.11	0.06	0.06	0.01	0.01	0.01	0.08	0.16	0.08	0.06	0.01	0.00	0.04	0.05	0.02	0.01	0.02	0.02	0.00	0.01	0.04	0.01	0.00	0.00	0.01	0.01	0.01
ln3-A	0.08	0.15	0.09	0.08	0.01	0.01	0.01	0.02	0.20	0.10	0.07	0.01	0.01	0.02	0.00	0.02	0.01	0.02	0.01	0.00	0.00	0.01	0.00	0.00	0.00	0.00	0.00	0.00
ln2-A	0.31	0.42	0.36	0.32	0.13	0.13	0.13	0.23	0.32	0.37	0.34	0.03	0.04	0.01	0.05	0.07	0.04	0.00	0.02	0.01	0.01	0.03	0.01	0.01	0.01	0.01	0.01	0.07
ln1-A	0.27	0.38	0.33	0.27	0.09	0.09	0.09	0.17	0.30	0.33	0.30	0.03	0.06	0.03	0.01	0.06	0.03	0.00	0.02	0.00	0.01	0.01	0.00	0.00	0.00	0.00	0.01	0.06
ln4-B	0.05	0.05	0.05	0.05	0.05	0.05	0.05	0.11	0.05	0.05	0.07	0.00	0.00	0.00	0.00	0.03	0.03	0.00	0.01	0.01	0.01	0.00	0.00	0.00	0.00	0.01	0.01	0.01
ln3-B	0.04	0.04	0.04	0.04	0.04	0.04	0.04	0.09	0.04	0.04	0.05	0.01	0.00	0.01	0.00	0.02	0.03	0.00	0.01	0.01	0.00	0.00	0.00	0.00	0.01	0.01	0.00	0.01

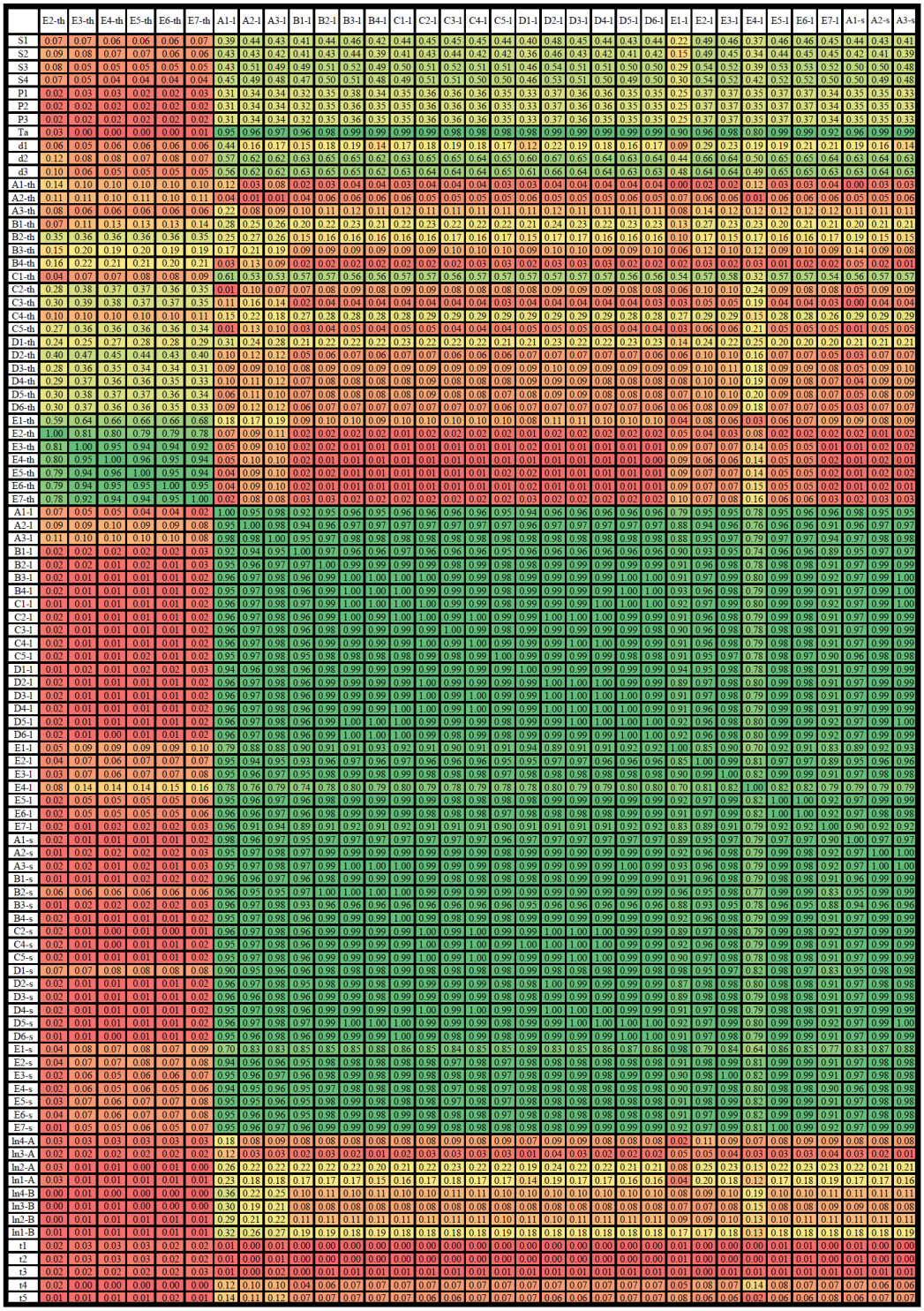

	E2-th	E3-th	E4-th	E5-th	E6-th	E7-th	A1-l	A2-l	A3-l	B1-l	B2-l	B3-l	B4-l	C1-l	C2-l	C3-l	C4-l	C5-l	D1-l	D2-l	D3-l	D4-l	D5-l	D6-l	E1-l	E2-l	E3-l	E4-l	E5-l	E6-l	E7-l	A1-s	A2-s	A3-s
S1	0.07	0.07	0.06	0.06	0.06	0.07	0.39	0.44	0.43	0.41	0.44	0.46	0.42	0.44	0.45	0.45	0.45	0.44	0.40	0.48	0.45	0.44	0.43	0.44	0.22	0.49	0.46	0.37	0.46	0.46	0.45	0.44	0.43	0.41
S2	0.09	0.08	0.07	0.07	0.06	0.06	0.43	0.43	0.42	0.41	0.43	0.44	0.39	0.41	0.43	0.44	0.42	0.42	0.36	0.46	0.43	0.42	0.41	0.42	0.15	0.49	0.45	0.34	0.44	0.45	0.45	0.42	0.41	0.39
S3	0.08	0.05	0.05	0.05	0.05	0.05	0.43	0.51	0.49	0.49	0.51	0.52	0.49	0.50	0.51	0.52	0.51	0.51	0.46	0.54	0.51	0.51	0.50	0.50	0.29	0.54	0.52	0.39	0.53	0.53	0.52	0.50	0.50	0.48
S4	0.07	0.05	0.04	0.04	0.04	0.04	0.45	0.49	0.48	0.47	0.50	0.51	0.48	0.49	0.51	0.51	0.50	0.50	0.46	0.53	0.51	0.50	0.49	0.50	0.30	0.54	0.52	0.42	0.52	0.52	0.50	0.50	0.49	0.48
P1	0.02	0.03	0.03	0.02	0.02	0.03	0.31	0.34	0.34	0.32	0.35	0.38	0.34	0.35	0.36	0.36	0.36	0.35	0.33	0.37	0.36	0.36	0.35	0.35	0.25	0.37	0.37	0.35	0.37	0.37	0.34	0.35	0.35	0.33
P2	0.02	0.02	0.02	0.02	0.02	0.02	0.31	0.34	0.34	0.32	0.35	0.36	0.35	0.35	0.36	0.36	0.36	0.35	0.33	0.37	0.36	0.36	0.35	0.35	0.25	0.37	0.37	0.35	0.37	0.37	0.34	0.35	0.35	0.33
P3	0.02	0.02	0.02	0.02	0.02	0.02	0.31	0.34	0.34	0.32	0.35	0.36	0.35	0.35	0.36	0.36	0.36	0.35	0.33	0.37	0.36	0.35	0.35	0.35	0.25	0.37	0.37	0.35	0.37	0.37	0.34	0.35	0.35	0.33
Ta	0.03	0.00	0.00	0.00	0.00	0.01	0.95	0.96	0.97	0.96	0.98	0.99	0.99	0.99	0.99	0.98	0.98	0.98	0.98	0.99	0.99	0.99	0.99	0.99	0.90	0.96	0.98	0.80	0.99	0.99	0.92	0.96	0.99	0.99
d1	0.06	0.05	0.06	0.06	0.06	0.06	0.44	0.16	0.17	0.15	0.18	0.19	0.14	0.17	0.18	0.19	0.18	0.17	0.12	0.22	0.19	0.18	0.16	0.17	0.09	0.29	0.23	0.19	0.19	0.21	0.21	0.19	0.16	0.14
d2	0.12	0.08	0.08	0.07	0.08	0.07	0.57	0.62	0.62	0.63	0.65	0.65	0.62	0.63	0.65	0.65	0.64	0.65	0.60	0.67	0.65	0.64	0.63	0.64	0.44	0.66	0.64	0.50	0.65	0.65	0.64	0.63	0.64	0.63
d3	0.10	0.06	0.05	0.05	0.05	0.05	0.56	0.62	0.62	0.63	0.65	0.65	0.62	0.63	0.64	0.64	0.64	0.65	0.61	0.66	0.64	0.64	0.63	0.63	0.48	0.64	0.64	0.49	0.65	0.65	0.63	0.63	0.64	0.63
A1-th	0.14	0.10	0.10	0.10	0.10	0.10	0.12	0.03	0.08	0.02	0.03	0.04	0.04	0.03	0.04	0.04	0.04	0.03	0.03	0.04	0.04	0.04	0.04	0.04	0.00	0.02	0.02	0.12	0.03	0.03	0.04	0.00	0.03	0.03
A2-th	0.11	0.11	0.10	0.11	0.10	0.11	0.04	0.01	0.01	0.04	0.06	0.06	0.06	0.06	0.05	0.05	0.05	0.05	0.06	0.05	0.05	0.05	0.06	0.05	0.07	0.06	0.06	0.01	0.06	0.06	0.06	0.05	0.05	0.06
A3-th	0.08	0.06	0.06	0.06	0.06	0.06	0.22	0.08	0.09	0.10	0.11	0.12	0.11	0.12	0.11	0.11	0.11	0.11	0.11	0.12	0.11	0.11	0.11	0.11	0.08	0.14	0.12	0.12	0.12	0.12	0.12	0.11	0.11	0.11
B1-th	0.07	0.11	0.13	0.13	0.13	0.14	0.28	0.25	0.26	0.20	0.22	0.23	0.21	0.22	0.23	0.22	0.22	0.22	0.21	0.24	0.23	0.22	0.23	0.23	0.13	0.27	0.23	0.23	0.20	0.21	0.21	0.20	0.21	0.21
B2-th	0.35	0.36	0.36	0.36	0.36	0.35	0.25	0.27	0.26	0.15	0.16	0.16	0.16	0.16	0.16	0.17	0.16	0.17	0.15	0.17	0.17	0.16	0.16	0.16	0.10	0.17	0.15	0.17	0.16	0.16	0.17	0.19	0.15	0.15
B3-th	0.15	0.20	0.19	0.20	0.19	0.19	0.17	0.21	0.19	0.09	0.09	0.09	0.09	0.09	0.09	0.10	0.10	0.10	0.09	0.10	0.10	0.09	0.09	0.10	0.06	0.12	0.10	0.12	0.09	0.10	0.09	0.14	0.09	0.08
B4-th	0.16	0.22	0.21	0.21	0.20	0.21	0.03	0.13	0.09	0.02	0.02	0.02	0.02	0.02	0.02	0.02	0.03	0.03	0.02	0.03	0.03	0.03	0.02	0.02	0.02	0.03	0.02	0.03	0.01	0.02	0.02	0.05	0.02	0.01
C1-th	0.04	0.07	0.07	0.08	0.08	0.09	0.61	0.53	0.53	0.57	0.57	0.56	0.56	0.57	0.57	0.56	0.57	0.57	0.57	0.57	0.57	0.57	0.56	0.56	0.54	0.57	0.58	0.32	0.57	0.57	0.54	0.56	0.57	0.57
C2-th	0.28	0.38	0.37	0.37	0.36	0.35	0.01	0.10	0.07	0.07	0.08	0.09	0.08	0.09	0.09	0.08	0.08	0.08	0.08	0.09	0.09	0.09	0.08	0.08	0.06	0.10	0.10	0.24	0.09	0.08	0.08	0.05	0.09	0.09
C3-th	0.30	0.39	0.38	0.37	0.37	0.35	0.11	0.16	0.14	0.02	0.04	0.04	0.04	0.04	0.04	0.04	0.04	0.03	0.04	0.04	0.04	0.04	0.04	0.03	0.03	0.05	0.05	0.19	0.04	0.04	0.03	0.00	0.04	0.04
C4-th	0.10	0.10	0.10	0.10	0.10	0.11	0.15	0.22	0.18	0.27	0.28	0.28	0.28	0.28	0.29	0.29	0.29	0.29	0.29	0.29	0.29	0.29	0.28	0.28	0.27	0.29	0.29	0.15	0.28	0.28	0.26	0.29	0.29	0.29
C5-th	0.27	0.36	0.36	0.36	0.36	0.34	0.01	0.13	0.10	0.03	0.04	0.05	0.04	0.05	0.05	0.04	0.04	0.04	0.05	0.05	0.05	0.05	0.04	0.04	0.03	0.06	0.06	0.21	0.05	0.05	0.05	0.01	0.05	0.05
D1-th	0.24	0.25	0.27	0.28	0.28	0.29	0.31	0.24	0.28	0.21	0.22	0.22	0.22	0.23	0.22	0.22	0.22	0.21	0.21	0.23	0.22	0.22	0.23	0.23	0.14	0.24	0.22	0.25	0.20	0.20	0.20	0.21	0.21	0.21
D2-th	0.40	0.47	0.45	0.44	0.43	0.40	0.10	0.12	0.12	0.05	0.06	0.07	0.06	0.07	0.07	0.06	0.06	0.06	0.07	0.07	0.07	0.07	0.07	0.06	0.06	0.10	0.10	0.16	0.07	0.07	0.05	0.03	0.07	0.07
D3-th	0.28	0.36	0.35	0.34	0.34	0.31	0.09	0.09	0.10	0.08	0.09	0.09	0.09	0.09	0.09	0.09	0.09	0.09	0.09	0.10	0.09	0.09	0.09	0.09	0.09	0.10	0.11	0.18	0.09	0.09	0.08	0.05	0.09	0.10
D4-th	0.29	0.37	0.36	0.36	0.35	0.33	0.10	0.11	0.12	0.07	0.08	0.08	0.08	0.08	0.09	0.08	0.08	0.08	0.09	0.09	0.09	0.08	0.08	0.08	0.08	0.10	0.10	0.19	0.09	0.08	0.07	0.04	0.09	0.09
D5-th	0.30	0.38	0.37	0.37	0.36	0.34	0.06	0.11	0.10	0.07	0.08	0.08	0.08	0.08	0.09	0.08	0.08	0.07	0.08	0.09	0.09	0.08	0.08	0.08	0.07	0.10	0.10	0.20	0.09	0.08	0.07	0.05	0.08	0.09
D6-th	0.30	0.37	0.36	0.36	0.35	0.33	0.09	0.12	0.12	0.06	0.07	0.07	0.07	0.07	0.07	0.07	0.07	0.06	0.07	0.07	0.07	0.07	0.07	0.06	0.06	0.08	0.09	0.18	0.07	0.07	0.05	0.03	0.07	0.07
E1-th	0.59	0.64	0.66	0.66	0.66	0.68	0.18	0.17	0.19	0.09	0.10	0.10	0.09	0.10	0.10	0.10	0.10	0.10	0.08	0.11	0.11	0.10	0.10	0.10	0.04	0.08	0.06	0.03	0.06	0.07	0.09	0.04	0.08	0.09
E2-th	1.00	0.81	0.80	0.79	0.79	0.78	0.07	0.09	0.11	0.02	0.02	0.02	0.02	0.01	0.02	0.02	0.02	0.02	0.01	0.02	0.02	0.02	0.02	0.02	0.05	0.04	0.03	0.08	0.02	0.02	0.02	0.02	0.01	0.02
E3-th	0.81	1.00	0.95	0.94	0.94	0.92	0.05	0.09	0.10	0.02	0.02	0.01	0.01	0.01	0.01	0.01	0.01	0.01	0.01	0.02	0.01	0.01	0.01	0.01	0.09	0.07	0.07	0.14	0.05	0.05	0.01	0.02	0.02	0.02
E4-th	0.80	0.95	1.00	0.96	0.95	0.94	0.05	0.10	0.10	0.02	0.01	0.01	0.01	0.01	0.01	0.01	0.01	0.01	0.01	0.01	0.01	0.01	0.01	0.00	0.09	0.06	0.06	0.14	0.05	0.05	0.02	0.01	0.02	0.01
E5-th	0.79	0.94	0.96	1.00	0.95	0.94	0.04	0.09	0.10	0.02	0.02	0.01	0.01	0.01	0.01	0.01	0.01	0.02	0.02	0.01	0.01	0.01	0.01	0.01	0.09	0.07	0.07	0.14	0.05	0.05	0.02	0.01	0.02	0.02
E6-th	0.79	0.94	0.95	0.95	1.00	0.95	0.04	0.09	0.10	0.02	0.01	0.01	0.01	0.01	0.01	0.01	0.01	0.01	0.02	0.01	0.01	0.01	0.01	0.01	0.09	0.07	0.07	0.15	0.05	0.05	0.02	0.01	0.02	0.01
E7-th	0.78	0.92	0.94	0.94	0.95	1.00	0.02	0.08	0.08	0.03	0.03	0.02	0.02	0.02	0.02	0.02	0.02	0.02	0.03	0.02	0.02	0.02	0.02	0.02	0.10	0.07	0.08	0.16	0.06	0.06	0.03	0.02	0.03	0.03
A1-l	0.07	0.05	0.05	0.04	0.04	0.02	1.00	0.95	0.98	0.92	0.95	0.96	0.95	0.96	0.96	0.96	0.96	0.95	0.94	0.96	0.96	0.96	0.96	0.96	0.79	0.95	0.95	0.78	0.95	0.96	0.96	0.98	0.95	0.95
A2-l	0.09	0.09	0.10	0.09	0.09	0.08	0.95	1.00	0.98	0.94	0.96	0.97	0.97	0.97	0.97	0.97	0.97	0.96	0.97	0.97	0.97	0.97	0.97	0.97	0.88	0.94	0.96	0.76	0.96	0.96	0.96	0.91	0.96	0.97
A3-l	0.11	0.10	0.10	0.10	0.10	0.08	0.98	0.98	1.00	0.95	0.97	0.98	0.98	0.98	0.98	0.98	0.98	0.98	0.98	0.98	0.98	0.98	0.98	0.98	0.88	0.95	0.97	0.79	0.97	0.97	0.94	0.97	0.98	0.98
B1-l	0.02	0.02	0.02	0.02	0.02	0.03	0.92	0.94	0.95	1.00	0.97	0.96	0.96	0.97	0.96	0.96	0.96	0.95	0.96	0.96	0.96	0.96	0.96	0.96	0.90	0.93	0.95	0.74	0.96	0.96	0.89	0.95	0.97	0.97
B2-l	0.02	0.02	0.01	0.02	0.01	0.03	0.95	0.96	0.97	0.97	1.00	0.99	0.99	0.99	0.99	0.98	0.99	0.98	0.98	0.99	0.99	0.99	0.99	0.99	0.91	0.96	0.98	0.78	0.98	0.98	0.91	0.97	0.99	0.99
B3-l	0.02	0.01	0.01	0.01	0.01	0.02	0.96	0.97	0.98	0.96	0.99	1.00	1.00	1.00	1.00	0.99	0.99	0.98	0.99	0.99	0.99	0.99	1.00	1.00	0.91	0.97	0.99	0.80	0.99	0.99	0.92	0.97	0.99	1.00
B4-l	0.02	0.01	0.01	0.01	0.01	0.02	0.95	0.97	0.98	0.96	0.99	1.00	1.00	1.00	0.99	0.99	0.99	0.98	0.99	0.99	0.99	0.99	1.00	1.00	0.93	0.96	0.98	0.79	0.99	0.99	0.91	0.97	0.99	1.00
C1-l	0.01	0.01	0.01	0.01	0.01	0.02	0.96	0.97	0.98	0.97	0.99	1.00	1.00	1.00	1.00	0.99	0.99	0.98	0.99	0.99	0.99	1.00	1.00	1.00	0.92	0.97	0.99	0.80	0.99	0.99	0.92	0.97	0.99	1.00
C2-l	0.02	0.01	0.01	0.01	0.01	0.02	0.96	0.97	0.98	0.96	0.99	1.00	0.99	1.00	1.00	0.99	1.00	0.99	0.99	1.00	1.00	1.00	0.99	0.99	0.91	0.96	0.98	0.79	0.99	0.98	0.91	0.97	0.99	0.99
C3-l	0.02	0.01	0.01	0.01	0.01	0.02	0.96	0.97	0.98	0.96	0.98	0.99	0.99	0.99	1.00	0.99	1.00	0.99	0.99	0.99	0.99	0.99	0.98	0.90	0.96	0.98	0.78	0.98	0.98	0.98	0.91	0.97	0.99	0.99
C4-l	0.02	0.01	0.01	0.01	0.01	0.02	0.96	0.97	0.98	0.96	0.99	0.99	0.99	0.99	1.00	0.99	1.00	0.99	0.99	0.99	1.00	1.00	0.99	0.99	0.91	0.96	0.98	0.79	0.98	0.98	0.91	0.97	0.99	0.99
C5-l	0.02	0.01	0.01	0.02	0.01	0.02	0.95	0.97	0.98	0.95	0.98	0.98	0.98	0.98	0.99	0.98	0.99	1.00	0.99	0.99	0.99	0.99	0.98	0.98	0.91	0.95	0.97	0.78	0.98	0.97	0.90	0.96	0.98	0.98
D1-l	0.01	0.02	0.01	0.02	0.02	0.03	0.94	0.96	0.98	0.96	0.98	0.99	0.99	0.99	0.99	0.99	0.99	1.00	0.99	0.99	0.99	0.99	0.99	0.99	0.94	0.95	0.98	0.78	0.98	0.98	0.91	0.97	0.99	0.99
D2-l	0.02	0.01	0.01	0.01	0.01	0.02	0.96	0.97	0.98	0.96	0.99	0.99	0.99	0.99	1.00	0.99	0.99	0.99	0.99	1.00	1.00	1.00	0.99	0.99	0.89	0.97	0.98	0.80	0.99	0.98	0.91	0.97	0.99	0.99
D3-l	0.02	0.01	0.01	0.01	0.01	0.02	0.96	0.97	0.98	0.96	0.99	0.99	0.99	0.99	1.00	0.99	1.00	0.99	0.99	1.00	1.00	1.00	0.99	0.99	0.91	0.97	0.98	0.79	0.98	0.98	0.91	0.97	0.99	0.99
D4-l	0.02	0.01	0.01	0.01	0.01	0.02	0.96	0.97	0.98	0.96	0.99	0.99	0.99	0.99	1.00	0.99	1.00	0.99	0.99	1.00	1.00	1.00	0.99	0.99	0.91	0.97	0.98	0.79	0.98	0.98	0.91	0.97	0.99	0.99
D5-l	0.02	0.01	0.01	0.01	0.01	0.02	0.96	0.97	0.98	0.97	0.99	1.00	1.00	1.00	0.99	0.99	0.99	0.98	0.99	0.99	0.99	1.00	1.00	1.00	0.92	0.97	0.99	0.80	0.99	0.99	0.92	0.97	0.99	1.00
D6-l	0.01	0.01	0.00	0.01	0.01	0.02	0.95	0.97	0.98	0.96	0.98	0.99	0.98	0.99	0.98	0.99	0.98	0.98	0.98	0.99	0.99	0.99	0.99	0.99	0.91	0.96	0.98	0.79	0.98	0.98	0.91	0.97	0.99	0.99
E1-l	0.05	0.09	0.09	0.09	0.09	0.10	0.79	0.88	0.88	0.90	0.91	0.91	0.93	0.92	0.91	0.90	0.91	0.91	0.94	0.89	0.91	0.91	0.92	0.92	1.00	0.85	0.90	0.70	0.92	0.91	0.83	0.89	0.92	0.93
E2-l	0.04	0.07	0.06	0.07	0.07	0.07	0.95	0.94	0.95	0.93	0.96	0.97	0.96	0.97	0.96	0.96	0.96	0.95	0.95	0.97	0.97	0.96	0.96	0.96	0.85	1.00	0.99	0.81	0.97	0.97	0.89	0.95	0.96	0.96
E3-l	0.03	0.07	0.06	0.07	0.07	0.08	0.95	0.96	0.97	0.95	0.98	0.99	0.98	0.99	0.98	0.98	0.98	0.98	0.98	0.98	0.98	0.98	0.98	0.98	0.90	0.99	1.00	0.82	0.99	0.99	0.91	0.97	0.98	0.98
E4-l	0.08	0.14	0.14	0.14	0.15	0.16	0.78	0.76	0.79	0.74	0.78	0.80	0.79	0.80	0.79	0.78	0.79	0.78	0.78	0.80	0.79	0.79	0.80	0.80	0.70	0.81	0.82	1.00	0.82	0.82	0.79	0.79	0.79	0.79
E5-l	0.02	0.05	0.05	0.05	0.05	0.06	0.95	0.96	0.97	0.96	0.98	0.99	0.99	0.99	0.99	0.98	0.98	0.98	0.98	0.99	0.99	0.99	0.99	0.99	0.92	0.97	0.99	0.82	1.00	1.00	0.92	0.97	0.99	0.99
E6-l	0.02	0.05	0.05	0.05	0.05	0.06	0.96	0.96	0.97	0.96	0.98	0.99	0.99	0.99	0.98	0.98	0.98	0.97	0.98	0.98	0.98	0.98	0.99	0.99	0.91	0.97	0.99	0.82	1.00	1.00	0.92	0.97	0.98	0.98
E7-l	0.02	0.01	0.02	0.02	0.02	0.03	0.96	0.91	0.94	0.89	0.91	0.92	0.91	0.92	0.91	0.91	0.91	0.90	0.91	0.91	0.91	0.91	0.92	0.92	0.83	0.89	0.91	0.79	0.92	0.92	1.00	0.90	0.92	0.92
A1-s	0.02	0.01	0.01	0.01	0.01	0.02	0.98	0.96	0.97	0.95	0.97	0.97	0.97	0.97	0.97	0.97	0.97	0.96	0.97	0.97	0.97	0.97	0.97	0.97	0.89	0.95	0.97	0.79	0.97	0.97	0.90	1.00	0.97	0.97
A2-s	0.01	0.02	0.02	0.02	0.02	0.03	0.95	0.97	0.98	0.97	0.99	0.99	0.99	0.99	0.99	0.99	0.99	0.98	0.99	0.99	0.99	0.99	0.99	0.99	0.92	0.96	0.98	0.79	0.99	0.98	0.92	0.97	1.00	1.00
A3-s	0.02	0.02	0.01	0.02	0.01	0.03	0.95	0.97	0.98	0.97	0.99	1.00	1.00	1.00	0.99	0.99	0.99	0.98	0.99	0.99	0.99	0.99	1.00	0.99	0.93	0.96	0.98	0.79	0.99	0.98	0.92	0.97	1.00	1.00
B1-s	0.01	0.01	0.01	0.02	0.02	0.02	0.96	0.96	0.97	0.96	0.98	0.99	0.99	0.99	0.99	0.98	0.98	0.98	0.98	0.99	0.99	0.99	0.99	0.91	0.96	0.98	0.79	0.98	0.98	0.91	0.96	0.99	0.99	
B2-s	0.06	0.06	0.06	0.06	0.06	0.06	0.96	0.95	0.95	0.97	1.00	1.00	1.00	1.00	0.99	0.99	0.99	0.99	0.99	0.99	0.99	0.99	0.99	0.96	0.95	0.98	0.97	0.78	0.99	0.99	0.93	0.95	0.99	0.99
B3-s	0.01	0.02	0.02	0.02	0.02	0.03	0.96	0.97	0.98	0.93	0.96	0.96	0.96	0.96	0.96	0.96	0.96	0.96	0.95	0.96	0.96	0.96	0.96	0.96	0.88	0.93	0.95	0.78	0.96	0.95	0.88	0.94	0.96	0.96
B4-s	0.02	0.01	0.01	0.01	0.01	0.02	0.95	0.97	0.98	0.96	0.99	0.99	0.99	1.00	0.99	0.98	0.99	0.98	0.99	0.99	0.99	0.99	0.99	0.99	0.92	0.96	0.98	0.79	0.99	0.99	0.91	0.97	0.99	0.99
C2-s	0.02	0.01	0.00	0.01	0.00	0.01	0.96	0.97	0.98	0.96	0.99	0.99	0.99	0.99	1.00	0.99	1.00	0.99	0.99	1.00	1.00	1.00	0.99	0.99	0.89	0.97	0.98	0.79	0.99	0.98	0.92	0.97	0.99	0.99
C4-s	0.02	0.01	0.00	0.01	0.01	0.02	0.95	0.97	0.98	0.96	0.99	0.99	0.99	1.00	0.99	0.99	1.00	0.99	0.99	1.00	1.00	1.00	0.99	0.99	0.92	0.96	0.98	0.79	0.99	0.98	0.91	0.97	0.99	0.99
C5-s	0.02	0.01	0.01	0.01	0.01	0.02	0.95	0.97	0.98	0.96	0.99	0.99	0.99	0.99	1.00	0.99	1.00	0.99	0.99	0.99	1.00	1.00	0.99	0.99	0.90	0.97	0.98	0.78	0.98	0.98	0.91	0.97	0.99	0.99
D1-s	0.07	0.07	0.08	0.08	0.08	0.08	0.90	0.95	0.96	0.96	0.98	0.98	0.98	0.99	0.98	0.98	0.98	0.98	0.99	0.98	0.98	0.98	0.99	0.98	0.98	0.95	0.97	0.82	0.98	0.97	0.83	0.95	0.98	0.98
D2-s	0.02	0.01	0.01	0.01	0.01	0.02	0.96	0.97	0.98	0.95	0.98	0.99	0.98	0.99	0.99	0.99	0.99	0.98	0.98	1.00	0.99	0.99	0.99	0.99	0.87	0.98	0.98	0.80	0.98	0.98	0.91	0.97	0.98	0.98
D3-s	0.02	0.01	0.01	0.01	0.01	0.02	0.96	0.96	0.98	0.96	0.99	0.99	0.99	0.99	0.99	0.99	0.99	0.98	0.99	0.99	0.99	0.99	0.99	0.99	0.89	0.98	0.98	0.79	0.98	0.98	0.91	0.97	0.99	0.98
D4-s	0.02	0.01	0.01	0.01	0.01	0.02	0.95	0.97	0.98	0.96	0.99	0.99	0.99	0.99	1.00	0.99	1.00	0.99	0

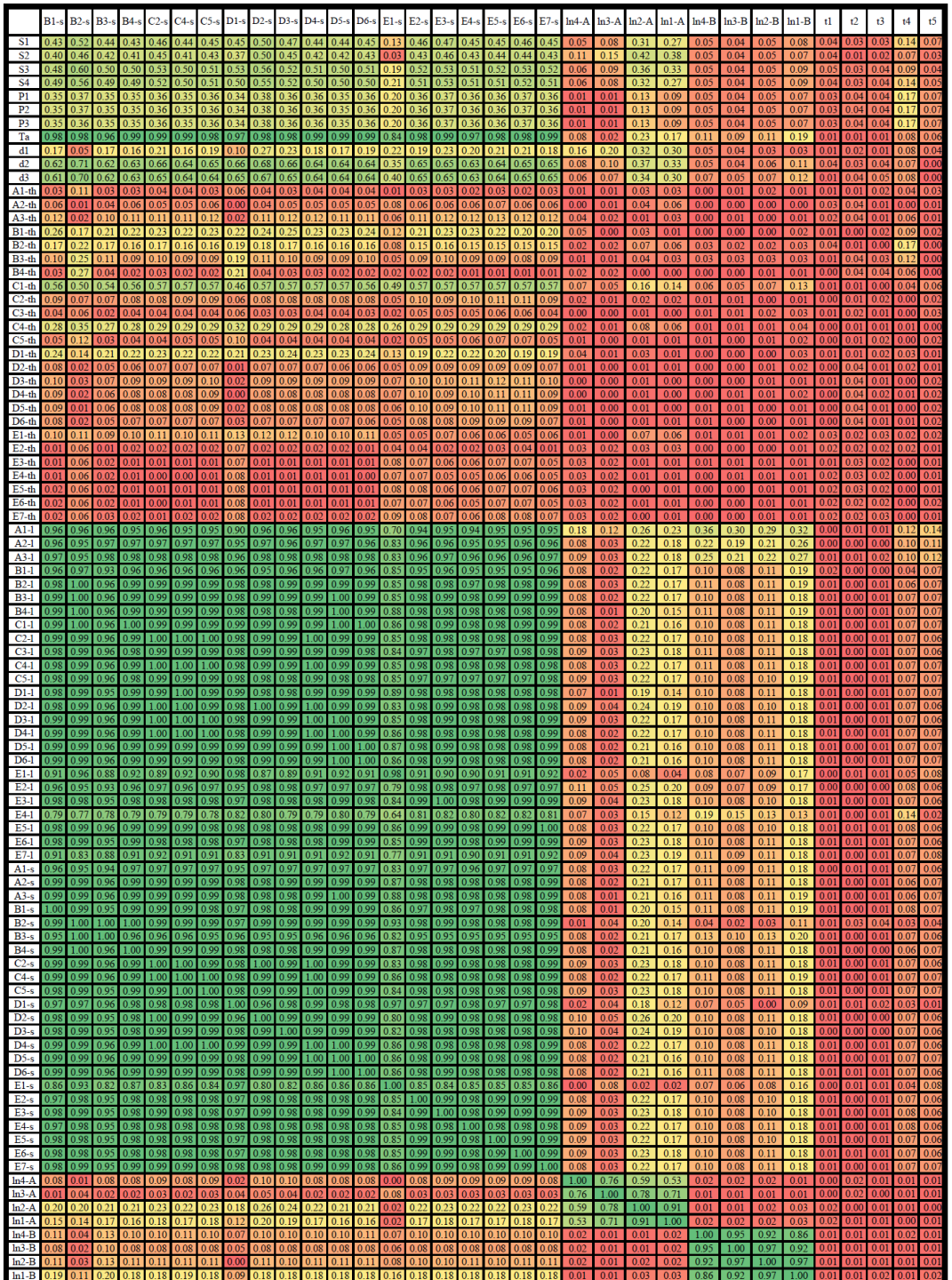

	B1-s	B2-s	B3-s	B4-s	C2-s	C4-s	C5-s	D1-s	D2-s	D3-s	D4-s	D5-s	D6-s	E1-s	E2-s	E3-s	E4-s	E5-s	E6-s	E7-s	ln4-A	ln3-A	ln2-A	ln1-A	ln4-B	ln3-B	ln2-B	ln1-B	t1	t2	t3	t4	t5
S1	0.43	0.52	0.44	0.43	0.46	0.44	0.45	0.45	0.50	0.47	0.44	0.44	0.45	0.13	0.46	0.47	0.45	0.45	0.46	0.45	0.05	0.08	0.31	0.27	0.05	0.04	0.05	0.08	0.04	0.03	0.03	0.14	0.07
S2	0.40	0.46	0.42	0.41	0.45	0.41	0.43	0.37	0.50	0.45	0.42	0.42	0.43	0.03	0.43	0.46	0.43	0.44	0.44	0.43	0.11	0.15	0.42	0.38	0.05	0.04	0.05	0.07	0.04	0.01	0.02	0.07	0.03
S3	0.48	0.60	0.50	0.50	0.53	0.50	0.51	0.53	0.56	0.52	0.51	0.50	0.51	0.19	0.52	0.53	0.51	0.52	0.53	0.52	0.06	0.09	0.36	0.33	0.05	0.04	0.05	0.09	0.05	0.03	0.04	0.09	0.04
S4	0.49	0.56	0.49	0.49	0.52	0.50	0.51	0.50	0.55	0.52	0.50	0.50	0.50	0.21	0.51	0.53	0.51	0.51	0.52	0.51	0.06	0.08	0.32	0.27	0.05	0.04	0.05	0.09	0.04	0.03	0.04	0.14	0.05
P1	0.35	0.37	0.35	0.35	0.36	0.35	0.36	0.34	0.38	0.36	0.36	0.35	0.36	0.20	0.36	0.37	0.36	0.36	0.37	0.36	0.01	0.01	0.13	0.09	0.05	0.04	0.05	0.07	0.03	0.04	0.04	0.17	0.07
P2	0.35	0.37	0.35	0.35	0.36	0.35	0.36	0.34	0.38	0.36	0.36	0.35	0.36	0.20	0.36	0.37	0.36	0.36	0.37	0.36	0.01	0.01	0.13	0.09	0.05	0.04	0.05	0.07	0.03	0.04	0.04	0.17	0.07
P3	0.35	0.36	0.35	0.35	0.36	0.35	0.36	0.34	0.38	0.36	0.36	0.35	0.36	0.20	0.36	0.37	0.36	0.36	0.37	0.36	0.01	0.01	0.13	0.09	0.05	0.04	0.05	0.07	0.03	0.04	0.04	0.17	0.07
Ta	0.98	0.98	0.96	0.99	0.99	0.99	0.98	0.97	0.98	0.98	0.99	0.99	0.99	0.84	0.98	0.99	0.97	0.98	0.98	0.99	0.08	0.02	0.23	0.17	0.11	0.09	0.11	0.19	0.01	0.01	0.01	0.08	0.06
d1	0.17	0.05	0.17	0.16	0.21	0.16	0.19	0.10	0.27	0.23	0.18	0.17	0.19	0.22	0.19	0.23	0.20	0.21	0.21	0.18	0.16	0.20	0.32	0.30	0.05	0.04	0.03	0.03	0.01	0.02	0.01	0.08	0.04
d2	0.62	0.71	0.62	0.63	0.66	0.64	0.65	0.66	0.68	0.66	0.64	0.64	0.64	0.35	0.65	0.65	0.63	0.64	0.65	0.65	0.08	0.10	0.37	0.33	0.05	0.04	0.06	0.11	0.04	0.03	0.04	0.07	0.00
d3	0.61	0.70	0.62	0.63	0.65	0.64	0.64	0.65	0.67	0.65	0.64	0.64	0.64	0.40	0.65	0.65	0.63	0.64	0.65	0.65	0.06	0.07	0.34	0.30	0.07	0.05	0.07	0.12	0.01	0.04	0.05	0.08	0.00
A1-th	0.03	0.11	0.03	0.03	0.04	0.04	0.03	0.06	0.04	0.03	0.04	0.04	0.04	0.01	0.03	0.03	0.02	0.03	0.02	0.03	0.01	0.01	0.03	0.03	0.00	0.01	0.02	0.01	0.01	0.01	0.02	0.04	0.03
A2-th	0.06	0.01	0.04	0.06	0.05	0.05	0.06	0.00	0.04	0.05	0.05	0.05	0.05	0.08	0.06	0.06	0.07	0.06	0.06	0.06	0.00	0.01	0.04	0.06	0.00	0.00	0.00	0.00	0.03	0.04	0.01	0.00	0.01
A3-th	0.12	0.02	0.10	0.11	0.11	0.11	0.12	0.02	0.11	0.12	0.12	0.11	0.11	0.06	0.11	0.12	0.12	0.13	0.12	0.12	0.04	0.02	0.01	0.03	0.00	0.01	0.00	0.01	0.02	0.04	0.01	0.06	0.01
B1-th	0.26	0.17	0.21	0.22	0.23	0.22	0.23	0.22	0.24	0.25	0.23	0.23	0.24	0.12	0.21	0.23	0.23	0.22	0.20	0.20	0.05	0.00	0.03	0.01	0.00	0.00	0.00	0.02	0.01	0.00	0.02	0.09	0.02
B2-th	0.17	0.22	0.17	0.16	0.17	0.16	0.16	0.19	0.18	0.17	0.16	0.16	0.16	0.08	0.15	0.16	0.15	0.15	0.15	0.15	0.02	0.02	0.07	0.06	0.03	0.02	0.02	0.03	0.04	0.01	0.00	0.17	0.00
B3-th	0.10	0.25	0.11	0.09	0.10	0.09	0.09	0.19	0.11	0.10	0.09	0.09	0.10	0.05	0.09	0.10	0.09	0.09	0.08	0.09	0.01	0.01	0.04	0.03	0.03	0.03	0.03	0.03	0.01	0.04	0.03	0.12	0.00
B4-th	0.03	0.27	0.04	0.02	0.03	0.02	0.02	0.21	0.04	0.03	0.03	0.02	0.02	0.02	0.02	0.02	0.01	0.01	0.01	0.01	0.02	0.02	0.00	0.00	0.00	0.00	0.00	0.01	0.01	0.00	0.04	0.06	0.00
C1-th	0.56	0.50	0.54	0.56	0.57	0.57	0.57	0.46	0.57	0.57	0.57	0.56	0.56	0.49	0.57	0.57	0.57	0.57	0.57	0.57	0.07	0.05	0.16	0.14	0.06	0.05	0.07	0.13	0.01	0.01	0.00	0.04	0.06
C2-th	0.09	0.07	0.07	0.08	0.08	0.09	0.09	0.06	0.08	0.08	0.08	0.08	0.08	0.05	0.10	0.09	0.10	0.11	0.11	0.09	0.02	0.01	0.02	0.02	0.01	0.01	0.00	0.01	0.00	0.01	0.02	0.00	0.02
C3-th	0.04	0.06	0.02	0.04	0.04	0.04	0.04	0.06	0.03	0.03	0.04	0.04	0.03	0.02	0.05	0.05	0.05	0.06	0.06	0.04	0.00	0.00	0.01	0.00	0.01	0.01	0.02	0.03	0.01	0.02	0.01	0.00	0.03
C4-th	0.28	0.35	0.27	0.28	0.29	0.29	0.29	0.32	0.29	0.29	0.29	0.28	0.28	0.26	0.29	0.29	0.29	0.29	0.29	0.29	0.02	0.01	0.08	0.06	0.01	0.01	0.01	0.04	0.00	0.01	0.01	0.01	0.00
C5-th	0.05	0.12	0.03	0.04	0.04	0.05	0.05	0.10	0.04	0.04	0.04	0.04	0.04	0.02	0.05	0.05	0.06	0.07	0.07	0.05	0.01	0.00	0.01	0.01	0.01	0.00	0.01	0.02	0.00	0.01	0.02	0.00	0.02
D1-th	0.24	0.14	0.21	0.22	0.23	0.22	0.22	0.21	0.23	0.24	0.23	0.23	0.24	0.13	0.19	0.22	0.22	0.20	0.19	0.19	0.04	0.01	0.03	0.01	0.00	0.00	0.00	0.03	0.01	0.01	0.02	0.03	0.01
D2-th	0.08	0.02	0.05	0.06	0.07	0.07	0.07	0.01	0.07	0.07	0.07	0.06	0.06	0.05	0.09	0.09	0.09	0.09	0.09	0.07	0.01	0.00	0.01	0.01	0.00	0.00	0.01	0.02	0.00	0.04	0.01	0.02	0.01
D3-th	0.10	0.03	0.07	0.09	0.09	0.09	0.10	0.02	0.09	0.09	0.09	0.09	0.09	0.07	0.10	0.10	0.11	0.12	0.11	0.10	0.00	0.00	0.01	0.00	0.00	0.00	0.01	0.01	0.01	0.01	0.04	0.01	0.00
D4-th	0.09	0.02	0.06	0.08	0.08	0.08	0.09	0.00	0.08	0.08	0.08	0.08	0.08	0.07	0.10	0.09	0.10	0.11	0.11	0.09	0.00	0.00	0.01	0.00	0.00	0.01	0.01	0.02	0.00	0.04	0.02	0.01	0.02
D5-th	0.09	0.01	0.06	0.08	0.08	0.08	0.09	0.02	0.08	0.08	0.08	0.08	0.08	0.06	0.10	0.09	0.10	0.11	0.11	0.09	0.01	0.00	0.01	0.00	0.01	0.01	0.00	0.01	0.00	0.04	0.01	0.00	0.02
D6-th	0.08	0.02	0.05	0.07	0.07	0.07	0.07	0.03	0.07	0.07	0.07	0.07	0.06	0.05	0.08	0.08	0.09	0.09	0.09	0.07	0.01	0.00	0.01	0.01	0.01	0.00	0.00	0.01	0.00	0.04	0.01	0.01	0.02
E1-th	0.10	0.11	0.09	0.10	0.11	0.10	0.11	0.13	0.12	0.12	0.10	0.10	0.11	0.05	0.05	0.07	0.06	0.06	0.05	0.06	0.01	0.00	0.07	0.06	0.01	0.01	0.01	0.02	0.03	0.02	0.03	0.02	0.02
E2-th	0.01	0.06	0.01	0.02	0.02	0.02	0.02	0.07	0.02	0.02	0.02	0.02	0.01	0.04	0.04	0.02	0.02	0.03	0.04	0.01	0.03	0.02	0.03	0.03	0.00	0.00	0.00	0.01	0.02	0.02	0.02	0.02	0.01
E3-th	0.01	0.06	0.02	0.01	0.01	0.01	0.01	0.07	0.01	0.01	0.01	0.01	0.01	0.08	0.07	0.06	0.06	0.07	0.07	0.05	0.03	0.02	0.01	0.01	0.01	0.01	0.01	0.01	0.01	0.03	0.02	0.00	0.01
E4-th	0.01	0.06	0.02	0.01	0.00	0.00	0.01	0.08	0.01	0.01	0.01	0.01	0.00	0.07	0.07	0.05	0.05	0.06	0.06	0.05	0.03	0.02	0.01	0.01	0.00	0.01	0.01	0.01	0.02	0.03	0.02	0.00	0.01
E5-th	0.02	0.06	0.02	0.01	0.01	0.01	0.01	0.08	0.01	0.01	0.01	0.01	0.01	0.08	0.08	0.06	0.06	0.07	0.07	0.06	0.03	0.02	0.00	0.01	0.00	0.00	0.01	0.01	0.02	0.03	0.02	0.00	0.01
E6-th	0.02	0.06	0.02	0.01	0.00	0.01	0.01	0.08	0.01	0.01	0.01	0.01	0.01	0.07	0.07	0.06	0.05	0.07	0.07	0.05	0.03	0.02	0.01	0.01	0.00	0.00	0.01	0.01	0.02	0.02	0.02	0.00	0.02
E7-th	0.02	0.06	0.03	0.02	0.01	0.02	0.02	0.08	0.02	0.02	0.02	0.02	0.02	0.09	0.08	0.07	0.06	0.08	0.08	0.07	0.03	0.02	0.00	0.01	0.00	0.00	0.01	0.01	0.02	0.02	0.03	0.00	0.01
A1-l	0.96	0.96	0.96	0.95	0.96	0.95	0.95	0.90	0.96	0.96	0.95	0.96	0.95	0.70	0.94	0.95	0.94	0.95	0.95	0.95	0.18	0.12	0.26	0.23	0.36	0.30	0.29	0.32	0.00	0.01	0.01	0.12	0.14
A2-l	0.96	0.95	0.97	0.97	0.97	0.97	0.97	0.95	0.97	0.96	0.97	0.97	0.96	0.83	0.96	0.96	0.95	0.95	0.96	0.96	0.08	0.03	0.22	0.18	0.22	0.19	0.21	0.26	0.00	0.00	0.00	0.10	0.11
A3-l	0.97	0.95	0.98	0.98	0.98	0.98	0.98	0.96	0.98	0.98	0.98	0.98	0.98	0.83	0.96	0.97	0.96	0.96	0.96	0.97	0.09	0.03	0.22	0.18	0.25	0.21	0.22	0.27	0.01	0.01	0.02	0.10	0.12
B1-l	0.96	0.97	0.93	0.96	0.96	0.96	0.96	0.96	0.95	0.96	0.96	0.97	0.96	0.85	0.95	0.96	0.95	0.95	0.95	0.96	0.08	0.02	0.22	0.17	0.10	0.08	0.11	0.19	0.02	0.00	0.00	0.04	0.07
B2-l	0.98	1.00	0.96	0.99	0.99	0.99	0.99	0.98	0.98	0.99	0.99	0.99	0.99	0.85	0.98	0.98	0.97	0.98	0.98	0.99	0.08	0.03	0.22	0.17	0.11	0.08	0.11	0.19	0.01	0.00	0.01	0.06	0.07
B3-l	0.99	1.00	0.96	0.99	0.99	0.99	0.99	0.98	0.99	0.99	0.99	1.00	0.99	0.85	0.98	0.99	0.98	0.99	0.99	0.99	0.08	0.02	0.22	0.17	0.10	0.08	0.11	0.18	0.01	0.00	0.01	0.07	0.07
B4-l	0.99	1.00	0.96	0.99	0.99	0.99	0.99	0.98	0.98	0.98	0.99	1.00	0.99	0.88	0.98	0.98	0.98	0.98	0.98	0.99	0.08	0.01	0.20	0.15	0.11	0.08	0.11	0.19	0.01	0.00	0.01	0.07	0.07
C1-l	0.99	1.00	0.96	1.00	0.99	0.99	0.99	0.99	0.99	0.99	0.99	1.00	1.00	0.86	0.98	0.99	0.98	0.98	0.99	0.99	0.08	0.02	0.21	0.16	0.10	0.08	0.11	0.18	0.01	0.00	0.01	0.07	0.07
C2-l	0.99	0.99	0.96	0.99	1.00	1.00	1.00	0.98	0.99	0.99	1.00	0.99	0.99	0.85	0.98	0.98	0.98	0.98	0.98	0.99	0.08	0.03	0.22	0.17	0.10	0.08	0.11	0.18	0.01	0.00	0.01	0.07	0.06
C3-l	0.98	0.99	0.96	0.98	0.99	0.99	0.99	0.98	0.98	0.99	0.99	0.99	0.99	0.84	0.97	0.98	0.97	0.97	0.98	0.98	0.09	0.03	0.23	0.18	0.11	0.08	0.11	0.18	0.01	0.00	0.01	0.07	0.06
C4-l	0.98	0.99	0.96	0.99	1.00	1.00	1.00	0.98	0.99	0.99	1.00	0.99	0.99	0.85	0.98	0.98	0.98	0.98	0.98	0.98	0.08	0.03	0.22	0.17	0.11	0.08	0.11	0.18	0.01	0.00	0.01	0.07	0.07
C5-l	0.98	0.99	0.96	0.98	0.99	0.99	0.99	0.98	0.98	0.98	0.99	0.99	0.98	0.85	0.97	0.97	0.97	0.97	0.97	0.98	0.09	0.03	0.22	0.17	0.10	0.08	0.10	0.19	0.01	0.00	0.01	0.07	0.07
D1-l	0.98	0.99	0.95	0.99	0.99	1.00	0.99	0.99	0.98	0.98	0.99	0.99	0.99	0.89	0.98	0.98	0.98	0.98	0.98	0.98	0.07	0.01	0.19	0.14	0.10	0.08	0.11	0.18	0.01	0.00	0.01	0.07	0.07
D2-l	0.98	0.99	0.96	0.99	1.00	1.00	0.99	0.98	1.00	0.99	1.00	0.99	0.99	0.83	0.98	0.99	0.98	0.98	0.98	0.98	0.09	0.04	0.24	0.19	0.10	0.08	0.10	0.18	0.01	0.00	0.01	0.07	0.06
D3-l	0.99	0.99	0.96	0.99	1.00	1.00	1.00	0.98	0.99	0.99	1.00	1.00	0.99	0.85	0.98	0.99	0.98	0.98	0.98	0.99	0.09	0.03	0.22	0.17	0.10	0.08	0.11	0.18	0.01	0.00	0.01	0.07	0.06
D4-l	0.99	0.99	0.96	0.99	1.00	1.00	1.00	0.98	0.99	0.99	1.00	1.00	0.99	0.86	0.98	0.98	0.98	0.98	0.98	0.99	0.08	0.02	0.22	0.17	0.10	0.08	0.11	0.18	0.01	0.00	0.01	0.07	0.07
D5-l	0.99	0.99	0.96	0.99	0.99	0.99	0.99	0.98	0.99	0.99	0.99	1.00	1.00	0.87	0.98	0.99	0.98	0.98	0.98	0.99	0.08	0.02	0.21	0.16	0.10	0.08	0.11	0.18	0.01	0.00	0.01	0.07	0.07
D6-l	0.99	0.99	0.96	0.99	0.99	0.99	0.99	0.98	0.99	0.99	0.99	1.00	1.00	0.86	0.98	0.99	0.98	0.98	0.98	0.99	0.08	0.02	0.21	0.16	0.10	0.08	0.11	0.18	0.01	0.00	0.01	0.07	0.07
E1-l	0.91	0.96	0.88	0.92	0.89	0.92	0.90	0.98	0.87	0.89	0.91	0.92	0.91	0.98	0.91	0.90	0.90	0.91	0.91	0.92	0.02	0.05	0.08	0.04	0.08	0.07	0.09	0.17	0.00	0.01	0.01	0.05	0.08
E2-l	0.96	0.95	0.93	0.96	0.97	0.96	0.97	0.95	0.98	0.98	0.97	0.97	0.97	0.79	0.98	0.98	0.97	0.98	0.97	0.97	0.11	0.05	0.25	0.20	0.09	0.07	0.09	0.17	0.00	0.00	0.00	0.08	0.06
E3-l	0.98	0.98	0.95	0.98	0.98	0.98	0.98	0.97	0.98	0.98	0.98	0.99	0.98	0.84	0.99	1.00	0.98	0.99	0.99	0.99	0.09	0.04	0.23	0.18	0.10	0.08	0.10	0.18	0.01	0.00	0.01	0.07	0.06
E4-l	0.79	0.77	0.78	0.79	0.79	0.79	0.78	0.82	0.80	0.79	0.79	0.80	0.79	0.64	0.81	0.82	0.80	0.82	0.82	0.81	0.07	0.03	0.15	0.12	0.19	0.15	0.13	0.13	0.01	0.00	0.01	0.14	0.02
E5-l	0.98	0.99	0.96	0.99	0.99	0.99	0.98	0.98	0.98	0.98	0.98	0.99	0.99	0.86	0.99	0.99	0.98	0.99	0.99	1.00	0.08	0.03	0.22	0.17	0.10	0.08	0.10	0.18	0.01	0.01	0.01	0.08	0.06
E6-l	0.98	0.99	0.95	0.99	0.98	0.98	0.98	0.97	0.98	0.98	0.98	0.99	0.99	0.85	0.99	0.99	0.98	0.99	0.99	0.99	0.09	0.03	0.23	0.18	0.10	0.08	0.11	0.18	0.01	0.01	0.01	0.07	0.06
E7-l	0.91	0.83	0.88	0.91	0.92	0.91	0.91	0.83	0.91	0.91	0.91	0.92	0.91	0.77	0.91	0.91	0.90	0.91	0.91	0.92	0.09	0.04	0.23	0.19	0.11	0.09	0.11	0.18	0.01	0.00	0.01	0.07	0.08
A1-s	0.96	0.95	0.94	0.97	0.97	0.97	0.97	0.95	0.97	0.97	0.97	0.97	0.97	0.83	0.97	0.97	0.96	0.97	0.97	0.97	0.08	0.03	0.22	0.17	0.11	0.09	0.11	0.18	0.00	0.01	0.01	0.07	0.06
A2-s	0.99	0.99	0.96	0.99	0.99	0.99	0.99	0.98	0.98	0.98	0.99	0.99	0.99	0.87	0.98	0.98	0.98	0.98	0.98	0.99	0.08	0.02	0.21	0.17	0.11	0.08	0.11	0.18	0.01	0.00	0.01	0.06	0.07
A3-s	0.99	0.99	0.96	0.99	0.99	0.99	0.99	0.98	0.98	0.98	0.99	1.00	0.99	0.88	0.98	0.98	0.98	0.98	0.98	0.99	0.08	0.01	0.21	0.16	0.11	0.08	0.11	0.19	0.01	0.00	0.01	0.06	0.07
B1-s	1.00	0.99	0.95	0.99	0.99	0.99	0.98	0.97	0.98	0.98	0.99	0.99	0.99	0.86	0.97	0.98	0.97	0.98	0.98	0.98	0.08	0.01	0.20	0.15	0.11	0.08	0.11	0.19	0.01	0.00	0.01	0.08	0.07
B2-s	0.99	1.00	1.00	1.00	0.99	0.99	0.99	0.97	0.99	0.99	0.99	0.99	0.99	0.93	0.98	0.99	0.98	0.98	0.98	0.99	0.01	0.04	0.20	0.14	0.04	0.02	0.03	0.11	0.01	0.03	0.04	0.03	0.04
B3-s	0.95	1.00	1.00	0.96	0.96	0.96	0.95	0.96	0.95	0.95	0.96	0.96	0.96	0.82	0.95	0.95	0.95	0.95	0.95	0.95	0.08	0.02	0.21	0.17	0.13	0.10	0.13	0.20	0.01	0.00	0.01	0.07	0.06
B4-s	0.99	1.00	0.96	1.00	0.99	0.99	0.99	0.98	0.98	0.98	0.99	0.99	0.99	0.87	0.98	0.98	0.98	0.98	0.98	0.99	0.08	0.02	0.21	0.16	0.10	0.08	0.11	0.18	0.01	0.00	0.00	0.06	0.07
C2-s	0.99	0.99	0.96	0.99	1.00	1.00	0.99	0.98	1.00	0.99	1.00	0.99	0.99	0.83	0.98	0.99	0.98	0.98	0.98	0.99	0.09	0.03	0.23	0.18	0.10	0.08	0.11	0.18	0.01	0.00	0.01	0.07	0.06
C4-s	0.99	0.99	0.96	0.99	1.00	1.00	1.00	0.98	0.99	0.99	1.00	0.99	0.99	0.86	0.98	0.98	0.98	0.98	0.98	0.99	0.08	0.02	0.22	0.17	0.11	0.08	0.11	0.19	0.01	0.00	0.01	0.07	0.07
C5-s	0.98	0.99	0.95	0.99	0.99	1.00	1.00	0.98	0.99	0.99	1.00	0.99	0.99	0.84	0.98	0.98	0.98	0.98	0.98	0.98	0.09	0.03	0.23	0.18	0.10	0.08	0.11	0.18	0.01	0.00	0.01	0.07	0.07
D1-s	0.97	0.97	0.96	0.98	0.98	0.98	0.98	1.00	0.96	0.98	0.98	0.98	0.98	0.97	0.97	0.97	0.98	0.97	0.97	0.98	0.02	0.04	0.18	0.12	0.07	0.05	0.00	0.09	0.01	0.01	0.02	0.03	0.01
D2-s	0.98	0.99	0.95	0.98	1.00	0.99	0.99	0.96	1.00	0.99	0.99	0.99	0.99	0.80	0.98	0.99	0.98	0.98	0.98	0.98	0.10	0.05	0.26	0.20	0.10	0.08	0.11	0.18	0.01	0.00	0.00	0.07	0.06
D3-s	0.98	0.99	0.95	0.98	0.99	0.99	0.99	0.98	0.99	1.00	0.99	0.99	0.99	0.82	0.98	0.98	0.98	0.98	0.98	0.98	0.10	0.04	0.24	0.19	0.10	0.08	0.10	0.18	0.00	0.00	0.00	0.07	0.06
D4-s	0.99	0.99	0.96	0.99	1.00	1.00	1.00	0.99	0.99	0.99	1.00	1.00	0.99	0.86	0.98	0.98	0.98	0.98	0.98	0.99	0.08	0.02	0.22	0.17	0.10	0.08	0.11	0.18	0.01	0.00	0.01	0.07	0.06
D5-s	0.99	0.99	0.96	0.99	0.99	0.99	0.99	0.98	0.99	0.99	1.00	1.00	1.00	0.86	0.98	0.99	0.98	0.98	0.98	0.99	0.08	0.02	0.21	0.16	0.10	0.08	0.11	0.18	0.01	0.00	0.01	0.07	0.07
D6-s	0.99	0.99	0.96	0.99	0.99	0.99	0.99	0.98	0.99	0.99	0.99	1.00	1.00	0.86	0.98	0.99	0.98	0.98	0.98	0.98	0.08	0.02	0.21	0.16

5.4 Some discussions on day by day correlation analysis results

5.4.1. Correlation between the air temperature and strain in the abutment

After this preliminary screening analysis, a closer look at the day-by-day correlation data can be performed, on an as-needed basis. As an example, Figure 5.5 shows the daily correlation results between the short strain gauge at location A3 (A3-s) and the data recorded by the ambient air temperature sensor (T_a).

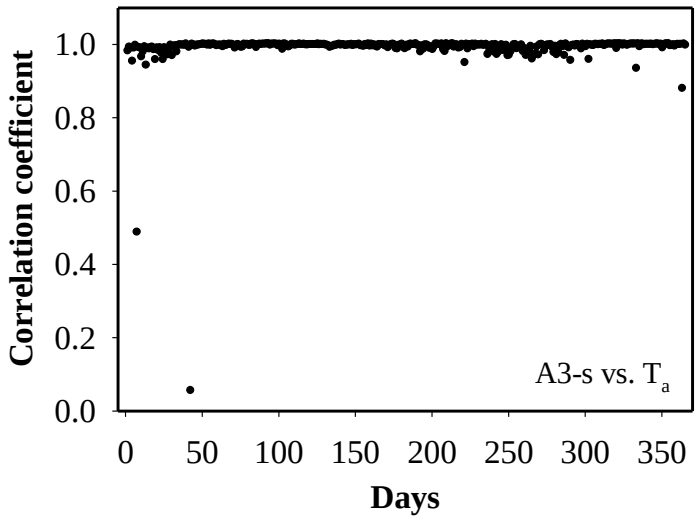

Figure 5.5 The daily correlation coefficient values between the ambient air temperature (T_a) and measured strain for the short gauge at location A3 (A3-s)

As shown in Figure 5.5, the daily calculated correlation coefficients are very high, with values that are typically very close to 1.0. This observation indicates that the changes in strain for this sensor were strongly linked to changes in ambient air

temperature. This observation led to the correction process for strain gauge data that is described in more detail in Chapter 6.

5.4.2. Correlation between the pressure measured by the abutment pressure cells

The correlation between the pressures recorded by the abutment pressure cells installed beneath the bridge bearing seat in the abutment was also investigated. The results showed that the trend for the first cell (d1, the uppermost cell) is different from the second and the third cell (d2 and d3), as shown in Figure 5.6 and Figure 5.7. The details regarding the effect of parameters on the measured pressure by the abutment pressure cells has been discussed in Chapter 9 using Figure 5.6 and 5.7.

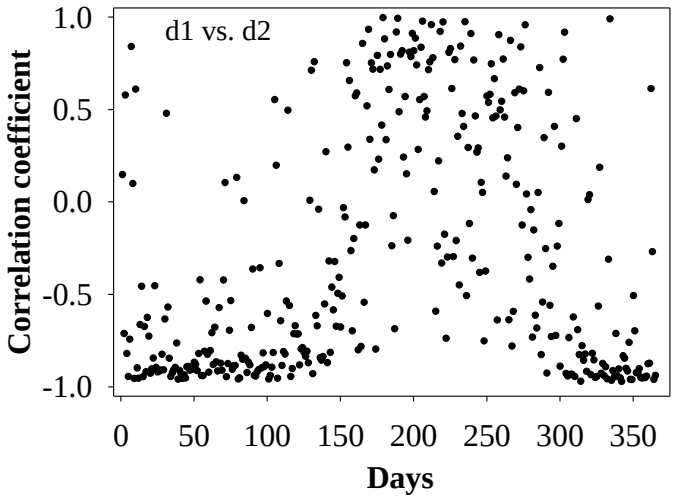

Figure 5.6 The daily correlation coefficient values between the measured total stress by pressure cells d1 and d2

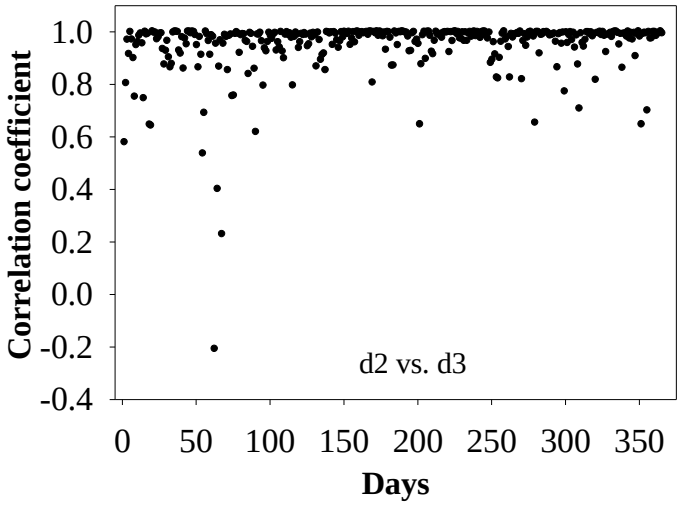

Figure 5.7 The daily correlation coefficient values between the measured total stress by pressure cells d2 and d3

As shown, the correlation between the measured pressure by d2 and d3 is very high and close to 1. However, this is not the case for the correlation between d1 and d2. This observation implies that pressure recorded by d1 does not follow the same trend as the pressure recorded by the other abutment pressure cells.

5.4.3. Correlation between the abutment pressure and the air temperature

The correlation coefficients between air temperature and the measured pressure by d1 and d2 over the first year of operation are presented in Figure 5.8 and Figure 5.9, respectively. As shown in these figures, the ρ between the pressure recorded by d2 and

air temperature was mostly negative, similar to what was observed in Figure 5.6. Since d2 and d3 are highly correlated, the same general trend in behavior was also observed for d3. Conversely, ρ values between air temperature and the pressure recorded by d1 are mostly positive, which is the opposite behavior from what was observed for the d2 and d3 sensors. These details show that the air temperature affects the measured pressure by the abutment pressure cells differently, indicating fairly complex behavior of the structure in this region (or perhaps sensor failure or other significant sensor error). These observations are discussed in more detail in Chapter 9.

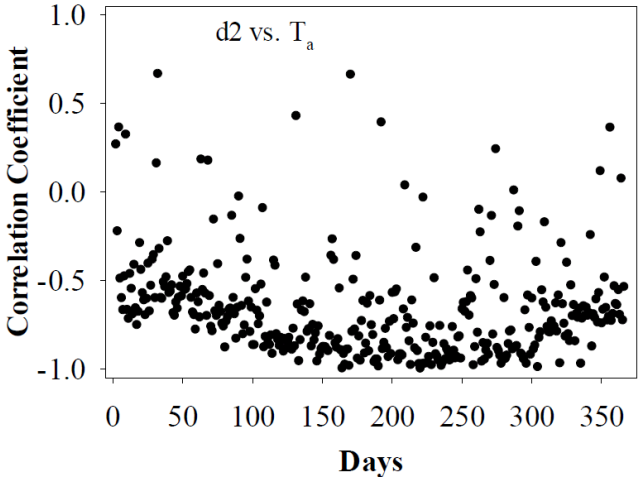

Figure 5.8 The daily correlation coefficient values between the ambient air temperature (T_a) and total stress measured by pressure cell d2

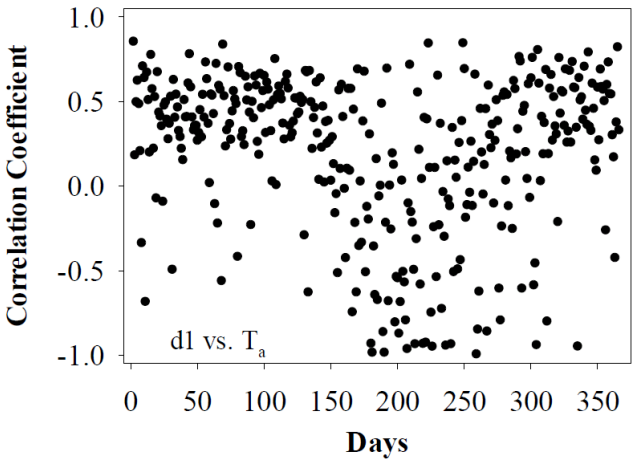

Figure 5.9 The daily correlation coefficient values between the ambient air temperature (T_a) and total stress measured by pressure cell d1

5.4.4. Correlation between the pressure measured by the foundation pressure cells and air temperature

In a similar fashion, we can also look at the daily results from correlation analysis of other sensors, for example between the total pressure cell S4 and the data recorded by the ambient air temperature sensor (T_a), as shown in Figure 5.10. As shown in this figure, the calculated correlation coefficients between these two variables were mostly negative which means that increases in air temperature often occurred at the same time as decreases in the total pressure in the foundation.

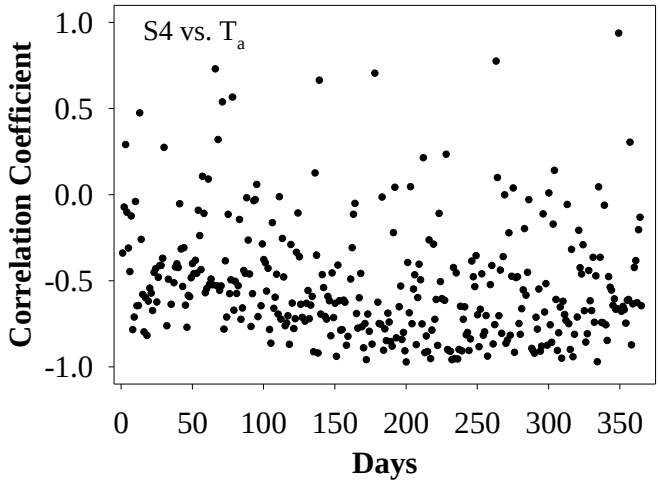

Figure 5.10 The daily correlation coefficient values between the ambient air temperature (T_a) and the measured total pressure by pressure cell S4

As shown in Figure 5.10, most of the calculated ρ values are negative. The ρ values are not very close to -1 however, which means some other factors are also affecting the measured total pressure values other than the air temperature.

5.4.5. Correlation between the pressures measured by neighboring foundation pressure cells

The daily ρ between the total pressure values recorded by different pressure cells was also high, which shows their trend is very similar (e.g., Figure 5.11). This indicates that the source of change in foundation pressure is the same for all the cells.

The total pressures measured by the foundation pressure cells are evaluated and discussed in more detail in Chapter 9.

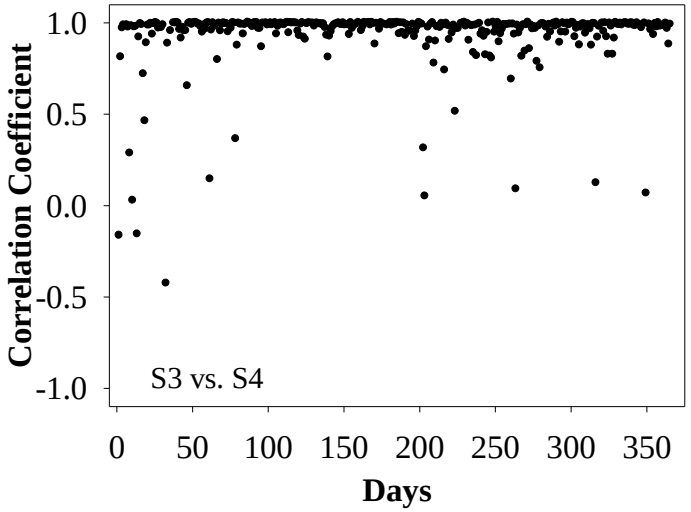

Figure 5.11 The daily correlation coefficient values between sensor S3 and sensor S4 measured total pressures

As shown in Figure 5.11, the daily correlation coefficient values are more than 0.95 most of the time. From this data, it can be inferred that the changes in pressure recorded by the different pressure cells are highly correlated and the root cause of this variation would likely be the same.

5.4.6. Correlation between the pressure measured by the foundation pressure cells and pore pressure measured by the piezometers

Another observation made via correlation analysis was the relationship between the pressure measured by the foundation pressure cells and the pore pressure measured by the piezometers. Figure 5.12 presents the corresponding results for cell S4. As can be observed, the total pressure measured by foundation cell S4 is strongly correlated with the pore pressure measured by piezometer P1 for most of the days, which indicates the change in the measured pressure by the foundation pressure cells is induced by the change in the pore pressure. However, there are a few days that the correlation was not as strong, which infers that there are other mechanisms which affect the change in total pressure.

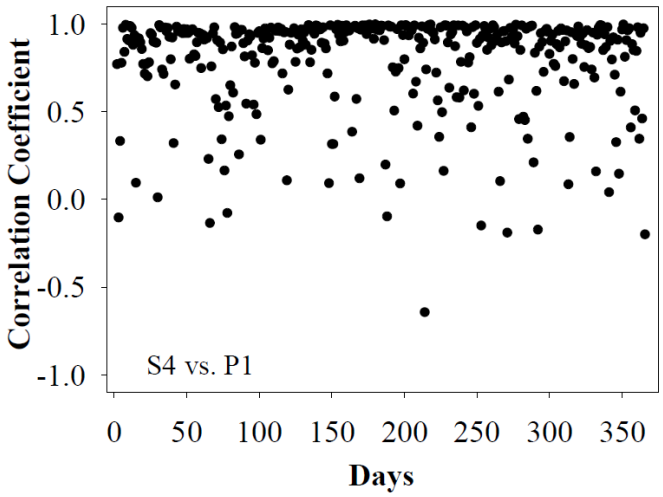

Figure 5.12 The daily correlation between the total pressure measured by S4 and pore pressure measured by P1

Similar correlation behavior to what is shown in Figure 5.12 was also observed for the other foundation pressure cells. This indicates that the change in pore pressure is the most significant source of change in the foundation total pressure, which is not surprising given that the total pressure cells are submerged beneath the water level in the channel. As a result, it was decided to calculate the effective pressure from the total pressure by subtracting the pore pressure determined from the piezometer sensor readings:

$$\sigma' = \sigma - u \tag{5.9}$$

In this equation, σ' is the calculated effective pressure, σ is the total pressure measured by the total pressure cell, and u is the pore pressure determined from the piezometer sensor readings.

After determining the effective pressure from the measured total pressures, a correlation analysis was conducted between the effective pressure and other sensor responses. Figure 5.13 shows the daily correlation between the effective pressure measured by S3 and S4 (E3 vs. E4). As shown, this figure is very similar to Figure 5.11 (S3 vs. S4), with somewhat fewer low correlation points; this indicates that the effective pressures measured by the pressure cells are generally more correlated than the total pressures (though not by an overly significant amount).

Figure 5.14 displays the correlation between the effective pressure of cell S4 (E4) and air temperature (T_a). As shown, the results are similar to Figure 5.10 (S4 vs. T_a) and there is not a significant difference between these two figures.

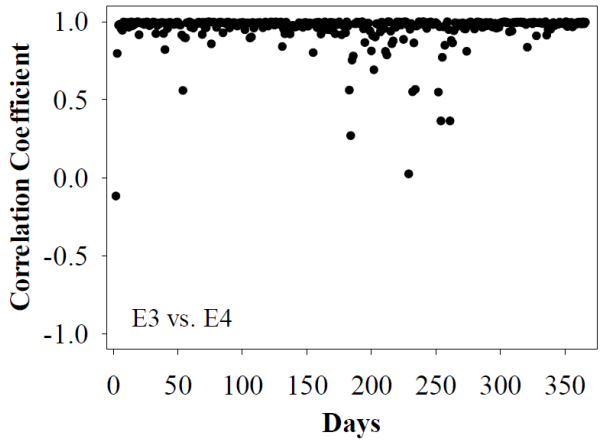

Figure 5.13 The daily correlation coefficient values between the calculated effective pressure by pressure cell S3 and S4 (E3 vs. E4)

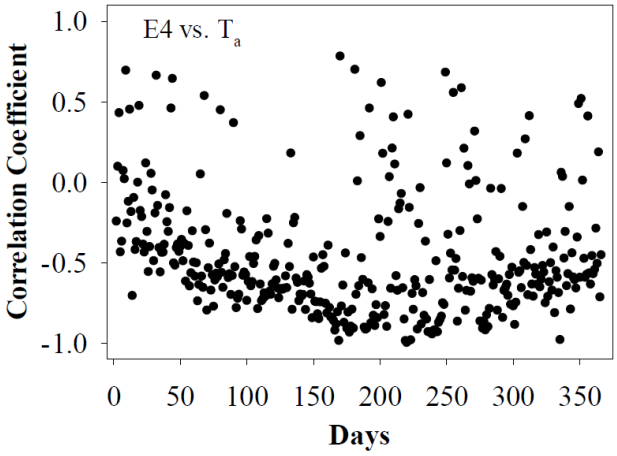

Figure 5.14 The daily correlation coefficient values between the ambient air temperature (T_a) and the calculated effective pressure by pressure cell S4 (E4)

5.5 Correlation analysis results

From the findings that are presented in this chapter, it can be concluded that correlation analysis is a powerful tool to develop an understanding about how values measured by different sensors relate to each other. The most significant outcomes from the correlation analysis that was performed are as follows:

1- Temperature changes have a strong relationship to measured strains by the strain gauges. The effects of temperature on measured strains are discussed in more detail in the next chapter.

2- The measured strain by different strain gages are correlated very well. This indicates that the rate of strain change in different places in the GRS abutment may be similar.

3- The changes in pore water pressure or abutment water content do not have a strong correlation with the abutment or foundation deformation. Since the foundation water pressure and abutment water pressure are correlated well, this indicates that significant amounts of pore water pressure were not generated in the foundation during construction and operation and the majority of the water pressure measured by the piezometers can be attributed to changes in the river water level.

4- The air temperature changes affect the measured pressure by the foundation pressure cells in an inverse way since the correlation

coefficient between these sensor types was mostly negative. This will be shown and discussed in more detail in Chapter 9.

5- The air temperature changes also affect the measured pressure by the abutment pressure cells. Its effect on the two lower abutment cells are similar to its effect on the foundation pressure cells. However, the air temperature effect on the uppermost cell was different from its effect on the other cells. In this case, the correlation coefficient was mostly positive. This will be shown and discussed in more detail in Chapter 9.

6- The measured pressure by the foundation pressure cells are highly correlated which implies that the source of change in foundation pressure is the same. The same thing occurred for the two lower abutment cells. The corresponding details are presented in Chapters 6 and 8.

7- The abutment temperature changes were not very uniform. The temperature at the locations closer to the facing wall were not highly correlated with the temperature at the locations further away from the facing wall. This behavior likely occurs because the locations close to the facing wall are more exposed to the air and as a result their corresponding temperature changes track more closely with daily swings in air temperature. On the other hand, the temperature changes in the area which are not close to the facing wall are more uniform, and are largely not affected by daily swings in temperature.

8- The total pressure measured by the foundation pressure cells are correlated well on a daily basis with the pore pressures measured by piezometers. This indicates that the daily changes in total pressure is considerably affected by the pore pressure. The effective pressure was consequently calculated to remove the effect of changes in pore pressure resulting from changes in the level of the water in the channel.

REFERENCES

Johnson, R. and Wichern, D. (2002). “Applied multivariate statistical analysis.” 5(8). Upper Saddle River, NJ: Prentice hall.

Pearson K. (1920). “Notes on the history of correlation.” Biometrika 13, 25–45.

R Development Core Team (2011). “R: A language and environment for statistical computing.” R Foundation for Statistical Computing, Vienna, Austria. ISBN 3-900051-07-0, URL http://www.R-project.org/.

Chapter 6

AN OBSERVATIONAL APPROACH TO CORRECTING FIELD STRAIN MEASUREMENTS TO ACCOUNT FOR TEMPERATURE EFFECTS

6.1 Introduction

Field sensors play an increasingly important role in civil engineering projects, as advances in data acquisition techniques and wireless (cellular) data logging approaches have allowed for remote, real-time structural health monitoring (e.g., Brownjohn, 2007; Fraser et al., 2009; Hu et al., 2013). Measurements of deformation or strain have historically played a critical role in assessing the behavior of geotechnical structures in the field, and may even allow for development of "early warning" systems that can provide indications about a catastrophic failure before it occurs (e.g., Lee and Wu, 2004; Intrieri et al., 2012; Lehtonen et al., 2015; Ong et al., 2015). Proper signal processing algorithms and corrections for the effect of temperature are critical for accurate reporting of measured field strains, and are essential to avoid reporting of "false positives" during structural health monitoring – i.e., the reporting of incorrect large displacement or high strain events that are in fact due to electrical or temperature issues (e.g., Hall and Deighan, 1986; Khan and Wang, 2001; A-iyeh, E., 2013). These type of "false positive" events can lead to mistrust of the accuracy of a field monitoring system post-installation, which can reduce attention to future system warnings, and increase response time if a failure event is impending or in the process of occurring.

Numerous failures of reinforced earth structures such as mechanically stabilized earth (MSE) walls, geosynthetic reinforced soil (GRS) walls, or geosyntethic reinforced slopes have been documented in the engineering literature (e.g., Yoo and Jung, 2006; Hossain et al., 2011; Xue et al., 2014). The use of these structures has generally become quite widespread for many different retained soil applications, due to their many performance and cost saving benefits (e.g., Adams et al., 2011; Yonezawa et al., 2014; Costa et al., 2016). Unfortunately however, the failure rate of these structures is generally significantly higher than other geotechnical engineering structures, which is generally attributed to poor design, poor construction, poor backfill compaction, or the existence of internal or external water (e.g., Koerner and Koerner, 2013; Valentine, 2013). Consequently, the use of structural health monitoring systems for reinforced earth structures may provide many practical benefits for owners or engineers that are responsible for the performance of the structure over the long-term.

When performing internal strain monitoring of reinforced earth structures, it is common practice to measure the strain of the reinforcing elements at various locations, whether they be metal strips, geogrids, or woven or non-woven geosynthetics (e.g., Walsh et al., 2009; Leshchinsky et al., 2010; Stuedlein et al., 2010; Warren et al., 2010; Nicks et al., 2016). A variety of strain gauge technologies have historically been utilized for this purpose, including vibrating wire strain gauges (electrically based), foil strain gauges (electrically based), and fiber Bragg grating gauges (fiber optic based) (e.g., Ma and Wu, 2004; Briançon et al., 2006; Allen and Bathurst, 2013). Various strain gauge attachment techniques have been employed to affix the sensors to the

reinforcement, which generally correspond to the type of strain gauge that is being used, and the type of reinforcement material that the gauge needs to be attached to (e.g., Sluimer and Risseeuw, 1982; Leshchinsky and Fowler, 1990; Berkheimer, 2007; Won and Kim, 2007; Walsh, 2009).

This chapter presents localized strain results measured for a heavily instrumented geosynthetic reinforced soil (GRS) bridge abutment, which was constructed as part of an integrated bridge system (IBS) (e.g., Adams et al., 2011). Foil strain gauges were selected for strain monitoring for this project, following recommendations made by Warren et al. (2010). Given the difficulty that has historically been observed with attaching strain gauges to GRS-IBS reinforcement (e.g., Warren et al., 2010), two different strain gauge attachment techniques were utilized for this project (Leshchinsky and Fowler, 1990; Wu et al., 2013), with each strain gauge point of monitoring having two independent measurements of strain. Temperature measurements were also made at each strain monitoring location, using embedded thermistors.

Data collected using the embedded strain gauges and thermistors, ambient temperature monitoring instrumentation, and a variety of other sensors together provided extremely useful information about the overall performance of the GRS-IBS (e.g., Chapters 4-5, 7-9). Using the recorded data, an observational approach to correcting field strain measurements to account for temperature effects was developed, which follows a long history of use of the observational method in geotechnical engineering (e.g., Peck, 1969). The presented approach is useful for engineers that need

to correct measured foil strain gauge results for the effect of temperature under complex field conditions.

6.2 Project details

The details regarding the project including the geometrical specifications and instrumentation systems were presented in Chapter 3. Strain and temperature monitoring locations in the west abutment are shown in Figure 6.1, with all of the points that are shown being located along the roadway centerline.

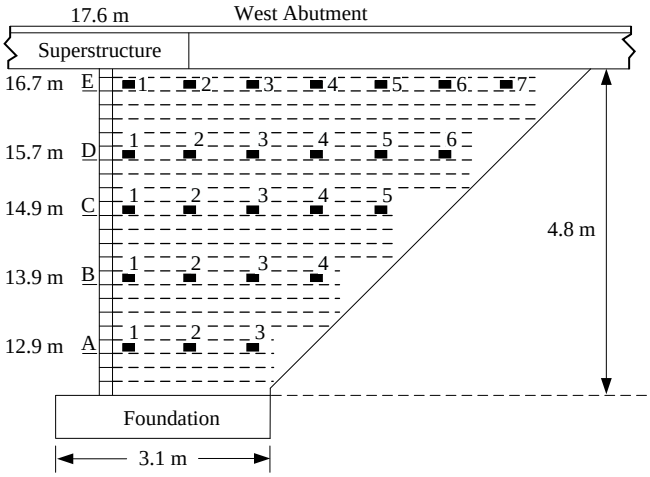

Figure 6.1 Typical section of the west GRS-IBS abutment, along the roadway centerline. Strain and temperature monitoring locations along select geosynthetic layers are shown

At each monitoring point shown in Figure 6.1, two different strain gauges and attachment techniques were utilized, with the goal being to have independent and complimentary measures of strain (as shown in Figure 6.2 for location B1). The details

regarding the strain gauge attachment techniques were presented in Chapter 3. As discussed in that chapter, for the first strain monitoring technique, a "long" strain gauge (5.71 cm, Vishay Micro-Measurements EA-06-20CBW-120) was attached following the general methodology outlined by Leshchinsky and Fowler (1990). For the second strain monitoring technique, a "short" strain gauge (0.95 cm, Vishay Micro-Measurements EP-08-250BG-120) was attached following the general methodology outlined in Chapter 3, in accordance with recommendations made by Wu et al. (2013). Step-by-step photos of the attachment process and additional details about the adhesives and other materials used for gauge attachment and waterproofing are discussed in more detail in Chapter 3.

A thermistor was also installed at each monitoring location shown in Figure 6.1, to investigate the effect of soil temperature changes on the strain readings. Ambient air temperature conditions were measured using a thermistor positioned at the location of the project dataloggers. In total, these sensors provided an accurate picture of spatial changes in the temperature within the GRS abutment that occurred in response to changes in ambient temperature conditions, on a daily and seasonal basis.

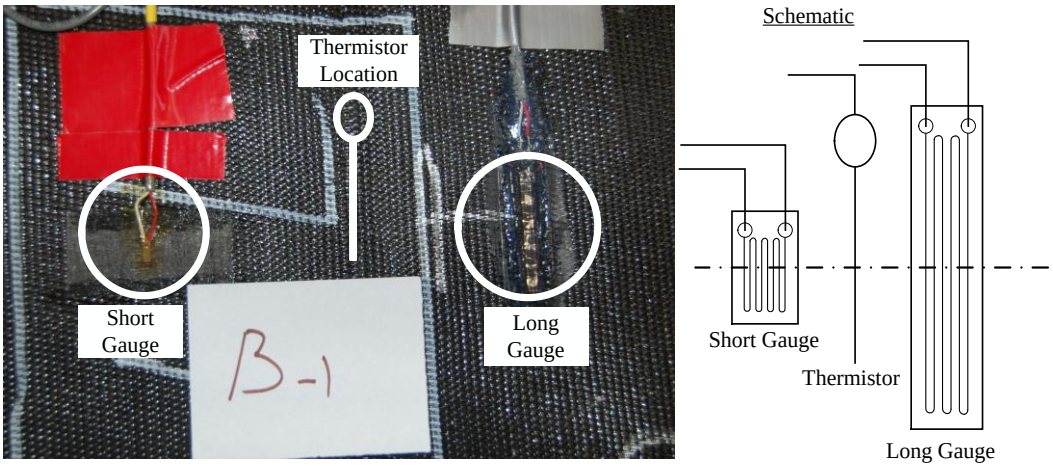

Figure 6.2 Strain monitoring location B-1, with separate measurements of strain being made by "short" and "long" strain gauges: (a) photo, and (b) schematic. (Note: thermistor installed later, in the field)

6.3 Measuring geosynthetic strains using foil strain gauges

Traditional foil strain gauges relate physical deformation over the length of the gauge (strain) to changes in electrical resistance across the gauge resistor (Figure 6.3a). Changes in temperature of the gauge itself changes its inherent electrical resistance, leading to different relationships between strain and resistance for different gauge temperatures (e.g., Vishay Micro-Measurements, 2007). Consequently, it is necessary to correct measured resistance values for the effect of temperature to get consistent and accurate measurements of strain from the gauge. Additionally, in common usage, strain gauges are part of a larger electrical circuit that involves an input signal wire, an output signal wire, and a datalogger (Figure 6.3b). Changes in temperature of the input and output wires also affects their internal electrical resistance,

leading to changes in the overall resistance values that are measured by the datalogger; these changes in temperature also need to be corrected for to get accurate strain measurements.

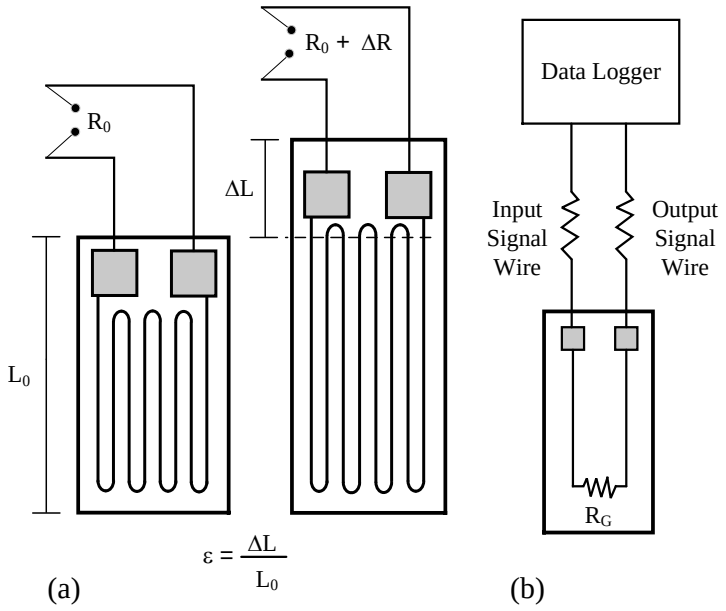

Figure 6.3. Foil strain gauge: (a) Change in resistance with change in length of the gauge, and (b) Strain gauge as part of a circuit

For typical levels of strain in civil engineering applications, changes in resistance (in ohms) across a foil gauge are typically quite small. Consequently, foil strain gauges are commonly used in a Wheatstone bridge configuration with a voltage excitation source, to more accurately capture small changes in resistance (Figure 6.4). Two and three-wire Wheatstone quarter-bridge configurations are commonly utilized in practice, as shown in Figures 4a and 4b, respectively (e.g., Vishay Micro-Measurements, 2005). In this figure, R_1 is the initial resistance of the gauge, ΔR is the

change in gauge resistance that occurs when the gauge is strained, R_{L1}, R_{L2}, and R_{L3} are the respective lead wire resistances, and R_2, R_3, and R_4 are resistive elements of the bridge. V_{EX} and V_o are the excitation and output voltages, respectively. The associated changes in gauge resistance that occur when a gauge is strained can be determined from changes in the measured output voltage using Equation 6.1 for a two-wire Wheatstone quarter-bridge and using Equation 6.2 for a three-wire Wheatstone quarter-bridge. In these equations, V_{EX} and R_1 are known, the R_L values are measured in the field prior to connecting the datalogger, R_2, R_3, and R_4 are known values of bridge resistance, and the change in resistance at the strain gauge location (ΔR) can be calculated directly from the change in measured output voltage (ΔV_o). For most Wheatstone quarter-bridge configurations, the bridge resistors are selected to have the same resistance as the gauge resistor, i.e., $R_1 = R_2 = R_3 = R_4$. Also, for a given sensor, the lead wire lengths are essentially the same, which means that $R_{L1} = R_{L2} = R_{L3} = R_L$, which allows the equations that are utilized to be simplified:

$$\Delta R = \frac{-4\frac{\Delta V_o}{V_{EX}}R_1}{1+2\frac{\Delta V_o}{V_{EX}}} - 2R_L \tag{6.1}$$

$$\Delta R = \frac{-4\frac{\Delta V_o}{V_{EX}}(R_1+R_L)}{1+2\frac{\Delta V_o}{V_{EX}}} \tag{6.2}$$

Strain values at the gauge location are determined using Equation 6.3, for the change in resistance values (ΔR) calculated using either Equation 6.1 or Equation 6.2:

$$\varepsilon(\%) = \frac{\Delta R}{R_1} \times \frac{1}{GF} \times 100 \qquad (6.3)$$

In this equation, ε is the calculated strain in percent, R_1 is the initial measured resistance of the strain gauge (ohm), ΔR is the change in resistance in the strain gauge as straining occurs (ohm), and GF is the gauge factor provided by the manufacturer (Vishay Micro-Measurements), which usually has a value around 2.0 for the type of gauges that were used in the current study. The "zero-strain" gauge resistance (R_1) was approximately 120 ohms for both gauges that were used.

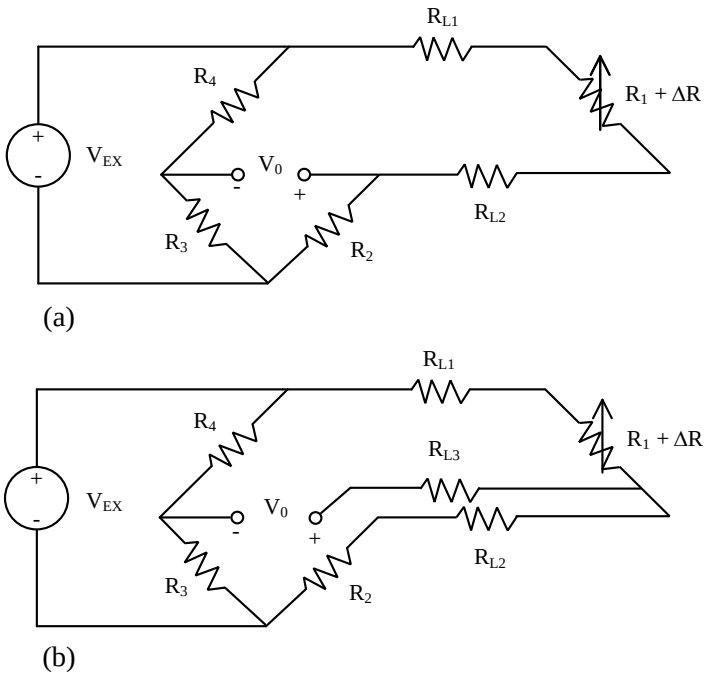

Figure 6.4. Common Wheatstone quarter-bridge configurations: (a) two-wire, and (b) three wire

Using a three-wire Wheatstone quarter-bridge configuration serves to compensate for the effect of wire temperature changes on foil strain gauge measurements (e.g., Vishay Micro-Measurements, 2005). However, it cannot remove the effect of changes in gauge temperature on the resistance readings. In order to isolate and examine the separate effects of changes in wire temperature from changes in gauge temperature, the current field study elected to use a two-wire quarter-bridge configuration approach.

6.4 Correcting measured strain readings for changes in gauge temperature

According to the data sheet provided by the manufacturer, equations having the following form should be used to correct measured strain readings for the effect of temperature change at the gauge location (Vishay Micro-Measurements 2007).

$$\varepsilon_{cor,g} = \varepsilon_{uncor} - \varepsilon_{T/O} \tag{6.4}$$

$$\varepsilon_{T/O} = A_0 + A_1 T + A_2 T^2 + A_3 T^3 + A_4 T^4 + A_5 T^5 \tag{6.5}$$

where ε_{uncor} is a measurement of uncorrected strain determined from Equation 6.3, $\varepsilon_{cor,g}$ is the temperature-corrected strain, $\varepsilon_{T/O}$ is an adjustment to the measured (uncorrected) strain to account for temperature effects on the gauge itself, in units of micro strain ($\mu\varepsilon$), T is the measured temperature at the gauge location (℃), and the A_i values are experimentally determined coefficients which are provided by the gauge manufacturer (Vishay Micro-Measurements) for each type of strain gauge that was used.

It is assumed in these equations that the gauge was balanced at a "room temperature" value; between 20℃ and 25℃ is common, Vishay Micro-Measurements uses 24℃ , which means that $\varepsilon_{T/O}$ is equal to zero at 24℃ . If the initial "zero" reading for a given strain gauge is recorded at a different temperature than 24℃ (i.e., T_1), the adjustment to the measured strain value ($\varepsilon_{T/O}$) for a given field strain reading taken at a different gauge temperature (i.e., T_2) should be calculated using Equation 6.6.

$$\varepsilon_{T/O} = \varepsilon_{T/O}(T_2) - \varepsilon_{T/O}(T_1) \quad (6.6)$$

For the "long" gauges that were used in the current study (Vishay Micro-Measurements):

A_0 = -7.26E+1, A_1 = 4.61E+0, A_2 = -7.44E-2, A_3 = 3.18E-4, A_4 = -3.00E-7 and A_5 = -1.83E-12

For the "short" gauges that were used in the current study (Vishay Micro-Measurements):

A_0 = 1.6E+1, A_1 = 1.29E+0, A_2 = -9.11E-2, A_3 = 4.13E-4, A_4 = -4.51E-7 and A_5 = 0

These A_i values were determined based on temperature calibration tests conducted by Vishay Micro-Measurements over a range of temperatures from –73℃ to 260℃. Figure 6.5 displays the effect of gauge temperature changes on the gauge reading for the long and short strain gauges; to more closely confirm to the range of temperature

expected in the field, only results from -10℃ to 40℃ are shown. As shown, the different gauges respond very differently to changes in temperature. For the long gauges, any increase in temperature increases the adjustment to temperature-induced strain over the range of temperatures shown. For the short gauges, increases in temperature initially increase the adjustment to temperature-induced strain until 9℃, after which point it decreases.

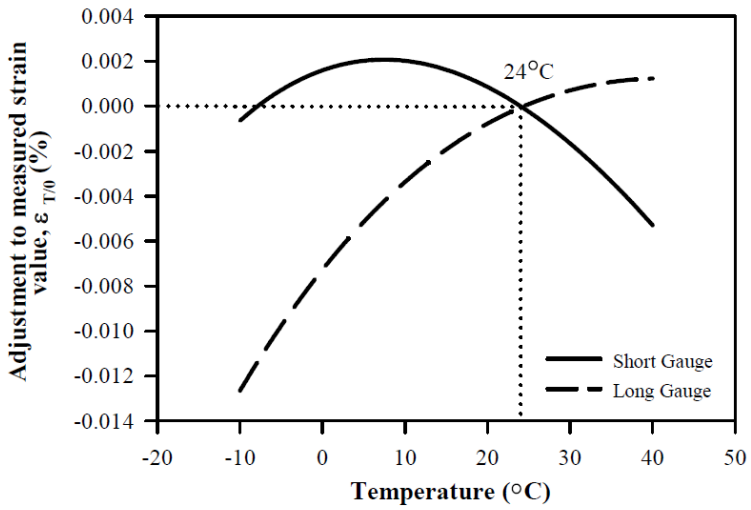

Figure 6.5. The effect of gauge temperature changes on the measured strain values, for "long" and "short" strain gauges

In this project, the temperature at the location of the gauges was generally changing between 0 and 30 ℃ (with most of the temperature changes being in the range of 5 to 25℃). As shown in Figure 6.5, a change in temperature from 0 to 30 ℃ for the long strain gauges results in a change in the adjustment to strain of approximately 0.00797% (with an average change of approximately 0.000266%/℃). Similarly, for the short strain gauges, a change in temperature from 0 to 30 ℃ results in a change in

the adjustment to strain of approximately 0.00325%. As a result of the shape of the curve, changes in temperature from 0 to 15℃ yield negligible changes in strain for the short strain gauge, and average changes in induced strain of approximately 0.000218%/℃ for temperature changes from 15 to 30℃.

6.5 Considering the effects of wire temperature change

In an instrumented geosynthetic reinforced structure, loading of the structure via self-weight dead loads or external dead/live loads will induce straining of the geosynthetic, which should be measured by a properly installed strain gauge. In addition to actual mechanical strains that occur, gauges will also exhibit apparent strain behavior that occurs as a result of foil gauge or wire temperature changes. This apparent strain needs to be corrected for to isolate the mechanical strain measurements. Otherwise, the actual strain induced by the structural deformation cannot correctly be captured. Foil gauge temperature corrections are typically applied using the approach that is described in the previous section. The effect of changes in wire temperature can be mitigated using a three-wire Wheatstone bridge approach (Vishay Micro-Measurements 2005). Alternatively, if a two-wire Wheatstone bridge approach is utilized, the effect of wire temperature changes needs to be corrected for.

To accomplish this correction, it is useful to know how wire resistance changes with temperature. In the current study, a 24-gauge (American Wire Gauge standard) three-conductor copper wire provided by Carol was utilized to connect the gauges to the data acquisition system. In order to assess the effect of temperature

changes on the wire resistance, a resistance test on 305 m of the wire was conducted in an adjustable constant-temperature room. To perform this test, the total resistance (in ohms) along the length of the entire wire spool was measured at different temperatures between 25 and 45℃ (Figure 6.6). As shown, the changes in wire resistance versus temperature are linear, with a slope of 0.1512 ohms /℃.

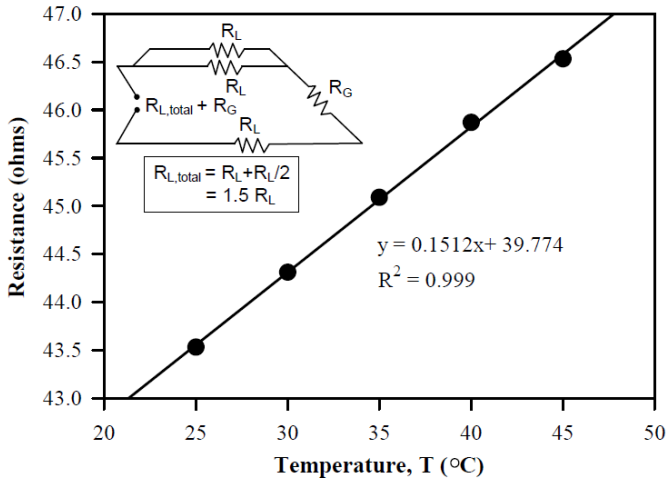

Figure 6.6. Changes in resistance vs. temperature for a 305 m lead wire

In order to duplicate the field wiring configuration (a two-wire setup, as shown in Figure 6.4a), two of the wires were twisted together for the direct resistance measurements that were made, as shown in Figure 6.6. For this configuration, the total resistance across the gauge and wires is equal to $1.5R_L$, where R_L is the resistance of a single wire. The resistance data shown in Figure 6.6 consequently corresponds to the change in resistance for all three wires ($1.5R_L$) versus change in temperature.

Direct measurements of change in wire resistance with change in wire temperature are best determined in a controlled laboratory setting using the approach

that is shown in Figure 6.6. However, an alternative approach that is more useful for practicing engineers who may not have easy access to the necessary facilities is to calculate the same slope as what is shown in Figure 6.6 using the equation:

$$m_t = \frac{(R-R_0)}{(T-T_0)} = R_0\alpha \tag{6.7}$$

where $R - R_0$ is the change in wire resistance, $T - T_0$ is the change in wire temperature, R_0 is the initial wire resistance at temperature T_0, and α is the wire temperature coefficient, which depends on the wire material properties. Values of R_0 are typically specified by the wire manufacturer for a specific length of wire (305 m is common), for "room temperature" wire with $T_0 = 20$ ℃. The wire temperature coefficient is controlled largely by the wire material properties; for solid core copper wiring, an α value of 0.0039 is commonly used (e.g., Griffith, 2000).

For this field project, the length of the lead wires generally varied from 24 to 36 m depending on the location of the gauge in the abutment, with an average length of approximately 30.5 m. Using Equation 6.3 with R_0 and GF equal to 120 ohms and 2.0, respectively, yields an approximate strain change of 0.0063(%)/℃ for 30.5 m of wire. Comparing the effect of wire temperature change with the effect of gauge temperature change on strain for a two-wire Wheatstone bridge configuration (0.0063%/℃ vs. 0.000266%/℃ and 0.000218%/℃), it can be observed that the effect of wire temperature changes is about 25 times larger than the effect of gauge temperature changes for the length of wires that were used in this study.

As shown in Figure 6.7, the lead wire path utilized for strain gauge installation in the field has some portion of the wire passing through the air, and some portion of the wire passing through the ground. As shown in Figure 6.1, the wire installation path for each sensor was by necessity different, as was the length of the lead wires. The portion of the wire that is above the ground will be affected by changes in air temperature, with a given change in air temperature being fairly constant along the exposed length of the wire, provided that the wire does not pass through sunny vs. shady spots. The portion of the wire that is below the ground passes through a soil profile that is likely to have a varying temperature profile that is affected by both deeper ground temperatures (which are more stable) and overlying air temperatures (which will vary on a daily and seasonal basis). In order to correct measured wire resistance values for changes in temperature, the variation in temperature along the length of the wire in the field needs to be addressed, in a fashion that is proportional to the relative temperatures that the wire is actually being exposed to. To accomplish this task, the embedded array of thermistors at locations A1 through E7 was extremely useful for understanding the general ground temperature distribution over time during the course of the study, and correcting for changes in ground temperature accordingly.

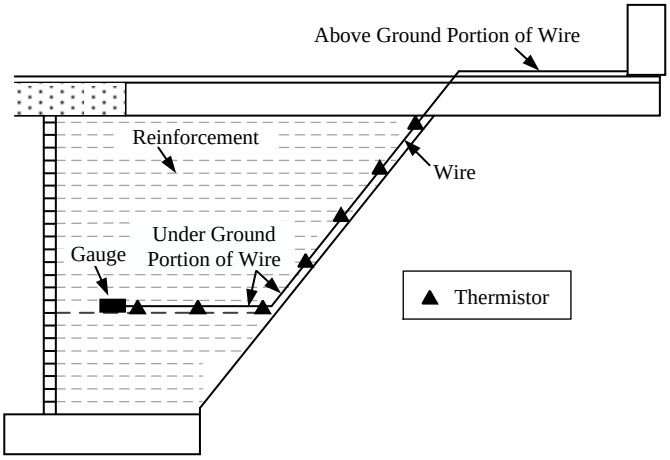

Figure 6.7. Lead wire path for an installed strain gauge, which is affected by changes in air temperature and changes in ground temperature

6.6 Strain gauge data correction process

Figure 6.8a shows the uncorrected strain readings (ε_{uncor}) for gauge A3-s (the third short gauge in layer A) over a one-year duration. As shown in this figure, the ε_{uncor} is changing between 0.04% and 0.22%, with a total variation in range of approximately 0.18%. Figure 6.8b shows measured strain values for this sensor that have been corrected to account for the effects of changes in gauge temperature ($\varepsilon_{cor,g}$). As can be observed, there is not a significant difference between Figures 8a and 8b, indicating that the effect of changes in gauge temperature was generally minimal for the ranges of ground temperature that were encountered at the embedded strain gauge locations.

Figure 6.8 shows a low frequency sinusoidal behavior that can be attributed to seasonal temperature fluctuations; note how the strain increases in the warming spring and summer months, and decreases in the cooling fall and winter months. The high frequency "noise" shown in Figure 6.8 can be attributed to changes in temperature that occur over a daily cycle. Figure 6.9 displays locally recorded air temperatures (T_a) recorded over the same time period as Figure 6.8. As shown in Figure 6.9, similar low frequency and high frequency patterns of behavior can be observed. To allow for comparisons of behavior on a daily basis, Figure 6.10 displays both strain and air temperature over a month of continuous operation. As shown, the trends for $\varepsilon_{cor,g}$ and T_a are similar and generally follow the same pattern.

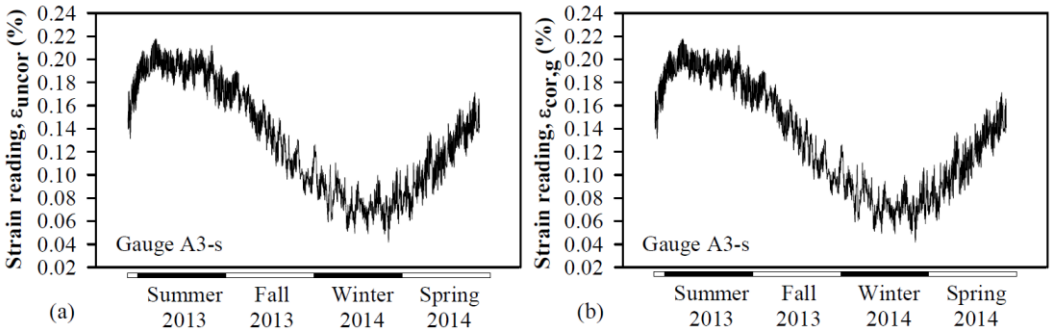

Figure 6.8 Strain values for gauge A3-s over a one-year duration: (a) raw measured strain values, uncorrected, and (b) measured strain values, corrected for the effect of changes in gauge temperature

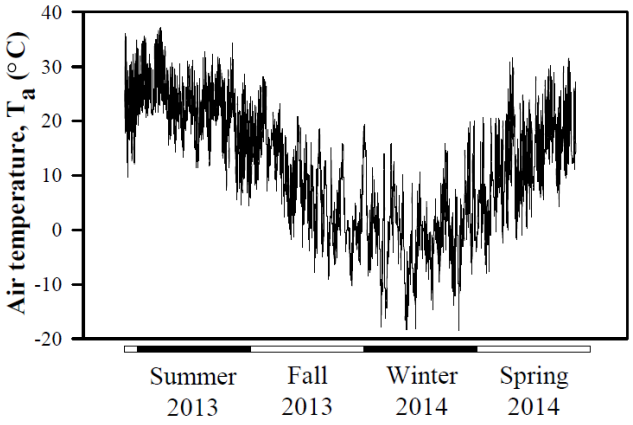

Figure 6.9. Air temperature changes over a one-year duration

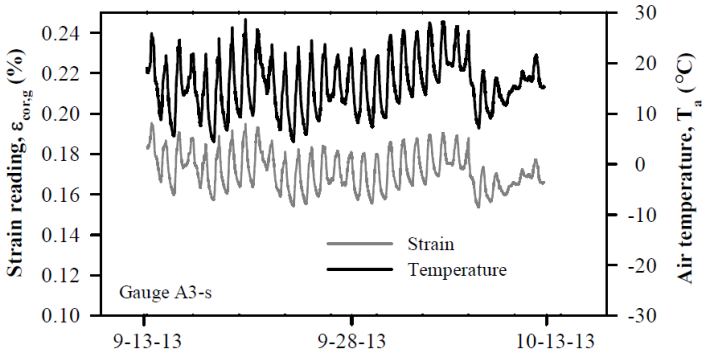

Figure 6.10. Air temperature and strain changes for gauge A3-s over one month of operation

Figure 6.11 shows the results from a regression analysis between gauge temperature corrected strain ($\varepsilon_{cor,g}$) and air temperature (T_a) for data recorded over a single day for gauge A3-s; the corresponding slope (m_a), intercept, and coefficient of determination (R^2) for this regression are shown on the figure. Using a script-based code written in R (R Core Team, 2014), this type of regression analysis was repeated for each day of recorded data, for data collected over the course of one year. Figure

6.12 shows the resulting distribution of the 365 calculated slope (m_a) values, which is somewhat normally distributed with an average value of 0.00170%/°C.

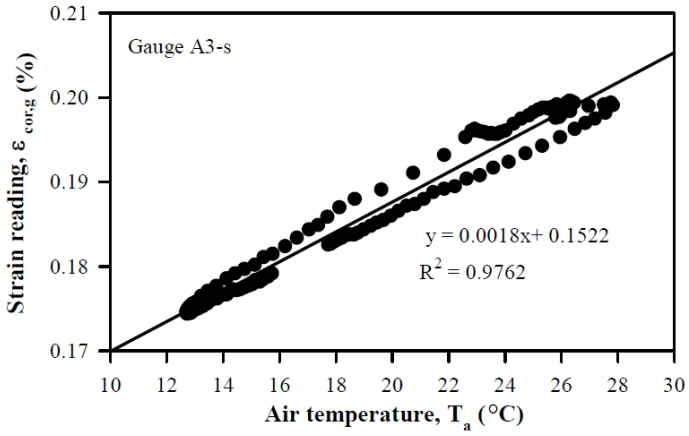

Figure 6.11. Example relationship between gauge temperature corrected strain (for gauge A3-s) and air temperature for data recorded over a single day

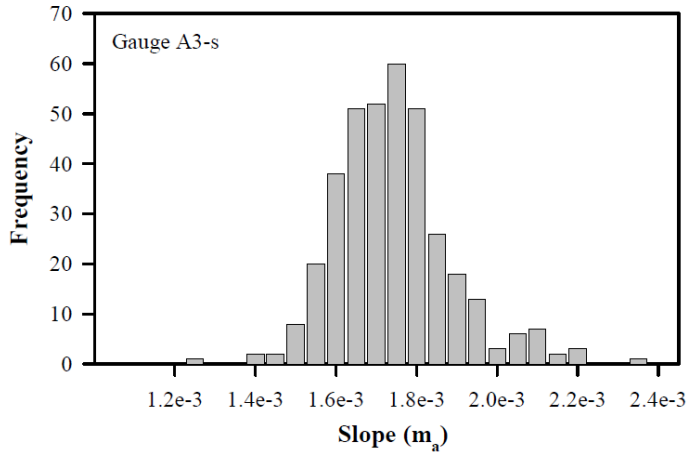

Figure 6.12. Distribution of the calculated slope values for gauge temperature corrected strain (for gauge A3-s) vs. air temperature for daily regression analyses conducted using one year of data

Using this information, the measured strain can be corrected to filter out the daily noise that occurred as a result of temperature change along the exposed portion of the wire. Following the relatively linear relationship that was observed for the daily strain vs. temperature behavior, it is reasonable to assume the following equation is representative of the underlying behavior:

$$\varepsilon_{cor,g}[T_a] = m_a T_a + \varepsilon_0 \quad (6.8)$$

In this equation, $\varepsilon_{cor,g}$ is the measured strain values, corrected for the effect of changes in gauge temperature, T_a is the air temperature in ℃, m_a is the average slope (from Figure 6.12), and ε_0 is the apparent strain reading that would be measured at an air temperature of 0℃. In conventional practice, measured strain values are corrected to an arbitrary (non-zero) temperature value that is specified by the practitioner; for example, in the current study the measured strain values were corrected to a constant ambient air temperature of 25.6℃, which was the initial air temperature measured at the site. In order to employ the correction process in this fashion, a change-based approach can be utilized, as shown in Figure 6.13.

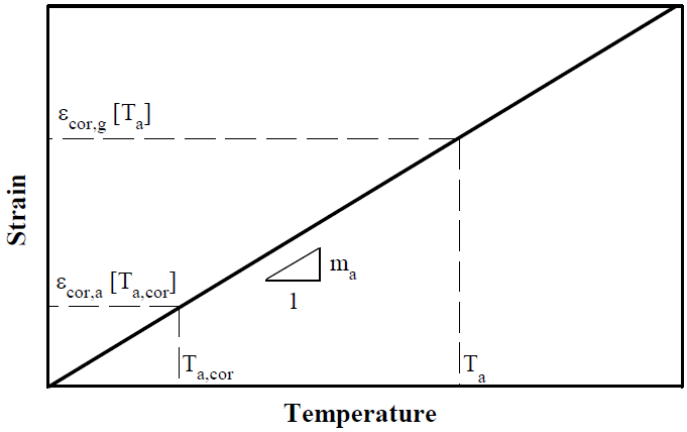

Figure 6.13. The conversion of $\varepsilon_{cor,g}[T_a]$ to $\varepsilon_{cor,a}[T_{a,cor}]$ using the average daily slope (m_a)

Considering an arbitrary fixed air temperature that measured strain values are to be corrected to ($T_{a,cor}$), it can be written that:

$$\varepsilon_{cor,a}[T_{a,cor}] = m_a T_{a,cor} + \varepsilon_0 \quad (6.9)$$

Based on Figure 6.13 and using Equations 6.8 and 6.9, in order to adjust the measured strain values ($\varepsilon_{cor,g}$) recorded over a variety of air temperature (T_a) values to corrected strain values ($\varepsilon_{cor,a}$) for an arbitrarily defined constant temperature ($T_{a,cor}$) of 25.6℃, the following equation should be used:

$$\varepsilon_{cor,a}[T_{a,cor}] = \varepsilon_{cor,g}[T_a] - m_a(T_a - T_{a,cor}) \quad (6.10)$$

where $\varepsilon_{cor,a}$ is the corrected strain for the effect of air temperature along the exposed portion of the wire length.

The gauge temperature corrected ($\varepsilon_{cor,g}$) and wire air temperature corrected strain ($\varepsilon_{cor,a}$) values that result when this process is applied to the measured data are shown in Figure 6.14.

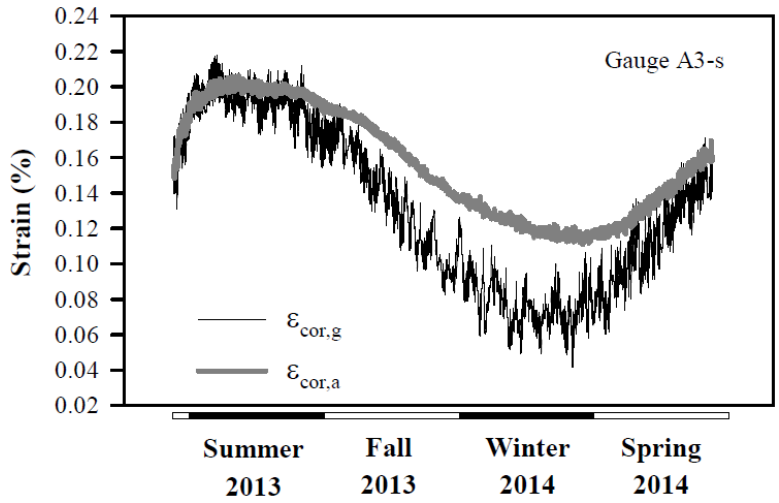

Figure 6.14. The gauge temperature corrected ($\varepsilon_{cor,g}$) and wire air temperature corrected strain ($\varepsilon_{cor,a}$) values for gauge A3-s

As shown in Figure 6.14, the applied correction significantly filters out the daily noise in the measured data that is induced by changes in air temperature along the exposed length of the wire. The remaining fluctuations in measured strain can be attributed to changes in temperature along the length of the wire that is buried in the ground (l_s), which also needs to be corrected for to get a clearer picture of the actual strains that occurred in the geosynthetic fabric. At any given point in time, the wire

passes through backfill soils that have a varying temperature profile; moreover, this temperature profile changes with time in response to changes in ambient air temperature. In order to account for this variation in temperature along the embedded length of the wire, an average soil temperature along the length of each wire was determined ($T_{s,ave}$), using data from the embedded array of thermistors at locations A1 through E7. As each strain gauge wire has a unique path that passes along its own soil temperature profile (i.e., Figure 6.7), the associated values of $T_{s,ave}$ are different for each strain gauge. To determine the appropriate value of $T_{s,ave}$ for each strain gauge, a weighted average approach was utilized to account for variations in temperature over various increments of the wire, i.e.,

$$T_{s,ave} = \frac{T_{t1}l_{s1}+T_{t2}l_{s2}+\cdots+T_{tn}l_{sn}}{l_{s1}+l_{s2}+\cdots+l_{sn}} \tag{6.11}$$

where, $T_{s,ave}$ is the average temperature of the underground length of the wire (l_s), T_{ti} is the temperature at the location of *i*th thermistor along the path of the wire, and l_{si} is the incremental length of the wire assigned to *i*th thermistor, such that:

$$l_{s1} + l_{s2} + \cdots + l_{sn} = l_s \tag{6.12}$$

Unfortunately, given that the ground temperature varies along the length of the wire, it is often not possible to use temperature values recorded only at the gauge location to correct for the effect of ground temperature. As an example, Figure 6.15 shows the difference between ground temperatures measured only at the location of

gauge A3-s, versus average ground temperatures along the length of the wire to gauge A3-s, over a one-year duration.

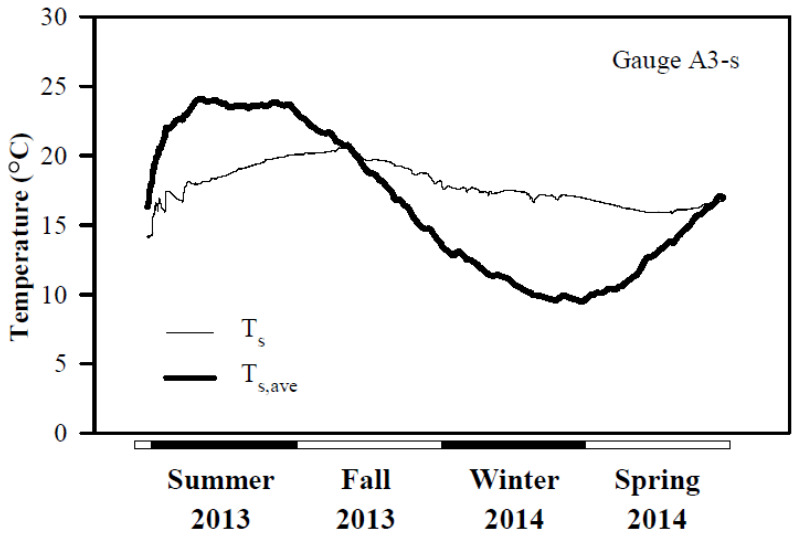

Figure 6.15. Ground temperatures at the location of gauge A3-s (T_s) relative to average ground temperatures along the length of the wire to A3-s ($T_{s,ave}$) over a one-year duration

Figure 6.16 compares air temperature corrected strain values ($\varepsilon_{cor,a}$) with ground temperatures measured at the location of gauge A3-s (T_s), over a one-year duration. Figure 6.17 compares air temperature corrected strain values ($\varepsilon_{cor,a}$) with average ground temperatures along the length of the wire to A3-s ($T_{s,ave}$), over a one-year duration. As can be observed, much stronger correlation exists for the average ground temperature values, which is not surprising. Moreover, as shown in Figure 6.17, the R^2 value is very close to 1.0, which indicates that temperature changes in the

underground portion of the wire are likely the root cause of the remaining observed changes in strain.

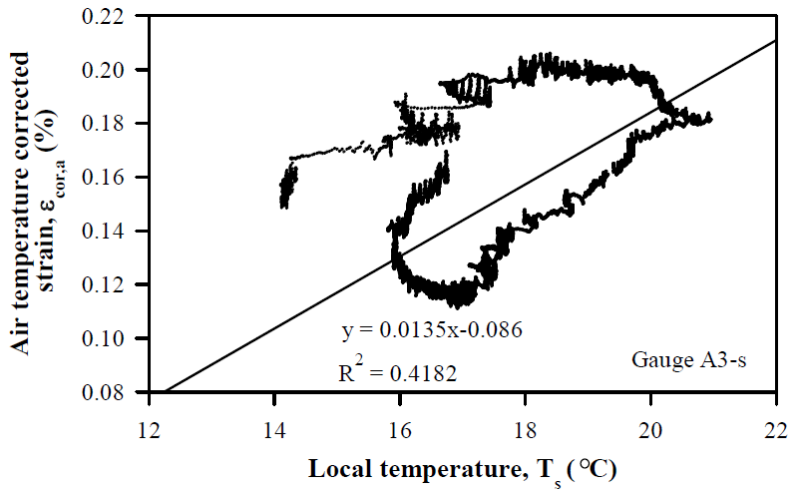

Figure 6.16. Relationship between air temperature corrected strain ($\varepsilon_{cor,a}$) and temperature measured at the location of gauge A3-s (T_s)

An equation having a similar form as Equation 6.10 was then used to correct for the effects of changes in underground wire temperature, to yield the final corrected strain reading:

$$\varepsilon_{cor} = \varepsilon_{cor,s}[T_{s,ave,cor}] = \varepsilon_{cor,a}[T_{s,ave}] - m_s(T_{s,ave} - T_{s,ave,cor}) \qquad (6.13)$$

where, $T_{s,ave,cor}$ is an arbitrary fixed soil temperature that measured strain values are to be corrected to, m_s is the average slope (i.e., from Figure 6.17), and ε_{cor} is the final corrected strain.

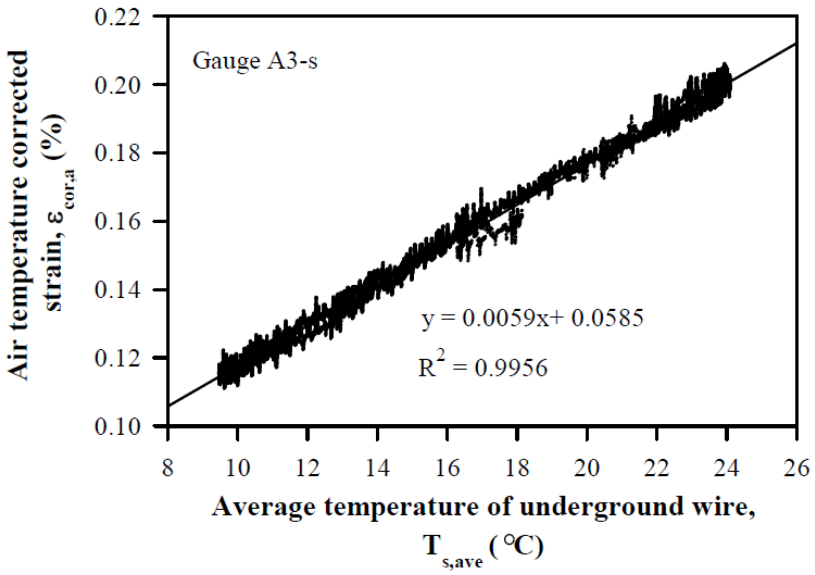

Figure 6.17. Relationship between air temperature corrected strain ($\varepsilon_{cor,a}$) and average ground temperature along the length of the wire to gauge A3-s ($T_{s,ave}$)

After performing the correction process described in Equations 6.4-6.13, the strain gauge data was corrected for the effects of both wire and sensor temperature. Figure 6.18 presents the raw (uncorrected) strain data measured for gauge A3-s (ε_{uncor}) alongside the final strain gauge data that results after the correction process has been applied (ε_{cor}). As shown, for this sensor, the change in strain over the course of one year was negligible, i.e., structural deformation due to loading or long-term creep of the geosynthetic did not occur.

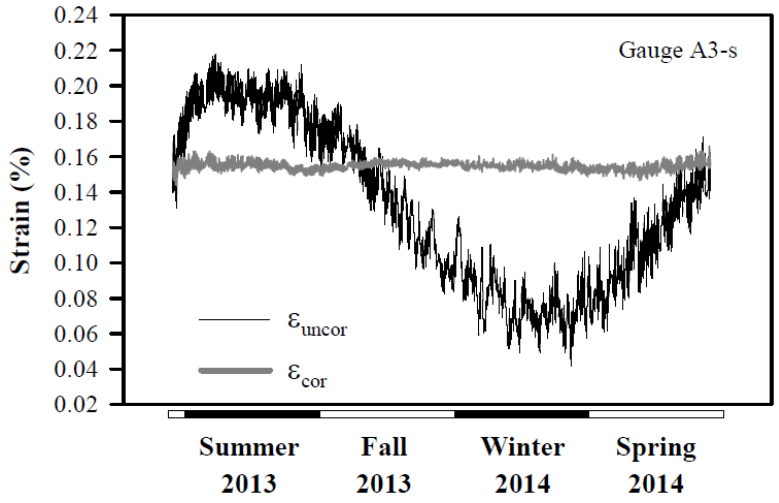

Figure 6.18. A comparison of raw (ε_{uncor}) and corrected strains (ε_{cor}) measured for gauge A3-s

The step-by-step process outlined in Equations 6.4-6.13 was broken down to show the relative contributions of the different temperature fluctuations to the overall corrections that are applied. From this discussion, it can be concluded that that the main source of the observed change in strain (i.e., the "apparent strain" that was measured, not the actual strain that occurred) was changes in wire temperature. Moving forwards, researchers and practicing engineers can correct for the effects of changes in wire temperature using a more straightforward calculation process that utilizes a single weighted-average temperature (T) for the total length of the wire (l_t), which includes temperature contributions from both its above ground and underground lengths, as follows:

$$l_t = l_a + l_s \tag{6.14}$$

$$T = \frac{T_a l_a + T_{s,avg} l_s}{l_t} \quad (6.15)$$

$$\varepsilon(T_0) = \varepsilon_{cor,g}(T) - m(T - T_0) = \varepsilon_{cor} \quad (6.16)$$

where, T_0 is an arbitrary fixed temperature that measured strain values are to be corrected to, T is the average temperature of the wire including both the above ground and underground portions, and m is the slope of the regression line from comparisons of gauge temperature corrected strain versus average temperature. An example of what this type of data looks like is shown in Figure 6.19, which presents the relationship between gauge temperature corrected stain ($\varepsilon_{cor,g}$) and average temperature (T) for gauge A3-s. As shown, since this gauge did not experience any significant strain outside of the temperature-induced apparent strain that occurred, the two variables are highly correlated with R^2 being very close to 1.0. The observed slope m = 0.0076 is a value that is proportional to the total length of the wire (l_t).

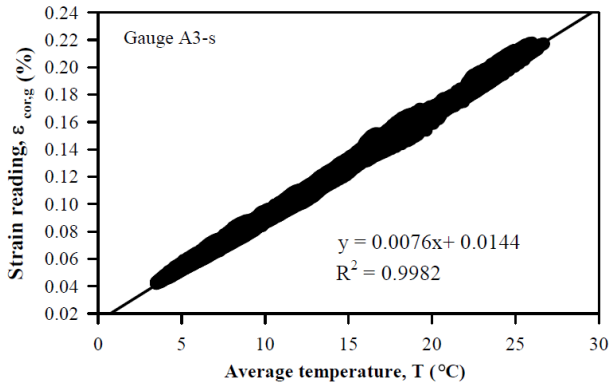

Figure 6.19. Relationship between gauge temperature corrected strain ($\varepsilon_{cor,g}$) and average temperature along the length of the wire for gauge A3-s (T)

From the observations made in this section, it is concluded that if the length of the wire exposed to air (l_a), the wire length under the ground (l_s), the air temperature (T_a) and the average wire temperature along its path under the ground ($T_{s,avg}$) are known, measured strain values made using a two-wire Wheatstone quarter-bridge configuration can be corrected following a straightforward process. This process was developed using an observational approach that employs an array of inexpensive temperature transducers.

6.7 Estimation of strain induced by structural deformation and creep

For gauge A3-s presented in the last section, the only significant source of observed strain change was apparent strains induced by changes in temperature. Therefore, the correlation between the measured strain and average temperature was very high. However, it is common for gauges that are used on real projects to experience actual strain over the same time frame as when temperature-induced apparent strains are being recorded; in other words, actual strain values and apparent strain values will be superimposed on top of each other. In this situation, the correlation between the measured strain and temperature (e.g., Figure 6.19) is not as high as the case where no structural deformation or creep deformation occurs for the geosynthetic. Consequently, an observational approach using direct field data such as the one shown in Figure 6.19 cannot be used to directly determine the slope *m* that is needed to correct for the effect of changes in temperature.

Fortunately, a simpler approach to determining *m* is available, as this slope is directly related to the resistance characteristics of the wire at varying temperatures, relative to the change in resistance that corresponds to sensor strain. In particular, the wire temperature calibration process that is used in Figure 6.6 provides the essential information that is needed. As shown in Figure 6.6, the changes in wire resistance versus temperature are linear for 305 m of wire, with a slope of 0.1512 ohms /℃. Using this data in Equation 6.3 with R_0 and GF equal to 120 ohms and 2.0, respectively, yields an approximate strain change of 0.063(%)/℃ for 305 m of wire. For shorter lengths of wire used in the field (l_t), the following relationship will hold true for this wire:

$$\frac{m}{l_t} = \frac{0.063(\%)/℃}{305\ m} \tag{6.17}$$

This allows *m* to be calculated directly using the equation:

$$m = 0.063(\%)/℃ \times \frac{l_t}{305\ m} \tag{6.18}$$

For example for gauge A3-s, which has a total wire length of 36.6 m, m = 0.063(%)/℃× 36.6 m / 305 m = 0.0076(%)/℃. This value for *m* is exactly the same as the value that was independently calculated using the regression analysis approach from the observational method (Figure 6.19), which supports the use of this direct calculation method for *m*.

This method can be applied to other sensors on this project (or to sensors on other projects) to remove the effect of apparent strains induced by temperature. For

example, strain gauge B3-l has a total wire length (l_t) of 30.5 m, with the length of the wire exposed to air (l_a) of 7 m, and an embedded length in the ground (l_s) of 23.5 m. Figure 6.20 presents the measured strain (ε_{uncor}) for strain gauge B3-l over three years of operation. The air temperature (T_a) and the average wire temperature under the ground ($T_{s,avg}$) over the same duration are also shown in this figure. The average ground wire temperatures were calculated using the approach outlined in Equation 6.11, which utilized various temperature values recorded by the thermistors installed along the path of the wire under the ground. The average temperature (T) over the total length of the wire (l_t) is then calculated using Equation 6.15, with the results from this process being shown in Figure 6.21. Following the approach in the previous paragraph, the calculated value of m for this sensor is determined to be 0.0063(%)/℃ (m = 0.063(%)/℃× 30.5 m / 305 m). Finally, the corrected strain (ε_{cor}) can be calculated using Equation 6.16, yielding the results shown in Figure 6.22.

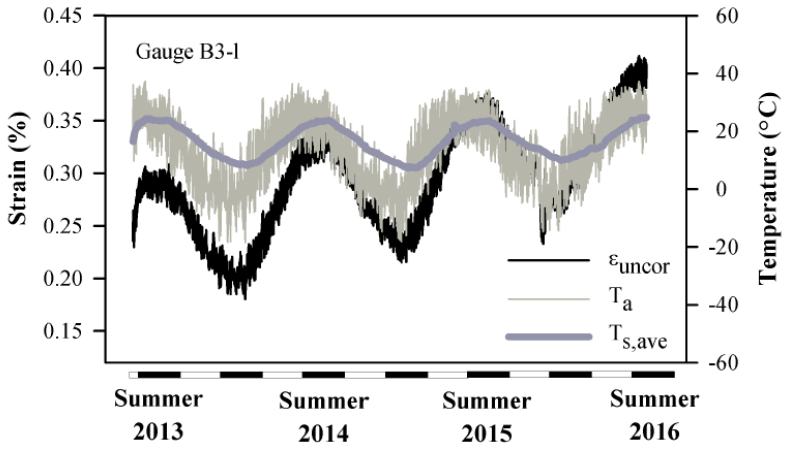

Figure 6.20. The measured strain (ε_{uncor}), air temperature (T_a), and average wire path temperature under the ground ($T_{s,avg}$) for strain gauge B3-l over three years of operation.

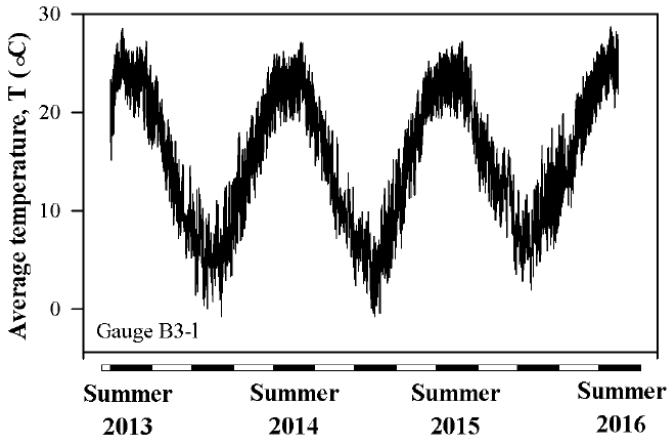

Figure 6.21. The average temperature (T) for the total length of the wire (l_t) for strain gauge B3-l over three years of operation.

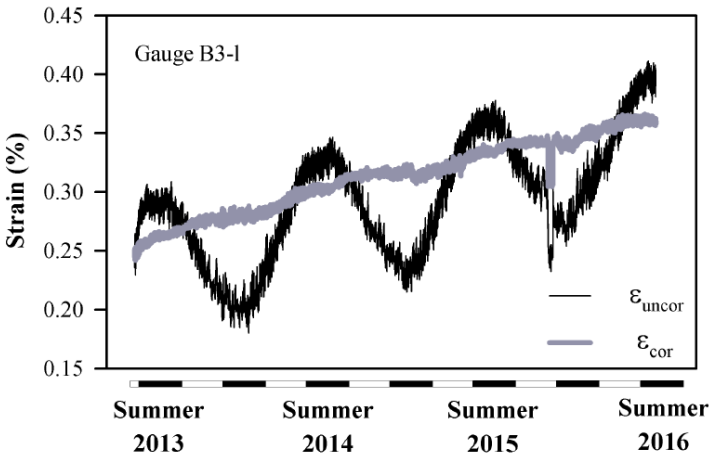

Figure 6.22. The measured strain readings (ε_{uncor}) and the temperature corrected strain (ε_{cor}) values for strain gauge B3-l over three years of operation.

The results shown in Figure 6.22 correspond to relatively small creep strains in the geosynthetic at the location of gauge B3-l. The root cause of these accumulating strains is unknown, but is believed to be caused in part by gradual stress redistributions in the GRS abutment over time. It should be noted that the overall magnitude of creep strain that is observed over a three-year period was quite small, on the order of 0.10%.

6.8 Conclusion

This chapter evaluated the effect of foil gauge and connecting wire temperature changes on the strain readings in a GRS abutment that was instrumented with a two-wire configuration Wheatstone quarter-bridge measurement system. Although the measured strain values were fairly small, it was necessary to correct for temperature effects to examine the long-term strain behavior of the geosynthetic layers,

particularly to assess if any creep or stress-redistribution behavior had occurred. Observation of results indicate that changes in wire temperature have a more significant effect than changes in strain gauge temperature with respect to the values of strain that are measured. The relative effect of wire temperature change is more pronounced if the level of actual strain that occurs at the gauge location is small, and the temperature fluctuations are large; this induces a noticeable "apparent strain" effect.

Using observed field data from a distributed array of temperature sensors, a straightforward mathematical correction approach is presented for correcting foil strain gauge measurements to account for temperature effects. The presented methodology follows basic principles of physics and electric circuits theory, and is supported by direct field measurements from an instrumented GRS structure. Representative results from two strain gauges are presented, for data collected over an extended period of time (up to three years post-construction).

The presented approach and associated framework for data correction are useful for practicing engineers and other researchers, as the general concepts from this study can be applied to data collected from many instrumented field projects. The general observational approach that is discussed may be useful in the future for "training" structural health monitoring systems, particularly those that may employ machine learning algorithms in real time to avoid reporting false positives about problematic behavior.

Following the methodology presented in this chapter, the strains measured by all the sensors in the west abutment over the first three years of operation were

corrected; the results from this correction process are shown in more detail in Appendix G. As shown in Appendix G, for the gauges which are still working properly, the maximum change in the corrected strain is less than 0.1% over the first three years of in-service operation of the structure. In some cases, the gauges stopped working properly; the long-term failure of gauges is generally attributed to the presence of water. For some of the failed gauges, measured strains are greater than 0.1%. However, these measured results were generally considered to be not reliable, given the eventual gauge failure that occurred. From the corrected strain data, it can be observed that the overall internal strains in the abutment are quite small. Continuous monitoring of the structure is recommended over the long term to assess the creep behavior of the abutment.

The same procedure that was described in this chapter was utilized to correct the data of the strain gauges attached to the bottom of the concrete bridge. The corresponding strains including the measured and corrected values are presented in Appendix H for the gauges which continued working after the completion of construction (b2, b3, b4, b6 and b8). As shown in Appendix H, the corrected values are nearly constant and less than 0.06% for most of the monitoring period. It appears that gauge b3 stopped properly working at some point in the second year, as its readings increased in a fashion that did not correspond to the readings indicated by the other nearby strain gauges.

REFERENCES

A-iyeh, E. (2013). "Thermal output and thermal compensation models for apparent strain in a structural health monitoring-based environment." Master of Science Dissertation, University of Manitoba.

Adams, M., Nicks, J., Stabile, T., Wu, J., Schelatter, W. and Hartmann, J. (2011). "Geosynthetic reinforced soil integrated bridge system interim implementation guide." Publication No. FHWA-HRT-11-026, Federal Highway Administration, Washington, DC.

Allen, T. and Bathurst, R. (2013). "Performance of an 11 m high block-faced geogrid wall designed using the K-stiffness method." Canadian Geotechnical Journal 51(1), 16-29.

Berkheimer, S. (2007). "Instrumented geogrid reinforced mechanically stabilized earth wall undergoing large settlement." Master's Thesis, University of Delaware.

Briançon, L., Nancey, A., Robinet, A., Voet, M. (2006). "Set up of a warning system integrated inside a reinforced geotextile for the survey of railway." Proceedings of the 8th International Geosynthetics Conference, Yokohama, Japan, 857-860.

Brownjohn, J., (2007). "Structural health monitoring of civil infrastructure." Philosophical Transactions of the Royal Society of London A: Mathematical, Physical and Engineering Sciences, 365(1851), 589-622.

Costa, C., Zornberg, J., de Souza Bueno, B. and Costa, Y. (2016). "Centrifuge evaluation of the time-dependent behavior of geotextile-reinforced soil walls." Geotextile and Geomembrane, 44(2), 188-200.

Fraser, M., Elgamal, A., He, X. and Conte, J. (2009). "Sensor network for structural health monitoring of a highway bridge." J. Comput. Civil Eng. 24(1), 11-24.

Griffith, B. (2000). "Radio-electronic transmission fundamentals." SciTech Publishing. Chicago

Hall, P., Deighan III, R. (1986). "On using strain gauges in electronic assemblies when temperature is not constant." Components, Hybrids, and Manufacturing Technology, IEEE Transactions on 9(4), 492-497.

Hossain, M., Kibria, G., Khan, M., Hossain, J. and Taufiq, T. (2011). “Effects of backfill soil on excessive movement of MSE wall.”" Journal of Performance of Constructed Facilities, 26(6), 793-802.

Hu, X., Wang, B. and Ji, H. (2013). “A wireless sensor network-based structural health monitoring system for highway bridges.” Computer-Aided Civil and Infrastructure Engineering, 28(3), 193-209.

Intrieri, E., Gigli, G., Mugnai, F., Fanti, R. and Casagli, N. (2012). “Design and implementation of a landslide early warning system.” Engineering Geology, 147, 124-136.

Khan, A. and Wang, X. (2001). “Strain measurements and stress analysis. Prentice Hall.”

Koerner, R., Koerner, G. (2013). “A data base, statistics and recommendations regarding 171 failed geosynthetic reinforced mechanically stabilized earth (MSE) walls.” Geotextile and Geomembrane, 40, 20-27.

Lee, K., Wu, J. (2004). “A synthesis of case histories on GRS bridge-supporting structures with flexible facing.” Geotextile and Geomembrane, 22(4), 181-204.

Lehtonen, V., Meehan, C., Länsivaara, T. and Mansikkamäki, J. (2015). “Full-scale embankment failure test under simulated train loading.” Géotechnique, 65(12), 961-974.

Leshchinsky, D. and Fowler, J. (1990). “Laboratory measurement of load-elongation relationship of high-strength geotextiles.” Geotextile and Geomembrane. 9(2), 145-164.

Leshchinsky, D., Imamoglu, B. and Meehan, C. (2010). “Exhumed geogrid-reinforced retaining wall.” Journal of Geotechnical and Geoenvironmental Engineering, 136(10), 1311-1323.

Ma, C. and Wu, J. (2004). Field performance of an independent full-height facing reinforced soil wall. Journal of performance of constructed facilities, 18(3), 165-172.

Nicks, J., Esmaili, D. and Adams, M. (2016). “Deformations of geosynthetic reinforced soil under bridge service loads.” Geotextile and Geomembrane, 44(4), 641-653.

Ong, D., Leung, C., Chow, Y. and Ng, T. (2015). “Severe damage of a pile group due to slope failure.” Journal of Geotechnical and Geoenvironmental Engineering, 141(5), 04015014.

Peck, R. (1969). “Advantages and limitations of the observational method in applied soil mechanics.” Géotechnique, 19(2), 171-187.

R Core Team (2014). “R: A language and environment for statistical computing. R Foundation for Statistical Computing.” Vienna, Austria. URL http://www.R-project.org/.

Sluimer, G. and Risseeuw, P. (1982). “A strain-gauge technique for measuring deformations in geotextiles.” Proceeding Second International Conference on Geotextiles, Las Vegas, USA, 835-838.

Stuedlein, A., Bailey, M., Lindquist, D., Sankey, J., Neely, W. (2010). “Design and performance of a 46-m-high MSE wall.” Journal of Geotechnical and Geoenvironmental Engineering, 136(6), 786-796.

Valentine, R. (2013). “An assessment of the factors that contribute to the poor performance of geosynthetic-reinforced earth retaining walls.” H.I. Ling (Ed.), et al., Proc. International Symposium on Design and Practice of Geosynthetic-Reinforced Soil Structures, Bologna, Italy, October 14-16, DEStech Publication Inc., Lancaster, PA, 318-327.

Vishay Micro-Measurements (2005). “The three-wire quarter bridge circuit.” Application Note TT-612.

Vishay Micro-Measurements, V. (2007). “Strain gage thermal output and gage factor variation with temperature.” Technical Note TN-504-1.

Walsh, N. (2009). “High strength geotextile: Strain monitoring at Cherry Island landfill.” Master's Thesis, University of Delaware.

Walsh, N., Meehan, C. and Leshchinsky, D. (2009). “Lessons learned: Field installation of strain gages on high-strength geotextile.” Proceeding of International Foundations Congress and Equipment Expo '09 (IFCEE09), Contemporary Topics in Ground Modification, Problem Soils, and Geo-Support, Geotechnical Special Publication No. 187, Orlando, FL, March 15-19, 2009, ASCE, Reston, VA, 369-376.

Warren, K., Christopher, B. and Howard, I. (2010). “Geosynthetic strain gage installation procedures and alternative strain measurement methods for roadway applications.” Geosynthetic International, 17(6), 403-430.

Won, M., Kim, Y. (2007). “Internal deformation behavior of geosynthetic-reinforced soil walls.” Geotextile and Geomembrane, 25(1), 10-22.

Wu, J., Nicks, J., Pham, T. and Adams, M. (2013). "Composite Behavior of Geosynthetic Reinforced Soil Mass." Publication No. FHWA-HRT-10-077, Federal Highway Administration, Washington, DC.

Xue, J., Chen, J., Liu, J. and Shi, Z. (2014). "Instability of a geogrid reinforced soil wall on thick soft Shanghai clay with prefabricated vertical drains: A case study." Geotextile and Geomembrane, 42(4), 302-311.

Yonezawa, T., Yamazaki, T., Tateyama, M. and Tatsuoka, F. (2014). "Design and construction of geosynthetic-reinforced soil structures for Hokkaido high-speed train line." Transportation Geotechnics, 1(1), 3-20.

Yoo, C., Jung and H. (2006). "Case history of geosynthetic reinforced segmental retaining wall failure." Journal of Geotechnical and Geoenvironmental Engineering, 132(12), 1538-1548.

Chapter 7

LIVE LOAD TESTING OF THE CONSTRUCTED GRS-IBS

7.1 Introduction

Live load testing is recommended for evaluating the structural response of a constructed GRS-IBS, either immediately after construction or during operation, to ascertain the safety of the structure or to assess its load-carrying capacity (Adams et al. 2011, Lawrence 2014, Phillips 2014). Live load testing and other types of nondestructive field testing has been used in the past by researchers to achieve a variety of goals including better estimation of bridge load rating, determination of the response of non-deteriorated and deteriorated components, and evaluation of the transverse distribution characteristics of the bridge superstructure (e.g., Schulz et al. 1995, Chajes et al. 1997; Cai and Shahawy 2003, Fang et al. 2004, Bhattacharya et al. 2005, DelGrego et al. 2008, Lawrence et al. 2011). Different guidance manuals and codes have recommended various procedures for live load testing, which often include the use of heavily loaded trucks for live load application (e.g., the Manual for Bridge Rating through Load Testing (e.g., Transportation Research Board (TRB) 1998, AASHTO LRFD 2013). A review of available literature on this topic shows that field load tests have been performed to investigate not only the stability of bridge structures but also the stability of abutments (such as geosynthetic reinforced abutments, which includes

MSE or GRS walls) and foundations, since the assessment of the geotechnical stability of the abutments and foundations of any bridge is critical and bridges can be structurally stable but experience failure because of abutment mechanical instability, foundation failure, or scour issues (e.g., Berg et al. 2009, Adams et al. 2011). From a design standpoint, the abutments of any bridge must be assessed to ensure that they will be externally and internally stable against both dead and live loads. To evaluate the relative safety and load-displacement response of reinforced abutments, a number of researchers have conducted live load testing in the field or in the lab; the results of these tests have in some cases had an influence on existing design code recommendations (e.g., Helwany et al. 1996, Adams et al. 2002, Lee and Wu 2004, Adams et al. 2007, Bathurst et al. 2009, Vennapusa et al. 2012, Nicks et al. 2013, Wu and Pham 2013, Iwamoto 2014).

After completion of construction of the GRS abutments, and following placement of the bridge superstructure, it can be useful to preload the bridge prior to asphalt paving (Adams et al. 2011); this type of preloading is particularly beneficial because it helps the bridge superstructure to "settle in" to the bridge bearing seat, which can help to prevent later pavement cracking that can occur if the bridge is not preloaded. For the current study, this preloading process was conducted in a careful way, such that it could also serve as a meaningful live load test for the structure. This type of testing can provide valuable information about the expected in-service performance of the structure, and can provide feedback that may also be useful for the bridge load rating process. This chapter presents the results of live load testing of the constructed GRS-

IBS using heavily loaded trucks. In the next sections, the live load test details and the corresponding results are discussed.

7.2 Live load test details

Trucks with a single axle on the front and double axles on the rear were utilized to conduct the load test (Figure 7.1). The spacing between the two rear axles and between the front axle and the center of the two rear axles are shown in Figure 7.2. The spacing between the front wheels and also the rear wheels are also shown in Figure 7.2. The criteria used to select the maximum truck weight was based on the AASHTO LRFD Design Load of HL93, which consists of a Design Truck having a total weight of 72 kips and a Lane Load of 0.64 kip/ft and the Design Tandem Load having a total weight of 50 kips and Lane Load of 0.64 kip/ft.

During the live load testing, the weight of the trucks was increased in a series of consistent increments in order to assess the deformation response of the structure at different load levels. Four levels of truck load were used for this process: (1) empty trucks, (2) trucks approximately 1/3 full of soil, (3) trucks approximately 2/3 full of soil, and (4) trucks completely full of soil. In order to examine the effect of the position of the trucks on the response of the structure, the trucks were positioned in different locations on the bridge and the abutments. The various truck positions that were utilized for truck live load testing are shown in Figures 7.3a through 7.3j. As shown in these figures, the trucks were positioned on both abutments as well as the bridge. For

each empty or loaded truck, total applied loads were measured directly using separate scales for each truck tire (or tire group if a double tire was present); the corresponding tire weights are presented in Table 7.1. The live load case number, respective position of the loaded trucks, and the weight are presented in Table 7.2. In order to compare the applied live and dead load, Table 7.3 illustrates the ratio between the live load induced by the trucks and the total applied dead load by the bridge and the reinforced soil to the west abutment (as illustrated in Figure 7.4) for different load cases. As shown in Table 7.3, the maximum live to total dead load ratio is less than 13 percent. As shown in Figure 7.3i, for load cases 16 to 19, one of the trucks moved from the west abutment to the east abutment and the corresponding data was measured for four different truck positions. In other cases, the trucks did not move and were just stopped in their loading position prior to collecting the sensor data.

Figure 7.1 Truck type utilized for live load testing

Figure 7.1 Truck type utilized for live load testing (Continued)

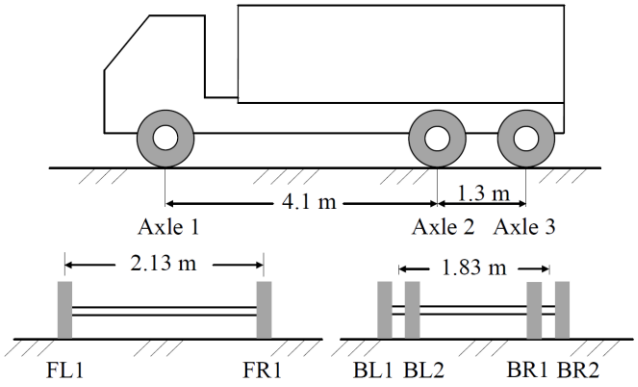

Figure 7.2 Axle and wheel load configuration of the trucks

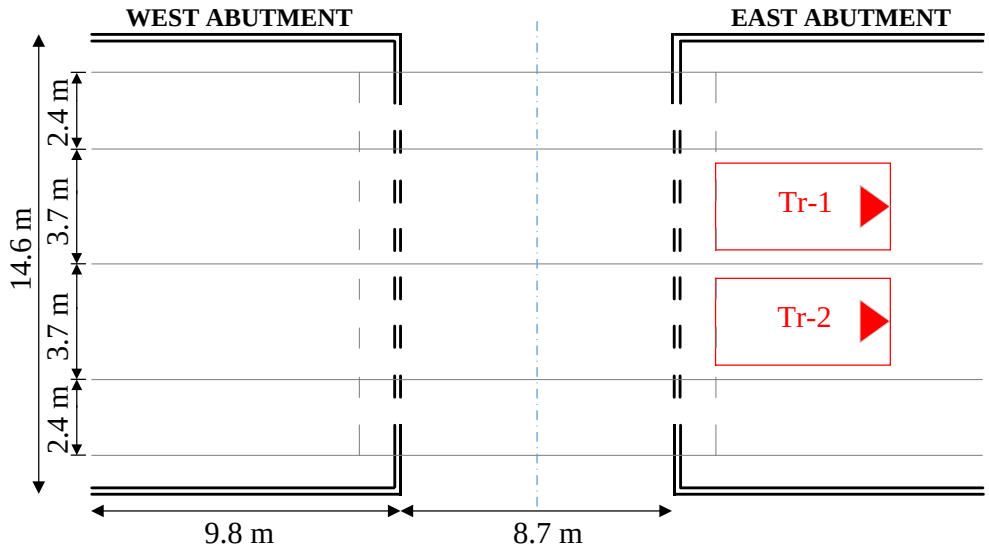

Figure 7.3a Live load test, truck position number 1 (P1) – trucks facing east.

Used for Live Load Test Nos. 1, 4 and 7.

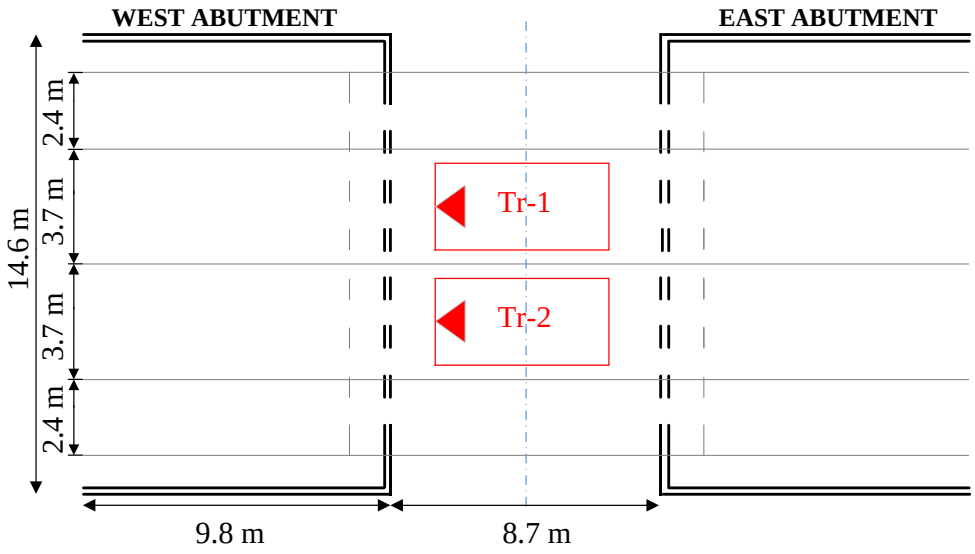

Figure 7.3b Live load test, truck position number 2 (P2) – trucks facing west.

Used for Live Load Test Nos. 2, 5, 8 and 13.

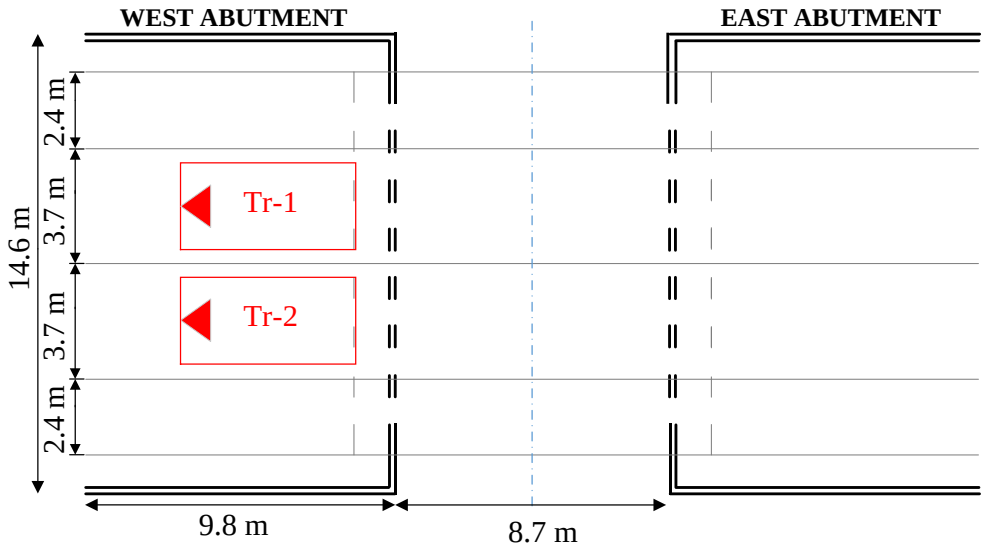

Figure 7.3c Live load test, truck position number 3 (P3) – trucks facing west. Used for Live Load Test Nos. 3, 6 and 9.

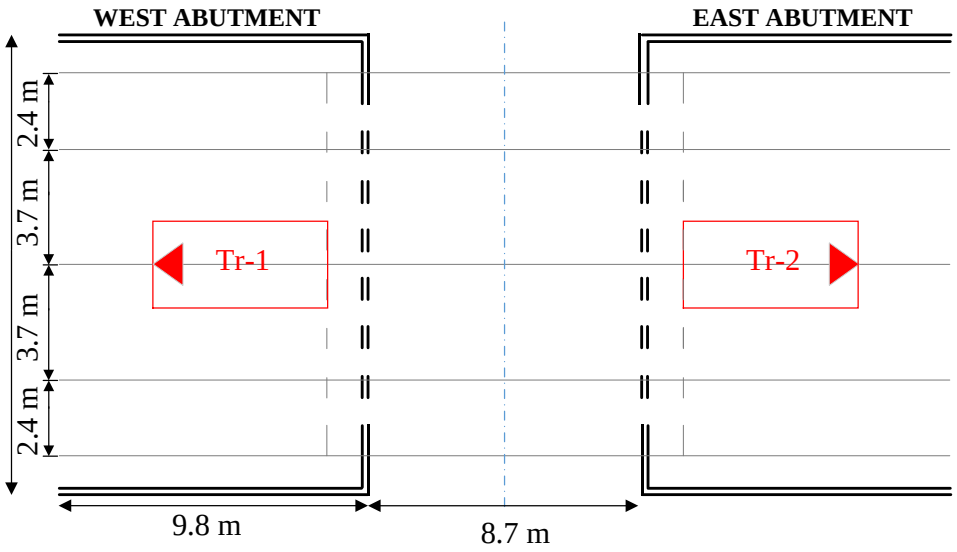

Figure 7.3d Live load test, truck position number 4 (P4) – trucks facing both east and west. Used for Live Load Test No. 10

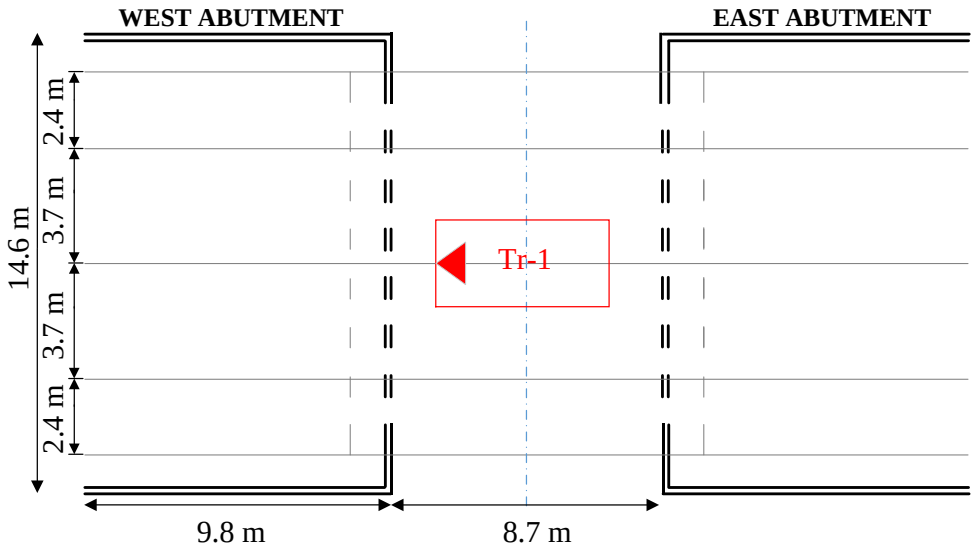

Figure 7.3e Live load test, truck position number 5 (P5) – single truck facing west. Used for Live Load Test No. 11.

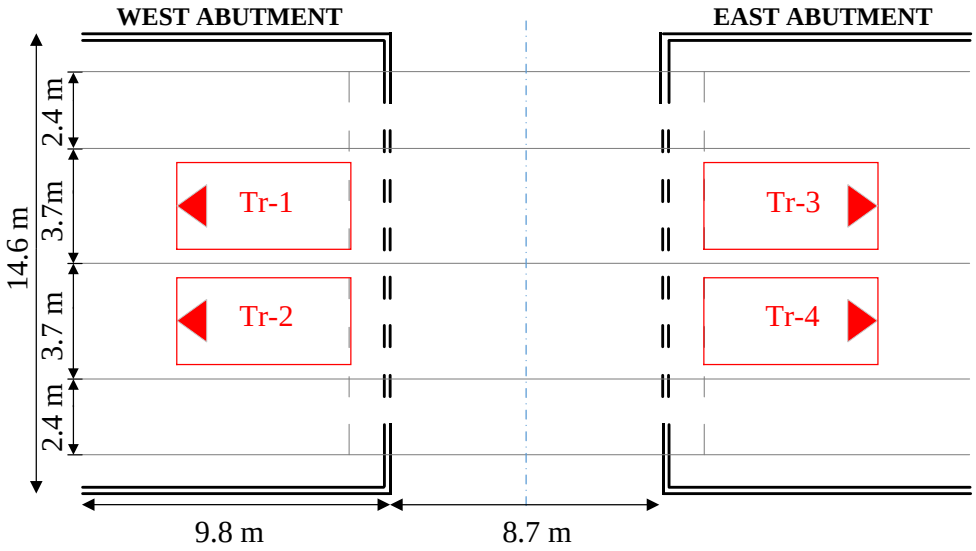

Figure 7.3f Live load test, truck position number 6 (P6) –trucks facing west. Used for Live Load Test No. 12.

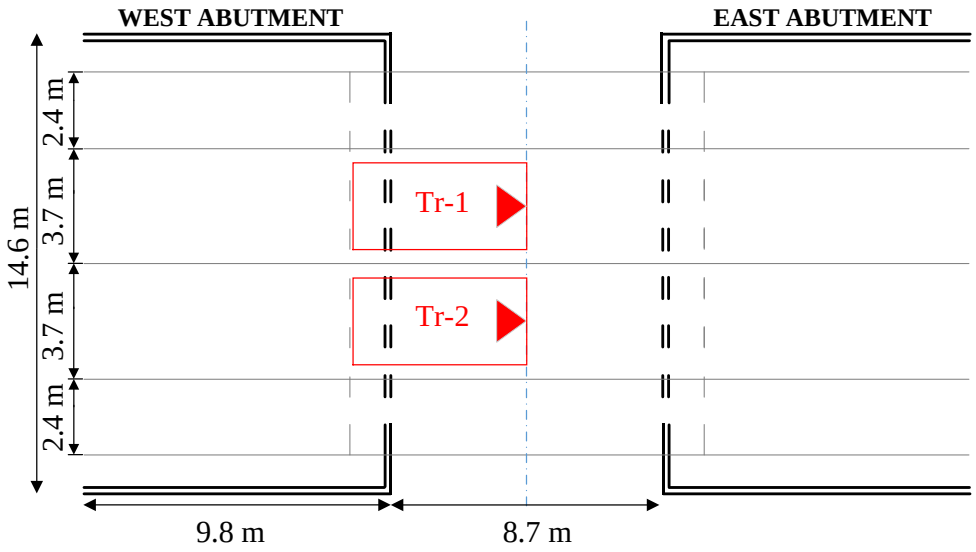

Figure 7.3g Live load test, truck position number 7 (P7) –trucks facing both east and west. Used for Live Load Test No. 14.

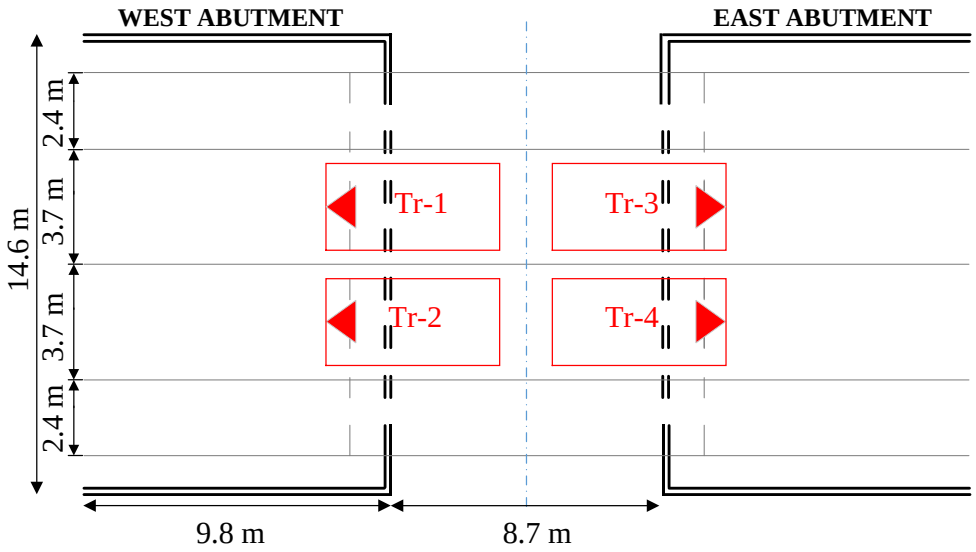

Figure 7.3h Live load test, truck position number 8 (P8) – four trucks, facing both east and west. Used for Live Load Test No. 15.

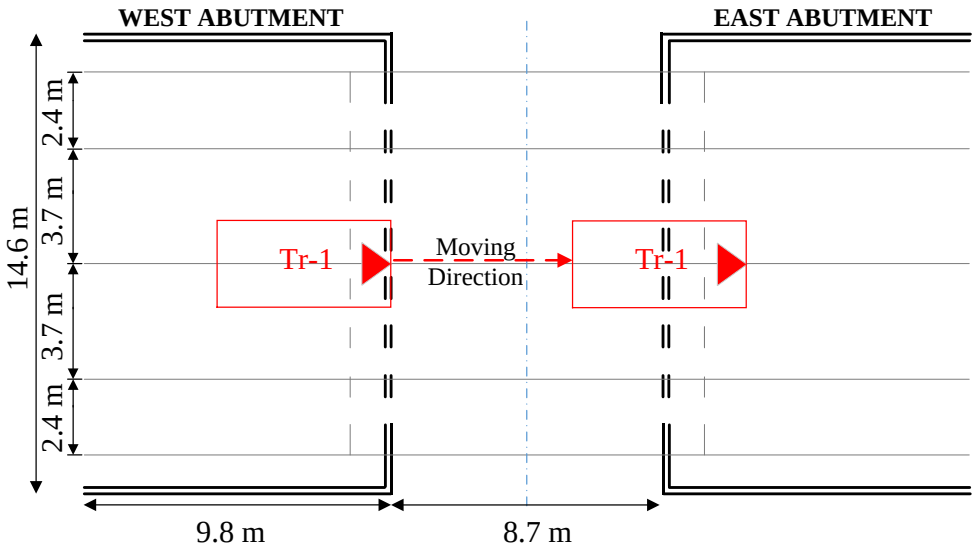

Figure 7.3i Live load test, truck position numbers 9 to 12 (P9- P12) – moving truck test, from west to east. Used for Live Load Test Nos. 16-19.

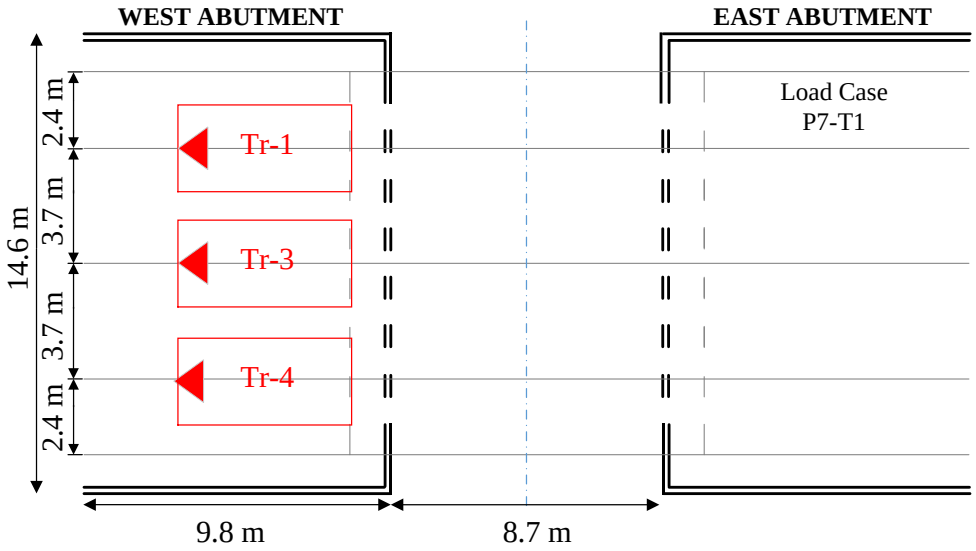

Figure 7.3j Live load test, truck position number 13 (P13) – three trucks, facing west. Used for Live Load Test No. 20.

Table 7.1 Applied load under each tire or two-tire group (scale weight) for each of the trucks and load levels that was used for live load testing

Truck Load Level	Truck No.	FL1 (kN)	FR1 (kN)	BL1 (kN)	BR1 (kN)	BL2 (kN)	BR2 (kN)	Total (kN)
Empty Trucks	1	25.8	27.8	17	16.8	15.7	14.9	**118.0**
	2	26.3	27.4	18	20.9	18.3	17.6	**128.4**
	3	-	-	-	-	-	-	-
	4	-	-	-	-	-	-	-
1/3 Full Capacity	1	31.4	32.6	28.8	29.6	28.3	28.4	**179.1**
	2	32.6	32.8	30.0	31.2	30.8	28.1	**185.5**
	3	-	-	-	-	-	-	-
	4	-	-	-	-	-	-	-
2/3 full Capacity	1	31.0	31.4	36.3	38.7	34.7	35.0	**207.2**
	2	28.4	30.9	36.3	41.1	34.4	40.3	**211.5**
	3	-	-	-	-	-	-	-
	4	-	-	-	-	-	-	-
Full Capacity	1	32.1	33.1	47.2	49.7	45.3	45.5	**253.0**
	2	35.9	34.9	53.0	53.5	55.4	48.0	**280.6**
	3	35.9	38.4	48.3	50.3	46.5	47.1	**266.5**
	4	33.1	34.3	50.0	49.8	46.8	48.4	**262.5**

Table 7.2 Live load case numbers, respective truck positions, and the associated weight of trucks used for live load testing

Live Load Case	Truck Position	Truck Weight Utilized (kN)				
		T1	T2	T3	T4	Total
1	P1	118	128.4	-	-	246.4
2	P2			-	-	
3	P3			-	-	
4	P1	179.1	185.5	-	-	364.6
5	P2			-	-	
6	P3			-	-	
7	P1	207.2	211.5	-	-	418.7
8	P2			-	-	
9	P3			-	-	
10	P4	266.5	280.6	-	-	547.1
11	P5	266.5	-	-	-	266.5
12	P6	266.5	280.6	253.0	262.5	1062.6
13	P2	266.5	280.6	-	-	547.1
14	P7	266.5	280.6	-	-	547.1
15	P8	266.5	280.6	253.0	262.5	1062.6
16-19	P9-P12	266.5	-			266.5
20	P13	266.5	-	253.0	262.5	782.0

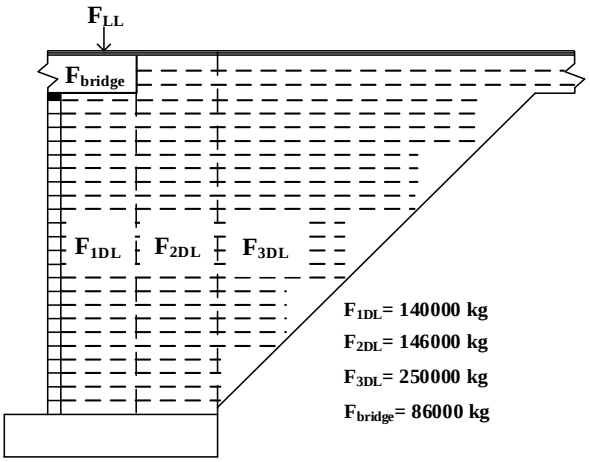

Figure 7.4 Abutment dead load by section and bridge dead load split equally over both of the abutments

7.2.1 Assessing the applied load on a per-abutment basis

As presented in the previous section, the trucks were positioned in a variety of different locations including entirely on the bridge, entirely on the abutments and moving from one abutment to the other one. In load test Case Nos. 1, 2, 3 4, 5, 6, 7, 8, 9 and 13, two trucks (one per lane) were utilized either on the east abutment, in the middle of the bridge or on the west abutment. In test No. 10, the two trucks were positioned with each one on either abutment (along the centerline), and in test No. 11 only one truck was left in the middle of the bridge on the centerline. Four trucks were utilized in load test Nos. 12 and 15. In test No. 12 the trucks were left on the abutments (two per each abutment, in each lane) while in test 15 the trucks were left on the bridge (two at the centerline of the bridge, back to back, in each lane). Two trucks (one per

lane) were positioned on the bridge in test No. 14 such that they were close to the west abutment and not in the middle of the bridge, yielding an asymmetrical load case (unlike many of the other load cases). In tests 16 through 19, one truck was moved from the west to the east abutment on the centerline. Finally, in Test No. 20, three trucks were left on the west abutment for a couple of days to investigate the response of the abutment and the foundation under a heavy load for a longer time.

Table 7.3 The ratio between the abutment live load and various components of the total dead load for the different load cases

Load Case	F_{LL} [1] (kg)	F_{LL}/F_{1DL} (%)	F_{LL}/F_{2DL} (%)	F_{LL}/F_{3DL} (%)	F_{LL}/F_{bridge} (%)	$F_{LL}/\Sigma F_{DL}$ [2] (%)
1	24640	17.6	16.88	9.86	28.65	4.0
2	12320	8.8	8.44	4.93	14.33	2.0
3	24640	17.6	16.88	9.86	28.65	4.0
4	34640	24.7	23.73	13.86	40.28	5.6
5	18230	13.0	12.49	7.29	21.20	2.9
6	34640	24.7	23.73	13.86	40.28	5.6
7	41870	29.9	28.68	16.75	48.69	6.7
8	20935	14.9	14.34	8.37	24.34	3.4
9	41870	29.9	28.68	16.75	48.69	6.7
10	26650	19.0	18.25	10.66	30.99	4.3
11	13325	9.5	9.13	5.33	15.49	2.1
12	51550	36.8	35.31	20.62	59.94	8.3
13	27325	19.5	18.72	10.93	31.77	4.4
14	27325	19.5	18.72	10.93	31.77	4.4
15	51550	36.8	35.31	20.62	59.94	8.3
16-19	26650	19.0	18.25	10.66	30.99	4.3
20	78200	55.9	53.56	31.28	90.93	12.6

Note 1: Live load force values presented here assume equal division of the total live load that was applied over both abutments. For asymmetric loading patterns (e.g., Figure 7.3g, LL Case 14), this assumed behavior is likely not realistic. Since the purpose of this table is only to show the "rough" load levels, only this type of simplistic load distribution approach was utilized here. This issue is discussed in more detail in the following section.

Note 2: $\Sigma F_{DL} = F_{1DL+} F_{2DL+} F_{3DL+} F_{bridge}$

Since the trucks were positioned at different locations on the bridge or abutment, it is reasonable to expect that the pattern of load application to each abutment will naturally be different for each load case. Unfortunately, simple mechanics-based approaches to determining the proportionate load distribution on a per-abutment basis and across the width of the bridge bearing seat may not work well for structures such as the GRS-IBS, which can exhibit complex soil-structure interaction behavior upon loading. For load cases where the trucks were left entirely on the abutment, the expected loading behavior is even more complicated, because the loads are applied as individual wheel loads to the reinforced abutment rather than as a more even uniform (hopefully) bridge bearing seat pressure.

For trucks parked entirely on the bridge in a symmetrical fashion, the calculation of the applied pressure per abutment is generally easier, with fewer and more reasonable assumptions being made during the calculation process. Table 7.4 presents the calculated pressure for the west abutment for those load cases in which the trucks were positioned on the bridge in a symmetrical manner (load cases No. 2, 5, 8, 11, 13 and 15). For these load cases, it is straightforward and reasonable to assume an equal distribution of the total live load over both of the abutments, i.e., a balanced load application between the east abutment and the west abutment. The next assumption that was made was that of complete bridge rigidity, which implies that the total applied truck loads will be distributed uniformly over both of the bridge bearing seats. From the array of sensors that was utilized at the project site, the validity of this assumption cannot be directly verified, as nearly all of the sensors were deployed along the structure's

centerline. As shown in Table 7.4, the applied bearing pressure directly beneath the bridge increases with increases in the truck loads, as expected. The maximum calculated applied pressure (48.4 kPa) belongs to Load Case No. 15 in which four heavy trucks were utilized.

A second approach to looking at applied pressure beneath the bridge bearing seat caused by the live load on the bridge is to examine the results from the total pressure cells d1 through d3. Unfortunately, the type of sensor that was used at these locations was shown to exhibit a variable pressure response over time (as shown in Chapter 9), and the measured results can consequently be considered fairly unreliable. Moreover, significant variability in measured pressures was observed between sensors d1 to d3, possibly due to redistribution of stress at deeper depths within the embankment. As sensor d1 is closest to the point of load application, its results can be considered to be the most representative of the applied stresses. Consequently, Table 7.4 presents the measured pressure values for sensor d1. The measured pressure by this cell prior to load testing was subtracted from the measured pressures during load testing to come up with the induced pressure by the live loads. It can be observed that the measured values are often quite a bit different than those calculated from the assumed uniform bearing pressure approach; this difference may be due to the aforementioned problems with this pressure cell, or due to problems with the uniform pressure assumption.

To explore the assumption of a uniform applied bearing pressure further, a simple Finite Element (FE) analysis was also conducted using ABAQUS 6.13 (2013) for comparison purposes. In this case, the bridge was modelled as a slab and the bridge

contact area with the abutments as a spring foundation. Since the level of strain in the bridge was expected to be low during the live load testing, elastic behavior was assumed for the concrete bridge. The modulus of elasticity and Poisson's ratio of the bridge concrete were assumed to be 20 E6 kPa and 0.22, respectively, and the stiffness of the spring foundation per unit area for dense granular material of the abutment beneath the bridge was considered to be 100,000 kN/m/m^2 (e.g., Bowles 1988). A sensitivity analysis was conducted to investigate the effect of spring stiffness on the induced pressure, by varying the stiffness values between 80,000 to 120,000 kN/m/m^2. Over this range of spring stiffnesses, it was observed that the induced pressure on the foundation does not significantly change. Figure 7.5 shows the finite element mesh that was utilized for the bridge in this analysis. In total, 36,275 10-node quadratic tetrahedron elements were utilized to mesh the bridge.

In order to verify the FE analysis results, a simulation using only a line load on the middle span of the bridge was performed. The results indicated that the deformations around the middle of the bridge span were essentially the same as elsewhere on the bridge, with the springs at the center of the bridge span deflecting the same amount as the springs on either side.

The corresponding applied pressures predicted by the FE analysis at the center of the bridge bearing seat are presented in Table 7.4. As shown, the agreement between the FE approach and the uniform pressure assumption values is stronger (RMSE=1.4) than the agreement between the cell d1 measured values and the uniform pressure assumption values (RMSE=4.0).

Table 7.4 The results from different approaches for estimating the applied pressure induced by a given live load event

Load case No.*	Uniform pressure (Approach 1)	Measured by cell d1 (Approach 2)	FE result (Approach 3)
2	11.2	7.4	12.9
5	16.6	10.8	16.8
8	19.0	17.9	19.3
11	14.9	20.4	13.8
13	24.9	22.2	22.5
15	48.4	51.4	46.9
RMSE	2 vs 1: 4.0	2 vs 3: 4.7	1 vs 3: 1.4

Note: Only the results from symmetric load cases are presented in this table.

As indicated by the variable results in Table 7.4, evaluation of the applied pressure to the abutment induced by the live load on the bridge is not a simple problem. As a result of this observation, for future studies it is recommended that additional load cells should be placed across the width of the bridge beam seat, to more accurately capture the actual pressures applied during live load testing. For this purpose, vibrating wire total pressure cells are recommended. Also, during this type of work, it is highly recommended that the exact position of the trucks on the bridge be recorded, to allow for more accurate follow-up calculations with FE analysis.

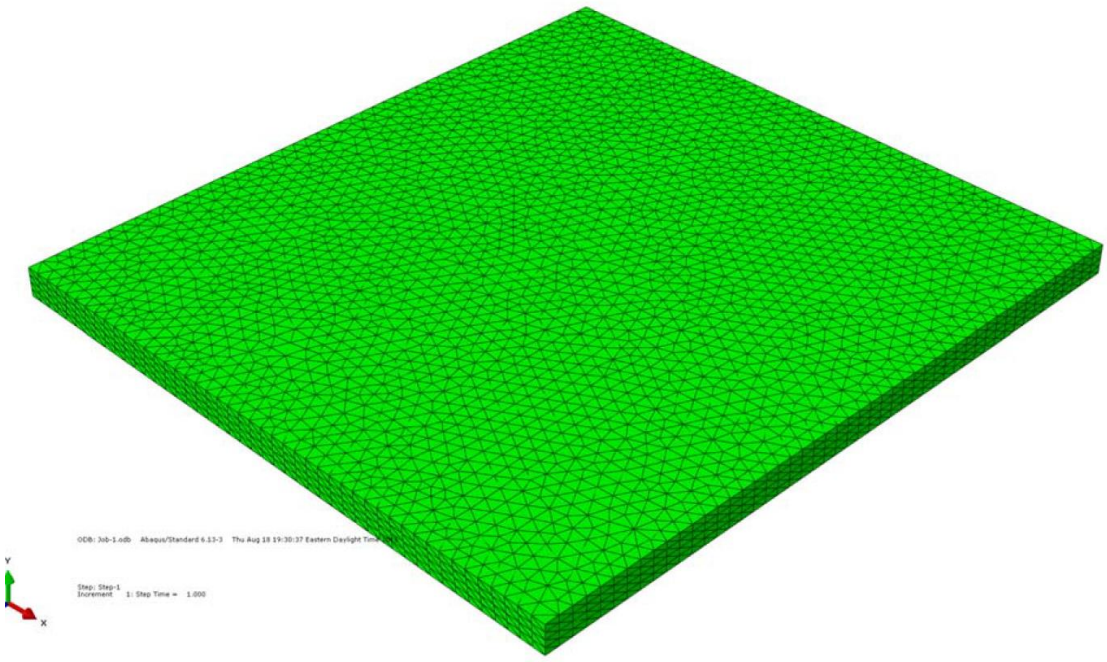

Figure 7.5 The utilized mesh for FE analysis

7.3 Test results

7.3.1 Strain in the abutments

The strain gauge locations for the east and west abutments are shown in Figure 3.28. The strain in the abutments was recorded during the live load test for both abutments. Since the data for the east abutment had to be collected manually, which was a time-consuming process, only data corresponding to load cases 4, 7, 10, 12 and 15 were measured for this abutment. The change in the west abutment strain during the load test is presented in Figures 7.6 and 7.7 for load cases 2, 5, 8, 11, 13 and 15, for the long and short strain gauges, respectively. In a similar fashion, the corresponding results

for the east abutment and load cases 4, 7, 10, 12 and 15 are presented in Figure 7.8 and 7.9, for the long and short strain gauges, respectively.

In general, it can be observed that the increase in the strain measured by both the long and short strain gauges was small even during the heaviest load cases. The results did not show any remarkable change in strain level for different loading conditions. Generally speaking, the maximum strain increase was less than 0.025 percent, as shown in Figures 7.6 through 7.9. As shown in these figures, the maximum strain measured by both the long and short gauges was not significantly different. However, the general shape of the strain distribution measured by the long and short gauges was different. With respect to the shape of the strain distribution, the strain can be observed to generally decrease away from the facing wall, which is rational behavior since areas closer to the facing wall are more affected by the live load applied to the bridge. Since the measured induced strains are very low, no definitive comparison between the reliability of the short and long strain gauges can be made for the live load testing that was performed.

Generally, these results showed that even under fairly significant load, the changes in strain in the reinforcement were not significant. Given that this reinforcement can support significant additional changes in strain before failure, this indicates that this embankment should perform quite well in the future with respect to live load events on that bridge, and the fashion that the associated strains are carried in the reinforcement.

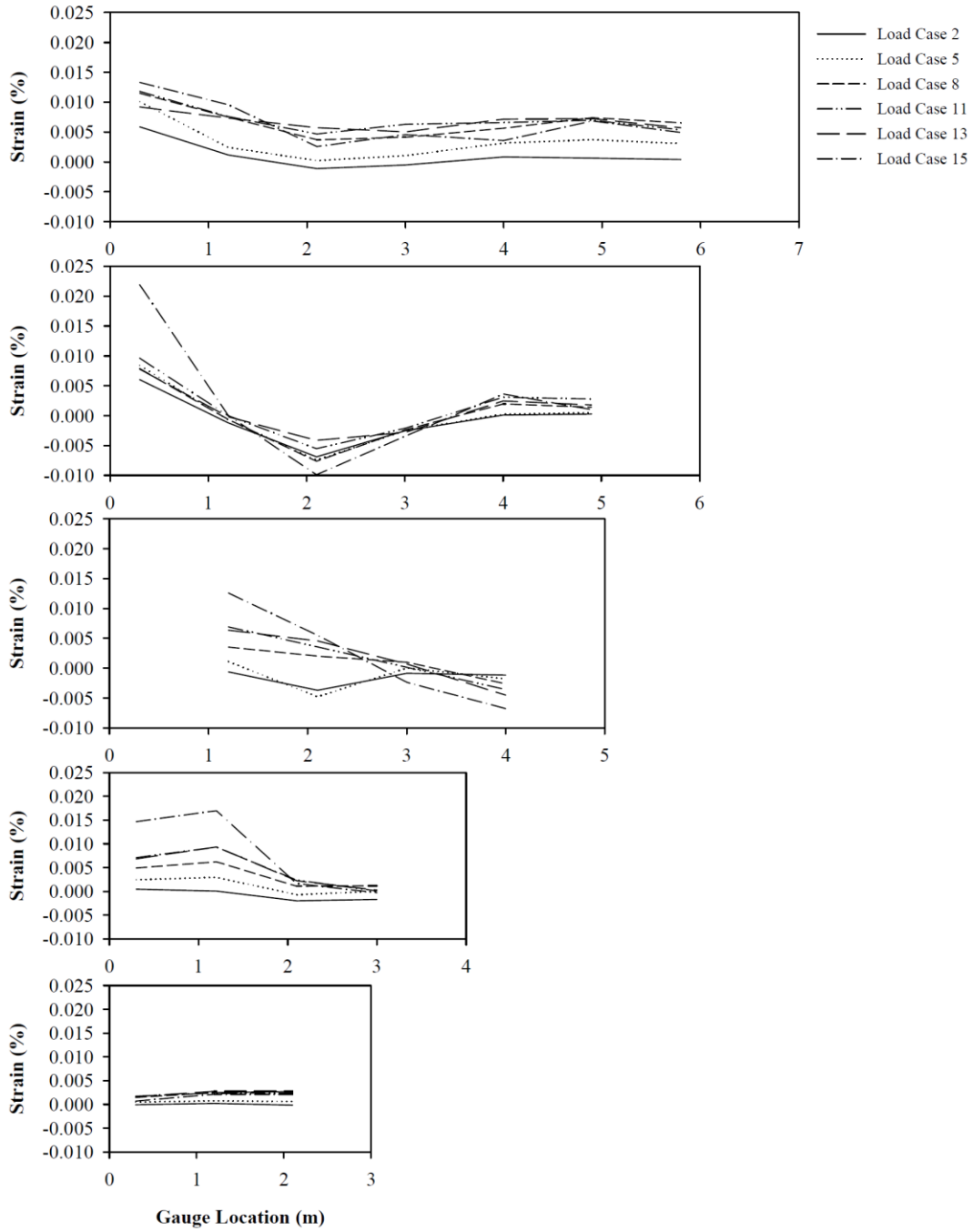

Figure 7.6 Increase in strain due to truck live load for Test Nos. 2, 5, 8, 11, 13 and 15, for different elevations in the west abutment (measured by long strain gauges)

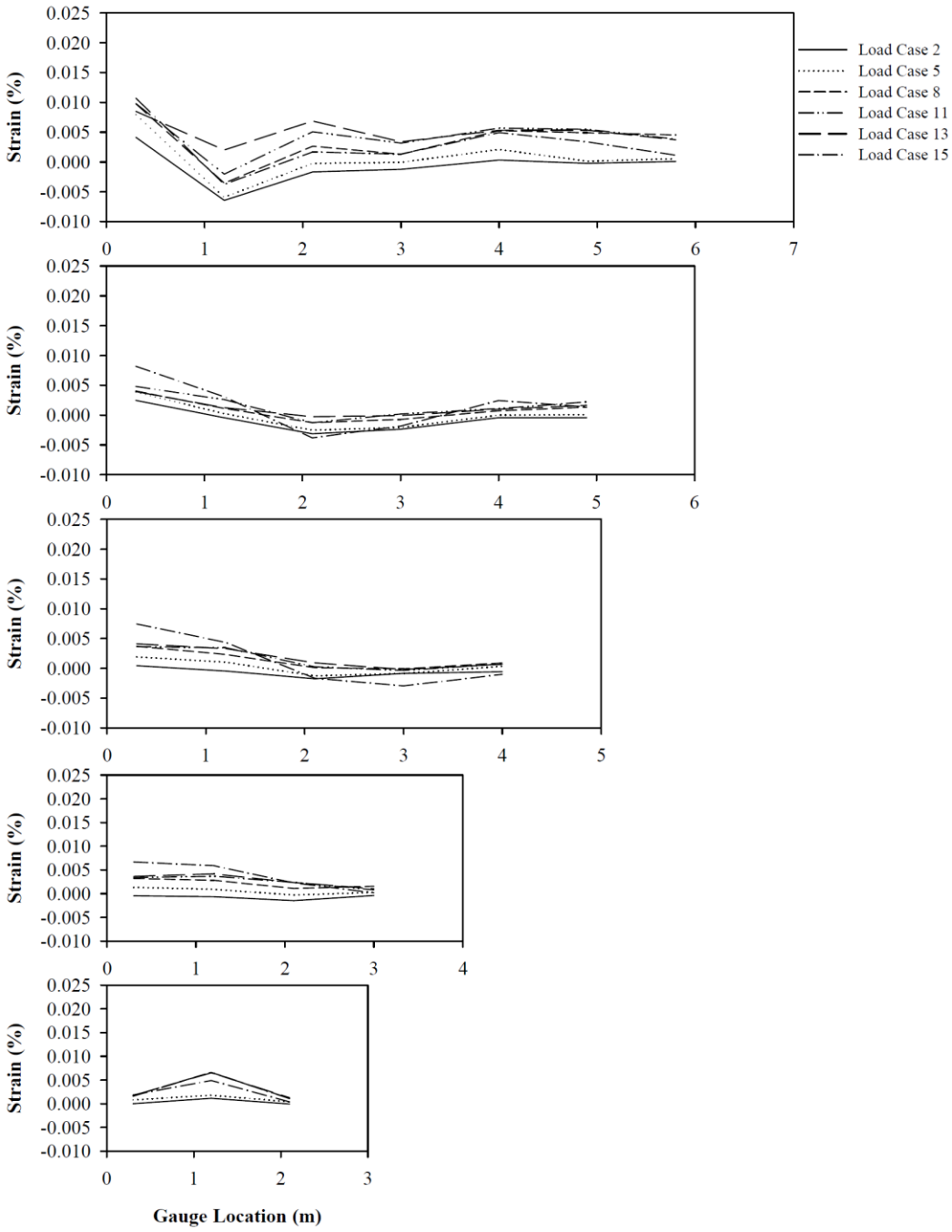

Figure 7.7 Increase in strain due to truck live load for Test Nos. 2, 5, 8, 11, 13 and 15, for different elevations in the west abutment (measured by short strain gauges)

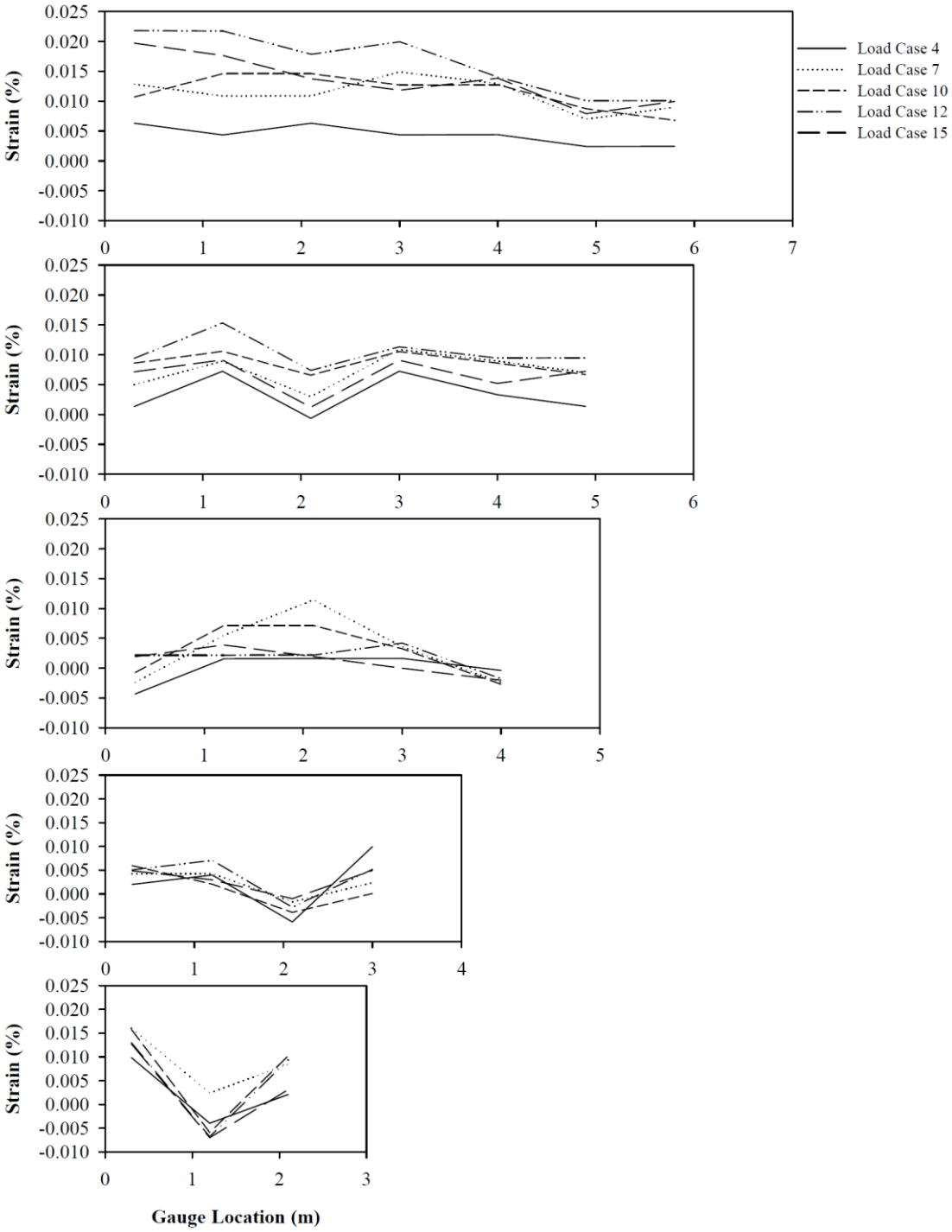

Figure 7.8 Increase in strain due to truck live load for Test Nos. 4, 7, 10, 12, and 15, for different elevations in the east abutment (measured by long strain gauges)

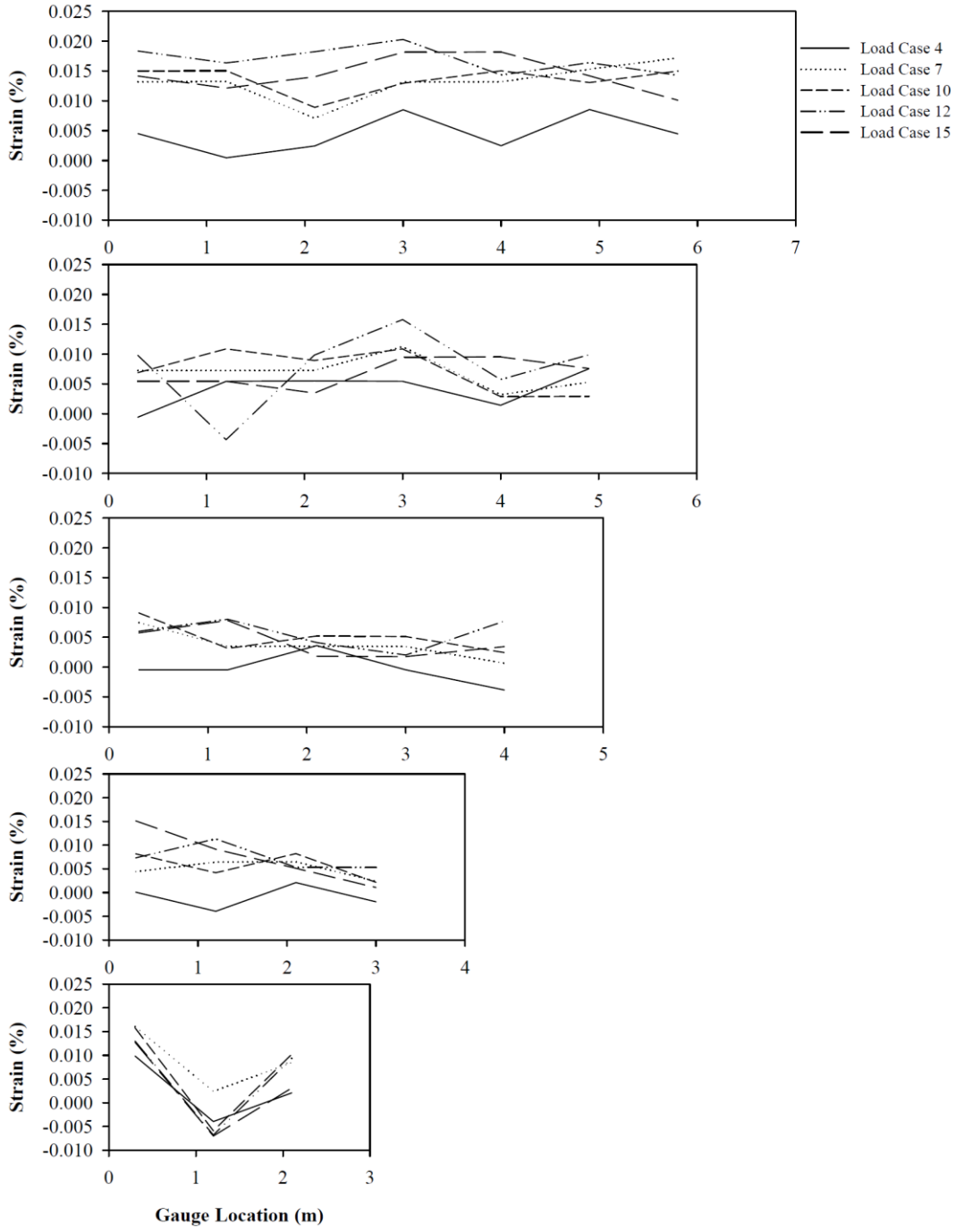

Figure 7.9 Increase in strain due to truck live load for Test Nos. 4, 7, 10, 12, and 15, for different elevations in the east abutment (measured by short strain gauges)

7.3.1.1 The relationship between the applied pressure to the west abutment and the induced strain

Figures 7.10 and 7.11 illustrate the relationship between the calculated applied pressure by the live load (Table 7.4) and the induced strain measured by the long and short gauges, respectively. Figures 7.12 and 7.13 present the corresponding results for measured applied pressure by the live load (Table 7.4). The results are presented only for the first sensor of each layer (A1 to E1, except C1 which was not working) which are the closer ones to the facing wall and are more affected by the live load. The results showed that the correlation between the measured strain and the measured applied pressure is stronger than the correlation between the measured strain and the calculated applied pressure. However, as the measured strain is very low and may not be very reliable, these correlation results should be interpreted with that fact in mind. The weakest and strongest correlations were observed in the case of the A and D layers, respectively. The correlations between the measured strain and the applied pressures determined using finite element analysis were very similar to the correlations between the measured strain and the calculated applied pressure; consequently, the correlation results for this data set are not presented here.

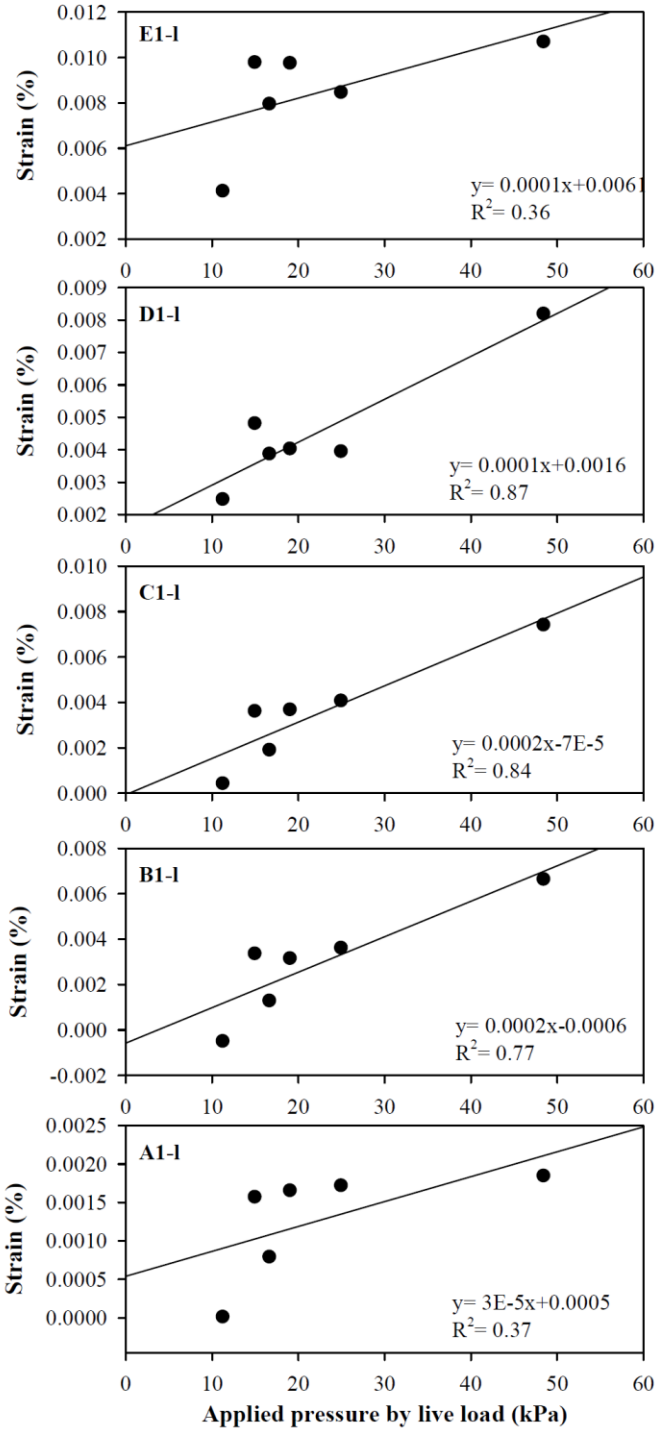

Figure 7.10 Relationship between the measured induced strain and calculated applied pressure (measured by the long strain gauges)

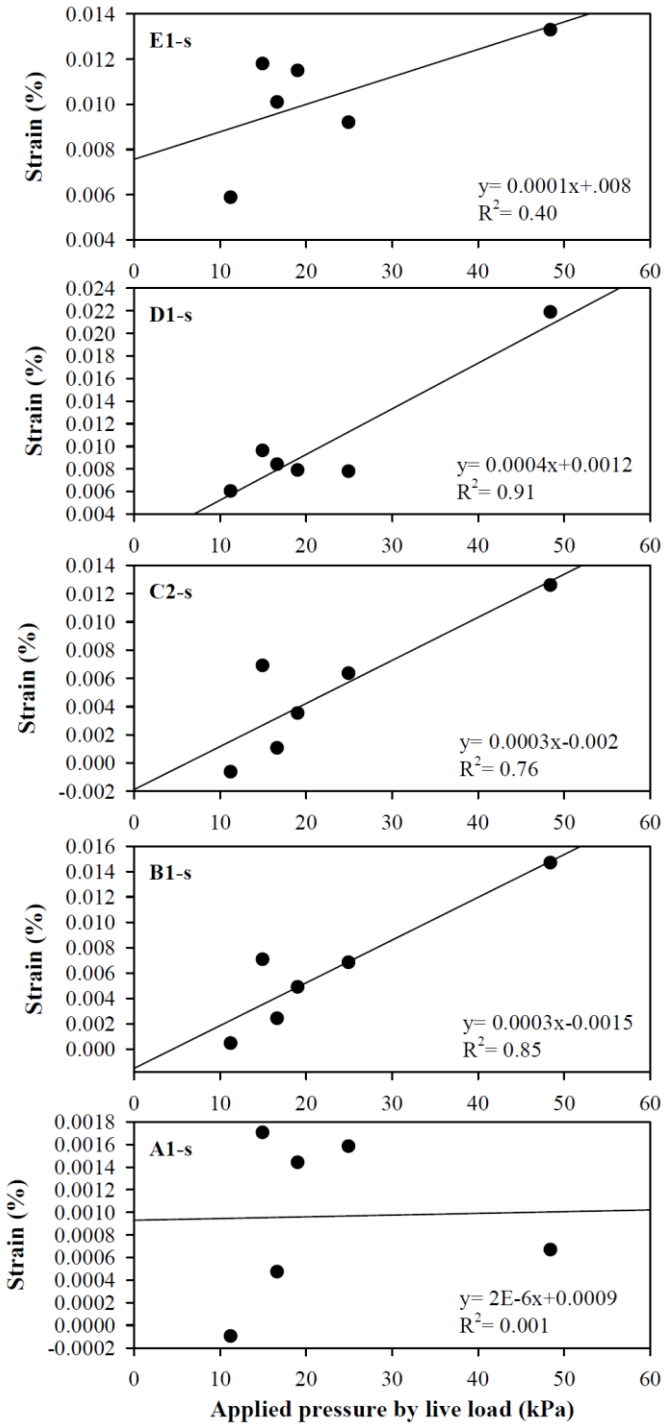

Figure 7.11 Relationship between the measured induced strain and calculated applied pressure (measured by the short strain gauges)

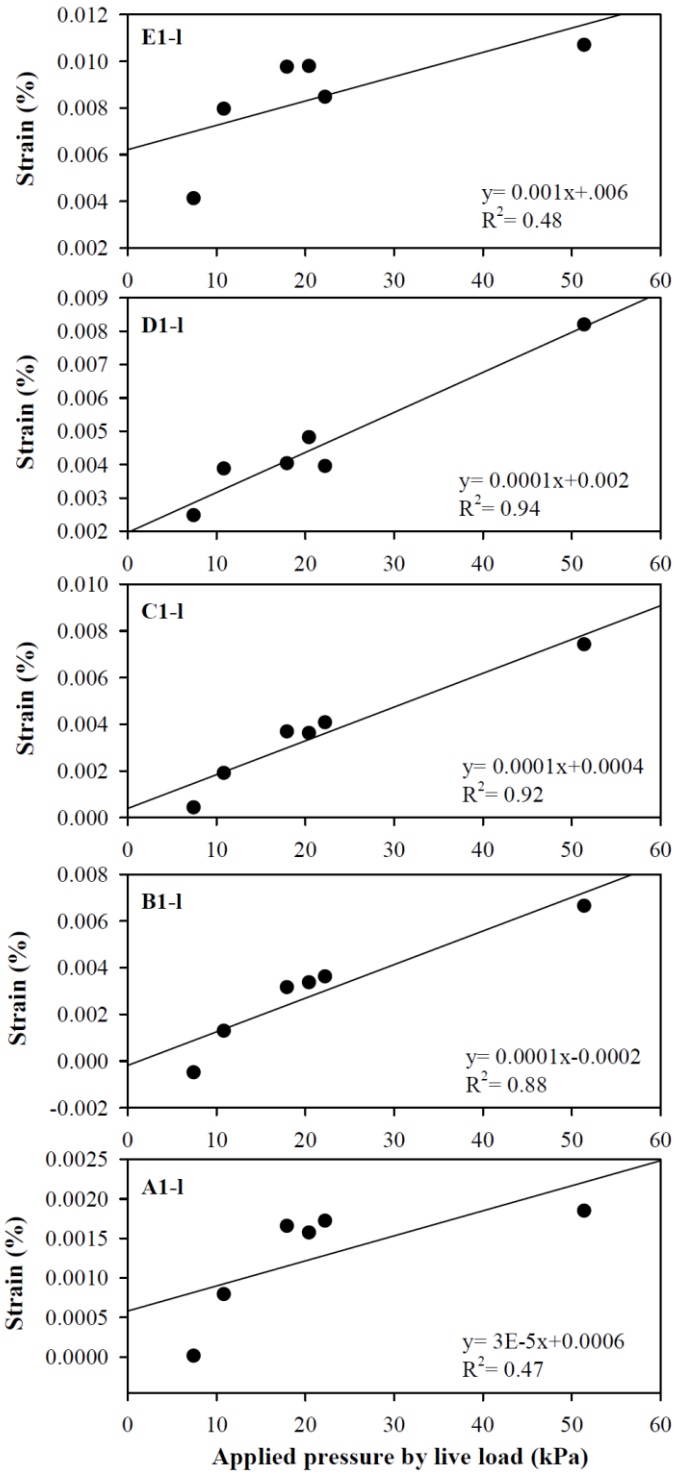

Figure 7.12 Relationship between the measured induced strain and measured applied pressure (measured by the long strain gauges)

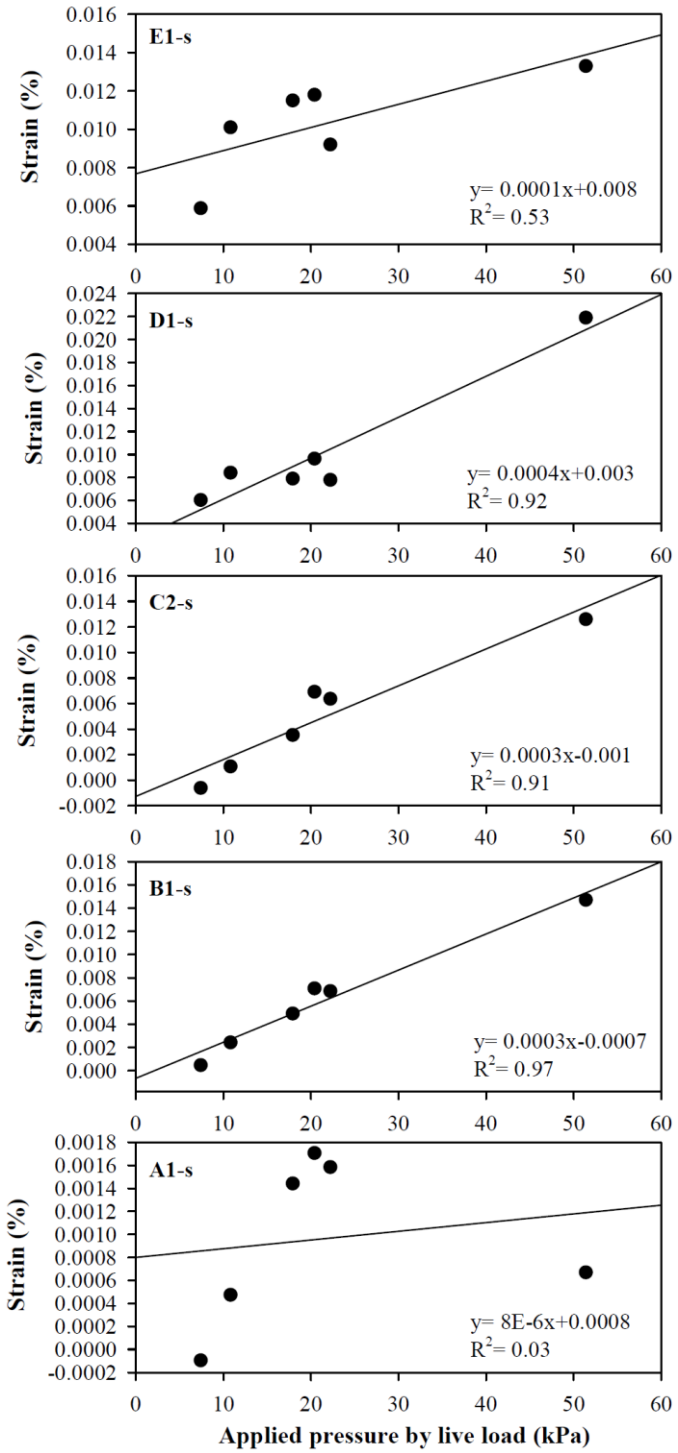

Figure 7.13 Relationship between the measured induced strain and measured applied pressure (measured by the short strain gauges)

7.3.2 Displacement of facing walls

The lateral deflection and settlement of the facing walls were measured during the live load test. As presented in Chapter 3, the targets are installed on both abutments at three elevations (16.45 m, 15.24 m and 14.02 m). There are five targets at each elevation across the facing walls.

As discussed in Chapter 4, the measured deformation during live load testing was very low and was not different across the facing walls. Figure 7.14 shows the changes in lateral deflection in the centerline of the west and east facing walls during truck load testing. According to the results, the maximum recorded value is about 10 mm. As noted in Chapter 4, the maximum precision of the surveying process was 6 mm, which is enough noise to induce remarkable error in the readings. Consequently, a series of measurement error bands were added to the surveying graphs to show how the reading could vary.

The same process was repeated to evaluate the settlement of the west and east facing walls during the live load test. Figure 7.15 illustrates the changes in settlement in the centerline of the west and east facing walls during the live load testing. The maximum measured settlement during load testing was less than 5 mm.

In order to evaluate the lateral deflection and settlement across the east and west facing walls during live load testing, the corresponding graphs were prepared as shown in Figures 7.16 through 7.19 for load case Nos. 2, 5, 8, 11, 13 and 15 for different elevations. As shown, there is not any significant trend in change in the settlement with the increase in the load level. This can be attributed to the precision of the surveying

operation which had some errors in the measured values. Additionally, the deformation distribution across the facing walls does not follow any specific trend. However, the maximum measured deflection and settlement on both facing walls did not exceed 12 mm and 10 mm, respectively during the load test.

These observations indicate that the abutments performed well under heavy live loads with very negligible settlement and lateral deformation. Even with consideration of probable error induced by the surveying operation, the maximum lateral deflection does not exceed 14 mm and the maximum settlement does not reach 8 mm. Therefore, it can be concluded that the heavy live trucks load did not induce any significant displacement to the abutments.

7.3.2.1 The relationship between the applied pressure and facing walls deformation

In section 7.3.1.1, the correlation between the applied pressure and the abutments strain was investigated. The relationship between the applied pressure by the live load and the facing walls deformation was investigated as well. Unfortunately, no specific trend could be captured since the surveying operation was not sufficiently precise. In fact, it could also be noted from Figures 7.16 through 7.19 that there is no strong correlation between these two parameters. For future studies, it is recommended that for this type of strong structure with very low deformation, a high-precision surveying operation should be utilized.

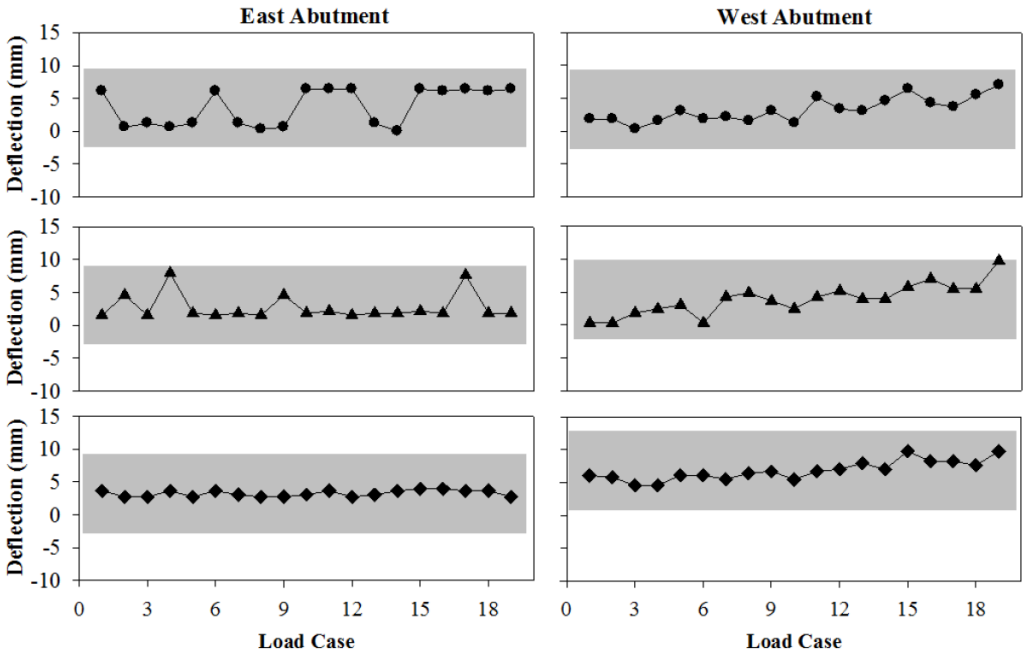

Figure 7.14 Lateral deflection of the centerline of the facing walls during the load test

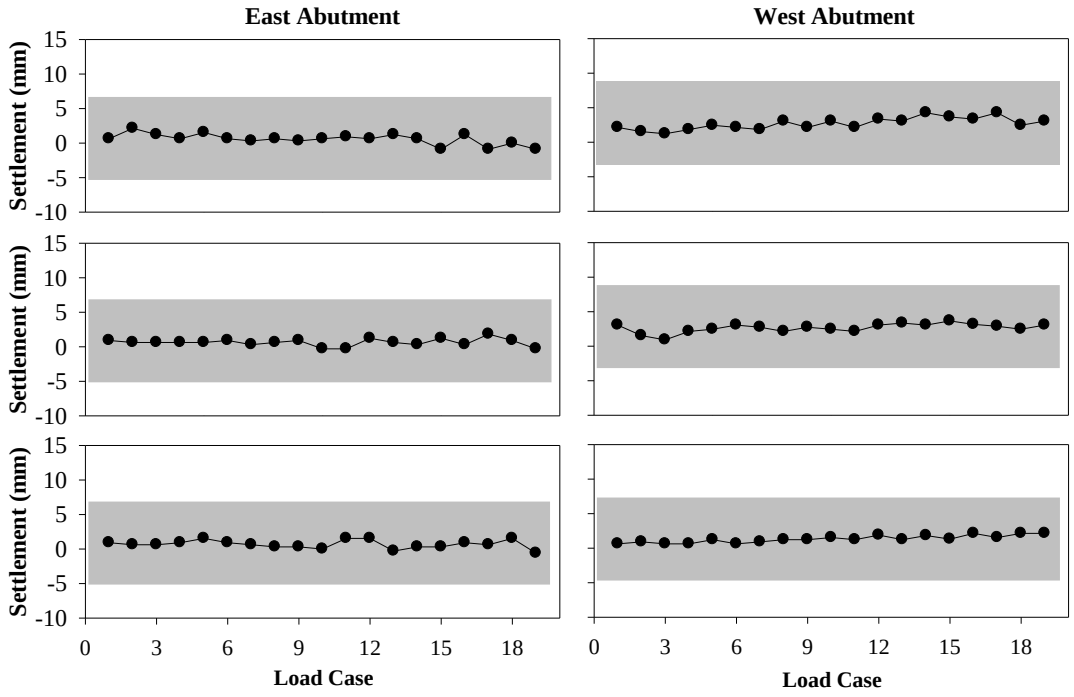

Figure 7.15 Settlement of the centerline of the facing walls during the load test

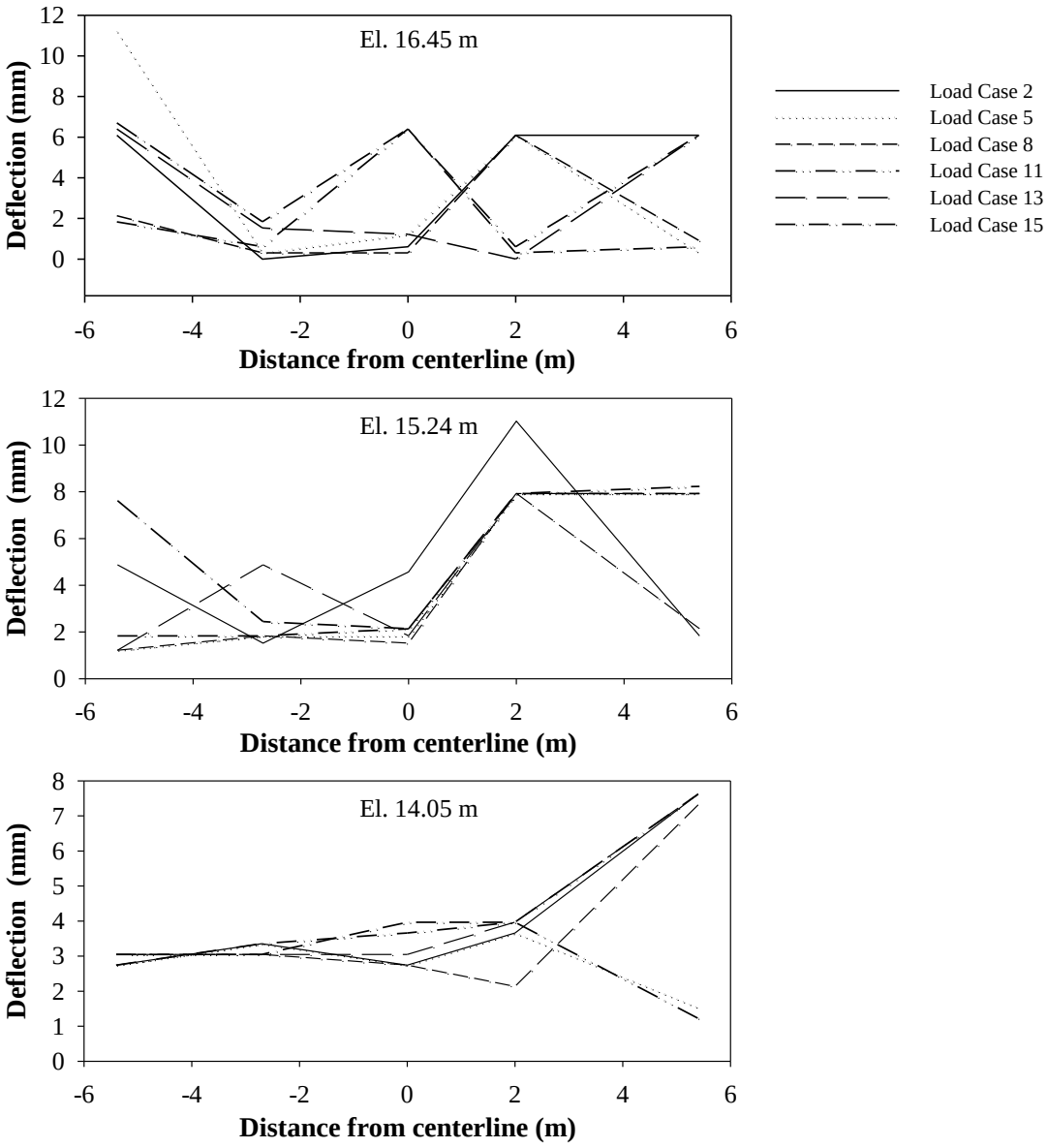

Figure 7.16 Lateral deflection across the east facing wall for different elevations

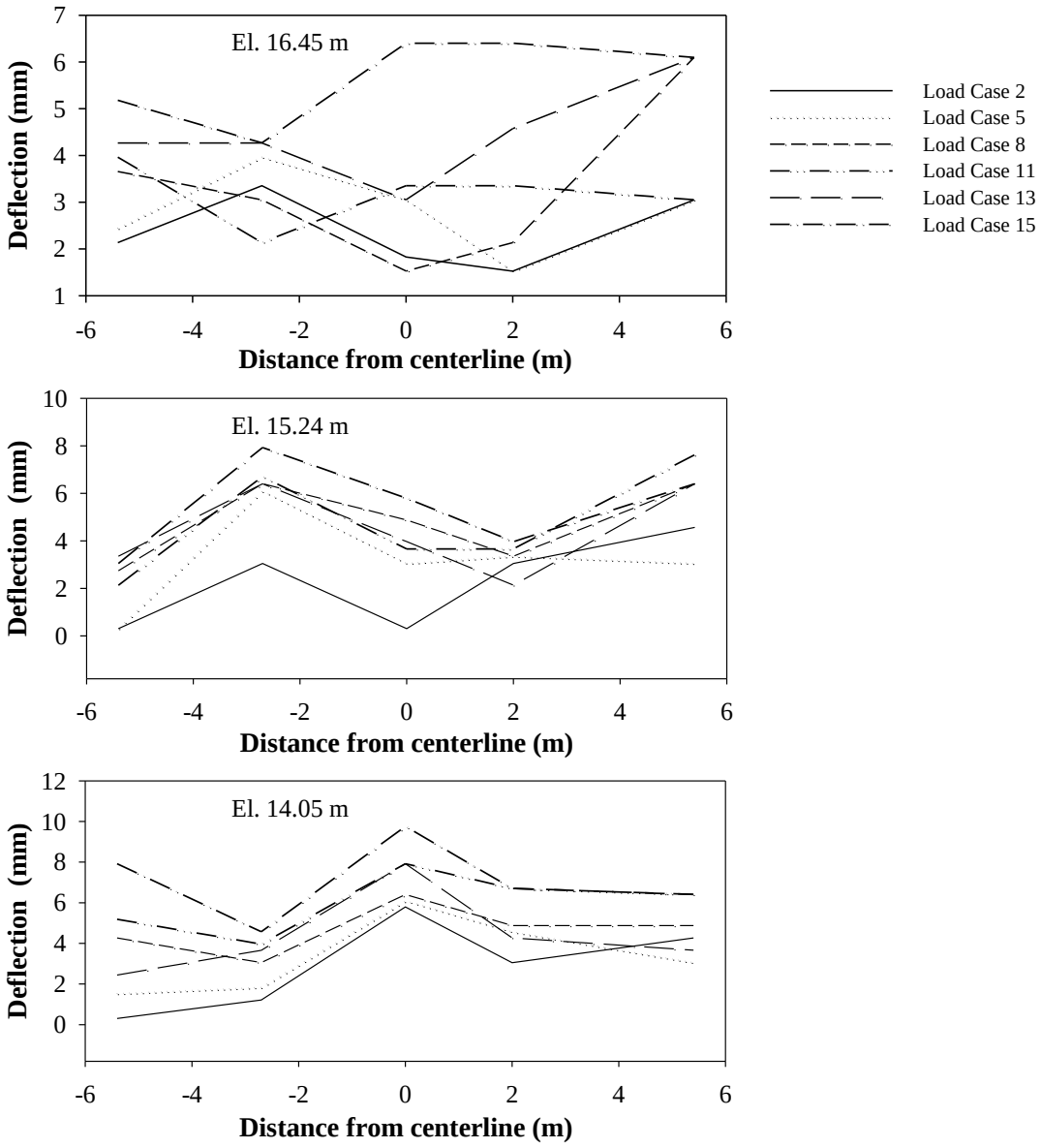

Figure 7.17 Lateral deflection across the west facing wall for different elevations

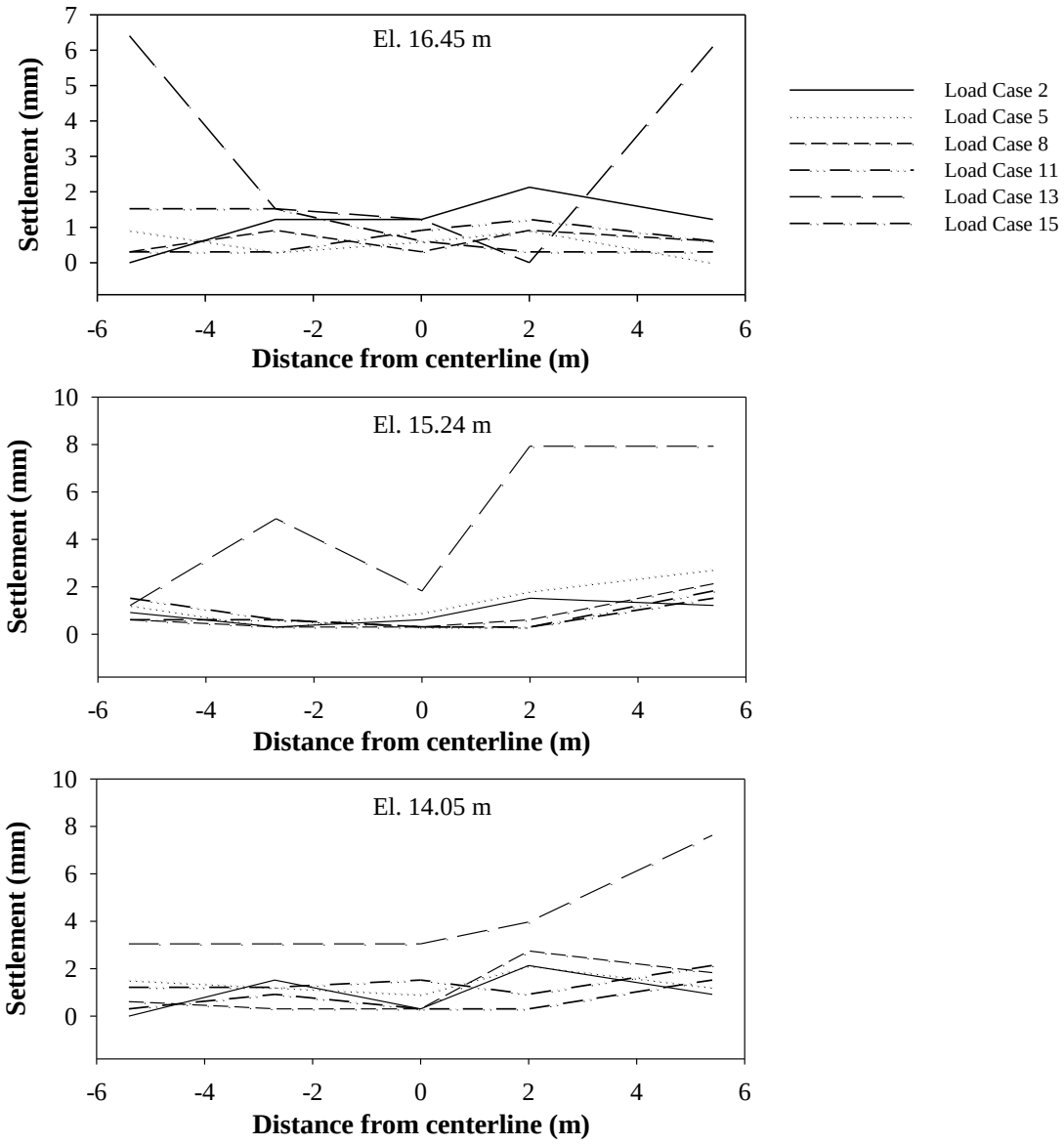

Figure 7.18 Settlement across the east facing wall for different elevations

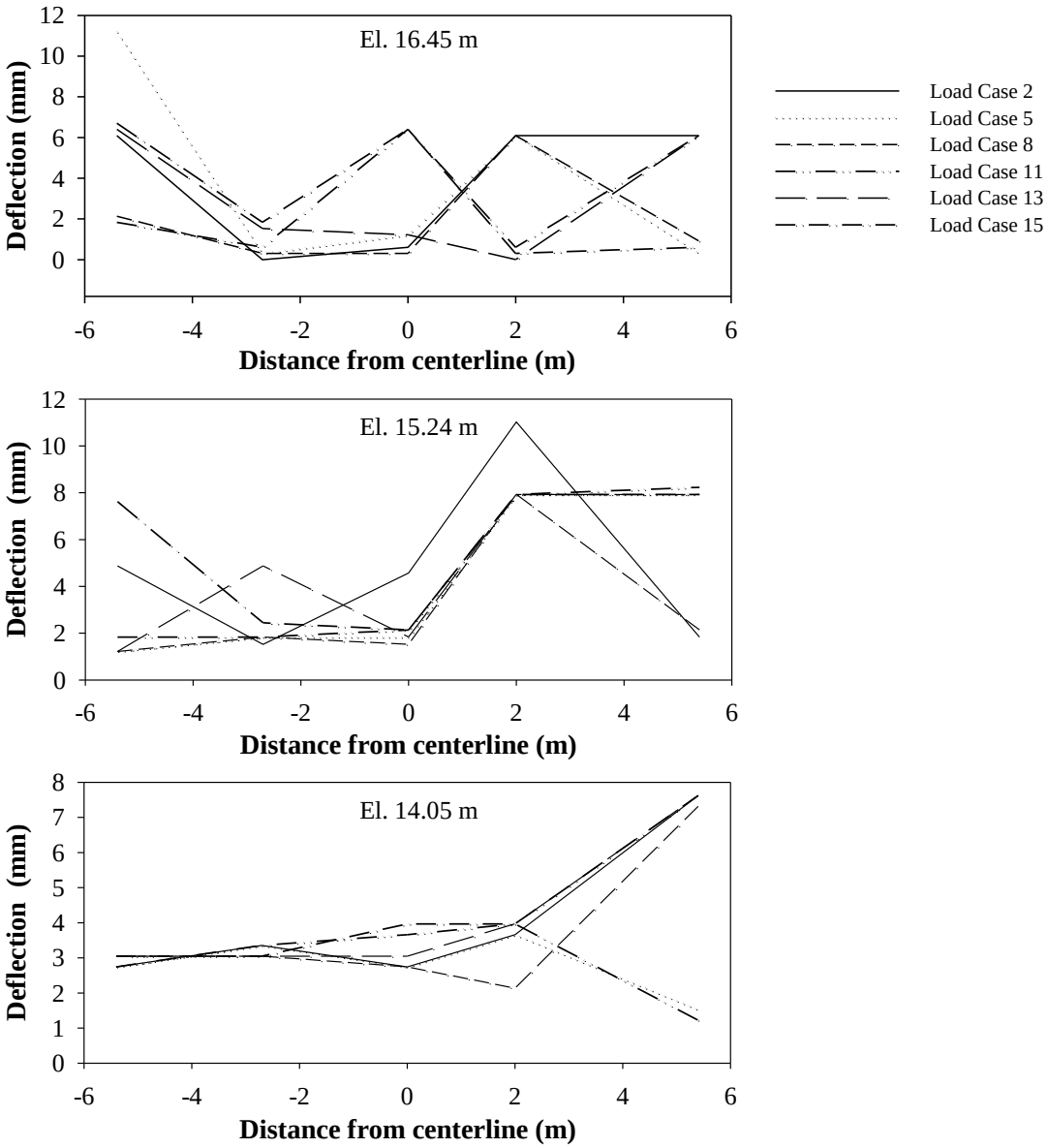

Figure 7.19 Settlement across the west facing wall for different elevations

7.3.3 Inclinometer sensors

Figures 7.20 and 7.21 present the increase in lateral deflection during load testing for load case Nos. 2, 5, 8, 11, 13 and 15 in the E-W and N-S directions. As shown, the maximum increase in measured deflection in the E-W and N-S directions is less than 0.1 mm. The maximum increase is not associated with the heaviest load case. Since the measured values are very low perhaps the precision of the sensors was not enough to capture this small change of deflection. The results showed that the induced deformation in the foundation by the live load is negligible even for the heaviest load case.

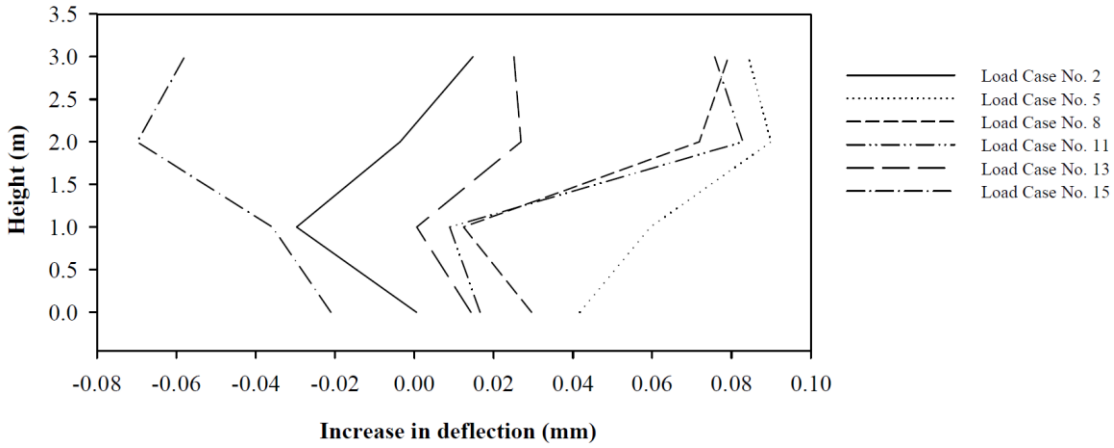

Figure 7.20 Increase in lateral deflection in the E-W direction during the load test

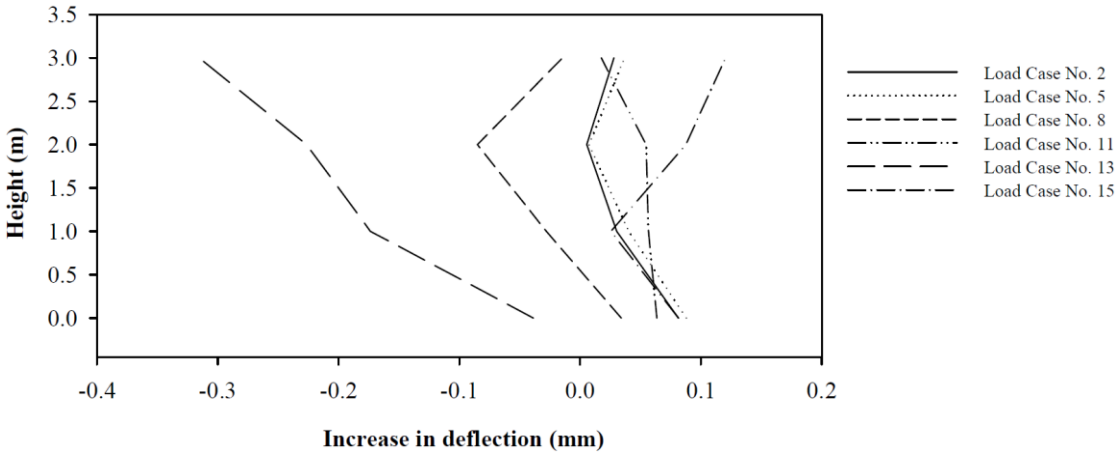

Figure 7.21 Increase in lateral deflection in the N-S direction during the load test

7.3.4 Pressures in the foundation

As described in Chapter 3, four pressure transducers were installed beneath the foundation of the GRS-IBS structure to record the applied pressure distribution in this area. The corresponding results for the time of construction and three years of operation are presented in Chapters 4, 8 and 9. The applied pressure distribution beneath the RSF foundation is also examined in more detail in Chapter 8. It will be shown in Chapter 8 that the pressure is not uniform beneath the RSF.

Figure 7.22 shows the resulting pressure distributions beneath the foundation for various live load events. As expected, the applied bearing pressure beneath the RSF increases as the truck loads increase. The pressure distribution after the bridge placement and before the live load test is also presented in this figure, for comparison purposes. In order to compare the pressure values before and after the live load test, Figure 7.23 shows the maximum pressure distribution induced by the live load and the pressure distribution before the live load test. The maximum increase in pressure

shown in this figure corresponds to load case 14, in which two full capacity trucks were placed on the bridge close to the west abutment with the rear axles on the abutment, as shown in Figure 7.3g. Given the heavy weight of loading and relative truck positions, it is logical that this load case corresponded to the maximum applied pressure measurements.

Load Case 15 induced the second highest pressure in the foundation. For this load case, four full capacity trucks were placed on the bridge, with two of them close to the west abutment and other two close to the east abutment, as shown in Figure 7.3h. Based on what is shown in Figure 7.22, these two load cases (14 and 15) have induced the maximum pressure in the foundation and their corresponding pressure distribution lines are separated from the other load cases. The induced pressure by the trucks to the foundation pressure cells for case 12 which includes two heavy trucks positioned entirely on the west abutment was lower than load cases 14 and 15. It can be inferred that in order to induce the maximum pressure to the foundation, the heavy trucks should be positioned entirely on the bridge and close to the abutment. Another finding in Figures 7.22 and 7.23 is that the induced pressure to the first load cell (S1), which is located in front of facing wall beneath the RSF, does not significantly change with changes in the live load.

As shown in Figure 7.23, the maximum increase in pressure (14%) occurs in cell no. 2, which is located beneath the facing wall and always exhibits the largest of the recorded pressure values. The increase in pressure in cells No. 3 and 4 are about 12.6 and 11.0 percent, respectively, with cell No. 1 (which is located at the very front

of the footing) only increasing 5.3%. It should be noted that the pressure distribution beneath the footing is not uniform or trapezoidal, as is commonly assumed for design purposes – this will be discussed in more detail in the next chapter.

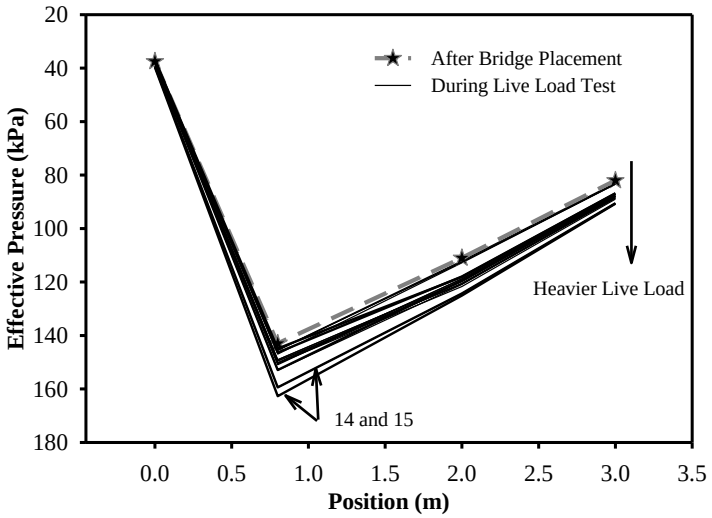

Figure 7.22 Pressure distributions beneath the foundation for various live load events

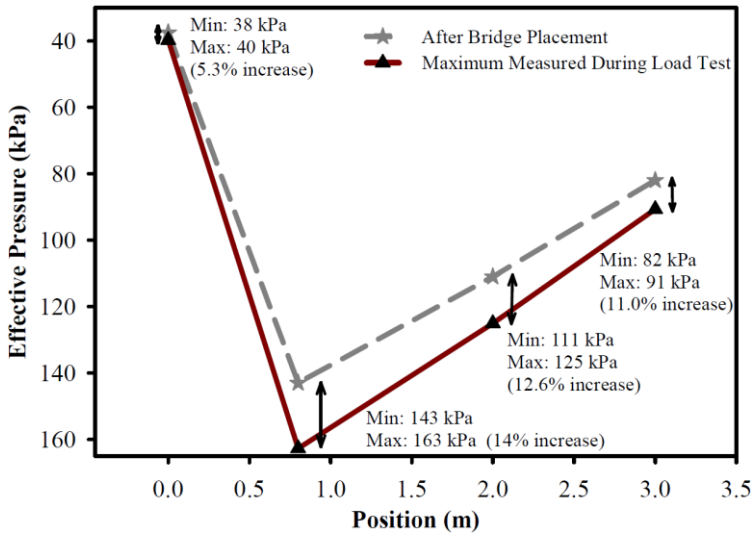

Figure 7.23 The maximum increase in measured pressure during the live load test (DL+LL), relative to the applied pressure immediately after bridge superstructure placement (DL only)

7.3.4.1 Factor of safety against bearing capacity failure

Based on the clay foundation strength parameters discussed in Chapter 3, the calculated ultimate bearing capacity of the foundation (q_u) was approximately 500 kPa. If the maximum induced pressure by the trucks in the foundation is considered as the applied pressure (q_{app}) the factor of safety against bearing capacity failure ($F.S_{bearing}$) can be calculated as follows:

$$F.S_{bearing} = \frac{q_u}{q_{app}} = \frac{500}{162} = 3.09 \quad (7.1)$$

This calculated factor of safety meets the required design criteria. Moreover, note that this is a very conservative approach to determining the bearing

capacity, as the worst case pressure is not uniformly applied beneath the RSF, but rather only at one location. Consequently, the assumptions about bearing capacity made during the design stage can be validated from the live load testing that was performed. Additional information about the actual applied bearing pressures beneath the RSF at various levels of loading (including with live load test loads) is provided and discussed in significant detail in Chapter 8.

7.3.5 Stresses in the abutments

As discussed in Chapter 3, in order to evaluate the stresses in the abutments induced by the live loads, three pressure transducers (d1, d2 and d3) were installed in upper elevations of the west abutment (at elevations of 16.7 m, 15.7 m and 14.9 m above sea level). These transducers were utilized to measure the induced pressures during the truck live load test and the measured pressure values are shown in Figure 7.24. As shown in this figure, for many of the lighter load cases, the maximum pressure was recorded by the middle transducer (d2). However, for the four heaviest load cases (14, 15, 17 and 18), the maximum recorded pressure was recorded at the location of the uppermost transducer (d1). The trucks were closer to the west abutment than the center of the bridge in these load cases as well. In general, it can be clearly observed that the maximum induced pressures corresponded to load cases 14, 15, 17, and 18, which are clearly separated from the lighter load applied pressure behaviors; this separation is more pronounced for the upper pressure cells (d1 and d2). One interesting observation is that load case 12 in which two heavy trucks were entirely positioned on the west

abutment did not induce the maximum pressure to the cells. This indicates that in order to apply the maximum pressure to the bridge abutment, the trucks should be entirely positioned on the bridge and close to the abutment.

Figure 7.25 illustrates the difference between the minimum and maximum pressures recorded by the transducers prior to and during the truck live load testing. As seen, the maximum difference occurs in the sensor at the highest elevation, which is about 56 kPa (a 79% increase) followed by the middle and lowest pressure transducers with pressure differences of 23 kPa (a 25% increase) and 13 kPa (a 15% increase), respectively.

It is shown in Chapter 9 that the air temperature affects the pressure cell readings. The corresponding details are discussed in that chapter. Therefore, part of the increase in measured induced pressure by cell d1 may have not occurred only due to the increase in the load but also by the increase in the air temperature.

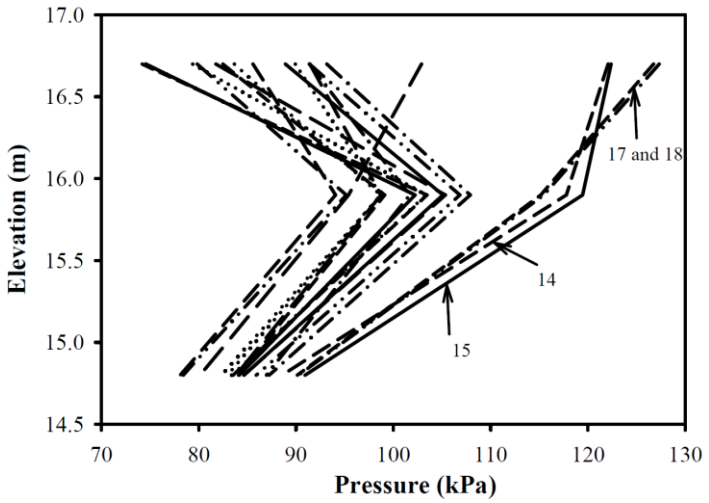

Figure 7.24 Pressure distribution in the abutment behind the facing wall during the live load test

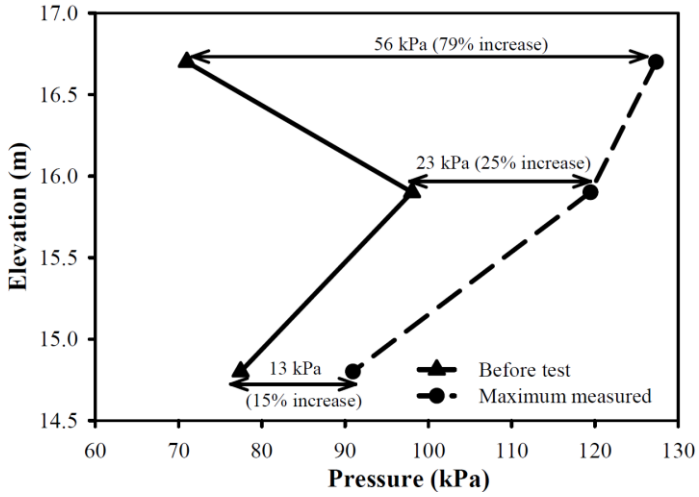

Figure 7.25 Difference between the minimum and maximum pressure behind the facing wall

7.3.5.1 Factor of safety against abutment bearing capacity failure

As shown in Figures 7.24 and 7.25, the maximum applied load per abutment including both bridge dead and live loads is about 127 kPa. The ultimate applied pressure per abutment is about 600 kPa based on the design criteria explained in Chapter 3. Therefore the factor of safety of internal stability against ultimate capacity during LL testing is about 4.7.

$$F.S_{abutment} = \frac{q_u}{q_{app}} = \frac{600}{127} = 4.7 \quad (7.2)$$

7.3.6. Piezometers and water content sensors

There was no significant changes in the abutment water content and foundation pore pressure during load testing.

Since the load testing was conducted in only one day and there was no rain on that day, no change in abutment water content was expected. The foundation pore pressure did not change during live load testing for two reasons. First, there was no precipitation on the test day to increase the water level in the river. Second, it was a bridge replacement project where the new structure had approximately the same weight as the structure that it was replacing; consequently, no significant excess pore pressure was produced.

7.4 Conclusion

This chapter describes the approach that was utilized to capture the response of the GRS-IBS structure using a live load test. Trucks were utilized to conduct the test and different vehicle arrangements and loads were implemented. The findings of the test are as follows:

1- The increase in the lateral strain was not significant during the load test even for the fullest trucks load case. According to the results, the maximum increase in the abutment strain was less than 0.03 percent measured with both long and short gauges. The maximum increase generally occurred at measurement points closer

to the facing wall and at a higher elevation, which was rational since these areas were more influenced by the applied live loads.

2- Since the level of change in strain induced by the live load was very low, the correlation between the applied pressure by the live load and induced strain was not very strong, even for the first strain gauges of each layer which are more affected by the live load.

3- No significant increase in the facing wall deformations was observed during the live load test. The maximum lateral deflection and settlement across the facing walls measured by the surveying targets was less than 12 mm.

4- There was not a strong correlation between the applied pressure to the abutment and the measured facing wall deformation by the surveying operation. This lack of agreement was attributed to the precision of the surveying operation. Since the level of deformation in GRS-IBS structures was generally quite low, it was suggested to utilize a more precise surveying system in the future.

5- The induced pressure by the live load to the abutments was evaluated for the different load cases with the trucks on the bridge. Three different methods; manual calculation using static equilibrium force, measured data by the uppermost abutment pressure cell, and finite element (FE) analyses were utilized to evaluate the induced pressure. Measured pressures differed significantly from those calculated assuming a uniform applied pressure distribution, which in turn were in good agreement with the pressures predicted by the FE analyses. The discrepancy in these results could be partially due to errors with the pressure

cells, which did not all show good agreement with each other in terms of measured behavior. From the recorded data, it is not clear if the applied bearing pressures were uniformly distributed across the bridge bearing seat; for future studies, the use of additional pressure cells across the width of the beam seat is suggested for developing a more complete understanding of the applied pressure behavior in this area.

6- Increasing the live load increased the pressure in the foundation beneath the RSF based on the measured values by the foundation pressure cells. According to the results, the maximum increase occurred at the location of the cell beneath the facing wall (S2) and the minimum at the location of the cell in front of RSF (S1). The maximum increase in measured pressure was more that 14 percent during the load test. However, the factor of safety against foundation bearing capacity failure was still greater than 3.0. Heavy trucks entirely positioned on the bridge close to the abutment induced the maximum increase in the foundation pressure.

7- Increasing the live load increased the pressure in the abutments. For most of the cases, the maximum pressure was measured with the second cell (d2) while for the heaviest truck load cases, the upper cell (d1) indicated the largest recorded pressure values. The reason for this discrepancy may have been the effect of the air temperature on the recorded total pressure values, which will be discussed in more detail in Chapter 9. There was an obvious change in the abutment pressure with a change in the truck weights. In a similar fashion as to the foundation

pressure, heavy trucks entirely positioned on the bridge close to the abutment induced the maximum increase in the abutment pressure.

8- The maximum increase in the abutment pressure was measured by cell d1, which recorded a 79 percent increase in pressure during the load test. The increase in pressure measured by the second cell (d2) and the third cell (d3) during the load test were 25 and 15 percent, respectively. The factor of safety against the abutment bearing capacity failure was still quite high even during the largest load test events, with a value of 4.7 under the largest applied live loads.

9- According to the current GRS-IBS interim implementation guide (Adams et al. 2011), the maximum applied surcharge to the GRS abutment is not recommended to exceed 4000 psf, which is about 191 kPa. The maximum applied live load per abutment in this project was about 50 kPa, as shown in Table 7.4. The bridge applied dead load per abutment was about 80 kPa, which consequently means that the total applied surcharge was about 130 kPa. The performance of the bridge under this amount of surcharge was quite satisfactory and the live load testing results showed that the GRS-IBS structure is very stable against heavy surcharges applied by the bridge dead and live loads. All induced deformations were quite low and all induced pressures were far less than the allowable pressures. Based on the structure's performance under 130 kPa applied surcharge to its abutments, it can be predicted that the abutments of this structure can also handle a 191 kPa surcharge as well, without catastrophic ultimate limit state failure. As a result, it can be hypothesized that limiting the surcharge to 191 kPa may be an overly conservative

recommendation for GRS-IBS structures, particularly if a similar structure would have been constructed on a stronger foundation. (For the current structure, global stability mechanisms of failure through the foundation controlled the design, rather than internal mechanisms of failure).

REFERENCES

AASHTO (American Association of State Highway and Transportation Officials) (2013). "LRFD Bridge Design Specifications, Customary U.S. Units" Sixth Edition with 2013 Interim, AASHTO, Washington, D.C.

Adams, M., Lillis, C., Wu, J. and Ketchart, K. (2002). "Vegas mini pier experiment and postulate of zero volume change." In Proceedings, Seventh International Conference on Geosynthetics, 389-394.

Adams, M. T., Ketchart, K., & Wu, J. T. (2007). Mini pier experiments–geosynthetic reinforcement spacing and strength as related to performance.*Proceedings, Geo-Denver*.

Adams, M., Nicks, J., Stabile, T., Wu, J., Schelatter, W. and Hartmann, J. (2011). "Geosynthetic Reinforced Soil Integrated Bridge System Interim Implementation Guide", Federal Highway Administration, Publication No. FHWA-HRT-11-026, Washington, D.C.

Bathurst, R, Nernheim, A., Walters, D., Allen, T., Burgess, P. and Saunders, D. (2009). "Influence of reinforcement stiffness and compaction on the performance of four geosynthetic reinforced soil walls." Geosynthet. Int., 16(1), 43–59.

Berg, R. Christopher, B. and Samtani, N. (2009). "Design and construction of mechanically stabilized earth walls and reinforced soil slopes", Federal Highway Administration, Publication No. FHWA-NHI-10-024, Washington, D.C.

Bhattacharya, B., Li, D., Chajes, M. J. and Hastings, J. (2005). "Reliability-based load and resistance factor rating using in-service data." J. Bridge Eng., 10(5), 530–543.

Bowles, J. (1988). "Foundation analysis and design", The McGraw-Hill Companies, Inc., New York.

Cai, C., and Shahawy, M. (2003). "Understanding capacity rating of bridges from load tests." Pract. Period. Struct. Des. Constr., 8(4), 209–216.

Chajes, M., Mertz, D., and Commander, B. (1997). "Experimental load rating of a posted bridge." J. Bridge Eng., 1(1), 1–10.

DelGrego, M., Culmo, M., and DeWolf, J. (2008), "Performance evaluation through field testing of Century-Old railroad truss bridge," Journal of Bridge Engineering, 13(2), 132-138.

Fang, I., Chen, C. and Chang, I. (2004) "Field static load test on Kao-Ping-His cable-stayed bridge," J. Bridge Engineering, 9, 531-540.

Helwany, S., Tatsuoka, F., Tateyama, M. and Kojima, K. (1996). "Effects of facing rigidity on the performance of geosynthetic-reinforced soil retaining walls. Soils and Foundations." 36(1), 27-38.

Iwamoto, M. (2014). "Observations from load tests on geosynthetic reinforced soil." Masters dissertation, University of Hawaii at Manoa.

Lawrence, J. (2014). "Structural health monitoring of the first geosynthetic reinforced soil--integrated bridge system in Hawaii." Master thesis, University of Hawaii at Manoa.

Lawrence, T., Ritter, C. and Gergely, J. (2011). "Bridge monitoring and performance evaluation." Geotechnical and Geological Engineering, 29(5), 919-926.

Lee, K., Wu, J. (2004). "A synthesis of case histories on GRS bridge-supporting structures with flexible facing". Geotextiles and Geomembranes, 22 (4), 181–204.

Nicks, J., Adams, M., Ooi, P. and Stabile, T. (2013). "Geosynthetic reinforced soil performance testing—Axial load deformation relationships" (No. FHWA-HRT-13-066).

NCHRP-234, "Manual for bridge rating through load-testing,", Research Results Digest, No. 234, Transportation Research Board, National research Council, Washington, DC, USA, 1998.

Phillips, E. (2014). "Investigation of Required Tensile Strength Predicted by Current Reinforced Soil Design Methodologies". Master thesis, Virginia Tech.

Schultz J., Commander B., Goble G.and Frangpol D. (1995). "Efficient field esting and load Rating of Short – And Medium – Span Bridges." Structural Engineering review, 7(3), 181-194.

Vennapusa, P., White, D., Klaiber, F., Wang, S. and Gieselman, H. (2012). "Geosynthetic reinforced soil for low-volume bridge abutments."

Version, A. B. A. Q. U. S. (2013). 6.13. Analysis User's Guide, Dassault Systems.

Wu, J. and Pham, T. (2013). “Load-carrying capacity and required reinforcement strength of closely spaced soil-geosynthetic composites.” Journal of Geotechnical and Geoenvironmental Engineering, 139(9), 1468-1476.

Chapter 8

APPLIED BEARING PRESSURE BENEATH A REINFORCED SOIL FOUNDATION USED IN A GEOSYNTHETIC REINFORCED SOIL INTEGRATED BRIDGE SYSTEM

8.1 Introduction

Geosynthetic reinforced soil integrated bridge system (GRS-IBS) technology has seen recent adoption across many regions of the United States, as a cost effective solution for constructing small- to medium-span bridges (e.g., Adams et al. 2011, Talebi et al. 2014). A typical GRS-IBS utilizes closely spaced layers of geosynthetic reinforcement and compacted granular fill material to provide direct bearing support for structural bridge members (Figure 8.1a). Interim implementation guidelines for GRS-IBS technology (Adams et al. 2011) recommend the use of a reinforced soil foundation (RSF) to support the dead loads that are applied by the reinforced soil abutment and bridge superstructure, as well as any live loads that are applied by traffic on the bridge or abutment. In conventional practice, the RSF is composed of high-quality granular fill material that is thoroughly compacted on top of a geotextile fabric; the fabric is then wrapped around and on top of the fill layer to completely encapsulate it (Figure 8.1b). The resulting geosynthetic "mattress" supports

the applied loads above it, increasing the structure's bearing capacity and reducing its settlement under working load conditions relative to what would be observed if the structure was constructed directly on the native soils (Leshchinsky and Marcozzi 1990).

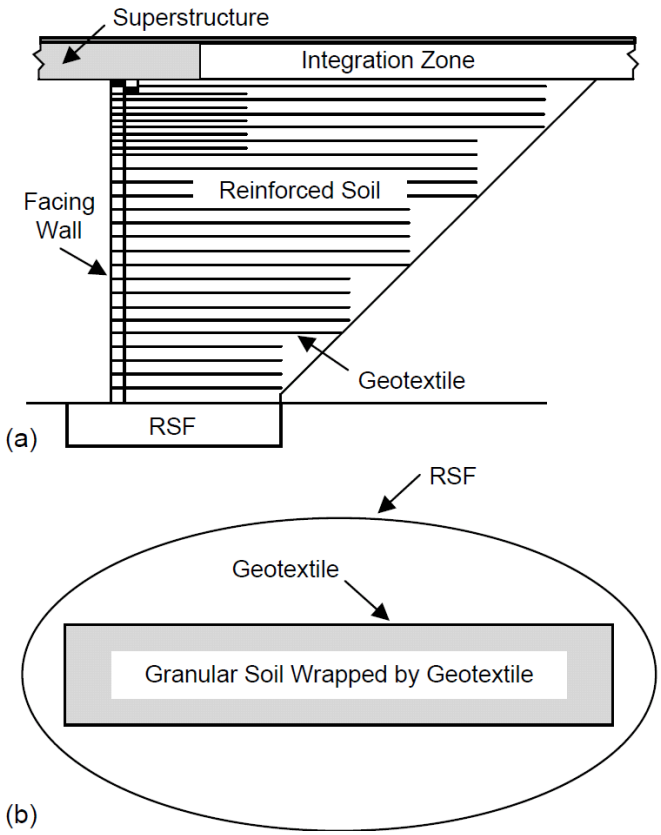

Figure 8.1. GRS-IBS structure: (a) Typical section view through a GRS bridge abutment, and (b) Reinforced soil foundation (RSF).

Numerous potential mechanisms of failure must be assessed as part of the GRS-IBS design process, comprising both internal (within the abutment or structure) and external (global, outside of the abutment or structure) failure modes (Adams et al.

2011). This chapter will focus on two vertical failure mechanisms of potential concern: (1) catastrophic bearing capacity failure of the GRS abutment(s), a vertical ultimate limit state failure mechanism, and (2) excessive settlement of the GRS abutment(s), a vertical serviceability limit state failure mechanism. Either of these failure mechanisms can occur as a result of excessive loading (dead load, live load) via the GRS abutment or bridge superstructure, sufficiently weak or overly compressible foundation soils, or some combination of these two conditions.

Current GRS-IBS design methodologies recommend a Meyerhof-type approach for performing bearing capacity analysis of an eccentrically loaded footing, which is based upon an underlying assumption of rigid body mechanics; this assumed behavior yields a trapezoidal applied pressure distribution beneath the RSF that is converted to a uniform applied pressure that acts over reduced RSF dimensions for purposes of analysis (Meyerhof 1953, Adams et al. 2011). For performing settlement analyses, little direct guidance is given in the GRS-IBS interim implementation guide, with the reader instead being told that: "The settlement of the underlying foundation soils is determined separately using classic soil mechanics theory for immediate (elastic) and consolidation settlement.", and "Nevertheless, settlement of the foundation soil should be assessed as with any other spread footing according to FHWA guidance." (Adams et al. 2011). Both of these statements generally imply that, for settlement purposes, the applied pressure distribution beneath the foundation is uniform. Following classical elastic theory approaches that are commonly used in settlement analyses, such as those extrapolated from Boussinesq (1885) or Westergaard (1938), the

changes in stress that are induced by GRS-IBS construction are applied directly to the foundation soil (the elastic medium) in the analysis process.

The recommended methods for vertical ultimate limit state (ULS) analysis and serviceability limit state (SLS) analysis of GRS-IBS structures consequently make some significant assumptions about the applied pressure distribution beneath the RSF, which correspond to methodologies that were originally developed for rigid concrete foundations. However, RSF behavior can reasonably be expected to be more flexible than the behavior of traditional concrete foundations (e.g., Leshchinsky and Marcozzi 1990). This flexible foundation behavior has the potential to change the applied pressure distribution beneath the RSF significantly, which can have effects on the bearing capacity and settlement analyses of these structures.

The current study presents measurements of applied bearing pressure beneath a RSF for a GRS-IBS constructed over a fine-grained soil foundation. Four total pressure transducers were utilized to measure values of applied bearing pressure directly beneath the RSF, with pressure values being measured at various intervals during the GRS-IBS construction process, after bridge superstructure placement, and with various levels of live load upon the bridge superstructure. In general, the load levels that were applied to the instrumented GRS-IBS in this study correspond to an "in-service" level of loading, rather than loading at the SLS or ULS. Even at this lower level of loading, it is quite evident that rigid foundation behavior was not observed for the instrumented GRS-IBS. Consequently, an empirical approach for predicting foundation behavior was developed from the actual data that was measured, which can

be used to predict values of applied pressure at different load levels. The proposed empirical methodology provides a framework for data collection for future GRS-IBS studies, from which an improved understanding of GRS-IBS field behavior can be developed.

8.2 Ultimate limit state analysis of a GRS-IBS – vertical bearing capacity

The current approach to vertical bearing capacity analysis of GRS-IBS structures assumes rigid foundation behavior, a fully mobilized active earth pressure condition behind the reinforced soil in the GRS-IBS, and an equilibrium based approach to design that converts applied pressures to equivalent forces (Meyerhof 1953, Adams et al. 2011), as shown schematically in Figure 8.2. It should be noted that for simplicity this design approach assumes that the reinforced soil zone ends at the back end of the RSF (e.g., Figure 8.2), even if the upper layers of geosynthetic reinforcement actually extend beyond this point, which is typical for most designs (e.g., Figure 8.1a).

As shown in Figure 8.2, the assessment of vertical bearing capacity necessitates the calculation of the resultant active earth pressures that are applied by the self-weight of the retained soil and any surcharges that are applied above the retained soil zone (Equation 8.1). This pressure diagram is then converted to an equivalent active earth pressure force (Equation 8.2).

$$\sigma_a = K_a \gamma H + K_a q_s \tag{8.1}$$

$$P_a = \frac{1}{2} K_a \gamma H^2 + K_a q_s H \tag{8.2}$$

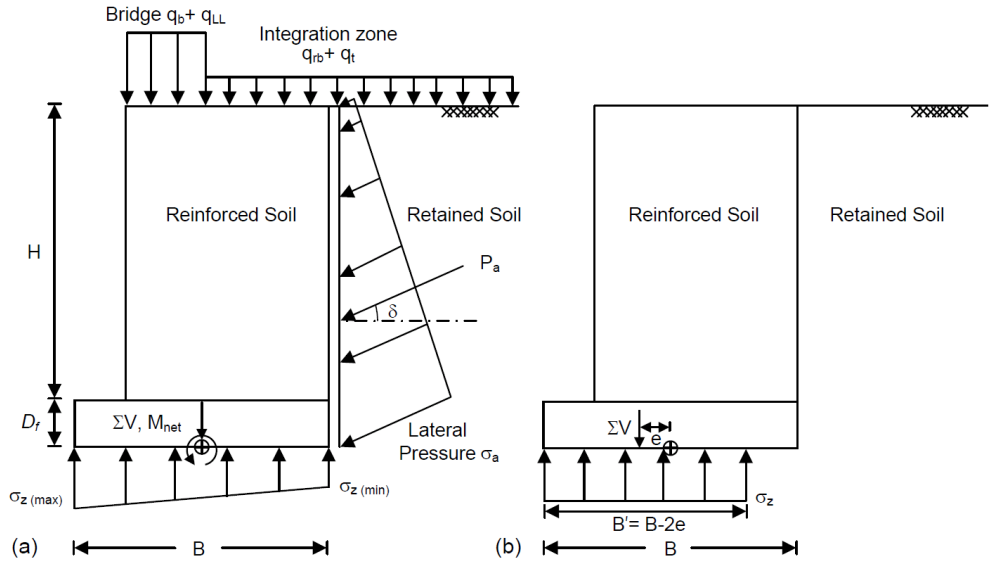

Figure 8.2. Vertical bearing capacity analysis of a GRS-IBS (ultimate limit state), following Meyerhof's (1953) approach: (a) applied trapezoidal stress distribution beneath the rigid foundation, and (b) reduced footing width and uniform applied pressure approach used with conventional bearing capacity analysis theory.

In these equations, σ_a is the active earth pressure at a depth H, K_a is the active earth pressure coefficient, γ is the retained soil unit weight, H is the height of the retained soil, q_s is the total surcharge that is applied by the integration zone dead load and the associated traffic live load (i.e., $q_s = q_{rb} + q_t$), and P_a is the resultant active earth pressure force applied by the retained soil and surcharge loads. The active earth pressure coefficient is typically determined using the methodologies presented by either Rankine (1857) or Coulomb (1776). If a Rankine (1857) approach is used for analysis, a horizontally sloped backfill yields a resultant active earth pressure force that acts horizontally, i.e., with $\delta = 0°$. If a Coulomb (1776) approach is used with a horizontally

sloped backfill, the resultant active earth pressure will act at an angle, i.e., with $\delta > 0°$ (Figure 8.2a).

The applied stress distribution beneath the foundation is calculated by assuming the entire GRS-IBS structure acts as a coherent mass (Adams et al. 2011). This approach is consistent with what is recommended in other guidelines and standards for design of MSE and GRS structures (e.g., Holtz et al. 1998; Wu et al. 2006; FHWA 2009; BS8006-1 2010; AASHTO 2012), for calculating the applied bearing pressure for ULS analysis. Following this approach, the net effect of the applied vertical and horizontal loads yields a trapezoidal applied pressure distribution beneath the rigid foundation (Figure 8.2a). The trapezoidal shape of this applied pressure distribution is caused by the loads that are applied external to the free body, which have a net rotational effect at the level of the foundation (M_{net}). The net rotational effect to the foundation caused by M_{net} is also commonly expressed using an equivalent force system (Figure 8.2b), in which the sum of the vertical loads is assumed to act at a distance (e) from the center of the foundation. This distance (e) corresponds to the "eccentricity" of loading on the foundation, which can be calculated using the following equation:

$$e = \frac{B}{2} - \frac{M_{net}}{\sum V} \tag{8.3}$$

In this equation, B is the width of the foundation, M_{net} is the net moment about the center of the foundation caused by all of the applied loads (i.e., the difference between the overall driving moments and the overall resisting moments), and $\sum V$ is the sum of the vertical forces acting on the foundation, which includes the weight of the

reinforced soil, the weight of the RSF, the weight of the facing elements, the weight of the superstructure, and any applied surcharges acting on the rigid body. The magnitude of M_{net} and the associated eccentricity of loading is significantly influenced by the magnitude and position of the resultant active earth pressure force, and in some cases for GRS-IBS structures, the dead load (DL) and live loads (LL) that are associated with the bridge superstructure. Once the eccentricity has been determined, the maximum and minimum stresses beneath the foundation can be calculated using the following equations:

$$\sigma_{z_{max}} = \frac{\sum V}{B}(1 + \frac{6e}{B}) \tag{8.4}$$

$$\sigma_{z_{min}} = \frac{\sum V}{B}(1 - \frac{6e}{B}) \tag{8.5}$$

where $\sigma_{z_{max}}$ and $\sigma_{z_{min}}$are the maximum and minimum induced pressure beneath the foundation, respectively.

Meyerhof (1953) recommended that the trapezoidal shape of the applied pressure distribution (Fig 8.2a) be converted to an equivalent uniform pressure distribution that acts over a reduced footing width B' (Figure 8.2b), which is determined using the following equation:

$$B' = B - 2e \tag{8.6}$$

This reduced footing width is used with the general bearing capacity equation to calculate the ultimate bearing capacity of the foundation soils (e.g., Das

2015). For purposes of comparison with ultimate or allowable foundation pressures, applied bearing pressures are assumed to be uniform, and to act only over this reduced footing width (Figure 8.2b).

8.3 Serviceability limit state analysis of a GRS-IBS – vertical settlement

The current approach to settlement analysis of GRS-IBS structures assumes that loads applied above the level of the foundation can be converted to applied stresses acting directly on the foundation, as shown in Figure 8.3. Following this approach, the foundation soil is modeled as an elastic medium, and elastic stress theory can be used to determine the change in stresses at various depths of interest beneath the point of stress application for settlement calculation purposes following conventional approaches (e.g., Boussinesq 1885, Westergaard 1938). For simplicity in the analysis process, it is generally easiest to determine the stresses at various points in the foundation by defining two distinct zones of applied stress, as shown schematically in Figure 8.3a: (1) Zone 1, which induces changes in stress beneath the RSF due to loads applied directly above the RSF, and (2) Zone 2, which induces changes in stress beneath the RSF due to loads adjacent to the RSF.

The stresses acting in Zone 1 include the dead load applied by the self-weight of the reinforced soil (q_a), plus either the bridge dead load plus the bridge live load acting over the width of the bridge bearing seat ($q_b + q_{LL}$), or the integration zone dead load plus any traffic live load ($q_{rb} + q_t$) (Figure 8.3b). Zone 1 can consequently best be modeled using the principle of superposition with two finite loaded areas having different constant surcharges. The stresses acting in Zone 2 include the dead load

applied by the self-weight of the retained soil (q_b), plus the integration zone dead load plus any traffic live load ($q_{rb} + q_t$) (Figure 8.3b). The stresses acting in Zone 2 can consequently best be modeled using a semi-infinite loaded area with a constant surcharge, as the loaded area generally extends far to the right of the structure for the sketch shown in Figure 8.3b.

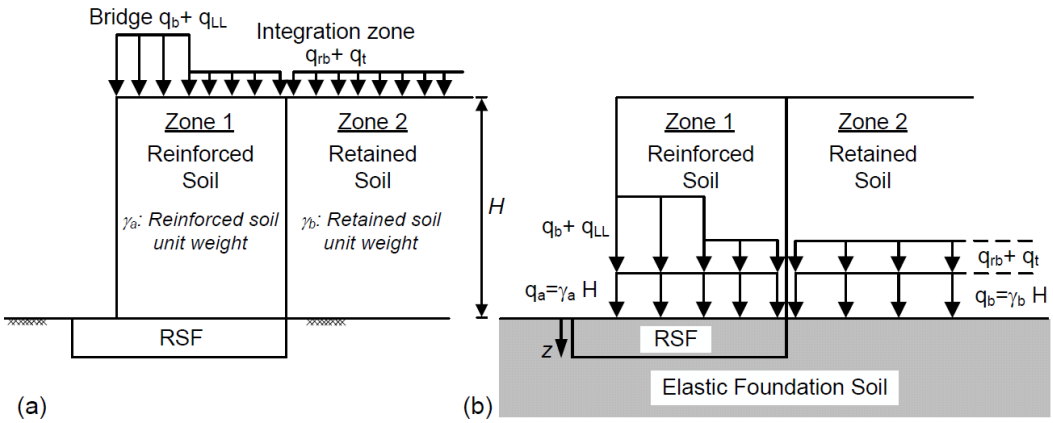

Figure 8.3. Settlement analysis of a GRS-IBS (serviceability limit state), following conventional elastic stress theory: (a) A GRS-IBS abutment, with a reinforced soil zone (Zone 1) and a retained soil zone (Zone 2), with different applied surcharge loads, and (b) Conversion of loads applied above the level of the foundation to equivalent surcharges loading a uniform elastic half-space.

For simplicity in the analysis process, it is generally easiest to assume that the RSF itself is part of the elastic half-space, and all stresses that induce settlement are applied directly to the top of the RSF. In this case, the elastic zone depth measurement, *z*, starts from the top of the RSF, as shown in Figure 8.3b. This assumption implies that

the RSF has the same elastic properties as the underlying foundation soil, which may or may not be the case, depending upon the existing foundation soils that are present at a given site. In most cases, this assumed behavior for the RSF is likely a conservative assumption, given the relatively stiff and strong behavior that is characteristic of typical RSF construction. Also, for simplicity, the boundary between the reinforced soil zone and the retained soil zone is generally assumed to be a vertical line up from the heel of the RSF (Figure 8.3a); in reality, the length of the reinforcement varies with the height of the wall for most constructed GRS abutments, as shown in Figure 8.1a.

8.4 Applied pressures beneath the GRS-IBS foundation during construction and after bridge load application

The constructed GRS-IBS was instrumented to measure values of applied bearing pressure directly beneath the RSF. Four total pressure transducers were utilized for this purpose (S1 to S4), as shown in Figure 8.4. The transducers were used to measure the applied vertical stress at various intervals during the GRS-IBS construction process, after bridge superstructure placement, and with various levels of live load upon the bridge superstructure.

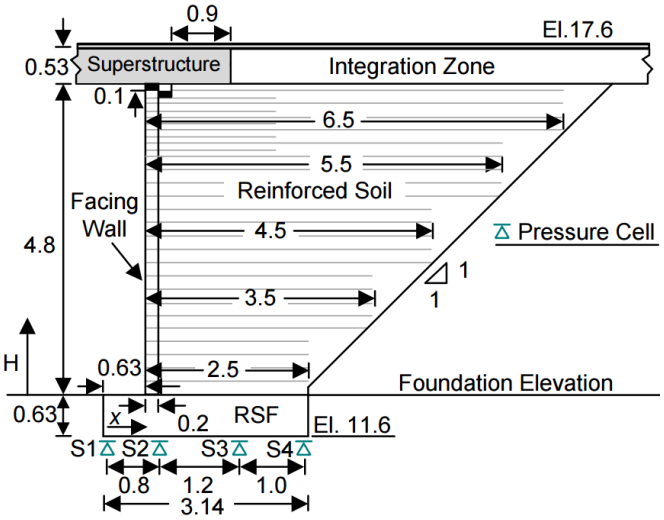

Figure 8.4. GRS-IBS cross-section along the roadway centerline (all dimensions shown are in m).

Figure 8.5 shows the progress of wall construction over time for the instrumented GRS abutment; note that the measurement of wall height that is shown in this figure is taken from the top of the RSF, as shown in Figure 8.4. Figure 8.6 shows the corresponding values of applied bearing pressure that were measured beneath the RSF, for different stages of wall construction. As shown in Figure 8.4, the horizontal distance (x) is measured from the beginning of the RSF; for reference purposes, the location of the wall face (the width of the CMU block wall facing elements used to construct the GRS abutment) is also shown.

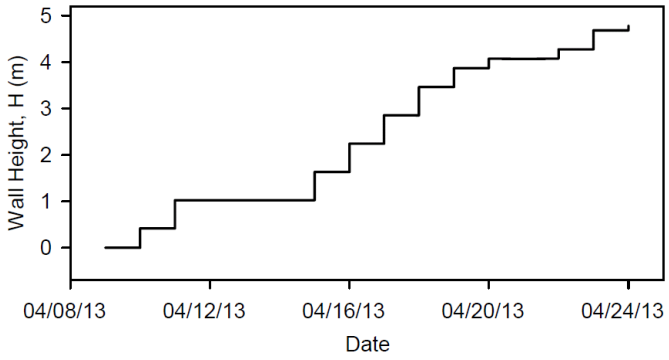

Figure 8.5. Increase in GRS abutment height over time during the construction process.

As shown in Figure 8.6, for each stage in the construction process, the maximum applied vertical pressure (σ_z) was observed in the second cell (S2), which is located beneath the reinforced soil zone fairly close to the wall face. With the exception of the first few construction increments, the minimum applied vertical pressure was generally observed for the cell which is located beneath the "toe" of the RSF, which extends beyond the face of the wall (S1). The third (S3) and fourth pressure cells (S4) generally recorded the second highest and third highest pressure values, respectively.

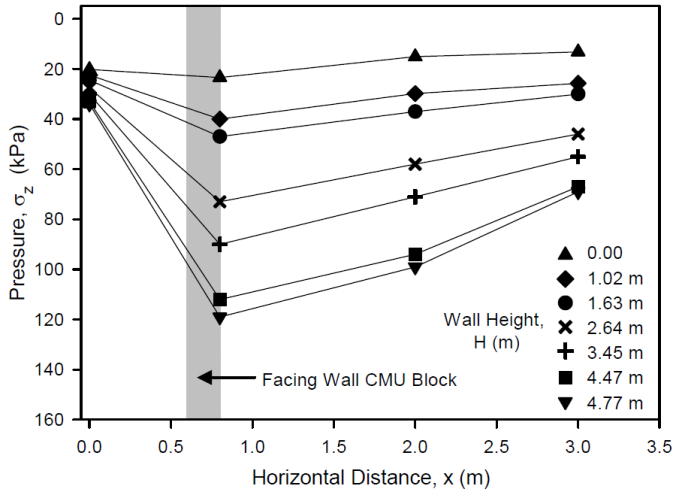

Figure 8.6. Applied bearing pressures measured during construction of the GRS abutment.

From these results, it is clear that the portion of the RSF that extends beyond the face of the wall does not behave like a "rigid" foundation, as the distribution over the total base width of the RSF is not trapezoidal in shape. This is not surprising, as significant confining stresses are not applied to the stone that is encapsulated in the RSF outside of the wall face, which gives this "toe section" of the RSF the ability to deform (flex) more freely, resulting in reduced applied bearing pressures in this area. This observation is particularly important, as it shows that very little stresses are carried by the toe of the RSF, the exact opposite of what is assumed by the trapezoidal stress distribution with Meyerhof's (1953) approach to vertical bearing capacity (the recommended design methodology for vertical ultimate limit state that is currently used in conventional GRS-IBS design procedures).

After abutment construction, the bridge superstructure was placed directly on the GRS abutments (inducing a q_b surcharge over the front portion of the GRS abutment), and the integration zone was constructed (inducing a q_{rb} surcharge over the rear portion of the GRS abutment). This resulted in application of significant additional dead loads (DL) to each abutment, of approximately 80 kPa near the face of the wall (distributed over the 0.9 m bridge bearing seat, as shown in Figure 8.4), and 8 kPa over the remaining portion of the reinforced soil zone. This application of load caused a noticeable change in the applied bearing pressure at the four sensor locations, as shown by the DL line in Figure 8.7.

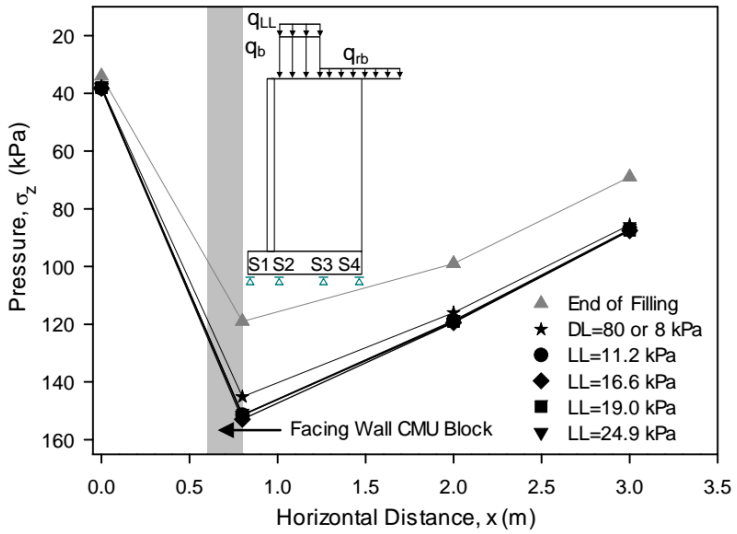

Figure 8.7. Applied bearing pressures caused by: (1) deployment of the bridge superstructure and construction of the transition zone (DL application), and (2) application of various levels of live load at mid-span on the bridge using heavy vehicle loads (LL application).

As part of a larger live load testing series (as discussed in Chapter 7), a number of symmetrical live loads (LL) were placed on the bridge post-construction, in the form of two heavy dump trucks that were parked side-by-side, each one in the middle of each roadway lane at the center of the bridge span. These loads induced an applied LL bearing pressure on each abutment (q_{LL}), which was applied over the bridge bearing seat area. Four levels of live load application (Load cases 2, 5, 8 and 15 in Chapter 7) were explored using this approach, with the trucks being parked empty, and at one-third, two-third, and completely full bed load levels; prior to loading the bridge each time, the truck weights were measured directly using scales. As discussed in Chapter 7, assuming a roughly equal distribution of the applied truck loads over both bridge abutments, and a uniform applied pressure over the bridge bearing seat, these truck live load levels corresponded to finite area surcharges of 11.2 kPa, 16.6 kPa, 19.0 kPa, and 24.9 kPa, respectively; these loads were applied in addition to the superstructure and transition zone dead loads. Additional changes in applied bearing pressure that occurred as a result of these LL events are shown in Figure 8.7.

As shown in Figure 8.7, significant changes in applied bearing pressure beneath the RSF occurred due to application of the DL, and only minor changes in applied pressure occurred with application of different live loads to the bridge. In a similar fashion as what was observed for changes in stress during GRS abutment construction, the largest changes in pressure were observed for sensor S2 (≈30 kPa), with sensors S3 and S4 exhibiting smaller (and roughly the same) changes in stress, and sensor S1 exhibiting very little change in stress. The increases in stress at each sensor

location were generally between 12 to 25 percent of the stresses that were measured at the end of GRS abutment construction. It should be noted here that the assumption of balanced truck loads over each abutment and a uniform applied pressure over the bridge bearing seat may differ from the actual behavior of this structure under load; this means that the calculated values of applied DL and LL are approximate in nature.

8.5 Calculation of applied bearing pressure following conventional ultimate limit state (ULS) and serviceability limit state (SLS) design approaches

For the constructed GRS-IBS, it is instructive to look at the shape of the applied pressure diagrams that are calculated using conventional design methodologies, relative to the actual applied bearing pressure distributions that were measured.

8.5.1 Vertical Bearing Capacity

Figure 8.8 shows the trapezoidal applied pressure distributions that result for a rigid foundation having different wall heights at different stages during the construction process. As shown, Figure 8.8a corresponds to the applied pressure distribution calculated for the assumption of a Rankine (1857) active earth pressure distribution behind the reinforced soil zone, with $\delta = 0$. Figure 8.8c shows the results for a Coulomb (1776) active earth pressure distribution, with $\delta = \phi'$. Note that the applied pressure distribution is very different for the Rankine and Coulomb assumptions, due to the downdrag effect that a significant value of δ has at the interface

of the reinforced soil and retained soil zones. Figures 8.8b and 8.8d show the same data presented in a fashion that allows for easy comparison between measured and calculated values for each sensor. Ideally, the presented results would fall along a 1:1 line, which clearly did not occur.

Figure 8.9 shows the trapezoidal applied pressure distributions that result from rigid foundation behavior, after application of the respective DL and LL events, relative to the measured values. Figures 8.9a and 8.9c show the results from approaches that utilize Rankine and Coulomb methodologies for determining the active earth pressure distribution behind the reinforced soil zone, respectively. Figures 8.9b and 8.9d present the corresponding measured stress vs. calculated stress plots, with the results again showing a strong deviation from the 1:1 line for the S1 and S4 sensors, but with the S2 and S3 sensors showing more reasonable results.

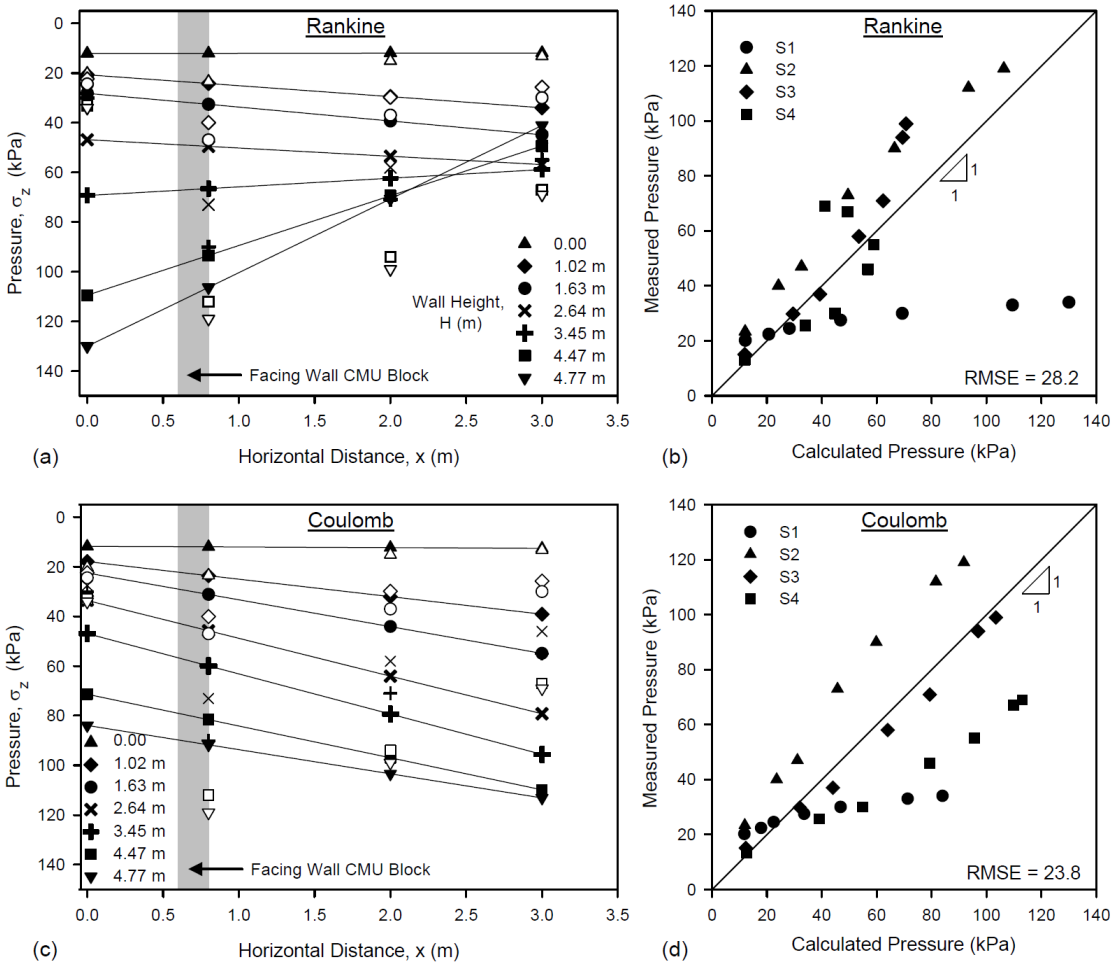

Figure 8.8. Applied bearing pressure beneath the RSF during construction, using a rigid foundation approach to vertical bearing capacity analysis: (a) Assuming development of a Rankine active earth pressure condition in the retained soil zone, (b) Measured stresses vs. calculated stresses determined using a Rankine earth pressure assumption, (c) Assuming development of a Coulomb active earth pressure condition in the retained soil zone, and (d) Measured stresses vs. calculated stresses determined using a Coulomb earth pressure assumption. Note that the open symbols in figures (a) and (c) correspond to measured values, and the solid symbols connected with a line correspond to calculated values.

It should be noted that the use of an active horizontal earth pressure condition to determine the applied stress distribution for ULS analysis, as recommended by Adams et al. (2011), is a significant assumption, especially for the smaller stress cases that correspond to the lower wall heights at the beginning of the construction process. In particular, it takes some lateral movement of the GRS abutment to reach an active condition behind the reinforced soil zone. It is not clear if sufficient wall movement has occurred under the in-service load conditions to achieve a fully active earth pressure condition. This assumed behavior will certainly have an effect on the results from the analyses described above. That being said, if one assumes that the other extreme in behavior holds true, i.e., the "at rest" earth pressure condition, the general shape of the results is still the same, only with larger applied bearing pressures being observed due to the larger applied earth pressures. The general conclusions from this section are consequently not significantly affected.

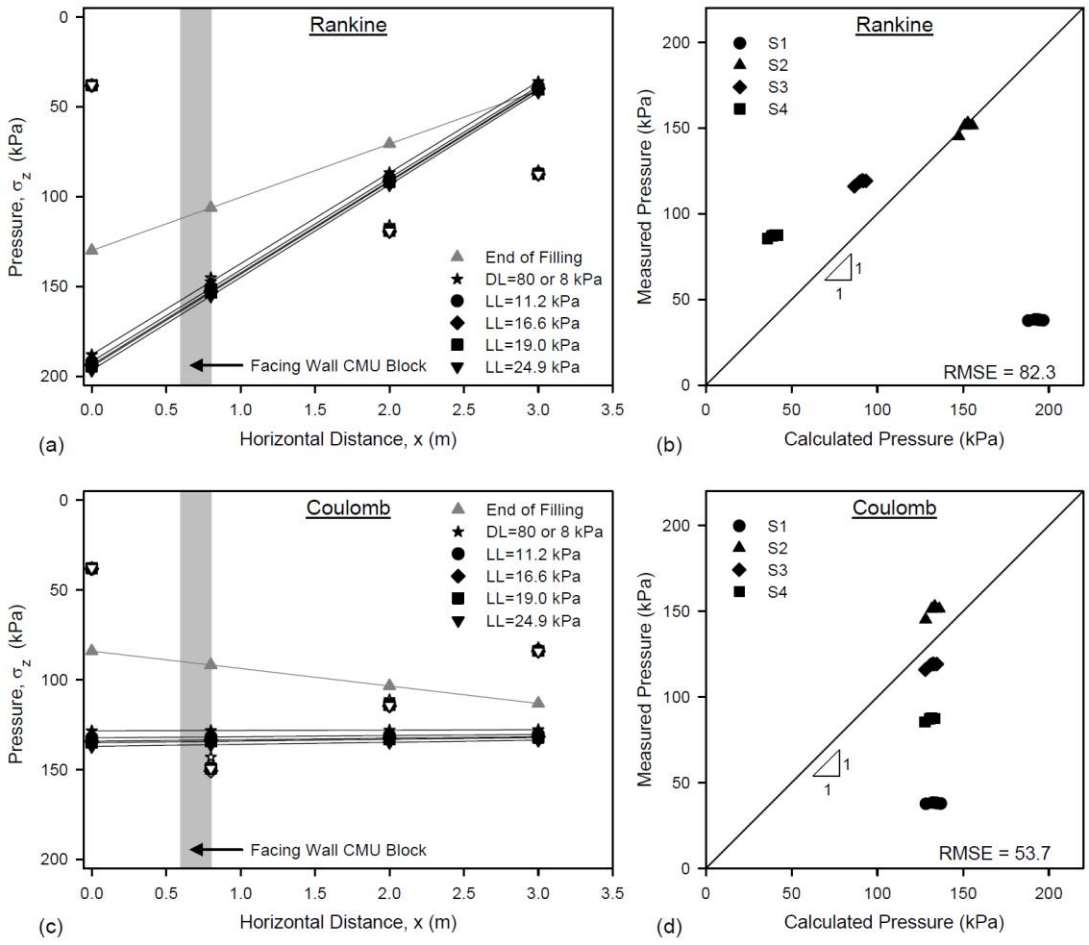

Figure 8.9. Applied bearing pressure beneath the RSF after DL and LL placement, using a rigid foundation approach to vertical bearing capacity analysis: (a) Assuming development of a Rankine active earth pressure condition in the retained soil zone, (b) Measured stresses vs. calculated stresses determined using a Rankine earth pressure assumption, (c) Assuming development of a Coulomb active earth pressure condition in the retained soil zone, and (d) Measured stresses vs. calculated stresses determined using a Coulomb earth pressure assumption. Note that the open symbols in figures (a) and (c) correspond to measured values, and the solid symbols connected with a line correspond to calculated values.

8.5.2 Vertical Settlement

As noted previously, a number of assumptions need to be made to use elastic stress theory to calculate the changes in stress beneath the RSF due to GRS abutment construction, placement of the bridge and transition zone DLs, and application of various levels of LL to the bridge superstructure. In particular, as shown in Figure 8.3, the elastic foundation medium was assumed to start at the ground surface, with the RSF being a part of the foundation and having the same stiffness as the underlying foundation soils. All loads applied above this point are assumed to be converted to equivalent surcharges that are applied directly to the elastic medium. Boussinesq's (1885) elastic stress theory was then utilized to determine changes in stress versus depth beneath the applied stresses, specifically here to calculate the theoretical applied pressures at the sensor locations. Figure 8.10a shows the applied pressure distributions that result for the different construction wall heights. Figure 8.10b presents the measured versus calculated values determined using Boussinesq's method for each of the four sensors. As shown, the agreement between the measured and the calculated values at the location of sensor S3 is excellent, with the other sensors showing much more significant deviation.

Figure 8.11 shows the applied pressure distributions that result from elastic stress theory analysis, after application of the respective DL and LL events, relative to the measured values. Figure 8.11a shows the results from Boussinesq's method, and Figure 8.11b shows the corresponding measured stress vs. calculated stress plots. In

general, good agreement was not observed between the measured and calculated values, even for sensor S3.

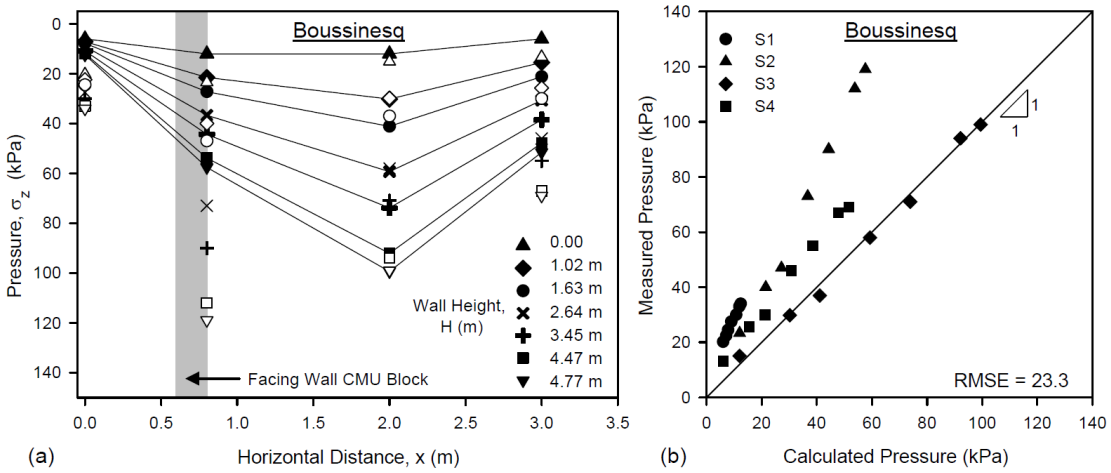

Figure 8.10. Applied bearing pressure beneath the RSF during construction, determined using elastic stress theory: (a) Results from Boussinesq's method, and (b) Measured stresses vs. calculated stresses. Note that the open symbols in figure (a) correspond to measured values, and the solid symbols connected with a line correspond to calculated values.

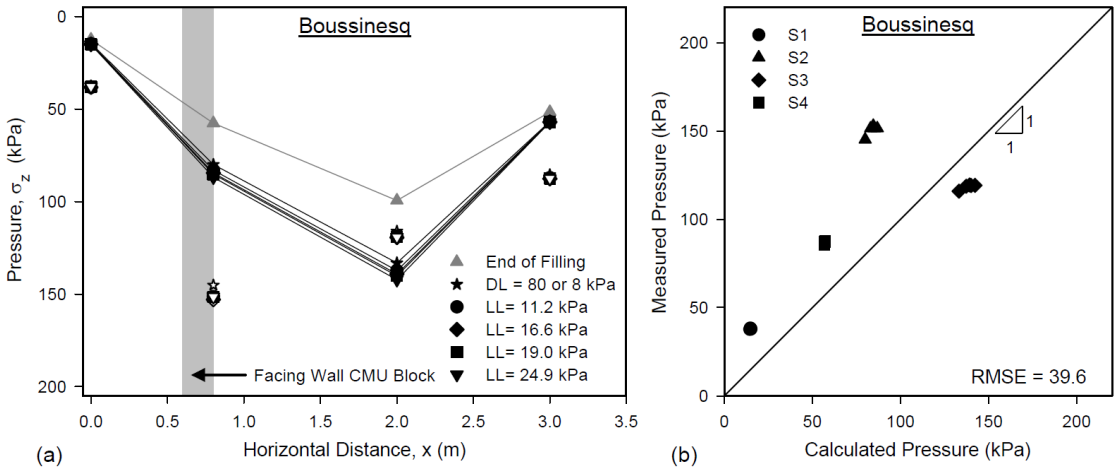

Figure 8.11. Applied bearing pressure beneath the RSF after DL and LL placement, determined using elastic stress theory: (a) Results from Boussinesq's method, and (b) Measured stresses vs. calculated stresses. Note that the open symbols in figure (a) correspond to measured values, and the solid symbols connected with a line correspond to calculated values.

8.6 Calculation of applied bearing pressure using an empirical approach

The applied bearing pressures that were measured during construction (Figure 8.6), after placement of the bridge DL (Figure 8.7), and during LL testing (Figure 8.7) indicate that the applied pressure distribution(s) beneath the bridge are clearly not uniform or trapezoidal in nature. The measured shape of the applied pressure distribution beneath the RSF that underlies the GRS abutment (in particular the toe of the RSF) also indicates that the RSF foundation is likely behaving in a flexible way. It is hypothesized by the authors that portions of the RSF without confinement will be able to flex more freely than areas that have more significant overburden, which should

induce a stiffer foundation behavior. To examine this phenomenon further, the authors recommend an empirical approach to estimating the applied bearing pressures beneath a geosynthetic-encapsulated RSF. This "observational approach" to understanding applied bearing pressures is consistent with the long history of use of the observational method in geotechnical engineering (Peck, 1969), in particular for understanding complex geotechnical problems.

Figure 8.12 shows the applied pressures that are measured by each sensor (S1-S4) versus the corresponding wall height for each stage of the GRS abutment construction process. As shown, for each sensor, the results are predictable, following a linear trend in measured behavior that is unique for each sensor location. Using these simple regression models, it is possible to make predictions for each of the sensors about what the applied pressure should be at each sensor location for various stages in the GRS abutment construction process; the results from this type of prediction are presented in Figure 8.13. Figure 8.13 illustrates that an empirical approach to stress prediction can yield results that are better than conventional ultimate limit state analysis using Meyerhof's bearing capacity theory (Figure 8.8) or serviceability limit state analysis using Boussinesq's elastic theory (Figure 8.10), especially for predicting GRS abutment behavior under "in-service" loading conditions.

A similar empirically-based simple linear regression approach can be applied to the results from the DL and LL events that the bridge was subjected to (Figure 8.14). In Figure 8.14, the applied bearing pressure beneath the RSF is calculated by assuming a roughly equal distribution of the applied bridge DL and truck LLs over both

bridge abutments, with an assumed uniform applied pressure over the bridge bearing seat. Unfortunately, this data set is dominated by the change in stress that occurs with the application of the bridge DL, leading to a fairly skewed data set it terms of data point grouping (Figure 8.14).

Despite this limitation, this type of empirical approach to determining applied bearing pressures still yields better results (Figure 8.15) than conventional ultimate limit state analysis using Meyerhof's bearing capacity theory (Figure 8.9) or serviceability limit state analysis using Boussinesq's elastic theory (Figure 8.11). These findings are similar to what was observed by the sensors for the construction-induced changes in stress. Not surprisingly, the relative change in slope between the DL/LL events and the wall construction events is different on a sensor-by-sensor basis, as the DL/LL events only induce loading over the bridge bearing seat area, while the GRS abutment construction process applies load over a larger area.

Of course, one major limitation of this type of empirically-based approach to stress prediction is that effectively predicting the applied pressure behavior at the SLS or the ULS requires extrapolation beyond the measured stresses at the "in-service" loading condition. In this regard, it would be interesting to see if the empirically-observed applied stress behavior holds true if the structure is loaded to SLS or ULS conditions, or alternatively, to identify the point in the loading process where the empirical linear model begins to break down. Despite this limitation, the observational approach towards assessment of applied bearing pressures beneath the RSF is instructive for enhancing our understanding about the assumed foundation behavior.

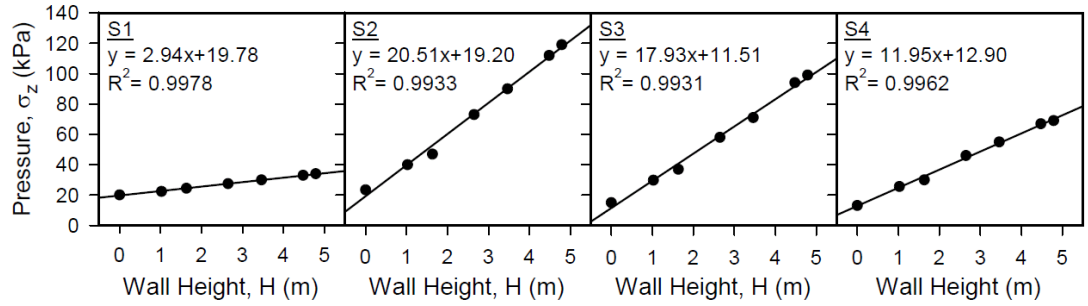

Figure 8.12. Linear relationship between measured applied pressure beneath the RSF and GRS abutment height.

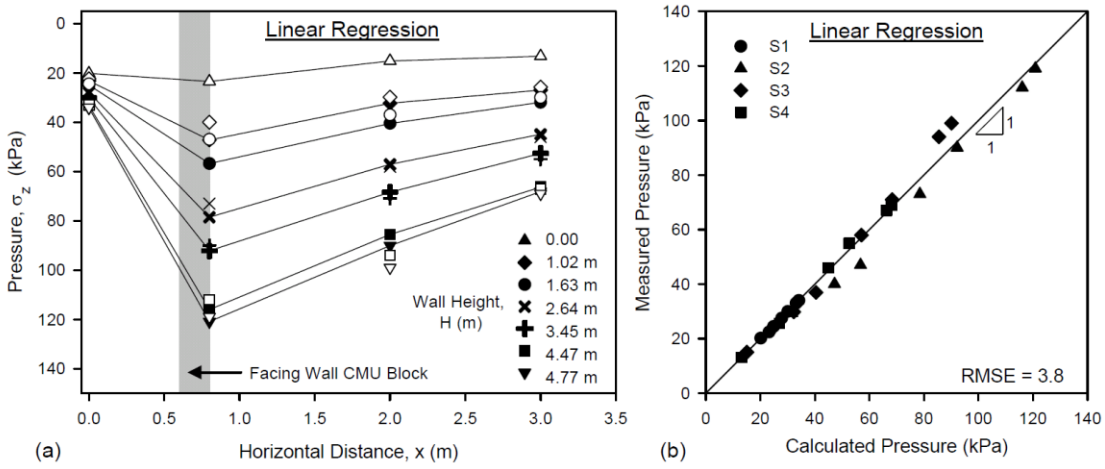

Figure 8.13. Applied bearing pressure beneath the RSF during construction, determined using an empirical approach: (a) Results from the empirical prediction method, and (b) Measured stresses vs. calculated stresses. Note that the open symbols in figure (a) correspond to measured values, and the solid symbols connected with a line correspond to calculated values.

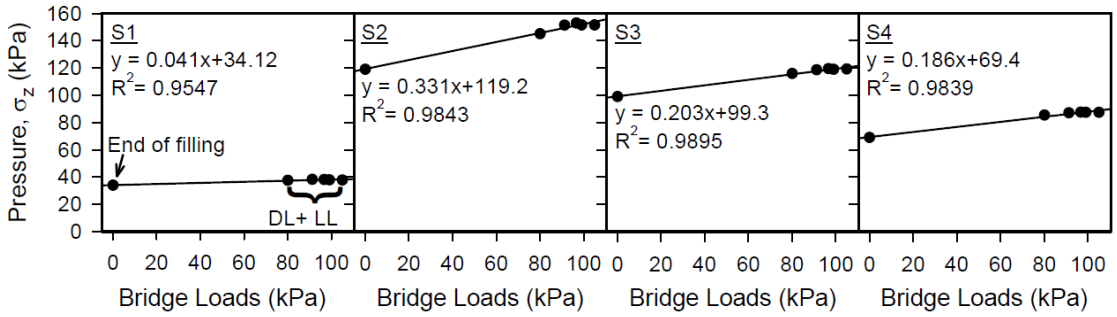

Figure 8.14. Linear relationship between measured applied pressure beneath the RSF and stress applied by the superstructure from the applied DL and LL.

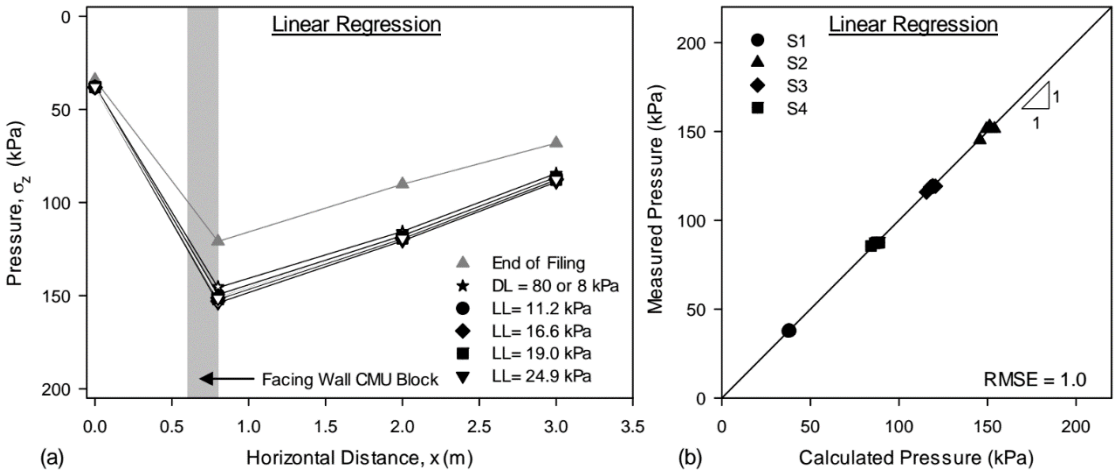

Figure 8.15. Applied bearing pressure beneath the RSF after DL and LL placement, determined using an empirical approach: (a) Results from the empirical prediction method, and (b) Measured stresses vs. calculated stresses. Note that the open symbols in figure (a) correspond to measured values, and the solid symbols connected with a line correspond to calculated values.

8.7 Conclusion

This chapter describes the current approaches to vertical ultimate limit state (ULS) and serviceability limit state (SLS) analysis of GRS abutments – specifically, the approaches that are used to determine the applied pressure distribution beneath the base of the reinforced soil foundation (RSF) for vertical bearing capacity and vertical settlement analyses. Data from an instrumented GRS-IBS that was constructed over a fine-grained soil foundation is presented, which illustrates the relatively poor predictive capabilities of these current design methodologies for capturing the actual applied pressure behavior beneath the type of RSF that is commonly used for GRS-IBS construction.

Four total pressure transducers were utilized to measure values of applied bearing pressure directly beneath the RSF for the instrumented case history, with pressure values being measured at various intervals during the GRS-IBS construction process, after bridge superstructure placement, and with various levels of live load upon the bridge superstructure. The measured data shows that the RSF behaves in a fairly flexible way under load, particularly outside of the face of the wall, yielding an applied pressure distribution that is neither uniform nor trapezoidal. This observed behavior is significantly different than what conventional GRS-IBS design methodologies assume.

Consequently, an empirical approach is developed for applied bearing pressure prediction using the recorded data from construction, and also separately for bridge dead-load and live-load application. Results from the empirical approach that is presented agree much more closely with measured values than those from the

conventional design methodologies. This empirical approach is a useful first step for researchers, as it draws important attention to this issue, and provides a framework for collecting meaningful field data on future projects which accurately capture real GRS-IBS foundation behavior. Additional empirical data in this area will eventually lead to improved GRS-IBS analysis methodologies, as it will allow for improved mathematical model calibrations.

REFERENCES

AASHTO (2012). "LRFD Bridge Design Specifications." Sixth ed. AASHTO, Washington, D.C.

Adams, M., Nicks, J., Stabile, T., Wu, J., Schelatter, W. and Hartmann, J. (2011). "Geosynthetic reinforced soil integrated bridge system Interim Implementation Guide." Publication No. FHWA-HRT-11-026. Federal Highway Administration, Washington, DC.

Boussinesq, J. (1885). "Application des potentiels à l'étude de l'équilibre et du mouvement des solides élastiques: principalement au calcul des déformations et des pressions que produisent, dans ces solides." des efforts quelconques exercés sur une petite partie de leur surface ou de leur intérieur: mémoire suivi de notes étendues sur divers points de physique. mathematique et d'analyse, (Vol. 4). Gauthier-Villars. (In French).

BS8006-1 (2010). "Code of practice for strengthened/reinforced soils and other fills." British Standard Institution, London

Coulomb, C. (1776). "Essai sur une application des règles de maximis & minimis à quelques problèmes de statique, relatifs à l'architecture. De l'Imprimerie Royale." (In French).

Das, B. (2015). "Principles of foundation engineering." Eighth ed. Cengage Learning, Boston, MA.

FHWA (2009). "Design of mechanically stabilized earth walls and reinforced soil slopes." Publication No. FHWA-NHI-10-024. Federal Highway Administration, Washington, D.C.

Holtz, R., Christopher, B., and Berg, R. (1998). "Geosynthetic design & construction guidelines." Publication No. FHWA-HI-95-038. Federal Highway Administration, Washington, DC.

Leshchinsky, D. and Marcozzi, G. (1990). "Bearing capacity of shallow foundations: rigid versus flexible models." Journal of Geotechnical Engineering, 116 (11), 1750-1756.

Meyerhof, G. (1953). "The bearing capacity of foundations under eccentric and inclined loads." Proc. Third International Conference on Soil Mechanics and Foundation Engineering, Zurich, 1, 440-445.

Peck, R. (1969). “Advantages and limitations of the observational method in applied soil mechanics.” Geotechnique, 19 (2), 171-187.

Rankine, W. (1857). “On the stability of loose earth.” Philosophical Transactions of the Royal Society of London, 147, 9-27.

Talebi, M., Meehan, C. L., Cacciola, D. V., and Becker, M. L., 2014. Rapid Replacement. Civil Engineering, ASCE, April 2014, 64-69 and 81.

Westergaard, H. (1938). “A problem of elasticity suggested by a problem in soil mechanics: soft material reinforced by numerous strong horizontal sheets.” Contributions to the Mechanics of Solids, Stephen Timoshenko 60th Anniversary Volume, MacMillan, New York, 260-277.

Wu, J., Lee, K., Helwany, S. and Ketchart, K. (2006). “Design and construction guidelines for geosynthetic-reinforced soil bridge abutments with a flexible facing.” Rep. No. 556, Transportation Research Board.

Chapter 9

INVESTIGATION OF THE GRS-IBS PERFORMANCE OVER THREE YEARS OF IN-SERVICE OPERATION

9.1 Introduction

In this chapter, the performance of the GRS-IBS structure is investigated using the measured data by different types of sensors. The data from the first three years of operation is considered in this investigation. The data collection process was discussed in Chapter 3, the collected data were presented in Chapter 4 and the correlation analysis for data interpretation was explained in Chapter 5.

The volumetric water content sensors were installed in the west abutment to investigate the possible effect of induced effective stress by changes in the abutment suction on the stability of the abutment. In a similar fashion, installation of the piezometers in the foundation and the lowermost level of the west abutment was intended to capture changes in pore water pressure in the fine-grained foundation soils, to assess the potential influence of water pressures on the behavior of the structure. Taken together, these sensors provide useful information for investigating the effect of water and water content on the stability of the structure.

Previous studies have shown the effect of precipitation on the performance of reinforced backfills. Ng and Pang (2000) indicated that under real conditions, about 60% of the rainfall infiltrates into the soil. This amount of infiltration may affect the

response of the backfill, depending on its permeability. Additionally, for GRS-IBS structures over a water crossing, any precipitation tends to increase the level of the water in the river, which may have adverse effect on the stability of the reinforced backfill since it decreases the soil strength in the reinforced soil zone, in the backfill, and in the foundation. The effect of water on the performance of reinforced earth structures has been studied by many researchers. For example, Koerner and Koerner (2013) and Valentine (2013) illustrated that over 60% of failures and poor performance of geosynthetic reinforced soil structures are caused by internal or external water. In addition, structures constructed using fine grained backfill material have experienced significantly more failure, which indicates the importance of backfill material selection on the overall performance of the structure.

Increasing levels of suction tend to increase the effective stress between soil particles (Fredlund et al. 1978), which in turn has the tendency to decrease the abutment deformation under load and increase its stability. The importance of suction on the behavior of reinforced soil abutments has recently been investigated by some researchers (e.g, Yoo and Jung 2006, Leshchinsky 2009, Leshchinsky and Tatsuoka 2013, Yoo 2013, Esmaili et. al 2014 and Vahedifard et al. 2015). In spite of its importance, the effect of suction is not accounted for in design methods proposed by design manuals for reinforced soil structures (e.g., FHWA 2009 and AASHTO 2014).

The adverse effect of decreases in soil suction on the performance of low quality reinforced backfills has been emphasized by researchers through experiments and numerical simulation (e.g., Yoo and Jung 2006, Kim and Borden 2013, Yoo 2013

and Esmaili et. al 2014). Using some experiments, Portelinha et al. (2013) showed that the use of non-woven geotextile as reinforcement element in backfill material increase the drainage capacity of reinforced backfills, which decreases their potential for failure.

As discussed in Chapter 3, thermistors were also installed in the GRS-IBS structure to investigate changes in the abutments' temperatures and their likely influence on the response of the structure. Air temperature was also recorded simultaneously using a thermistor located within the datalogger housing, to look for relationships between changes in the abutment and air temperature.

A review of available literature indicates that the effect of temperature change on the response of MSE and GRS abutments has been investigated by researchers. To date, most researchers have focused on the effect of air temperature change on the bridge expansion and contraction and induced pressure and deformation to the abutment. However, in a few studies, temperature sensors have been installed in the reinforced soil backfill to evaluate the effect of the abutment temperature changes on the structure's response. Using installed thermistors, Buttry et al. (1996) reported the influence of temperature and seasonal changes on the response of a 3.5 m high GRS segmental retaining wall. They concluded that the changes in temperature affected the stress level and deformation in the wall. Abu-Hejleh et al. (2001) summarized and discussed typical measured air temperatures, in comparison with soil temperatures at locations nearest to the wall facing and farthest from the wall facing in a GRS abutment using the data gathered by the thermistors installed in the abutment. They reported a cyclic lateral movement of the facing wall induced by the temperature change.

According to these studies, the abutment temperature changes can influence the deformation and pressure distribution to some extent.

In order to investigate the deformation of the GRS-IBS abutments, foil strain gauges and surveying targets were installed in the abutments and on the facing walls, respectively. Two different types of strain gauges were utilized for comparison purposes. As discussed in Chapter 2, monitoring the deformation of reinforced structures is very common for MSE and GRS construction and many researchers have used the data from the strain gauges and surveying targets to analyze the response of reinforced earth structures (e.g., Wu et al. 2008, Iwamato et al. 2013, Yang et al. 2013, Jiang et al. 2016, Lawrence 2014 and Nicks et al. 2016). Monitoring results from the strain gauges and the surveying targets have been discussed later in this chapter and conclusions regarding the deformation of the structure have been made from this data.

Inclinometer sensors were installed in the clay foundation to monitor its deformation during construction and operation. The results for the time of construction were presented in Chapter 4. In this chapter, the long term performance of the clay foundation has been evaluated using the measured data. The literature review shows that the stability of the foundation of reinforced structures (including GRS walls and abutments) has been widely investigated by researchers (e.g., Abu-Hejleh et al. 2002, Skinner and Rowe 2005, Wu 2006, Adams et al. 2007, Vennapusa et al. 2012, Helwany et al. 2003, Santos et al. 2013 and 2014, Miyata et al. 2015), due to the critical effect that foundation behavior can have on the overall performance of the structure. Details regarding the long-term performance of the clay foundation including creep

deformation are discussed in this chapter based on the collected data from the inclinometer sensors.

For the GRS-IBS structure studied in this report, vibrating wire pressure cells were in the foundation and abutment to monitor the pressure distribution beneath the RSF and within the abutment close to the beam seat during construction and operation. The results from the literature review on the applied pressure distribution beneath reinforced soil structures (including GRS ones) was presented in Chapter 8. The abutment pressure cells have also been utilized by researchers in the lab and also real field cases to investigate the response of the abutments to the induced pressure by live and dead load (e.g., Abu-Hejleh et al. 2003, Warren et al. 2010, Vennapusa et al. 2012, Iwamoto 2014, Lawrence 2014 and Zhang et al. 2016). The distribution of the pressure in the abutment and its effect on the deformations, lateral pressure, the force in geotextile, pullout resistance and etc. have been evaluated in these studies and some recommendations for changes to the design standards have been made.

The long term performance of the vibrating wire pressure cells showed significant amount of change in pressure beneath the RSF foundation and within the abutment. As shown later in this chapter, the main source of this change is the cell temperature changes. This effect of temperature on VW pressure cells has been addressed by some researchers (e.g., Weiler and Kulhawy 1982, Dunnicliff and Green 1988, Dunnicliff 1997, Sellers 2000 and Daigle and Zhao 2004). The temperature sensitivity of the cells is affected by the fluid inside of it and any temperature increase cause the fluid to expand against the rigid metal plates generating a change in measured

pressure. Dunnicliff (1997) mentioned that simulating field restraints and boundary conditions in the laboratory is not an easy task and significantly different temperature effects may be reported between a cell installed in the field and a cell tested in the laboratory. Dunnicliff and Green (1988) consequently suggested that designing the pressure cell for minimum sensitivity to temperature variation will be the best solution to consider temperature effects. Sellers (2000) utilized simple assumptions and approximations to develop Equations 9.1 and 9.2 to account for the temperature effects on hydraulic pressure cells. The equations consider properties of both the soil and pressure cell, for an embedded earth and a contact pressure cell.

$$CF = \frac{1.5EKD}{R} \qquad \text{for embedded pressure cells} \tag{9.1}$$

$$CF = \frac{3.0EKD}{R} \qquad \text{for contact pressure cells} \tag{9.2}$$

In these equations, *CF* is the temperature calibration factor (kPa/°C), *E* is the modulus of elasticity of the soil in contact with the pressure cell (GPa), *K* is the coefficient of thermal expansion of the fluid inside the pressure cell (which equals 10^{-6}/°C for the fluid that was used), *D* is the thickness of the fluid inside the pressure cell (mm), and *R* is the radius of the pressure cell (mm).

Yang et al. (2001) and Daigle and Zhao (2004) found that the equations developed by Sellers (2000) did not produce accurate temperature correction factors, and estimating an appropriate value for the modulus of elasticity of the surrounding soil is critical in the total pressure cell calibration procedure. Daigle and Zhao (2004) mentioned that calculation of the temperature correction using Equations 9.1 and 9.2

would give a much higher value of CF in this case than the empirical CF values observed from field data. They finally concluded that these equations are only useful in understanding the behavior of pressure cells in installed conditions.

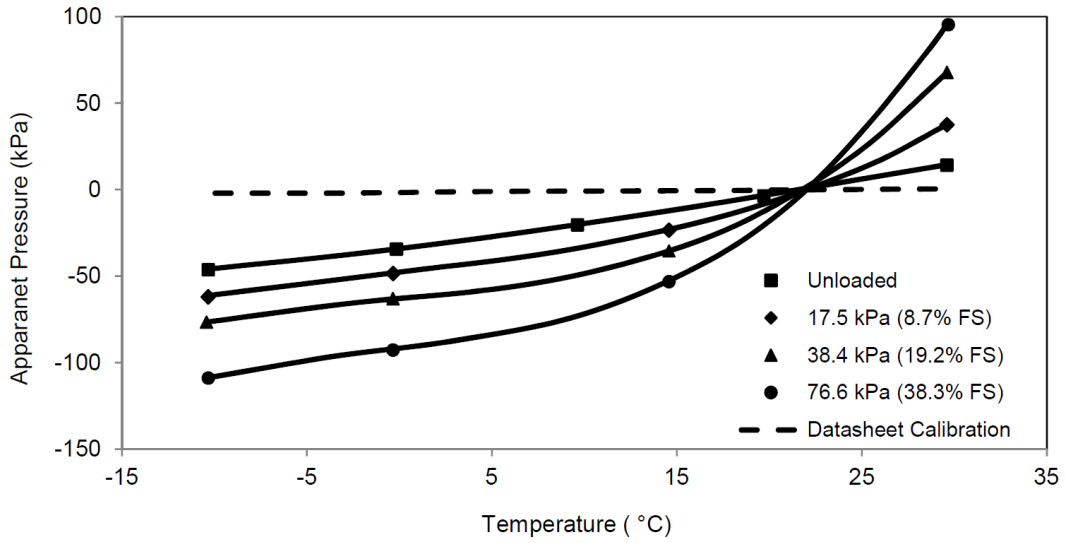

Figure 9.1 Temperature calibration of 228 mm diameter pressure cells under load (Modified After Daigle and Zhao 2004)

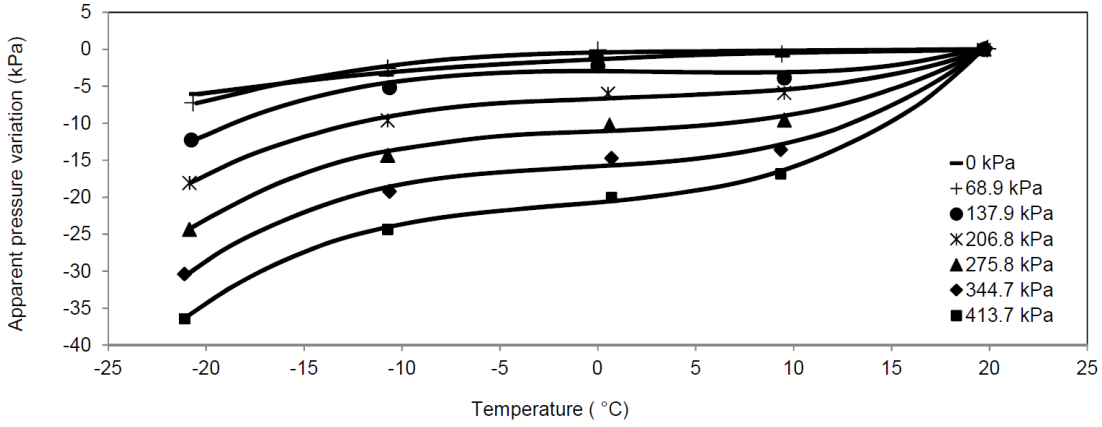

Figure 9.2 Temperature calibration of 230 mm diameter pressure cells under load (Modified after Huntley and Valsangkar 2016)

Daigle and Zhao (2004) and Huntley and Valsangkar (2016) performed temperature calibration tests on unloaded and loaded pressured cells and concluded that the correction factors were dependent not only on temperature, but also on the pressure applied to the cell. As the applied load increased, so did the absolute value of the apparent pressure due to the temperature effect. They both reported a nonlinear relationship between the applied pressure and the temperature in the case of loaded cells and a linear relationship if the cell was unloaded, as shown in Figure 9.1 and 9.2. Daigle and Zhao (2004) also reported that the effect of temperature changes on the measured pressure is more pronounced in case of cells with smaller diameter. Furthermore, Daigle and Zhao (2004) found that the temperature sensitivity of pressure cells appeared to be related to one or more parameters that were specific to the cell. They consequently concluded that all utilized cells in the field need to be calibrated for temperature change effect as each cell is unique.

Given these observations regarding the effect of the cell temperature on the measured pressure response for vibrating wire pressure cells, it is clear that developing an accurate methodology for correcting measured pressure values for temperature is not straightforward, as it depends both on the nature of the cell itself and on its installed condition in the field (i.e., the surrounding soil stiffness). This means that every pressure cell has to be calibrated post-installation in the field over the range of expected temperatures, which is simply not practical for many field projects that are under a tight time deadline.

Another challenge with interpreting the data from the pressure cells was the effect of the air temperature on the readings. According to the literature, air temperature changes induce expansion and contraction of the bridge superstructure (e.g., Abu-Hejleh et al. 2002 and 2006, Puppala et al. 2009, Lawrence 2014, Warren et al. 2014 and Tatsuoka et al. 2016) which as a result changes the pressure between the bridge and the integrated abutment as the bridge moves into and away from the abutment. Although this issue has been widely reported by researchers for integral bridge abutments (e.g., Abu- Hejleh et al. 2006, Efretuei 2013, Horvath 2005, Puppala et al. 2009), there is more limited experience with this behavior for GRS-IBS structures to date. Using the measured data from a GRS-IBS structure, Warren et al. (2010) concluded that the bridge expansion induced by increases in ambient temperature increased the lateral pressure between the bridge and the abutment and decreased the abutment vertical pressure. Warren et al. (2014) stated that the integrated approach in the GRS-IBS was flexible and moved successfully with thermally induced superstructure deformations. According to Warren et al. (2014), within 3.5-year monitoring period, the GRS approach remained engaged with the superstructure as it expanded during temperature increases and contracted during temperature decreases. Using the data from a GRS-IBS constructed in Hawaii, Lawrence (2014) also reported the effect of the bridge expansion and contraction on the measured pressure. With increase in the ambient temperature, the vertical pressure on the installed pressure cells beneath the bridge footing decreased and vice versa. It was concluded that the bridge induced thermal expansion and contraction,

which might have pushed the abutment backward and forward and changed the vertical pressure as a result.

The effect of daily air temperature changes on the pressure in the abutment and beneath the RSF was also observed for the GRS-IBS studied in this report, with the corresponding details being provided later in this chapter.

9.2 Analysis of the collected data by different types of instruments

In this section, the performance of the structure over three years of operation has been investigated using the measured data by different sensors.

9.2.1 Volumetric water content and pore pressure

In order to measure the change in the moisture content of the abutment and its possible effects on the response of the structure, volumetric water content sensors were installed in the west abutment, as shown in Chapter 3.

Figure 9.3 displays the change in water content at the site for each sensor over three years of operation. Sensor t5 stopped working at an early stage of the operational period. As shown in the figure, the abutment water content did not significantly vary for the most of the period. However, a jump in the abutment water content was observed in the winter and spring of each year, with the jump in the second year being even higher than the first year. Since the amount of rainfall precipitation over

the three years was not significantly different (Figure 9.7), this increase might be attributed to the snowfall and the corresponding rate of infiltration.

One possible explanation for this observed behavior is as follows: The snowfall in the first year was appreciably higher than the second and third years. This may have allowed the pattern of water infiltration into the abutment in the second year to be different than the first year. If this is the case, it can be concluded that changes in the abutment water content are likely influenced not only by the amount of precipitation but also by the type of it (rain or snow), and the relative rate of snowmelt from year to year.

Histograms of the volumetric water content measured by the sensors are presented in Figure 9.4. As shown, water contents between 22 to 26 percent were the most frequent in occurrence for all of the sensors. There is a slight increase in water content associated with the highest probability from the top to the bottom. More noise was observed in the data collected by sensor t4, as shown in Figures 9.3 and 9.4. This sensor was close to the water level and was more affected by water fluctuation because of its elevation.

The graphs in Figure 9.3 also show a slight increase in the abutment water content within three years of operation. Consequently, it is recommended that this trend should be monitored into the future to see if it continues, and if it corresponds to any significant influence on the response of the structure. As shown later in this chapter, there is a slight increase in the abutments' strain within three years of operation, of

which a part may be associated with an increase in the abutment water content. As stated in the literature review, an increase in water content changes the matric suction conditions in the embankment as well as the effective stress, and it can induce more deformation to the abutment.

Figure 9.5 shows the minimum and maximum measured water content values in the west abutment. As shown, the maximum water content occurred at the middle elevation.

Figures 9.6 and 9.7 show the water elevation in the river (based on piezometers readings) and the daily accumulated precipitation, respectively for three years of operation. Based on what is shown in these figures and Figure 9.3, the increase in precipitation affects the water level in the river, and also influences the water content in the abutment. In fact, the water content is changing due to the change in precipitation over time and the water level in the river.

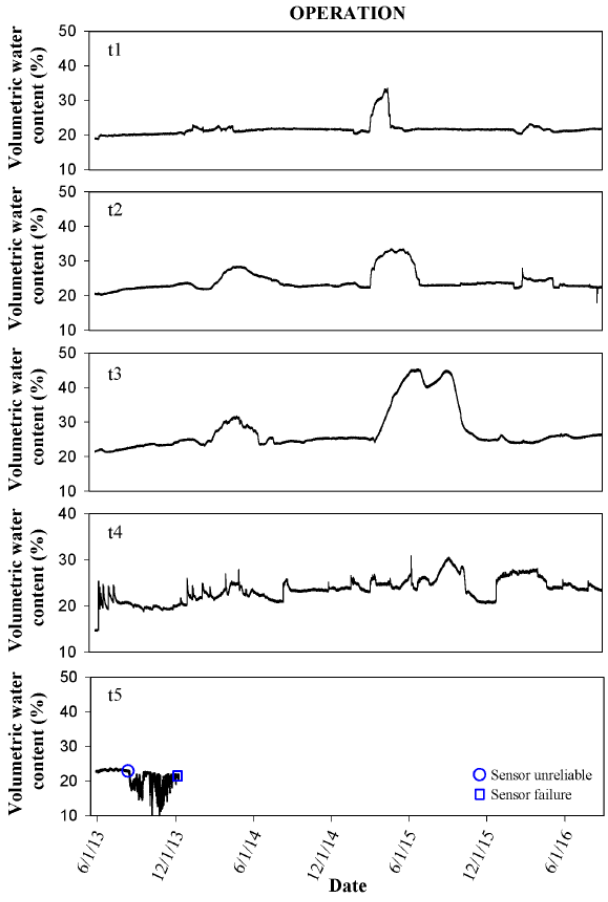

Figure 9.3 Change in volumetric water content over three years of operation

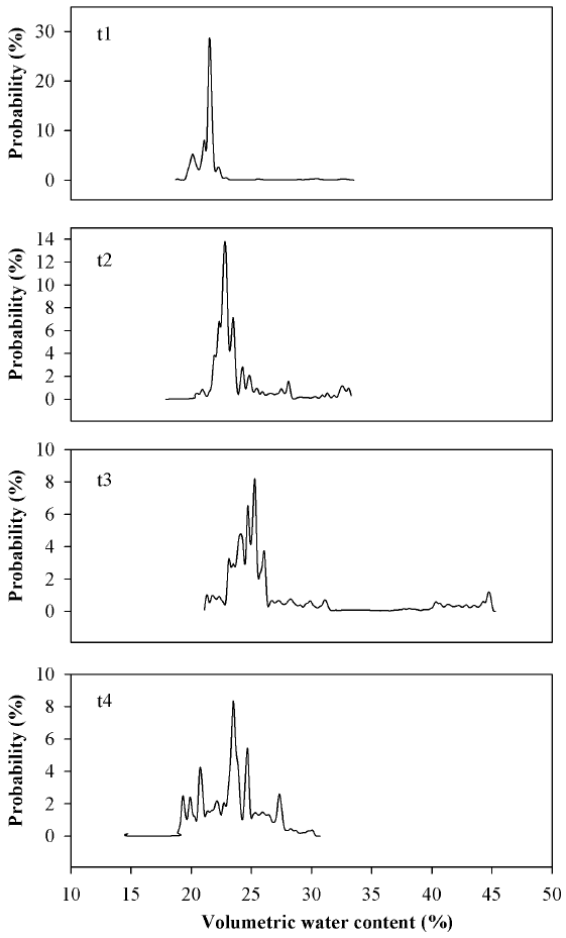

Figure 9.4 Histogram of the volumetric water content of the west abutment considering three years of data

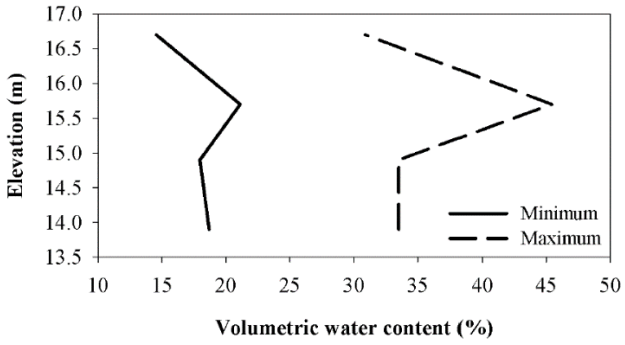

Figure 9.5 Profile of the minimum and maximum measured water content

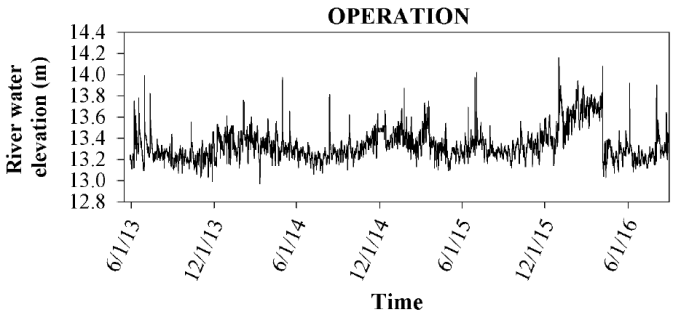

Figure 9.6 Change in river water elevation over three years of operation

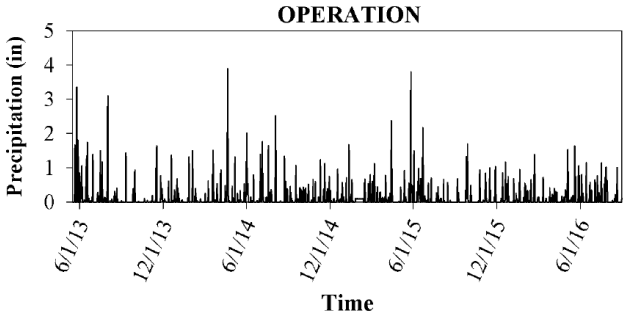

Figure 9.7 Precipitation over three years of operation

The effect of changes in the abutment water content was investigated over three years of operation. As shown in Chapter 5, there was not a strong correlation between the change in the abutment strain and changes in its water content. The results also did not show any strong effect of the increase in water content on the facing deformation and foundation displacements. It can be concluded that the structure's response was not significantly influenced by the abutment water content over the range of changes that were observed, which indicates the pore water pressure did not affect the reinforced soil nor geotextile strength. It should be noted though that the results only

reflect the first three years of operation. The long-term effect of the water on the stability of the abutment needs be examined again after a couple of additional years have passed.

Three vibrating wire piezometers were installed to monitor pore water pressure in the clay foundation during construction and operation as explained in Chapters 3 and 4. Figure 9.8 presents the change in pore pressure for all piezometers during the first three years of operation. No significant changes in pore water pressure was reported during construction. The only generated pressure was due to the change in the river water elevation due to rainfall. It can be inferred that no consolidation settlement occurred during construction. This behavior was expected since the GRS-IBS structure was a replacement for a previous bridge having approximately the same size and weight, which meant that the clay foundation was preconsolidated. As a result, no significant excess pore water pressure was generated and no significant settlement occurred.

Comparing Figure 9.8 with daily accumulated precipitation (Figure 9.7) shows a strong agreement between these two parameters. Any increase in precipitation increases the pore pressures in the structure and the foundation. The corresponding histogram for water level elevation in the river is shown in Figure 9.9. As shown, the difference between the minimum and maximum head of water in the river is only about 1.0 m during three years of operation. The performance of the structure was satisfactory for this water level variation. As shown in Chapter 5, there was not a strong correlation between the water level and the deformation of the abutment. This behavior was also expected, since the abutment was constructed using high quality material with high

draining capacity. However, the monitoring of the structure should be continued into the future to investigate its response to heavier flood incidents that may occur.

The results from the piezometers were also utilized to calculate the effective pressure beneath the RSF, which occurs at the time of abutment construction, bridge placement and live load testing, as was presented in Chapters 7 and 8. The results of the pressure distribution beneath the RSF over three years of operation will be presented later in this chapter.

Based on what was measured by the water content sensors and the piezometers within three years of operation, it can be observed that the structure's stability is not influenced by the presence of either internal or external water. The deformation of the abutments was quite small even for higher water content values and a higher water level in the river.

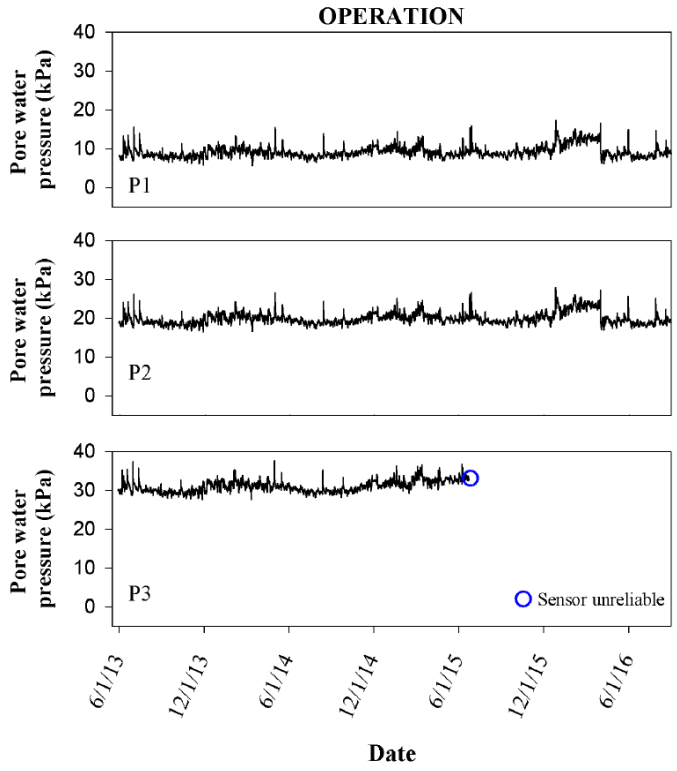

Figure 9.8 Measured pore water pressure by piezometers during three years of operation

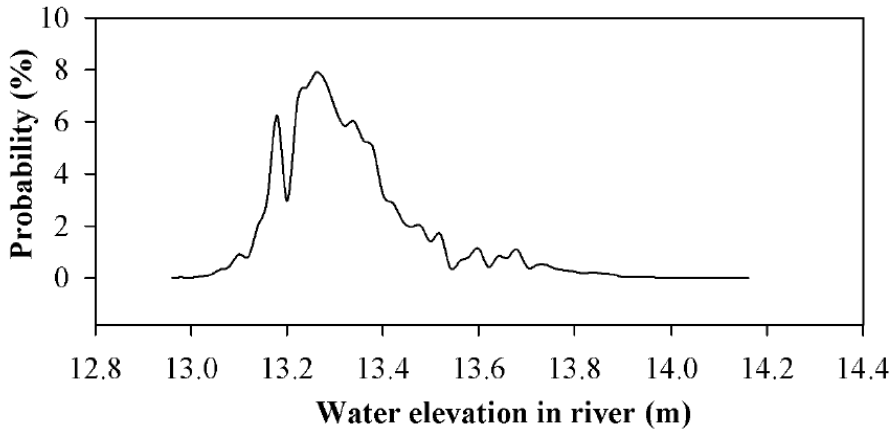

Figure 9.9 Histogram of the water elevation in the river considering three years of data

9.2.2 Temperature in the abutments measured by the thermistors

The model number used for the installed thermistors was YSI 55000, as provided by Therm-x. These thermistors provide "highly accurate and stable temperature sensing for applications of temperature measurement, control, indication and compensation" (Therm-x 1998). These thermistors have a high temperature range, up to 200°C, and improved stability compared to epoxy or plastic encapsulated thermistors.

As mentioned in Chapters 3 and 4, there are 50 thermistors installed in this project (25 per abutment). The thermistors were installed at the location of the strain gauges to investigate the effect of the temperature changes on the gauge reading.

Figure 9.10 presents the recorded thermistor temperatures for all of the instrumented layers of the west abutment (A to E) for the first three years of operation. The corresponding data for the east abutment, which were collected manually, are presented in Figure 9.11.

The temperature changes in the west and east abutments are similar and following the same trend. The seasonal temperature change is more pronounced from the bottom to the top of the abutment. While the temperature in Layers A and F is mostly changing between 10℃ and 20℃, the thermistors in layers E and J are ranging from 0℃ to 35℃ , with a "noisier" signal that fluctuates more on a daily basis. There are two reasons for this phenomenon: First, the layer E is closer to the ground surface and is exposed more directly to changes in the air temperature. Second, layer A is under water

most of the time and its temperature is more uniform than the other layers which are not submerged. The temperature in Layers B and G is mostly changing between 5℃ and 20℃ while the corresponding values for Layers C and H are 0℃ and 23℃. Finally, the temperature variation in Layers D and I is between 0℃ and 26℃.

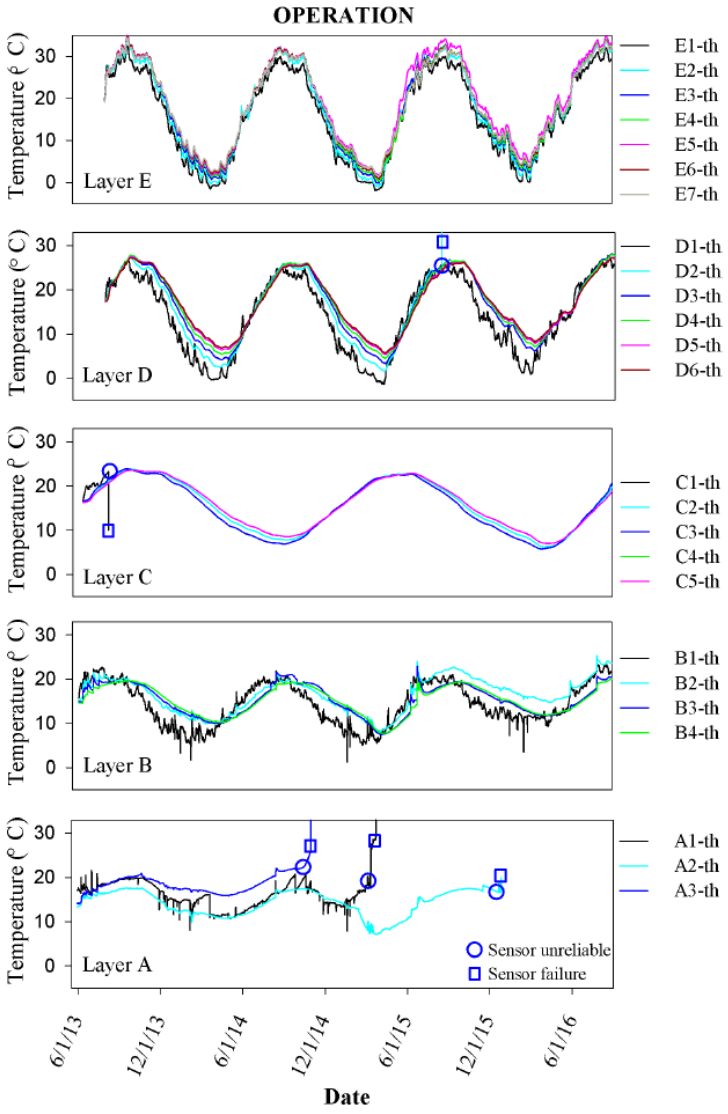

Figure 9.10 Temperature recorded by the thermistors in the west abutment over three years of operation

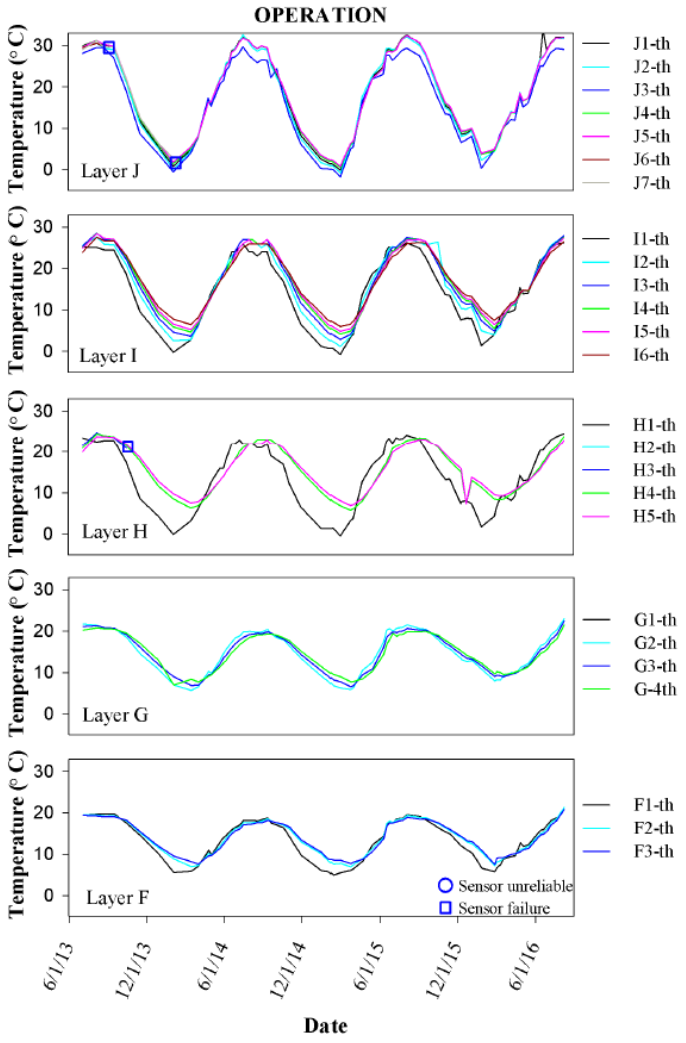

Figure 9.11 Temperature recorded by the thermistors in the east abutment over three years of operation

As shown in these figures, the majority of the sensors are still working after three years which indicates that the process that was used for waterproofing the thermistors was successful. The details regarding lost thermistors were presented in Chapter 4.

In order to investigate the temperature distribution in the abutment, the data from the west abutment were utilized to prepare temperature contour plots. Figures 9.12 and 9.13 display the temperature contours for a hot and a cold day (1 August 2013 and 20 February 2013) for every four hours. As shown, the daily temperature changes in the abutment are negligible while there is an obvious difference between the hot and cold day temperature changes. In the hot weather, the maximum temperature is measured at the top and temperature decreases from the top to the bottom. In different elevations, the maximum temperature does not occur close to the facing wall and the temperature behind the wall becomes nearly constant, specifically for the upper elevations. On the other hand, in the cold weather, the minimum temperature occurs at the top, with the maximum at the bottom of the abutment. The temperature increases backward into the abutment in this case, without becoming constant.

Since the hot and cold weather contours were different, a separate series of plots were prepared to investigate the monthly changes of temperature in the abutment, as shown in Figure 9.14. The temperature data of the first day of each month at 2:00 p.m. was considered in these plots. The gradual change in the shape of the contours can be observed in this figure through the different months. As shown, the temperature distribution in the abutment does not follow the same trend during different months and seasons.

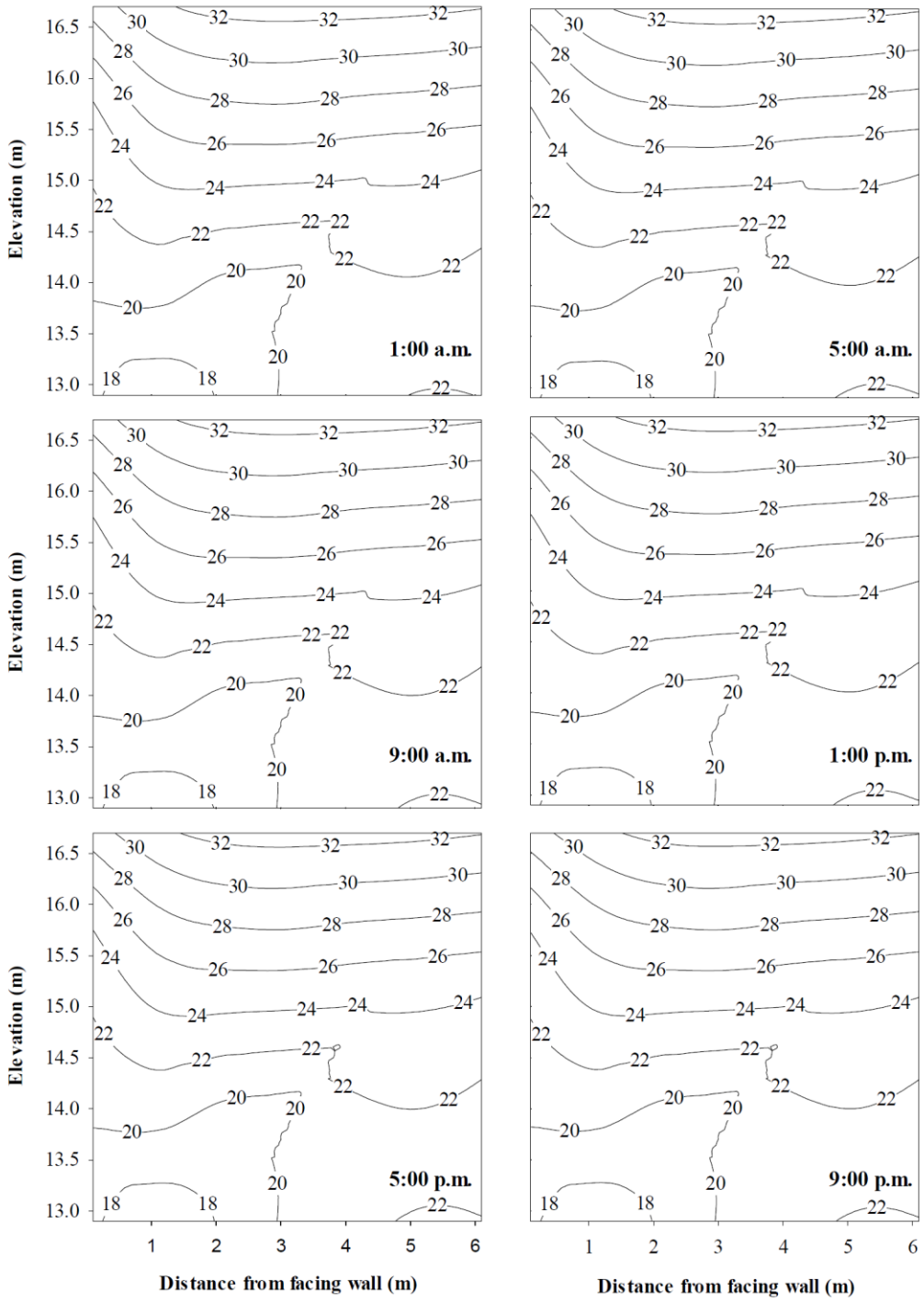

Figure 9.12 The temperature contours in the west abutment on 1/8/13 in different hours

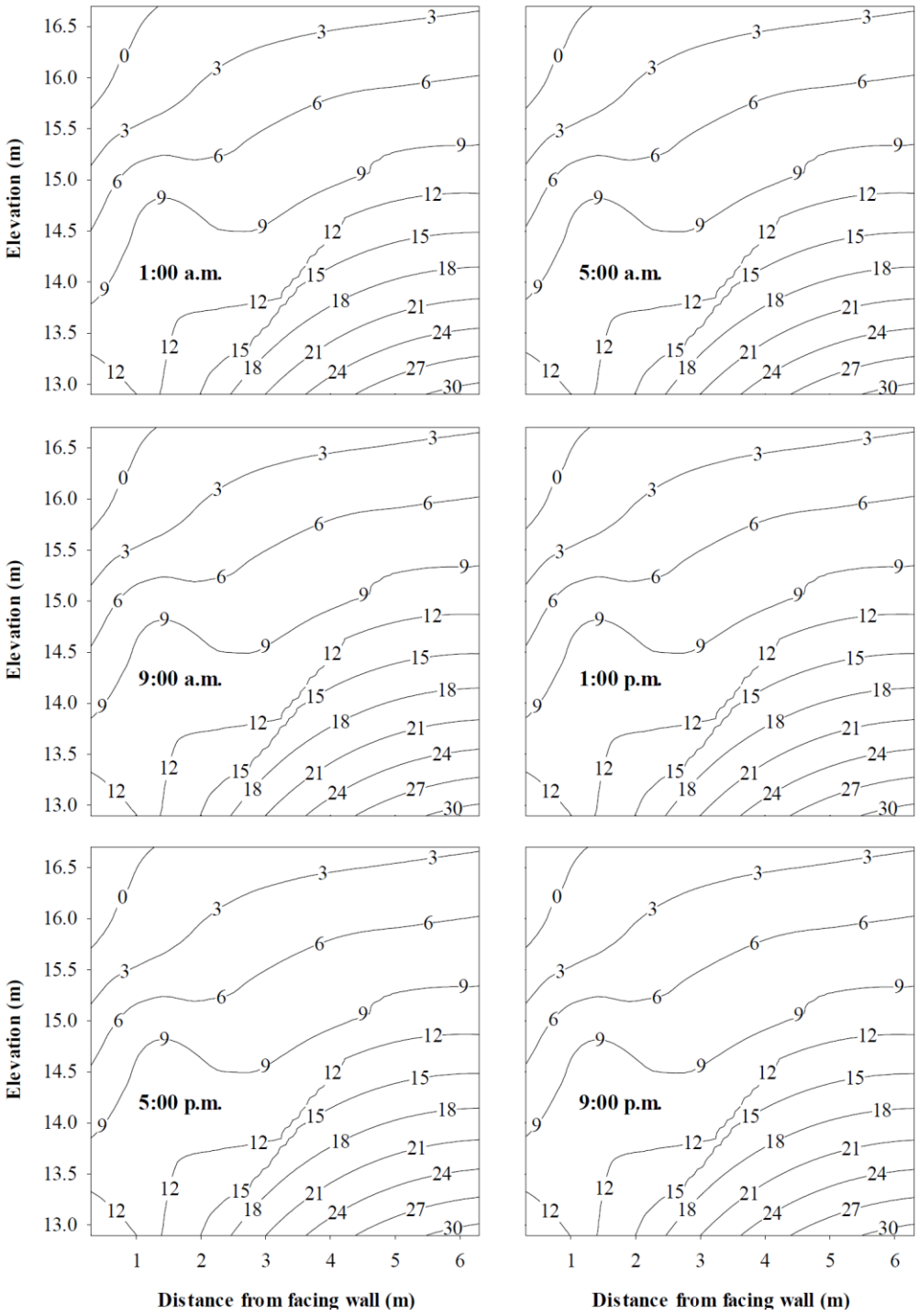

Figure 9.13 The temperature contours in the west abutment on 2/20/14 in different hours

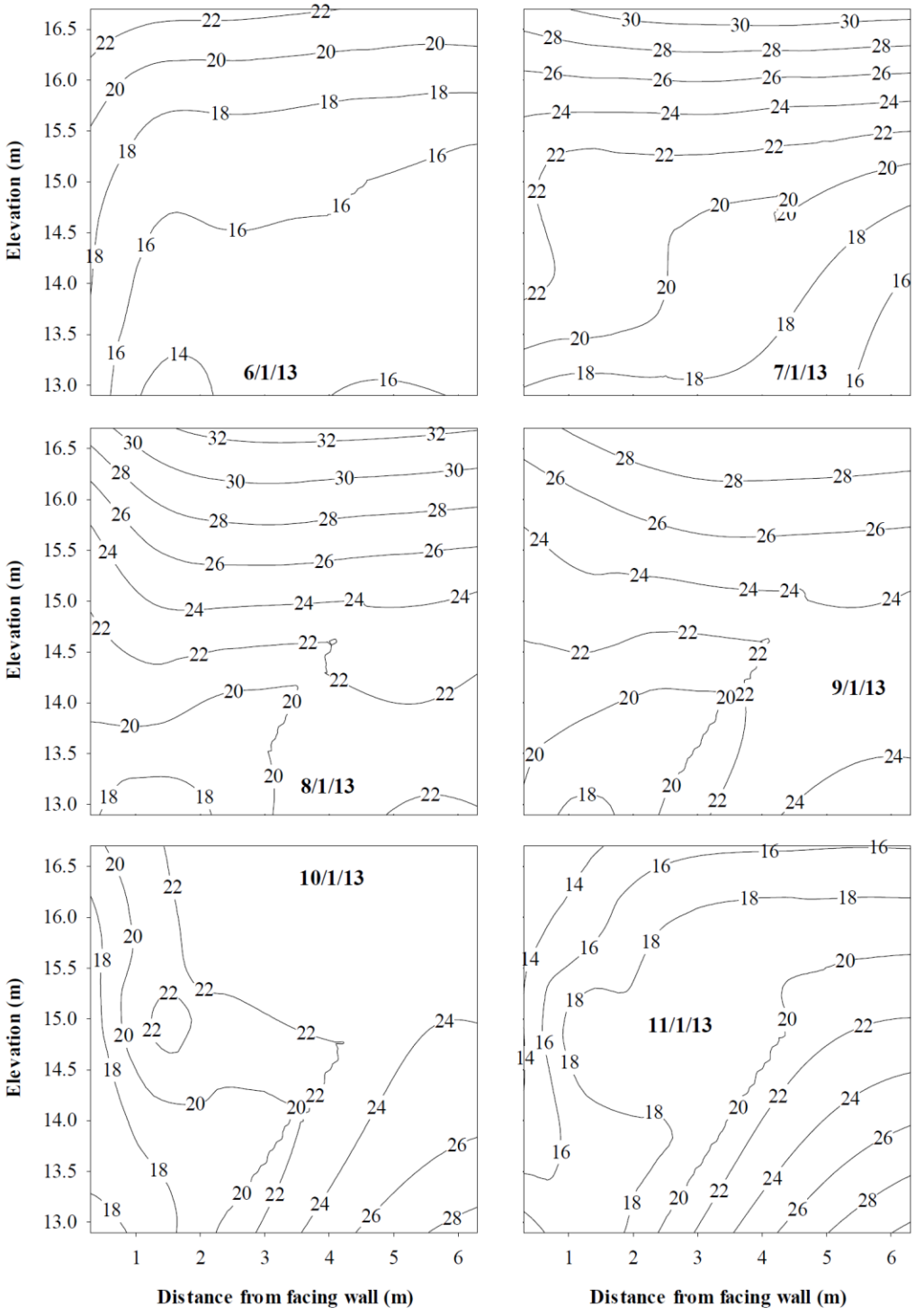

Figure 9.14 The temperature contours in the west abutment on the first day of each month for one year

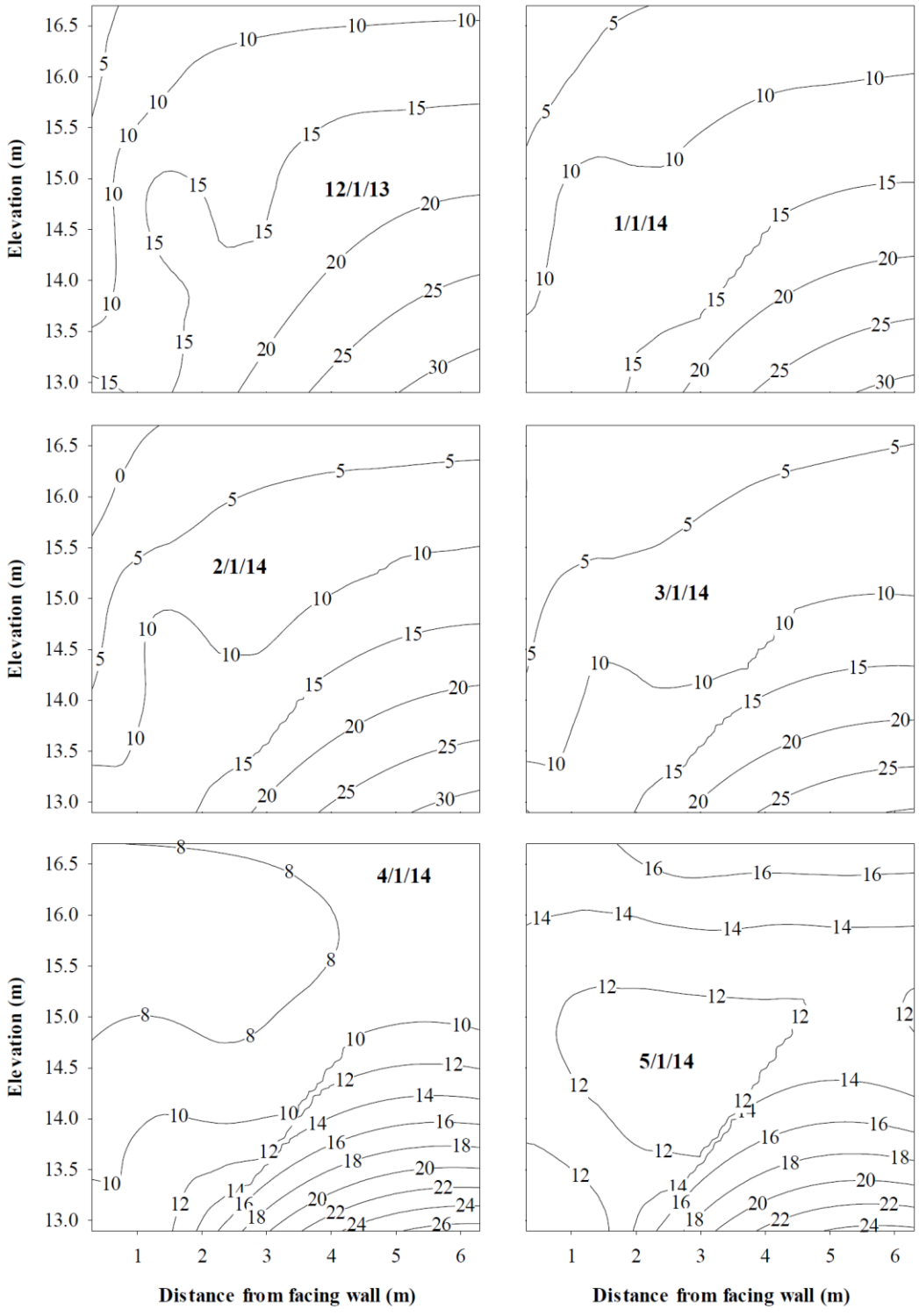

Figure 9.14 Continued

Figure 9.15 shows the outside temperature over the first three years of operation. Comparing Figures 9.10, 9.11 and 9.12 indicates that the temperature in the abutment is changing in response to changes in the ambient air temperature. In general, the changes in temperature inside the abutment are much smoother than what occurs outside the abutment. This is rational because inside the abutment is not directly exposed to the air, and temperatures within the abutment respond more gradually due to the intrinsic thermal inertia of the abutment, i.e., the time it takes for the soil mass of the abutment to change its overall temperature in response to an external forcing temperature at its boundaries. Not surprisingly, the thermistors which are closer to the facing wall (the Th-1's) are experiencing more temperature fluctuation because of their location.

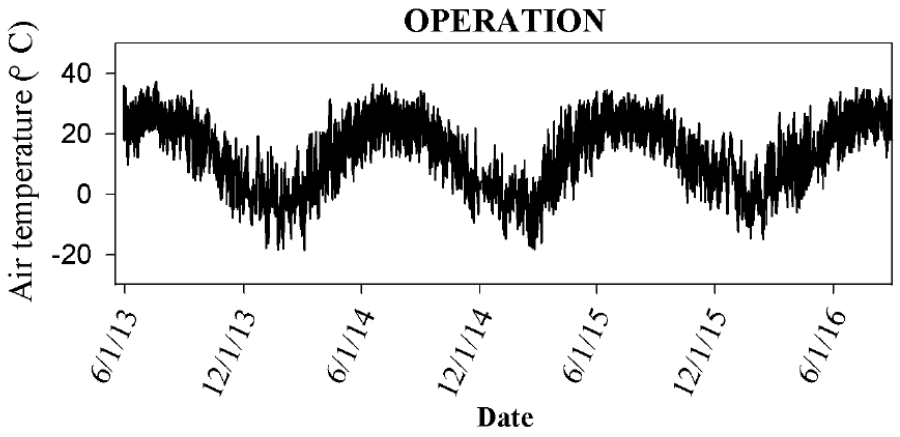

Figure 9.15 Air temperature changes over three years of operation

It can also be observed that seasonal changes in temperature for the upper geosynthetic layers are more in agreement with the air temperature because these layers are closer to the ground surface. For this reason, the temperature extremes in Layer E

track much more closely with the air temperature than the measured values for the underlying geosynthetic layers. The soil peak temperature occurs after the air peak temperature, with the lag between these two values becoming more pronounced backwards and downwards (i.e., further into the abutment).

9.2.3 Strain in the abutment measured by the strain gauges

Values of geosynthetic strain measured in the abutments during construction and load testing were presented in Chapters 4 and 7. The effect of temperature on the long term performance of the gauge readings was discussed in Chapter 6 and the long term strains measured for the strain gauges installed in the west abutment were corrected for the effect of temperature following the methodology presented in Chapter 6; the resulting corrected strains are presented in Appendix G. Generally, as shown in Appendix G, the developed strains in the abutments were very low and the maximum corrected strain did not exceed 0.5% in both abutments. This indicates the relatively high strength of the abutments under the service load conditions. In order to evaluate the development of creep in the west abutment, Figure 9.16 and 9.17 show the measured strain for each instrumented layer at the beginning and after three years of operation (or the last time when the sensor was working properly). Sensors C1-s and C3-s stopped working at the beginning of operation and their corresponding data are not presented in Figure 9.17.

As shown in Figures 9.16 and 9.17, small amounts of long-term deformation were developed in the abutment at different elevations. The creep measured by the sensors in Layer A was generally higher than the other layers. Since this layer has been submerged most of the time, its associated measured data may not be reliable. The other sensors reliability should also be considered in the creep analysis. As shown in Appendix G, in some cases the changes in strain were abrupt which likely does not correspond to real creep behavior. It is more likely that sensors that exhibit a sudden change in behavior may have stopped working properly; it is well-known that fabric-bonded strain gauges tend to have a relatively high rate of failure compared to other in situ sensor technologies (e.g., Warren et al. 2008).

In order to compare the measured strain by the long and short gauges, another set of graphs were provided for strains measured at the beginning of operation (Figure 9.18). As shown, in some cases the long gauges measured higher strain and in some other cases the short ones did so. From these results, it can be observed that there is no clear trend that was observed for the strains measured by the long- and short-gauges relative to each other; consequently, no clear conclusion can be made on strain reading difference with respect to gauge type.

Finally, a creep analysis was conducted to evaluate the effect of gauge type on measured creep (Figure 9.19). This figure shows the difference between the final and initial readings for both the long and short gauges. As shown, the long gauges have measured higher creep deformation in most of the cases (except one case). Part of this difference might be associated with the respective ability of the gauges to measure creep

accurately. The gauges' material and their attachment technique using different bonding agents may have affected the gauges' ability to measure creep accurately. In particular, at this small of a strain level, it is possible that at least some of the strain that is being observed is actually creep in the adhesive between the gauge and the geosynthetic, rather than creep in the geosynthetic itself. It seems that the long gauges are more susceptible to damage and creep in the long term and their data are less reliable; additional data is needed to confirm if this initial observation and conjecture is substantiated over the long term. The water in the river appeared to be destructive to both the long and short gauges in the lowest instrumented level (Layer A), inducing a gauge failure rate that was higher than what was observed for instrumented layers located above the river elevation. From the data that was recorded (and later smoothed), it was estimated that the creep that is occurring in the abutment was generally less than 0.1 percent over three years (on average). Strain gauges that have failed over the three year period (A1-l, A1-s, A2-l, A2-s, A3-l, A3-s, B1-l, B2-s, B3-s, B4-l, C1-s, C2-l, C2-s, C3-l, C3-s, C4-l, C4-s, D1-s, D2-l, D2-s, D3-s, D5-l, D5-s, D6-l, D6-s, E4-l, E4-s, E6-s, E7-l, F1-s, F1-l, H3-s, H3-l and I4-s) generally have high measurements of final strain thus resulting in abnormally large values of creep. However, these measurements are deemed unreliable due to the sensor failure.

Since the data for the east abutment were collected manually at a much lower frequency of data acquisition than for the west abutment, the data correction procedure which was explained in Chapter 6 could not be accurately applied to the east abutment. However, the long term collected data for the east abutment generally

followed a similar trend in behavior to the west abutment, with the maximum strain for the east abutment also being less than 0.5 percent. The average amount of creep in the east abutment did not exceed 0.1% as well. The continuous increase in the abutment water content which was shown in Figure 9.3 may have also induced some strain in the abutment.

9.2.3.1 Force in the reinforcement element

If the relationship between the force and strain in the geotextile is known (Figure 9.20, which was drawn using geosynthetic test data provided by the manufacturer) then the force in the geotextile can be calculated from the measured strain. If the maximum strain in the geotextile is considered as 0.5% based on the measured data then the maximum developed force in the geotextile will be about 5 kN/m based on Figure 9.18. The strength of the geotextile at 2% strain should not be less than 23.3 kN/m, which was calculated from the geosynthetic's ultimate strength determined from ASTM D4595, divided by 3.5 to account for various factors that can affect the installed strength of the geosynthetic, as shown in Chapter 3. Under the applied working load conditions, the factor of safety against the reinforcement stresses exceeding this level of acceptability is therefore:

$$F.S_{\text{reinf. failure}} = \frac{23.3}{5} = 4.7 \tag{9.3}$$

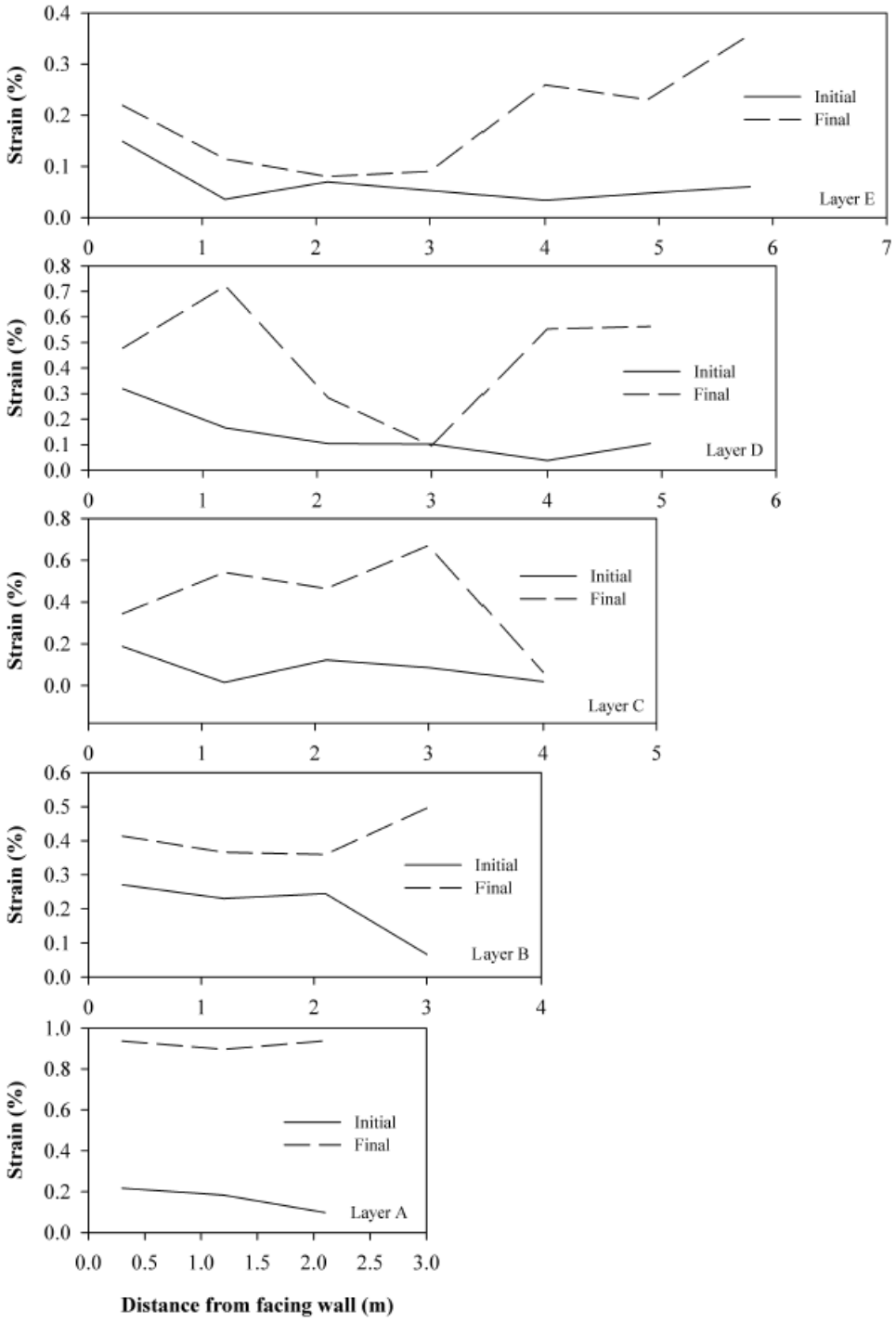

Figure 9.16 The initial and final strain readings by the long gauges over three years of operation

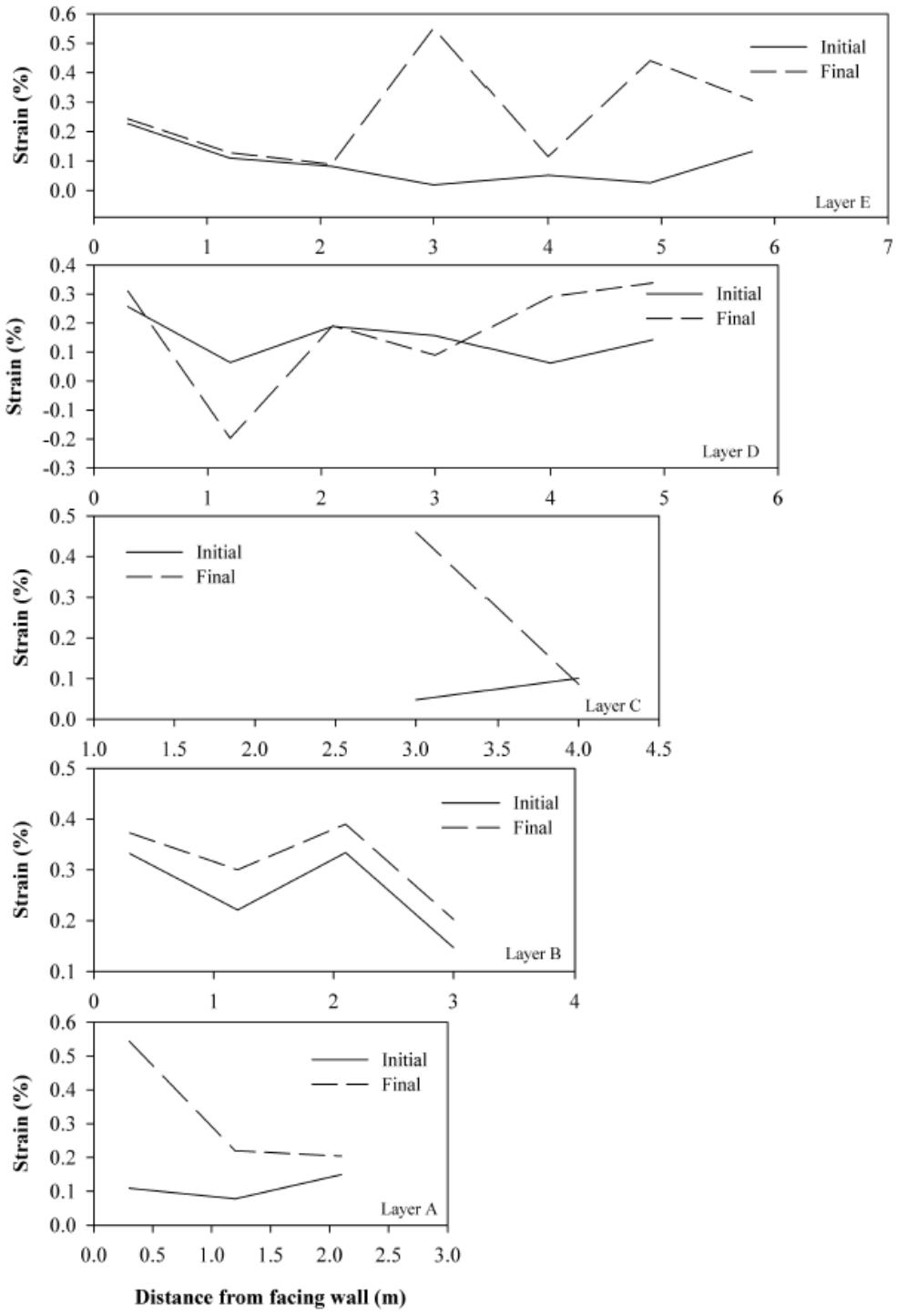

Figure 9.17 The initial and final strain readings by the short gauges over three years of operation

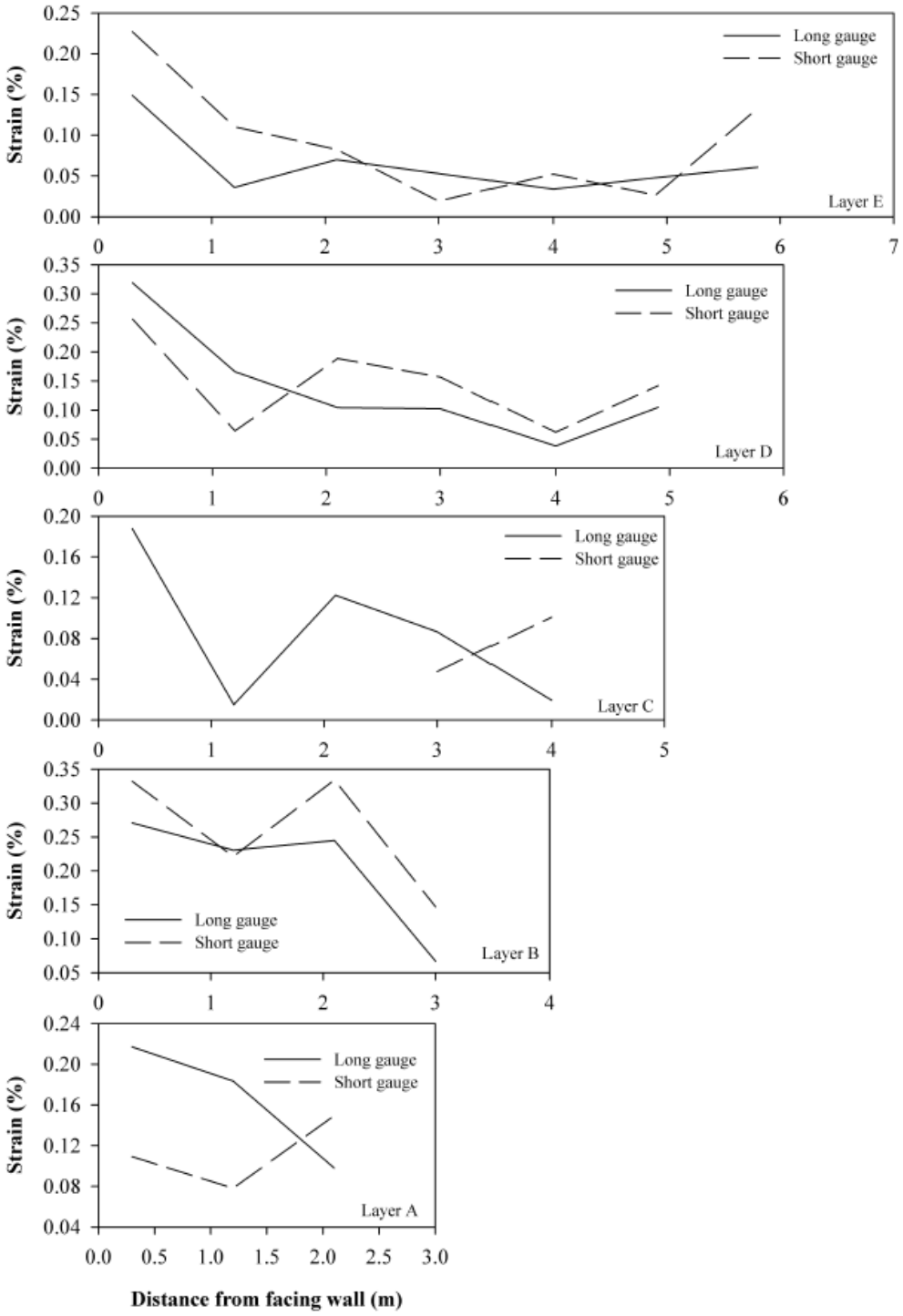

Figure 9.18 The relative strain readings measured by the long and short gauges at the beginning of operation

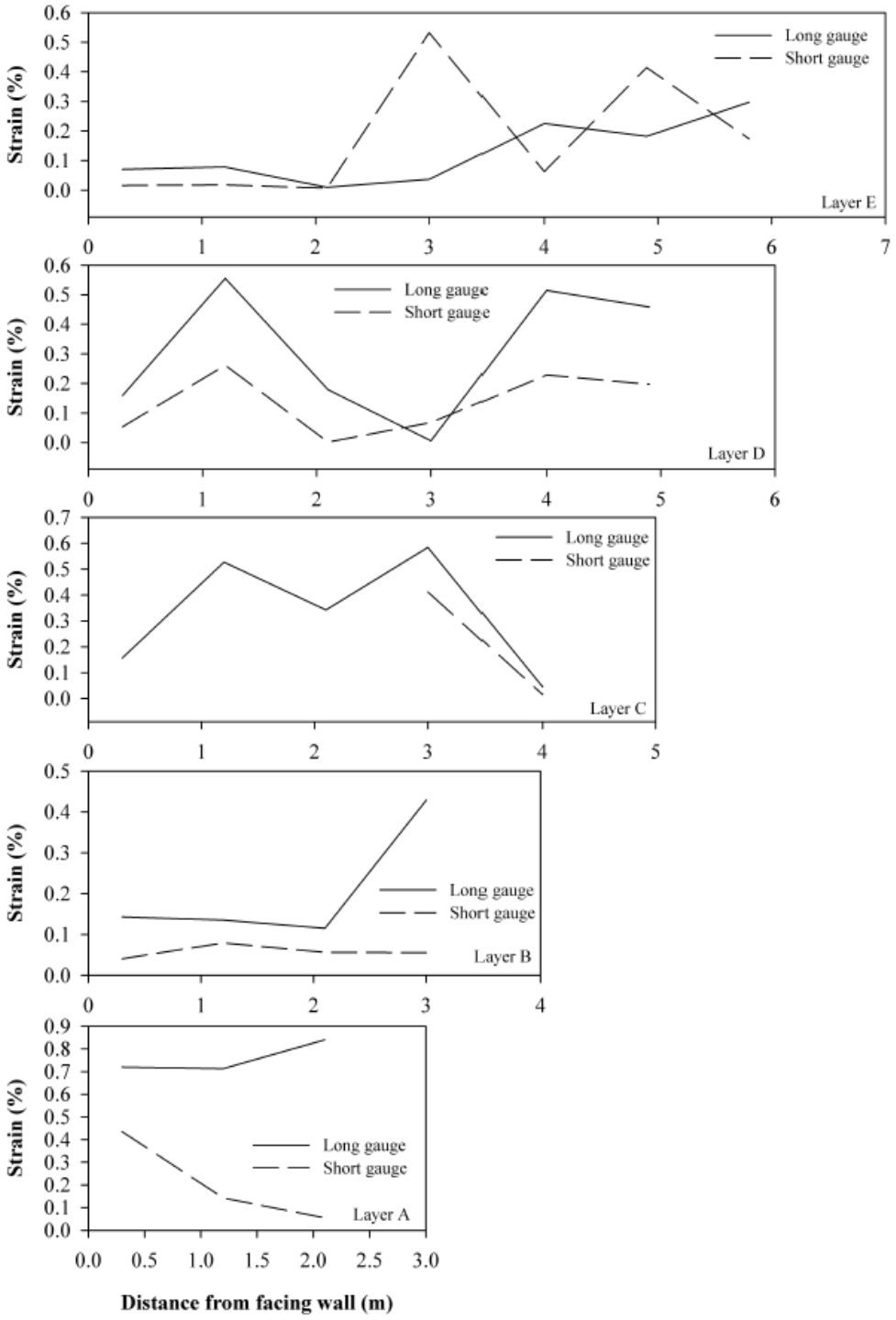

Figure 9.19 The creep strain (change in strain from initial to final conditions) measured by the long and short gauges over three years of operation

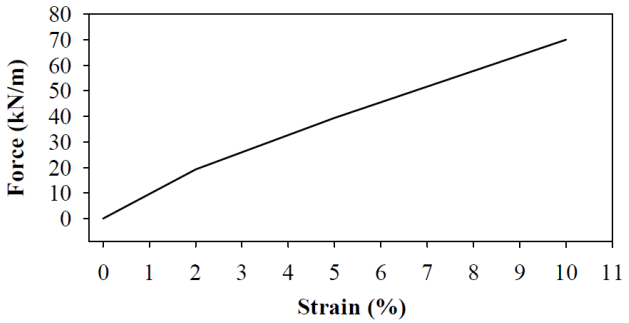

Figure 9.20 Relationship between the strain and force in the utilized geotextile, based upon data provided by the manufacturer

9.2.4 Facing wall movements measured by the surveying operation

The data collected during live load testing and over three years of operation were presented in detail in Chapter 4. It was shown that the measured deformation for the section beneath the bridge centerline was similar to the other sections. Generally, the facing wall deflection and settlement were small within the first three years of operation. The maximum measured settlement and also the lateral wall deflection were both less than 12 mm, a very low amount of overall deformation.

Adams et al. (2011) noted that for GRS-IBS construction it is common for most of the deformation to occur during the construction of the abutments, with an additional pronounced amount of movement occurring upon placement of the bridge superstructure. The collected data showed that there was a slight increase in settlement within three years of operation, relative to what was observed with the live load testing. It should also be mentioned that the targets were installed on the abutments at the end

of construction and before the bridge placement which means the measured deformation did not include the deformation induced by abutment construction.

Based on measured data by the targets, Figures 9.21 and 9.22 presents the contours of the east and the west wall deflection within three years of operation. As shown, the contours do not follow any specific trend monthly or annually. As noted earlier, the precision of the surveying operation was not high enough to capture very small displacements. As shown in these figures, the maximum lateral deflection was 12 mm, which was measured on the east wall.

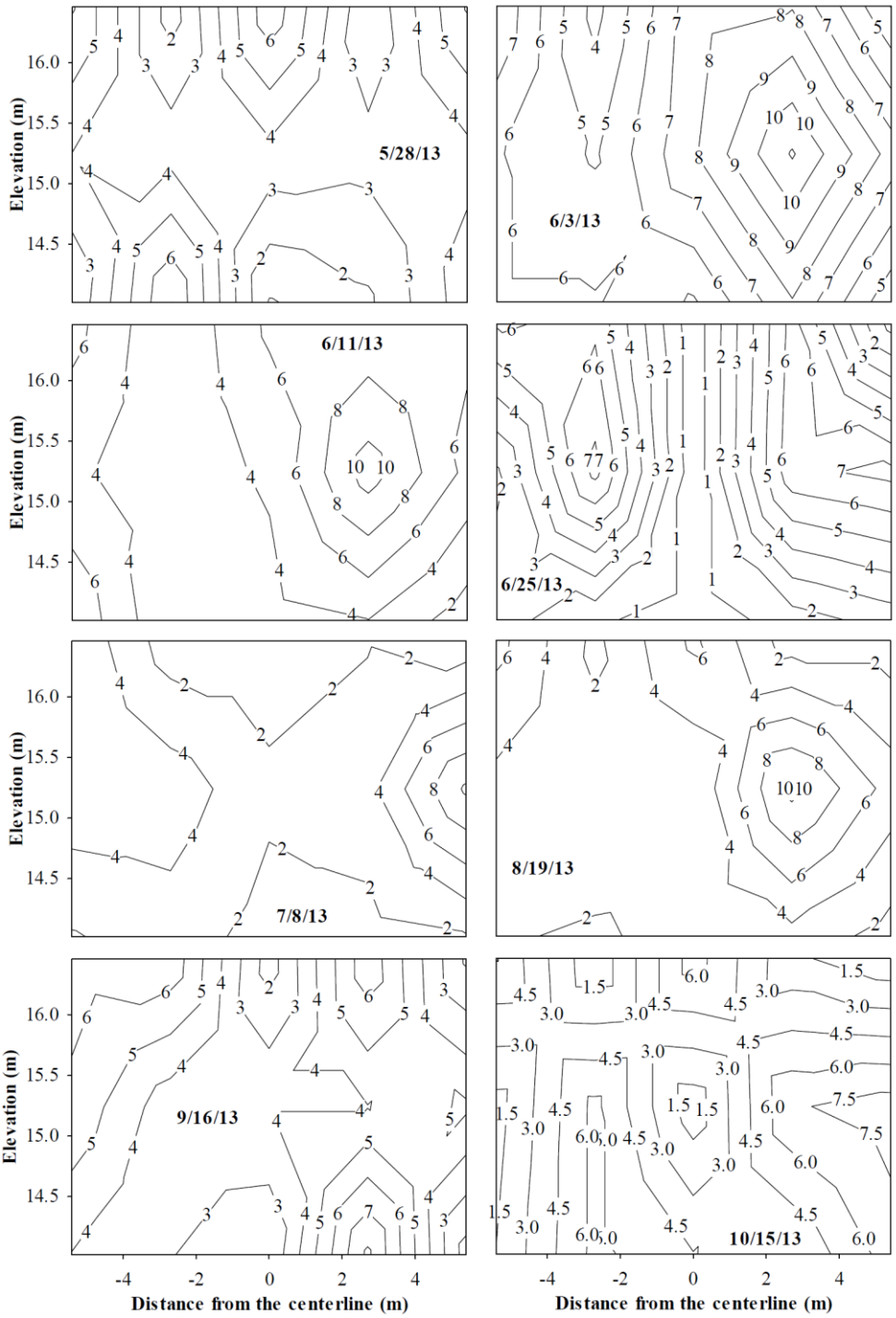

Figure 9.21 Contour plots of the east facing wall deflection over three years of operation

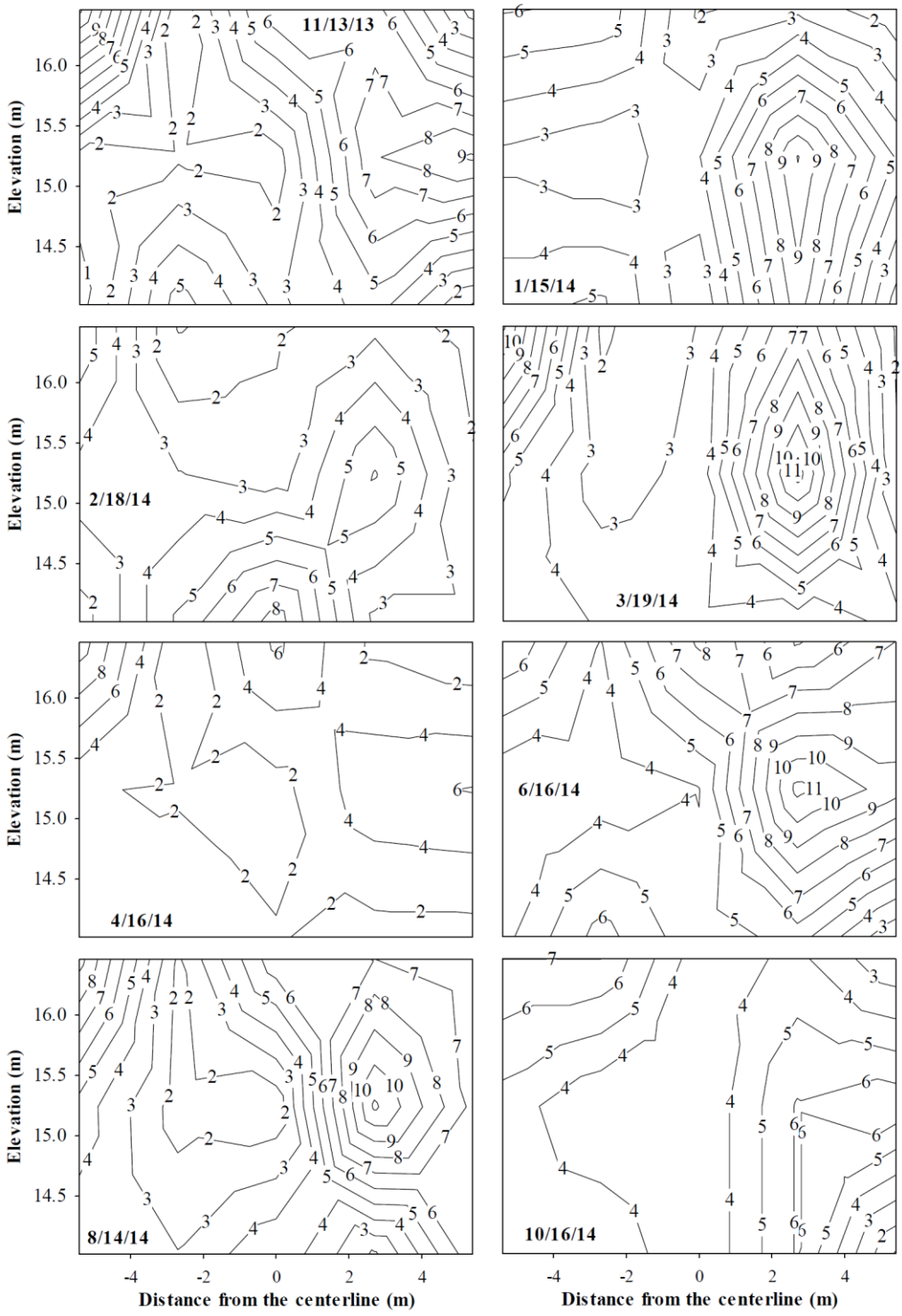

Figure 9.21 Continued

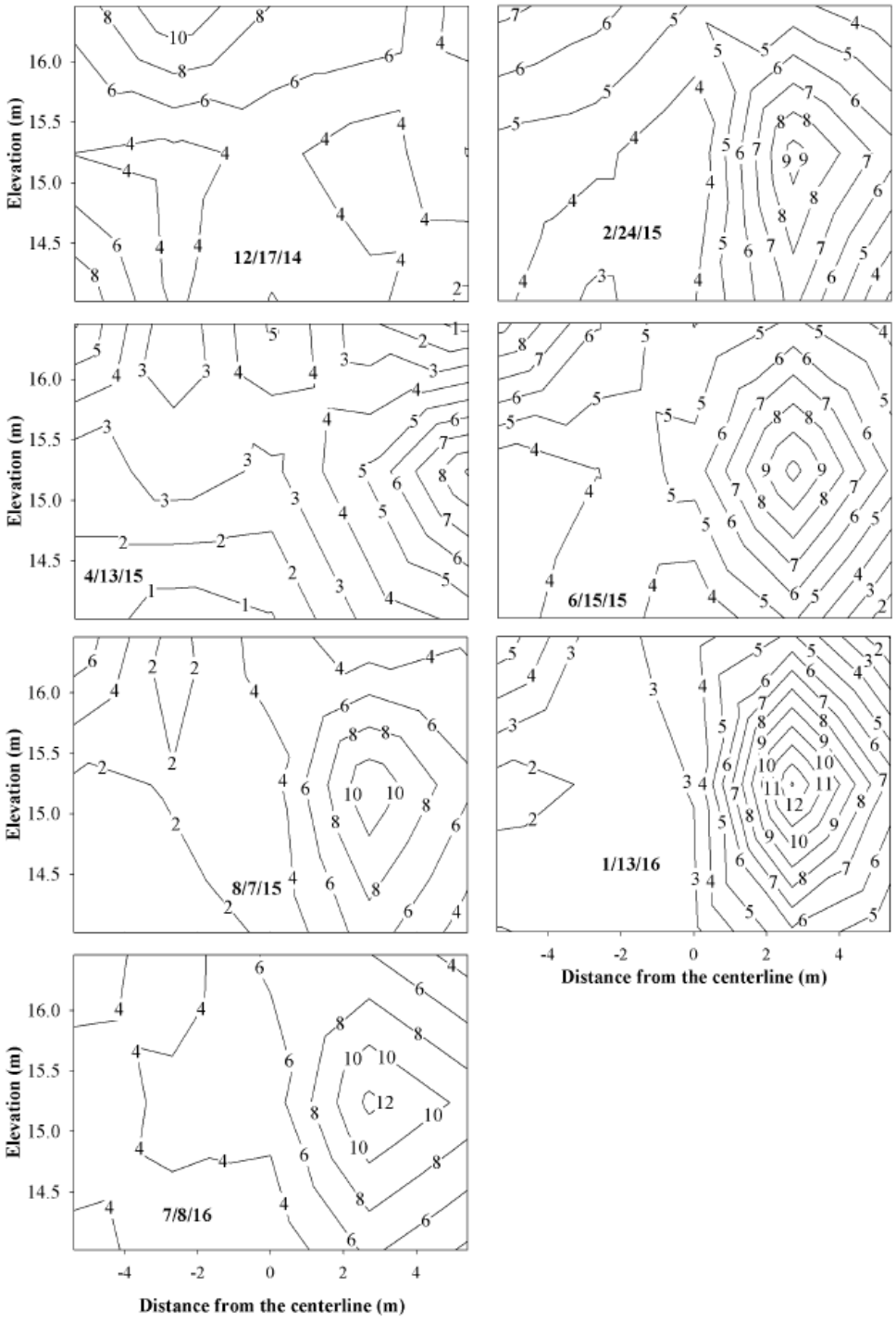

Figure 9.21 Continued

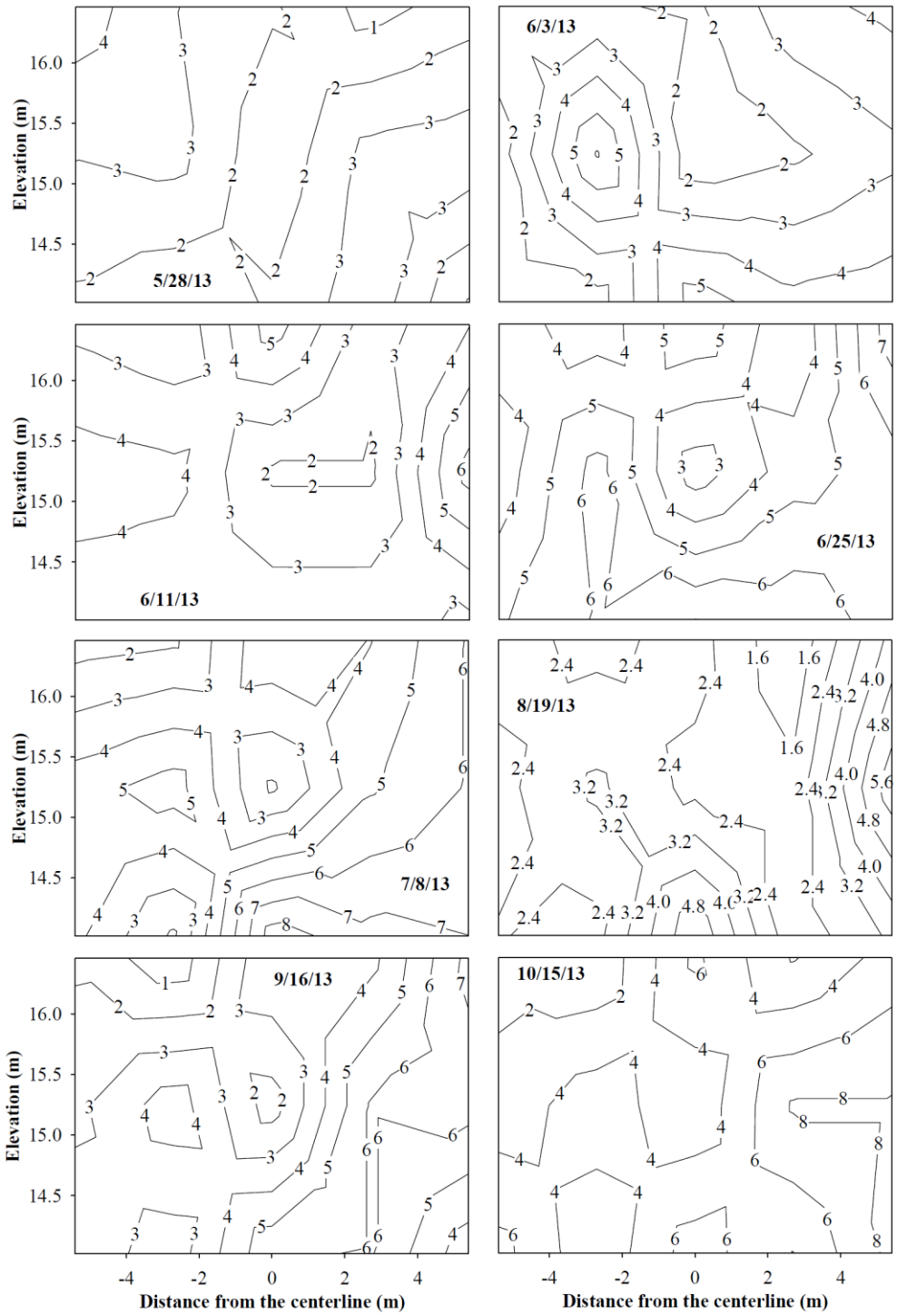

Figure 9.22 Contour plots of the west facing wall deflection over three years of operation

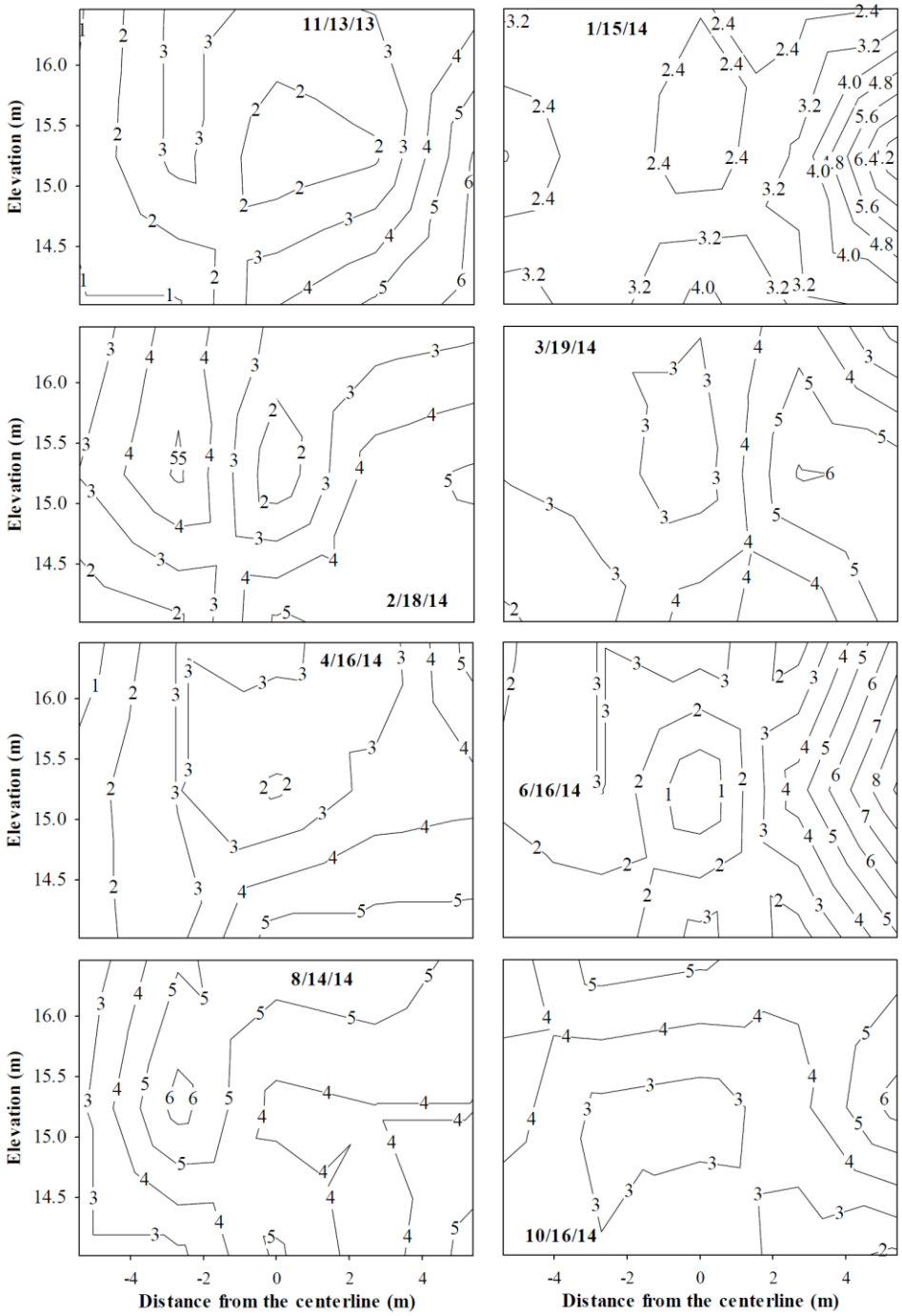

Figure 9.22 Continued

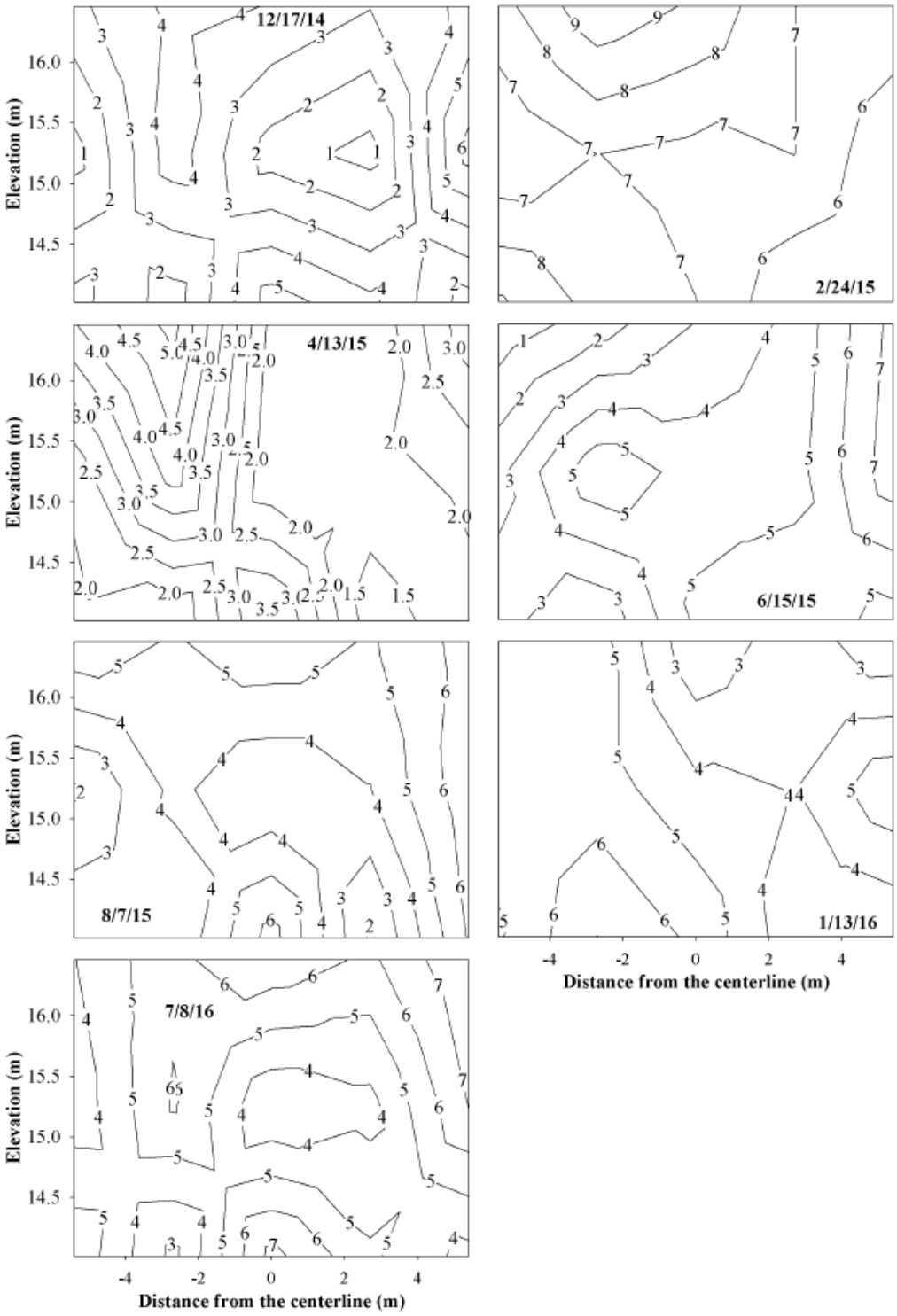

Figure 9.22 Continued

Figures 9.23 and 9.24 show contour plots of the east and west facing walls' settlement over three years of operation. Again here, the change in the facing walls settlement does not follow any specific trend monthly and annually. The maximum settlement was about 12 mm, as shown in these figures.

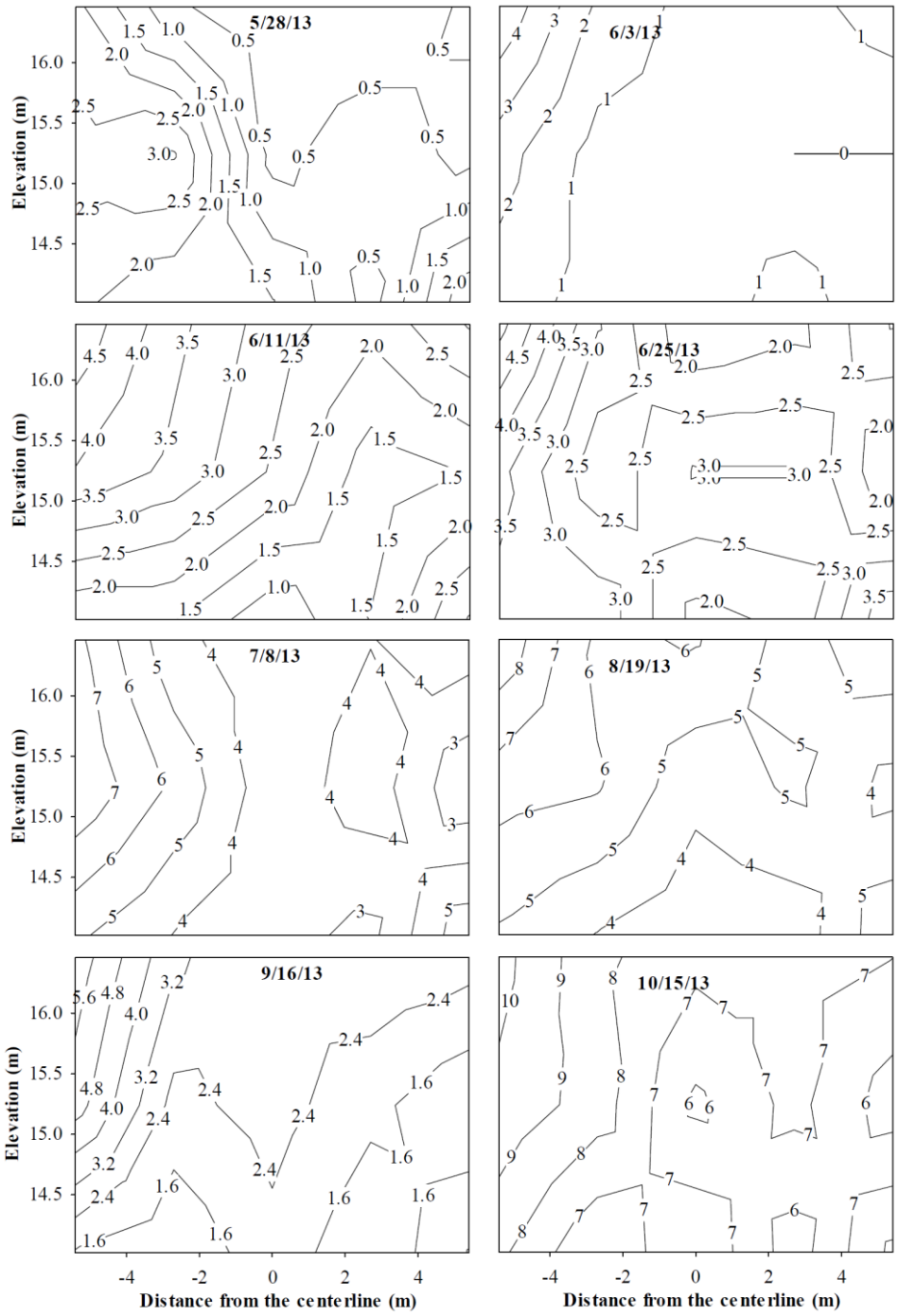

Figure 9.23 Contour plots of the east facing wall settlement over three years of operation

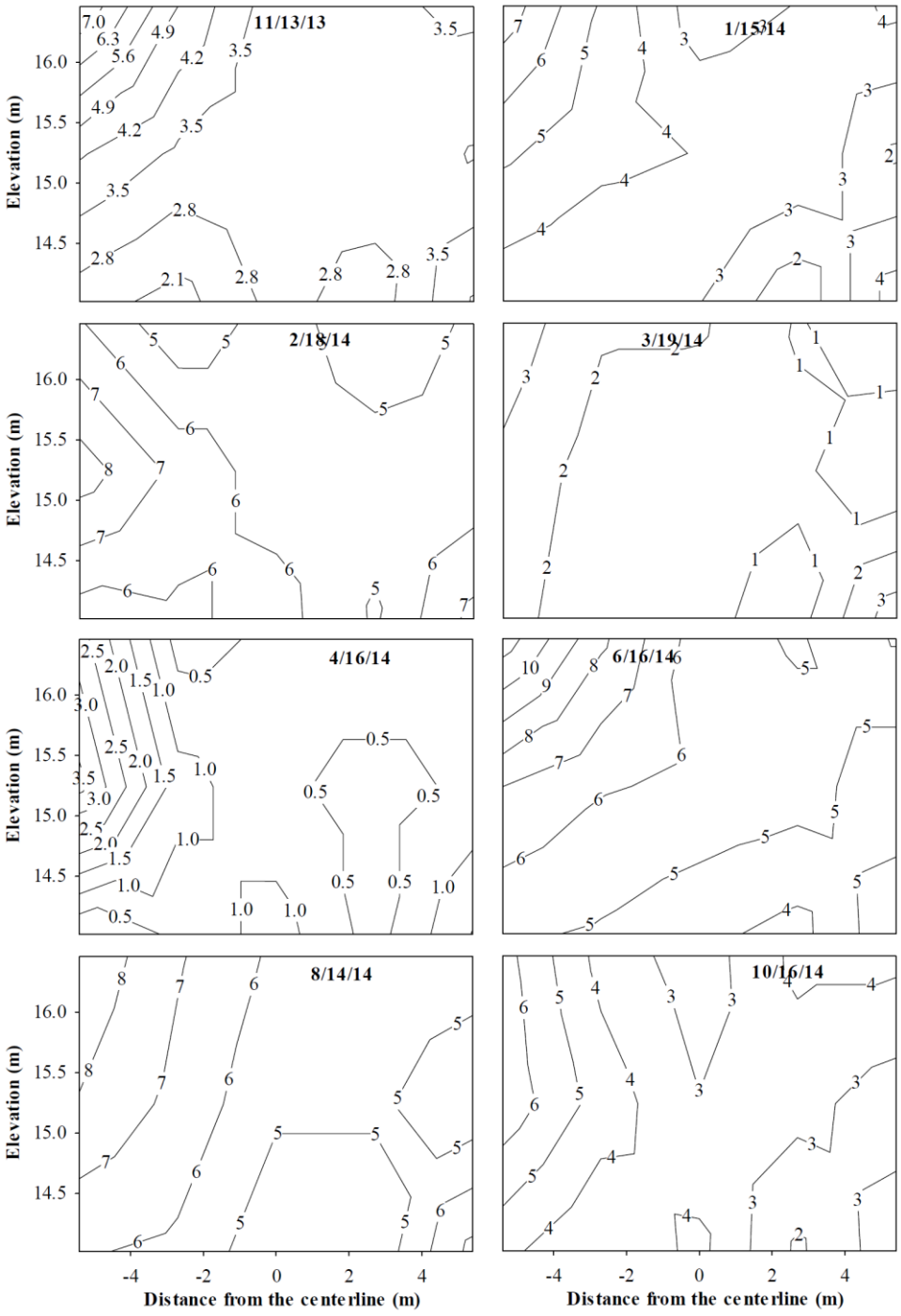

Figure 9.23 Continued

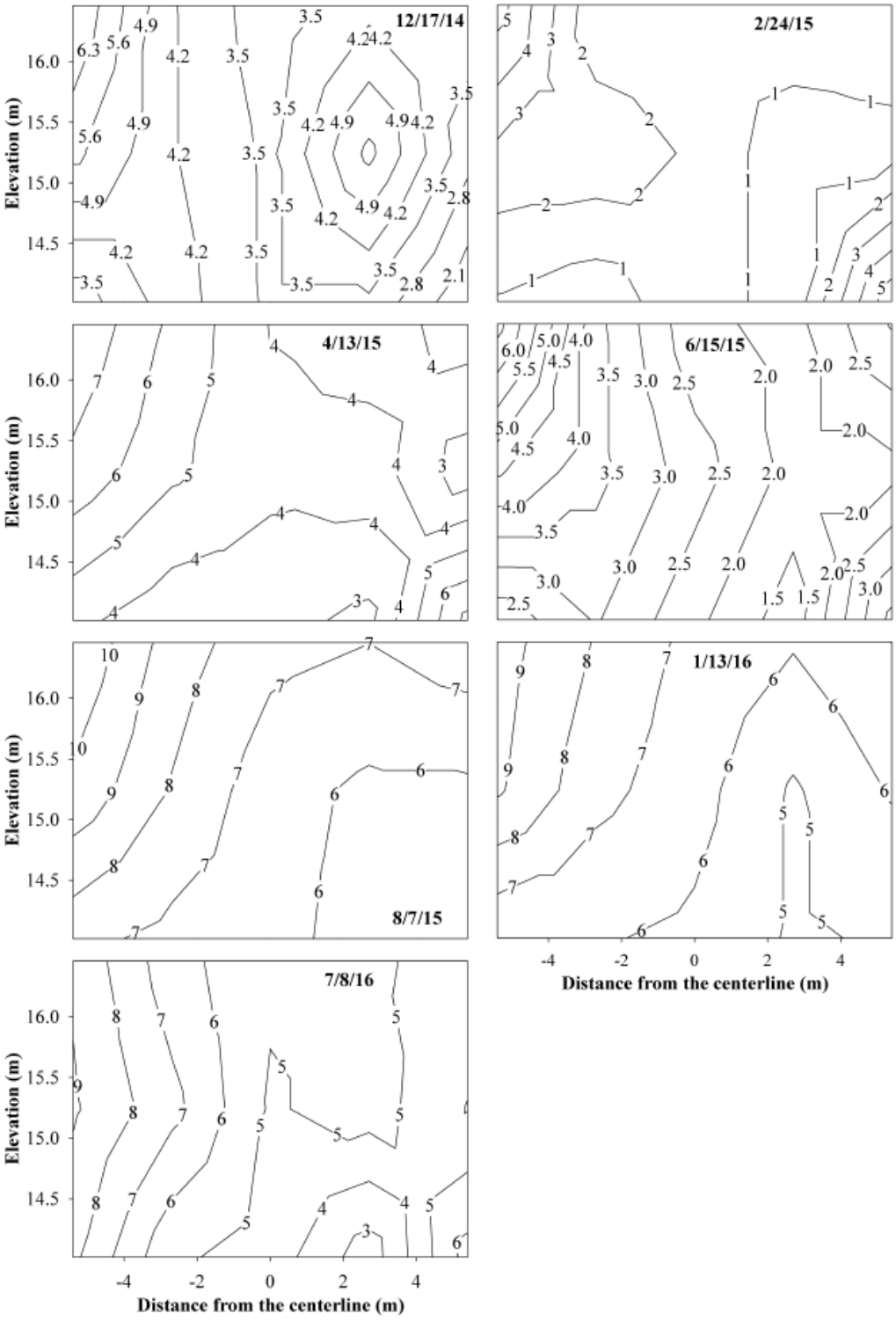

Figure 9.23 Continued

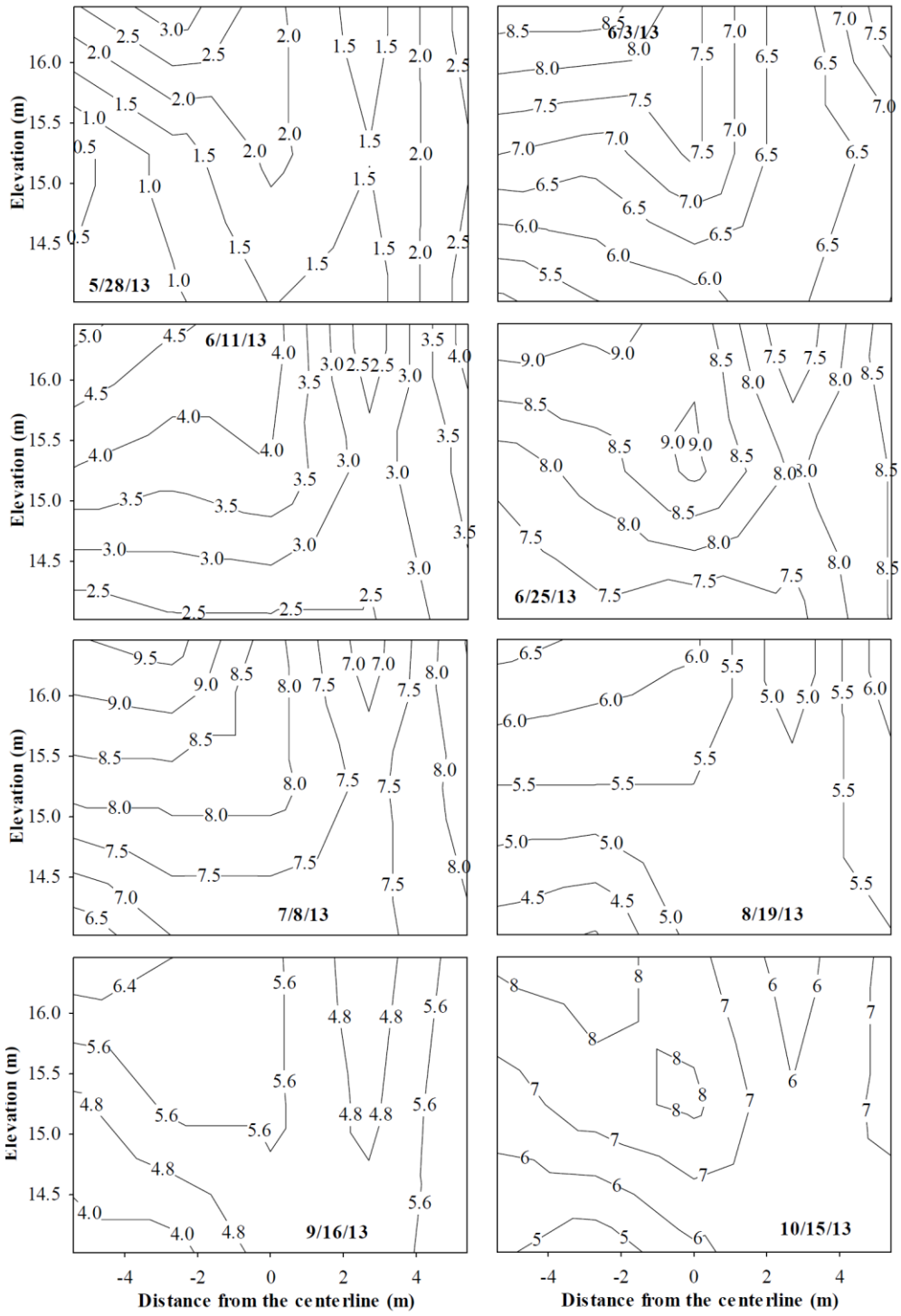

Figure 9.24 Contour plots of the west facing wall settlement over three years of operation

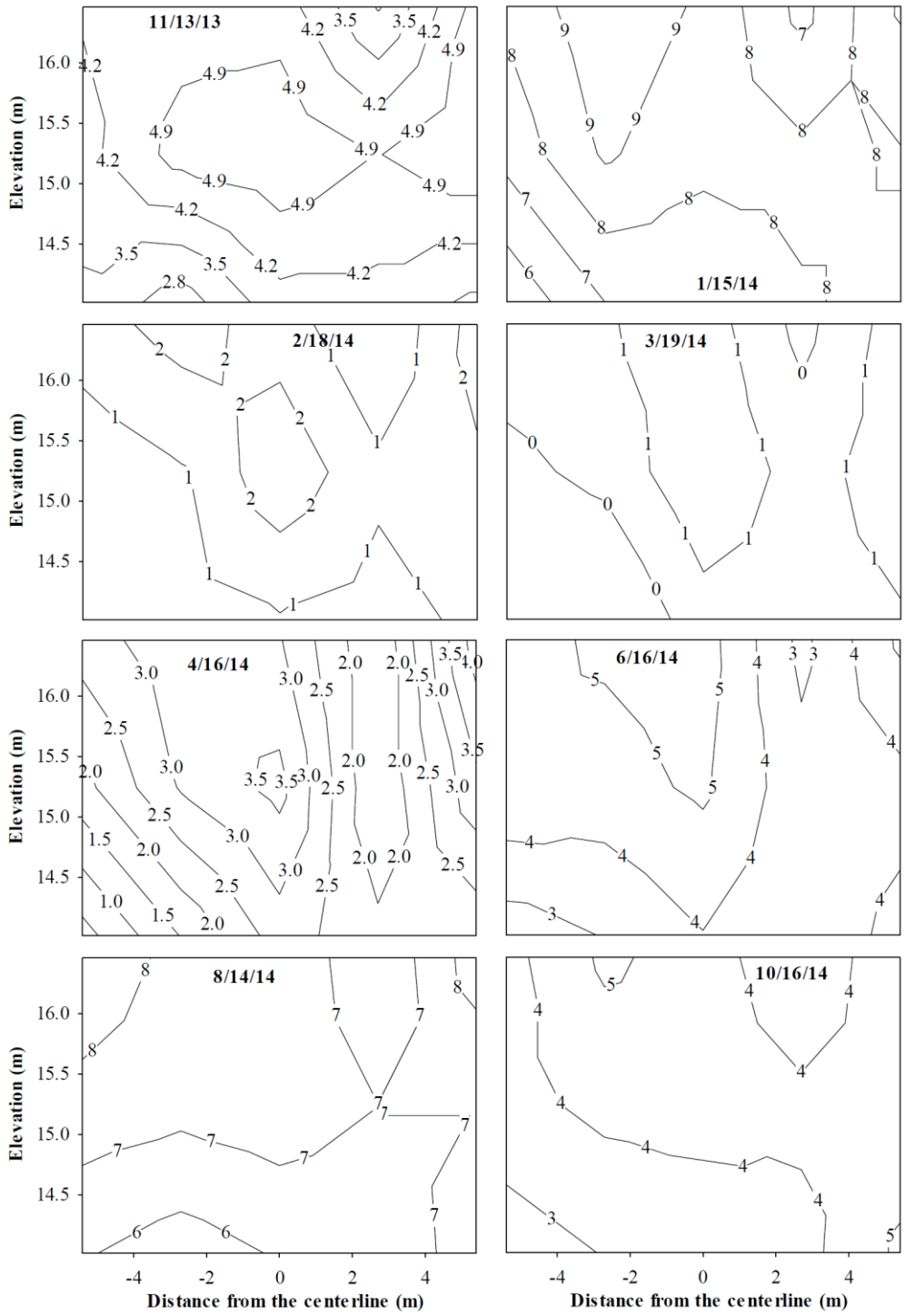

Figure 9.24 Continued

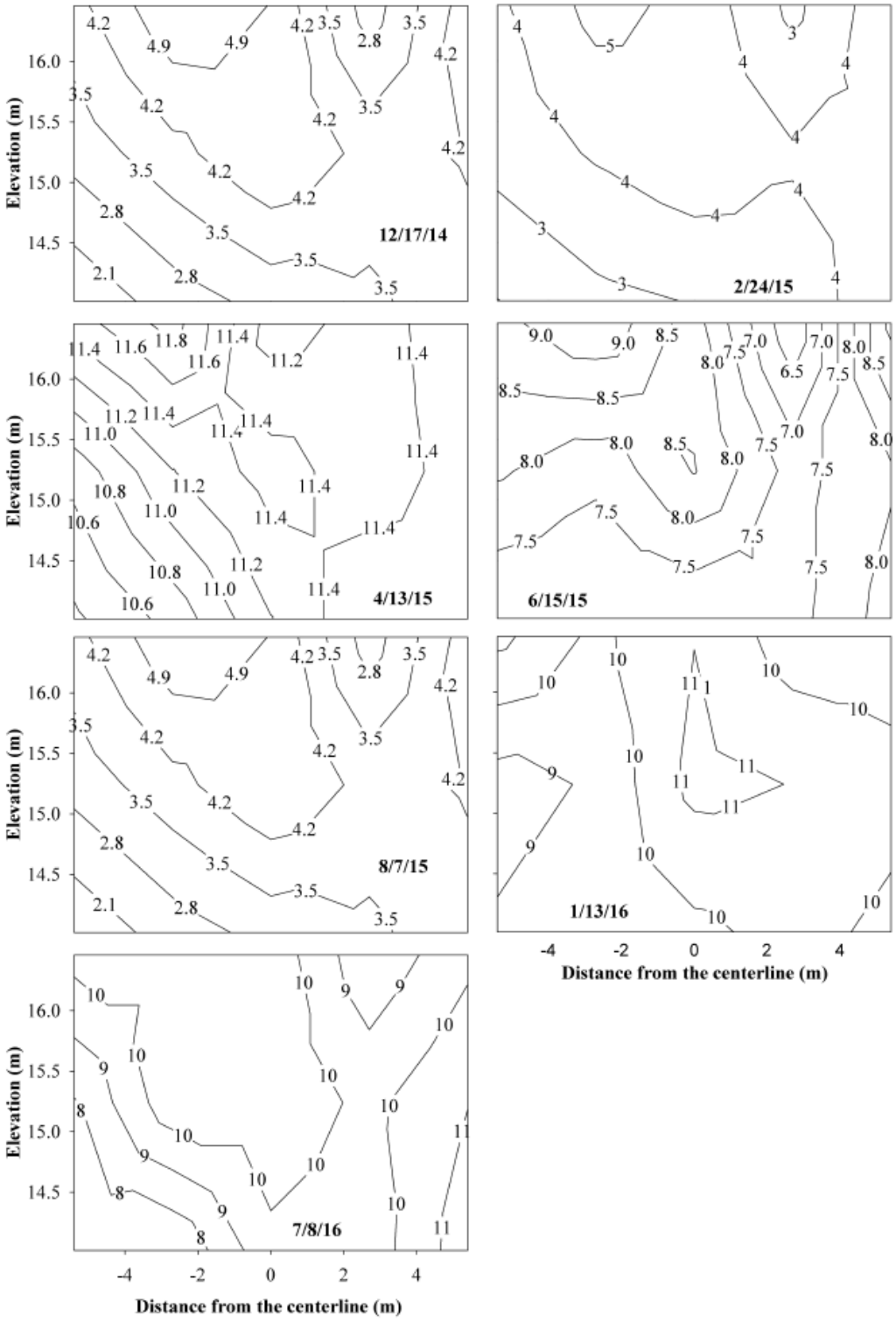

Figure 9.24 Continued

Considering the height of the GRS abutment walls ($H_{wall} = 4.8$ m) and the maximum measured settlement ($D_v = 12$ mm), the maximum vertical strain of the GRS abutment that occurred as a result of placement of the superstructure, during live load testing, and over three years of in-service performance is:

$$\varepsilon_V = \frac{D_v}{H_{wall}} = 0.25\% \tag{9.4}$$

According to the GRS-IBS Interim Implementation guide, the maximum vertical strain should be limited to 0.5% due to application of the superstructure DL and any additional LL over the in-service life of the structure (Adams et al. 2011). Therefore, the induced vertical strain in this project is less than recommended allowable vertical strain.

According to the GRS-IBS Interim Implementation guide the horizontal strain is calculated using the following equation (Adams et al. 2011):

$$\varepsilon_L = \frac{D_L}{b_{q,vol}} \tag{9.5}$$

In this equation, ε_L is the horizontal strain, D_L is the maximum horizontal deformation and $b_{q,vol}$ is the width of the load along the top of the wall (including the setback). Using the corresponding values for D_L and $b_{q,vol}$, we have:

$D_L = 12\ mm$

$b_{q,vol} = 1.1\ m$

$\varepsilon_L = 1.09\%$

According to the GRS-IBS Interim Implementation guide, the maximum lateral strain for this structure should not exceed 1 percent (Adams et al. 2011). The calculated strain is a little higher than the allowable strain. However, the precision of the surveying operation should be considered in the interpretation of these results. In such a case, taking an average of the varying results over time might be more representative of the actual wall lateral deflection. The average lateral deflection of both walls over three years of operation is very close and about 4 mm. Using this as D_L results in 0.4% of horizontal strain. This value is in a good agreement with horizontal strain measured by the strain gauges, as discussed in Section 9.4.

9.2.4.1 Investigating the trend of facing walls lateral deformation and settlement

As noted in Chapter 4 and earlier in this chapter, the error associated with the surveying operation was significant relative to the actual deformation that occurred, which made interpretation of the data difficult. So in order to have a rough estimate of the actual facing walls' deformation trend over three years of in-service operation, a regression analysis was conducted on the measured data for each target on the west and east facing walls as shown in Figures 9.25 and 9.26 for lateral deflection and settlement, respectively. As can easily be observed, due to the relatively large surveying error relative to the actual movements that occurred, the resulting correlations are generally poor, with fairly low R^2 values. Despite the relatively low correlation that was observed, Figures 9.25 and 9.26 indicate that there is an increase in both lateral deflection and

settlement over time for most of the cases. Tables 9.1 and 9.2 present the slope of the trend of change in lateral deflection in units of mm/year, for the data collected over three years of in-service operation for the targets on the west and east facing walls, respectively. The corresponding settlement values are presented in Tables 9.3 and 9.4. The maximum and minimum calculated slope for each case are also presented in the tables. For the lateral deflection, the maximum and minimum calculated slopes were 2.19 mm/year and -0.584 mm/year, respectively, while the corresponding values for the settlement were 1.5695 mm/year and 0.4745 mm/year. The average of the observed slopes for the lateral deflection and settlement were about 0.380 mm/year and 1.123 mm/year, respectively. The magnitude of this value implies that the increase in the facing walls' lateral deflection and settlement were about 1.14 mm and 3.369 mm (respectively) over three years, which is insignificant. Replacing this value in Equation 9.5 results in a 0.103% increase in horizontal strain, which is in a good agreement with the measured average creep strain by the abutment strain gauges (about 0.1%), as discussed in Section 9.2.3.

This increase in the facing walls' deformation is in agreement with what was shown in Chapter 4. As mentioned there, there was an increase in the facing walls deformations during three years of in-service operation relative to what had occurred during the live load testing period (Figures 4.5 through 4.24).

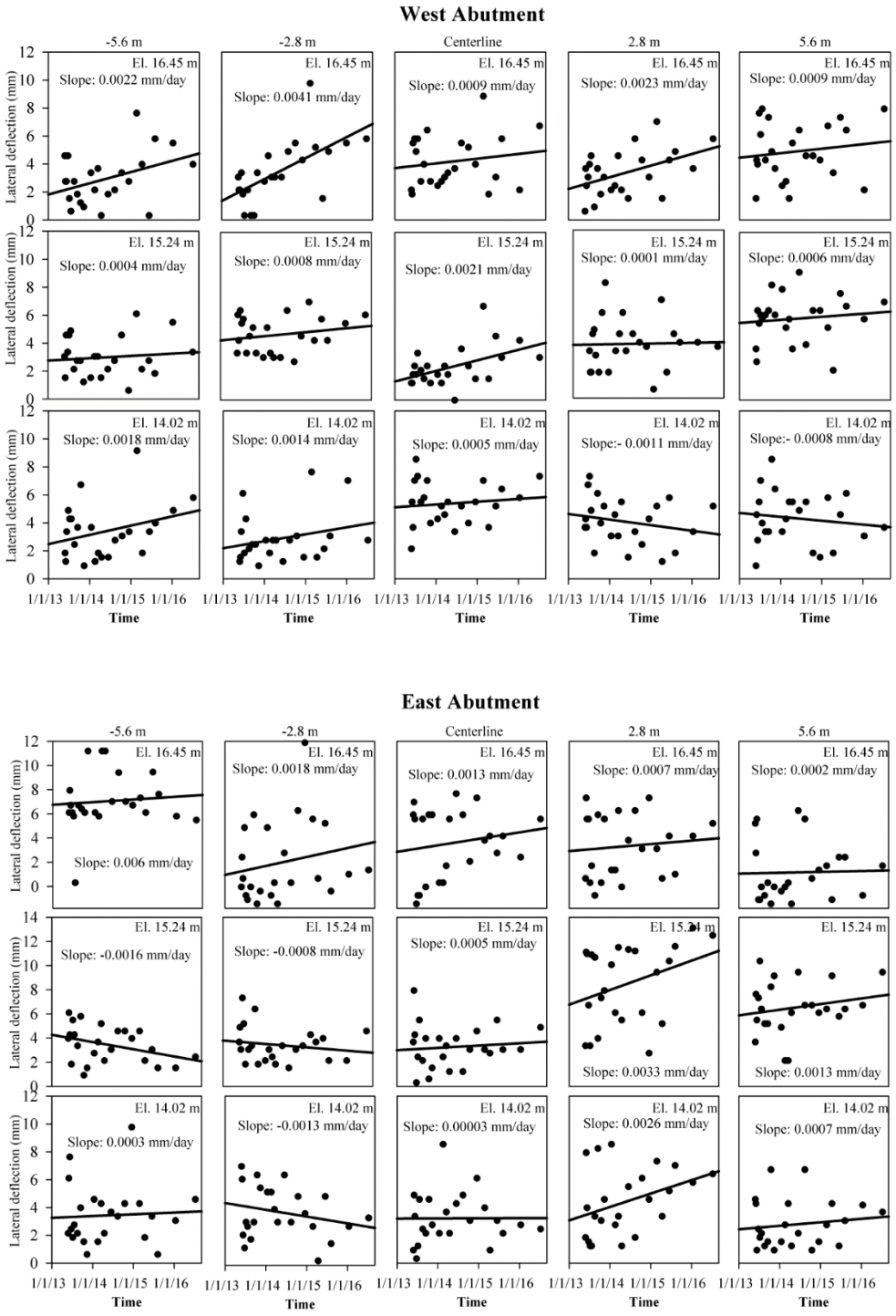

Figure 9.25 Changes in the west and east abutment walls' lateral deflection over three years of operation

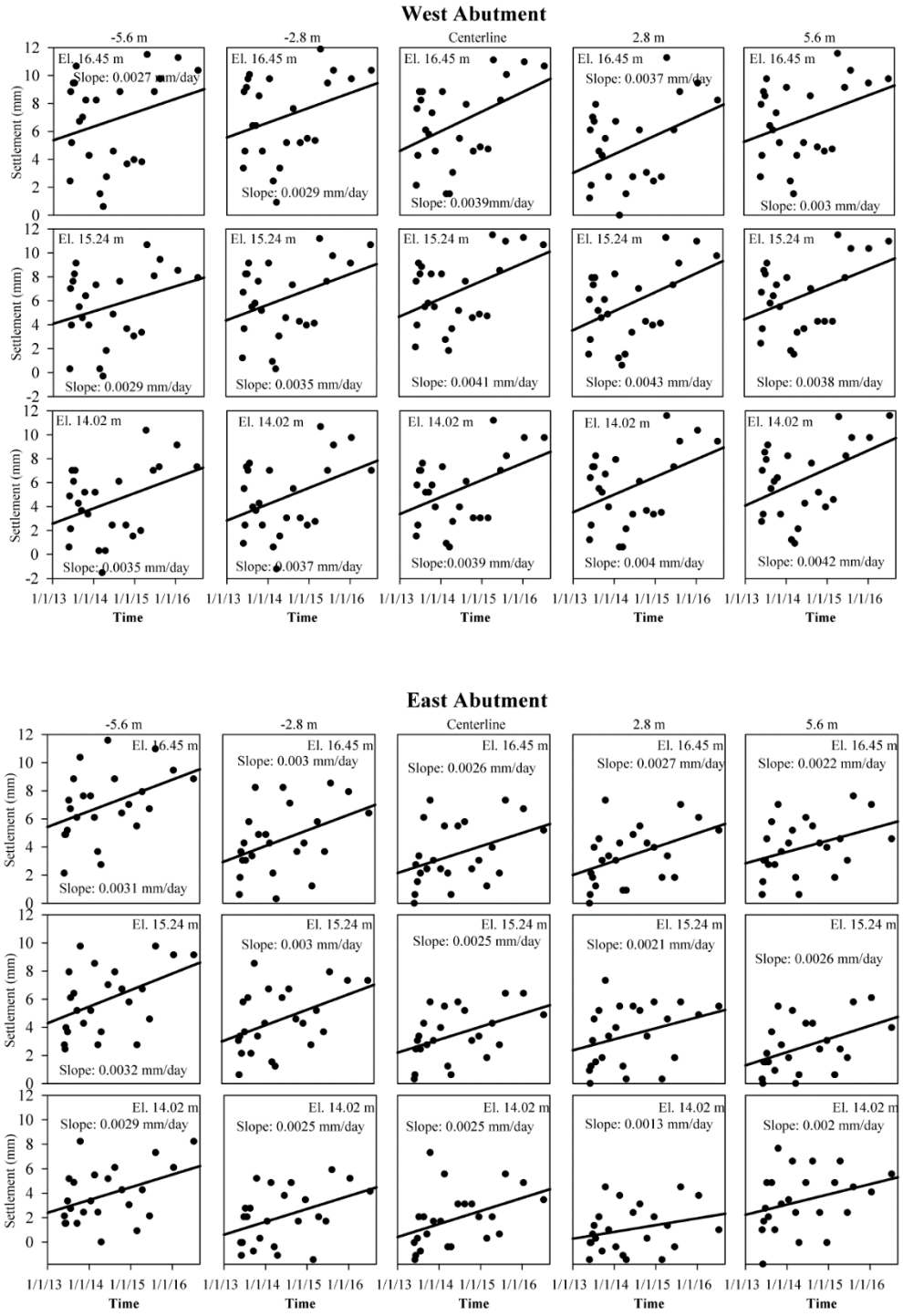

Figure 9.26 Changes in the west and east abutment walls' settlement over three years of operation

Table 9.1 The slope of the trend of change in lateral deflection over three years of in-service operation, for the targets on the west facing wall (mm/year)

Elv. \ Offset from Centerline (m)	-5.6	-2.8	0	2.8	5.6
16.45	0.803	1.4965	0.3285	0.8395	0.3285
15.24	0.146	0.292	0.7665	0.0365	0.219
14.02	0.657	0.511	0.1835	-0.4015	-0.292

Table 9.2 The slope of the trend of change in lateral deflection over three years of in-service operation, for the targets on the east facing wall (mm/year)

Elv. \ Offset from Centerline (m)	-5.6	-2.8	0	2.8	5.6
16.45	2.19	0.657	0.4745	0.2555	0.073
15.24	-0.584	-0.292	0.1825	1.2045	0.4745
14.02	0.1095	-0.4745	0.0109	0.949	0.2555

Table 9.3 The slope of the trend of change in settlement over three years of in-service operation, for the targets on the west facing wall (mm/year)

Elv. \ Offset from Centerline (m)	-5.6	-2.8	0	2.8	5.6
16.45	.9855	1.0585	1.4235	1.3505	1.095
15.24	1.0585	1.2775	1.4965	1.5695	1.387
14.02	1.2775	1.3505	1.4235	1.46	1.533

Table 9.4 The slope of the trend of change in settlement over three years of in-service operation, for the targets on the east facing wall (mm/year)

Offset from Centerline (m) / Elv.	-5.6	-2.8	0	2.8	5.6
16.45	1.1315	1.095	0.949	0.9855	0.803
15.24	1.168	1.095	0.9125	0.7665	0.949
14.02	1.0585	0.9125	0.9125	0.4745	0.73

9.2.5 Bridge strain gauges

As discussed in Chapter 3, long strain gauges were attached to the bottom surface of the bridge beams before their placement, at the middle of each beam. The measured data for the gauges which continued to work after the bridge superstructure placement were presented in Chapter 4, and the measured and corrected data for these strain gauges were presented in Appendix H. As shown in the appendix, the corrected data showed that strain was nearly constant and less than 0.05%, for all of the working gauges. As shown in Appendix H, the strain trend measured by all the gauges was similar. Gauge b3 stopped properly working in the second year.

A significant amount of research has already been conducted examining the effect of temperature on the response of concrete bridges (e.g., Hoffman et al. 1983, Branco and Mendes 1993, Roberts-Wollman et al. 2003, Kim and Laman 2010, Song et al. 2016). According to the literature, the surface temperature of a concrete bridge cross section is influenced by the air temperature, the solar energy, convection caused by the wind vector, and various forms of precipitation. These transient and random parameters

all together cause a non-uniform distribution of temperature across the bridge cross section. The relatively low thermal conductivity of concrete allows the non-uniform distribution of temperature to exist, given the relatively dynamic temperature forcing functions that are being applied to the structure. The temperature at the top and the bottom surfaces of the bridge are consequently different – the top is often hotter, given the effect of solar radiation directly on the bridge deck, and consequently the top surface tends to expand more than the bottom surface. Under this condition, the bridge beams tend to bow upward, as shown in Figure 9.27b. This figure shows the effect of temperature gradient on the deformation of a simply supported beam. It can be seen in this figure that when the temperature gradient across the beam is not uniform, the increase in temperature increases the tensile strain at top surface relative to what is observed on the bottom surface.

In order to investigate the effect of air temperature on the bridge beam strain, the corrected strain for Gauge b6 over three years of operation can be compared against the ambient air temperature over the same time period, as shown in Figure 9.28. As shown, these two parameters change seasonally in an inverse way. In order to examine the fluctuation in observed bridge strain and ambient temperature on a daily basis, Figure 9.29 presents the same two data plots again, over a 5-day period. As can be observed again in this figure, when the temperature increases the tensile strain decreases, and vice versa. Since the strain gauges are attached to the bottom surface of the bridge, this inverse response is consistent with the behavior that is shown in Figure

9.27b. The likely effect of the deformed shape of the bridge induced by the air temperature change on the pressure in the abutment is discussed later in this chapter.

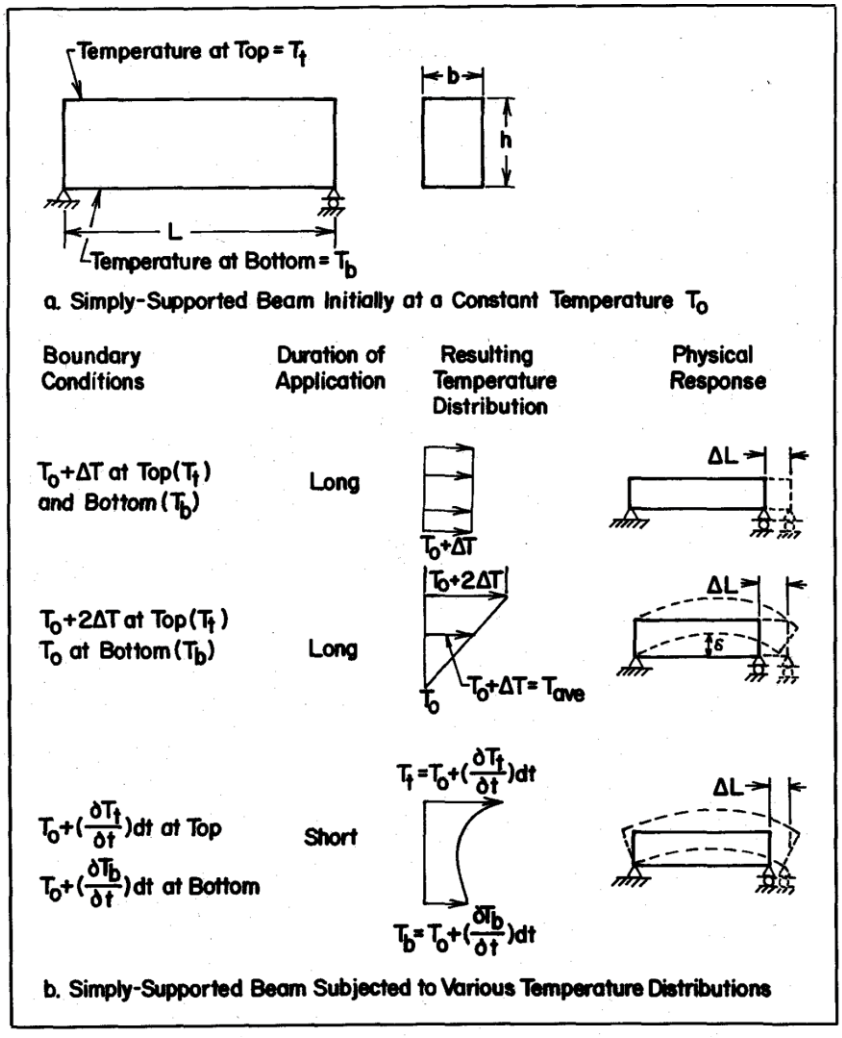

Figure 9.27 Influence of thermal boundary conditions on a simply supported beam (Hoffman et al. 1983)

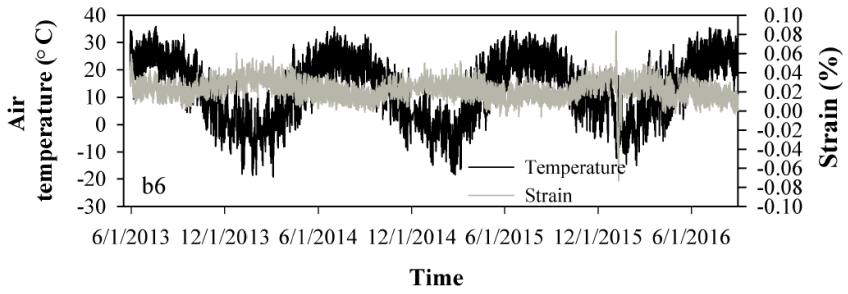

Figure 9.28 Changes in the corrected strain measured by Gauge b6 along with recorded air temperatures over three years of operation

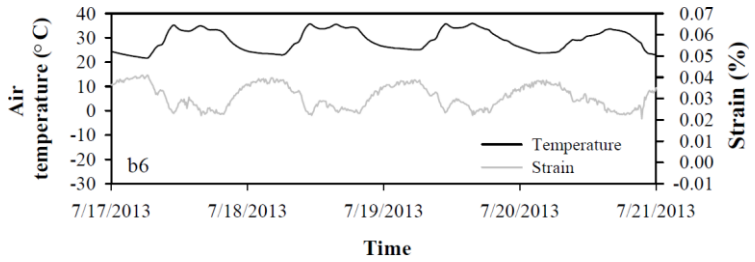

Figure 9.29 Changes in the corrected strain measured by Gauge b6 along with recorded air temperatures over a five-day period

9.2.6 Inclinometer sensors

Four In-Place Inclinometer (IPI) sensors were installed in the clay foundation layer (In-1 to In-4) to monitor displacement of this layer during construction and subsequent bridge operations. There was a relatively stiff sandy layer beneath the clay layer; consequently, the inclinometer casing was advanced through the clay layer and was terminated in the sandy soil.

The IPI sensors that were utilized in this project provide an in-place alternative to traditional traversing probe-type inclinometers, by employing a fixed chain of sensors affixed to a series of connected rods. Vertical biaxial IPIs were used, allowing for displacement measurements in both the N-S and E-W directions. The system consists of a sensor housing containing an accelerometer, gauge extension tubes to make up defined gauge lengths and wheel assemblies.

Figures 9.30 and 9.31 display the foundation deformation over three years of operation in the E-W and N-S directions, respectively. As shown, there was a slight increase in movement at the beginning of in-service operation, which is likely associated with the foundation initial settlement and movement due to construction and load testing of the GRS abutment. Both the abutment and the superstructure are involved with (and consequently are affected by) this deformation development. As shown in Figure 9.31, there is significant noise in the inclinometer signal in the N-S direction, relative to what was measured in the E-W direction. This behavior is attributed to the mechanism of fixture that is utilized between the inclinometer sections and the inclinometer casing itself; in particular, the spring-loaded wheels tend to fix the inclinometer sections strongly in the E-W direction (the primary direction of inclinometer movement that was assessed), while allowing a small amount of movement to occur in the out-of-plane N-S direction.

As shown in the figures, the rate of deformation in the foundation stabilized shortly into the monitoring timeframe, remaining at a constant level of movement beyond that point; this indicates satisfactory behavior with respect to shear or movement

in the foundation soils beneath the abutment. In order to investigate the trend of the foundation deformation over the first three years of operation more closely, Figures 9.30 and 9.31 were redrawn after removing the noise using a frequency-based filtering approach. Figures 9.32 and 9.33 show new graphs which present the resulting foundation deformation in the E-W and N-S directions. The initial increase in the foundation deformation is more obvious in these figures since the noise is not shown and also the vertical scale is exaggerated in way that just covers the deformation range for each sensor. As can be more clearly observed in these figures, the initial rate of deformation significantly decreases after about two months of operation. As shown, beyond that point there is a slight creep that occurs for some of the sensors, which is more noticeable in the N-S direction. The maximum creep deformation in the E-W direction is about 0.8 mm at the location of the uppermost sensor (In-1) while the corresponding value for the N-S direction is about 1.5 mm for sensor In-1. It can be inferred that more creep deformation occurred in the N-S direction than the E-W direction. The maximum measured deflections in the E-W and N-S directions are about 10 mm and 4 mm, respectively, which occurs in the uppermost sensor (In-1).

Using the data presented in Figures 9.30 and 9.31, the initial and final foundation deflection in the E-W and N-S directions can be determined; the results from this assessment are shown in Figures 9.34 and 9.35 for the E-W and N-S directions, respectively. As shown, the creep occurred in the clay foundation and the creep amount in the N-S direction is higher than the E-W direction, though both creep amounts are fairly small.

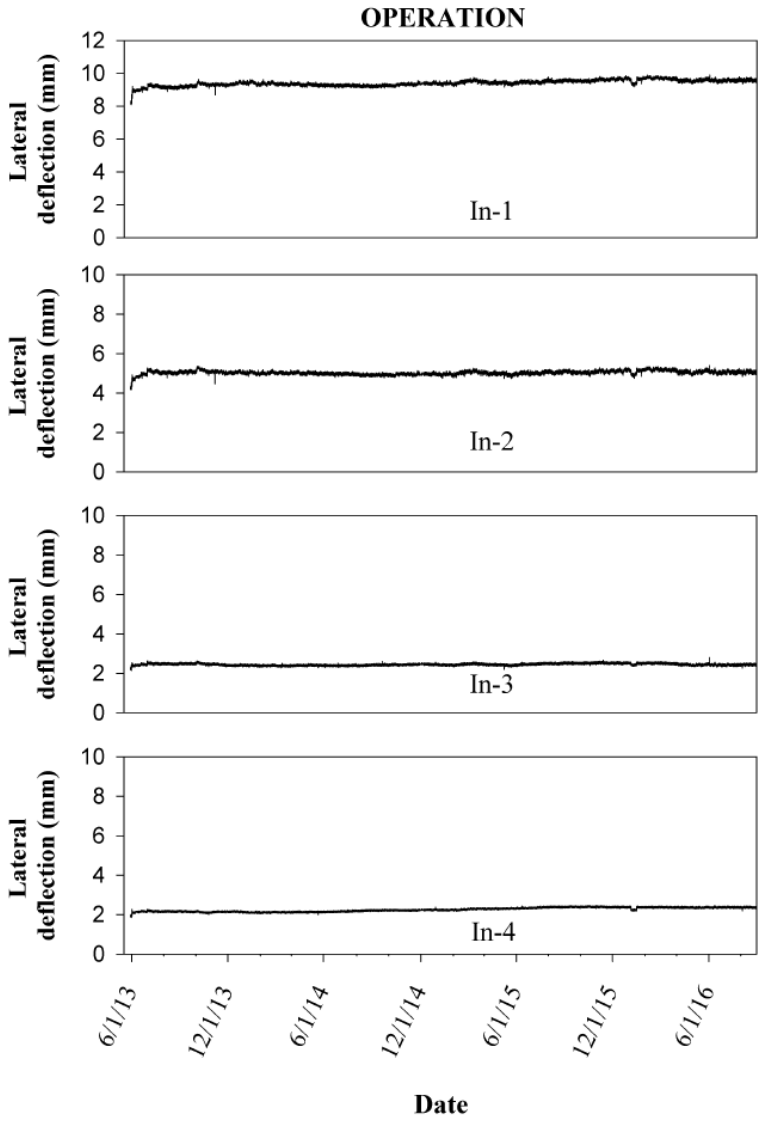

Figure 9.30 Lateral deflection recorded by the inclinometer sensors in the E-W direction over three years of in-service operation

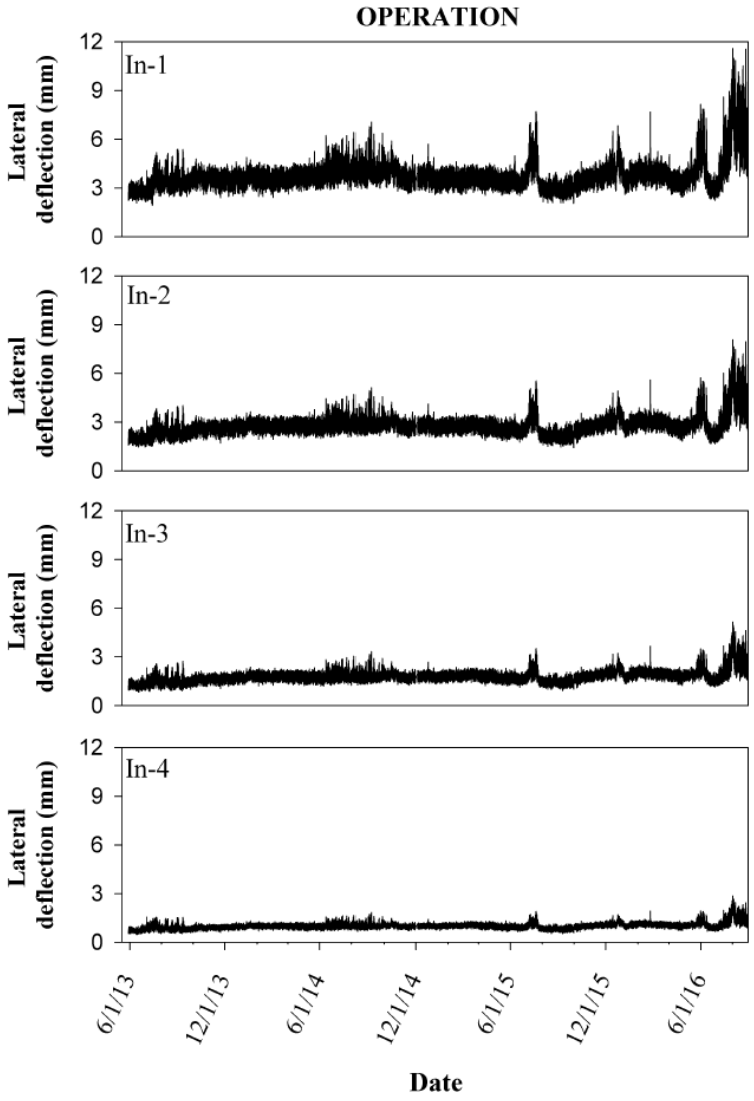

Figure 9.31 Lateral deflection recorded by the inclinometer sensors in the N-S direction over three years of in-service operation

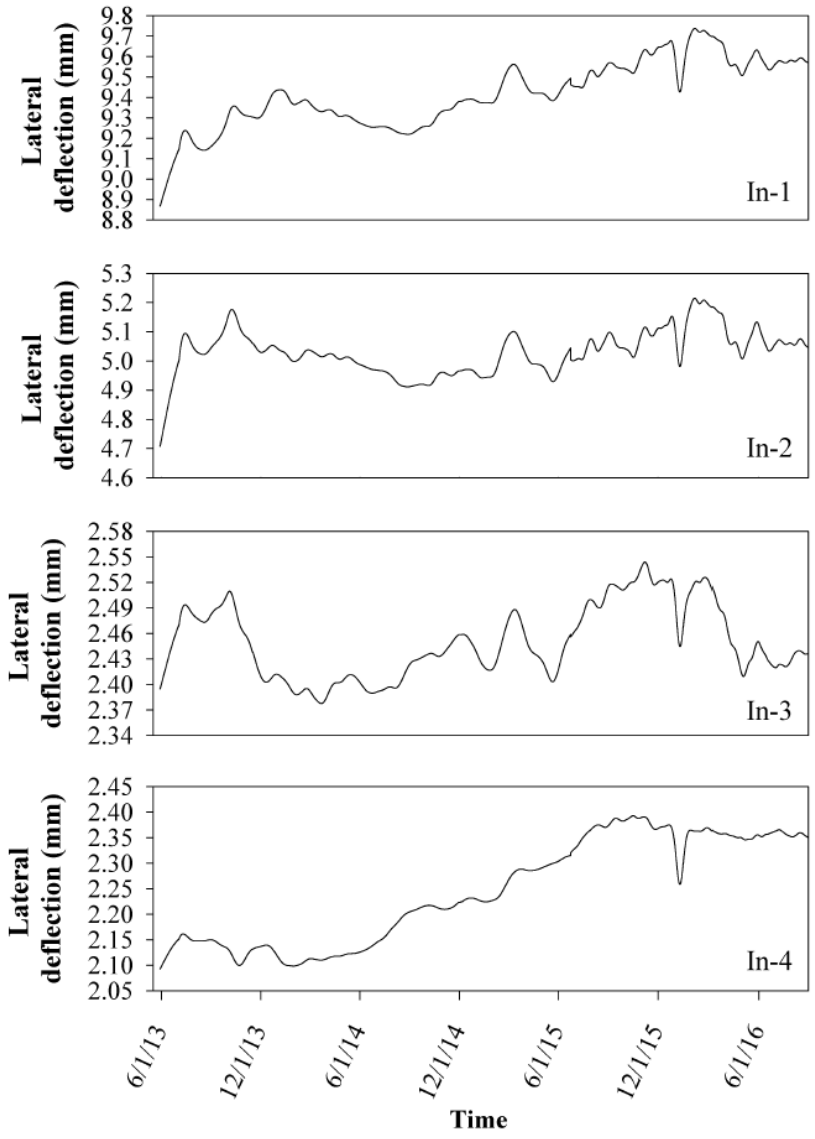

Figure 9.32 Filtered values of foundation lateral deflection in the E-W direction, recorded by the inclinometer sensors over three years of in-service operation

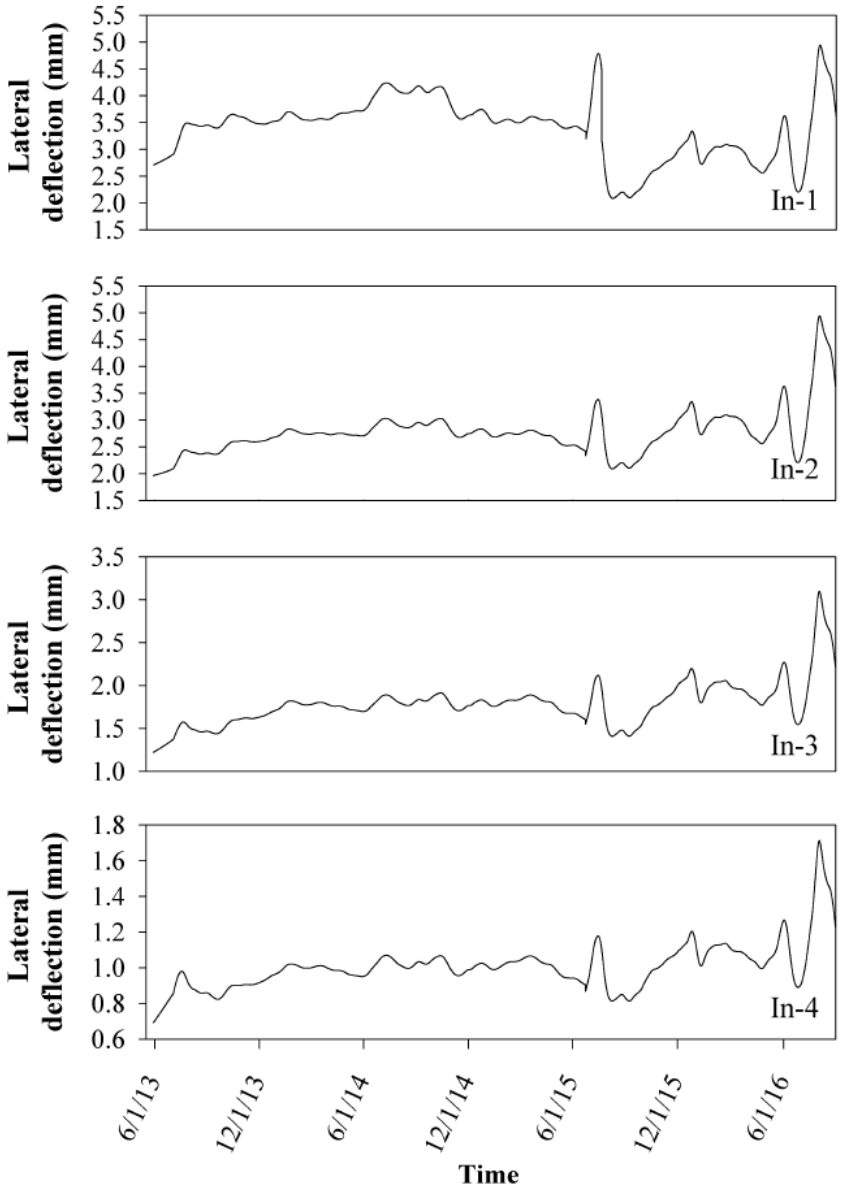

Figure 9.33 Filtered values of foundation lateral deflection in the N-S direction, recorded by the inclinometer sensors over three years of in-service operation

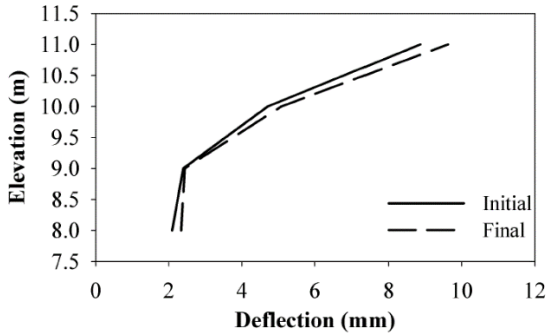

Figure 9.34 The initial and final foundation deflection in the E-W direction

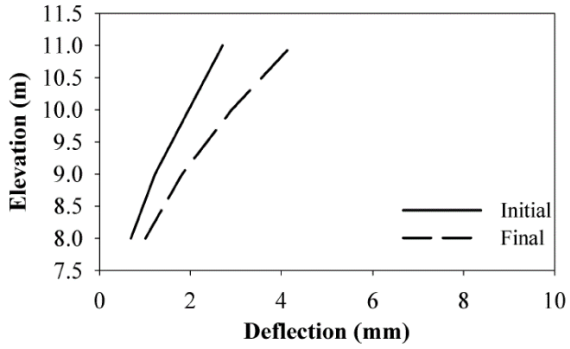

Figure 9.35 The initial and final foundation deflection in the N-S direction

9.2.7 Foundation pressure cells

As discussed in earlier chapters in this report, four vibrating wire static pressure cells (Model #P6, itmsoil USA) were installed beneath the GRS-IBS foundation (S1 to S4), and one more between the end of the concrete bridge superstructure and the integration zone (S5). The pressure range for these cells was 0-300 kPa. The cell installed between the bridge and the abutment (S5) stopped working early on into the in-service monitoring period, with its data not being reliable to use in

the data analysis. Therefore, what is presented in the next sections regarding measured pressures is only related to the cells installed beneath the RSF (S1 to S4).

The vibrating wire (VW) pressure cells consisted of a circular flat cell formed from two sheets of stainless steel welded around their periphery. The narrow gap between plates was filled with hydraulic oil. Vibrating wire transducers were connected to the cells by a short length of stainless steel tubing, forming a closed hydraulic system. An armored cable connected the transducers to the logger.

The cells have very good long-term stability according to the manufacturer but they are sensitive to temperature, and allowance for temperature variations is necessary when incorporating the results. Therefore, the cells accommodate a thermistor to monitor temperature if such variations are anticipated. The effect of the cell temperature on the readings will be discussed in this section.

VW pressure cells measure total stress, which for soils is the combination of effective stress and pore-water pressure. It was shown in Chapter 5 that there is a good correlation between the total pressure measured by the foundation cells and the pore pressure measured by the piezometers. The effective pressure was consequently calculated to remove the effect of pore pressure. It was possible to calculate the effective pressure since both total stress and pore pressure were recorded at the same time. What is discussed in the next section is regarding both total and effective pressures.

It is very important to calculate the effective pressure given that in geotechnical engineering application, the long-term stability of the soil is governed by

the effective stress. For example, for bearing capacity analysis, the effective induced stress by the structure needs to be compared with the soil's bearing capacity. Without having the pore water pressure information, the measured total stress might be misleading and not representative for the actual stress state.

The collected data by these cells for the time of construction and during the load testing were presented in the previous chapter. In the next section, the pressure variation beneath the foundation during three years of operation is discussed.

9.2.7.1 Long term performance of the cells

Figure 9.36 presents the changes in total and effective pressure recorded by the foundation pressure cells over three years of operation. As shown, there is a significant amount of noise in the data and the measured data was also seasonally fluctuating. Even after removing the effect of water pressure, much of the high-frequency noise and low frequency signal variation still remains. This signifies that there are other factors which are affecting the measured total pressures over time.

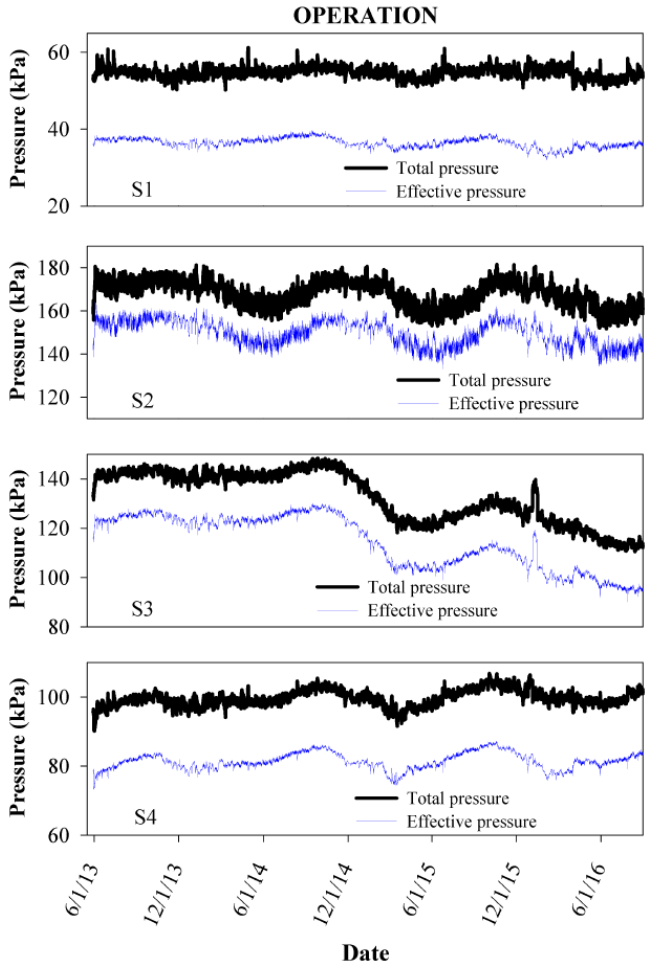

Figure 9.36 Measured total and effective pressures by foundation pressure cells over three years of operation

Figure 9.37 presents the minimum, average and maximum recorded effective pressure for pressure cells S1 to S4. The difference between the minimum and maximum measured values can be clearly observed in this figure. It will be shown later in this section that the main source of change in the measured pressure is the cell temperature changes.

Figure 9.38 displays the histogram of the measured effective pressure by the foundation pressure cells. As shown, the effective stress distributions do not follow a normal distribution. In the case of cells S1 and S4 the distributions are closer to a normal distribution; for S2 and S3 the distributions are quite far from the normal distribution.

As discussed in Chapter 8, the pressure distribution was not uniform beneath the foundation. The maximum pressure was observed at the location of S2, which was installed beneath the facing wall, while the minimum occurred at the location of S1, at the front toe of the foundation. The foundation pressure distribution was almost linear behind the facing wall, as it was during construction and upon application of dead and live loads to the GRS abutments via the bridge superstructure.

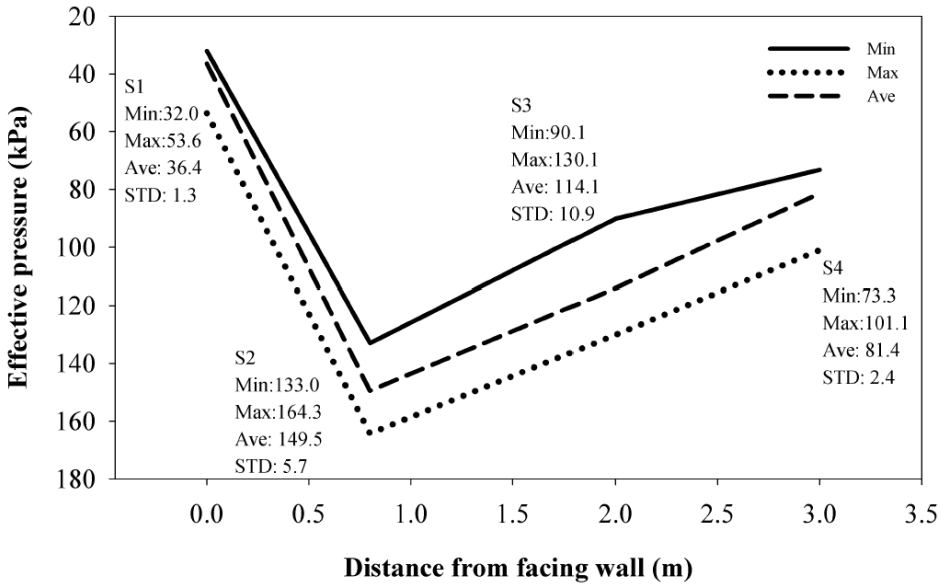

Figure 9.37 The changes in pressure distribution beneath the RSF foundation over three years of operation

As discussed in Section 4.1, a review of available literature showed that the readings of vibrating wire pressure cells are appreciably influenced by their temperature. The corresponding complexities with the calibration of the cells for the effect of temperature were also explained in that section. Accordingly, in the next part of this section, the effect of the cell temperature on the pressure readings is discussed.

Figure 9.39 displays the recorded effective pressures and the cell temperature for three years of operation and for cells S1 to S4. According to this figure, the trend for measured pressure and the cell temperature are significantly similar. When cell temperature increases the pressure consequently increases and when the cell temperature decreases the pressure decreases, as well.

This implies that the main source of change in pressure is the cells' temperature change, which is expected. According to the figure, it appears that cell S3 is not working properly since its corresponding readings do not follow the cell temperature anymore. Data monitoring over the course of three years confirmed this assumption.

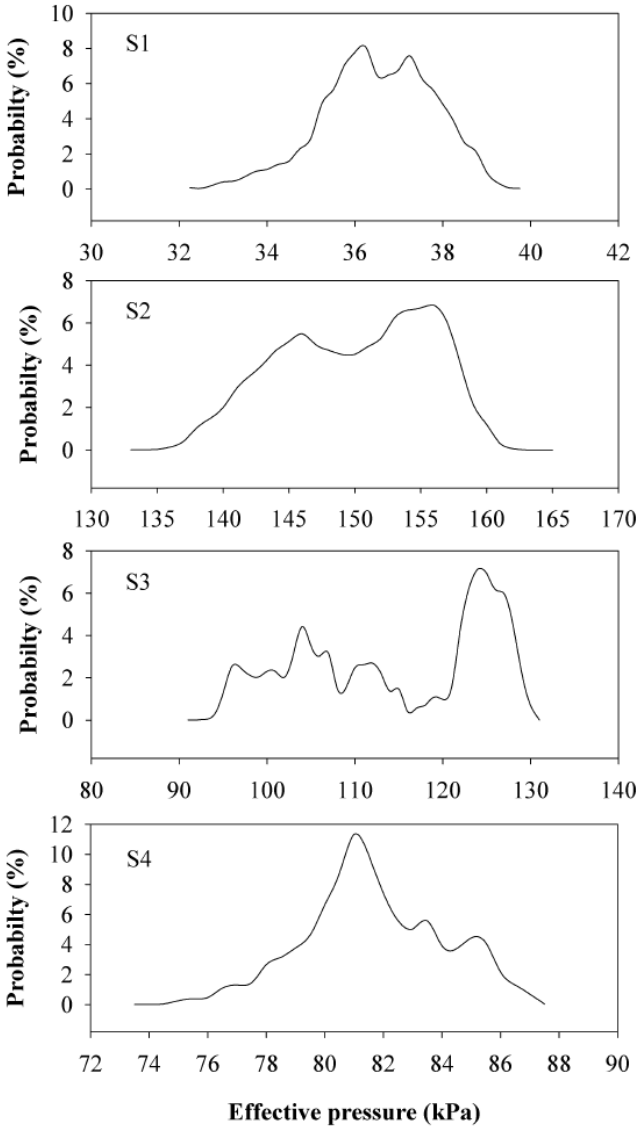

Figure 9.38 Histograms of foundation effective pressure based on three years of recorded cell pressure data

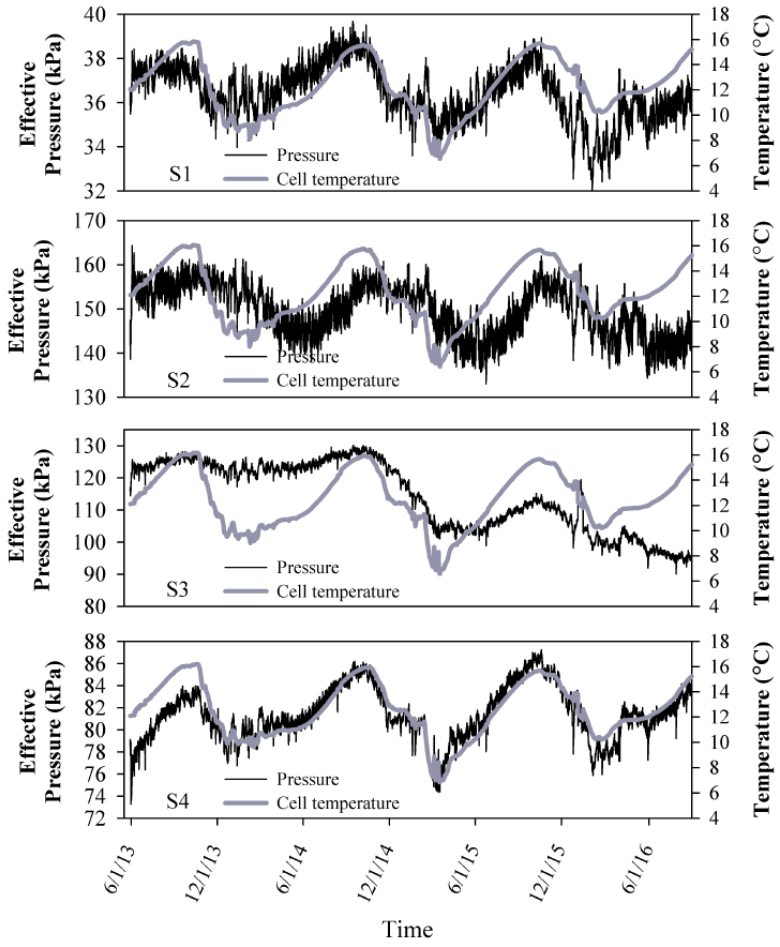

Figure 9.39 Changes in cell temperature alongside changes in the measured effective pressure

In order to investigate the effect of cell temperature on the measured pressure, it is helpful to remove the high-frequency noise from Figure 9.39, in order to compare the low-frequency trends between effective pressure and cell temperature. To accomplish this task, a frequency-based filtering approach was applied to the effective pressure graphs to filter out the high frequency noise in the signal. After filtering the

noise, new graphs were prepared which only show the low-frequency trend of changes in effective pressure (Figure 9.40).

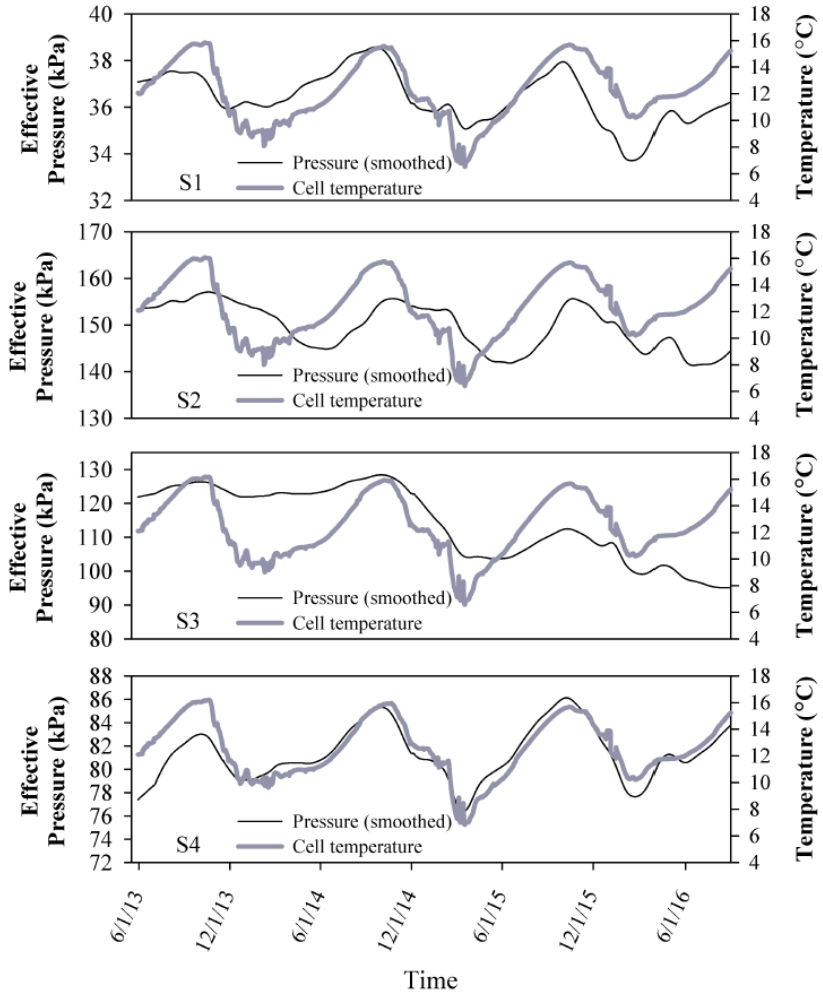

Figure 9.40 The foundation pressure cells' temperature changes versus filtered and smoothed effective pressure values

As shown in this figure, both the cell temperature and measured pressure follow the same general trend. However, some exceptions can be seen in the figure. In

the case of cell S2, there is a delay between the change in cell temperature and pressure particularly in cold seasons. A regression analysis was conducted to investigate the strength of correlation between the filtered effective pressure and cell temperature, as shown in Figure 9.41.

As shown in this figure, there is a direct correlation between the cell temperature and measured pressure. Increases in cell temperature correspond to increases in cell pressure and vice versa. As discussed earlier, this behavior is as expected and is similar to what has been observed by other researches. However, the correlation is not overly strong, particularly in case of cell S2. As observed in the last paragraph, there is a delay between the change in cell temperature and pressure, especially in the cold seasons in the case of cell S2. To investigate this, another correlation was performed in which this delay was considered (Figure 9.42). In this analysis, an adjustment of 14 days was considered between the temperature and pressure readings, for the entire data series. As shown, adjusting for a 14-day delay has significantly increased the correlation between the two values. This confirms the delay between increase in cell temperature and pressure for cell S2; the reason for this delay is not clear.

As shown in Figures 9.41 and 9.42, the slope of correlation has increased with the increase in the level of pressure. While the minimum slope belongs to cell S1 (0.32 kPa/°C), cell S2 has the maximum slope (0.835 kPa/°C in Figure 9.41 and 1.46 kPa/°C in Figure 9.42). This indicates that the change in pressure with the change in cell

temperature increases for higher levels of pressure. This is consistent with what was observed by earlier researches, as shown in Figures 9.1 and 9.2.

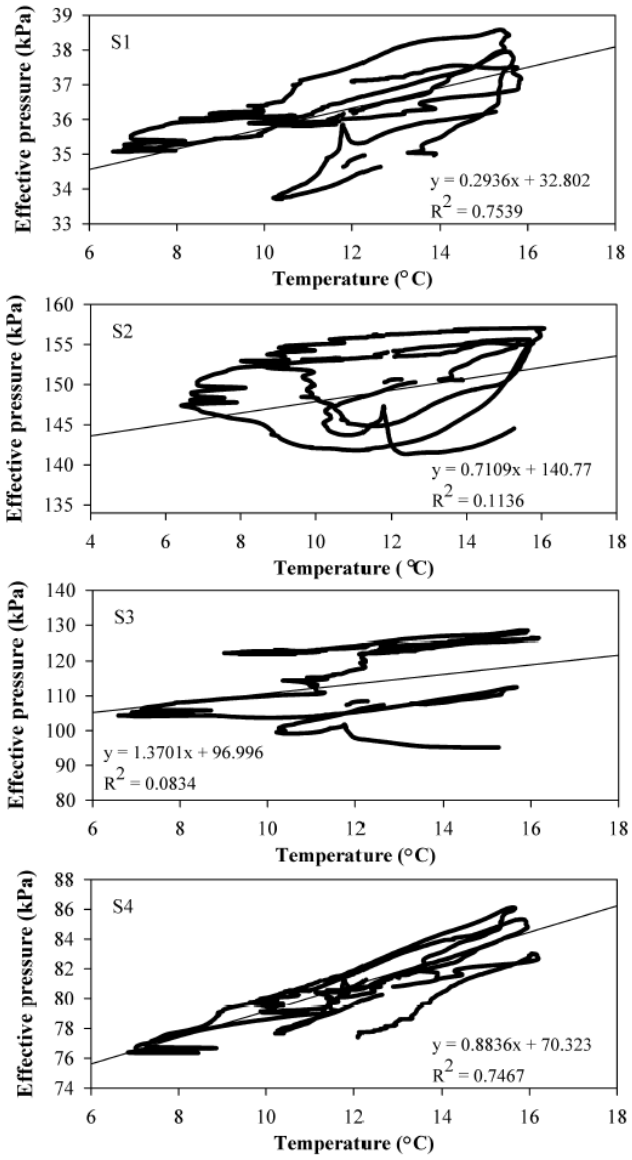

Figure 9.41 Correlation between the filtered effective pressure and temperature for the foundation pressure cells (Note: S3 stopped working properly at some point in the second year).

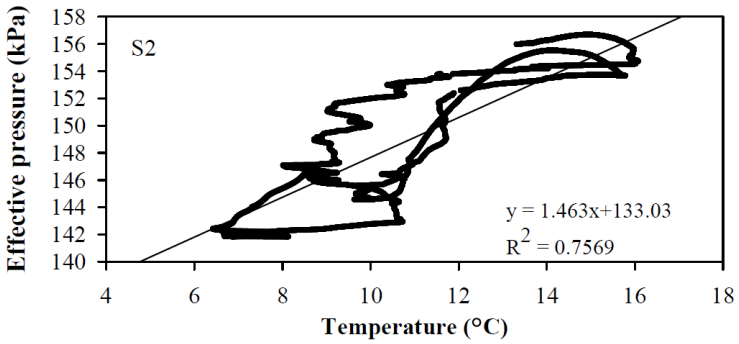

Figure 9.42 Correlation between the cell temperature and filtered effective pressure for cell S2, with a 14 day adjustment between the two measured parameters

Another observation in Figure 9.40 was the correlation between the cell temperature and measured pressure during increasing and decreasing temperature periods. Over three years of operation, the cells' temperature first goes up in summer and goes down in winter and again goes up and down in the following summer and winter (Figure 9.40). Finally, it again increases for the third time. To investigate the effect of the increase or decrease of cell temperature on the correlation, the correlation analysis was separately repeated for increasing and decreasing temperature periods. The corresponding results for cells S1, S3 and S4 are shown in Figures 9.43, 9.44 and 9.45. The results for cell S2 are not presented because of the aforementioned delay. The results for cell S3 are shown only for the period which it was working properly.

As shown in the figures, the slope of the correlation changes in hot and cold weather. For cells S3 and S4, the correlation becomes stronger relative to Figure 9.43

for cell S1, with higher R-squared values. For cell S1, the correlation is not as strong when temperature goes up the first time but the correlation increases for the rest of the period. The slope of the correlation for cells S3 and S4 is higher than the corresponding one for S1, which is expected given the higher level of pressure. In addition, for cell S3, when the temperature goes up the slope of correlation changes between 1.0 and 1.09 while for cell S4 it changes between 1.0 and 1.3. The slope of the correlation is 0.76 as for cell S3 when the temperature decreases and changes between 0.68 and 0.96 in case of cell S4. Generally, the slope is higher when the temperature increases. The results show that the cells may response differently to the temperature changes in hot and cold weather.

Generally, the cell temperature change can significantly affect the pressure reading. Table 9.5 presents the difference between the minimum and maximum pressure, as determined from the data presented in Figure 9.40, which shows the trend of the pressure changes after filtering the daily noise. As shown, the ratio for all cells except cell S3 is about 1.20. In case of cell S3 the ratio is higher since the cell stopped properly working at some point in the second year.

Table 9.5 The ratio between the minimum and maximum effective pressure for the foundation pressure cells over three years of operation

Pressure cell	The ratio
S1	1.24
S2	1.24
S3	1.44
S4	1.19

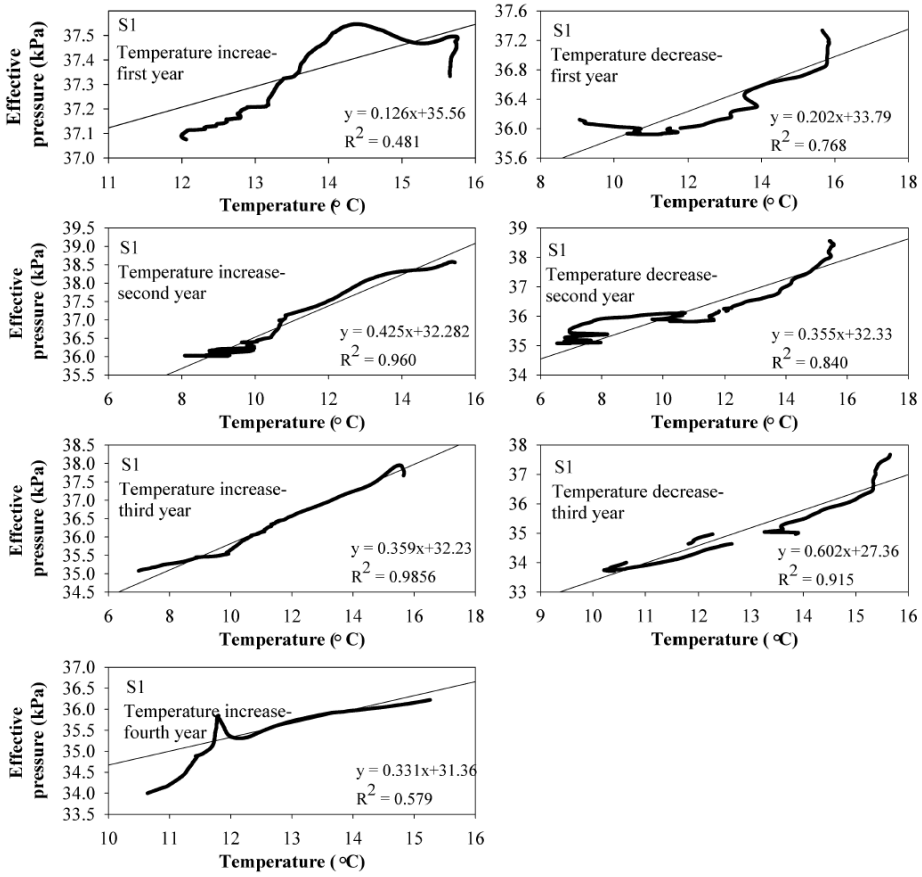

Figure 9.43 Seasonal correlation between cell temperature and measured pressure for cell S1

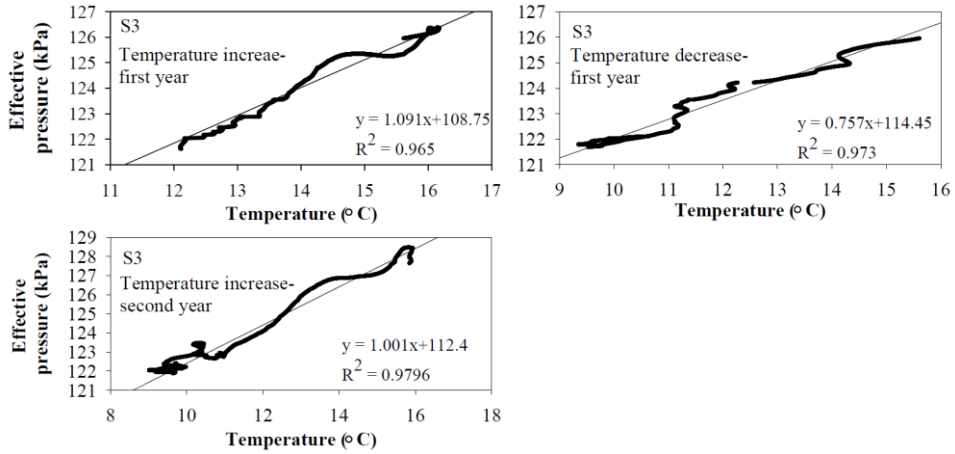

Figure 9.44 Seasonal correlation between cell temperature and measured pressure for cell S3 (Note: S3 stopped working properly at some point in the second year).

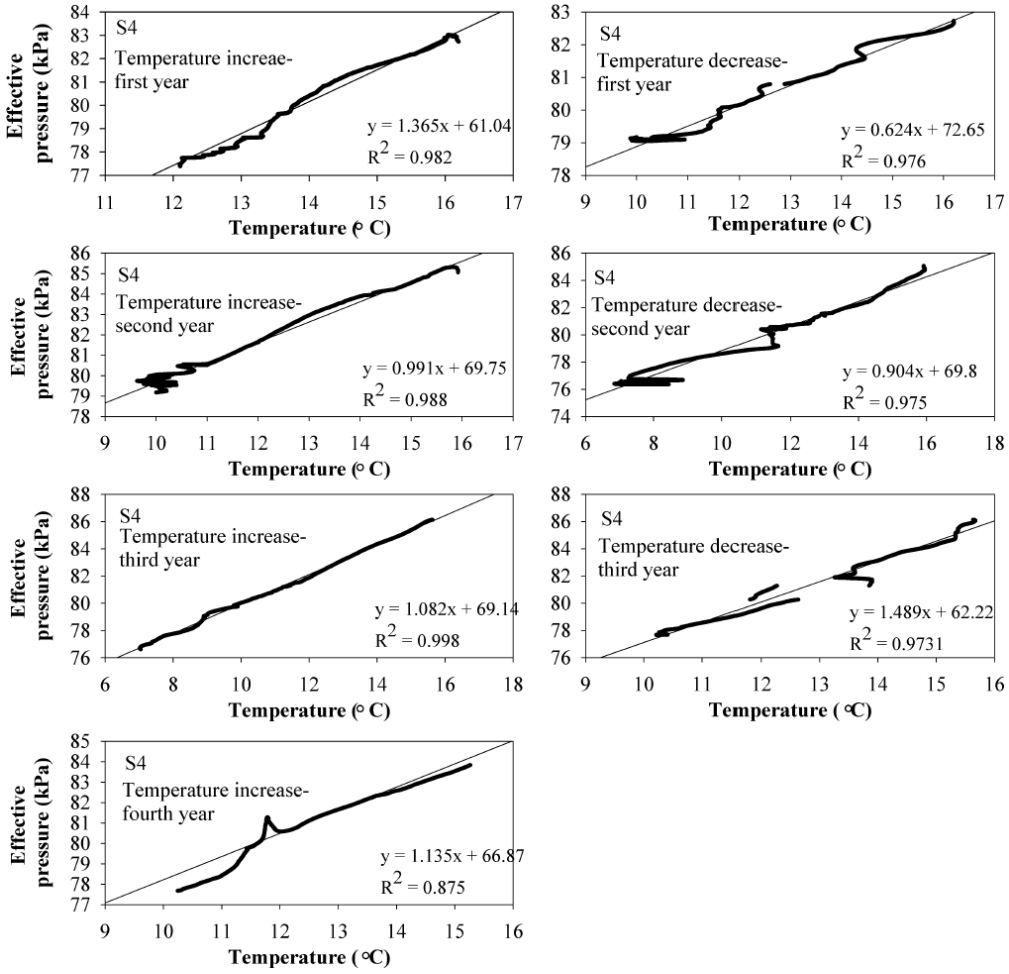

Figure 9.45 Seasonal correlation between cell temperature and measured pressure for cell S4

9.2.7.2 The effect of air temperature on foundation pressure cells

There are also pressure changes with high frequency which appear as noise in the shape of the pressure curve. This noise is mostly associated with the air temperature as shown in Figure 9.46. This figure presents the effective pressure changes as well as air temperature changes over four days of operation. As shown, any change in air temperature corresponds to an inverse response with effective pressure; i.e., when

the air temperature increases, the effective pressure decreases and vice versa. The source of this correlation is not clear. This behavior may be attributed to the bridge contraction and expansion with air temperature, which was discussed previously. If this is the case, when temperature increases the superstructure tends to expand which induces compressive pressure to the integrated zone, with a tendency to lift the bridge deck at the abutment. As a result, the foundation pressure decreases. The opposite response occurs when the air temperature decreases. This observed behavior is consistent with what has been reported by Lawrence (2014) for a GRS-IBS constructed in Hawaii. Warren et al. (2010) also reported a slight abutment pressure release induced by the steel girder expansion in a GRS-IBS structure.

There is always a delay between the air temperature and pressure peak values (about three hours). This observed behavior seems rational since it takes time to transfer the effect of external temperature into the structure.

In order to assess the typical daily change in the measured effective pressure upper and lower envelopes were drawn on the top and bottom boundaries of the graphs in a way that they covered the most of the measured data. The results are shown in Figure 9.47. As shown, except for a few points which do not fit between the upper and lower envelopes for the most of the period, the difference between the upper and lower measured values are about 2, 10, 5 and 2.5 kPa for cells S1, S2, S3 and S4, respectively. This range of daily change of the data is less than 6% of the average measured pressure values for each cell, as shown in Figure 9.37.

This inverse relationship between the air temperature and the foundation pressure was also shown in Chapter 5 in Figure 5.10. As discussed there, the daily correlation coefficient between the air temperature and foundation pressure was mostly negative, which indicates their inverse relationship.

9.2.7.3 Factor of safety against foundation bearing capacity failure

If the maximum applied pressure recorded by any of the GRS abutment sensors (e.g., S1, S2, S3, S4) after bridge placement is considered (164 kPa), the factor of safety against foundation bearing capacity failure can be calculated as:

$$F.S_{foundation\ bearing} = \frac{q_{u,found}}{q_{app,found}} = \frac{500}{164} = 3.1 \quad (9.6)$$

In this equation $q_{u,found}$ is the ultimate bearing capacity of the clay foundation and $q_{app,found}$ is the applied bearing pressure. Note that the above calculation makes a very conservative assumption, that the maximum applied pressure recorded by any sensor is actually a uniform applied bearing pressure. As shown in Chapter 8, this is clearly not the case. Consequently, the actual factor of safety against ultimate bearing capacity failure of the abutment is likely much larger than 3.1.

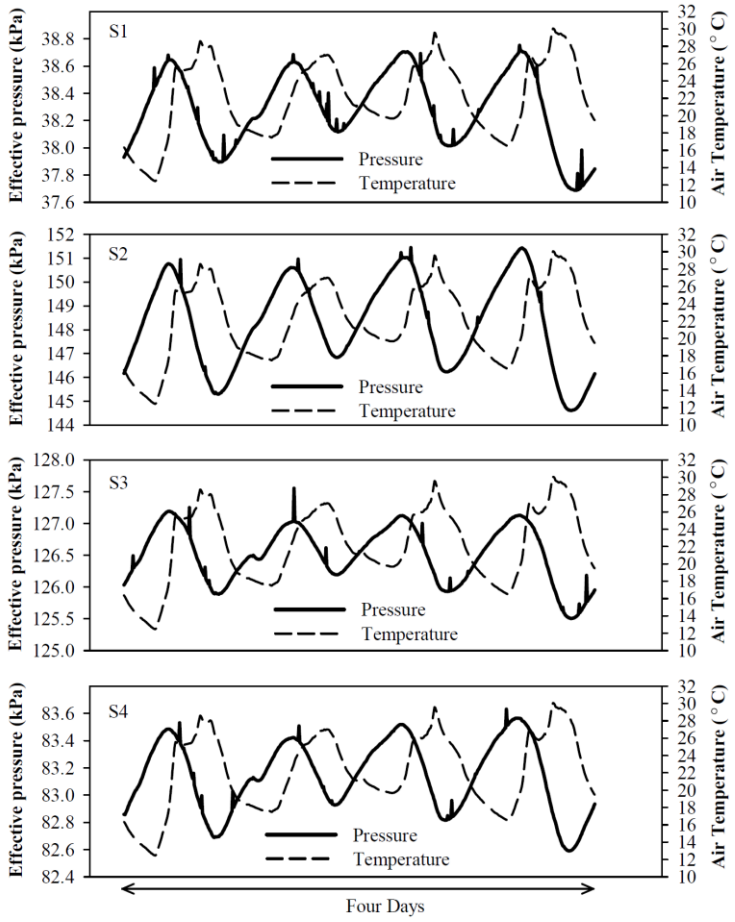

Figure 9.46 Air temperature changes alongside the associated effective foundation pressure changes

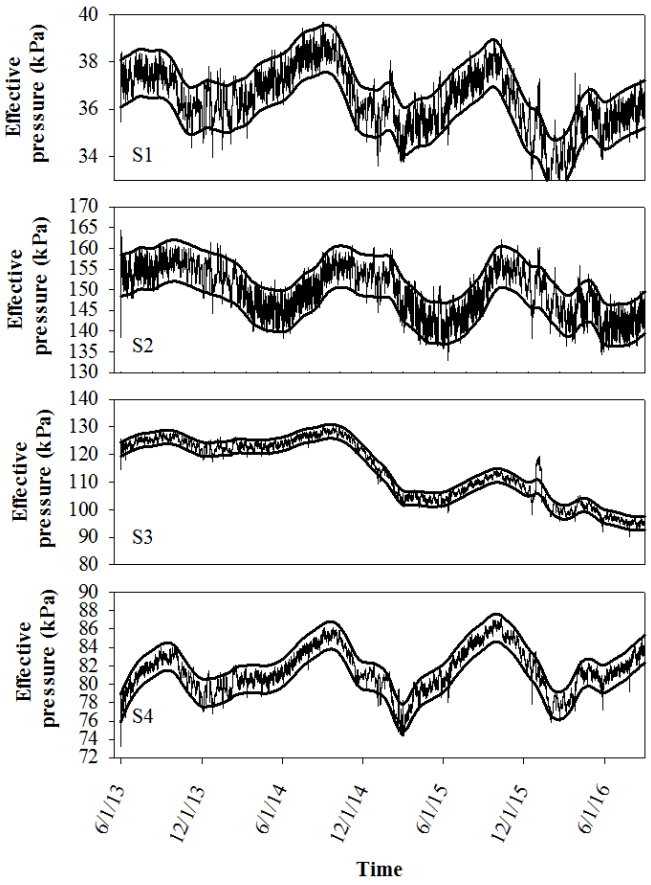

Figure 9.47 Upper and lower envelopes covering most of the measured data by the foundation pressure cells

9.2.8 Abutment pressure cells

Three pressure cells were installed in the west abutment to measure the induced pressure in this area. The cells were installed in the upper levels of the abutment to capture the effect of the live loads and also the bridge dead load. The induced pressure in the abutment by the truck live load tests were measured by these cells, with the corresponding results being presented in Chapter 7. These pressure cells are also capable

of measurement of instantaneous pressure produced by live load on the road provided a data logger with a high frequency of data collection is utilized. For budget reasons, the logger utilized for the current study was not able to collect the data with sufficiently high frequency to examine the occurrence of specific live load events on the bridge during in-service operation. However, in the future it is possible to replace the currently deployed datalogger with a new data logger that has the capability to investigate the effect of very instantaneous loads. The pressure transducers utilized at this location were custom made and were a combination of a vibrating wire pressure cell and a foil strain gauge-based pore pressure transducer. It was fabricated by itmsoil America and the purpose of this combination was to enable the cell to measure nearly instantaneous pressures.

Figure 9.48 demonstrates the changes in abutment pressure over three years of operation that were recorded by the cells. As shown in this figure and in a similar fashion as the foundation pressure cells, the pressure is changing seasonally and also daily. The daily changes induce a significant amount of noise in the measured pressure. This daily and seasonal change in pressure implies that the temperature influences the measured values by the cells similar to what was seen in case of the foundation pressure cells. Since the pressure cells included foil strain gauge-based pore pressure transducers to measure the pressure, some temperature effects on the cells' wires and their corresponding readings may have also been induced, in a similar fashion as what was observed in case of foil strain gauges (as discussed in Chapter 6).

Based on the measured pressure over three years of operation, the profile of minimum, maximum and average measured pressure in the abutment is presented in Figure 9.49. As shown, there is a big gap between the minimum and maximum measured values.

In order to investigate the probability distribution of measured pressures, the histograms of the abutment measured pressure are presented in Figure 9.50. As shown, the distribution is not normal and there is not even a clear peak value in case of cells d2 and d3. The histogram of cell d1 is more similar to a normal distribution.

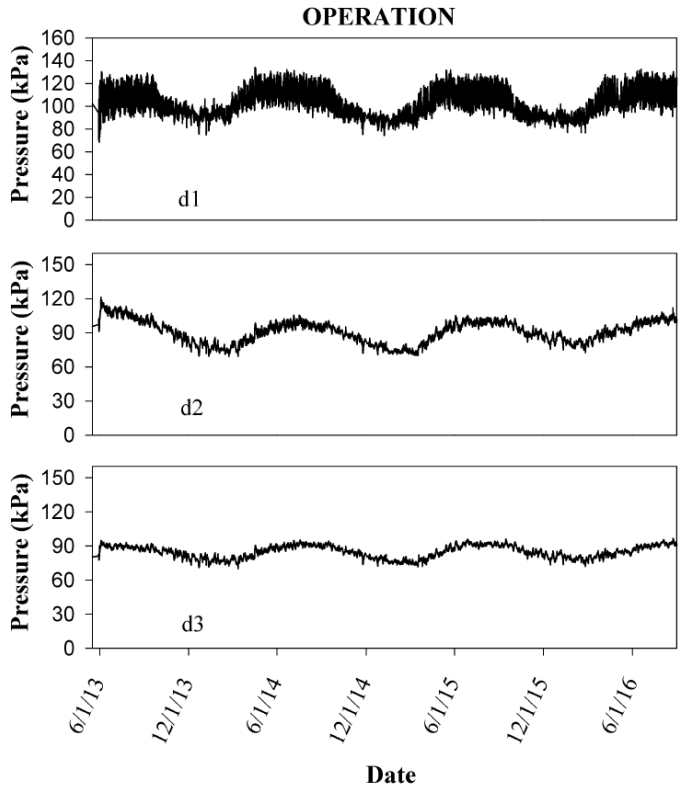

Figure 9.48 Measured pressure by the abutment cells over three years of operation

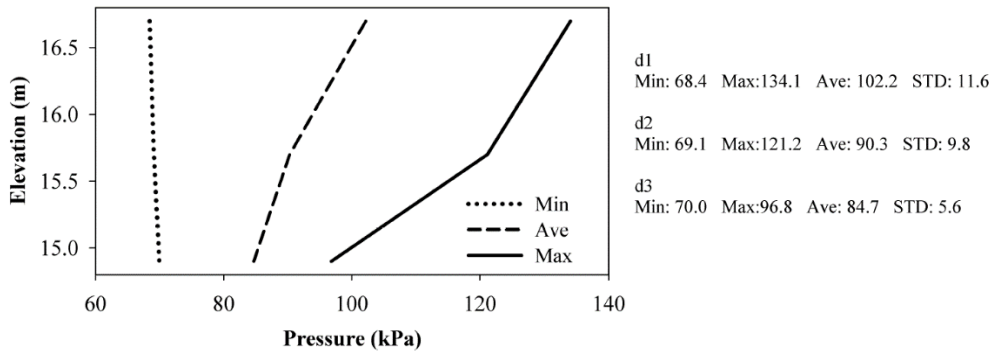

Figure 9.49 Minimum, maximum and average measured abutment pressures over three years of operation

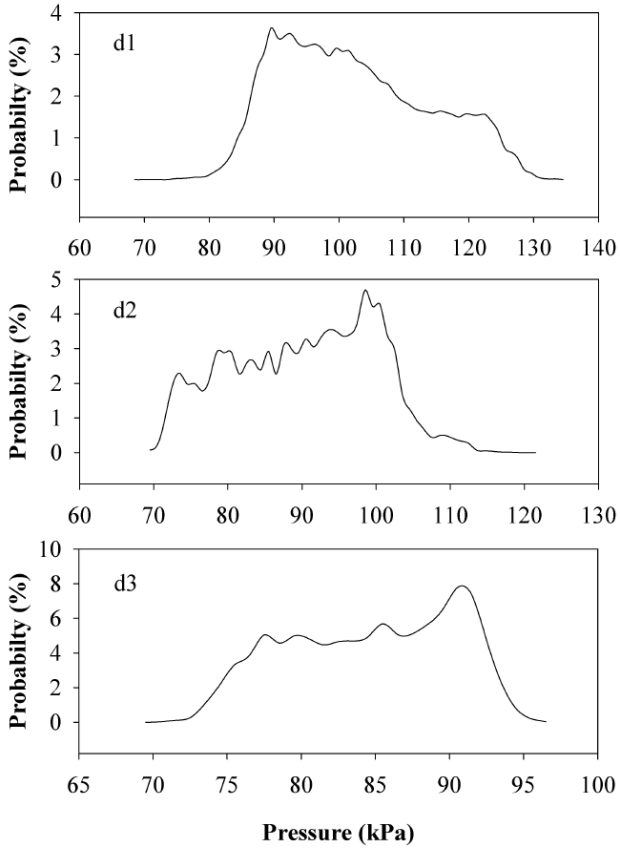

Figure 9.50 Histogram of abutment measured pressure over three years of operation

Based on what presented in Figures 9.48 through 9.50, the significant change in the measured pressure within three years of operation is clear. In the next section, possible reasons for this change are explored.

9.2.8.1 The effect of cell temperature on the abutment pressure cells

The effect of the cell temperature on the measured pressures is shown in Figure 9.51. As shown, the response is very similar to what shown in Figure 9.39 for the foundation pressure cells. This behavior appears rational since these cells are also vibrating wire type and the change in cell temperature has the same effect on them as it does on the foundation cells. It should be mentioned that unlike the foundation cells, these cells did not have a thermistor to measure their temperature. To estimate the cells temperature, the temperature measured by the thermistors on the left and right side of the cells were utilized. As shown in the figure, the cell temperature clearly affects the measured pressure. It is consequently believed that the seasonal change of measured pressure is apparent and not structural.

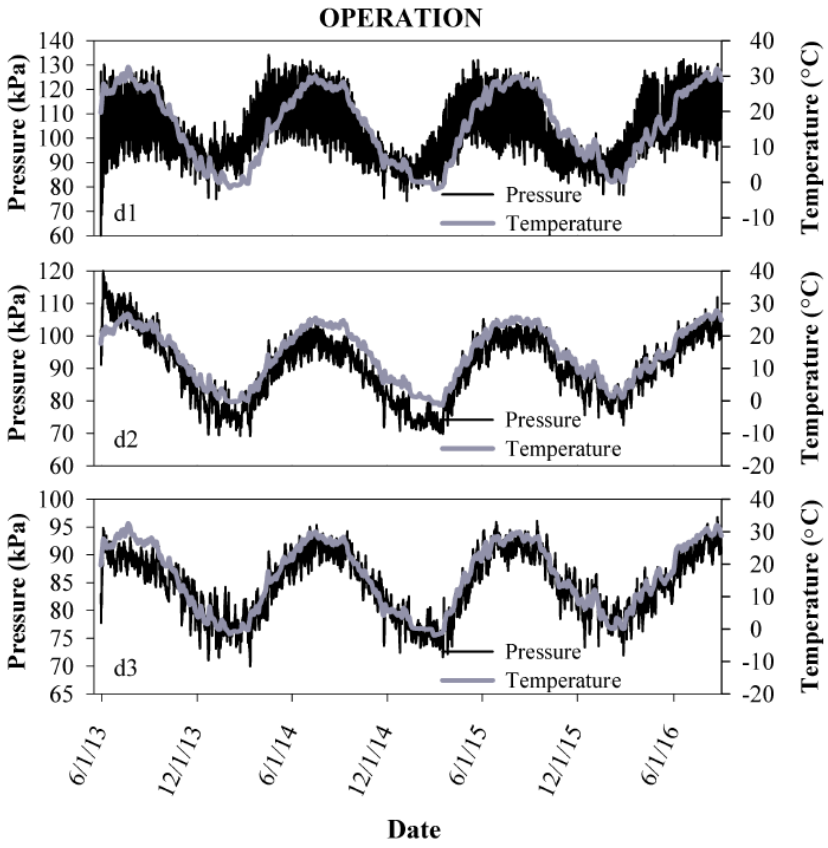

Figure 9.51 The effect of the cell temperature on the measured pressure by the abutment pressure cells

In order to investigate the effect of the cells' temperature on the associated readings, a frequency-based filtering process was applied to the pressure graphs in Figure 9.51 to filter out high frequency noise. After filtering this noise, new graphs were prepared which only show the trend of changes in pressure. The output of this process is shown in Figure 9.52; it can be observed that there is a good agreement between the cells' measured pressure trend and the cells' estimated temperature.

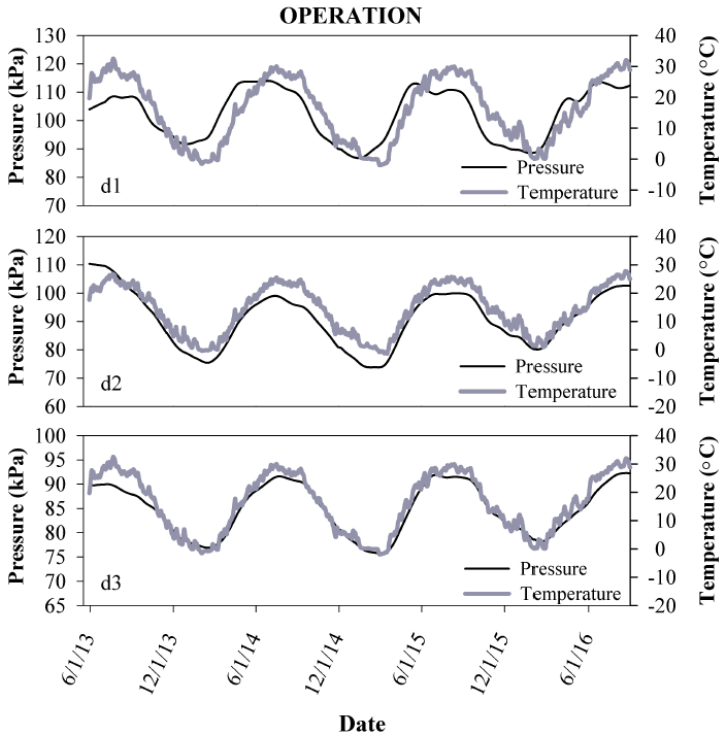

Figure 9.52 Smoothed pressure measured by the abutment pressure cells together with the cells' temperature estimated using the abutment thermistor readings

Regression analysis was conducted to find out the strength of the correlation between these two parameters, as shown in Figure 9.53. The results show a strong correlation for cells d2 and d3 with R-squared values greater than 0.9. However the correlation for cell d1 was not as strong, with an R-squared value of about 0.7. As mentioned earlier, there was no thermistor installed at the cells' exact locations and their temperature was estimated using the installed thermistors in the abutment, an approximation which likely affected the results. According to Figure 9.53, any increase in a given cell's temperature increases the cell's pressure, which is similar to the effect

that temperature has on foundation pressure cell readings. The slope of the correlation varies between 0.636 kPa/°C and 1.13 kPa/°C for cells d3 and d2, respectively. From these figures, it can be inferred that the seasonal changes in the measured pressure can be primarily attributed to changes in the pressure cells' temperature. The other source of daily changes might be attributed to the effect of wire temperature changes since changes in wire temperature can change the resistance of the overall circuit, affecting the corresponding readings like what was observed for the foil strain gauges that were attached to the geosynthetic. However, as shown in Chapter 5, the daily correlation between the pressure measured by the abutment cells and air temperature was generally much weaker than the daily correlation between the strains measured by the strain gauges and air temperature. In addition, for the strain gauges on the geosynthetic, the correlation between the strain and air temperature was similar for all the gauges, but the daily correlation between pressure measured by Cell d1 and air temperature was different from the daily correlations measured for Cells d2 and d3. These observations indicate that wire temperature changes are not the only source of the noise that was observed in the abutment pressure cells' readings, as was the case for the foil strain gauges that were bonded to the geosynthetic.

Generally, the cell temperature change can significantly affect the pressure reading. Table 9.6 presents the difference between the minimum and maximum pressure, based off of the data shown in Figure 9.52, which shows the trend of the pressure changes after filtering the daily noises. As shown, the ratio for the cells changes from 1.4 to 2.0.

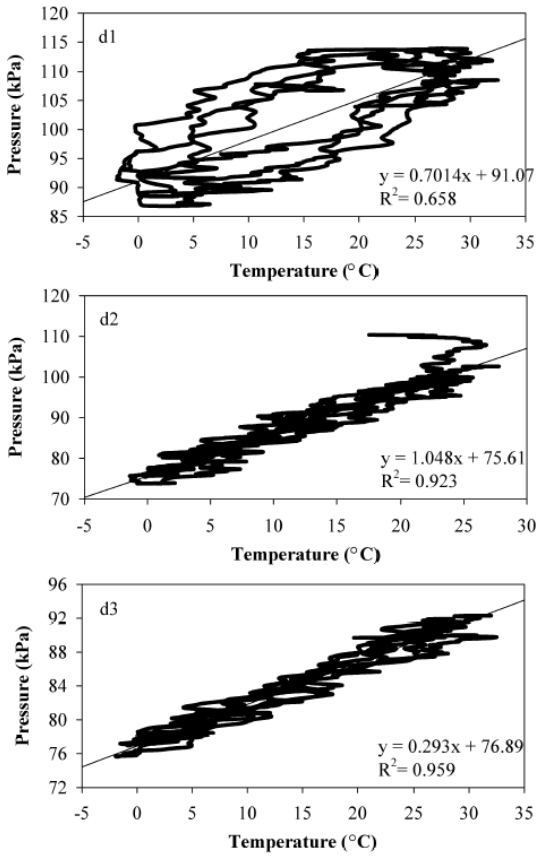

Figure 9.53 The correlation between the cells' estimated temperatures and measured pressures

Table 9.6 The ratio between the minimum and maximum pressure for the abutment pressure cells over three years of operation

Pressure cell	The ratio
d1	1.96
d2	1.75
d3	1.38

9.2.8.2 The effect of air temperature on the abutment pressure cells

The changes in measured pressure together with the changes in air temperature over four days are displayed in Figure 9.54. This figure clearly presents the changes in pressure with the changes in air temperature. As can be observed, the effect of the air temperature on cell d1 is significantly different from its effect on the other two cells.

Any increase in air temperature increases the measured pressure by cell d1, while simultaneously decreasing the measured pressure by the other two cells. The inverse effect of the air temperature on measured pressure was already discussed for the foundation pressure cells. It was noted previously that air temperature changes induces contraction and expansion to the superstructure which may change the pressure in the foundation. The same conclusion can be made in the case of the pressure in the abutment, as shown for the d2 and d3 cells. However, the effect on cell d1 is not inverse but direct for most of the three years of operation.

As discussed in Chapter 5, the correlation between cells d2 and d3 was strong while it was weak between d1 and d2 (Figures 5.6 and 5.7). In addition, the correlation coefficient between d2 and air temperature (Figure 5.8) was mostly negative similar to what was observed for the foundation pressure cells (Figure 5.10), and the discrepancies in Figure 5.8 were even less than Figure 5.10.

As shown in Figure 5.9, the correlation between the measured pressure by cell d1 and the air temperature was mostly positive but very erratic which means that there were also days that the response of the cell d1 to the air temperature change was similar to the two other cells. Therefore, the response of cell d1 to the air temperature was complicated. It might be concluded that the location and the elevation of the cell d1 is such that the effect of the air temperature change on it is direct most of the time, depending on the amount of the change in air temperature and its gradient. In case of the other two cells, the effect of the air temperature change is inverse most of the time. The effect of the air temperature on the bridge expansion and contraction may have some effects on the measured pressure by the cells.

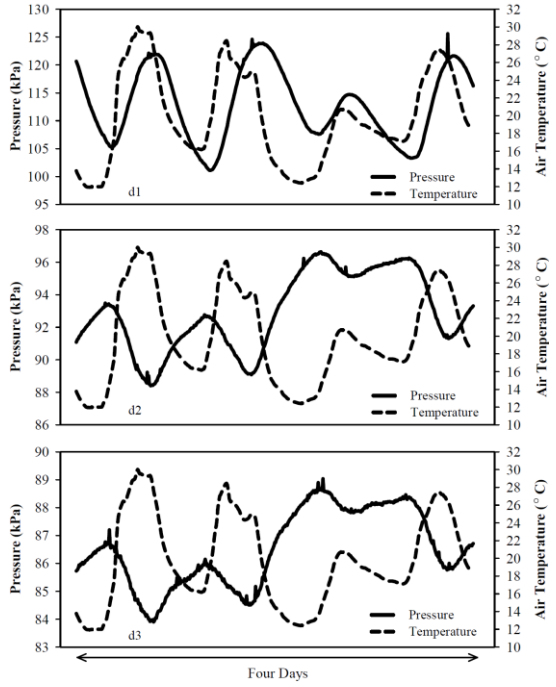

Figure 9.54 The effect of the air temperature on the measured pressure by the abutment cells

The amount of the decrease or increase in measured pressure with the increase or decrease in air temperature is not constant or proportional. For instance, for those sample four days shown in Figure 9.54, a 18°C increase in air temperature increased the induced pressure to cell d1 as high as 16 kPa while a 12°C increase in air temperature increased the induced pressure to cell d1 as high as 23 kPa, which is significant compared with the average value that was recorded (about 102 kPa). Since the reinforcement elements are designed based on the applied pressure, this change in pressure induced by the air temperature can significantly affect the applied pressure to the reinforcement element, which should be considered in design. The effect of the air temperature on the uppermost cell is more significant than its effect on the lower cells. For instance, a 12°C decrease in air temperature decreases the induced pressure to cell d1 as high as 18 kPa while increases the induced pressure to cell d2 as high as 8 kPa, as shown in Figure 9.54. As with the foundation pressure cells, there is always a delay between the air temperature and foundation pressure peak values, which is associated with the time that is needed to transfer the air temperature change to the abutment.

In order to assess the typical daily change in the measured abutment pressure, an upper and lower envelope were drawn on the top and bottom boundaries of the graphs in a way that they covered the most of the measured data. The results are shown in Figure 9.55. As shown, except for a few points which did not fall between the upper and lower envelopes, for the most of the period the difference between the upper and lower measured values are about 19, 14 and 9 kPa for cells d1, d2 and d3, respectively. Comparing with the average pressure values for each cell (shown in Figure

9.49), this range of daily change of the data is between 10 to 16 percent. The corresponding value for the foundation pressure cells were less than 6%. This indicates that the effect of temperature change is more pronounced for the abutment pressure cells, which is not surprising given that they are foil-based sensors and not vibrating wire ones (as the foundation pressure cells were).

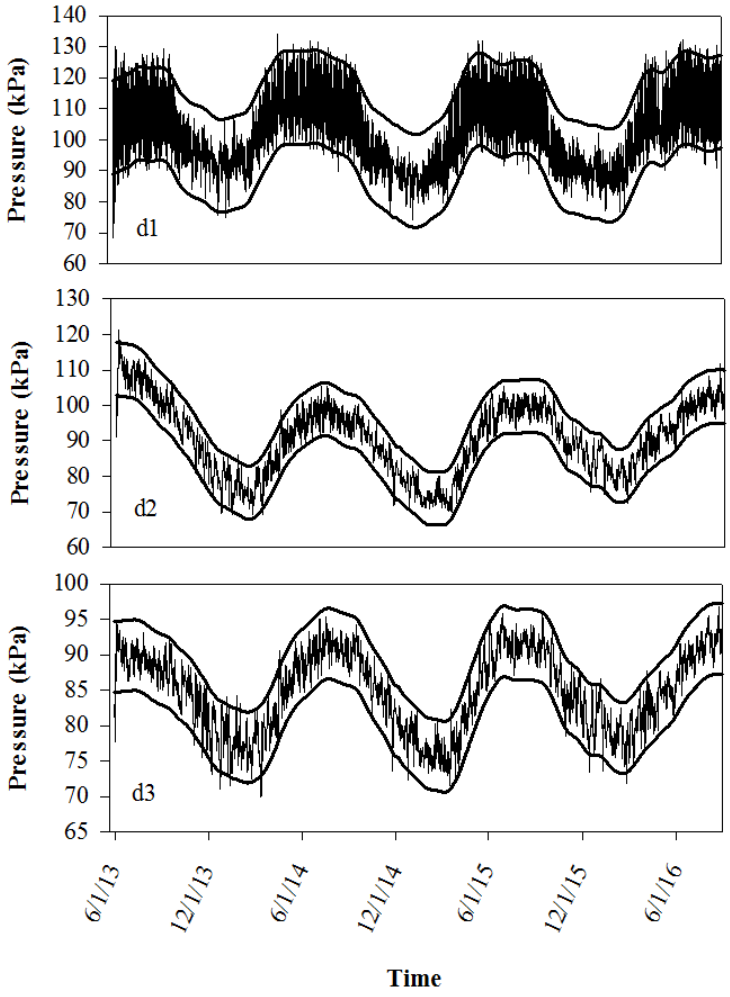

Figure 9.55 Upper and lower envelopes covering most of the measured data from the abutment pressure cells

9.8.2.3 Factor of safety against abutment bearing capacity failure

The factor of safety against abutment bearing capacity failure can be calculated in a similar fashion as what was done for the foundation bearing capacity failure (Equation 9.7). The maximum measured pressure after the bridge placement ($q_{app,abut}$) was about 134 kPa (Figure 9.49). The ultimate applied pressure per abutment ($q_{u,abut}$) is about 600 kPa according to the design criteria (Adams et al. 2011 and Chapter 3), which implies that:

$$F.S_{abutment\ bearing} = \frac{q_{u,abut}}{q_{app,abut}} = \frac{600}{134} = 4.5 \quad (9.7)$$

It should be noted that this calculation is also quite conservative in its approach, as it assumes the maximum applied pressure at any point in time by any sensor is applied continuously, which is clearly not the case (as shown in Figure 9.49).

9.3 Conclusion

In this chapter, the behavior of the GRS-IBS structure was investigated over three years of in-service operation. The measured data by different types of sensors were discussed and the details were presented for each type of sensor that was utilized in the structure. A summary of the results is as follows:

1- The water content of the abutments changed seasonally based on what was measured by the water content sensors. The maximum water content was measured in the winter and spring seasons while the minimum was measured in the summer. The

corresponding trend was in a good agreement with the river water level and precipitation data. The precipitation by itself increases the water content in the abutments and also increases the water level in the river which affects the abutment water content as well. The maximum water content measured in the second year was higher than the first and third years of operation. The water content in the abutment might be affected by both the amount and type of precipitation and the subsequent rate of infiltration. No obvious correlation was observed between the water content increase and the deformation of the structure. The amount of the measured strain was still very low even for the points with the highest measured water contents. It was concluded that the structure's response over three years of operation was not significantly influenced by the abutment water content.

2- In order to measure the water pressure in the foundation and the abutment, three piezometers were installed. The measured piezometric data did not show any generation of significant excess pore pressures during construction and operation. It was inferred that very little observable consolidation settlement occurred over three years of operation. The water pressure was only changing with the water level in the river. The maximum change in river water level was about 1 m over three years of operation. However, no significant effect of the increase in river water level was observed on the GRS-IBS structure's responses. This behavior was not surprising, as the abutment was constructed using an open-graded free draining backfill.

3- Thermistors were utilized to measure the changes in the abutment temperature and its effect on the response of the GRS-IBS. The results showed that the abutment temperature changes seasonally. The temperature in the area close to the

facing wall and near the top of the abutment experienced more daily changes in temperature since they are closer to the air and are more influenced by the air temperature. The daily and monthly temperature contour graphs indicated that the temperature does not significantly change over the course of a single day. However, the temperature distribution in the abutment is different in hot and cold weather.

4- The long-term monitoring of the strain gauges showed the development of a small amount of creep strain in the abutment. The average amount of creep did not exceed 0.1% over three years. The measured creep by the long gauges was typically higher than what was measured by the short ones. The maximum strain in both abutments was less than 0.5 percent. The sensors' malfunction should be noted in interpretation of creep data. Part of the increase in the abutment strain may have been associated with the continuous increase in the abutment water content. The abutment water content needs to be cautiously monitored to investigate its possible effect on the structure stability in future years.

5- The facing walls' deflection and settlement were measured using surveying targets. The lateral deflection was very small along the width and the height of both facing walls. The maximum measured deflection and settlement was about 12 mm. The corresponding maximum vertical and lateral strain were 0.25% and 1.09%, respectively. There was relatively significant error associated with the surveying operation (6 mm), as compared with the measured values. The average lateral deflection over three years of operation was about 4 mm for both facing walls, which corresponded to 0.4% lateral strain. This value is in good agreement with what was measured by the

strain gauges. The results showed a slight tendency for increase in both the lateral deflection and settlement of the facing walls over time, i.e., minor creep behavior.

6- The clay foundation lateral deflection was measured using four inclinometer sensors. The lateral deflection increased during construction and at the beginning of in-service operation but the rate of the deformation decreased for both the E-W and N-S directions. Some very minor creep deformation behavior was observed, which was higher in the N-S direction. This may indicate some abutment lateral deflection toward the wing walls. The maximum deflection was less than 10 mm, which is not significant.

7- The effective pressure beneath the RSF was measured using four vibrating wire pressure cells over three years of operation. The maximum pressure occurred beneath the facing wall, with the pressure varying generally linearly backward. The minimum pressure was measured in front of the RSF foundation, which was expected since there was no abutment on top of it; these results are consistent with what was discussed in Chapter 7. The measured pressure was significantly changing over time due to the cells' temperature, with a fluctuation in value of about 20%. Changes in cell temperature induce fluctuations in the measured pressure values over time. As discussed, the cell temperature effect on the pressure reading is complicated, since it depends on different factors such as temperature, pressure, the properties of the cell, and installation effects. It was also shown that there was an inverse correlation between the daily air temperature changes and the measured pressure, which induces additional noise to the measured data on a daily basis. This may be attributed to the bridge expansion

and contraction induced by the air temperature changes, which pushes the abutment backward and forward. Increases in the air temperature correspond to decreases the foundation pressure and vice versa. The daily changes of the pressure induced by the air temperature was commonly less than 6% of the average effective pressure.

8- The abutment pressure was measured using three pressure cells in the elevations near the top of the wall. The results clearly showed the effect of the cell temperature on the pressure on a seasonal basis, as was observed for the foundation cells. It was shown that the pressure changes nearly linearly with changes in the cells' temperatures. The measured pressure was significantly changing due to the cells' temperature (between 20% to 50%). There was also a relationship between the daily air temperature changes and the measured pressure. The air temperature correlation with the two lower cells measured pressure (d2 and d3) was mostly inverse, similar to what was observed for the foundation pressure cells. In contrast, its correlation with the uppermost cell measured pressure was mostly direct. Any decrease on increase in air temperature significantly changed the pressure measured by pressure cell d1. Bridge induced deformation by the air temperature changes may also affect the pressure in the upper elevations of the abutment. The ratio between the daily changes of the measured pressure and the average pressure was typically between 10 to 16 percent.

References

AASHTO (2014). "AASHTO LRFD bridge design specifications." 7th ed. Washington, DC: American Association of State Highway and Transportation Officials

Abu-Hejleh, N., Wang, T. and Zornberg, J. (2001). "Performance of geosynthetic-reinforced walls supporting bridge and approaching roadway structures." In GeoDenver 2000 Congress.

Abu-Hejleh, N., Hanneman, D., White, D., Wang, T. and Ksouri, I. (2006). "Flowfill and MSE Bridge Approaches: Performance, Coast, and Recommendations for Improvements (No. CDOT-DTD-R-2006-2)." Colorado Department of Transportation, Research Branch.

Abu-Hejleh, N., Zornberg, J., Wang, T., Watcharamonthein, J. (2002). "Monitored displacement of unique geosynthetic-reinforced soil bridge abutments." Geosynthetics International, 9 (1), 71–95.

Abu-Hejleh, N., Zornberg, J., Elias, V. and Watcharamonthein, J. (2003). "Design assessment of the founders/meadows GRS abutment structure." In Proc., 82nd Annual TRB Meeting.

Adams, M., Nicks, J., Stabile, T., Wu, J., Schelatter, W. and Hartmann, J. (2011). "Geosynthetic Reinforced Soil Integrated Bridge System Interim Implementation Guide." Federal Highway Administration, Publication No. FHWA-HRT-11-026, Washington, DC.

Adams, M., Schlatter, W. and Stabile, T. (2007). "Geosynthetic-reinforced soil integrated abutments at the bowman road bridge in defiance county, Ohio." Proceedings, Geo-Denver, 1-11.

ASTM D4595 (2011). "Standard test method for tensile properties of geotextiles by the wide-width strip method." ASTM International, West Conshohocken, PA.

Branco, F. and Mendes, P. (1993). "Thermal actions for concrete bridge design." Journal of Structural Engineering, 119(8), 2313-2331.

Buttry, K., McCullough, E. and Wetzel, R. (1996). "Temperatures and related behavior in segmental retaining wall system." Transportation Research Record: Journal of the Transportation Research Board, (1534), 19-23.

Daigle, L. and Zhao, J. (2004). "The influence of temperature on earth pressure cell readings." Canadian geotechnical journal, 41(3), 551-559.

Dunnicliff, J. (1997). “Temperature sensitivity of earth pressure cells.” Geotechnical Instrumentation News, 15(2): 42.

Dunnicliff, J. and Green, G. (1988). “Geotechnical instrumentation for monitoring field performance.” John Wiley & Sons, Inc., New York.

Efretuei, E. (2013). “Thermal impact on soil-structure interaction for integral bridges.” University of Leeds.

Esmaili, D., Hatami, K. and Miller, G. (2014). “Influence of matric suction on geotextile reinforcement-marginal soil interface strength.” Geotextiles and Geomembranes, 42(2), 139-153.

FHWA (2009). “Mechanically stabilized earth walls and reinforced soil slopes design and construction guidelines”. Volume I, publication No. FHWANHI-10-025.

Fredlund, D. G., Morgenstern, N. R. and Widger, R. A. (1978). “The shear strength of unsaturated soils.” Canadian geotechnical journal, 15(3), 313-321.

Helwany, S., Wu, J. and Froessl, B. (2003). “GRS bridge abutments—an effective means to alleviate bridge approach settlement.” Geotextiles and Geomembranes, 21(3), 177-196.

Hoffman, P., McClure, R. and West, H. (1983). “Temperature study of an experimental segmental concrete bridge.” PCI Journal, 28(2), 78-97.

Horvath, J. (2005). “Integral-abutment bridges: geotechnical problems and solutions using geosynthetics and ground improvement.” In West Virginia University.

Huntley, S. and Valsangkar, A. (2016). “Laboratory thermal calibration of contact pressure cells installed on integral bridge abutments.” Canadian Geotechnical Journal, 53(6), 1013-1025.

Iwamoto, M. (2014). “Observations from load tests on geosynthetic reinforced soil”. Doctoral dissertation, University of Hawaii.

Jiang, Y., Han, J., Parsons, R. and Brennan, J. (2016). “Field Instrumentation and Evaluation of Modular-Block MSE Walls with Secondary Geogrid Layers.” Journal of Geotechnical and Geoenvironmental Engineering, 05016002.

Kim, W. and Borden, R. (2013). “Numerical simulation of MSE wall behavior induced by surface-water infiltration.” Journal of Geotechnical and Geoenvironmental Engineering, 139(12), 2110-2124.

Kim, W. and Laman, J. (2010). “Integral abutment bridge response under thermal loading.” Engineering Structures, 32(6), 1495-1508.

Koerner, R. and Koerner, G. (2013). “A data base, statistics and recommendations regarding 171 failed geosynthetic reinforced mechanically stabilized earth (MSE) walls.” Geotextiles and Geomembranes, 40, 20–27.

Lawrence, J. (2014). “Structural health monitoring of the first geosynthetic reinforced soil--integrated bridge system in Hawaii.” Doctoral dissertation, University of Hawaii at Manoa.

Leshchinsky, D. (2009). “On global equilibrium in design of geosynthetic reinforced wall.” Journal of Geotechnical and Geoenvironmental Engineering, 135(3), 309–15

Leshchinsky D and Tatsuoka F. (2013). “Performance, design, and redundancy, geosynthetic reinforced walls in the public sector.” Geosynthetics 31(3), 12–21.

Miyata, Y., Bathurst, R. and Miyatake, H. (2015). “Performance of three geogrid-reinforced soil walls before and after foundation failure.” Geosynthetics International, 22(4), 311-326.

Ng C and Pang Y. (2000). “Influence of stress state on soil–water characteristics and slope stability.” Journal of Geotechnical and Geoenvironmental Engineering, 126(2), 157–66

Nicks, J., Esmaili, D. and Adams, M. (2016). “Deformations of geosynthetic reinforced soil under bridge service loads.” Geotextiles and Geomembranes, 44(4), 641-653.

Portelinha, F., Bueno, B. and Zornberg, J. (2013). “Performance of nonwoven geotextile-reinforced walls under wetting conditions: laboratory and field investigations.” Geosynthetic International, 20(2), 90–104.

Puppala, A., Saride, S., Archeewa, E., Hoyos, L. and Nazarian, S. (2009). “Recommendations for design, construction, and maintenance of bridge approach slabs: Synthesis report.” Rep. No. FHWA/TX-09/6022, 1.

Roberts-Wollman, C., Breen, J. and Cawrse, J. (2002). “Measurements of thermal gradients and their effects on segmental concrete bridge.” Journal of Bridge Engineering, 7(3), 166-174.

Santos, E., Palmeira, E. and Bathurst, R. (2013). "Behaviour of a geogrid reinforced wall built with recycled construction and demolition waste backfill on a collapsible foundation." Geotextiles and Geomembranes, 39, 9-19.

Santos, E., Palmeira, E. and Bathurst, R. (2014). "Performance of two geosynthetic reinforced walls with recycled construction waste backfill and constructed on collapsible ground." Geosynthetics International, 21(4), 256-269.

Sellers, B. (2000). "Temperature effects on earth pressure and concrete stress cells – some theoretical considerations." Geotechnical Instrumentation News, 18(1), 23–24.

Skinner, G.D., Rowe R.K. (2005). "A novel approach to estimating the bearing capacity stability of geosynthetic reinforced retaining walls constructed on yielding foundations." Canadian Geotechnical Journal, 42(3), 763-779.

Song, X., Melhem, H., Li, J., Xu, Q. and Cheng, L. (2016). "Effects of Solar Temperature Gradient on Long-Span Concrete Box Girder during Cantilever Construction." Journal of Bridge Engineering, 21(3), 04015061.

Tatsuoka, F., Tateyama, M., Koda, M., Kojima, K., Yonezawa, T., Shindo, Y. and Tamai, S. (2016). "Recent research and practice of GRS integral bridges for railways in Japan." Japanese Geotechnical Society Special Publication, 2(68), 2307-2312.

Therm-x (1998). "YSI precision thermistors and probes."

Vahedifard, F, Leshchinsky, B, Mortezaei, K and Lu, N. (2015). "Active earth pressures for unsaturated retaining structures." Journal of Geotechnical and Geoenvironmental Engineering, 141(11), 04015048.

Valentine, R. (2013). "An assessment of the factors that contribute to the poor performance of geosynthetic-reinforced earth retaining walls." In: Ling HI et al., editors. Proc. international symposium on design and practice of geosynthetic-reinforced soil structures, Bologna, Italy, October 14– 16. Lancaster, PA: DEStech Publication Inc., 318–27.

Vennapusa, P., White, D., Klaiber, F., Wang, S. and Gieselman, H. (2012). "Geosynthetic reinforced soil for low-volume bridge abutments."

Warren, K., Christopher, B. and Howard, I. (2008). "Techniques Used to Measure Strain on Geosynthetics in Dynamic Applications." GeoCongress 2008: Characterization, Monitoring, and Modeling of GeoSystems, 541-548.

Warren, K. A., Schlatter, W., Adams, M., Stabile, T. and LeGrand, D. (2010). "Preliminary Results for a GRS Integrated Bridge System Supporting a Large Single Span Bridge." In Earth Retention Conference 3, 612-619.

Warren, K., Whelan, M., Hite, J. and Adams, M. (2014). "Three-Year Evaluation of Thermally Induced Strain and Corresponding Lateral End Pressures for a GRS IBS in Ohio." In Geo-Congress 2014 Technical Papers: Geo-characterization and Modeling for Sustainability, 4238-4251

Weiler, W., and Kulhawy, F. (1982). "Factors affecting cell stress measurements in soil. Journal of the Geotechnical Engineering Division." ASCE, 108(GT12), 1529–1548.

Wu, J. (2006). "Design and construction guidelines for geosynthetic-reinforced soil bridge abutments with a flexible facing." Transportation Research Board.

Wu, J., Ketchart, K. andAdams, M. (2008). "Two full-scale loading experiments of geosynthetic-reinforced soil (GRS) abutment wall. International Journal of Geotechnical Engineering."

Yang, M., Drumm, E., Bennett, R., and Mauldon, M. (2001). "Temperature effects on contact earth pressure cells: inferences from long term field instrumentation." Geotechnical Instrumentation News, 19(2), 25–28.

Yang, K., Utomo, P. and Liu, T. (2013). "Evaluation of force-equilibrium and deformation-based design approaches for predicting reinforcement loads within geosynthetic-reinforced soil structures." Journal of GeoEngineering, 8(2), 41-54.

Yoo, C. (2013). "Effect of rainfall on performance of geosynthetic reinforced soil wall using stress-pore pressure coupled analysis." In Geo-Congress 2013: Stability and Performance of Slopes and Embankments III, 566-573).

Yoo, C., and Jung, H. (2006). "Case history of geosynthetic reinforced segmental retaining wall failure." Journal of Geotechnical and Geoenvironmental Engineering, 132(12), 1538-1548.

Zhang, J., Zheng, J., Zhao, D., & Chen, S. (2016). "Field study on performance of new technique of geosynthetic-reinforced and pile-supported embankment at bridge approach." Science China Technological Sciences, 59(1), 162-174.

Chapter 10

CONCLUSIONS AND RECOMMENDATIONS FOR FUTURE RESEARCH

10.1 Introduction

This report presented an in-depth discussion on the design, construction, instrumentation and performance of the first geosynthetic reinforced soil integrated bridge system (GRS-IBS) that was constructed in the state of Delaware. Internal and external stability of the structure were evaluated during the design process, and the results from these analyses were used to establish the recommended materials, dimensions, and construction requirements for the structure. An extensive instrumentation system was designed in order to monitor the behavior of the GRS-IBS during construction, truck live load testing and in-service operation including water content sensors, thermistors, piezometers, surveying targets, strain gauges, inclinometer sensors, foundation pressure cells and abutment pressure cells. The majority of the aforementioned sensors used in the study were installed in the west abutment, with only surveying targets, strain gauges and thermistors being installed in the east abutment for independent confirmation of the GRS behavior. According to the results, the structure was stable during construction, live load testing and over three years of in-service operation. Based on data collected from the installed GRS-IBS instrumentation, it can be concluded that all measured deformations, strains and pressure were less than the allowable values.

10.2 Conclusions

1. The construction of the first GRS-IBS in Delaware was completed in about two months. During construction, different instruments were installed in the abutments. Prior to their installation in the field, strain gauges were affixed to the geosynthetic layers in the University of Delaware laboratory using two different attachment techniques, in order to minimize any field work stoppages during the construction process.

2. The overall behavior of the GRS-IBS was monitored during construction using the installed instrumentation. Generally, the deformation was very low and the maximum measured strains in the abutments were less than 0.5 percent. Placement of the bridge superstructure increased the geosynthetic strain level in the abutments, though not by a significant amount. The maximum effective pressure beneath the reinforced soil foundation (RSF) was less than 150 kPa and its distribution was not uniform. The maximum pressure was measured beneath the facing wall, with the applied pressure beneath the RSF decreasing in a fairly linear fashion moving into the abutment (away from the bridge superstructure). The minimum pressure was measured beneath the front of RSF (beneath the front "toe" of the structure), at the point where there was no abutment constructed on top of the RSF. The applied pressure beneath the GRS abutment increased in a relatively linear fashion during construction, tracking closely with increases in the abutment height. Placement of the bridge superstructure caused a significant jump in the applied pressure distribution, which was not surprising. The maximum measured pressure within the GRS abutment was recorded at the location of

the uppermost abutment cell after the bridge placement, which was also as expected. The deflection and settlement of the GRS abutment facing walls was very low during construction and after bridge superstructure placement. The maximum corresponding measured values were less than 12 mm, which included errors in the surveying approach (on the order of $\pm$6 mm); the actual abutment deflections and settlements were consequently likely less than 12 mm.

3. GRS-IBS construction was followed by live load testing using heavy trucks to evaluate the response of the structure. Different responses of the structure to different applied live loads were evaluated using the installed instruments. The results did not show any significant response of the structure to the applied live loads, with the induced deformation and pressures by the live load being in the allowable range. The maximum increase in the abutment strain during live load testing was less than 0.03 percent. The maximum increase in the foundation measured pressure during live load testing was about 14 percent. In addition, the maximum increase in the abutment pressure was measured by cell d1, which recorded a 71 percent increase in pressure during the load test. The factor of safety against abutment bearing capacity failure during live load testing was still quite high even for the heaviest load tests, where it was approximately equal to 4.7. The load cases with the trucks entirely positioned on the bridge and near to the west abutment induced the maximum pressure to the pressure cells installed in that abutment and also the ones beneath the RSF. No significant increase in the facing walls deformation was observed during the live load testing.

4. After completion of construction for the GRS-IBS, the in-service behavior of the structure was monitored over the long term. This report consequently presents data collected for the first three years of in-service operation of the structure. Data collection for the west abutment was performed using automated data loggers that simultaneously recorded data every 10 minutes, in order to ascertain that no significant event such as a flood is missed. As a result of this relatively high frequency of data collection for static system performance assessment, numerous data points were collected, which necessitated using data management techniques. The statistical analysis program "R" was utilized for this purpose, and the raw data were converted to engineering values using the instruments' respective calibration factors. The data was also rounded carefully for each type of sensor, with the degree of rounding for each sensor type being selected following the general accuracy and precision values reported by the manufacturer for each sensor. In order to minimize errors associated with computer memory usage, a data filtering process was also utilized to reduce the recorded data from a time interval of every 10 minutes to a time interval of 20 minutes. The data in the east abutment were collected manually using a handheld datalogger with a rotary switch for sensor selection, with an approximate data recording frequency of every two weeks to one month.

5. Daily correlation analyses were performed using the R program, in order to evaluate the strength of the correlation between different measured sensor responses. The results showed a strong correlation between the air temperature and strain in the abutment. In addition, the correlation analyses indicated the effect of the air temperature

on the foundation and abutment pressures measured by the pressure cells. The foundation pressure was correlated well with the pore pressure, which implies that there was a significant effect of pore pressure on the total pressure (which is not surprising). The pore pressure was consequently subtracted from the total pressure to calculate the effective pressure. No correlation was observed between the abutment pore pressure or water content versus the abutment deformation, which indicates that the presence of water in the abutment does not influence its deformation.

6. The water content in the abutments was slightly increasing over three years of in-service operation. There was a noticeable increase in water content in different elevations of the abutments in the winter and spring. The amount of precipitation and the rate of water infiltration into the abutment affect the water content in the abutment. Additionally, precipitation increases the water level in the river, which also increases the water content in the lower portion of the abutment. The abutment's deformation did not show a significant change with increases in the abutment's water content, even in the wetter seasons of the year.

7. The measured strain by the abutment strain gauges was corrected for the effect of air temperature and abutment temperature changes. An innovative approach was developed for performing this correction, which utilized an average abutment temperature recorded by numerous thermistors along the wire path. This approach is useful for correcting data recorded by foil strain gauges that are used with a two-wire Wheatstone bridge configuration.

8. The development of strain in the abutments was analyzed based on readings taken over three years of in-service operation. A very small amount of creep was observed, which was generally slightly less than 0.1% for the strain gauges which remained properly working. The long strain gauges measured a slightly higher creep than the short strain gauges, which may be attributed to the durability of the gauges themselves or (more likely), some small amount of creep in the adhesive that was used over time. The continuous increase in the abutment water content which was discussed in Chapter 9 may have induced some small amount of deformation to the abutment as well, which was not detectable via the surveying readings given their overall level of precision.

9. A methodology was developed to predict the effective pressure beneath the RSF during construction of the abutment and after surcharge application by the bridge dead and live load. It was shown that the induced pressure changes linearly at each location beneath the RSF for both load cases. It was also demonstrated that conventional bearing capacity and settlement design approaches do not do a good job of predicting the actual applied pressure distribution beneath the RSF foundation.

10. The investigation of the long term performance of the structure over three years of in-service operation did not show any significant change in the recorded values that were measured by the different sensors. The abutment strains did not exceed 0.5 percent and the facing walls' deformation was almost constant, which indicated the high strength of the abutments. The foundation and abutment pressures did not exceed the allowable values. However, the pressure cells' temperature changes

did appear to track closely with seasonal changes in the measured pressure and the air temperature changes tracked closely with the daily changes in the measured pressure; taken together, these effects together produced significant noise in the corresponding pressure graphs. Since a given cell's temperature change influences its pressure, the consequent induced pressure changes are believed to be apparent pressures, i.e., they do not correspond to actual changes in pressure. The maximum to minimum pressure ratio was about 1.10 for the foundation pressure cells and between 1.2 and 1.5 for the abutment pressure cells. The effect of changes in air temperature induced an apparent change in pressure into the pressure cell readings. It also likely changed the actual applied pressure regime to the abutment, due to thermal expansion and contraction of the bridge superstructure. It is difficult to differentiate between air temperature effects on the sensor measured pressures (due to changes in fluid pressure in the cell that are caused by changes in temperature) and actual changes in pressure that correspond to thermal straining of the GRS-IBS itself. The daily changes in the measured pressures were about 6% of the average pressure for the foundation cells and between 10% and 16% of the average pressure for the abutment cells.

11. Many of the installed sensors are still functioning properly after three years of operation. Our experience on this project indicates the importance of careful water proofing and appropriate sensor protection during installation.

10.3 Main Contributions

1. An extensive instrumentation system was utilized to monitor the behavior of the GRS-IBS structure and the data were collected every 10 minutes, which resulted in a large amount of collected data. In order to manage the large amount of data and also in order to have a better understanding of the performance of the structure, a correlation analysis was conducted between the different responses measured by different sensors. This correlation analysis clearly showed some important correlations including the effect of air temperature on the measured strain by the foil strain gauges and also its effect on the measured pressure in the foundation and the abutment.

2. The significant effect of wire temperature changes on the measured strain by the foil strain gauges was discussed and quantified in this report. A robust methodology was developed to correct this effect and the results showed the effectiveness of this methodology.

3. It was shown in this report that the deformation of the abutments and the facing walls of the GRS-IBS structure was very low. The maximum horizontal strain in the abutment was less than 0.5% and the facing walls lateral deformation and settlement was less than 12 mm, which were less than what is usually observed in conventional GRS and MSE structures. This observation also implies that sensors with higher precision and resolution should be utilized to measure the deformation of GRS-IBS structures.

4. It was shown in this report that the measured pressure distribution beneath the RSF foundation of the GRS-IBS structure was not in agreement with what

was predicted using conventional analysis/design approaches. It was also shown that the developed pressure beneath the toe of the RSF was not significant and the minimum pressure was measured at this location, while the maximum pressure beneath the RSF was measured close to the location of the facing wall. The pressure was linearly changing beneath the RSF behind the facing wall. Additionally, the increases in the measured pressure beneath the RSF with increases in the height of the abutment and also with increases in the applied surcharge was linear. An empirical approach was subsequently developed to predict the pressure distribution beneath the foundation during construction and bridge surcharge application. The strong agreement between the calculated pressure values using this empirical approach with the measured pressure showed the effectiveness of the developed approach.

5. The induced deformation by the heaviest live load was quite insignificant. The corresponding applied pressure by the heaviest live load was 130 kPa per abutment. This implies that the performance of the abutments under 190 kPa pressure (which is the allowable pressure to the abutment in the GRS-IBS manual) may still be quite satisfactory and the developed deformation under 190 kPa pressure will likely not be significant either. So it was recommended in this report to review the currently specified criteria for allowable pressure to the abutment, particularly for GRS-IBS structures that have a strong foundations.

10.4 Recommendations for Future Rfesearch

6. The monitoring for this GRS-IBS project should be continued to investigate the long term response of the structure into the future. Specifically, the abutments and foundation deformation should be monitored to evaluate any creep deformation which usually occurs over a longer term. Since most of the strain gauges are properly working, their data can be utilized for creep assessment. The effect of increase in the abutment water content on its deformation should also be investigated.

7. The effect of pressure cell temperature on the measured pressure was discussed in this report. It was shown that this effect is significant and complicated because some factors such as temperature, pressure, the properties of the cell and even the cells' installed condition in the field can affect the measured pressures. In spite of the importance of the issue, the literature review showed that only limited research has been conducted on the effect of cell temperature on measured total pressure cell readings. For future projects, it is recommended that all pressure cells should be calibrated in the lab under different pressure and temperature conditions, with an experimental setup that is designed to simulate their installed condition in the field as closely as possible. The effect of temperature gradients during periods of decreasing and increasing temperature also needs to be evaluated. Research conducted by others has indicated that each pressure cell should be calibrated separately, since the calibration factors for different pressure cells are unique.

8. The influence of air temperature changes on the induced pressure in the abutment and the foundation of GRS-IBS structures needs to be investigated further. As

discussed in this report, it appears that the bridge expansion and contraction caused by changes in the air temperature induce some changes in the applied pressure in the abutment and the foundation. It is recommended that a few pressure cells should be installed between the bridge and the approach road to continuously measure the induced pressure by the bridge to the abutment. The correlation between the changes in this measured pressure and applied pressure to the abutment and foundation should then be evaluated. The effect of temperature gradient on the induced pressure should also be assessed. 3D finite element coupled (stress-temperature) analyses are also recommended using reliable pressure and temperature data that has been collected in the field.

9. For future studies, it is recommended that sensors with higher resolution and precision should be utilized to monitor the performance of GRS-IBS structures, given the relatively small amounts of strain and deflection that were observed in the current study. Specifically, the abutment strain gauges and surveying operation system should be capable of capturing very low levels of deformation and strain with a high precision.

10. It is recommended that a few pressure cells be utilized across the width of the bridge beam bearing seat, in order to capture the induced pressure by the live load during live load testing. This will be useful for assessing if the applied pressure distribution across the width of the superstructure is uniform (or alternatively, how non-uniform it us) for a given live load on the bridge.

Appendix A

SITE EXPLORATION

This appendix presents data collected from a geotechnical site exploration conducted by the Delaware Department of Transportation at the Br. 1-366 field site, including the borehole logs and summary of associated data collected as a result of the exploration process. As shown in the following pages, two boreholes were drilled at the site (CC-1 and CC-2), one through each of the existing bridge abutments. Field and laboratory soil classification results taken from the borehole samples indicated that the soil encountered during the site exploration consisted of both granular and fine materials, ranging in USCS classification from SM-SC to CL. According to the standard penetration test results, this material was generally at a "medium dense" state.

As shown in the boring logs, beneath the uppermost sandy layer which exists primarily in the bridge backfill zone, a fairly thin stiff orange sandy clay layer was observed, which transitioned rather quickly to a grayish-brown silty fine sandy clay layer. This layer continued to an approximate depth of 29-30 ft[1]. This layer is medium stiff to stiff and in some depths includes organic material. Generally, it appears as if this

[1] The system of units utilized in the appendices of this report are English units while the system of units utilized in the chapters of this dissertation are SI units. This choice of two systems of units is intentional, as SI units are more commonly used in dissertations and journal publications, and English units are used by the Delaware Department of Transportation, the primary funding sponsor for this project who provided support with obtaining a significant amount of the Appendix data.

layer became siltier with depth. After this clay layer, a fine sand layer with some silt was observed again. This fine sand layer was classified as dense to very dense and was shown to extend to the end of the borehole exploration. A summary simplified cross section was developed from these data for purposes of engineering analysis of the GRS-IBS, as shown in Figure 3.3.

STATE OF DELAWARE
DEPARTMENT OF TRANSPORTATION
MATERIALS AND RESEARCH

BORING CC-1

Project Name: Chesapeake City Road over Guthrie Run **Location:** New Castle County Delaware
State Contract #: T201007102 **Federal Contract #:**
Station/Offset: **Northing:** **Easting:**
Boring Surface Elev.: **Reference:**
Date Started: 12/8/11 **Date Completed:** 12/8/11

Wt. of Sample Hammer: 140 Lbs. **Average Fall:** 30 IN.
Type of: **D-Sampler:** Split Barrel O.D. **O.D. of Sampler:** 2 IN.
S-Sampler: O.D. **O.D. of Samp. Tube:** IN.
U-Sampler: O.D. **O.D. of Samp. Tube:** IN.
Core Bit: O.D. **O.D. of Rock Core:** IN.

Hollow Stem Auger Diameter: 3 1/4" Inches **From Depth of:** 0.0' **To:** 59.75'
Mud Rotary: **From Depth of:** **To:**

Water Level Readings

Date	Depth to Water (ft)	Caved Depth (ft)
12/8/11	15.5	
12/8/11	10.9	13.1

Boring Contractor: Walton Corporation **Equipment/Rig Type:** CME 55 Truck
Driller: Bill Holden **Logged By:** T. Kane

Depth (ft.)	Water Level	No.	Sample Depth	Blows/6"	Sample Description	AASHTO Class.	Remarks
2.53		1	2.0'	5 8 1 11	Wet medium dense orange silty fine to coarse sand w/some fine gravel and clay.	A-2-4(0)	Fill
			4.0'		17"" RECOVERY		
5.06							
		2	6.0'	4 4 5 6	Wet loose gray silty fine sand w/some coarse sand, trace of fine gravel.	A-2-4(0)	Fill
7.59			8.0'		18"" RECOVERY		
10.12		3	10.0'	4 8	Wet medium dense gray silty fine sand w/some coarse sand, trace of fine gravel and clay.	A-2-4(0)	Fill
	▽		11.0'		8"" RECOVERY		
		3A	11.0'	11 14	No sieve analysis - Indication of wet very stiff orange clayey silt w/some sand.		
			12.0'		8" RECOVERY		
12.65		4	12.0'	11 16 9 6	Wet medium dense orange clayey coarse sand and fine gravel w/some silt, trace of fine sand.	A-2-6(1)	
			14.0'		10" RECOVERY		
		5	14.0'	5 7 11 8	No sieve analysis - Indication of wet very stiff orange sandy clay.		
15.18	▽		16.0'		2" RECOVERY		

Remarks: Associates from University of Delaware were present for drilling.

Reviewed By: Hany Fekry **Soils Supervisor:** Aaron Wieczorek

Figure A.1 Borehole CC-1 log

STATE OF DELAWARE
DEPARTMENT OF TRANSPORTATION
MATERIALS AND RESEARCH

Project Name: Chesapeake City Road over Guthrie Run **Boring No.:** CC-1
State Contract:

Depth (ft.)	Water Level	No.	Sample Depth	Blows/6"	Sample Description	AASHTO Class.	Remarks
		6	16.0'	8 6 7 6	Saturated stiff orange fine sandy clay w/trace of coarse sand and silt.	A-7-6(16)	
17.71			18.0'		12" RECOVERY		
		7	18.0'	3 4 7 6	Saturated stiff green fine sandy clay w/some silt, trace of coarse sand, fine gravel and organic matter.	A-6(4)	
			20.0'		16" RECOVERY		
20.24		U-1	20.0'				Shelby Tube - Press Sample
			22.0'		19" RECOVERY		
		8	22.0'	4 4 6 7	Saturated stiff green fine sandy silt w/trace of coarse sand and organic matter.	A-4(0)	
22.77			24.0'		23" RECOVERY		
		9	24.0'	5 6 7 8	Saturated stiff gray fine sandy silt w/some clay, trace of coarse sand.	A-4(1)	
25.3			26.0'		24" RECOVERY		
		10	26.0'	4 4 7 9	Saturated stiff gray fine sandy silt.	A-4(0)	
27.83			28.0'		10" RECOVERY		
		11	28.0'	4 7 4 8	Saturated very stiff grayish black silt w/some fine sand, trace of coarse sand.	A-4(1)	
			30.0'		22" RECOVERY		
30.36							
		12	30.5'	10 23 19	No sieve analysis - Indication of saturated dense grayish black organic clayey sand.		
		14	32.0' 32.5'	39 50	No sieve analysis - Indication of saturated very dense gray organic silty sand.		
32.89			34.0'		4"" RECOVERY		
		15	34.0'	11 10 13 14	Saturated medium dense gray fine sand w/some coarse sand, trace of silt and fine gravel.	A-3	
35.42			36.0'		24" RECOVERY		
		16	36.0'	20 15 36 35	Saturated very dense gray fine sand w/some coarse sand, trace of silt and fine gravel.	A-3	
37.95			38.0'		18" RECOVERY		
		17	38.0'	10 24 36 40	Saturated very dense gray fine sand w/some silt, trace of coarse sand.	A-2-4(0)	
			40.0'		17" RECOVERY		

Figure A.1 Continued

STATE OF DELAWARE
DEPARTMENT OF TRANSPORTATION
MATERIALS AND RESEARCH

Project Name: Chesapeake City Road over Guthrie Run **Boring No.:** CC-1
State Contract:

Depth (ft.)	Water Level	No.	Sample Depth	Blows/6"	Sample Description	AASHTO Class.	Remarks
40.48		18	40.0' – 42.0'	34 42 50	Saturated very dense gray fine sand w/trace of coarse sand and silt. 15" RECOVERY	A-3	
43.01		19	42.0' – 44.0'	9 14 24 26	Saturated dense gray fine sand w/some coarse sand and silt. 19" RECOVERY	A-2-4(0)	
45.54		20	44.0' – 46.0'	9 17 26 32	Saturated dense gray coarse to fine sand w/some silt. 14" RECOVERY	A-1-b	
48.07		21	46.0' – 48.0'	16 29 32 35	Saturated very dense gray coarse to fine sand w/ trace of silt. 16" RECOVERY	A-1-b	
50.6		22	48.0' – 50.0'	19 30 50	Saturated hard light gray fine sandy silt w/trace of coarse sand. 18" RECOVERY	A-4(0)	
53.13		23	53.0' – 55.0'	7 5 7 12	Saturated stiff light gray clay w/trace of fine sand. 12" RECOVERY	A-7-6(21)	
55.66							
58.19		24	58.0' – 60.0'	11 17 44 50	Saturated very dense light gray fine to coarse sand w/trace of silt. 14" RECOVERY	A-3	
60.72					End Boring		
63.25							

Figure A.1 Continued

STATE OF DELAWARE
DEPARTMENT OF TRANSPORTATION
MATERIALS AND RESEARCH

BORING CC-2

Project Name: Chesapeake City Road over Guthrie Run **Location:** New Castle County Delaware
State Contract #: T201007102 **Federal Contract #:**
Station/Offset: **Northing:** **Easting:**
Boring Surface Elev.: **Reference:**
Date Started: 12/8/11 **Date Completed:** 12/8/11

Wt. of Sample Hammer: 140 **Lbs.** **Average Fall:** 30 **IN.**
Type of: D-Sampler: Split Barrel **O.D.** **O.D. of Sampler:** 2 **IN.**
S-Sampler: **O.D.** **O.D. of Samp. Tube:** **IN.**
U-Sampler: **O.D.** **O.D. of Samp. Tube:** **IN.**
Core Bit: **O.D.** **O.D. of Rock Core:** **IN.**

Hollow Stem Auger Diameter: 3 1/4" **Inches** **From Depth of:** **To:**
Mud Rotary: **From Depth of:** 34.0' **To:** 60.0'

Water Level Readings

Date	Depth to Water (ft)	Caved Depth (ft)
12/8/11	11.4	
12/8/11	11.4	14.0

Boring Contractor: Walton Corporation **Equipment/Rig Type:** CME 55 Truck
Driller: Jason Truver **Logged By:** GTA

Depth (ft.)	Water Level	No.	Sample Depth	Blows/6"	Sample Description	AASHTO Class.	Remarks
2.53		1	2.0'	1 1 4 5	Wet firm gray fine sandy silt w/some coarse sand and clay, trace of fine gravel.	A-4(0)	7" Crushed Concrete. 7" Hot-mix. Fill
			4.0'				
		2	4.0'	6 6 7 11	Wet stiff brownish gray fine sandy silt w/some coarse sand, trace of fine gravel.	A-4(0)	Fill
5.06			6.0'				
7.59							
10.12		3	10.0'	4 4 2 3	Wet loose brown coarse to fine sand w/some silt, trace of fine gravel.	A-1-b	Fill
	▼		12.0'				
12.65		4	12.0'	1 5 8 8	Saturated medium dense brown coarse to fine sand and fine gravel w/trace of silt.	A-1-b	Fill
			14.0'		12" RECOVERY		
		5	14.0'	6 16 11 5	No sieve analysis - Indication of saturated medium dense gray sand w/trace of silt and fine gravel.		
15.18			16.0'		8" RECOVERY		

Remarks: Associates from University of Delaware were present for drilling.

Reviewed By: Hany Fekry **Soils Supervisor:** Aaron Wieczorek

Figure A.2 Borehole CC-2 log

STATE OF DELAWARE
DEPARTMENT OF TRANSPORTATION
MATERIALS AND RESEARCH

Project Name: Chesapeake City Road over Guthrie Run **Boring No.:** CC-2
State Contract:

Depth (ft.)	Water Level	No.	Sample Depth	Blows/6"	Sample Description	AASHTO Class.	Remarks
		6	16.0'	3 3 8 9	Saturated stiff brown clay w/some fine sand and fine gravel, trace of coarse sand and silt.	A-7-6(13)	
17.71			18.0'		24" RECOVERY		
		7	18.0'	3 3 5 7	Saturated firm grayish brown silty fine sandy clay w/trace of coarse sand, fine gravel and organic matter.	A-6(8)	Organic Content = 2.1%
20.24			20.0'		22" RECOVERY		
		U-1	20.0'				Shelby Tube - Press Sample
			22.0'		24" RECOVERY		
		U-2	22.0'			A-4(4)	Shelby Tube - Press Sample
22.77			24.0'		24" RECOVERY		
		U-3	24.0'			A-6(6)	Shelby Tube - Press Sample
25.3			26.0'		24" RECOVERY		
		U-4	26.0'				Shelby Tube - Press Sample
27.83			28.0'		24" RECOVERY		
		U-5	28.0'				Shelby Tube - Press Sample
			30.0'		24" RECOVERY		
30.36		13	30.0'	5 8 12 23	Saturated medium dense gray organic silty fine sand w/some fine gravel and clay, trace of coarse sand.	A-2-4(0)	Organic Content = 21.98%
			32.0'		24" RECOVERY		
		14	32.0'	25 32 33 30	Saturated very dense gray fine sand w/some coarse sand, trace of fine gravel, silt and organic matter.	A-3	Organic Content = 1.19%
32.89			34.0'		24" RECOVERY		
		15	34.0'	10 15 21 24	Saturated dense gray fine sand w/some silt, coarse sand and organic matter, trace of fine gravel.	A-2-4(0)	Organic Content = 4.83%
35.42			36.0'		18" RECOVERY		
		16	36.0'	24 34 42 50	Saturated very dense gray fine sand w/some coarse sand and silt, trace of fine gravel and organic matter.	A-2-4(0)	Organic Content = 1.51%
37.95			38.0'		21" RECOVERY		
		17	38.0'	11 18 17 20	Saturated dense gray fine sand w/trace of coarse sand, fine gravel, silt and organic matter.	A-3	Organic Content = 1.83%
			40.0'		18" RECOVERY		

Figure A.2 Continued

STATE OF DELAWARE
DEPARTMENT OF TRANSPORTATION
MATERIALS AND RESEARCH

Project Name: Chesapeake City Road over Guthrie Run **Boring No.:** CC-2
State Contract:

Depth (ft.)	Water Level	No.	Sample Depth	Blows/6"	Sample Description	AASHTO Class.	Remarks
40.48		18	40.0'	22 24 26 29	Saturated medium dense gray fine sand w/some coarse sand, trace of fine gravel, silt and organic matter.	A-3	Organic Content = 1.46%
			42.0'		24" RECOVERY		
		19	42.0'	15 27 32 50	Saturated very dense gray fine sand w/some coarse sand, trace of fine gravel, silt and organic matter.	A-3	Organic Content = 1.56%
43.01			44.0'		20" RECOVERY		
		20	44.0'	4 12 30 29	Saturated dense gray fine sand w/trace of coarse sand, fine gravel, silt and organic matter.	A-3	Organic Content = 0.73%
45.54			46.0'		18" RECOVERY		
		21	46.0'	10 15 27 29	Saturated dense gray fine to coarse sand w/trace of silt, fine gravel and organic matter.	A-3	Organic Content = 0.47%
48.07			48.0'		18" RECOVERY		
		22	48.0'	10 18 16 16	Saturated dense gray coarse to fine sand w/trace of silt, fine gravel and organic matter.	A-1-b	Organic Content = 0.47%
			50.0'		15" RECOVERY		
50.6							
53.13		23	53.0'	4 5 7 11	Saturated medium dense light gray fine sand w/ some coarse sand and silt, trace of fine gravel.	A-2-4(0)	
			55.0'		14" RECOVERY		
55.66							
58.19		24	58.0'	7 6 7 11	Saturated medium dense light gray silty fine sand w/trace of coarse sand and fine gravel.	A-2-4(0)	
			60.0'		20" RECOVERY		
60.72					End Boring.		
63.25							

Figure A.2 Continued

Appendix B

SOIL CLASSIFICATION TESTS

The results from soil classification tests performed by the Delaware Department of Transportation on samples taken from boring logs CC-1 and CC-2 at the Br. 1-366 site are provided in this appendix. As shown, 41 samples have been classified by DelDOT following the procedures outlined in AASHTO T 27/T 11. Using the results from classification tests provided by DelDOT, the author also performed side-by-side classification of the soils following the Unified Soil Classification System (ASTM D2487). Table B.1 presents the soil classification in the boreholes together with the interpreted soil stratification that was determined from these results.

As shown in Table B.1, the foundation soil classification varies from clays (CL and CH) to silty sands (SM and SP-SM) (ASTM D2487). The foundation material contained a silty fine sandy clay layer between an approximate depth of 14 ft and 30 ft (El 44 to 28 ft). The proposed base of the GRS-IBS structure is around an elevation of 40 ft, with the reinforced soil foundation (RSF) for the GRS-IBS extending below this point. Consequently, the proposed structure location is such that it bears directly on, or very close to directly on, this fine-grained foundation soil layer.

Table B.1 The soil classification in different depths of the drilled boreholes and the interpreted soil stratification

Sample Elevation (ft)	Sample Depth (ft)	Borehole CC-1 Soil Classification	Borehole CC-2 Soil Classification	Interpreted Soil Classification
56	2	SC-SM, A-2-4(0)	SC-SM, A-4(0)	SC-SM or SM, A-4(0)
54	4	-	SM, A-4(0)	
52	6	SM, A-2-4(0)	-	
48	10	SM, A-2-4(0)	SM, A-1(b)	
47	11	-	-	
46	12	SC, A-2-6(1)	SW-SM, A-1(b)	
44	14	-	-	
42	16	CL, A-7-6(16)	CH, A-7-6(13)	CL, A-6(8)
40	18	CL, A-6(4)	CL, A-6(8)	
38	20	-	-	
36	22	ML, A-4(0)	-	
34	24	ML, A-4(1)	-	
32	26	ML, A-4(0)	-	
30	28	ML, A-4(1)	-	
28	30	-	SM, A-2-4(0)	SP-SM, A-3
26	32	-	SP-SM, A-3	
24	34	SP-SM, A-3	SM, A-2-4(0)	
22	36	SP-SM, A-3	SP-SM, A-2-4(0)	
20	38	SM, A-2-4(0)	SP-SM, A-3	
18	40	SP-SM, A-3	SP-SM, A-3	
16	42	SM, A-2-4(0)	SP-SM, A-3	
14	44	SM, A-1-b	SP, A-3	
12	46	SP-SM, A-1-b	SP-SM, A-3	
10	48	SM, A-4(0)	SP, A-1-b	
5	53	CL, A-7-6(21)	SM, A-2-4(0)	CL, A-7-6(21)
0	58	SP, A-3	SM, A-2-4(0)	SP-SM, A-3

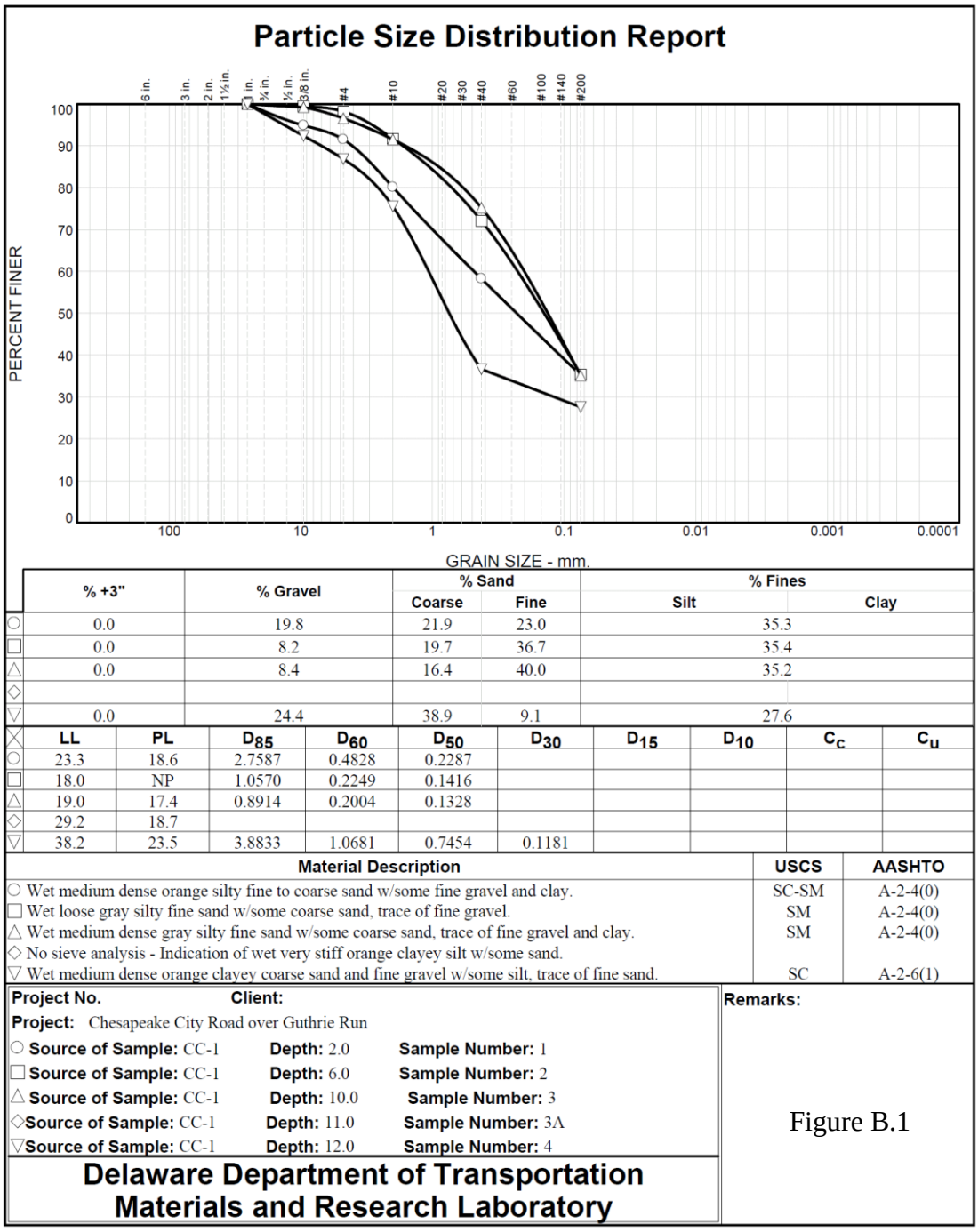

	% +3"	% Gravel	% Sand		% Fines	
			Coarse	Fine	Silt	Clay
○	0.0	19.8	21.9	23.0	35.3	
□	0.0	8.2	19.7	36.7	35.4	
△	0.0	8.4	16.4	40.0	35.2	
◇						
▽	0.0	24.4	38.9	9.1	27.6	

	LL	PL	D_{85}	D_{60}	D_{50}	D_{30}	D_{15}	D_{10}	C_C	C_u
○	23.3	18.6	2.7587	0.4828	0.2287					
□	18.0	NP	1.0570	0.2249	0.1416					
△	19.0	17.4	0.8914	0.2004	0.1328					
◇	29.2	18.7								
▽	38.2	23.5	3.8833	1.0681	0.7454	0.1181				

	Material Description	USCS	AASHTO
○	Wet medium dense orange silty fine to coarse sand w/some fine gravel and clay.	SC-SM	A-2-4(0)
□	Wet loose gray silty fine sand w/some coarse sand, trace of fine gravel.	SM	A-2-4(0)
△	Wet medium dense gray silty fine sand w/some coarse sand, trace of fine gravel and clay.	SM	A-2-4(0)
◇	No sieve analysis - Indication of wet very stiff orange clayey silt w/some sand.		
▽	Wet medium dense orange clayey coarse sand and fine gravel w/some silt, trace of fine sand.	SC	A-2-6(1)

Project No. **Client:**

Project: Chesapeake City Road over Guthrie Run

○ **Source of Sample:** CC-1 **Depth:** 2.0 **Sample Number:** 1

□ **Source of Sample:** CC-1 **Depth:** 6.0 **Sample Number:** 2

△ **Source of Sample:** CC-1 **Depth:** 10.0 **Sample Number:** 3

◇ **Source of Sample:** CC-1 **Depth:** 11.0 **Sample Number:** 3A

▽ **Source of Sample:** CC-1 **Depth:** 12.0 **Sample Number:** 4

Delaware Department of Transportation
Materials and Research Laboratory

Remarks:

Figure B.1

Figure B.1 Particle size distribution tests results, boring CC-1, Depths 0-13.5 ft

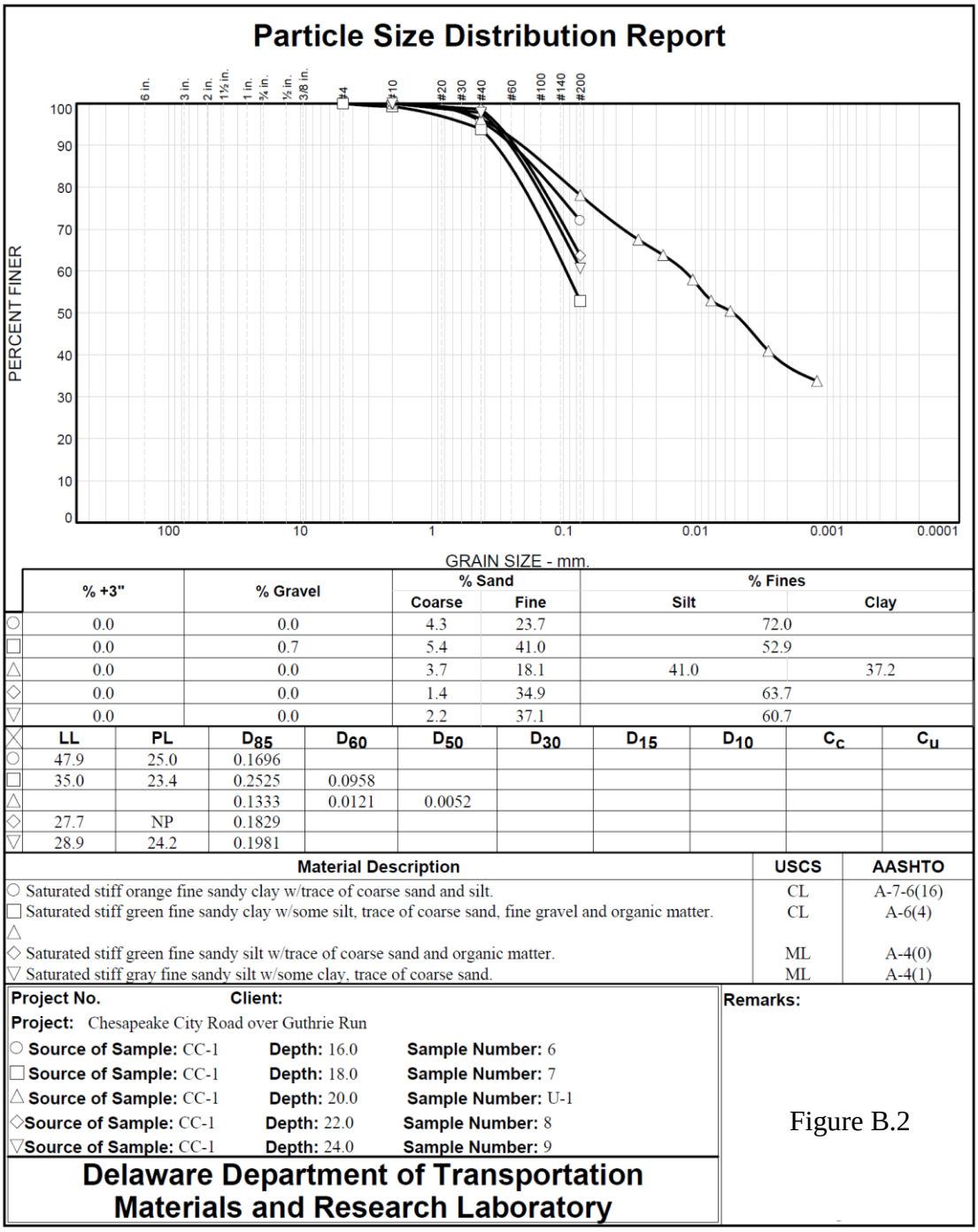

	% +3"	% Gravel	% Sand		% Fines	
			Coarse	Fine	Silt	Clay
○	0.0	0.0	4.3	23.7	72.0	
□	0.0	0.7	5.4	41.0	52.9	
△	0.0	0.0	3.7	18.1	41.0	37.2
◇	0.0	0.0	1.4	34.9	63.7	
▽	0.0	0.0	2.2	37.1	60.7	

	LL	PL	D_{85}	D_{60}	D_{50}	D_{30}	D_{15}	D_{10}	C_C	C_u
○	47.9	25.0	0.1696							
□	35.0	23.4	0.2525	0.0958						
△			0.1333	0.0121	0.0052					
◇	27.7	NP	0.1829							
▽	28.9	24.2	0.1981							

	Material Description	USCS	AASHTO
○	Saturated stiff orange fine sandy clay w/trace of coarse sand and silt.	CL	A-7-6(16)
□	Saturated stiff green fine sandy clay w/some silt, trace of coarse sand, fine gravel and organic matter.	CL	A-6(4)
△			
◇	Saturated stiff green fine sandy silt w/trace of coarse sand and organic matter.	ML	A-4(0)
▽	Saturated stiff gray fine sandy silt w/some clay, trace of coarse sand.	ML	A-4(1)

Project No. **Client:**

Project: Chesapeake City Road over Guthrie Run

○ **Source of Sample:** CC-1 **Depth:** 16.0 **Sample Number:** 6

□ **Source of Sample:** CC-1 **Depth:** 18.0 **Sample Number:** 7

△ **Source of Sample:** CC-1 **Depth:** 20.0 **Sample Number:** U-1

◇ **Source of Sample:** CC-1 **Depth:** 22.0 **Sample Number:** 8

▽ **Source of Sample:** CC-1 **Depth:** 24.0 **Sample Number:** 9

Remarks:

Delaware Department of Transportation
Materials and Research Laboratory

Figure B.2

Figure B.2 Particle size distribution tests results, boring CC-1, Depths 16-25.5 ft

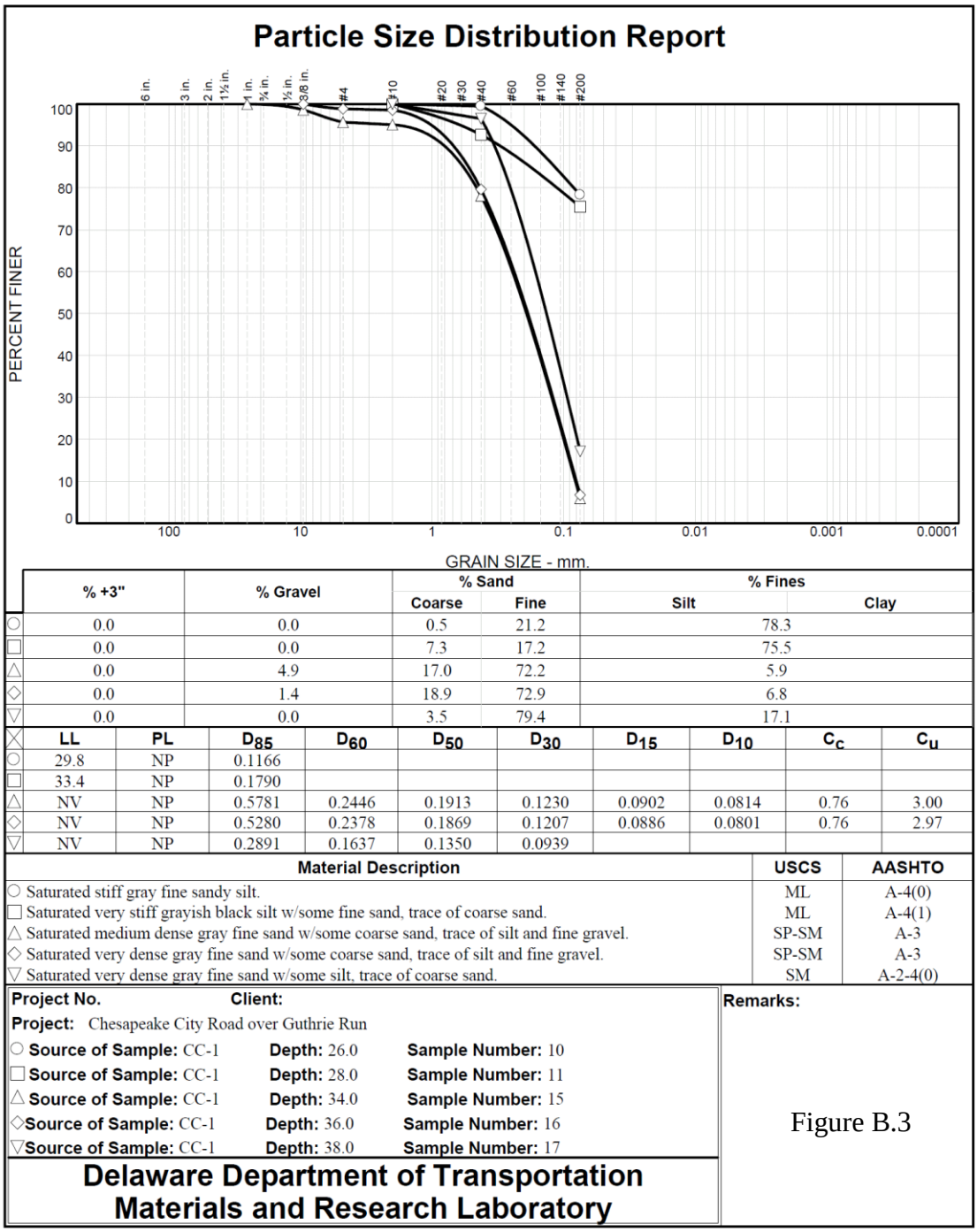

	% +3"	% Gravel	% Sand		% Fines	
			Coarse	Fine	Silt	Clay
○	0.0	0.0	0.5	21.2	78.3	
□	0.0	0.0	7.3	17.2	75.5	
△	0.0	4.9	17.0	72.2	5.9	
◇	0.0	1.4	18.9	72.9	6.8	
▽	0.0	0.0	3.5	79.4	17.1	

	LL	PL	D_{85}	D_{60}	D_{50}	D_{30}	D_{15}	D_{10}	C_c	C_u
○	29.8	NP	0.1166							
□	33.4	NP	0.1790							
△	NV	NP	0.5781	0.2446	0.1913	0.1230	0.0902	0.0814	0.76	3.00
◇	NV	NP	0.5280	0.2378	0.1869	0.1207	0.0886	0.0801	0.76	2.97
▽	NV	NP	0.2891	0.1637	0.1350	0.0939				

Material Description	USCS	AASHTO
○ Saturated stiff gray fine sandy silt.	ML	A-4(0)
□ Saturated very stiff grayish black silt w/some fine sand, trace of coarse sand.	ML	A-4(1)
△ Saturated medium dense gray fine sand w/some coarse sand, trace of silt and fine gravel.	SP-SM	A-3
◇ Saturated very dense gray fine sand w/some coarse sand, trace of silt and fine gravel.	SP-SM	A-3
▽ Saturated very dense gray fine sand w/some silt, trace of coarse sand.	SM	A-2-4(0)

Project No. **Client:**

Project: Chesapeake City Road over Guthrie Run

○ **Source of Sample:** CC-1 **Depth:** 26.0 **Sample Number:** 10

□ **Source of Sample:** CC-1 **Depth:** 28.0 **Sample Number:** 11

△ **Source of Sample:** CC-1 **Depth:** 34.0 **Sample Number:** 15

◇ **Source of Sample:** CC-1 **Depth:** 36.0 **Sample Number:** 16

▽ **Source of Sample:** CC-1 **Depth:** 38.0 **Sample Number:** 17

Delaware Department of Transportation
Materials and Research Laboratory

Remarks:

Figure B.3

Figure B.3 Particle size distribution tests results, boring CC-1, Depths 26-39.5

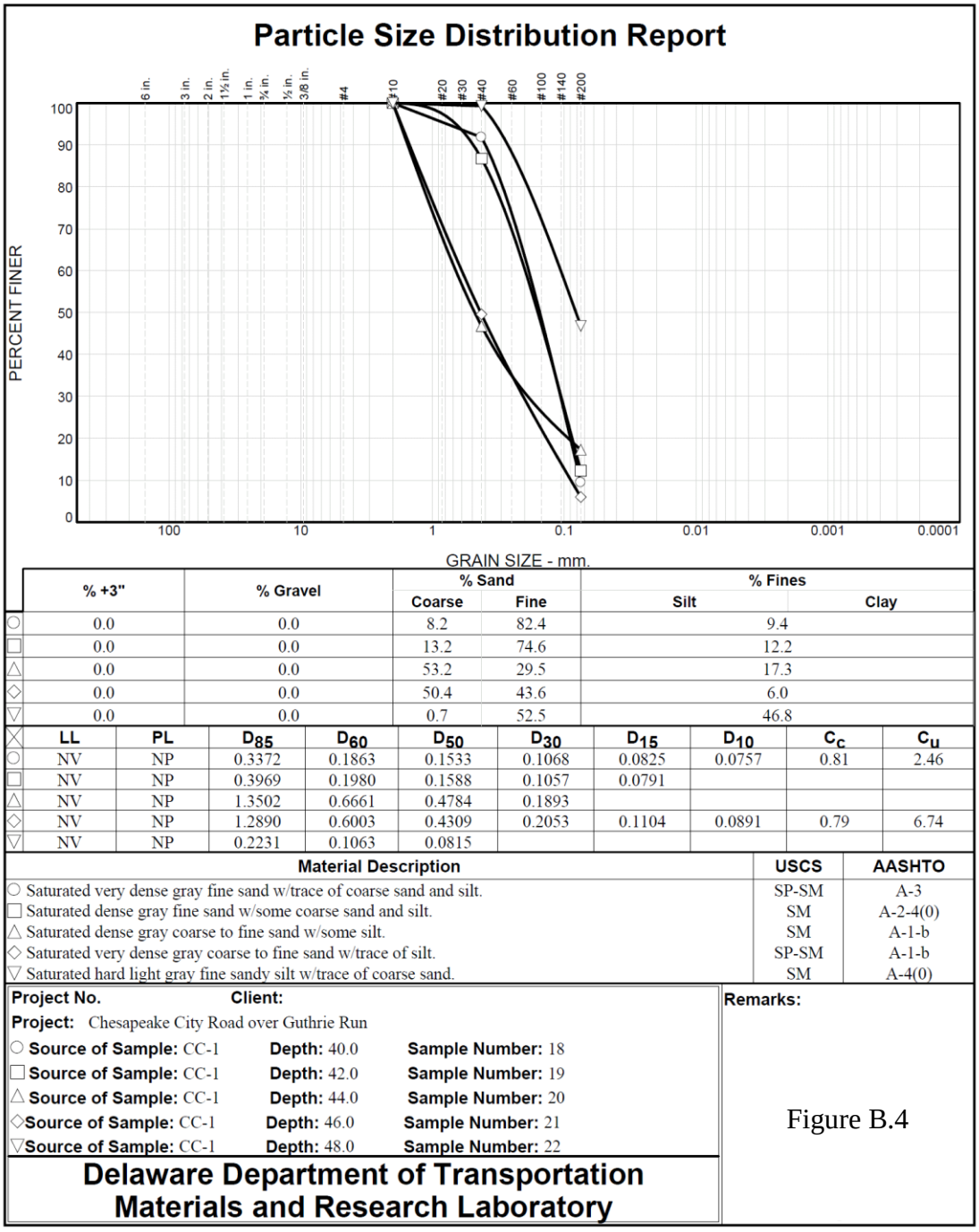

	% +3"	% Gravel	% Sand		% Fines	
			Coarse	Fine	Silt	Clay
○	0.0	0.0	8.2	82.4	9.4	
□	0.0	0.0	13.2	74.6	12.2	
△	0.0	0.0	53.2	29.5	17.3	
◇	0.0	0.0	50.4	43.6	6.0	
▽	0.0	0.0	0.7	52.5	46.8	

	LL	PL	D_{85}	D_{60}	D_{50}	D_{30}	D_{15}	D_{10}	C_C	C_u
○	NV	NP	0.3372	0.1863	0.1533	0.1068	0.0825	0.0757	0.81	2.46
□	NV	NP	0.3969	0.1980	0.1588	0.1057	0.0791			
△	NV	NP	1.3502	0.6661	0.4784	0.1893				
◇	NV	NP	1.2890	0.6003	0.4309	0.2053	0.1104	0.0891	0.79	6.74
▽	NV	NP	0.2231	0.1063	0.0815					

Material Description	USCS	AASHTO
○ Saturated very dense gray fine sand w/trace of coarse sand and silt.	SP-SM	A-3
□ Saturated dense gray fine sand w/some coarse sand and silt.	SM	A-2-4(0)
△ Saturated dense gray coarse to fine sand w/some silt.	SM	A-1-b
◇ Saturated very dense gray coarse to fine sand w/trace of silt.	SP-SM	A-1-b
▽ Saturated hard light gray fine sandy silt w/trace of coarse sand.	SM	A-4(0)

Project No. **Client:**

Project: Chesapeake City Road over Guthrie Run

○ **Source of Sample:** CC-1 **Depth:** 40.0 **Sample Number:** 18

□ **Source of Sample:** CC-1 **Depth:** 42.0 **Sample Number:** 19

△ **Source of Sample:** CC-1 **Depth:** 44.0 **Sample Number:** 20

◇ **Source of Sample:** CC-1 **Depth:** 46.0 **Sample Number:** 21

▽ **Source of Sample:** CC-1 **Depth:** 48.0 **Sample Number:** 22

Delaware Department of Transportation
Materials and Research Laboratory

Remarks:

Figure B.4

Figure B.4 Particle size distribution tests results, boring CC-1, Depths 40-49.5

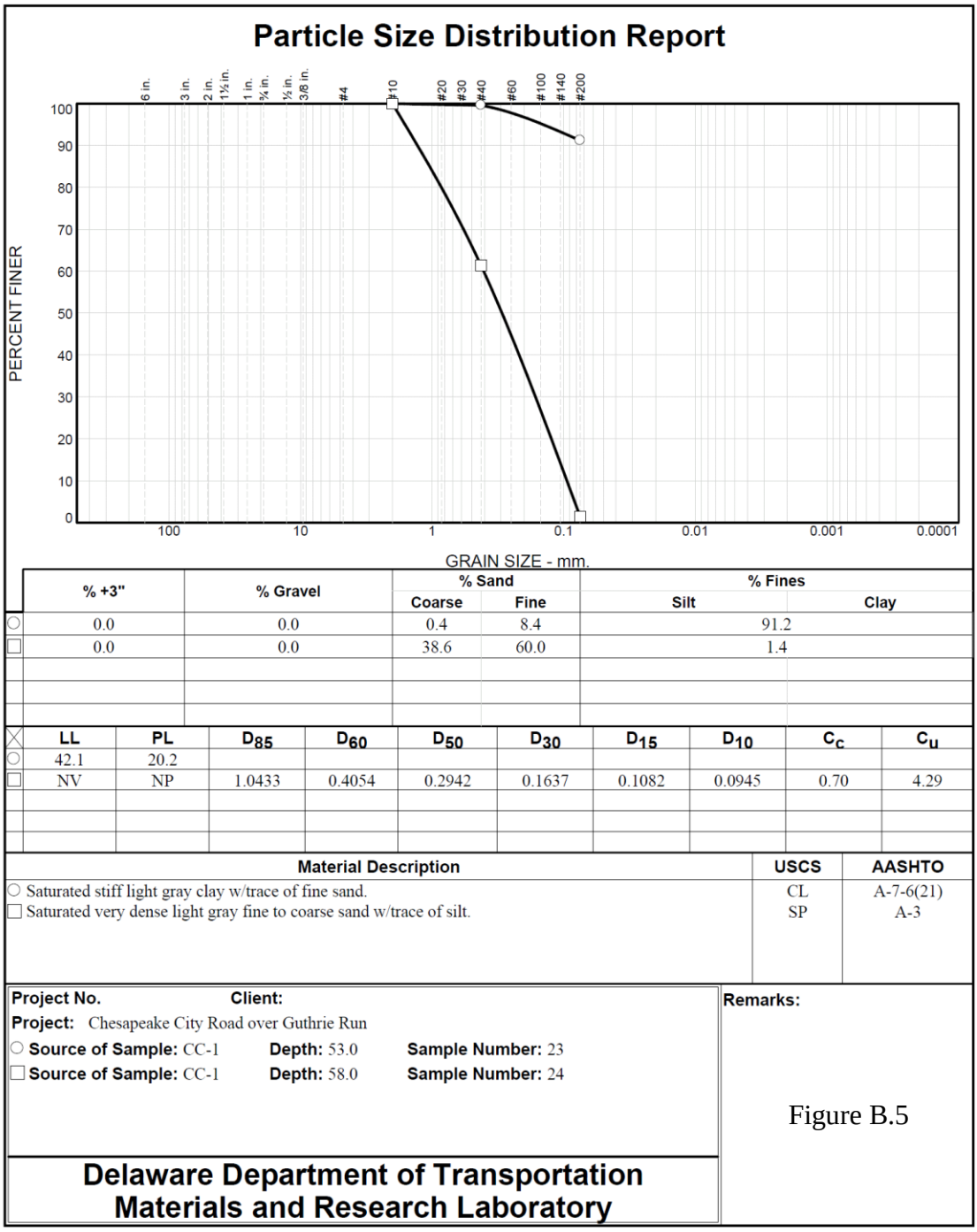

Figure B.5 Particle size distribution tests results, boring CC-1, Depths 53-59.5

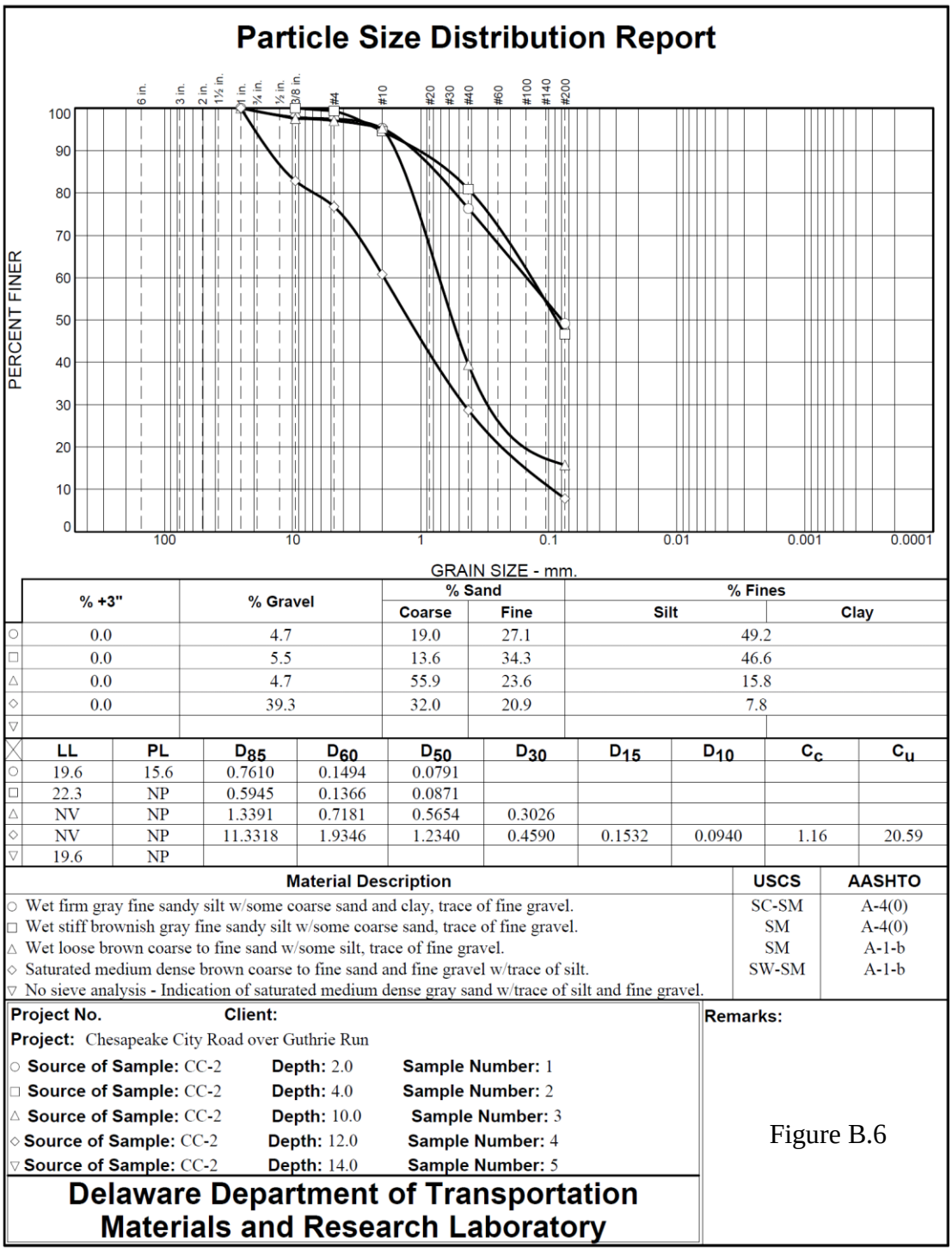

	% +3"	% Gravel	% Sand		% Fines	
			Coarse	Fine	Silt	Clay
○	0.0	4.7	19.0	27.1	49.2	
□	0.0	5.5	13.6	34.3	46.6	
△	0.0	4.7	55.9	23.6	15.8	
◇	0.0	39.3	32.0	20.9	7.8	
▽						

	LL	PL	D_{85}	D_{60}	D_{50}	D_{30}	D_{15}	D_{10}	C_c	C_u
○	19.6	15.6	0.7610	0.1494	0.0791					
□	22.3	NP	0.5945	0.1366	0.0871					
△	NV	NP	1.3391	0.7181	0.5654	0.3026				
◇	NV	NP	11.3318	1.9346	1.2340	0.4590	0.1532	0.0940	1.16	20.59
▽	19.6	NP								

	Material Description	USCS	AASHTO
○	Wet firm gray fine sandy silt w/some coarse sand and clay, trace of fine gravel.	SC-SM	A-4(0)
□	Wet stiff brownish gray fine sandy silt w/some coarse sand, trace of fine gravel.	SM	A-4(0)
△	Wet loose brown coarse to fine sand w/some silt, trace of fine gravel.	SM	A-1-b
◇	Saturated medium dense brown coarse to fine sand and fine gravel w/trace of silt.	SW-SM	A-1-b
▽	No sieve analysis - Indication of saturated medium dense gray sand w/trace of silt and fine gravel.		

Project No. **Client:**

Project: Chesapeake City Road over Guthrie Run

○ **Source of Sample:** CC-2 **Depth:** 2.0 **Sample Number:** 1

□ **Source of Sample:** CC-2 **Depth:** 4.0 **Sample Number:** 2

△ **Source of Sample:** CC-2 **Depth:** 10.0 **Sample Number:** 3

◇ **Source of Sample:** CC-2 **Depth:** 12.0 **Sample Number:** 4

▽ **Source of Sample:** CC-2 **Depth:** 14.0 **Sample Number:** 5

Remarks:

Delaware Department of Transportation
Materials and Research Laboratory

Figure B.6

Figure B.6 Particle size distribution tests results, boring CC-2, Depths 2-15.5

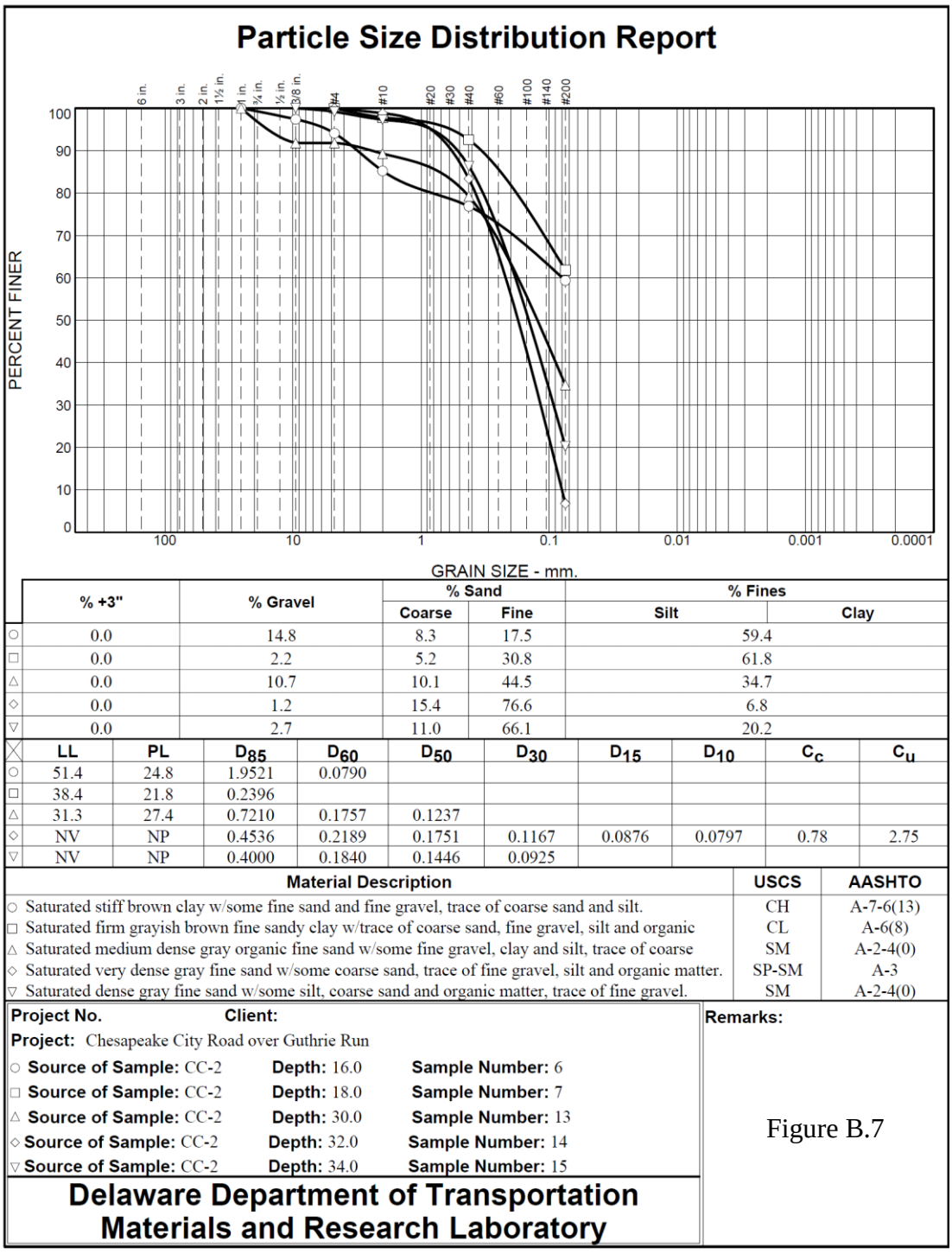

	% +3"	% Gravel	% Sand		% Fines	
			Coarse	Fine	Silt	Clay
○	0.0	14.8	8.3	17.5	59.4	
□	0.0	2.2	5.2	30.8	61.8	
△	0.0	10.7	10.1	44.5	34.7	
◇	0.0	1.2	15.4	76.6	6.8	
▽	0.0	2.7	11.0	66.1	20.2	

	LL	PL	D_{85}	D_{60}	D_{50}	D_{30}	D_{15}	D_{10}	C_c	C_u
○	51.4	24.8	1.9521	0.0790						
□	38.4	21.8	0.2396							
△	31.3	27.4	0.7210	0.1757	0.1237					
◇	NV	NP	0.4536	0.2189	0.1751	0.1167	0.0876	0.0797	0.78	2.75
▽	NV	NP	0.4000	0.1840	0.1446	0.0925				

	Material Description	USCS	AASHTO
○	Saturated stiff brown clay w/some fine sand and fine gravel, trace of coarse sand and silt.	CH	A-7-6(13)
□	Saturated firm grayish brown fine sandy clay w/trace of coarse sand, fine gravel, silt and organic	CL	A-6(8)
△	Saturated medium dense gray organic fine sand w/some fine gravel, clay and silt, trace of coarse	SM	A-2-4(0)
◇	Saturated very dense gray fine sand w/some coarse sand, trace of fine gravel, silt and organic matter.	SP-SM	A-3
▽	Saturated dense gray fine sand w/some silt, coarse sand and organic matter, trace of fine gravel.	SM	A-2-4(0)

Project No. **Client:**

Project: Chesapeake City Road over Guthrie Run

○ **Source of Sample:** CC-2 **Depth:** 16.0 **Sample Number:** 6

□ **Source of Sample:** CC-2 **Depth:** 18.0 **Sample Number:** 7

△ **Source of Sample:** CC-2 **Depth:** 30.0 **Sample Number:** 13

◇ **Source of Sample:** CC-2 **Depth:** 32.0 **Sample Number:** 14

▽ **Source of Sample:** CC-2 **Depth:** 34.0 **Sample Number:** 15

Delaware Department of Transportation
Materials and Research Laboratory

Remarks:

Figure B.7

Figure B.7 Particle size distribution tests results, boring CC-2, Depths 16-35.5

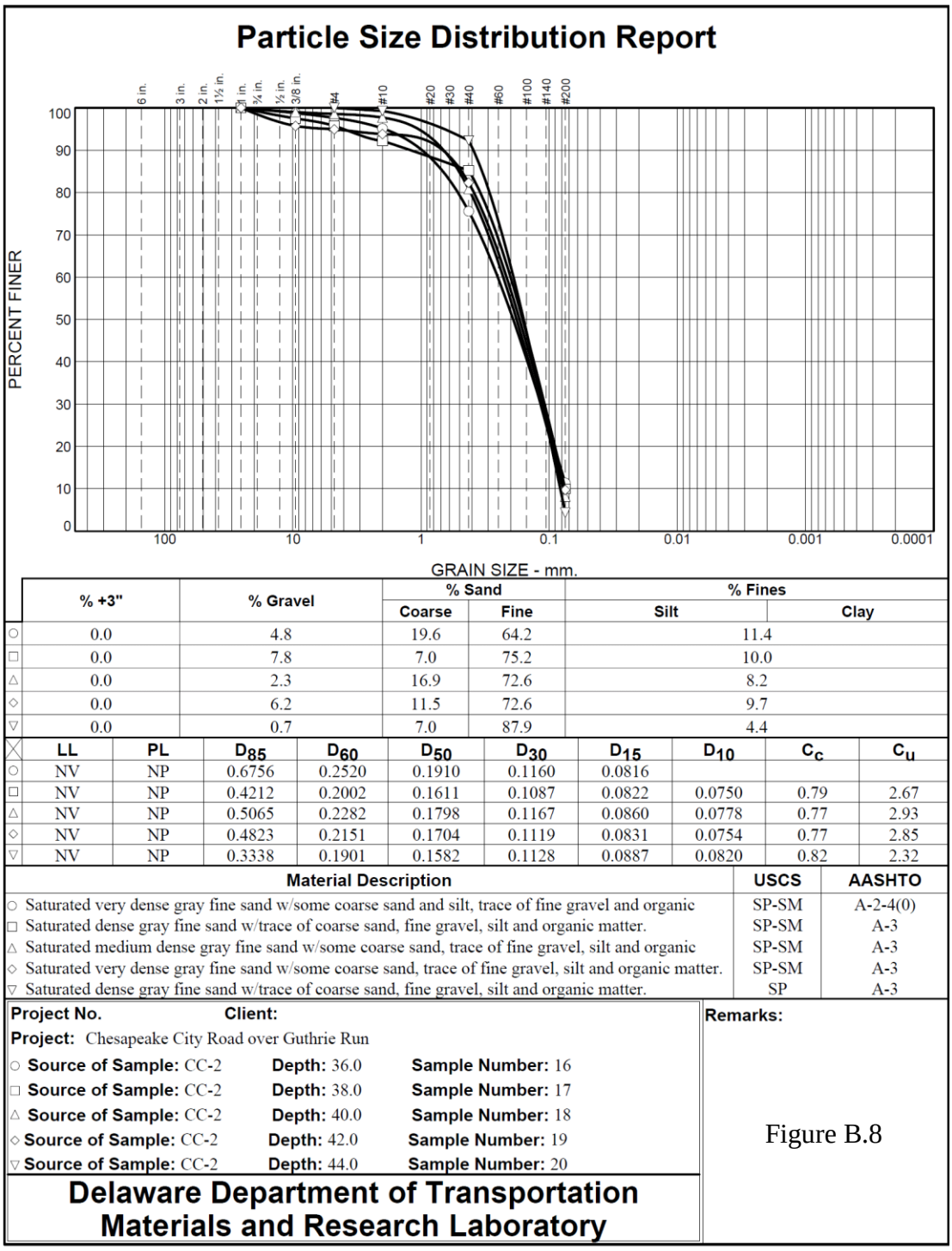

	% +3"	% Gravel	% Sand		% Fines	
			Coarse	Fine	Silt	Clay
○	0.0	4.8	19.6	64.2	11.4	
□	0.0	7.8	7.0	75.2	10.0	
△	0.0	2.3	16.9	72.6	8.2	
◇	0.0	6.2	11.5	72.6	9.7	
▽	0.0	0.7	7.0	87.9	4.4	

	LL	PL	D_{85}	D_{60}	D_{50}	D_{30}	D_{15}	D_{10}	C_c	C_u
○	NV	NP	0.6756	0.2520	0.1910	0.1160	0.0816			
□	NV	NP	0.4212	0.2002	0.1611	0.1087	0.0822	0.0750	0.79	2.67
△	NV	NP	0.5065	0.2282	0.1798	0.1167	0.0860	0.0778	0.77	2.93
◇	NV	NP	0.4823	0.2151	0.1704	0.1119	0.0831	0.0754	0.77	2.85
▽	NV	NP	0.3338	0.1901	0.1582	0.1128	0.0887	0.0820	0.82	2.32

	Material Description	USCS	AASHTO
○	Saturated very dense gray fine sand w/some coarse sand and silt, trace of fine gravel and organic	SP-SM	A-2-4(0)
□	Saturated dense gray fine sand w/trace of coarse sand, fine gravel, silt and organic matter.	SP-SM	A-3
△	Saturated medium dense gray fine sand w/some coarse sand, trace of fine gravel, silt and organic	SP-SM	A-3
◇	Saturated very dense gray fine sand w/some coarse sand, trace of fine gravel, silt and organic matter.	SP-SM	A-3
▽	Saturated dense gray fine sand w/trace of coarse sand, fine gravel, silt and organic matter.	SP	A-3

Project No. **Client:**

Project: Chesapeake City Road over Guthrie Run

○ **Source of Sample:** CC-2 **Depth:** 36.0 **Sample Number:** 16

□ **Source of Sample:** CC-2 **Depth:** 38.0 **Sample Number:** 17

△ **Source of Sample:** CC-2 **Depth:** 40.0 **Sample Number:** 18

◇ **Source of Sample:** CC-2 **Depth:** 42.0 **Sample Number:** 19

▽ **Source of Sample:** CC-2 **Depth:** 44.0 **Sample Number:** 20

Delaware Department of Transportation
Materials and Research Laboratory

Remarks:

Figure B.8

Figure B.8 Particle size distribution tests results, boring CC-2, Depths 36-45.5

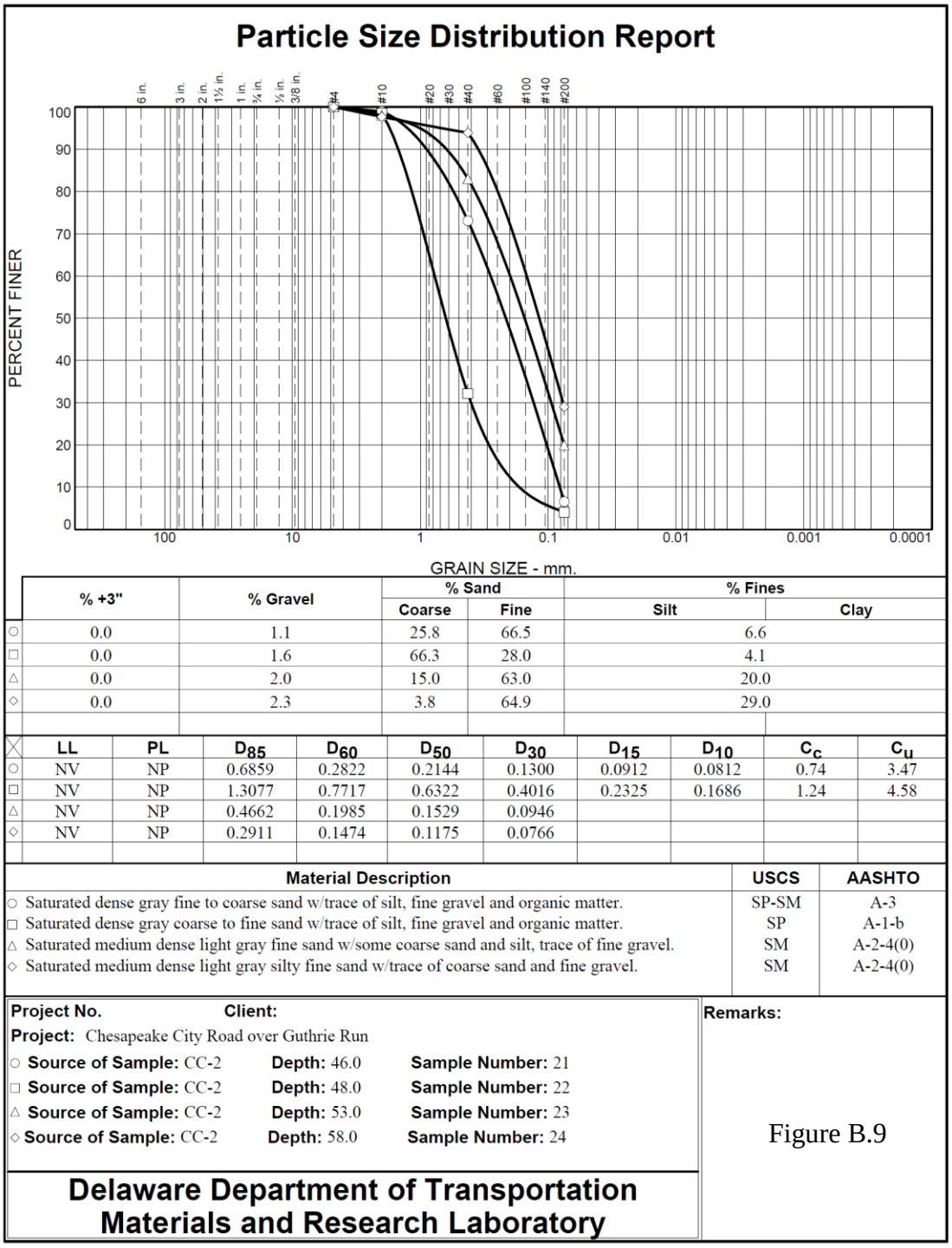

	% +3"	% Gravel	% Sand		% Fines	
			Coarse	Fine	Silt	Clay
○	0.0	1.1	25.8	66.5	6.6	
□	0.0	1.6	66.3	28.0	4.1	
△	0.0	2.0	15.0	63.0	20.0	
◇	0.0	2.3	3.8	64.9	29.0	

	LL	PL	D_{85}	D_{60}	D_{50}	D_{30}	D_{15}	D_{10}	C_c	C_u
○	NV	NP	0.6859	0.2822	0.2144	0.1300	0.0912	0.0812	0.74	3.47
□	NV	NP	1.3077	0.7717	0.6322	0.4016	0.2325	0.1686	1.24	4.58
△	NV	NP	0.4662	0.1985	0.1529	0.0946				
◇	NV	NP	0.2911	0.1474	0.1175	0.0766				

	Material Description	USCS	AASHTO
○	Saturated dense gray fine to coarse sand w/trace of silt, fine gravel and organic matter.	SP-SM	A-3
□	Saturated dense gray coarse to fine sand w/trace of silt, fine gravel and organic matter.	SP	A-1-b
△	Saturated medium dense light gray fine sand w/some coarse sand and silt, trace of fine gravel.	SM	A-2-4(0)
◇	Saturated medium dense light gray silty fine sand w/trace of coarse sand and fine gravel.	SM	A-2-4(0)

Project No. **Client:**

Project: Chesapeake City Road over Guthrie Run

○ **Source of Sample:** CC-2 **Depth:** 46.0 **Sample Number:** 21

□ **Source of Sample:** CC-2 **Depth:** 48.0 **Sample Number:** 22

△ **Source of Sample:** CC-2 **Depth:** 53.0 **Sample Number:** 23

◇ **Source of Sample:** CC-2 **Depth:** 58.0 **Sample Number:** 24

Remarks:

Delaware Department of Transportation
Materials and Research Laboratory

Figure B.9

Figure B.9 Particle size distribution tests results, boring CC-2, Depths 46-59.5

REFERENCES

AASHTO T11 (2005). "Materials finer than 75 μm (No. 200) sieve in mineral aggregates by washing." AASHTO Standard Method of Testing, American Association of State Highway and Transportation Officials, Washington, D.C.

AASHTO T27 (2014). "Sieve Analysis of Fine and Coarse Aggregates." AASHTO Standard Method of Testing, American Association of State Highway and Transportation Officials, Washington, D.C.

ASTM D2487 (2011). "Standard Practice for Classification of Soils for Engineering Purposes (Unified Soil Classification System)." ASTM International, West Conshohocken, PA.

Appendix C

CONSOLIDATION TESTS

Six consolidation tests were conducted by the Delaware Department of Transportation on specimens taken from boring logs CC-1 and CC-2 at the Br. 1-366 site, following the test procedure outlined in AASHTO T 216; the results from these tests are provided in this appendix. Table C.1 presents a summary of results from the consolidation tests including the sample depths, initial water contents (w_0), initial void ratios (e_0), compression indices (C_c), re-compression indices (C_r) and preconsolidation pressure (P_c'). The initial effective pressure, which was calculated using the estimated applied pressure by the existing structure at time of site exploration, is also presented in this table. According to the borehole logs, the water table was located at an approximate depth of 11 ft (i.e., at an elevation of 47 ft). The results from the consolidation testing showed the initial water content varied between 27% to 35%, the initial void ratio varied between 0.68 to 0.84, the compression index (C_c) ranged between 0.17 to 0.25, and the re-compression index ranged between 0.02 to 0.06.

Table C.1 Consolidation test results

Borehole	Depth (ft)	w_0 %	e_0	C_c	C_r	P_c' (tsf)
CC-1	20	30.8	0.78	0.24	0.06	1.92
CC-2	20	29.6	0.685	0.23	0.05	2.09
	22	27.7	0.701	0.17	0.02	3.57
	24	28.7	0.692	0.18	0.03	1.45
	26	27.8	0.704	0.2	0.03	2.32
	28	35.0	0.837	0.25	0.03	2.91

REFERENCES

AASHTO T216 (2007). “Standard method of test for one dimensional consolidation properties of soils.” AASHTO Standard Method of Testing, American Association of State Highway and Transportation Officials, Washington, D.C.

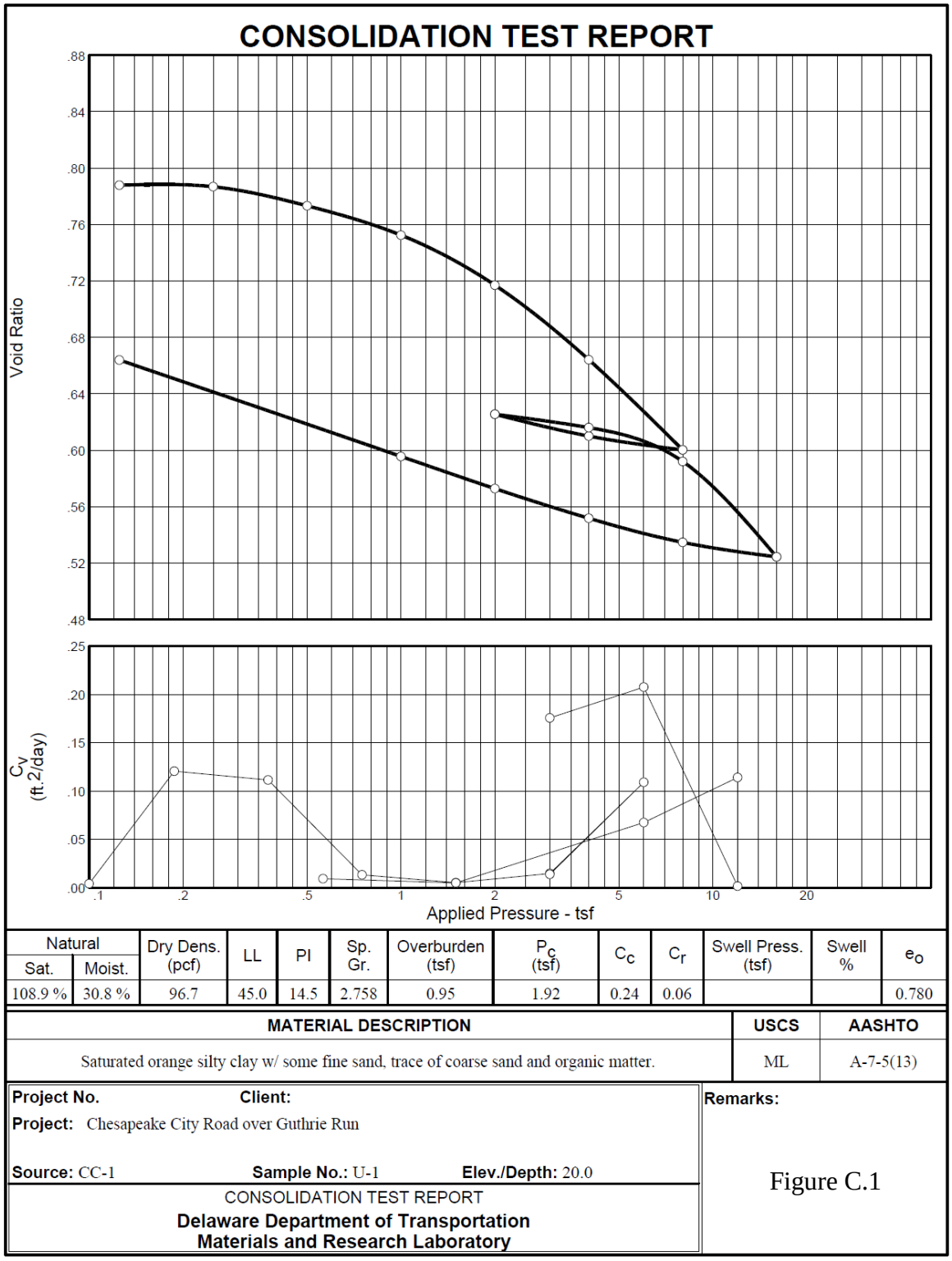

Natural Sat.	Natural Moist.	Dry Dens. (pcf)	LL	PI	Sp. Gr.	Overburden (tsf)	P_c (tsf)	C_c	C_r	Swell Press. (tsf)	Swell %	e_o
108.9 %	30.8 %	96.7	45.0	14.5	2.758	0.95	1.92	0.24	0.06			0.780

MATERIAL DESCRIPTION	USCS	AASHTO
Saturated orange silty clay w/ some fine sand, trace of coarse sand and organic matter.	ML	A-7-5(13)

Project No. **Client:**

Project: Chesapeake City Road over Guthrie Run

Source: CC-1 **Sample No.:** U-1 **Elev./Depth:** 20.0

CONSOLIDATION TEST REPORT

Delaware Department of Transportation
Materials and Research Laboratory

Remarks:

Figure C.1

Figure C.1 Consolidation test results for Sample U-1 from borehole CC-1

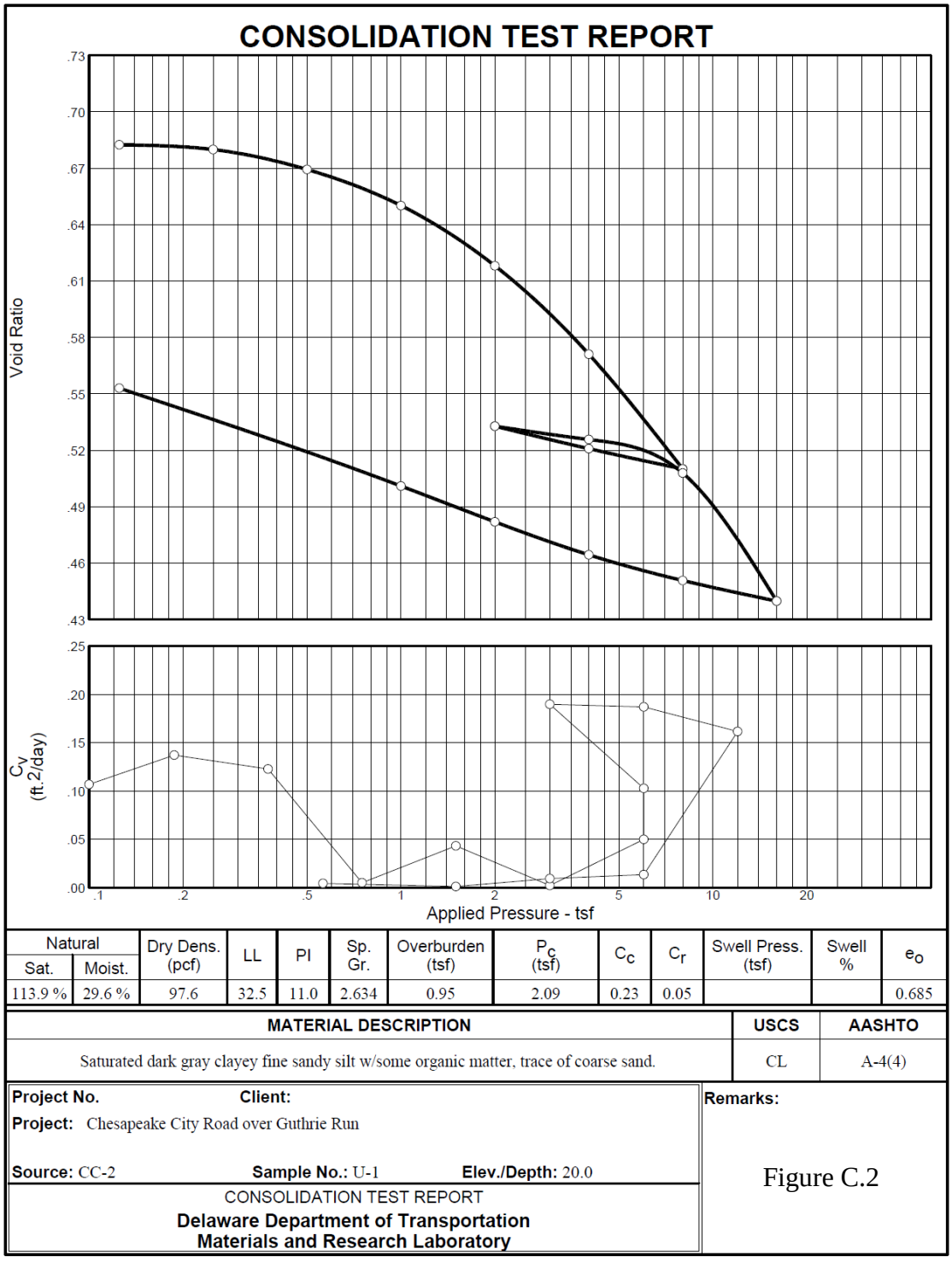

Natural Sat.	Natural Moist.	Dry Dens. (pcf)	LL	PI	Sp. Gr.	Overburden (tsf)	P_c (tsf)	C_c	C_r	Swell Press. (tsf)	Swell %	e_o
113.9 %	29.6 %	97.6	32.5	11.0	2.634	0.95	2.09	0.23	0.05			0.685

MATERIAL DESCRIPTION	USCS	AASHTO
Saturated dark gray clayey fine sandy silt w/some organic matter, trace of coarse sand.	CL	A-4(4)

Project No. **Client:**

Project: Chesapeake City Road over Guthrie Run

Source: CC-2 **Sample No.:** U-1 **Elev./Depth:** 20.0

CONSOLIDATION TEST REPORT

Delaware Department of Transportation
Materials and Research Laboratory

Remarks:

Figure C.2

Figure C.2 Consolidation test results for Sample U-1 from borehole CC-2

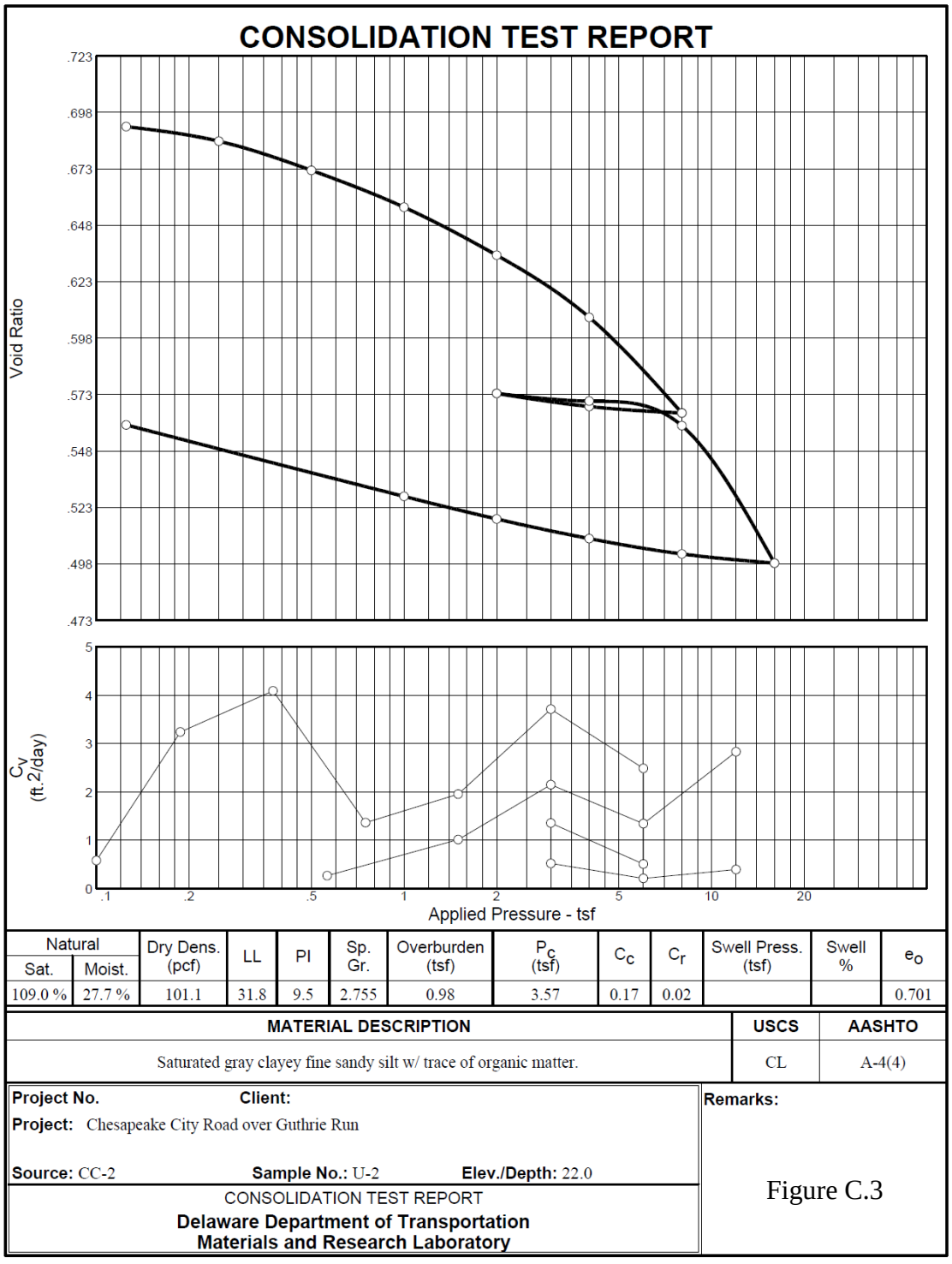

Natural Sat.	Natural Moist.	Dry Dens. (pcf)	LL	PI	Sp. Gr.	Overburden (tsf)	P_c (tsf)	C_c	C_r	Swell Press. (tsf)	Swell %	e_o
109.0 %	27.7 %	101.1	31.8	9.5	2.755	0.98	3.57	0.17	0.02			0.701

MATERIAL DESCRIPTION	USCS	AASHTO
Saturated gray clayey fine sandy silt w/ trace of organic matter.	CL	A-4(4)

Project No. **Client:**

Project: Chesapeake City Road over Guthrie Run

Source: CC-2 **Sample No.:** U-2 **Elev./Depth:** 22.0

CONSOLIDATION TEST REPORT

Delaware Department of Transportation
Materials and Research Laboratory

Remarks:

Figure C.3

Figure C.3 Consolidation test results for Sample U-2 from borehole CC-2

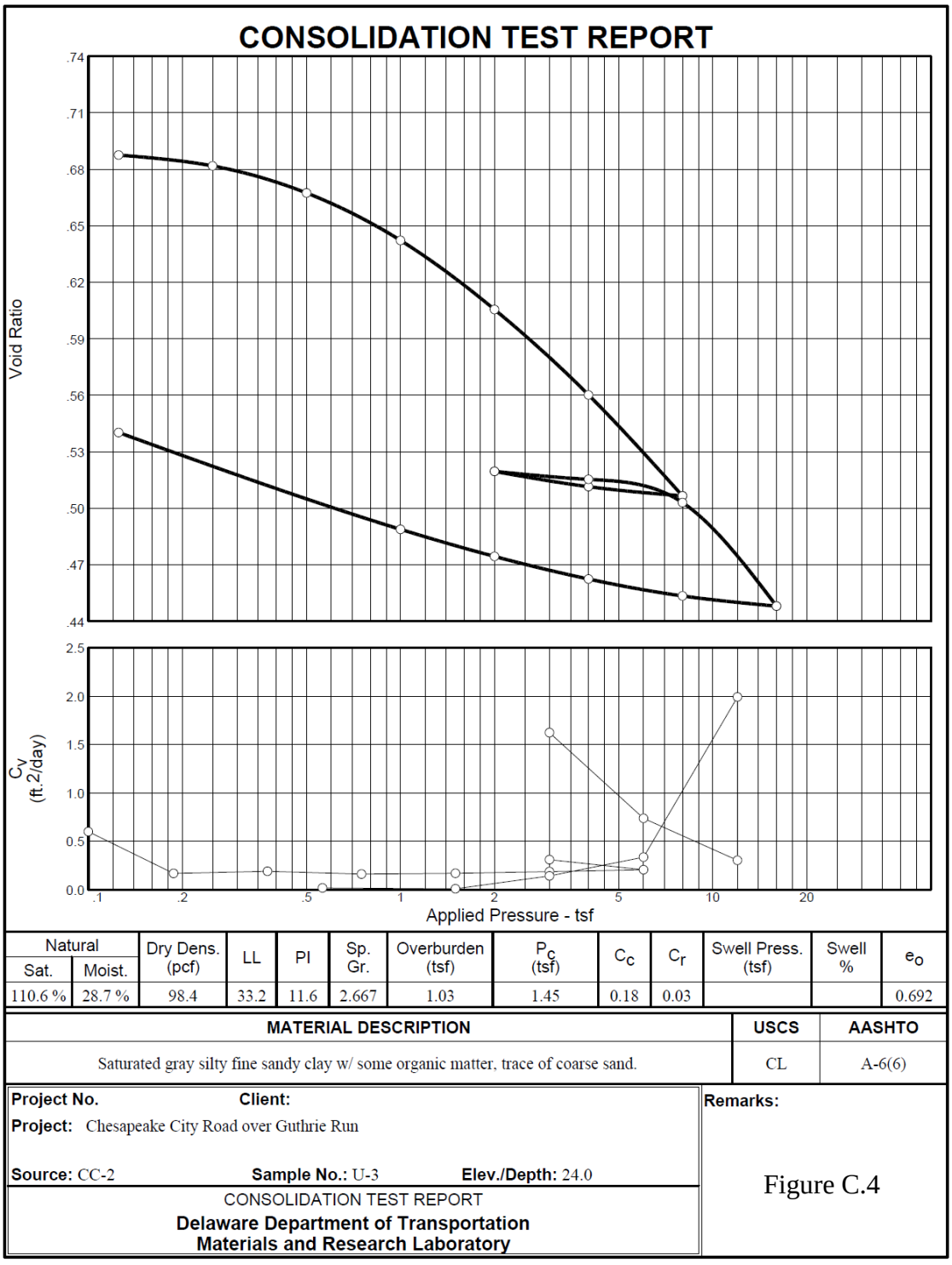

Natural Sat.	Natural Moist.	Dry Dens. (pcf)	LL	PI	Sp. Gr.	Overburden (tsf)	P_c (tsf)	C_c	C_r	Swell Press. (tsf)	Swell %	e_o
110.6 %	28.7 %	98.4	33.2	11.6	2.667	1.03	1.45	0.18	0.03			0.692

MATERIAL DESCRIPTION	USCS	AASHTO
Saturated gray silty fine sandy clay w/ some organic matter, trace of coarse sand.	CL	A-6(6)

Project No. **Client:**

Project: Chesapeake City Road over Guthrie Run

Source: CC-2 **Sample No.:** U-3 **Elev./Depth:** 24.0

CONSOLIDATION TEST REPORT

Delaware Department of Transportation
Materials and Research Laboratory

Remarks:

Figure C.4

Figure C.4 Consolidation test results for Sample U-3 from borehole CC-2

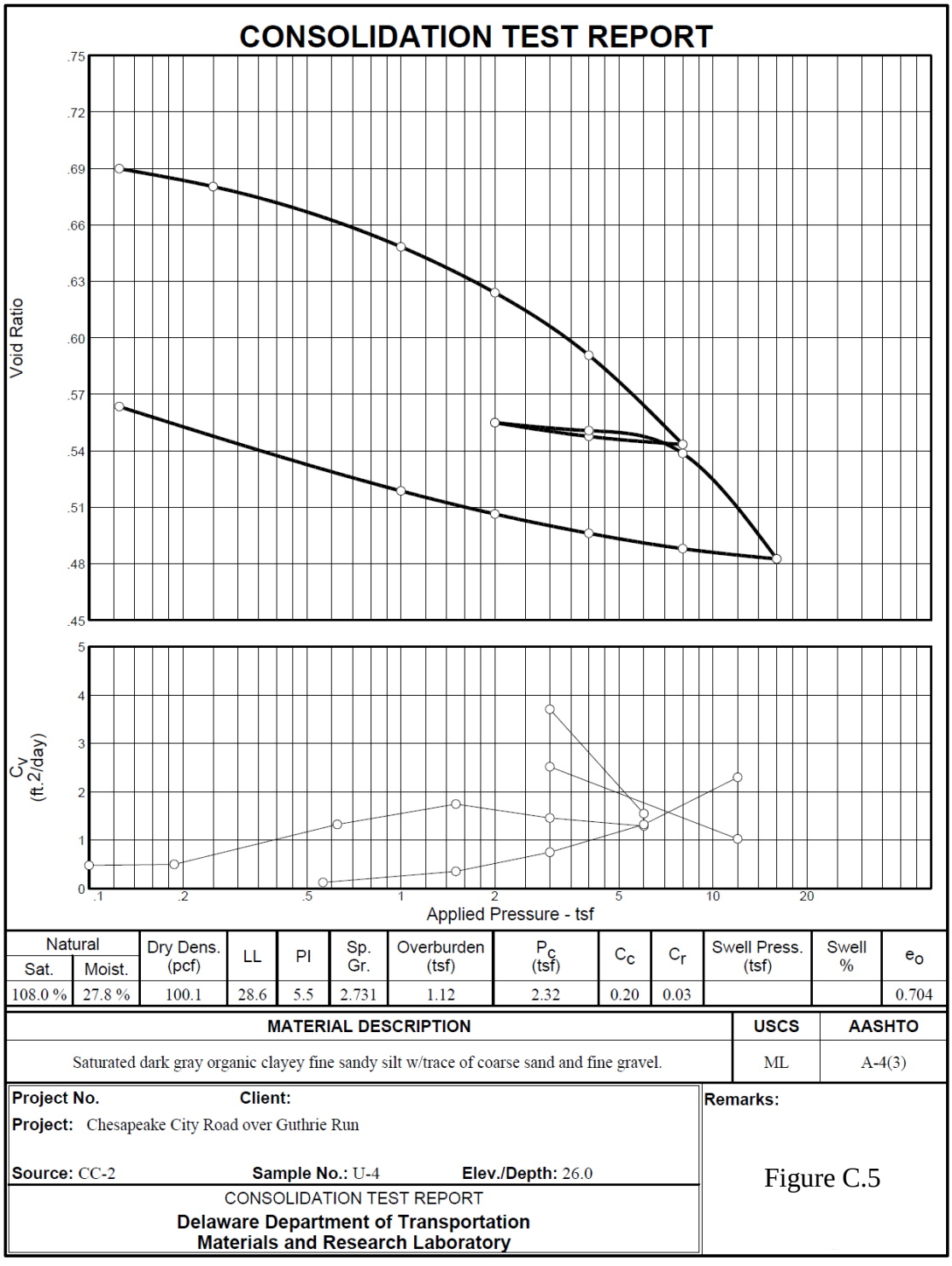

Natural Sat.	Natural Moist.	Dry Dens. (pcf)	LL	PI	Sp. Gr.	Overburden (tsf)	P_c (tsf)	C_c	C_r	Swell Press. (tsf)	Swell %	e_o
108.0 %	27.8 %	100.1	28.6	5.5	2.731	1.12	2.32	0.20	0.03			0.704

MATERIAL DESCRIPTION	USCS	AASHTO
Saturated dark gray organic clayey fine sandy silt w/trace of coarse sand and fine gravel.	ML	A-4(3)

Project No. **Client:**

Project: Chesapeake City Road over Guthrie Run

Source: CC-2 **Sample No.:** U-4 **Elev./Depth:** 26.0

CONSOLIDATION TEST REPORT

Delaware Department of Transportation
Materials and Research Laboratory

Remarks:

Figure C.5

Figure C.5 Consolidation test results for Sample U-4 from borehole CC-2

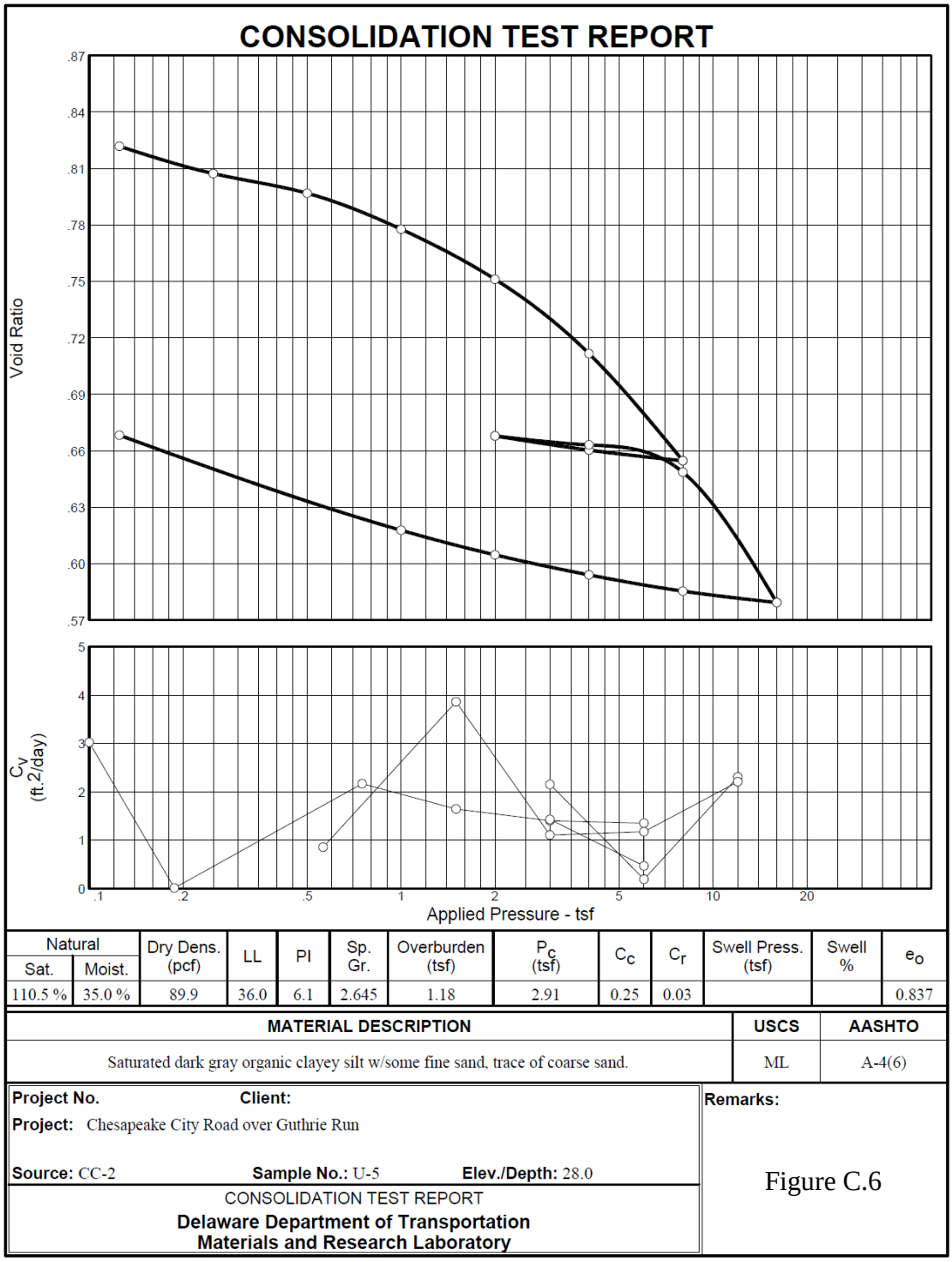

Natural Sat.	Natural Moist.	Dry Dens. (pcf)	LL	PI	Sp. Gr.	Overburden (tsf)	P_c (tsf)	C_c	C_r	Swell Press. (tsf)	Swell %	e_o
110.5 %	35.0 %	89.9	36.0	6.1	2.645	1.18	2.91	0.25	0.03			0.837

MATERIAL DESCRIPTION	USCS	AASHTO
Saturated dark gray organic clayey silt w/some fine sand, trace of coarse sand.	ML	A-4(6)

Project No. **Client:**

Project: Chesapeake City Road over Guthrie Run

Source: CC-2 **Sample No.:** U-5 **Elev./Depth:** 28.0

CONSOLIDATION TEST REPORT

Delaware Department of Transportation
Materials and Research Laboratory

Remarks:

Figure C.6

Figure C.6 Consolidation test results for Sample U-5 from borehole CC-2

Appendix D

UNCONFINED COMPRESSION TESTS

Two unconfined compression tests were conducted by the Delaware Department of Transportation on specimens taken from boring logs CC-1 and CC-2 at the Br. 1-366 site, following the test procedure outlined in AASHTO T 208. The unconfined compressive strengths measured in each of these tests were 1440 and 1760 psf, respectively.

UNCONFINED COMPRESSION TEST

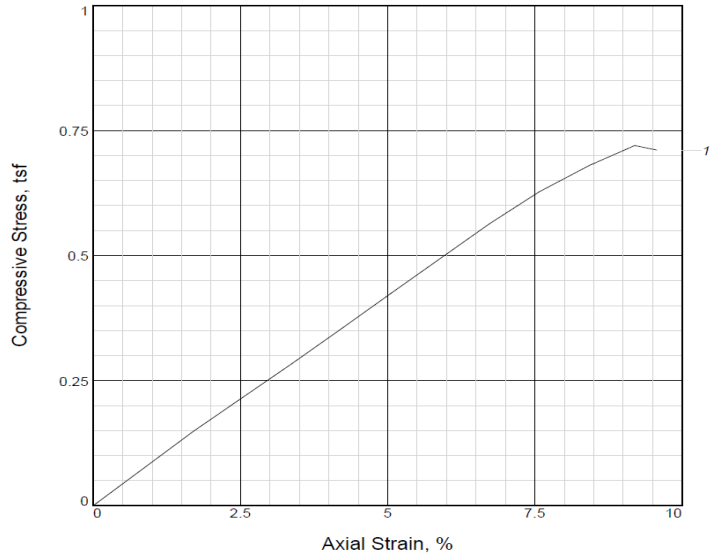

Sample No.	1			
Unconfined strength, tsf	0.720			
Undrained shear strength, tsf	0.360			
Failure strain, %	9.2			
Time to failure, min.	15			
Water content, %	27.5			
Wet density, pcf	127.8			
Dry density, pcf	100.2			
Saturation, %	105.6			
Void ratio	0.7183			
Specimen diameter, in.	2.88			
Specimen height, in.	5.60			
Height/diameter ratio	1.95			

Description: Saturated orange silty clay w/ some fine sand, trace of coarse sand and organic matter.

LL = 45.0	**PL =** 30.5	**PI =** 14.5	**GS=** 2.758	**Type:**

Project No.:
Date Sampled:
Remarks:

Client:

Project: Chesapeake City Road over Guthrie Run

Source of Sample: CC-1 **Depth:** 20.0
Sample Number: U-1

UNCONFINED COMPRESSION TEST
Delaware Department of Transportation
Materials and Research Laboratory

Figure D.1

Figure D.1 Unconfined Compression Tests Results for Sample U-1 from borehole CC-1

UNCONFINED COMPRESSION TEST

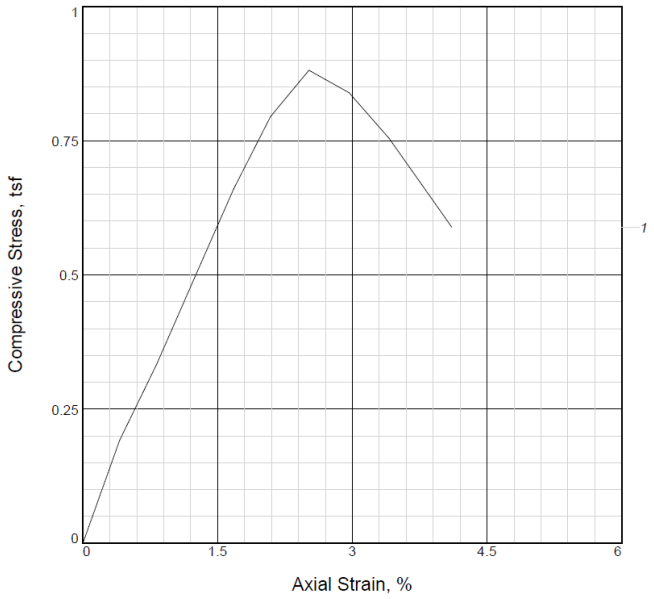

Sample No.	1			
Unconfined strength, tsf	0.881			
Undrained shear strength, tsf	0.441			
Failure strain, %	2.5			
Time to failure, min.	7			
Water content, %	26.6			
Wet density, pcf	125.9			
Dry density, pcf	99.5			
Saturation, %	100.5			
Void ratio	0.7288			
Specimen diameter, in.	2.88			
Specimen height, in.	5.60			
Height/diameter ratio	1.95			

Description: Saturated gray clayey fine sandy silt w/ trace of organic matter.

LL = 31.8	**PL =** 22.3	**PI =** 9.5	**GS=** 2.755	**Type:**

Project No.:
Date Sampled:
Remarks:

Figure D.2

Client:

Project: Chesapeake City Road over Guthrie Run

Source of Sample: CC-2 **Depth:** 22.0
Sample Number: U-2

UNCONFINED COMPRESSION TEST
Delaware Department of Transportation
Materials and Research Laboratory

Figure D.2 Unconfined Compression Tests Results for Sample U-2 from borehole CC-2

REFERENCES

AASHTO T208 (2015). “Standard Method of Test for Unconfined Compressive Strength of Cohesive Soil.” AASHTO Standard Method of Testing, American Association of State Highway and Transportation Officials, Washington, D.C.

Appendix E

UNCONSOLIDATED UNDRAINED TRIAXIAL TESTS

Four unconsolidated undrained triaxial tests were conducted at the University of Delaware on specimens taken from boring logs CC-1 and CC-2 at the Br. 1-366 site, following the test procedure outlined in ASTM D2850. The results from these tests showed that the undrained cohesion (c_u) of the material is approximately 2100 psf (Figure E.1). The recorded data from these tests is presented in this appendix, in Figures E.2 to E.5.

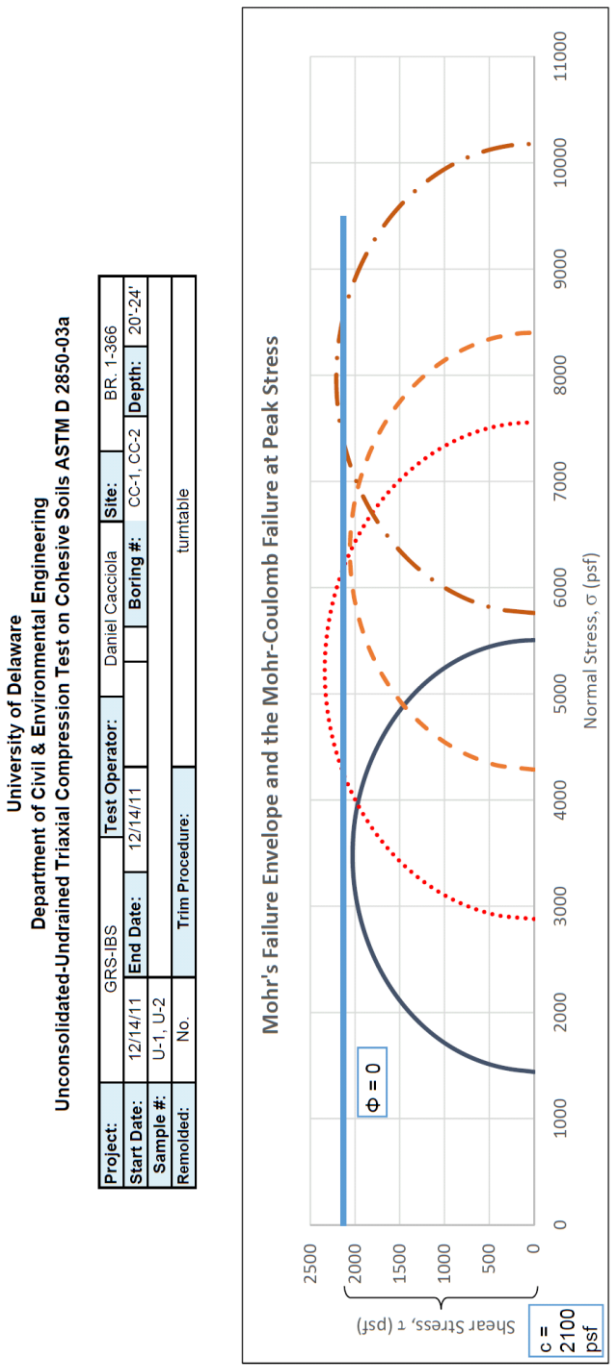

Figure E.1 The results from four UU triaxial tests for tests run on specimens U-1 and U-2 from borehole CC-1, and specimens U-1 and U-2 from borehole CC-2

University of Delaware
Department of Civil & Environmental Engineering
Unconsolidated-Undrained Triaxial Compression Test on Cohesive Soils ASTM D 2850-03a

Project:	GRS-IBS			Test Operator:		Daniel Cacciola		Site:	BR.1-366			
Start Date:		12/13/11	End Date:	12/13/11			Boring #:	CC-1	Tube #:	1	Depth:	20' - 22'
Sample #:	U-1	LL:	35	PL:	23	PI:	12	Classification:	CL			
Remolded:		No	Trim Proc.:	turntable		Particle Size Analysis ASTM D422						

WATER CONTENT DETERMINATION DATA				
	Before Failure	After Failure	Specimen Calculations:	
Sample Number	B-1 T-1 S-1	B-1 T-1 S-1	Average Water Content	24.8%
Pan Number	8	FJ-3		
Mass of Pan (g)	11.78	29.06		
Mass of Pan + Wet Soil (g)	16.78	77.52	Moist Unit Weight [pcf]	
Mass of Pan + Dry Soil (g)	15.79	67.87		
Mass of Wet Soil (g)	5.00	48.46		
Mass of Dry Soil (g)	4.01	38.81	Dry Unit Weight [pcf]	
Mass of Water (g)	0.99	9.65		
Water Content (%)	24.7%	24.9%		

UNCONSOLIDATED-UNDRAINED TRIAXIAL COMPRESSION TEST DATA					
Type of Sample	Undisturbed	Height/Diameter	2.54	Specific Gravity by ASTM D 854	2.65
Initial Diameter [in]	1.402	Initial Area [in^2]	1.544		
Initial Height [in]	3.564	Initial Volume [in^3]	5.502	Strain Rate [% per min]	0.3
Void Ratio (e)	0.657	Saturation (%)	100%	Station Number	2

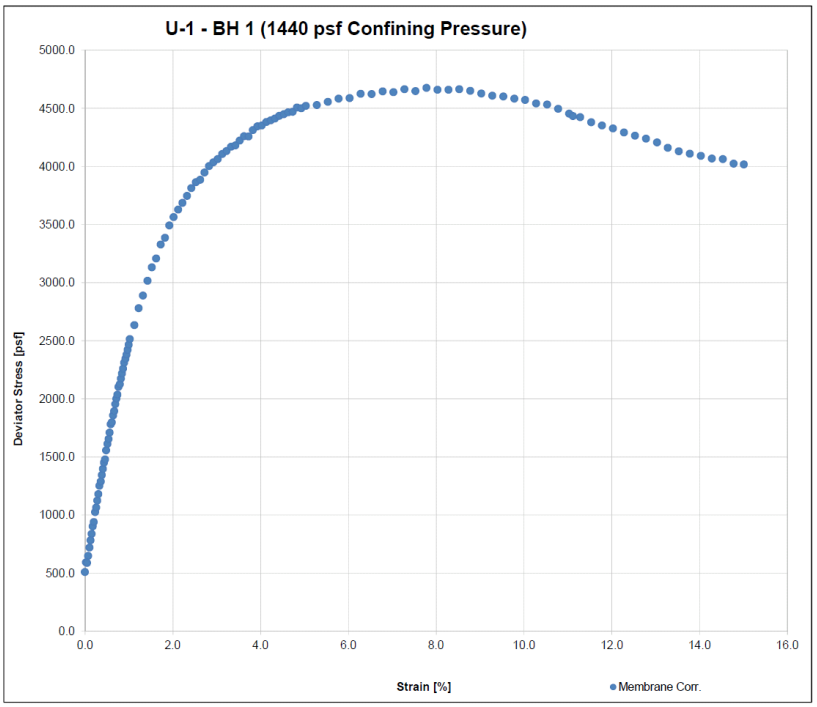

Failure Criteria - Max Stress	
Stress σ_d [psf]	4677.600
Strain (%)	7.780

Failure Criteria - 10% Strain	
Stress σ_d [psf]	4616.208
Strain (%)	10.030

PHOTO OF SPECIMEN AFTER FAILURE

Notes	The water content was calculated using trimmings before the test and from the entire specimen after the test. Reported stresses have been corrected for Trojan condom membranes using a modulus of 1390KPa and a thickness of 0.07mm per membrane. Two membranes were used.

Figure E.2 Unconsolidated Undrained Triaxial Tests Results for Sample U-1 from borehole CC-1

University of Delaware
Department of Civil & Environmental Engineering
Unconsolidated-Undrained Triaxial Compression Test on Cohesive Soils ASTM D 2850-03a

Project:	GRS-IBS			Test Operator:		Daniel Cacciola		Site:	BR.1-366			
Start Date:		12/13/11	End Date:	12/13/11			Boring #:	CC-1	Tube #:	1	Depth:	20' - 22'
Test #:	U-2	LL:	35	PL:	23	PI:	12	Classification:	CL			
Remolded:		No	Trim Proc.:	turntable		Particle Size Analysis ASTM D422						

WATER CONTENT DETERMINATION DATA

	Before Failure	After Failure	Specimen Calculations:	
Sample Number	B-1 T-1 S-2	B-1 T-1 S-2	Average Water Content	24.8%
Pan Number	5	T4-5		
Mass of Pan (g)	11.83	30.35		
Mass of Pan + Wet Soil (g)	18.86	88.38	Moist Unit Weight [pcf]	
Mass of Pan + Dry Soil (g)	17.48	76.72		
Mass of Wet Soil (g)	7.03	58.03		
Mass of Dry Soil (g)	5.65	46.37	Dry Unit Weight [pcf]	
Mass of Water (g)	1.38	11.66		
Water Content (%)	24.4%	25.1%		

UNCONSOLIDATED-UNDRAINED TRIAXIAL COMPRESSION TEST DATA

Type of Sample	Undisturbed	Height/Diameter	2.18	Specific Gravity by ASTM D 854	2.65
Initial Diameter [in]	1.461	Initial Area [in^2]	1.676		
Initial Height [in]	3.189	Initial Volume [in^3]	5.346	Strain Rate [% per min]	0.3
Void Ratio (e)	0.657	Saturation (%)	100%	Station Number	1

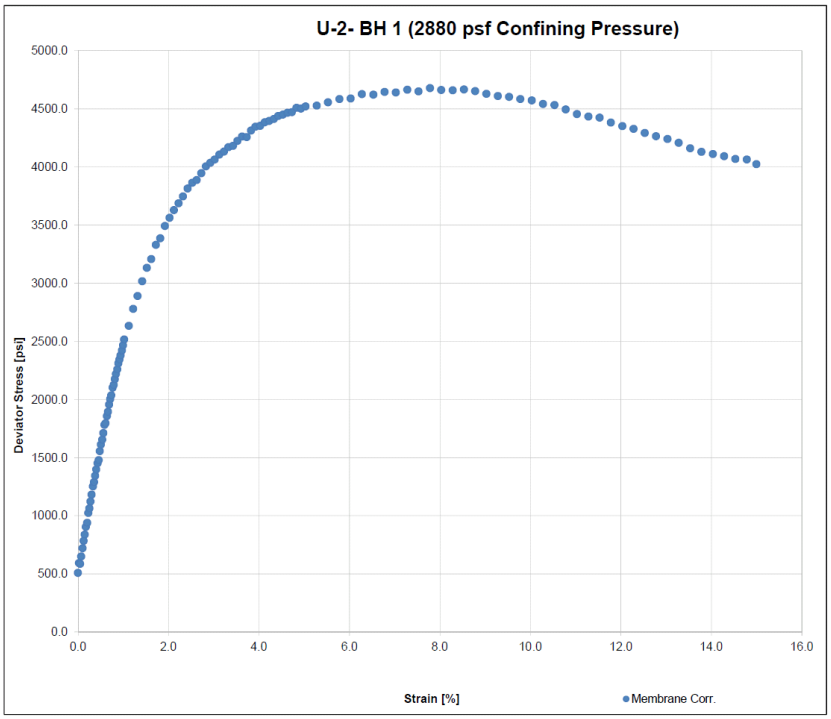

Failure Criteria - Max Stress	
Stress σ_d [psf]	4019.184
Strain (%)	8.280

Failure Criteria - 10% Strain	
Stress σ_d [psf]	3986.352
Strain (%)	10.000

PHOTO OF SPECIMEN AFTER FAILURE

Notes	The water content was calculated using trimmings before the test and from the entire specimen after the test. Reported stresses have been corrected for Trojan condom membranes using a modulus of 1390KPa and a thickness of 0.07mm per membrane. Two membranes were used.

Figure E.3 Unconsolidated Undrained Triaxial Tests Results for Sample U-2 from borehole CC-1

University of Delaware
Department of Civil & Environmental Engineering
Unconsolidated-Undrained Triaxial Compression Test on Cohesive Soils ASTM D 2850-03a

Project:	GRS-IBS			Test Operator:		Daniel Cacciola		Site:	BR.1-366			
Start Date:		12/14/11	End Date:	12/14/11			Boring #:	CC-2	Tube #:	2	Depth:	22'-24'
Sample #:	U-1	LL:	38	PL:	22	PI:	16	Classification:		CL		
Remolded:		No	Trim Proc.:		turntable			Particle Size Analysis ASTM D422				

WATER CONTENT DETERMINATION DATA

	Before Failure	After Failure	Specimen Calculations:	
Sample Number	B-2 T-2 S-1	B-2 T-2 S-1	Average Water Content	25.2%
Pan Number	105	99		
Mass of Pan (g)	12.09	16.01		
Mass of Pan + Wet Soil (g)	16.59	100.10	Moist Unit Weight [pcf]	126.97
Mass of Pan + Dry Soil (g)	15.72	82.51		
Mass of Wet Soil (g)	4.50	84.09		
Mass of Dry Soil (g)	3.63	66.50	Dry Unit Weight [pcf]	101.40
Mass of Water (g)	0.87	17.59		
Water Content (%)	24.0%	26.5%		

UNCONSOLIDATED-UNDRAINED TRIAXIAL COMPRESSION TEST DATA

Type of Sample	Undisturbed	Height/Diameter	2.44	Specific Gravity by ASTM D 854	2.65
Initial Diameter [in]	2.846	Initial Area [in^2]	6.362		
Initial Height [in]	6.958	Initial Volume [in^3]	44.263	Strain Rate [% per min]	0.3
Void Ratio (e)	0.668	Saturation (%)	100%	Station Number	-

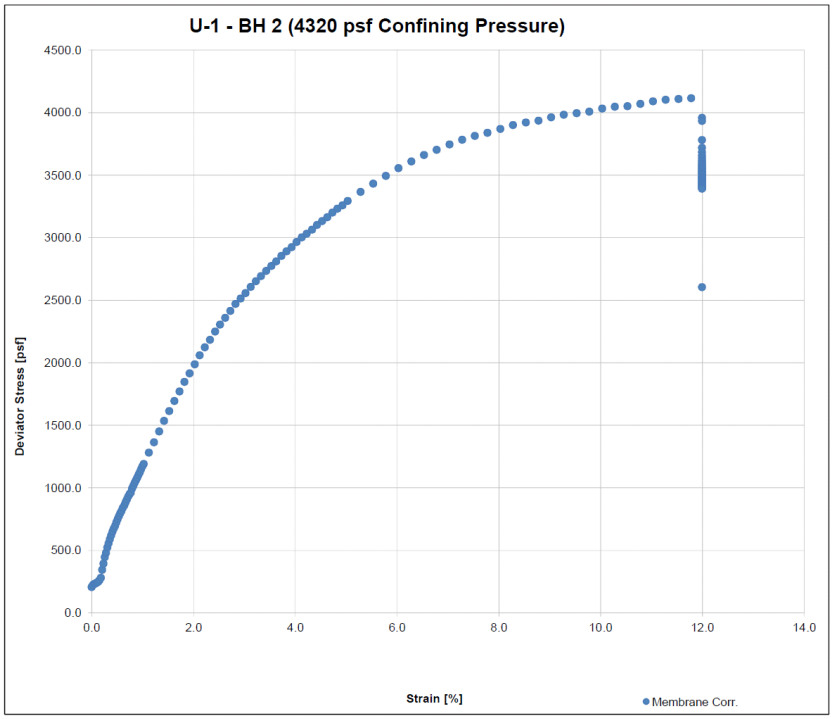

Failure Criteria - Max Stress	
Stress σ_d [psf]	4113.504
Strain (%)	7.210

Failure Criteria - 10% Strain	
Stress σ_d [psf]	4032.000
Strain (%)	10.030

PHOTO OF SPECIMEN AFTER FAILURE

Notes	The water content was calculated using trimmings before the test and from the entire specimen after the test. Reported stresses have been corrected for Trojan condom membranes using a modulus of 1390KPa and a thickness of 0.07mm per membrane. Two membranes were used.

Figure E.4 Unconsolidated Undrained Triaxial Tests Results for Sample U-1 from borehole CC-2

University of Delaware
Department of Civil & Environmental Engineering
Unconsolidated-Undrained Triaxial Compression Test on Cohesive Soils ASTM D 2850-03a

Project:	GRS-IBS			Test Operator:		Daniel Cacciola		Site:	BR.1-366			
Start Date:		12/14/11	End Date:	12/14/11			Boring #:	CC-2	Tube #:	2	Depth:	20' - 22'
Sample #:	U-2	LL:	39	PL:	22	PI:	17	Classification:		CL		
Remolded:		No	Trim Proc.:		turntable		Particle Size Analysis ASTM D422					

WATER CONTENT DETERMINATION DATA

	Before Failure	After Failure	Specimen Calculations:	
Sample Number	B-2 T-2 S-2	B-2 T-2 S-2	Average Water Content	25.7%
Pan Number	5	65		
Mass of Pan (g)	11.83	30.32		
Mass of Pan + Wet Soil (g)	12.71	128.00	Moist Unit Weight [pcf]	123.19
Mass of Pan + Dry Soil (g)	12.54	106.91		
Mass of Wet Soil (g)	0.88	97.68		
Mass of Dry Soil (g)	0.71	76.59	Dry Unit Weight [pcf]	97.97
Mass of Water (g)	0.17	21.09		
Water Content (%)	23.9%	27.5%		

UNCONSOLIDATED-UNDRAINED TRIAXIAL COMPRESSION TEST DATA

Type of Sample	Undisturbed	Height/Diameter	2.15	Specific Gravity by ASTM D 854	2.65
Initial Diameter [in]	2.868	Initial Area [in^2]	6.460		
Initial Height [in]	6.156	Initial Volume [in^3]	39.769	Strain Rate [% per min]	0.3
Void Ratio (e)	0.682	Saturation (%)	100%	Station Number	-

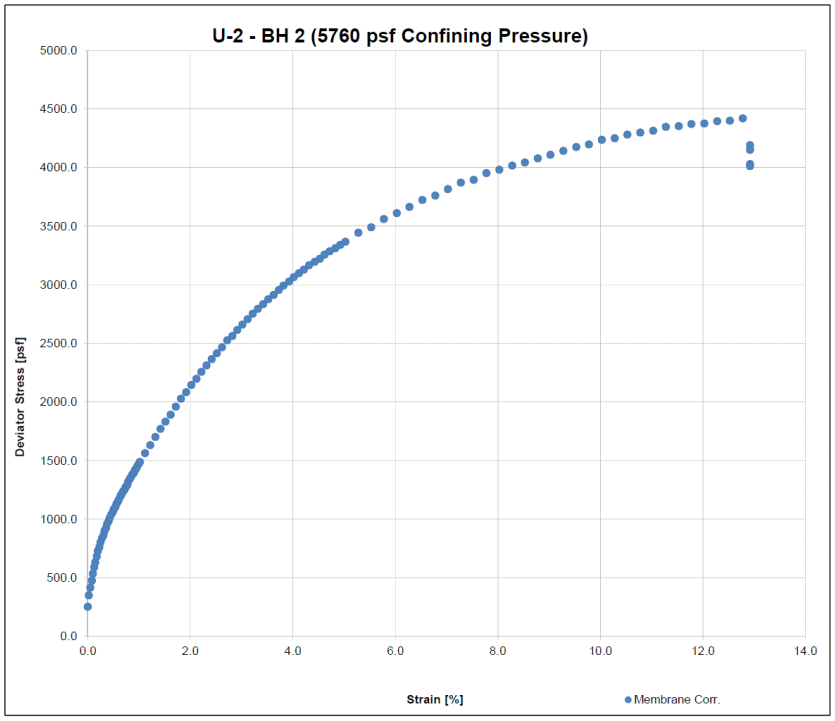

Failure Criteria - Max Stress	
Stress σ_d [psf]	4418.352
Strain (%)	12.780

Failure Criteria - 10% Strain	
Stress σ_d [psf]	4235.184
Strain (%)	10.000

PHOTO OF SPECIMEN AFTER FAILURE

Notes	The water content was calculated using trimmings before the test and from the entire specimen after the test. Reported stresses have been corrected for Trojan condom membranes using a modulus of 1390KPa and a thickness of 0.07mm per membrane. Two membranes were used.

Figure E.5 Unconsolidated Undrained Triaxial Tests Results for Sample U-2 from borehole CC-2

REFERENCES

ASTM D2850 (2015). “Standard Test Method for Unconsolidated-Undrained Triaxial Compression Test on Cohesive Soils.” ASTM International, West Conshohocken, PA.

Appendix F

ORGANIC CONTENT TESTS

A total of 11 organic content tests were conducted by the Delaware Department of Transportation on specimens taken from boring logs CC-1 and CC-2 at the Br. 1-366 site, following the test procedure outlined in AASHTO T 267 (Table F.1). As shown in Table F.1, the organic content ranges between 0.47% and 4.83% with an average of 1.7%.

Table F.1 Organic content test results

BR1-366 Organic Content	
Sample Number	Organic Content
7	2.1
13	2.19
14	1.19
15	4.83
16	1.51
17	1.83
18	1.46
19	1.56
20	0.73
21	0.47
22	0.47

REFERENCES

AASHTO T267 (1986). "Standard Method of Test for Determination of Organic Content in Soils by Loss of Ignition." AASHTO Standard Method of Testing, American Association of State Highway and Transportation Officials, Washington, D.C.

Appendix G

WEST ABUTMENT STRAIN DURING OPERATION

The measured strain by the long and short strain gauges of the west abutment and the corresponding corrected strain values are presented in this appendix. The correction procedure that was utilized is explained in detail in Chapter 6.

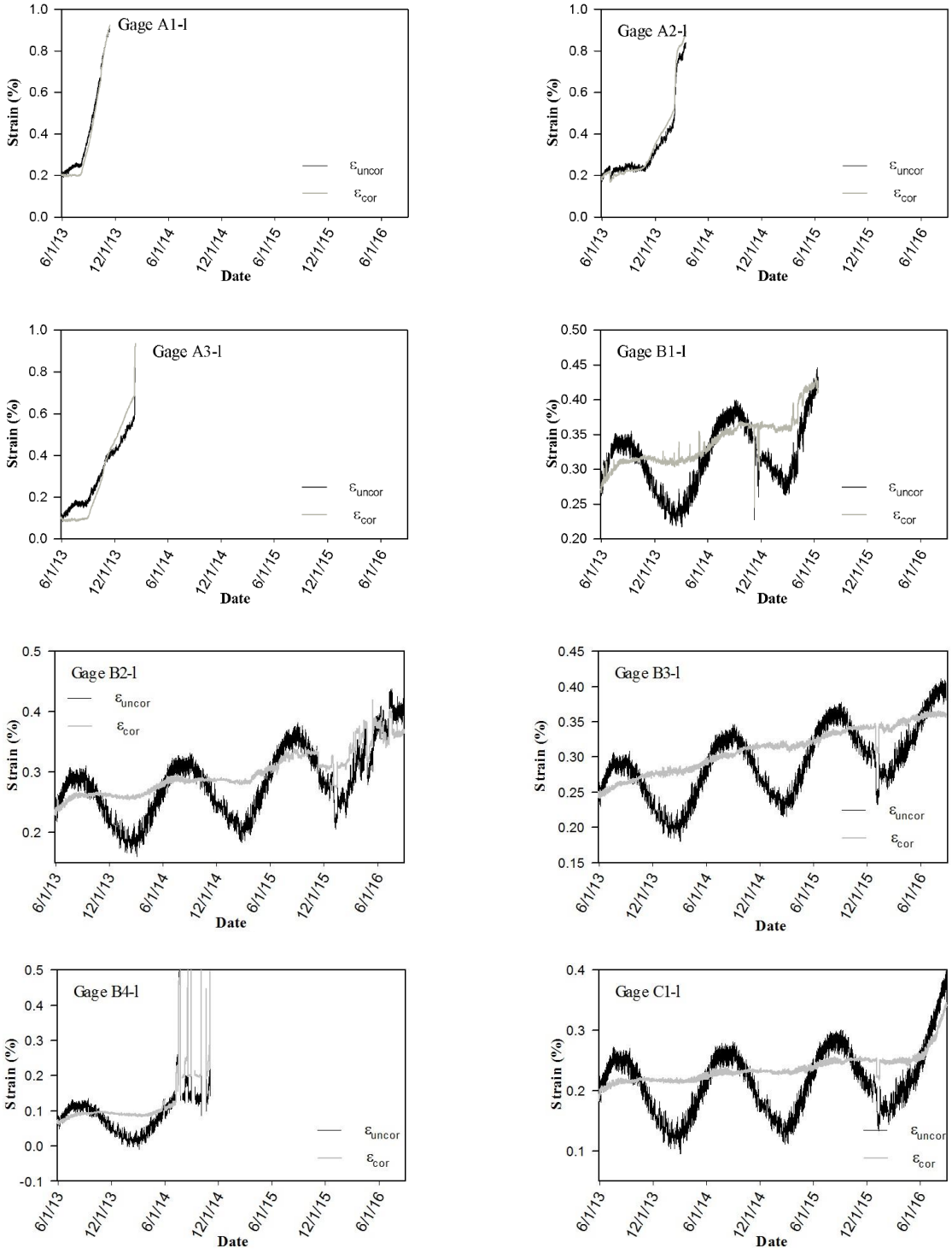

Figure G.1. Long term performance of the west abutment long strain gages

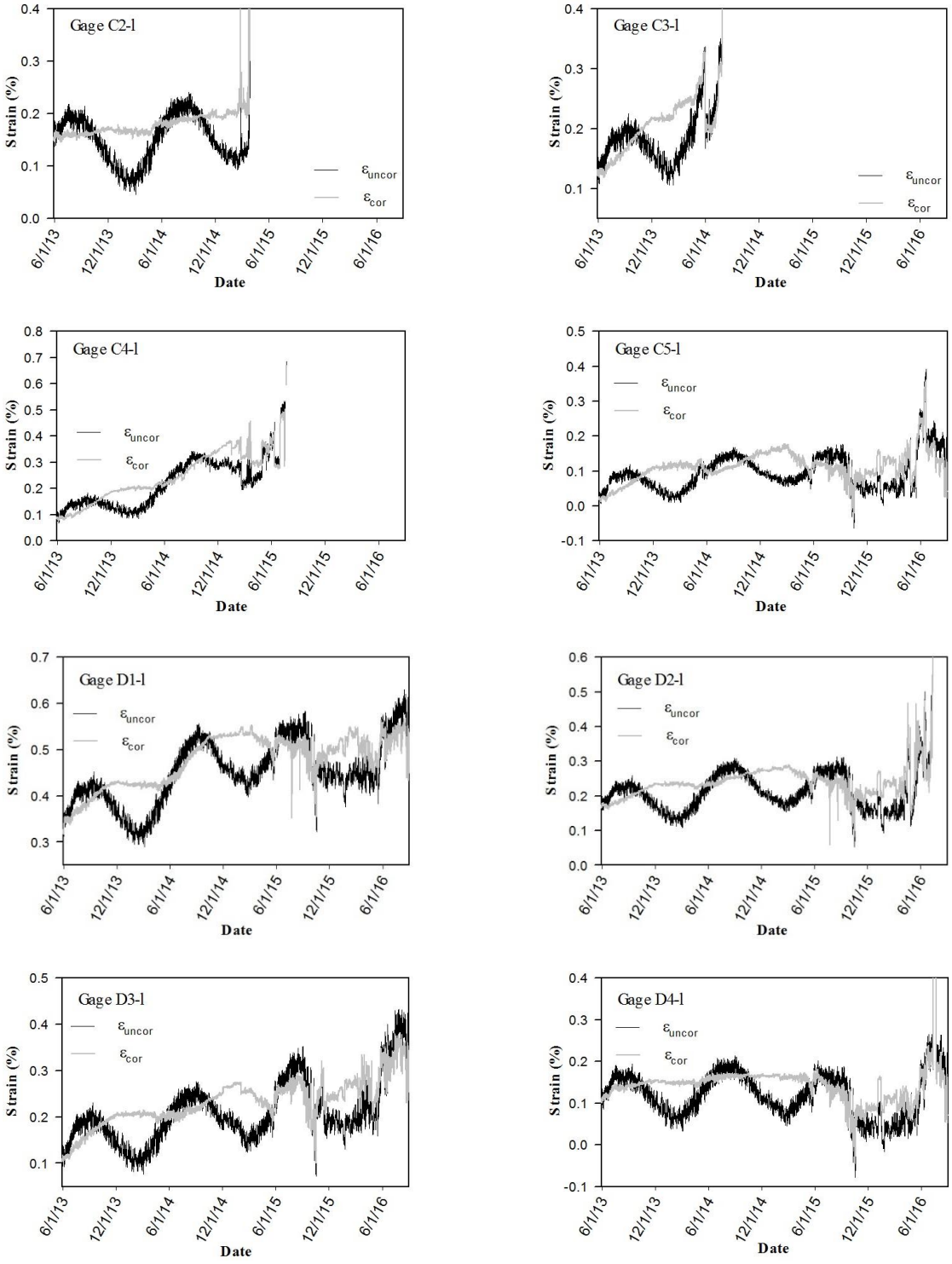

Figure G.1 Continued

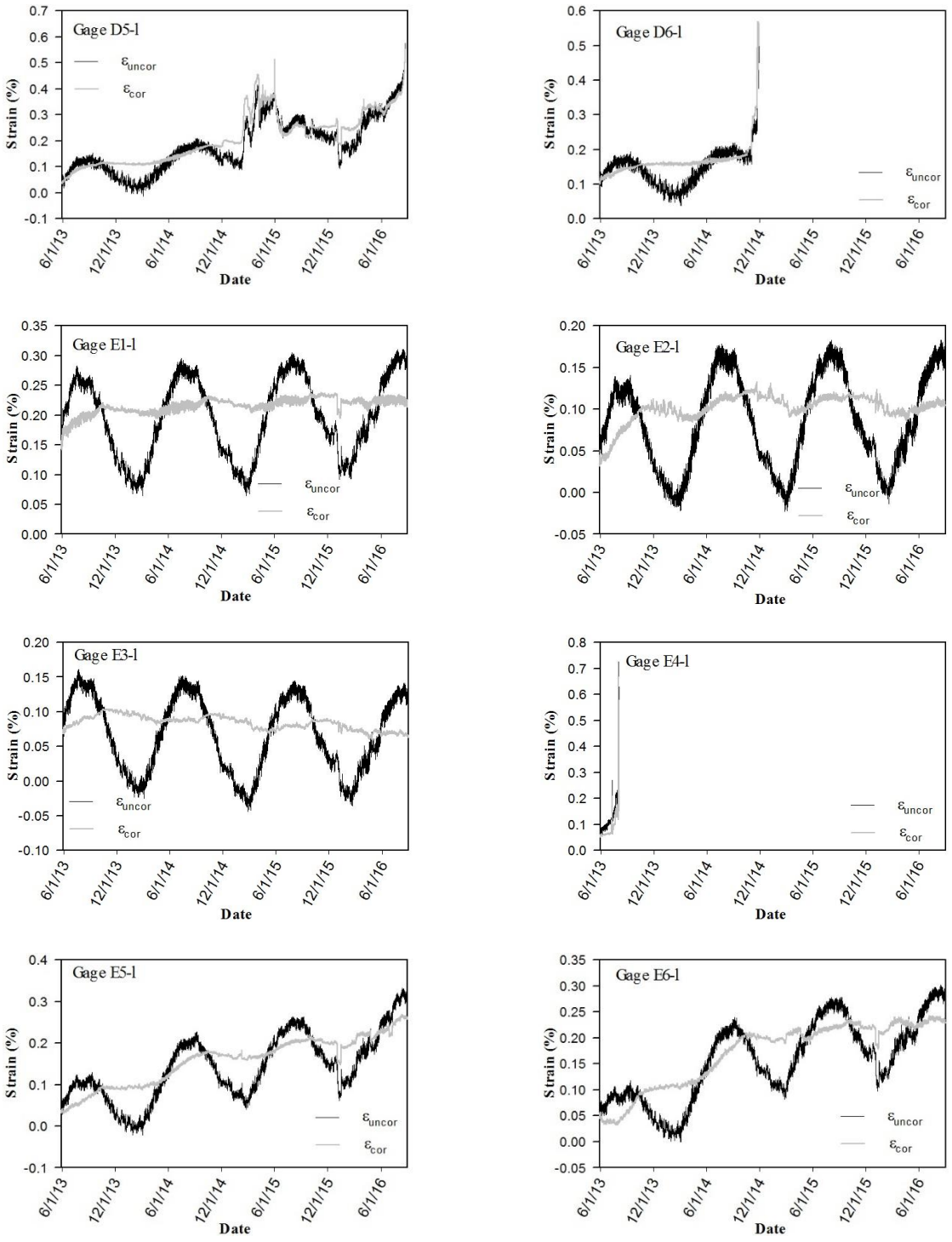

Figure G.1 Continued

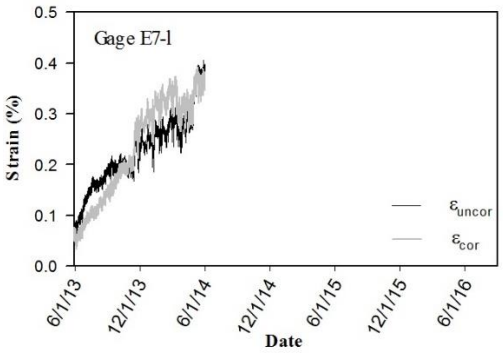

Figure G.1 Continued

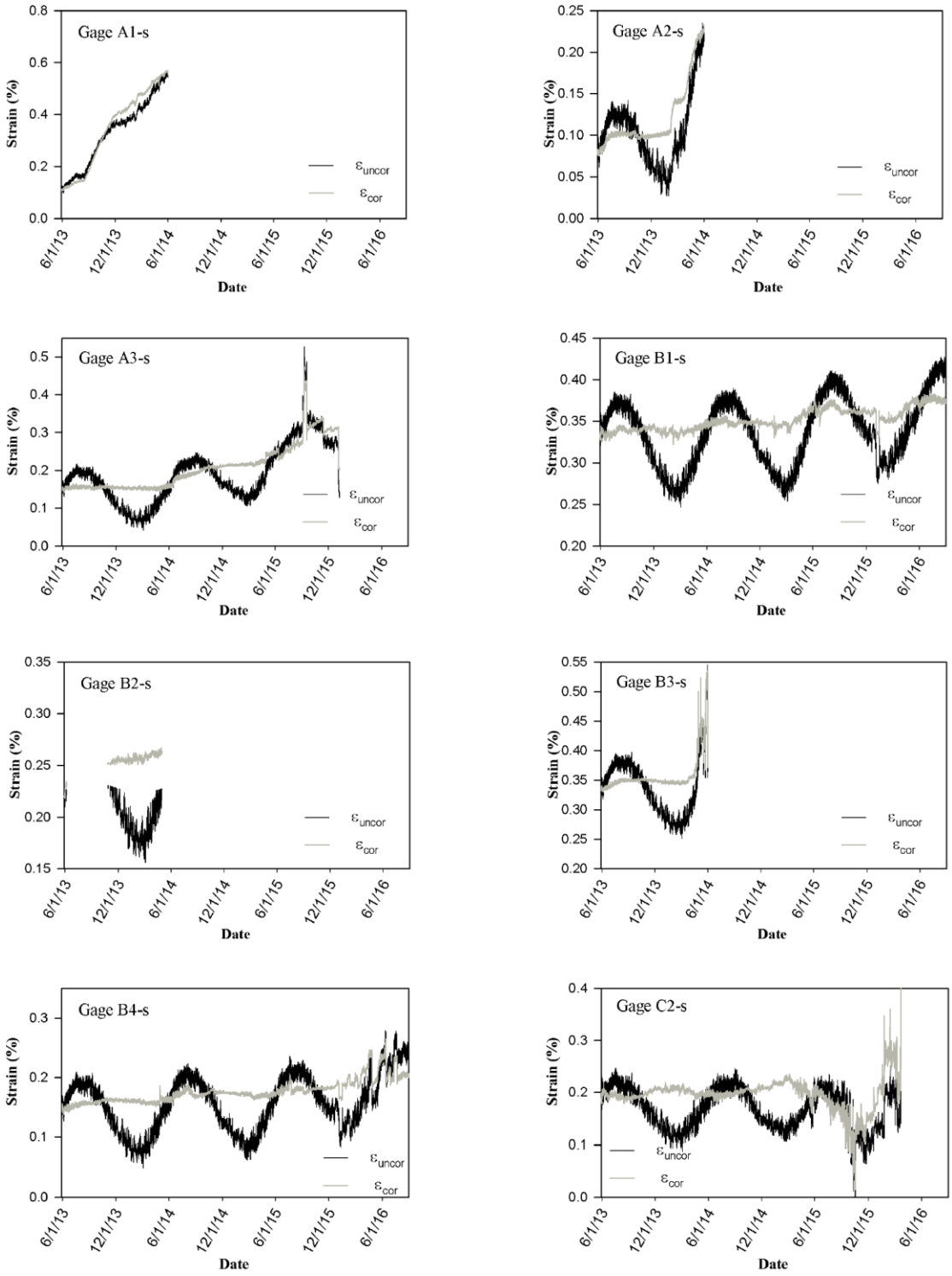

Figure G.2. Long term performance of the west abutment short strain gages

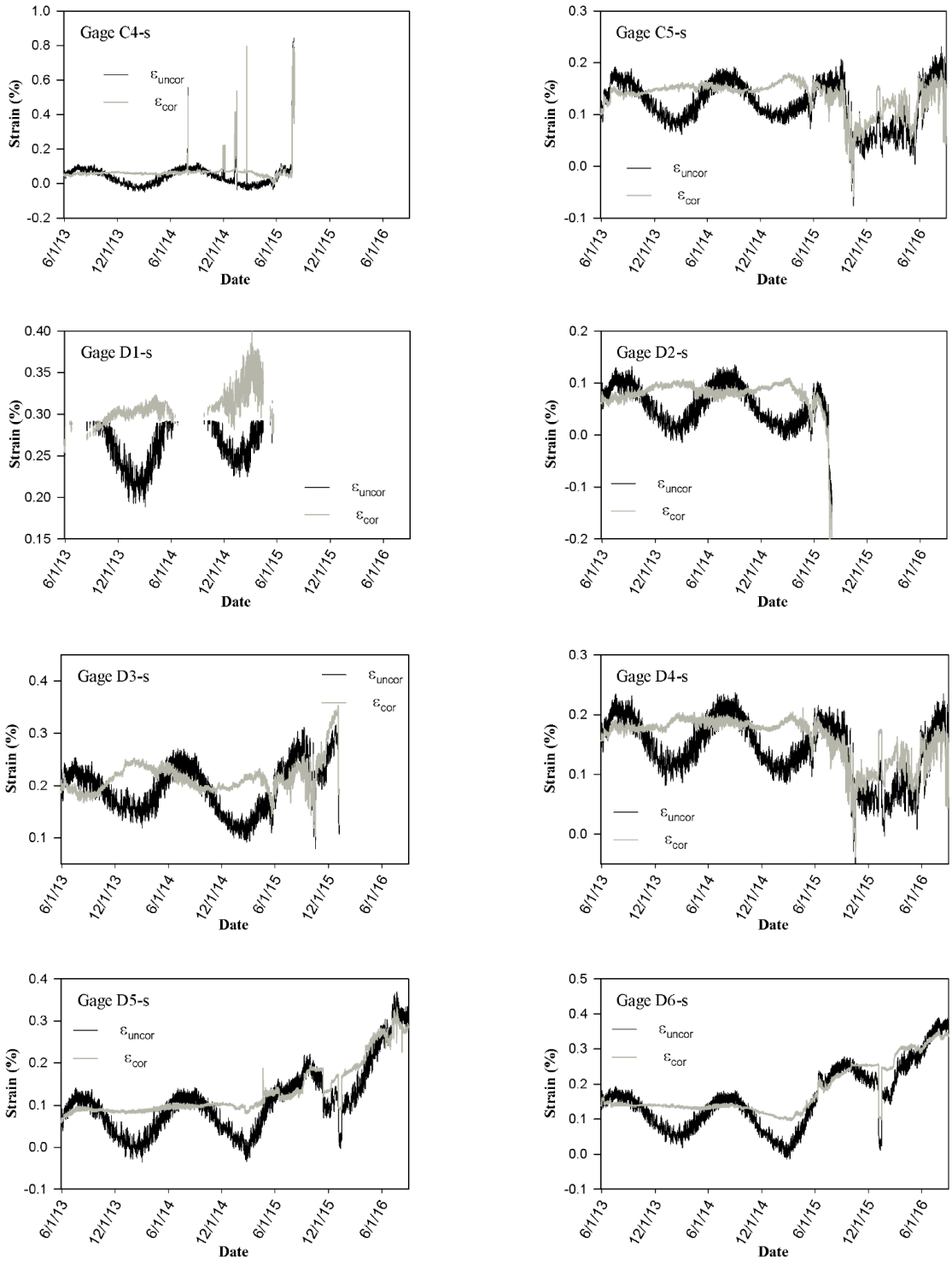

Figure G.2 Continued

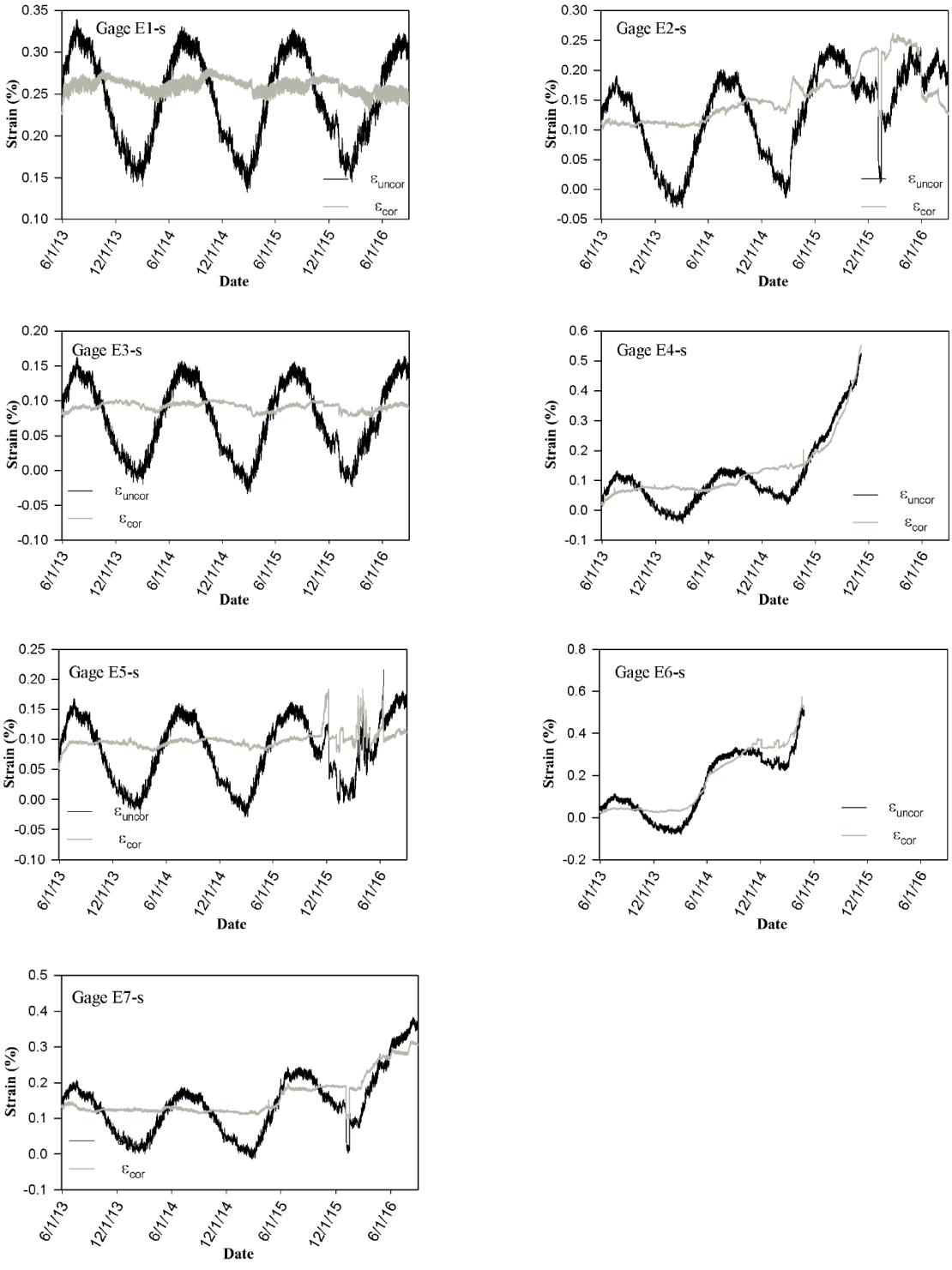

Figure G.2 Continued

Appendix H

BRIDGE STRAIN DURING OPERATION

Ten (10) long strain gauges were attached to the bottom of the bridge at its mid-span, in the direction of traffic travel. Five of the gauges stopped working immediately after placement of the superstructure (it is speculated that this observed behavior may have been caused by installation-related damage), while the other five continued to work over the first two years post-construction. The measured and corrected strains for the surviving bridge strain gauges are presented in this appendix. The correction procedure utilized was the same procedure as what was used for the abutment strain gauges, which is described in detail in Chapter 6.

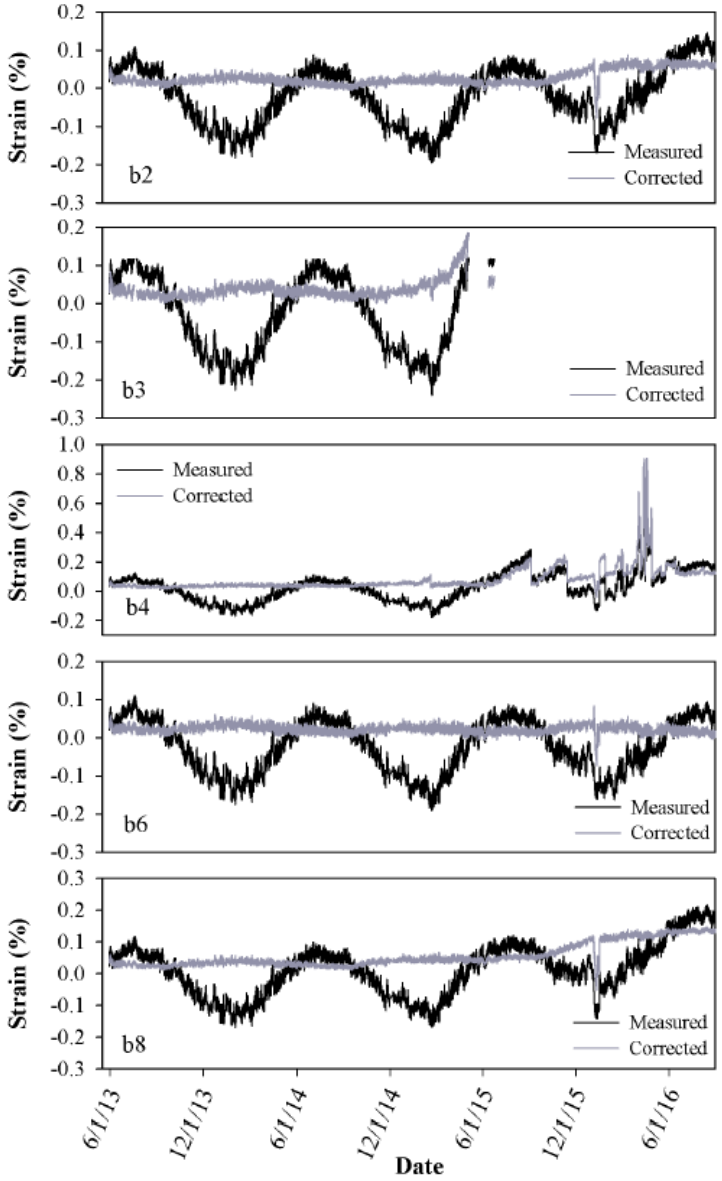

Figure H.1 Long-term measured strains determined using mid-span bridge strain gauges

Delaware Center for Transportation University of Delaware Newark, Delaware 19716

AN EQUAL OPPORTUNITY/AFFIRMATIVE ACTION EMPLOYER

The University of Delaware does not discriminate on the basis of race, color, national origin, sex, disability, religion, age, veteran status, gender identity or expression, or sexual orientation, or any other characteristic protected by applicable law in its employment, educational programs and activities, admissions policies, and scholarship and loan programs as required by Title IX of the Educational Amendments of 1972, the Americans with Disabilities Act of 1990, Section 504 of the Rehabilitation Act of 1973, Title VII of the Civil Rights Act of 1964, and other applicable statutes and University policies. The University of Delaware also prohibits unlawful harassment including sexual harassment and sexual violence. Inquiries or complaints may be addressed to:

Susan L. Groff, Ed. D.
Director, Institutional Equity & Title IX Coordinator
305 Hullihen Hall
Newark, DE 19716
(302) 831-8063
titleixcoordinator@udel.edu

For complaints related to Section 504 of the Rehabilitation Act of 1973 and/or the Americans with Disabilities Act, please contact:

Anne L. Jannarone, M.Ed., Ed.S.
Director, Office of Disability Support Services
Alison Hall, Suite 130,
Newark, DE 19716
(302) 831-4643
OR contact the U.S. Department of Education - Office for Civil Rights (https://wdcrobcolp01.ed.gov/CFAPPS/OCR/contactus.cfm).